MFHS 2014

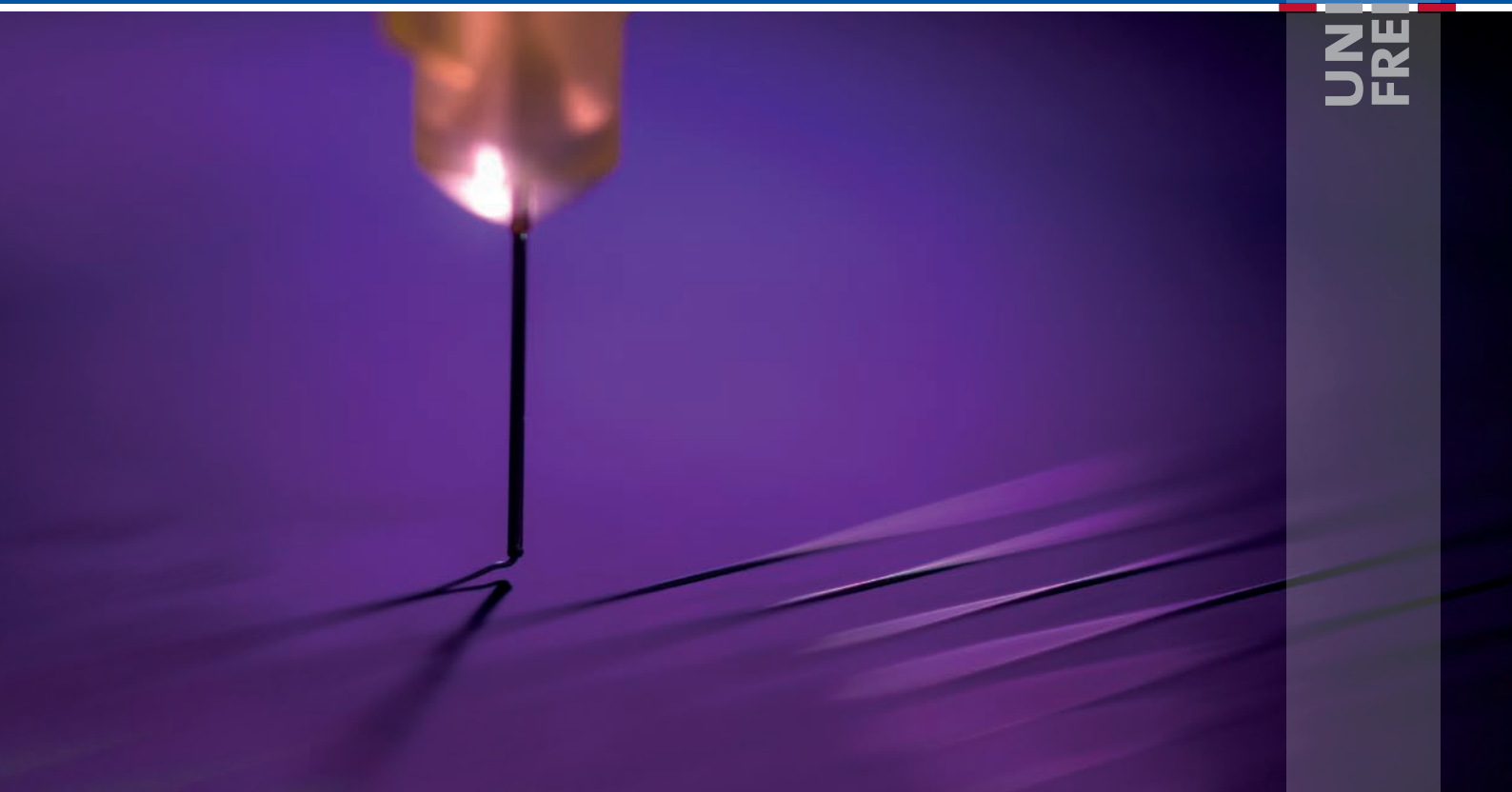2nd International Conference on MicroFluidic Handling Systems

8.-10. October 2014

University of Freiburg
Germany

Proceedings

Welcome to the 2nd International Conference on Microfluidic Handling Systems

Dear colleagues,

We are pleased to welcome you to the 2nd International Conference on Microfluidic Handling Systems (MFHS 2014) in Freiburg, as a follow-up to the successful first conference in Enschede in 2012.

Worldwide, accurate handling – i.e. analysis, dosage, measurement and control – of small and extremely small mass flow rates of both gases and liquids is becoming more and more important, driven by numerous applications. Examples of economically and societally relevant applications are e.g. improvement of medical infusion pump systems, increasing the efficiency of processes that extract oil from oil wells (enhanced oil recovery), systems that measure the energy content (calorific value or Wobbe Index) of natural gas and bio-gas, monitoring of ground water pollution and the production of pharmaceuticals by means of flow chemistry.

Whether in analytical instrumentation, flow chemistry, energy, semiconductor industry, food & beverage or life sciences – microfluidic handling systems are facing two major trends: (1) a need for accurate measurement and calibration facilities and (2) a need for complete functional systems rather than for the individual components. In the future, the impact of this field of research may become bigger and potentially large target markets may arise, especially when spin-off companies start manufacturing and selling their products, systems or pilot plants.

The MFHS 2014 focuses mainly on the technology, components, devices and systems that enable the application in microfluidic systems. It provides an excellent opportunity to bring together scientists and engineers from academia, research institutes and companies to present and discuss the latest results in the field of microfluidic handling systems. The conference goals are to stimulate interaction and knowledge exchange between the delegates in a friendly atmosphere. The most recent developments in the field of microfluidic sensors, actuators, interfaces, fluidic control systems and applications will be presented.

We are looking forward to seeing you at the MFHS 2014 conference!

Kind regards,

Dr. Peter Koltay   Dr. Joost Lötters   Prof. Gerald Urban
Conference Co-chairs

Conference Committee

Chairs

Prof. Dr. Gerald Urban

University of Freiburg, Germany
IMTEK – Department of Microsystems
Engineering
Lab for Sensors

Dr. Peter Koltay

University of Freiburg, Germany
IMTEK – Department of Microsystems
Engineering
Lab for MEMS Applications

Dr. Joost Lötters

University of Twente, The Netherlands
Department of Transducers Science
and Technology

Technical program Committee

Prof. Dr. Shuichi Shoji

Waseda University, Japan
Faculty of Science and Engineering

Dr. Klaus Stefan Drese

IMM Mainz
Germany

Prof. Dr. Han Gardeniers

University of Twente, The Netherlands
Mesoscale Chemical Systems

Dr. Holger Becker

microfluidic ChipShop
Germany

Prof. Dr. Miko Elwenspoek

University of Twente, The Netherlands
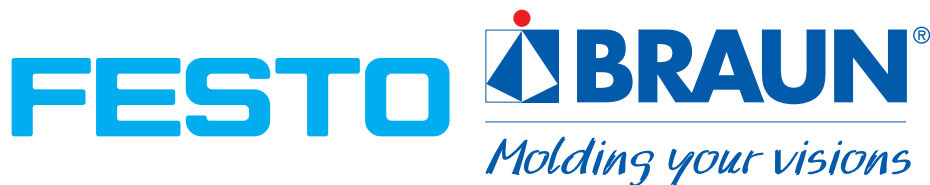Transducers Science and Technology

Dr. Martin Richter

Fraunhofer EMFT
Germany

Prof. Dr. Göran Stemme

KTH Royal Institute of Technology,
Sweden
Micro and Nanosystems

Conference sponsors

Program

Wednesday, 8th of October 2014

17:00 – 18:00 Registration

18:00 – 21:00 Welcome reception

Thursday, 9th of October 2014

08:00 – 09:00 Registration

09:00 – 09:15 Welcome & announcements

09:15 – 09:40 Invited talk 1
Smart Reagent Dosing - Novel Cartridge Concept for Highly Precise Dispensing of IVD Reagents down to the sub-μL Range
Dr. Jürgen Spinke
Director Enabling System Technologies
Roche Diagnostics GmbH, Germany

09:40 – 11:00 Session 1: Overview of the Field

11:00 – 11:30 Coffee break & exhibition

11:30 – 12:50 Session 2: Sensors

12:50 – 14:00 Lunch

14:00 – 15:20 Session 3: Actuators

15:20 – 15:45 Coffee break & exhibition

15:45 – 16:15 Invited talk 2
Lab on Chip for separations
Prof. Dr. Andreas Manz
Head of Research
KIST Europe (Korea Institute of Science and Technology Europe
Forschungsgesellschaft mbH), Germany

16:15 – 18:30 Poster session & exhibition

19:00　　　　Conference dinner

20:30　　　　Evening lecture

Friday, 10th of October 2014

08:00 – 09:00 Registration

09:00 – 09:15 Welcome & announcements

09:15 – 09:40 Invited talk 3
  (Multi-)Infusion: challenges and technical solutions for medication safety
  Dr. Annemoon Timmerman
  Clinical Physicist and Patient Safety Officer
  Faculty of Medicine (UMC), Utrecht University, The Netherlands

09:40 – 11:00 Session 4: Fluidic Control Systems

11:00 – 11:30 Coffee break & exhibition

11:30 – 12:50 Session 5: Applications

12:50   Closure of the conference, Best paper / poster award and Next Conference

13:15 – 14:00 Lunch

15:00 – 17:00 Optional: lab tour at HSG-IMIT, IMTEK and BioFluidix

Session A
(Thursday 09:40)

09:40 – 09:55 – A01 **PRIMARY STANDARD FOR NANOFLOW RATES**
Peter Lucas[1], Harm Tido Petter[1], Wouter Sparreboom[2], Joost Lötters[2]
[1]VSL, Netherlands; [2]Bronkhorst High-Tech, Netherlands

09:55 – 10:10 – A02 **A COMPACT MICRO CORIOLIS MASS FLOW SENSOR WITH FLOW BYPASS FOR A MONOPROPELLANT MICRO PROPULSION SYSTEM**
Jarno Groenesteijn[1], Marcel Dijkstra[1], Theo S.J. Lammerink[1], Joost C. Lötters[1,2], Remco J. Wiegerink[1]
[1]MESA+ Institute for Nanotechnology, University of Twente, Enschede, The Netherlands; [2]Bronkhorst High-Tech BV, Ruurlo, The Netherlands

10:10 – 10:25 – A03 **PERISTALTIC MICROPUMP WITH INTEGRATED ACTIVE DAMPING**
Axel Schumacher[1], Martin Götz[1], Gerhard Kattinger[1], Jürgen Merz[1], Simon Herrlich[1], Sven Spieth[1], Roland Zengerle[1,2]
[1]HSG-IMIT, Villingen-Schwenningen, Germany; [2]IMTEK, University of Freiburg, Freiburg, Germany

10:25 – 10:40 – A04 **CONTACTLESS BOILING: A WAY TO IMPROVE THE RELIABILITY OF MICROFLUIDIC PROCESSES?**
Cor Maria Rops[1], Balkrishna Patankar[2], Gert Jan Snijders[3], Cees v/d Geld[2]
[1]TNO technical sciences, Netherlands, The; [2]Eindhoven university of Technology, Netherlands, The; [3]Bronkhorst High-Tech BV, Netherlands, The

10:40 – 10:55 – A05 **3D PRINTED UNIBODY LAB-ON-A-CHIP INTEGRATION**
German Comina, Anke Suska, Daniel Filippini
Linköping University, Sweden

Session B
(Thursday 11:30)

11:30 – 11:45 – B01 **REAL-TIME COMPOSITION DETERMINATION OF GAS MIXTURES**

Egbert van der Wouden[1], Joost Lötters[1,2]
[1]Bronkhorst High-Tech B.V., the Netherlands; [2]University of Twente, Transducers Science and Technology

11:45 – 12:00 – B02 **METHOD FOR THE DETERMINATION OF THE THERMAL PROPERTIES OF GASES UNDER FLOW CONDITIONS**

Diego Fernando Reyes-Romero[1,2], Gerald Urban[1]
[1]University of Freiburg, Germany; [2]IST AG, Switzerland

12:00 – 12:15 – B03 **MICRO FLOW STANDARD FOR STEADY AND PULSATING FLOW**

Hugo Bissig, Martin Tschannen, Marc de Huu
Federal Institute of Metrology METAS, Switzerland

12:15 – 12:30 – B04 **DETECTION OF GAS KIND AND FLOW SPEED USING THERMAL FLOW SENSORS WITH DC EXCITATION IN A FLOWING FLUID**

Christoph J. Hepp[1], Florian T. Krogmann[1], Gerald A. Urban[2]
[1]Innovative Sensor Technology IST AG, Switzerland; [2]University of Freiburg, Freiburg Institute for Advanced Studies, Freiburg, Germany

12:30 – 12:45 – B05 **CALORIMETRIC FLOW SENSOR CHIP BASED ON SURFACE CHANNEL TECHNOLOGY**

Wouter Sparreboom[1], Egbert van der Wouden[1], Theo Lammerink[2], Joost Lötters[1,2]
[1]Bronkhorst High-Tech B.V., Ruurlo, The Netherlands; [2]University of Twente, Transducers Science and Technology, Enschede, The Netherlands

Session C
(Thursday 14:00)

14:00 – 14:15 – C01 **STARJET-BASED, PNEUMATICALLY ACTUATED LIQUID METAL DROPLET PRINTING AT UP TO 500 °C**
Björn Gerdes[1], Nils Lass[1], Lutz Riegger[1,2], Roland Zengerle[1], Peter Koltay[1,2]
[1]IMTEK University Freiburg, Germany; [2]BioFluidix GmbH

14:15 – 14:30 – C02 **DYNAMIC BEHAVIOUR OF A PIEZOELECTRIC MICROPUMP ACTUATOR**
Christoph Werner Jenke, Miriam Köhn, Martin Wackerle, Christoph Kutter, Martin Richter
Fraunhofer EMFT, Germany

14:30 – 14:45 – C03 **A DISPOSABLE, DISPENSING VALVE FOR NON-CONTACT MICROLITER APPLICATIONS IN 96-WELL PLATE FORMAT**
Sabrina Kartmann[1], Andreas Ernst[1,2], Roland Zengerle[1], Peter Koltay[1,2]
[1]IMTEK, University of Freiburg, Freiburg, Germany, Germany; [2]BioFluidix GmbH, Freiburg, Germany

14:45 – 15:00 – C04 **VOLUME CONTROLLABLE SEQUENTAIL GENERA -TION OF THREE DIFFERENT REAGENTS INCUBATED IN MICRO DROPLETS FOR DIGITAL FLOW SYNTHESIS**
Afshan Jamshaid[1,3], Dong Hyun Yoon[1], Tetsushi Sekiguchi[2], Shuichi Shoji[1]
[1]Waseda University, Japan,; [2]Nano Technology Research Center, Waseda University Tokyo, JAPAN; [3]Department of Physics, Syed Baber Ali School of Science & Engineering, Lahore University of Management Sciences(LUMS), Pakistan

15:00 – 15:15 – C05 **DECOUPLED MICROFLUIDIC FLUID HANDLING SYSTEM FOR COMBINATORIAL GENOME SEQUENCE ASSEMBLY**
Maïwenn Kersaudy-Kerhoas[1], Farid Amalou[1,2], Marc Desmulliez[3], Will Shu[4]
[1]Heriot-Watt University, Institute of Biological Chemistry, Biophysics and Bioengineering, United Kingdom; [2]Southampton University, Southampton, United Kingdom; [3]Heriot-Watt University, Institute of Sensors, Signals and Systems, United Kingdom; [4]Heriot-Watt University, Institute of Biological Chemistry, Biophysics and Bioengineering, United Kingdom

Session D
(Friday 09:40)

09:40 – 09:55 – D01 **MICROFLUIDIC DROPLET HANDLING BY ACOUSTO-PHORESIS ON BULK ACOUSTIC WAVE (BAW) DEVICES**
Ivo Leibacher, Peter Reichert, Jürg Dual
ETH Zurich, Switzerland

09:55 – 10:10 – D02 **A DISPENSING SYSTEM FOR SEDIMENTING METAL MICROPARTICLE SOLUTIONS BASED ON A CIRCULATION MIXER METHOD**
Andreas Ernst[1,2], Lutz Riegger[1,2], Peter Koltay[1,2]
[1]BioFluidix GmbH, Germany; [2]University of Freiburg, Lab for MEMS Applications, Freiburg, Germany

10:10 – 10:25 – D03 **A PICOLITER DISPENSER WITH DISPOSABLE CARTRIDGES FOR PRECISE AND CONTACT-FREE INJECTION OF DNA INTO OPEN MICROFLUIDIC STRUCTURES**
Julian Riba[1], Ludwig Gutzweiler[1], Lutz Riegger[1,2], Peter Koltay[1,2], Roland Zengerle[1], Andre Gross[1]
[1]University of Freiburg, Lab for MEMS Applications, Freiburg, Germany; [2]Biofluidix GmbH, Freiburg, Germany

10:25 – 10:40 – D04 **NANO-WORKBENCH: A COMBINED AFM-FEMTO-PIPETTE AND ROBOTIC NANOMANIPULATOR**
Hector Hugo Pérez Garza, Murali Krishna Ghatkesar, Urs Staufer
Delft University of Technology, The Netherlands

10:40 – 10:55 – D05 **FEEDBACK CONTROLLED MICRODOSING SYSTEM FOR NANOLITER PER SECOND DOSING RATES USING A CAPACITIVE PHASE BOUNDARY TIME-OF-FLIGHT FLOW SENSOR**
Sebastian Kibler, Laeschkir Lukman Hassan, Martin Richter, Christoph Kutter
Fraunhofer EMFT, Germany

Session E
(Friday 11:30)

11:30 – 11:45 – E01 **SEMI-CONTACT WRITING TECHNOLOGY & APPLICATIONS**
Ludwig Gutzweiler[1], Tobias Gleichmann[1], Peter Koltay[1,2], Roland Zengerle[1], Lutz Riegger [1,2]
[1]University of Freiburg, Lab for MEMS Applications, Freiburg, Germany; [2]BioFluidix GmbH, Freiburg, Germany

11:45 – 12:00 – E02 **MICROFLUIDIC SAMPLE PREPARATION CHIP FOR RNA-BASED PATHOGEN DETECTION**
Hendrik Hubbe[1], Sydney Hakenberg[1], Gregory Dame[1], Gerald Urban[1,2]
[1]University of Freiburg, Lab for Sensors, Germany; [2]University of Freiburg, Freiburg Institute for Advanced Studies, Germany

12:00 – 12:15 – E03 **MICROFLUIDIC SUBCRITICAL WATER EXTRACTION USING FREEZE VALVES AND ULTRASOUND**
Michael C. Lee[1], Aaron Noell[1], Jennifer Hasenoerhl[1,2], Nobuyuki Takano[1,3], Stewart Sherrit[1], Frank Grunthaner[1]
[1]Jet Propulsion Lab (JPL-Caltech), Pasadena, USA; [2]University of Idaho, Moscow, USA.; [3]California State University, Pomona, USA

12:15 – 12:30 – E04 **TOWARDS SYSTEM-LEVEL MODELING AND CHARACTERIZATION OF COMPONENTS FOR INTRAVENOUS THERAPY**
Dennis Alveringh[1], Remco J. Wiegerink[1], Joost C. Lötters[1,2]
[1]MESA+ Institute for Nanotechnology, University of Twente, Enschede, The Netherlands; [2]Bronkhorst High-Tech BV, Ruurlo, The Netherlands

12:30 – 12:45 – E05 **CELL SIZE DISCRIMINATION BASED ON THE MEASUREMENT OF THE EQUILIBRIUM VELOCITY IN RECTANGULAR MICROCHANNELS FOR POINT OF CARE DIAGNOSTICS**
Christian Sommer[1], Lisa Schott[1], Thomas Walther[2], Michael Baßler[1]
[1]Fraunhofer ICT-IMM, Germany; [2]Technische Universität Darmstadt

Poster Session
(Thursday 16:15)

P01 OXYGEN SUPPLY FOR CELL CULTURE SYSTEMS - MEASURED WITH FLUORESCENCE LIFETIME ANALYSIS AND MODELLED USING SIMULATIONX

Mathias Busek[1], Florian Schmieder[1], Stefan Grünzner[1], Kevin Hofmann[2], Uwe Grätz[2], Frank Sonntag[1]
[1]Fraunhofer IWS, Dresden, Germany; [2]ITI GmbH, Dresden, Germany

P02 CHARACTERIZATION AND CALIBRATION OF FLOW COMPONENTS IN THE RANGE OF 5 TO 500 NL/MIN

Martin Ahrens, Stephan Klein, Bodo Nestler, Christian Daminai
Lübeck University of Applied Sciences, Lübeck, Germany

P03 SIMULATION STUDY OF A NOVEL CAPACITIVE PRESSURE SENSOR CONCEPT BASED ON THE GEOMETRICAL DEFORMATION OF AN ELASTIC MEASURING CELL

Sabrina Kartmann[1], Malena Kellermann[1], Andreas Ernst[1,2], Roland Zengerle[1], Peter Koltay[1,2]
[1]IMTEK, University of Freiburg, Freiburg, Germany; [2]BioFluidix GmbH, Freiburg, Germany

P04 HOLLOW FIBER-BASED LAB-ON-A-CHIP DUAL PERFUSION SYSTEM WITH INTEGRATED FLUORESCENCE-BASED OXYGEN MONITORING

Florian Schmieder, Stefan Grünzner, Claudia Winkelmann, Frank Sonntag
Fraunhofer Institute for Material and Beam Technology IWS, Germany

P05 MODELLING AND CHARACTERIZATION OF A MULTIPARAMETER HOT-DISK SENSOR FOR DETERMINATION OF FLUID MIXTURE PROPERTIES

Bastian Schmitt, Kai Sauer, Andreas Schütze
LMT, Saarland University, Saarbrücken, Germany

P06 OPTO-ELECTRONIC FLOW SENSOR - VERY THIN IN DIRECTION OF FLOW

Ralf Müller[1], Dieter Petrak[2], Jens Zosel[3], Olaf Brodersen[1]
[1]CiS Forschungsinstitut für Mikrosensorik und Photovoltaik GmbH, Erfurt, Germany; [2]Ingenieurbüro FlowSensor GbR, Weimar, Germany; [3]Kurt-Schwabe-Institut für Mess- und Sensortechnik e.V. Meinsberg, Waldheim, Germany

P08 ON CHIP RNA-EXTRACTION COMBINED WITH REVERSE TRANSCRIPTION RT ON CHIP FOR IMPROVED PATHOGEN DETECTION

Dennis Trenkle[1], Sydney Hakenberg[1], Gerald Urban[1,2], Gregory Dame[1]
[1]IMTEK, University of Freiburg, Freiburg, Germany; [2]Freiburg Institute for Advanced Studies, University of Freiburg, Freiburg, Germany

P09 A ROBUST ELECTRICAL SENSOR FOR CONTACTLESS CONTROL OF MOVING PLUGS IN MICROFLUIDIC SYSTEMS WITH HIGH ACCURACY

Almuth Hoffmann[1,2], Karin Potje-Kamloth[1], Steffen Hardt[2], Michael Baßler[1]
[1]ICT-IMM (IMM), Germany; [2]Technische Universität Darmstadt, Germany

P10 PNEUMATICALLY ACTUATED PERISTALTIC MICRO PUMP - CHARACTERIZED WITH μPIV AND MODELLED USING SIMULATIONX

Mathias Busek[1], Kevin Hofmann[2], Uwe Grätz[2], Christoph Polk[1], Frank Sonntag[1]
[1]Fraunhofer IWS, Dresden, Germany; [2]ITI GmbH, Dresden, Germany

P11 MICROFLUIDIC DEVICE COMPONENTS FOR MULTISTEP ASSAYS

Elwin Xander Vrouwe, Monica Brivio, Marko Blom
Micronit Microfluidics, Netherlands, The

P12 UNIBODY THREE CHANNELS INJECTOR WITH INTEGRATED MANUAL PUMPS

Anke Suska, German Comina, Daniel Filippini
Linköping University, Sweden

P13 INTEGRATED PASSIVE CHECK-VALVES FOR 3D PRINTED FLUIDICS

German Comina, Anke Suska, Daniel Filippini
Linköping University, Sweden

P14 EMULSION PREPARATION USING STAINLESS STEEL EDGE MICROFLUIDIC DEVICES

Olesya Bliznyuk, Sami Sahin, Karin Schroën
WUR, Netherlands, The

P15 FREQUENCY AND VOLTAGE CHARACTERISTICS OF A PIEZO-ELECTRIC DIAPHRAGM PUMP

Tao Li
Nanyang Technological University, Singapore

P16 A STUDY ON SINGLE AND MULTILAYER MICROVALVES AND THEIR APPLICATION TO ANALYZE INFECTION PROBABILITY OF P. FALCIPARUM

Weichao Zhai, Eileen Nugent, Alexandra Grigore, Pietro Cicuta
University of Cambridge, United Kingdom

P17 SMART OPEN MICROFLUIDICS: AN AUTOMATED PLATFORM FOR THE DYNAMIC GENERATION OF FLUIDIC STRUCTURES DOWN TO THE SUB-NL-RANGE

Tobias Gleichmann[1], Ludwig Gutzweiler[1], Roland Zengerle[1,3], Peter Koltay[1,2], Lutz Riegger[1,2]
[1]IMTEK University Freiburg, Germany; [2]BioFluidix GmbH, Freiburg, Germany; [3]HSG-IMIT, Freiburg, Germany

P18 LOW FLOW LIQUID CALIBRATION SETUP

Tom Herman Platenkamp[1], Wouter Sparreboom[1], Gijs Hermanus Johannes Maria Ratering[1], Marcel Ronald Katerberg[1], Joost Conrad Lötters[1,2]
[1]Bronkhorst High-Tech B.V., Ruurlo, The Netherlands; [2]University of Twente, Transducers Science and Technology, Enschede, The Netherlands

P19 LOW FLOW CORIOLIS FLOW CONTROLLER WITH PIEZO OPERATED CONTROL VALVE

Marcel Ronald Katerberg[1], Gijs Hermanus Johannus Maria Ratering[1], Tom Herman

2$^{\text{nd}}$ International Conference on MicroFluidic Handling Systems
8 – 10 October 2014, University of Freiburg, Germany

13

Platenkamp[1], Jan Van de Geest[1], Sander Klein Hesselink[1], Joost Conrad Lötters[1,2]
[1]Bronkhorst High-Tech, Netherlands, The; [2]University of Twente, Transducer Science and Technology, Enschede, Netherlands, The

P20 MICROFLUIDIC DROPLET HANDLING BY ACOUSTOPHORESIS ON BULK ACOUSTIC WAVE (BAW) DEVICES

Ivo Leibacher, Peter Reichert, Jürg Dual
ETH Zurich, Switzerland

P21 COMPUTATIONAL DESIGN OF WETTING AND SPREADING BEHAVIOUR FOR ENHANCED IN-VITRO-DIAGNOSTIC APPLICATIONS

Adham Hashibon, Matthias Gurr, Pit Polfer, Frank Burmeister, Torsten Kraft
Fraunhofer IWM, Germany

P22 FAST PROTOTYPING OF MULTISENSOR CELL CULTURE CHIPS USING ULTRA-SHORT PULSE-LASER ABLATION AND PCB MICRO-MILLING

Sebastian Marcus Bonk[1], Paul Oldorf[2], Rigo Peters[2], Werner Baumann[1], Jan Gimsa[1]
[1]University Rostock, Germany; [2]Schweißtechnische Lehr und Versuchsanstalt, Rostock, Germany

P23 LIVE IMAGING STUDIES OF P. FALCIPARUM EGRESS AND INVASION OF ERYTHROCYTES BY USING MICROFLUIDIC DEVICES

Yen-Chun Lin[1], Weichao Zhai[1], Eileen Nugent[1], Alex Crick[1], Teresa Tiffert[2], Virgilio Lew[2], Julian Rayner[3], Pietro Cicuta[1]
[1]Cavendish Laboratory, University of Cambridge, United Kingdom; [2]Department of Physiology, Development and Neuroscience, University of Cambridge, United Kingdom; [3]Wellcome Trust Sanger Institute, Wellcome Trust Genome Campus, Cambridge, United Kingdom

P24 OPTIMIZATION OF THE MICROFLUIDIC DESIGN OF A MINIATURIZED COUNTER-CURRENT FLAME IONIZATION DETECTOR

Winfred Jan Kuipers[1], Michael Deilmann[1], Christian Koch[2], Jörg Müller[3]
[1]KROHNE Messtechnik GmbH, Duisburg, Germany; [2]KROHNE Innovation GmbH, Duisburg, Germany; [3]Hamburg University of Technology, Hamburg, Germany

P25 DEVELOPMENT OF A PORTABLE MULTI-PARAMETER CENTRIFUGAL MICROFLUIDIC ANALYSIS SYSTEM (CMAS) FOR WATER QUALITY MONITORING

Patrick Floris[1], Thomas Glennon[1], Conor O' Quigley[1], Eoghan Mc Namara[1], Yang Yang[1], Jens Ducrée[2], Alan Smeaton[1], Dermot Diamond[1], Kevin J. Fraser[1]
[1]Insight Centre for Data Analytics, National Centre for Sensor Research, Dublin City University, Ireland; [2]Biomedical Diagnostics Institute, National Centre for Sensor Research, Dublin City University, Dublin 9, Ireland

P26 THE LAB-ON-A-CHIP DESIGN & FOUNDRY SERVICE

Sebastian Hin[1], Daniel Baumann[2], Konstantinos Mitsakakis[1,2], Vanessa Klein[1], Oliver Strohmeier[1,2], Mark Keller[1,2], Dominique Kosse[1,2], Roland Zengerle[1,2,3], Felix von Stetten[1,2], Daniel Mark[1,2]
[1]Laboratory for MEMS Applications, Department of Microsystems Engineering - IMTEK, University of Freiburg, Georges-Koehler-Allee 106, 79110 Freiburg, Germany; [2]HSG-IMIT - Institut für Mikro- und Informationstechnik, Georges-Koehler-Allee 103, 79110 Freiburg, Germany; [3]BIOSS Centre for Biological Signalling Studies, University of Freiburg, 79110

Freiburg, Germany

P27 POROUS PILLAR ARRAY FORMATION USING ISOTROPIC XENON DIFLUORIDE ETCHING FOR LIQUID CHROMATOGRAPHY MICRO-CHIP

Kailing Shih[1], Muneki Isokawa[2], Takahiro Kanamori[2], Dong Hyun Yoon[1], Tetsushi Sekiguchi[3], Jun Mizuno[3], Takashi Funatsu[2], Makoto Tsunoda[2], Shuichi Shoji[1]

[1]Major in Nanoscience and Nanoengineering, Waseda University, Tokyo, Japan; [2]Graduate School of Pharmaceutical Sciences, The University of Tokyo, Tokyo, Japan; [3]Nanotechnology Research Center, Waseda University, Tokyo, Japan

P28 OVERVIEW OF IN VITRO MEASUREMENT STUDIES THAT EXPLORE THE CAUSES OF FLOW RATE VARIABILITY IN INFUSION THERAPY: WHAT ARE THE OPPORTUNITIES FOR MICROFLUIDICS?

Roland A. Snijder[1], Peter Lucas[2], Toine C.G. Egberts[3], Joris E.N. Jaspers[1], Joris H. Radermacher[1], Annemoon M.D.E. Timmerman[1]

[1]University Medical Center Utrecht, Medical Technology and Clinical Physics, Utrecht, Netherlands, The; [2]VSL Dutch Metrology Institute, Research, Delft, Netherlands, The.; [3]University Medical Center Utrecht, Clinical Pharmacy, Utrecht, Netherlands, The

P29 A MICROFLUIDIC FUEL CELL SIMULATION TO STUDY THE INFLUENCE OF THE POROUS ELECTRODE MORPHOLOGY ON ELECTRODE KINETICS

Mohammad Al-Halhouli[1,2], Jochen Kieninger[2], Olena Yurchenko[1,2], Patrick Daubinger[1], Gerald Urban[1,2,3]

[1]University of Freiburg, Freiburg Materials Research Centre - FMF, Freiburg, Germany; [2]University of Freiburg, Department of Microsystems Engineering - IMTEK, Freiburg, Germany; [3]University of Freiburg, Freiburg Institute for Advance Studies, Freiburg, Germany

P30 SMALL-ANGLE X-RAY AND NEUTRON SCATTERING IN COMBINATION WITH DROPLET MICROFLUIDICS

Sebastian Seiffert[1,2]

[1]Helmholtz-Zentrum Berlin, Germany; [2]Freie Universität Berlin, Germany

P32 UPSCALING MICROFLUIDIC EDGE DEVICES FOR THE PREPARATION OF LARGE AND SMALL UNIFORM DROPLETS

Samin Sahin, Karin Schroën

Food Process Engineering Group, Wageningen University, The Netherlands

Key notes

Lab on Chip for separations

Prof. Dr. Andreas Manz

Head of Research
KIST Europe (Korea Institute of Science and Technology Europe Forschungsgesellschaft mbH)

Smart Reagent Dosing – novel cartridge concept for highly precise dispensing of IVD reagents down to the sub-uL range

Dr. Jürgen Spinke

Director Project Management R&D
Roche Diagnostics GmbH, Germany

(Multi-)Infusion: challenges and technical solutions for medication safety

Dr. Annemoon Timmerman

Clinical Physicist and Patient Safety Officer
Faculty of Medicine (UMC), Utrecht University, The Netherlands

Speed up you mind!

Henning Beck

Neurobiologist and science slammer
Author of „Hirnrissig. Die 20,5 größten Neuromythen – und wie unser Gehirn wirklich tickt" (Hanser Verlag), 2014.
Neuro | Science | Entertainment | www.henning-beck.com

4. Fluidic control systems   **Presentation**

PRIMARY STANDARD FOR NANOFLOW RATES

P. Lucas[1], H.T. Petter[1], W. Sparreboom[2], J.C. Lötters[2]
[1] Dutch Metrology Institute (VSL), Delft, The Netherlands
[2] Bronkhorst High-Tech, Ruurlo, The Netherlands

Micro- and nanoflows are appearing more frequently in various applications, for example in life science and technology, automotive and lab-on-a-chip applications. Further, they are relevant for some medical applications, for example in (implanted) pain control pumps. For these applications, traceability can be important for a safe and sound usage.

As of yet there does not exist a validated primary standard for flow rates lower than, say, 20 µl/min. Therefore, this research, which is part of [4], aims at developing a primary standard for liquid volume flows for flow rates from 1 up to 1000 nl/min.

The approach followed is a standard based on volumetric expansion (comparable to an old-fashioned thermometer). The upper part of the given flow rate range can also be achieved with a gravimetric principle (e.g. [5]). However, for flow rates lower than, say 100 nL/min, the uncertainty due to for example evaporation makes this principle not applicable. Conventional syringe pumps are not feasible because the inner dimensions of the syringe cannot be determined with sufficient low uncertainty. A syringe pump based on a plunger rather than a piston may be an interesting alternative.

Recently, also good results for flow rates between 1 and 1000 nL/min have been achieved with a front-tracking system [1]. In this set up the velocity of the meniscus inside a capillary is measured. With the velocity and dimensions of the capillary known, the flow rate is deduced.

In Figure 1 a sketch of the volume-expansion standard is shown; the expanding liquid is contained in a reservoir placed inside a temperature controlled (water) bath. In Figure 2 the reservoir containing the expanding liquid is shown and in Figure 3 the complete set up.
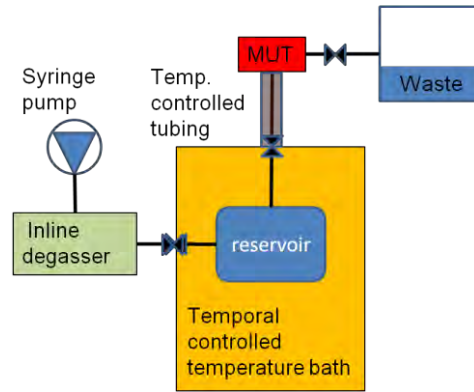

Figure 1. Sketch principle standard.

The driving force is the decrease in density over time. Hence, the flow rate follows from:

$$Q = -\frac{1}{\rho}\frac{dm}{dt}$$

where *m* is the mass of the expanding liquid and ρ is the density at the exit of the reservoir. Working out this equation gives the following main component:

$$Q = -\frac{Vk}{\rho_{MUT}}\left(\frac{\partial\rho}{\partial T}\right)$$

where *V* is the volume of the expanding liquid, *k* is the temperature gradient, ρ is the density and *T* is the temperature. Since the temperature is time controlled, one has a control over the time rate change of the density and thus also the volume flow rate.
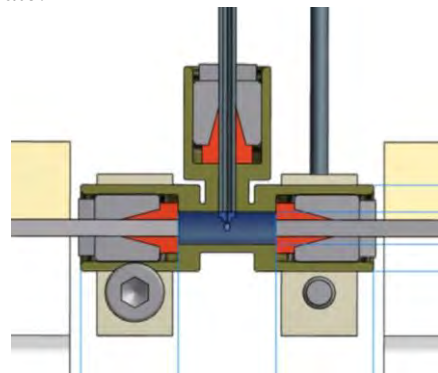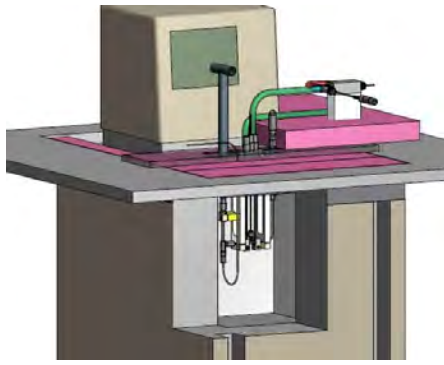

Figure 2 Close up reservoir. The temperature is measured in the center of the reservoir.

Figure 3 Set up primary standard for nano flow rates. The MUT is shown on the right (in white). The pink material is insulation, whereas the lever shown is to open and close one of the valves.

Because the flow rate depends on the (temporal) volume, density and liquid properties, the flow rate will be varying for a constant temperature gradient. This is because over time the temperature increases which leads to a different fluid properties. However, for sufficient small temperature gradients, say smaller than 0.02 K/s, the flow rate is fairly constant for at least 10 minutes.

In order to arrive at the correct flow rate, several corrections need to be made to the main component. Corrections are required for: the expansion of the reservoir itself, cooling down of the fluid elements when they travel through the capillaries that are not submerged (see Fig. 3) and a non-homogeneous temperature throughout the whole reservoir. Numerical modeling has been used to estimate the impact of the non-homogeneous temperature distribution [3]. Further, standard equations and material properties have been used to determine the volume expansion of the reservoir. Finally, it is straightforward to show that the impact of the cooling down is negligible when the volume of the capillaries is small compared to the volume of the reservoir, say smaller than 5%.

The flow rate can be made traceable directly to SI units. Therefore one needs to know the following parameters: (temporal) volume of the expanding liquid, temperature gradient and the liquid properties (density and expansion coefficient).

The volume of the expanding liquid follows from the mass difference between an empty and filled reservoir (and correction for the expansion of the reservoir itself). The temperature gradient

follows from temperature measurements inside the reservoir and just outside the reservoir (see Fig. 2). Finally, the liquid properties follow from the Tanaka equation [5]. Hence, pure and degassed water needs to be used.

The estimated uncertainty is around 2.5% (k=2), depending on the flow rate. The largest contributions are due to the expansion of the reservoir, the temperature gradient and the spatial variation in the temperature gradient. Linear regression [2] is used to determine the uncertainty in the temperature gradient.

In Fig. 5 a comparison is shown between the volume-expansion, a gravimetric standard and a chip-based Coriolis flow meter [4,5]. This flow meter has been calibrated by a gravimetric standard at zero flow and full scale (2 g/h). The calibration coefficients are then assumed to be constant over the complete range. In Fig. 4 the measured temperature and resulting temperature gradient are shown. From the temperature gradient the flow rate according to the volume-expansion standard is determined.

The top graph of Fig. 5 shows the balance read out. The middle graph shows the unfiltered data as given by the standard and the chip-based Coriolis meter (the results from the gravimetric standard are omitted because they are very noisy). Here, unfiltered means the discrete values are used to determine the temperature gradient. The bottom part of Fig. 5 shows fitted polynomials found by linear regression for a specific part of the calibration. This part is selected because in this part the temperature increase is homogenous throughout the whole reservoir (differences smaller than 1% of the mean temperature gradient). This selection results in a relative low uncertainty because the expansion of the water is only well-known in case the (temporal) temperature gradient is constant throughout the whole reservoir. In case all measurement data is included, the calibration uncertainty easily increases to 5% or more.

For the selected data points, the average deviation between the standard and chip-based flow meter is 2%. In Tab. 1 the average results for three repetitions are shown for a (mean) target flow rate of 333 nL/min and 2000 nL/min.
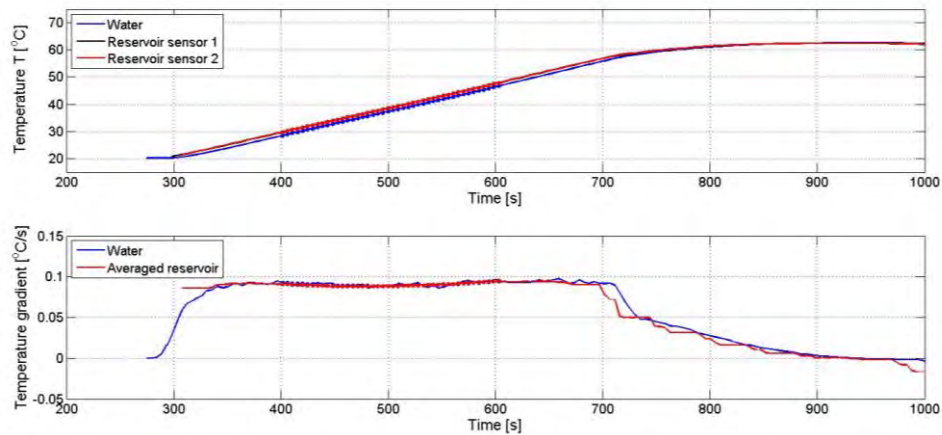
Figure 4 *Measured temperature of the expanding liquid (water inside the reservoir) and the reservoir itself. The temperature gradient follows from this temperature and results in the flow rate shown in Fig. 5.*
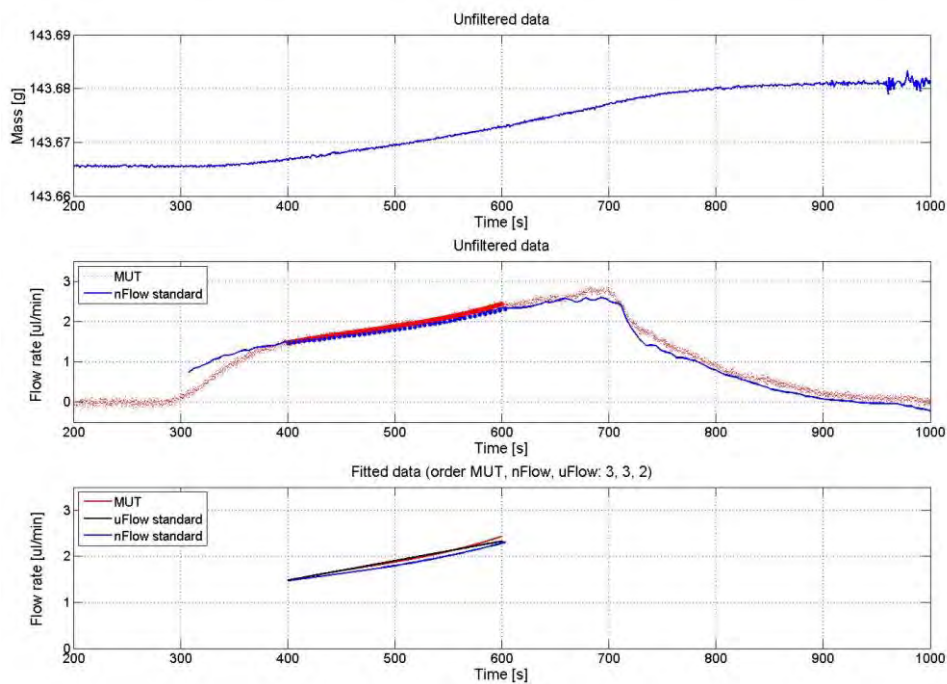
Figure 5 *Results comparison volume-expansion standard, a gravimetric standard and the chip-based Coriolis flow meter. The upper graph is the balance read out, the middle part the flow rate according to the chip-based flow meter and volume-expansion standard. The lower graph is the filtered flow rate of the three measurement standards which followed from linear regression of the 'unfiltered data'. The part between 400 s and 600 s is used to determine the average flow rate because in this part the temperature gradient is constant in the reservoir.*

Table 1 Results comparison volume-expansion standard (vol. exp.), a gravimetric standard (grav.) and the chip-based Coriolis flow meter (cori). For two target flow rates (333 nL/min and 2000 nL/min) three repetitions have been performed. The mean flow rate is given by $\hat{Q}$ and the relative standard deviation by σ.

	target: 333 nL/min		target: 2000 nL/min	
	$\hat{Q}$ (nL/min)	σ (%)	$\hat{Q}$ (nL/min)	σ (%)
vol. exp	364	2.1	1776	2.8
grav.	372	2.4	1816	2.5
cori	375	1.5	1796	3.3

REFERENCES

[1] Ahrens, M., Klein, S., Nestler, B. and Damiani, C., Design and uncertainty assessment of a setup for calibration of microfluidic devices down to 5 nL min^{-1}, *Measurement Science and Technology*, volume 25, 2014

[2] Cox, M.G., Harris, P.M., Software support for metrology best practice guide no. 6 – uncertainty evaluation, *NPL technical report*, 2006.

[3] Gersl, J. Numerical results for nano-flow generator fo VSL, technical report available at http://www.drugmetrology.com/images/Gersl_N umerical_Simulations_NFG.pdf

[4] Lucas, P. *et al.*, *Metrology for drug delivery*, 2012 - 2015, partners VSL, Cetiat, CMI, DTI, EJPD, IPQ, Tubitak, project summary at http://www.euramet.org/index.php?id=emrp_call _2011

[5] Tanaka, M. *et al.*, Recommended table for the density of water between 0 °C and 40 °C based on recent experimental reports, *Metrologia*, 38, 301-309, 2001

[6] Sparreboom, W., Geest, J. van de, Katerberg, M., Postma, F., Haneveld, J., Groenesteijn, J., Lammerink, T. Wiegerink, R. J. and Lötters, J.C. (2013) Compact mass flow meter based on a micro coriolis flow sensor. *Micromachines*, 4(1). pp. 22-33. ISSN 2072-666X

[7] Haneveld, J., Lammerink, T.S.J., Boer, M.J. de, Sanders, R.G.P., Mehendale, A. and Lötters, J., Dijkstra, M.A., and Wiegerink, R.J. (2010) Modeling, design, fabrication and characterization of a micro Coriolis mass flow sensor. *Journal of Micromechanics and Microengineering*, 20(6). p. 125001. ISSN 0960-1317

A COMPACT MICRO CORIOLIS MASS FLOW SENSOR WITH FLOW BYPASS FOR A MONOPROPELLANT MICRO PROPULSION SYSTEM

J. Groenesteijn[1], M. Dijkstra[1], T.S.J. Lammerink[1], J.C. Lötters[1,2] and R. J. Wiegerink[1]
[1]MESA+ Institute for Nanotechnology, University of Twente, Enschede, THE NETHERLANDS
[2]Bronkhorst High-Tech BV, Ruurlo, THE NETHERLANDS

ABSTRACT

We have designed, fabricated and tested a micromachined Coriolis flow sensor for the measurement of hydrazine (N_2H_4) propellant flow in a micro chemical propulsion system (μCPS). The sensor will be used for measurement and characterization of the μCPS in a simulated space vacuum environment. To reach the required flow range a bypass system is integrated. Initial measurements demonstrate an increase of the flow range in accordance with the designed bypass ratio. The sensor is operated as a two-port resonator in an oscillator circuit to improve frequency stability.

KEYWORDS

micro chemical propulsion system, Coriolis flow sensor, bypass channel, two-port resonator

INTRODUCTION

In recent years, integrated microfluidic systems have gained interest in a large variety of devices, e.g. (bio) chemical, medical, automotive, industrial and space applications. A major advantage of these systems is its potential for very small, accurate, reliable liquid and gas handling systems. In the EU project PRECISE, a MEMS-based mono-propellant μCPS for accurate altitude control of small satellites is being developed. The availability of such a system forms the basis for defining new mission concepts such as formation flying, advanced robotic missions and rendezvous manoeuvres[1]. To measure the hydrazine propellant flow of up to $20\,\mathrm{g\,h^{-1}}$, a flow sensor is required that is small and energy efficient and is capable of operating under vacuum conditions.

To achieve these requirements, we designed, fabricated and tested a micro-machined Coriolis mass flow sensor based on the sensor presented in [2]. That sensor uses a silicon-nitride micro-channel with a tube wall of $1.2\,\mu\mathrm{m}$ and is capable of measuring up to $1.2\,\mathrm{g\,h^{-1}}$ with a measurement accuracy of 1% of the full scale. An on-chip bypass system has been incorporated in the sensor to extend the measurement range to $20\,\mathrm{g\,h^{-1}}$. To be able to measure and characterize the μCPS in a simulated space vacuum environment, dedicated electronics have been developed for capacitive read-out of the sensor and to actuate the sensor using the mechanical structure as a two-port resonator in an oscillator circuit.

CORIOLIS MASS FLOW SENSOR

Coriolis mass flow sensors consist of a vibrating tube, as shown schematically in Figure 1. For the sensor presented here, this tube is actuated in torsional mode at frequency $\vec{\omega}_{am}$ by Lorentz force actuation using current $\vec{i}_a$ through a track on top of the channel. For this, a magnetic field $\vec{B}$ is applied by two permanent magnets to the side of the sensor. A mass flow $\vec{\Phi}_m$ inside the tube will induce Coriolis forces $\vec{F}_C$ that excite the other vibration mode, resulting in a vibration amplitude proportional to the mass flow. Capacitive comb-structures at each side of the rotational axis attached to the long side of the sensor are used to measure these vibrations. A mass flow will result in a phase shift between the two read-out signals.
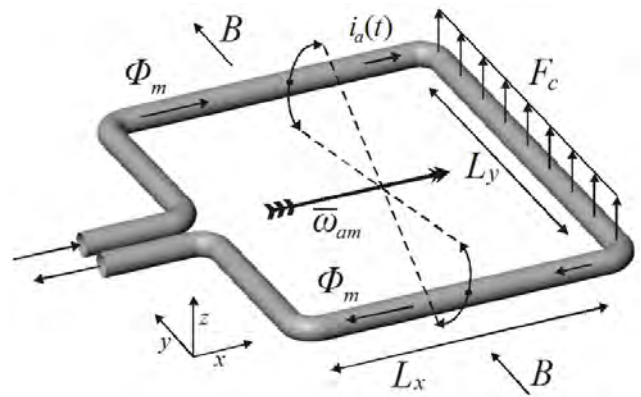
Figure 1: Schematic overview of the operation principle of a Coriolis mass flow sensor without bypass.

ON-CHIP BYPASS SYSTEM

To be able to measure the required $20\,\mathrm{g\,h^{-1}}$, bypass channels have been integrated on the chip, see figure 2. Using Bernoulli's equation and Poiseuille's law for tube flow, the ratio between the flow through the Coriolis channel and the flow through the bypass channel can be calculated. When channels are used with the same diameter, the ratio will initially only depend on the difference in channel length. At higher flows the bypass

ratio will decrease. A second order polynomial can be used as transfer function between the measured flow through the Coriolis channel and the total flow through the sensor.

Figure 2: Schematic view of the bypass sytem. At low flow, the length of the Coriolis channel and of the bypass channel determine the bypass-ratio.
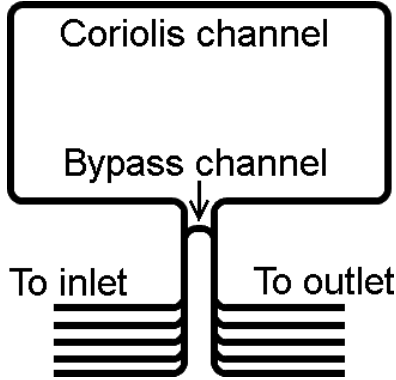
OSCILLATOR CIRCUIT

Previously, the Coriolis mass flow sensor was actuated using a DSP for generating a Lorentz actuation signal using the capacitive read-out signals as a reference. This method resulted in poor frequency stability and was sensitive to distortion and noise on the read-out signals. The electronics presented here use the mechanical structure of the Coriolis channel as a two-port resonator. On top of the Coriolis channel, there are two parallel metal tracks. Actuation current i_a runs through one of the tracks. When the channel is vibrating, there will be a changing magnetic flux through the second track on the channel, generating an electromotive force proportional to the speed of the channel resulting in an induction voltage. Figure 3 shows the transfer between the two tracks on top of the Coriolis channel, measured using a gain-phase analyser under ambient pressure and while the channels are filled with air. The phase shift at resonance is 0 degrees, so that an amplifier is sufficient to realise an oscillator. An automatic gain control has been added to control the amplitude of the vibrating tube. A schematic overview of the actuation circuit is shown in Figure 4. First the signal from the feedback track is amplified 5000 times. That signal is used to control the gain of the second stage.

FABRICATION

The fabrication process of the Coriolis flow sensor is described in detail by Haneveld et al. [3] and schematically shown in figure 5. First, a layer of low-stress LPCVD silicon-rich silicon nitride (SiRN) is deposited on a highly p-doped silicon wafer (a). Using
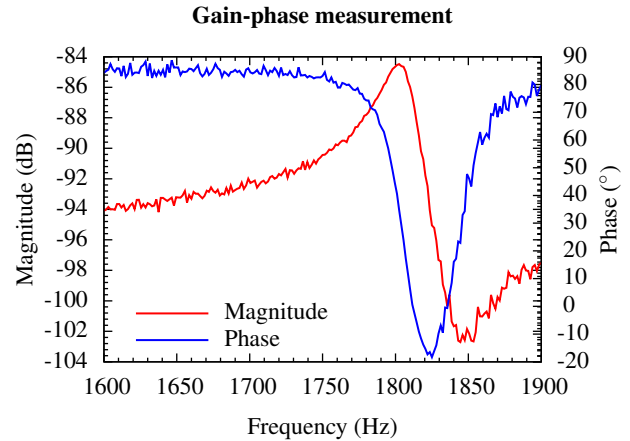

Figure 3: Gain-phase measurement for the Coriolis sensor operated as two-port resonator.
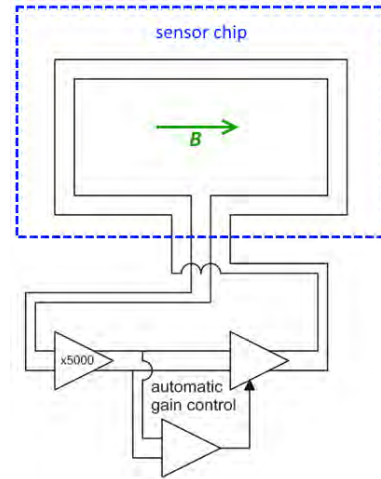
Figure 4: Schematic view of the actuation circuit using the mechanical structure of the Coriolis channel as two-port resonator while the channel is filled with water.

deep reactive ion etching (DRIE), fluid inlet/outlet holes are etched from the backside using a photoresist (PR) mask, whereas the SiRN layer on top acts as a stop layer. Next, a $1\,\mu m$ thick SiO_2 layer is deposited using TEOS and afterwards removed from the top side. A $50\,nm$ layer of chromium is sputtered to create the centrelines of the channels. The pattern is then transferred into the nitride layer by reactive ion etching (RIE) and subsequently the channels are etched in the silicon using isotropic plasma etching by SF_6 (b).

The SiO_2 layer and chromium mask are then removed and another SiRN layer is grown with a thickness of $1.8\,\mu m$ to form the channel walls and to seal the etch holes in the first nitride layer (c). A $10\,nm$ layer

Si   SiRN   SiO$_2$ PR   Au/Cr

(a) Fluid inlet/outlet holes from backside using DRIE.

(b) Channel etching by isotropic etching of silicon.

(c) Formation of channel walls and hole sealing by SiRN.

(d) Sputtering and patterning of electrodes (Au/Cr).

(e) Opening of release windows by RIE.

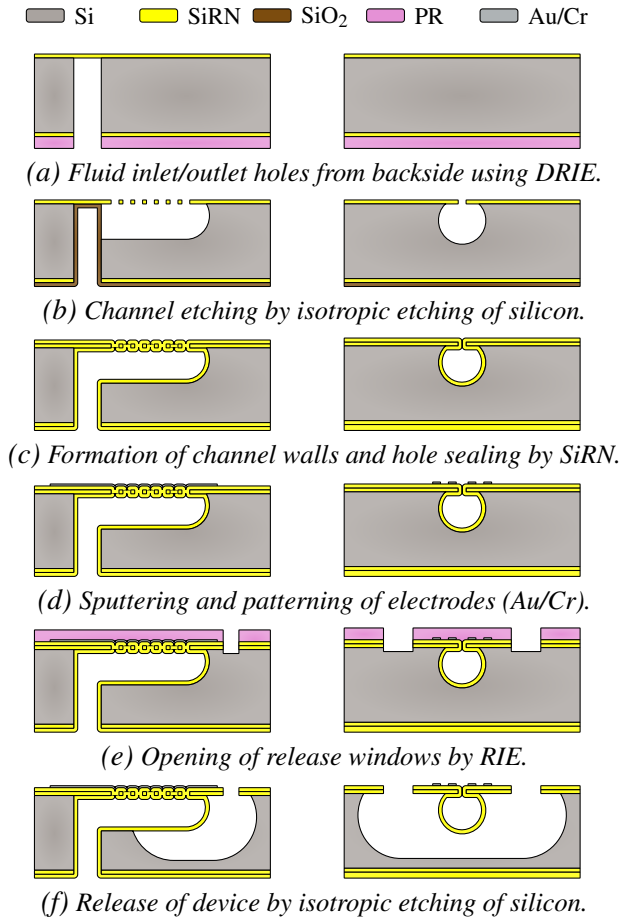*(f) Release of device by isotropic etching of silicon.*

Figure 5: Schematic view of the fabrication process. Left: through-wafer cross-section along the length of the tube. Right: through-wafer cross-section of the tube.

Figure 6: Photo of the fabricated sensor.

Figure 7: Photo of the complete sensing system.

of chromium and 200 nm layer of gold are sputtered (chromium serves as the adhesion layer for gold) and patterned to create the metal electrodes for actuation and read-out (d). Release windows are created by reactive ion etching (RIE) of the SiRN layer (e). Then, the structure is released by isotropic etching of silicon using SF$_6$ (f). A photograph of the finished sensor is shown in Figure 6 showing the location of the Coriolis channel, the bypass channel and the capacitive read-out structures. Figure 7 shows the sensor package with all the required electronics.

RESULTS

Mass flow measurement

The measurement setup is schematically shown in Figure 8. The sensing system is placed in a vacuum chamber which can be pumped down to a pressure of approximately 1×10^{-3} Pa. A Bronkhorst M12 mini CORI-FLOW Mass Flow controller is used to regulate the flow. The water reservoir is pressurized to 8 hPa.

The detection of the phaseshift is done using two Stanford Research SR830 lock-in amplifiers. Figure 9 shows the measurement results for four different sensors. One without bypass system (the red markers) and three with bypass system. The markers show the measurement results, the lines are quadratic fits of the measurement data for the sensors with bypass and a linear fit for the measurement data of the sensor without bypass. The dashed lines are the ratio's between the sensors with bypass system and the sensor without bypass system. As expected from the model, the ratio decreases at higher flow. The spread in bypass ratio is most probably caused by the relatively short bypass channel and by the spread in diameter of the channels caused by the fabrication process.

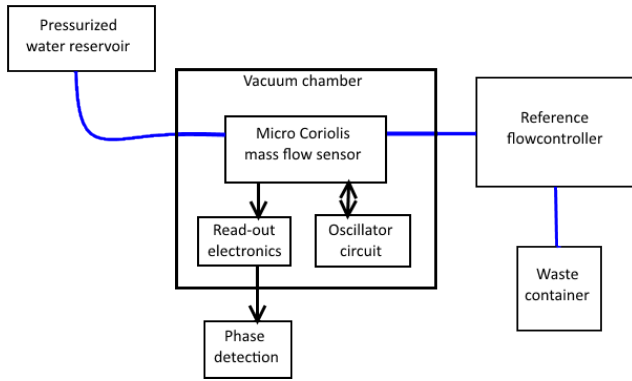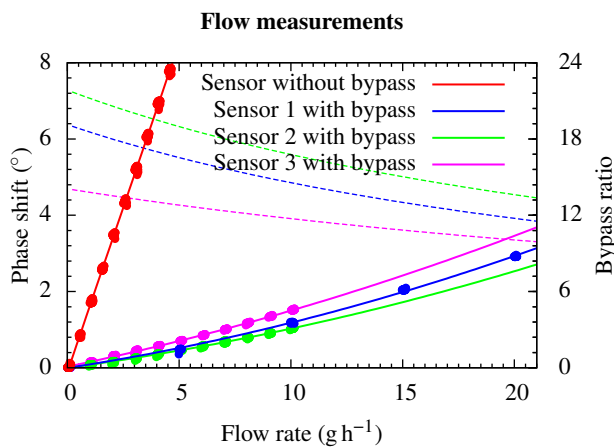*Figure 8: Schematic overview of the measurement setup*

Figure 9: Flow measurement using water. The dots are measurement points. The lines are linear and quadratic fits for the sensors without and with bypass respectively. The dashed lines are the bypass-ratios of the chips with bypass.
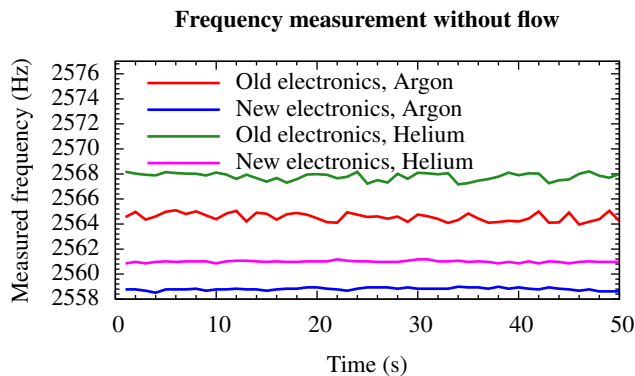

Figure 10: Measured frequency using the old and new actuation method. The channels are filled with either Argon or Helium.

Frequency stability

To measure the frequency stability of the oscillator circuit, the actuation frequency has been measured while the sensor channels were filled with either helium or argon. The measurement has been repeated with both the old actuation method and the new oscillator circuit. Using the old electronics, the standard deviation of these measurements is 0.33Hz for both gasses. Using the new electronics, this was reduced to 0.10Hz and 0.08Hz for Argon and Helium respectively indicating a three times better frequency stability using the self-oscillation circuit, resulting in a more accurate density measurement.

CONCLUSIONS

A micro Coriolis mass flow sensor for the measurement of hydrazine (N_2H_4) propellant flow in a µCPS has been developed. Measurements have been done both under atmospheric pressure as under vacuum to test the operation of the sensor. Using an on-chip bypass system, the measurement range has been increased to $20\,\mathrm{g\,h^{-1}}$. Further work will have to be done to test the sensor in a simulated space environment using hydrazine.

ACKNOWLEDGEMENTS

REFERENCES

[1] M. Gauer, D. Telitschkin, U. Gotzig, Y. Batonneau, H. Johansson, M. Ivanov, P. Palmer, and R. Wiegerink, "PRECISE-development of a MEMS-based monopropellant micro Chemical Propulsion System," in *48th AIAA Joint Propulsion Conference*, 2012.

[2] J. Haneveld, T. S. J. Lammerink, M. Dijkstra, H. Droogendijk, M. J. de Boer, and R. J. Wiegerink, "Highly sensitive micro Coriolis mass flow sensor," in *Proc. MEMS 2008*, 2008, pp. 920–923.

[3] J. Haneveld, T. S. J. Lammerink, M. J. de Boer, R. G. P. Sanders, A. Mehendale, J. C. Lötters, M. Dijkstra, and R. J. Wiegerink, "Modeling, design, fabrication and characterization of a micro Coriolis mass flow sensor," *J. Micromech. Microeng.*, vol. 20, p. 125001, 2010.

2nd International Conference on MicroFluidic Handling Systems
8 – 10 October 2014, University of Freiburg, Germany

24

PERISTALTIC MICROPUMP WITH INTEGRATED ACTIVE DAMPING

A. Schumacher[1], M. Götz[1], G. Kattinger[1], J. Merz[1], S. Herrlich[1,], S. Spieth[1], and R. Zengerle[1,2]*

[1] Institut für Mikro- und Informationstechnik der Hahn-Schickard-Gesellschaft für angewandte Forschung e.V. (HSG-IMIT), Villingen-Schwenningen, Germany

[2] University of Freiburg, Department of Microsystems Engineering – IMTEK, Laboratory for MEMS Applications, Freiburg, Germany

ABSTRACT

We present a novel peristaltic micropump with active damping for biotechnological or medical applications. The modular concept of the pump is based on a low-cost disposable fluidic pump chip and a reusable actuator unit. The disposable pump chip enables the cost-effective and easy exchange of all components being in contact with the liquid to be pumped. The reusable actuator unit consists of three piezo stack actuators that form an undamped peristaltic micropump. With an integrated pressure sensor measuring the flow pulsations and an additional piezo stack actuator whose movement is controlled in real-time in a closed-loop, active pulsation damping is implemented. The pump rate of water is proportional to the operation frequency and reaches 1 mL/min at 30 Hz. From 0 to 200 kPa backpressure, the pump rate varies less than ±10 %. With active damping, flow pulsations can be reduced by 80 to 90 %, compared to the undamped flow.

KEYWORDS

Peristaltic micropump, Pulsation-free flow, Active damping

INTRODUCTION

Pulsation-free and continuous liquid flows are necessary in many applications in process technology, biotechnology, as well as medicine. Although syringe pumps can provide nearly pulsation-free flows, they have only limited volumetric capacities in their reservoirs making them not suitable for real continuous or long-term flow applications, e.g. to operate circulating systems. On the other hand, several micropumps are available on the market [1-3] or are currently under development [4], but their flows are pulsating as a result of the applied actuation principles. Additional passive damping elements can be used to reduce pulsations [3], but these elements are based on large fluidic capacitances. In this work, a novel modular peristaltic micropump with an integrated active pulsation damping unit is presented. Thereby, the flow pulsations are detected by a pressure sensor and effectively reduced in real-time by an actuator.

CONCEPT & SOLUTION

The actively damped micropump consists of a low-cost replaceable and disposable pump chip which can be placed into a pump body containing the actuators (Fig. 1a). This way all liquid-contaminated parts can easily be removed and disposed. The pumping action is performed by means of three piezoelectric stack actuators. They displace the liquid in chambers inside the microfluidic pump chip which are connected by channels in a chain-like manner. Fig. 1.b illustrates the three different pump phases which are repeated continuously according to the actuation frequency during pumping. Only between phase 3 and phase 1, liquid is delivered from the outlet of pump chamber 3. Therefore, the flow rate of liquid is not constant, but pulsates with the actuation frequency.
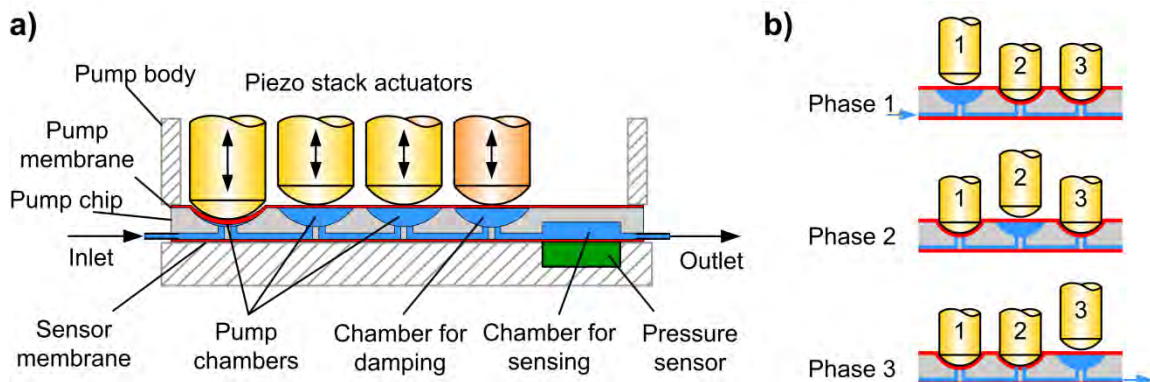

Figure 1: (a) Schematic view of the peristaltic micropump with active damping. (b) The three different pump phases of the undamped peristaltic micropump.
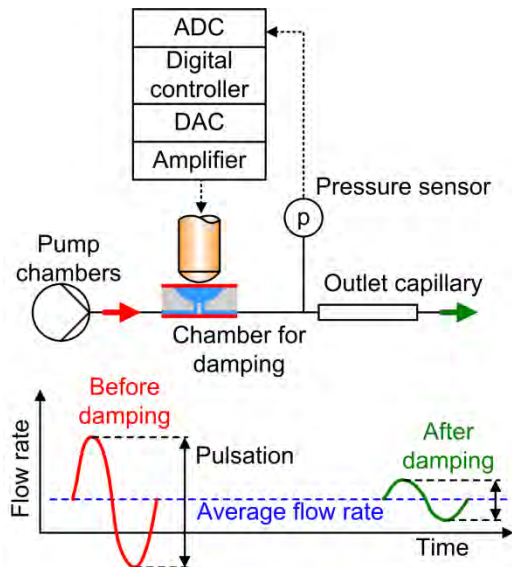
Figure 2: Principle of active flow pulsation damping.

A pressure sensor at the outlet is able to detect pressure pulsations. To reduce flow oscillations at the outlet capillary, a forth chamber is added containing a piezo stack-actuated flexible membrane.

Due to the Hagen-Poiseuille law, the pressure difference across the outlet capillary is proportional to the flow rate through it. Given the assumption that the pressure inside the outlet tubing, which is attached at the capillary, is constant, the flow pulsations can be detected by the associated pressure pulses. For this purpose, a modified commercial pressure sensor with integrated amplifier (MPX5500D, Freescale Semiconductor Inc.) is used, which is in direct contact with the sensor membrane. The membrane is actively controlled to compensate pressure oscillations at frequencies of the operation frequency at the outlet. The sensor signal is converted into a digital signal by an analog-to-digital converter (ADC) and digitally processed by a proportional-integral-derivative controller (PID controller). By conversion with a digital-to-analog converter (DAC) and amplification by a factor of 10, the appropriate signal for the damping actuator is generated (Fig. 2).

The metallic pump body made of stainless steel and aluminum provides a mechanically stable construction with respect to the arising actuation forces. Four spring-preloaded piezo stack actuators, each inside a steel housing (PST 150/4/40, Piezomechanik GmbH) as well as a pressure sensor which is used for active pulsation damping are integrated into the pump body (Fig.3.a). After insertion, the disposable pump chip is secured in a defined position by a self-locking eccentric cylinder connected to a handle (Fig. 3.b).

Without load, the used piezo actuators offer a maximum stroke of about 40 μm at an operating voltage of 150 V [5]. The stroke is transmitted to the pump membrane by means of a plunger adapted to the shape of the pump chamber. Due to the restoring force of the pump membrane as well as the applied backpressure, the maximum stroke of the actuator is reduced in practice to about 35 μm. As the depth of the pump chambers is set to 200 μm, the membranes have to be pre-deflected leaving a chamber height of about 35 μm at the minimum actuation voltage of the actuator. This results in a theoretical stroke volume of 0.9 μL for each chamber.
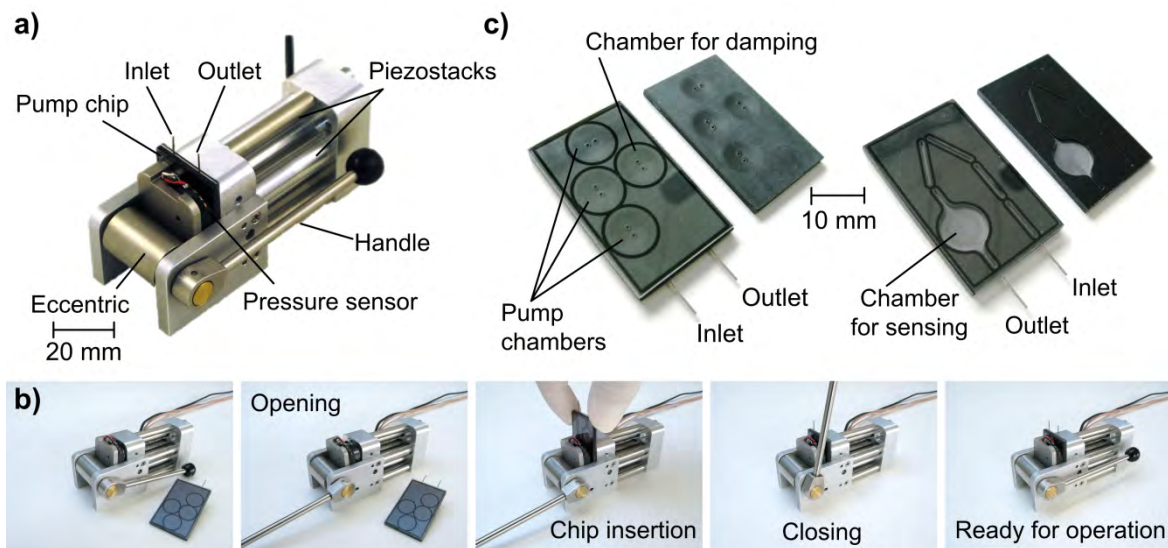

Figure 3: (a) Photograph of the peristaltic micropump with active damping. (b) Insertion procedure of the disposable pump chip into the reusable actuator unit. (c) Disposable pump chip. Front side (left) and rear side (right) with and without membrane, respectively.

The disposable pump chip is shown in Fig. 3.c from the front and the rear side. It consists of a black polymer body made of a polycarbonate (PC)/ acrylonitrile butadiene styrene (ABS) blend (Bayblend® T65, Bayer MaterialScience) having outer dimensions of $40 \times 25 \times 2$ mm³. It contains cavities, channels, and holes which have been fabricated by precision milling. Each pump chamber is acting as a valve, which is closed, when the actuator is extended at most, and the corresponding membrane is in this case pressed against the bottom of the pump chamber. Due to the fact that at any time at least one valve is closed, any backflow is prevented during pumping of liquid against external backpressure.

For future mass production, it is planned to fabricate the body by injection molding. The shape of the pump chambers is adapted to the deflection profile of a uniformly loaded circular plate with clamped edges [6] with a plate radius of 5 mm and a maximum center deflection of 200 μm. Both sides of the body are covered by transparent PC membranes (Makrofol® DE 1-1 CC, Bayer MaterialScience): The pump membrane on the front side covering the pump chambers has a thickness of 0.75 mm, whereas the sensor membrane on the rear side is 0.125 mm thick. To join the membranes with the body, laser plastic welding has been applied. Therefore, no additional substances such as adhesives are necessary, which could lead to clogging of the channels or possibly interact with the liquid. Fluidic connection to the chip is realized by two stainless steel capillaries at the inlet and outlet, respectively, adapted to commercially available plastic tubing with an inner diameter of 0.5 mm.

Figure 4: Electronic control unit.

A compact stand-alone electronic control unit shown in Fig. 4 is connected to the micropump, which contains the drivers and amplifiers for the piezo stacks, the AD-converter, a digital controller, the DA-converter, and the amplifier for the active damping as well as the PC interface to control the micropump.

CHARACTERIZATION & RESULTS

The micropump has been characterized by measuring the pump rates and the flow pulsations at different frequencies and backpressures. The pump rate has been determined by measuring the weight of pumped water over a fixed time interval by using a precision balance (ED623S, Sartorius AG). Backpressures from 0 to 200 kPa have been applied to the outlet tubing using a pressure controller (DPI 520, ICS Schneider Messtechnik GmbH) and a pressure reservoir. By measuring the transient pressure drop over an additional fixed flow resistance connected to the outlet tubing with a pressure sensor (MPX5500D, Freescale Semiconductor Inc.), the (remaining) flow pulsations have been monitored.

Fig. 5 shows the pump rates at actuation frequencies from 5 to 30 Hz, and backpressures from 0 to 200 kPa (average of four different 30-s-measurements in each case). The pump rate is nearly proportional to the frequency and reaches about 1 mL/min at 30 Hz. During variation of the backpressure from 0 to 200 kPa, the pump rate varies less than ±10 %.

Considering equal conditions (10 Hz, 200 kPa), a single time-resolved measurement of the flow rate with active damping (red curve) in comparison to the flow rate without damping (blue curve) is exemplarily shown in Fig. 6. Without damping, the flow rate reaches its maximum when liquid is delivered from pump chamber 3, whereas the pump rate is about zero during the remaining pump cycle. During liquid transfer from pump chamber 2 to 3, there is a small backflow into the pump chip causing a negative flow rate at this point. With active damping, the flow peaks are effectively reduced. The controller output signal
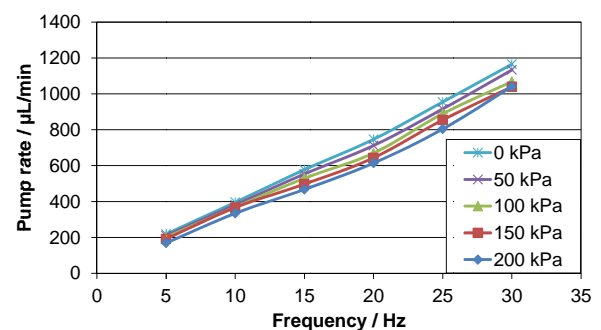

Figure 5: Pump rates measured at different frequencies and external backpressures.
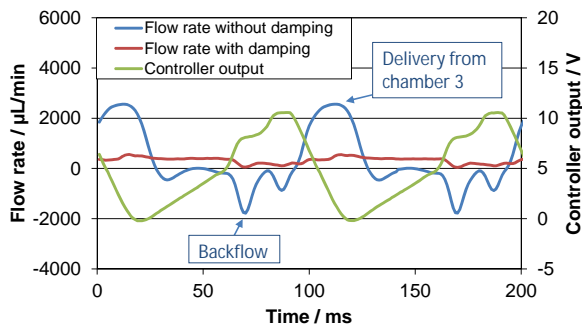
Figure 6: Time-resolved measurement of the flow rate with active damping (red curve) in comparison to the flow rate without damping (blue curve) (10 Hz, 200 kPa in each case). In addition, the signal for the damping actuator before amplification (green curve) is shown.

(green curve) resembles a triangular wave with a decrease during the delivery phase of pump chamber 3 and an increase during the rest of the pump cycle.

To evaluate quantitatively the effect of pulsation damping, the peak-to-peak amplitudes of the flow rates with damping have been set in direct relation to the amplitudes without damping. Fig. 7 shows the remaining percentage of pulsation after active damping at frequencies from 5 to 30 Hz and backpressures from 100 to 200 kPa. With active damping, flow pulsations can be reduced by 80 to 90 % compared to the undamped flow.

By reversing the waveforms of the control voltages of the piezo actuators, it is possible to pump in both directions. It could be verified that active damping is also effective during suction. After insertion of a dry pump chip, the pump is self-priming up to a backpressure of 5 kPa.
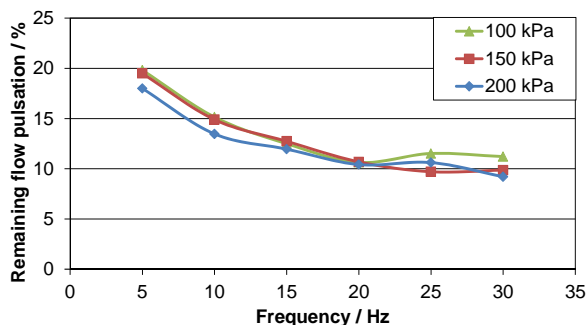

Figure 7: Relative flow pulsations after active damping (undamped = 100 %) measured at different external backpressures.

CONCLUSION

We presented a novel peristaltic micropump with an integrated active damping mechanism. Due to the modular setup with a low-cost pump chip and a reusable actuator unit, the pump fits the requirements of the medical field and health care industry. The pump rate is nearly independent from the backpressure and proportional to the actuation frequency, and can therefore be easily controlled. The integrated active damping unit is able to effectively reduce flow pulsations without the use of large fluidic capacitances which would cause undesirable dead volumes. The stand-alone control unit allows the easy use of the micropump for different applications.

ACKNOWLEDGEMENT

This work has been supported by the Federal Ministry of Economics and Technology on the basis of a decision by the German Bundestag. The authors acknowledge the support from Bayer MaterialScience for providing the materials for the pump chip, ModellTechnik Rapid Prototyping GmbH for fabricating the pump chip bodies, the machine shop facilities at HSG-IMIT for fabricating the mechanical components of the pump, and Cetoni GmbH for many useful discussions.

REFERENCES

[1] Bartels Microtechnik GmbH, Dortmund, Germany, www.bartels-mikrotechnik.de.

[2] Christian Bürkert GmbH & Co. KG, Ingelfingen, Germany, www.burkert.com.

[3] KNF Neuberger GmbH, Freiburg, Germany, www.knf.de.

[4] F. Trenkle, PMP-NC² - A normally-closed, backpressure independent peristaltic micropump featuring a modular setup, PhD thesis, University of Freiburg, 2011.

[5] Piezo-mechanical and electrostrictive stack and ring actuators: Product range and technical data, Piezomechanik GmbH, Oct. 2006, P. 6.

[6] S. Timoshenko, Theory of plates and shells, McGraw-Hill, 2nd edition 1987, p. 55.

CONTACT

* S. Herrlich, simon.herrlich@hsg-imit.de

5. Applications   Presentation

CONTACTLESS BOILING:
A WAY TO IMPROVE THE RELIABILITY OF MICROFLUIDIC PROCESSES?

C.M. Rops[1] , B. Patankar[2] , G.J. Snijders[3] and C.W.M. v/d Geld[2]
[1] TNO Technical Sciences, De Rondom 1, 5612 AP, Eindhoven, The Netherlands
[2] Eindhoven university of Technology, PO Box 513, 5600 MB Eindhoven, The Netherlands
[3] Bronkhorst High-Tech BV, Ruurlo, The Netherlands

ABSTRACT

The availability of MEMS production techniques allowed the mass production of small sized fluidic systems. The reduced cost price implies that crucial parts of a system become disposable units, improving the serviceability and the controllability. However, small channel diameters demand extra care on fouling, reliability and thermo-mechanical management. In the current investigation, a dedicated setup is realised which aims to obtain contactless boiling due to the presence of a thin gas blanket near the wall. The formation and the possible optimization of this bubbly cushion still needs further research. Understanding of the stability of the thin gas blanket or bubble cushion formation may lead to the demand for novel wall structures which can be realised by means of innovative 3D manufacturing techniques.

KEYWORDS

Contactless boiling, gas film, fouling, reliability, 3D rapid manufacturing.

INTRODUCTION

Since the 1980's production techniques have become available for MEMS (Micro Electro Mechanical Systems). This allows the mass production of small sized fluidic systems having a better control of process conditions and faster response times and functionality integration [1]. The significantly reduced cost price allows that crucial parts of the system may become disposable units. This gives opportunities to improve the controllability and the serviceability of high-tech systems. For example, in ALD (Atomic Layer Deposition) and CVD (Chemical Vapour Deposition) processes micro evaporators could have added value, given their controllability and serviceability.

However, small channel diameters demand extra care on fouling, reliability and thermo-mechanical management. Additionally, the maximum achievable heat flux is limited by various physical processes. For instance, the importance of body forces like gravity and inertia is less than the capillary forces which causes an increased probability of channel blockage [2]. Even explosive vapour bubble growth [3] with large pressure fluctuations [4] and flow instabilities [5] is observed.

Fouling and reliability of a micro system are obviously determined by the deposition and entrainment rates of particles at the wall. In addition, the heated wall of the micro evaporator may act as a catalyst leading to fouling accumulation undesired reactions. This may lead to uncontrolled behaviour of the micro evaporator over time [6]. A novel strategy to reduce the fouling and enhance the system stability is the creation of a thin gas blanket between the wall and the fluid. The flow pattern thus created resembles so-called inverted annular flow. Measurements in a porous conical channel give indications for the existence of such a vapour blanket [7].

The present investigation explores possibilities to obtain insights on lifting the boiling fluid off the wall, which enhance the reliability and stability of a once-through micro evaporator. It is attempted to lift the boiling liquid off the wall by feeding hot Nitrogen through a porous wall in a rectangular shaped channel. Next, the formation of the gas blanket is studied by means of high speed camera recordings. An experimental setup is made (section 2). Results are shown and discussed in section 3. Finally some conclusion and suggestions for future investigations are given.

EXPERIMENTAL SETUP
Channel layout

The measurement setup consists of three sections : (a) Glass top plate , (b) Porous heated metal and (c) Air chamber. In the glass top plate a rectangular slit is made to form the rectangular boiling channel with a height of 1.4mm and a width of 2mm, see Fig. 1. This allows a camera recording of the boiling flow from 3 sides. The side view possibility allowed to observe the existence of a gas layer when gas is injected via the pressurized air chamber.

The glass top is glued to the reactor using the Wurth Silicone Special 250 rubber. This silicone glue maintains its elasticity upto temperatures of 250˚C, to moderate the different thermal expansion coefficients

of steel and glass. The porous wall (SIKA-R 0.5AX) is made of small stainless steel particles sintered together with a typical hole size of about 0.5 micro meter and a typical volume porosity ~21%. The top and bottom surfaces are electro etched using the EDM technique. This ensures porosity of the top and bottom surfaces enabling air injection.
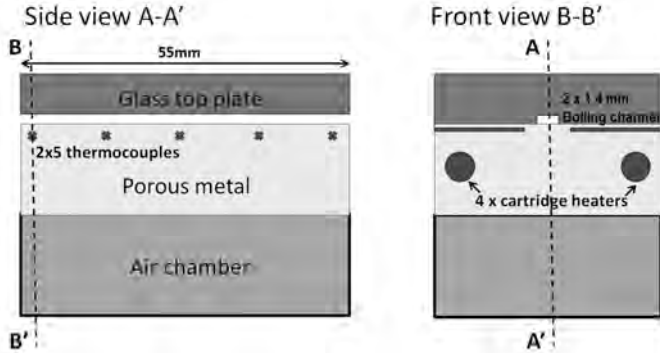

Figure 1: Schematic overview of the boiling channel.

On each side of the setup 5 thermocouples are inserted. The first thermocouple is placed at a distance of 1mm from the inlet. 4 cartridge heaters (Omega, Hi-Density ¼ inch) are used to heat the porous metal. The porous metal is insulated at the sides with Teflon to minimize the heat losses to the surroundings. The air chamber, to supply the pressurized air to the boiling channel, is connected to the porous wall by an air-tight fit using an O-ring.

Visualisation setup
The contactless flow boiling are recorded by means of a high speed camera using the setup as shown in Fig. 2.
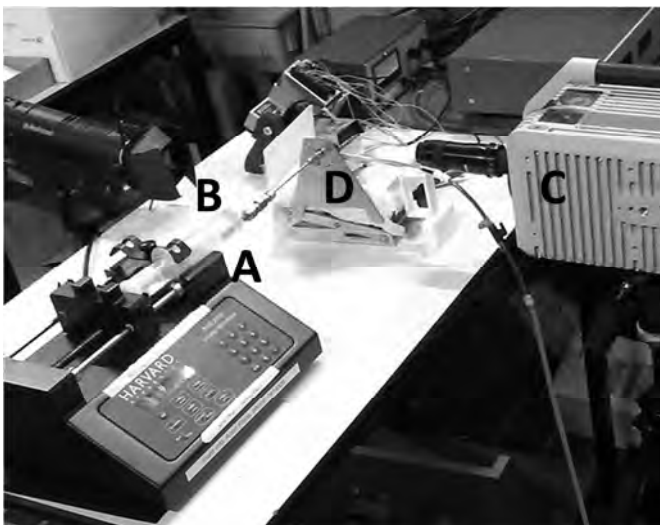

Figure 2: Overview of the setup: water supply (A), illumination (B), high-speed camera (C) and flow boiling channel (D).

The water is supplied by the means of a syringe pump (Harvard PHD 2000 series). No particular attention was given to degas the water prior to using it in the experiments. Air is supplied through the bottom wall of the channel using compressed air connected to the air chamber. The pressure at which air is supplied is measured using a pressure gauge with accuracy ± 5 mbar.

The high speed videos are recorded using a Photron FASTCAM SA-X2. Dedocool lamps (250W) are used as illumination. The light is diffused using a translucent diffuser plate.

Experimental procedure
The heating is controlled by varying the input to the cartridge heaters. The temperature of the first thermocouple is maintained at 130°C ± 1°C. In this investigation water flow rates between 35ml/hr to 280ml/hr are studied. The supply temperature of the water is at room temperature 20°C. Air is injected with two pressures in the air chamber, either 303 mbar ± 3 mbar or 602 mbar ± 3 mbar are employed. The air is heated up to the temperature of the porous wall by passing through the pores. The frame rate of the high-speed recordings is 1000 fps, with a shutter speed of 1/1000 s. A typical movie length is around 4-5 seconds real time. The spatial resolution of the movies was 512x1024 pixels. It is observed that in the first few mm all the characteristic features of bubble growth take place. Thus only the first 20mm of the channel are imaged, resulting in a spatial resolution of about 0.02 mm.

For each flow setting the following procedure is followed :
- Air pressure stabilized in the air chamber.
- Water flow set by the syringe pump.
- Heater is switched on and the temperature of the first thermocouple is stabilized at 130°C.
- Stabilization period of at least 5 minutes.
- The lights and camera are started. The focus is adjusted to ensure that a clear image.
- Recording of movies is started for a period of ~5 seconds.

EXPERIMENTAL RESULTS
Results
High speed recordings without air injection from the bottom wall are shown in Fig. 3. These images show that near the inlet multiple small bubbles are stuck to the channel wall. These semi spherical bubbles grow rather slowly. This is most likely due to the cold inlet temperature of the water. Further

downstream the boiling becomes more vigorous, and the typical flow reversal is observed, see Fig 3.
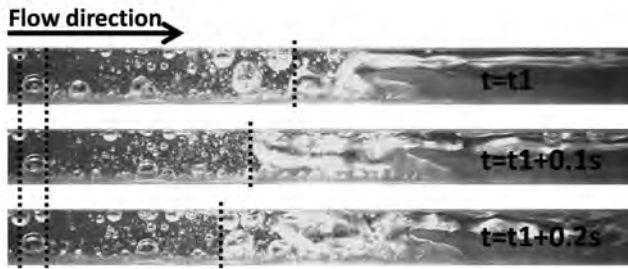

Figure 3. Typical high speed camera images of flow boiling without gas injection from the bottom wall. Temperature first thermocouple 130ºC, liquid water flow velocity ~0.01m/s.

The observed flow reversal can be linked to the high pressure fluctuations occurring in once-through micro boiling channels. These variations lead to an unstable system, and possibly malfunction. However, on inserting a gas through the heated wall the flow boiling behaviour changes, see Fig. 4.
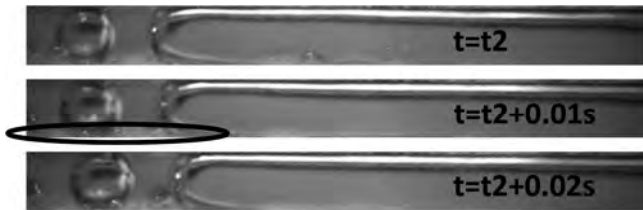

Figure 4. Typical high speed camera images of flow boiling with gas injection from the bottom wall. Temperature first thermocouple 130ºC, liquid water flow velocity ~0.01m/s.

Gas injection through the heated porous wall allows the spherical vapour bubbles to slide along the wall more easily. Next, no upstream vapour bubble growth is observed during the explosive bubble expansion. Furthermore, more elevated temperatures are measured downstream the boiling channel in case of gas injection. Based on first order energy calculations, the heat transferring capacity of the boiling channel with gas injection is less than without gas injection. However, both are still within the same order of magnitude. This corresponds to the findings in earlier work performed on contactless boiling [7].

These observations for gas injections hint towards the presence of a thin gas blanket near the porous wall. From the images very tiny bubbles (<50micron) seem to be present forming some sort of bubble cushion, see Fig. 4. The formation and the stability of the bubbly cushion still needs further research. Detailed high speed camera recordings near the wall are needed to properly characterise the gas behaviour.

Discussion

Understanding of the stability of a gas layer or bubble cushion formation may lead to the demand for novel wall structures. These wall structures may have a well-defined three dimensional shape, which can be realised by means of innovative 3D manufacturing techniques.

At TNO, in collaboration with Bronkhorst High-Tech, the possibilities are being explored regarding the employment of rapid manufacturing techniques. High accuracies and tight tolerances can be met, see Fig. 5. These techniques allow novel sensor and equipment design.
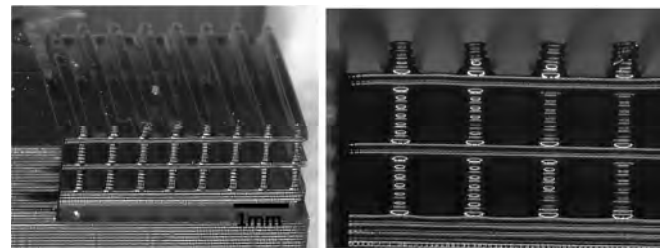
Figure 5. Typical example of rapid prototyping manufacturing technique, polymer hardening by laser. Well defined thin walls (~0.2mm), both in vertical as in horizontal direction.

Currently, layerwise sintering of metal particles is being explored, similar as in current rapid prototyping techniques. These innovations may lead to a well-defined porous and open metal wall, however equipped with bubble cushion or gas layer stabilizing structures.

The possibility to form an inherently stable gas layer, leads to micro fluidic systems which are less sensitive to fouling and have less violent flow behaviour. Due to the small size of the boiling systems it is possible to sinter multiple system in parallel which significantly reduces the cost price of a single unit. Therefore, this future investigation may open the door to a more sustainable and serviceable usage of micro fluidic components in industry.

CONCLUSIONS

A once through micro evaporator is constructed. This flow boiling channel allows a visual access from three sides. The bottom wall of the channel is a heated porous metal wall allowing air injection. A high-speed camera setup is realized, and recordings made of both with air injection through the porous wall and without air injection through the porous wall. The recordings with air injection show no upstream vapour bubble growth and a less violent flow behavior as opposed to no air injection flow boiling.

Layerwise sintering of micron sized metal particles is regarded as a viable manufacturing technique to support the developments in contactless boiling. The technique can be made cost efficient and permits the requirements posed on the system.

REFERENCES

[1] Tabeling, P. (2005). Introduction to microfluidics. Oxford university press.

[2] C.M. Rops, L.F.G. Geers, J. Westerweel, Explosive bubble growth during flow boiling in micro-channels, *Proceedings of 5th European Thermal-Sciences Conference*, Eindhoven, The Netherlands, 2008.

[3] L. Zhang, E.N.Wang, K.E. Goodson, and T.W. Kenny, Phase change phenomena in silicon microchannels, International journal of heat and mass transfer, 48, pp. 1572-1582, 2005.

[4] J.E. Kennedy, G.M. Roach Jr., M.F. Dowling, S.I. Abdel-Khalik S.M. Ghiaasiaan, S.M. Jeter, Z.H. Quershi, The onset of flow instability in uniformly heated horizontal microchannels, Journal of Heat Transfer, 122(1), p.p. 118-125, 2000.

[5] S.G. Kandlikar, Heat transfer mechanisms during flow boiling in microchannels, Journal of heat transfer, 126, pp. 8-16, 2004.

[6] J.F. Perry, Fouling in silicon microchannel designs used for IC chip cooling and its mitigation, Dissertation, Rochester Institute of Technology, 2008.

[7] C. M. Rops, G.J. Oosterbaan, C.W.M. Geld, Once-through contactless flow boiling in a micro evaporator , *Proceedings of 5th int. conf. on heat transfer and fluid flow in micro-scale*, Marseille, France, 2014.

CONTACT
* C.M. Rops, cor.rops@tno.nl

2. Actuators   Presentation

3D PRINTED UNIBODY LAB-ON-A-CHIP INTEGRATION

G. Comina, A. Suska and D. Filippini*
Optical Devices Laboratory, IFM – Linköping University, Sweden

ABSTRACT

Fast and affordable prototyping of lab-on-a-chip (LOC) devices built around a single monolithic 3D printed element (unibody) is demonstrated. A consumer grade stereo lithography (SL) 3D printer, is used to configure unibody-LOCs (ULOC) with different forms of sample delivery, transport, handling and readout. ULOC centralizes all complex fabrication procedures and entirely replaces the need for clean room access. Prototypes in this work cost 0.57US$ and can be produced in less than 30min, from design to testing. Here we demonstrate ULOC chemical sensing for optical readout and micromixing capabilities.

KEYWORDS

3D printer, lab-on-a-chip, fast prototyping, unibody, micromixers, chemical sensing.

INTRODUCTION

Conventional microfabrication techniques involve specialized resources and skills beyond the scope of many potential LOC users.[1-2] Simplified processes have been explored, although they still require dedicated skills and expensive clean room infrastructure.[2-4]

Additive 3D structuring, like in thermoplastic extrusion systems [5] and micro stereo lithography (SL) platforms, [3] can greatly simplify fabrication and minimize infrastructure costs.

ULOCs are possible due to the resolution presently achievable with consumer grade SL 3D printers. Previous demonstrations of 3D printed fluidics, made with affordable printers [6], had restrictions on resolution and surface roughness, which prevented regular LOC channel geometries and simple sealing procedures. In contrast, SL 3D printers support resolutions of 50µm [7,9], and surface roughness under 200nm, which permits channel sealing with regular adhesive tape. For similar resolutions, other additive systems cost 10 to 100 times more than the Miircraft printer [9] used in this work (2290 US$).

In addition, ULOC can accommodate different designs and operation principles using essentially the same concept. Here we demonstrate the fabrication of LOC devices, designed around a 3D printed single monolithic body, or unibody LOC (ULOC), which can be completed with simple additional procedures.

ULOC can thus integrate printed connectors to silicone tubing, complex geometric features to facilitate functionalization, and the inclusion of glass micro beads for continuous flow mixers.

EXPERIMENTAL

Device fabrication

Device structures were designed with free CAD software for Mac Os X 10.8.3 (Autodesk® Inventor® Fusion, Autodesk Inc.) on a MacBook Air computer (13-inch, late 2010, 1.86 GHz Intel Core 2 Duo, 4 GB 1067 MHz).

The devices were fabricated with a Miicraft® 3D printer, which is a stereo lithography (SL) platform (2299 US$) with 450ppi (~56µm) lateral resolution, and 50µm resolution in the vertical direction.

CADs were exported as .stl mesh files and converted to bitmap exposure patterns by the Miicraft® Suite software provided with the 3D printer. Further details of these recourses have been published elsewhere [8,9].

After optimization, devices were printed in the following conditions of exposure time, printing speed and vertical step size: 7s, 2cm/hour, 50µm. After printing, the devices were sonicated (FinnSonic m15) in industrial grade ethanol for 20s, and air-dried.

The printer uses a proprietary resin (138 US$ / 500 ml), with undisclosed formulations of a modified acrylate oligomer and monomer in combination with an epoxy monomer, a photo initiator, and additives.

The average device weight was 2.1 gr, which for the resin cost corresponds to 0.57 US$/device.

Surface roughness was measured with a stylus profiler (Dektak 6, Veeco Instrument Inc.) along 1mm tracks resolved in 6000 points. The average roughness was 182nm for the finished templates, which enables direct sealing with adhesive tape. Designs are conceived to exploit this aspect and simplify the fabrication to a single monolithic 3D printed body, so called unibody [8,9], around which the device is assembled.

The devices were subsequently sealed with adhesive tape (3M Ruban Adhesive Scotch® Nastro Adhesive). Excess tape was trimmed with a cutter and the tape was pressed against the unibody surface with

a cotton tip in order to eliminate trapped air in small blisters.

Mixers (Fig. 2) were firstly front-sealed with adhesive tape, and in the model incorporating beads (G1145 SIGMA Glass beads, acid-washed, 150-212 μm (70-100 U.S. sieve)), these were delivered dry from the backside of the through hole. Excess beads were brushed away from the unibody and the backside immediately sealed with adhesive tape.

The total fabrication time, including the assembly of the sensing sector and sealing, to produce a device ready for testing was less than 30 min.

H_2O_2 assay

The assay solution contained: 10 units/ml horseradish peroxidase (HRP) and 0.3 mM trehalose in physiological saline (0.9% NaCl in water). The assay was prepared as a surface film on a PDMS slab, which could be trimmed in small areas and directly transferred to the unibody sensing sector.

The liquid assay solution was delivered on top of hydrophilic PDMS surface and placed in a chamber at 35% relative humidity (RH) for 12h. The assay solution exposed to these conditions became a sticky thin gel coating the PDMS surface, easy to apply to the printout.

The fluorescent substrate Ampliflu Red (Sigma-Aldrich, St. Louis, MO, USA) was dissolved in DMSO to a concentration of 1 mg/ml. For the test solutions, Ampliflu Red stock solution was added to 0.9% NaCl normal saline (5 μl Ampliflu Red in 995μl 0.9% NaCl), and this preparation was directly used as control, and to produce 0.1μM and or 1μM hydrogen peroxide solutions, which resolve the lower limit of H_2O_2 in urine for whole body oxidative stress monitoring. The test solutions were prepared fresh directly before the experiment.

Imaging

Imaging of unibody printouts was carried out with an Olympus SZ60 stereo zoom microscope, provided with a Canon EOS 500D DSLR camera (15 MP, APS-C Cmos sensor).

Bright field and epi-fluorescene imaging was performed on a Zeiss Axiovert 40 cfl inverted routine microscope. Fluorescence excitation was provided by a Zeiss HBO50 illuminator, housing a mercury vapor short arc lamp HBO 50. The same Canon EOS 500D camera was used in both microscopes.

Imaging of mixing flows (Fig. 2) was carried out with a Samsung Galaxy Note 2, 8 Mpix rear side camera in full HD video acquisition mode (30fps). Backside illumination was provided by a iPod Touch screen (4th generation, 960 x 640 pixel screen resolution, with iOS 6) running a Led Torch v1.37 app (www.smalte.ch), set to pure white (rgb 255, 255, 255).

H_2O_2 fluorescence response (Fig. 1), for C, S and H concentrations, was time-lapsed captured at 10s interval with a Canon EOS 500D mounted on the Zeiss Axiovert 40 cfl. The image sequence was processed in Matlab R2008b with a dedicated script developed for this purpose. Signal noise was extracted from linear curve fitting to the response in the interval [10,12] min and used to compute the resolution.

RESULTS AND DISCUSSION

Fig.1a and b illustrate a unibody design with integrated connectors that seal to standard silicon tubing. Three channels were used to embed the calibration range, with a long section that enabled accurate fixed volume (3μL) sample delivery to the detection zone.

Special features, such as roofed channels (Fig.1 b), permit integration of separately prepared functional surfaces that seal independently to different unibody sectors (Fig. 1c). In this case transport sections were directly sealed with adhesive tape and the detection area with functionalized PDMS for H_2O_2 fluorescence detection [10]. Sample and reference concentrations were pipetted in the silicon tubing and injected with an air loaded syringe. Fig. 1e shows the detail of a pressure sealed tubing.

Time-lapse acquisition of fluorescence intensity, at 10s intervals, captured the assay time response from which a resolution of 0.098μM of H_2O_2 was determined. The result was compatible with the lowest clinically relevant limit of H_2O_2 in urine, for oxidative stress monitoring.
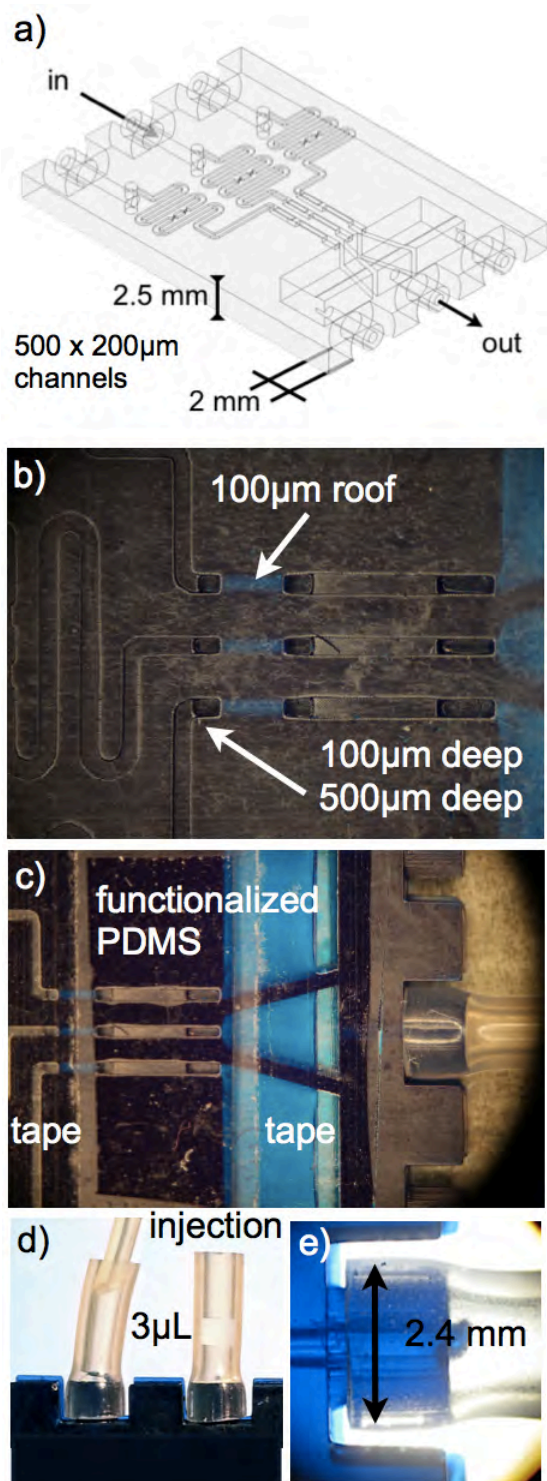
Fig. 1: ULOC configured for fluorescence detection of H_2O_2 on a microscopes stage and for 3µl manual sample delivery using a 5ml syringe loaded with air connected to integrated connectors. The three channels permit integration of the calibration range. The detection region was sealed with functionalized PDMS, and the transport areas independently sealed with adhesive tape.

Mixing is a common preparatory stage in chemical analyses, and accordingly, an important function to demonstrate with unibodies. Microfluidic dimensions favor laminar flow regimes, rendering mixing a slow diffusional process, whereas designs favoring turbulence improve the mixing performance.[11] Since the bodies in ULOC designs are conceived to accommodate the connectors, they entail a thickness of about 2.5 mm, which can be employed for fluidic purposes. In contrast with classical fabrication methods introducing multiple depths does not imply extra fabrication steps, masks or alignments.

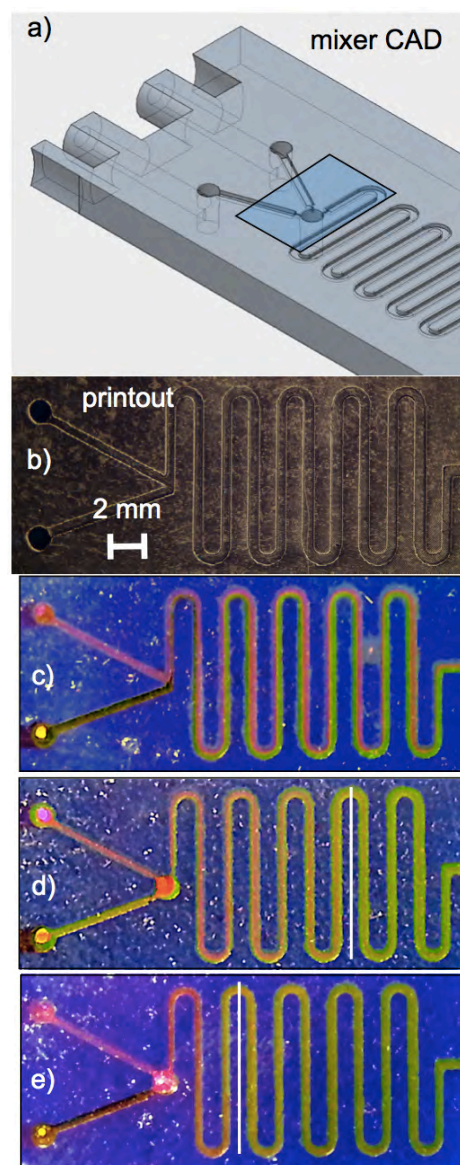*Fig. 2. Three ULOC micromixer designs showing their mixing efficiency at 30 µL/min. The devices were sealed with adhesive tape (3M Ruban Adhesive Scotch® Nastro Adhesive), and glass beads were used in e).*

Fig. 2a shows the unibody design. Since the channel height is proportional to the Reynolds number, a localized geometric feature such as a 1mm through hole, can improve the mixing efficiency in a

compact way. In addition, this space can be used to contain glass micro beads, which enhance turbulence even further.

Fig. 2b shows the printout of the diffusional mixer used as reference, and Fig. 2c corresponds to its performance at 30µL/min constant flow rate. The solutions did not mix at the distal side of the devise, whereas with the 1mm through hole the flows mixed at about 80% of the total length (Fig. 2d, white line). In the case of introducing 150µm diameter beads, the flows mixed at less that 40% of the device length, thus doubling the performance (Fig. 2e).

This work demonstrated the possibility of 3D printed LOC devices compatible with different sample delivery and handling approaches. Migration from established solutions, in classical LOC, were shown simple with ULOC fabrication, and requiring minimal infrastructure.

The advantage of direct additive printing is exploited to fabricate in a single step, the complex geometries required to support independent sealing of different device sectors. In addition, unibody design optimizes additive prototyping by minimizing material and by exploiting the planar dimension, where the printer can deliver sub micrometric surface roughness and reliable resin removal, which creates uniform channels over long distance ranges.

CONCLUSIONS

These results demonstrate that consumer grade 3D printers can drastically simplify custom LOC fabrication and still support complex features only accessible with advanced fabrication techniques.

ULOC architecture makes possible to exploit the surface smoothness granted by this fabrication method, thus simplifying assembly and minimizing materials and prototyping time.

These aspects were demonstrated at a convenient development cost of 0.57US$ per prototype, and for fabrication times under 30 min.

REFERENCES

[1] Fabrication, Implementation, and Applications, in Microfluidics and Nanofluidics Handbook, ed. S. Mitra and S. Chakraborty, CRC Press Taylor & Francis Group, Boca Raton, 2012.

[2] J. Love, D. Wolfe, H. Jacobs and G. Whitesides, Langmuir, 2001, 17, 6005.

[3] C. Sun, N. Fang, D. Wu and X. Zhang, Sens. Actuators, A, 2005, 121, 113.

[4] P. Preechaburana, D. Filippini, Lab Chip 11, 2011, 288.

[5] J. McDonald, M. Chabinyc, S. Metallo, J. Anderson, A. Stroock and G. Whitesides, Anal. Chem., 2002, 74, 1537.

[6] P. Kitson, M. Rosnes, V. Sans, V. Dragone, L. Cronin, "Configurable 3D-Printed millifluidic and microfluidic 'lab on a chip' reactionware devices", Lab Chip, 2012, 12, 3267.

[7] MiiCraft®, MiiCraft 3D Printer, http://www.miicraft.com/products/

[8] G. Comina, A. Suska, D. Filippini, "Low cost lab-on-a-chip prototyping with a consumer grade 3D printer", Lab Chip 14, 2014, 2978.

[9] G. Comina, A. Suska, D. Filippini, " PDMS lab-on-a-chip fabrication using 3D printed templates", Lab Chip 14, 2014, 424.

[10] M. Zhou, Z. Diwu, Z. Panchuk-Voloshina, N. Haugland, Anal. Biochem, 1997, 253, 162.

[11] N. Nguyen and Z. Wu, J. Micromech. Microeng., 2005, 15, R1.

CONTACT

* D. Filippini, danfi@ifm.liu.se

1. Sensors

REAL-TIME COMPOSITION DETERMINATION OF GAS MIXTURES

E.J. van der Wouden*[1] and J.C. Lötters[1,2]
[1] Bronkhorst High-Tech BV, Ruurlo, The Netherlands
[2] University of Twente, Transducers Science and Technology, Enschede, The Netherlands

ABSTRACT

In this paper we describe the development of a model and system to analyse the compositions of gas mixtures up to 4 components. We present measurements with binary and ternary mixtures, on compositions with components that range over an order of magnitude in the value for the measured physical properties. The system is consists of a coriolis, density, pressure and thermal flow sensor. With this system it is possible to measure the viscosity, density, heat capacity and flow rate of the medium. We demonstrate that if the properties of the individual components are known, binary mixtures can be analyzed within 1 % and ternary within 2 % accuracy.

KEYWORDS

Multi Parameter, gas mixtures, thermal flow sensor, coriolis flow sensor.

INTRODUCTION

In flow dosing systems there is a demand to not just measure or control flowrate, but also measure the type or composition of the flow. For instance in biogas production; here the measurement of methane and inert gas fractions can give information about the energy content and in this way serve as a quality control [1-5]. A second example is purging of reaction chambers in semiconductor industry. Many processes here involve toxic or explosive gasses. Before equipment, that contains these gasses, can be opened, it should to be properly purged. A real-time monitoring system of gas composition can help to indicate threshold levels for harmful gasses and signal when it is save to open the reaction chamber. In this way reduce costly down time of equipment and aid in operator safety. Here we show that by combining a medium independent Coriolis mass flow measurement with thermal and pressure sensors, we can extract physical properties of the medium. In a second calculation step, the composition can be calculated based on these measured medium properties

Model

The model presented in figure 1 links a pressure, density, thermal and Coriolis sensor [5]. The latter one acts as a medium independent mass flow sensor. The thermal sensor gives an output that is proportional to both the mass flow and heat capacity of the medium. Linking the two sensors yields an independent measurement of the heat capacity. Secondly, with an independent measurement of the medium density, the volume flow can be determined by combining density and mass flow. This finally gives the viscosity when the pressure needed to drive the volume flow through a fixed flow obstruction is measured in the laminar flow regime.
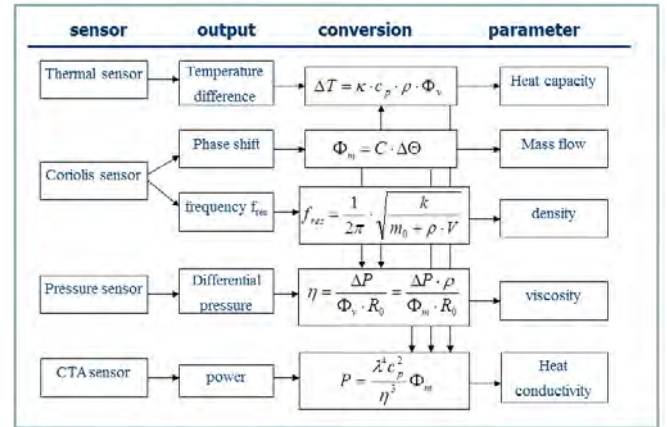

Figure 1: Schematic overview of the sensors, their relations and their transfer function.

When a gas mixture is composed of a limited number of components, the measured physical properties can be used to analyse this composition.

Formula one illustrates how the total heat capacity is a sum of the contribution of the two components. Since the total fraction is one, this equation can be solved and yield the compositing if the heat capacity of the two components. In the formula c_p, c_{p1}, c_{p2}, φ_1 and φ_2 are respectively the total heat capacity, the heat capacity of component 1 and two and the mass fractions of the two components.

$$cp = cp_1 * \varphi_{m1} + cp_2 * \varphi_{m2} \qquad (1)$$

Formula 1 can be expanded to include all the parameters measured in our system. When written as a function of the volume fraction and put into matrix form, this yields equation 2

In formula 1 and 2 cp, φ_m, φ, η and ρ are respectively the heat capacity at constant pressure, mass fraction, volume fraction, viscosity and the

density. The subscripts indicate mixture components.

$$\begin{pmatrix} \rho_1 & \rho_2 & \rho_3 & \rho_4 \\ \eta_1 & \eta_2 & \eta_3 & \eta_4 \\ 1 & 1 & 1 & 1 \\ \frac{c_{p1}}{\rho_{tot}} & \frac{c_{p2}}{\rho_{tot}} & \frac{c_{p3}}{\rho_{tot}} & \frac{c_{p4}}{\rho_{tot}} \end{pmatrix} * \begin{pmatrix} \varphi_1 \\ \varphi_2 \\ \varphi_3 \\ \varphi_4 \end{pmatrix} = \begin{pmatrix} \rho \\ \eta \\ 1 \\ c_p \end{pmatrix} \quad (2)$$

It becomes clear from formula 2, that with our system we are able to analyse gas mixtures of up to four components. For this analysis it is necessary that the physical constants of the components are known, and that at least one constant makes the gas distinguishable from the other components.

Results

A schematic drawing of the setup is shown in figure 2. The coriolis, thermal and pressure sensor are respectively a M13, F-111AC and P-502C all manufactured by Bronkhorst High-Tech B.V. The density meter is a northdome sensor purchased from Avenisense. Mixtures where supplied by controlling the gas flow of the individual components with thermal mass flow sensors at a constant total volume flow of 1 lit/ min. The pressure is measured over the thermal flow sensor, since over this section the flow is in the luminaire Hagen-Poiseuille regime, where there is a linear relation between pressure and volume flow.
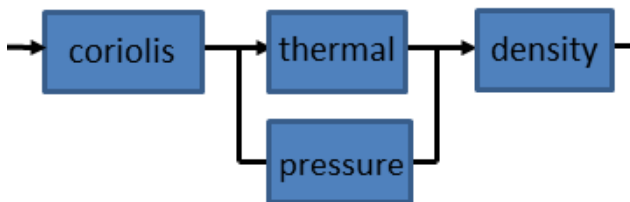

Figure 2: schematic of the measurement setup.

The first result shown in figure 2 gives the volume fraction of an air hydrogen mixture based on the measured heat capacity. The bottom graph in figure 2 shows a result for a methane nitrogen mixture. In the figure both the measured heat capacity as the heat capacity calculated based on the applied flow rates of the components are plotted. The inset of the picture shows the calculated and applied volume flow rate. The calculated fractions are calculated with the aid of formula 1 and converted to volume fractions.

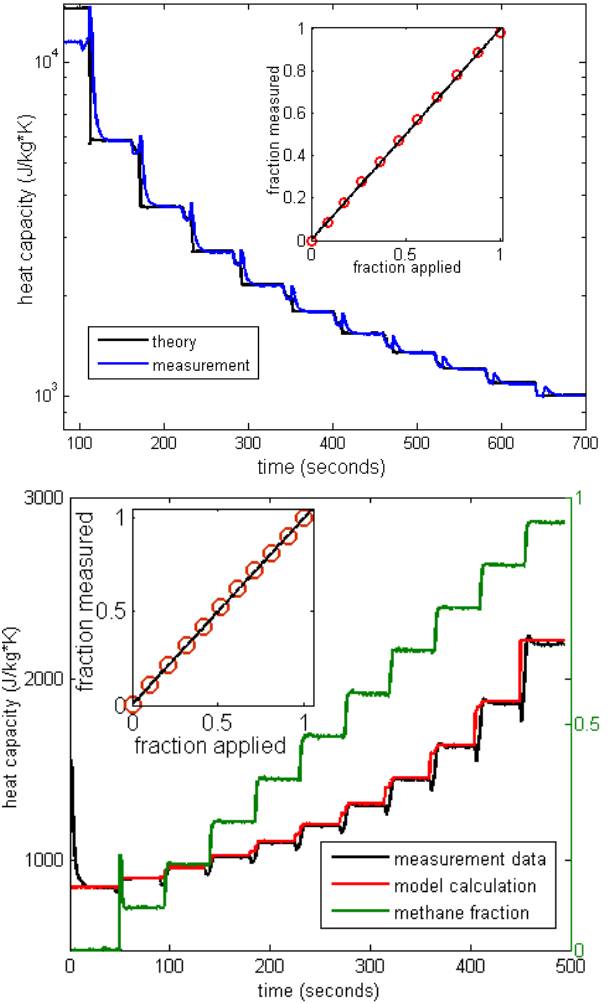In both cases the volume flow fractions, could be calculated with an accuracy of less than 1 %.

Figure 3: top) mole fraction of a hydrogen/air mixture based on the measured heat capacity. Bottom) mole fraction of methane/nitrogen mixture.

The measured heat capacity shows deviation for 100 % hydrogen, this most likely is due to slight contamination with air, due to the large difference in density and heat capacity the difference between theory and measurement can already be accounted for by a 0.1 v/v % air fraction in the hydrogen flow.

In figure for a measurement result is given for a mixture of hydrogen, air and argon. Since the mixture consists of only three fractions, three equations suffice to yield a solution. Since we measure the mass flow and pressure we can calculate the ratio between the density and viscosity, as can be seen in figure 1. Based on this parameter together with the measured heat capacity we calculate the volume fraction of the three components.
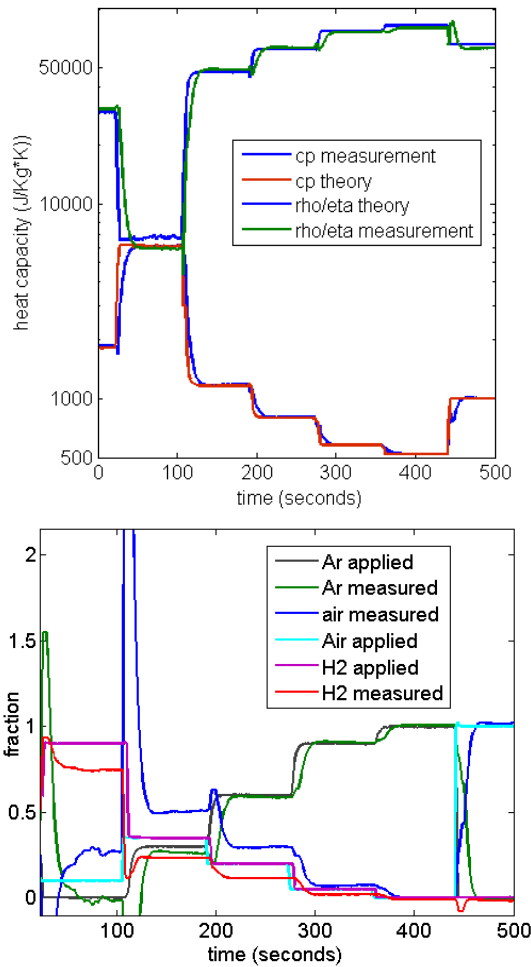
2$^{\text{nd}}$ International Conference on MicroFluidic Handling Systems
8 – 10 October 2014, University of Freiburg, Germany

38

Figure 4: Top) heat capacity and ratio between density and viscosity. Bottom) calculated volume fraction of the three components.

It can be seen in the top figure that for the ratio between density and viscosity as well as the heat capacity, there is a good agreement between the theory and the measurement results. This however, does not result in an accurate calculation of the volume fractions. The result in the bottom graph of figure 4 indicates that there is good correlation between applied and measured fractions, however, with large absolute variations.

The resulting variations are caused largely by selectivity of the measured parameters. It can be seen in the top part of figure 4 the 2 measured parameters are each other's inverse and hence cannot be used adequately to calculate the composition. By incorporating a separate density measurement the measurement can be more specific.

Table 1: gas properties of nitrogen and carbon oxide.

Property/ component	Nitrogen	carbon monoxide	Hydrogen
density	1.150	1.150	0.083
Heat capacity	1040	1043	14300
viscosity	$1.747 \cdot 10^{-5}$	$1.665 \cdot 10^{-5}$	$8.8 \cdot 10^{-6}$
Thermal conductivity	0.02487	0.026	0.176

Table 1 illustrates a limitation of this method. It can be seen that although heat capacity and density are very different for hydrogen and nitrogen, the product is the same. Furthermore it can be seen, that for carbon monoxide and nitrogen all the parameters listed in the table are almost identical. This is caused by the very similar molecular structure and atomic weight. To test if a density measurement can improve the results we have performed tests on a mixture of methane, nitrogen and carbon dioxide. We have selected a mixture of these three components since this resembles the composition of certain types of biogas.
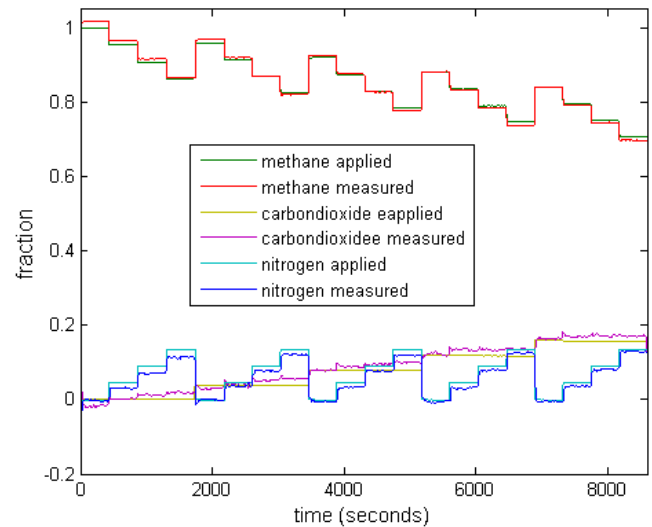
Figure 5: The caption should be placed after the figure.

Conclusions

We have designed and realized a system and model with which we can real-time determine the composition of gas mixtures, if the properties of the components of the mixture are sufficiently distinguishable. The model is based upon a multi-parameter flow measurement system, consisting of a Coriolis and thermal flow sensor, a density meter and a pressure sensor. The system enables direct measurement of flow rate and physical properties of gas mixtures. Binary mixtures have been measured with accuracy of better than 1 %. Ternary mixture has been measured within 2 % for a mixture of methane, nitrogen and carbon dioxide.

REFERENCES

[1] A.J. Mouris, Optimized fired heater control, Hydrocarbon Processing, November 2010, pp. 65–68

[2] P. Ulbig, D. Hoburg, Determination of the calorific value of natural gas by different methods, Thermochimica Acta, 382 (2002), pp. 27–35

[3] Lötters, J.C. and Lammerink, T.S.J. and Pap, M.G. and Sanders, R.G.P. and Boer, M.J. de and Mouris, A.J. and Wiegerink, R.J., Integrated micro Wobbe index meter; towards on-chip energy content measurement. In: IEEE 26th International Conference on Micro Electro Mechanical Systems, MEMS 2013, 20-24 January 2013, Taipei, Taiwan (pp. pp. 965-968)

[4] http://www.bright-sensors.com

[5] S. Udina, et al., A micromachined thermoelectric sensor for natural gas analysis: Multivariate calibration results, Sens. Actuators B: Chem. (2012), pp. 551–558

[6] J.C. Lötters, E. van der Wouden, J. Groenesteijn, W. Sparreboom, T.S.J. Lammerink, R.J. Wiegerink, Integrated multiparameter flow measurement system, In: 27th IEEE International Conference on Micro Electro Mechanical Systems, MEMS 2014, 26-30 January 2014, San Francisco, CA, USA (pp. 975-978)

CONTACT
* E.vanderWouden@bronkhorst.com

2. Actuators   Poster or Presentation
(please choose category from list)   (if requesting poster)

METHOD FOR THE DETERMINATION OF THE THERMAL PROPERTIES OF GASES UNDER FLOW CONDITIONS

D.F. Reyes-Romero[1,2], G. Urban[1]
[1] University of Freiburg, Laboratory for Sensors, Freiburg, Germany
[2] Innovative Sensor Technology AG, Ebnat-Kappel, Switzerland

ABSTRACT

This contribution presents a measuring technique for determining the thermal conductivity k and volumetric heat capacity ρc_p of gases in a channel under flow conditions. This method relies on the reduction of the penetration depth associated to the thermal oscillations produced by a heater placed on a wall of the channel. This turns the oscillatory heat transfer (at 200 Hz) between a germanium thermistor and an encircling chromium heater independent of the flow rate. The thermal conductivity of gases is successfully determined under flow conditions. The ultimate goal is to achieve independent flow measurement using a simple calorimetric flow sensor.

KEYWORDS

Flow sensor; thermal conductivity; gas characterization; AC thermal excitation

INTRODUCTION

The thermal transfer between two distinct static points inside a fluid in motion not only depends on the thermal properties of the fluid but also on its state of motion. In consequence, a direct measurement of the thermal conductivity and volumetric heat capacity of a fluid is not possible if its state of motion is unknown. Conversely, determining the flow velocity of a fluid in motion by using thermal techniques requires foreknowledge of its thermal properties. This restriction can be better described by the heat transfer equation [1]:

$$\rho c_p \frac{\partial T}{\partial t} + \rho c_p (\vec{u} \cdot \nabla T) = k \nabla^2 T + \dot{q} \qquad (1)$$

where T is the local temperature, u the velocity field and q the local heat generation. The relationship between temperature and heat generation is affected by both the thermal properties of the fluid and the velocity field.

It has been shown that it is possible to determine the thermal conductivity and thermal diffusivity ($\alpha = k/\rho c_p$) of stagnant liquids [2] or liquids moving with a known flow rate [3]. These methods use oscillatory thermal excitation to enable the derivative term in Eq. (1), which allows for determining the thermal diffusivity. The output signals, amplitude and phase of the temperature oscillations, are measured

and fitted to an analytical model along a wide frequency range. This renders these methods rather slow.

Another technique based on steady oscillatory thermal excitation for stagnant fluids is the 3ω method. A fine, thin-film, straight heater is subjected to an AC current. Its temperature, also sinusoidal, is then measured. The resulting amplitude and phase shift are related to the thermal properties of the fluid [5], [6]. This method also requires sweeping the frequency throughout a rather wide range, thus increasing the measurement time.

The challenge to determine the thermal properties of fluids in motion implies bringing them to state of motionless or known velocity. A by-pass or dead-end cavity is usually applied for this purpose [7]. However, this increases the complexity of the sensor. In this contribution, we present a method for measuring the thermal conductivity and volumetric heat capacity with a single micromachined calorimetric flow sensor.

SENSOR DESCRIPTION

The sensor features a circular, 1-mm-diameter, SiO_2-SiN_x, insulating membrane. Like typical calorimetric flow sensors, a heater is placed at the center of the membrane while two temperature sensors are placed up- and downstream (see Figure 1). The chromium heater closely surrounds an additional central thermistor (CT); this is a key feature that allows for fluid characterization.
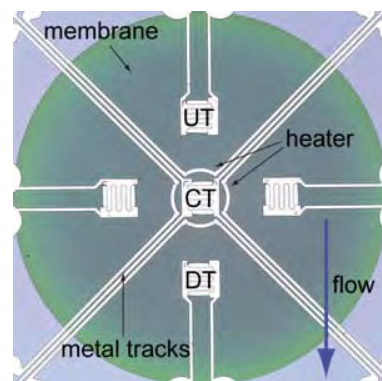

Figure 1. Close view of the SiO_2-SiN_x membrane including the central thermistor (CT) and the heater around it. Up- and downstream thermistors allow for flow measurement (UT, DT).

MEASUREMENT PRINCIPLE

As discussed before, to measure the thermal properties of fluid in motion, it is necessary to confine the heat exchange between the heater and the fluid to a region where the fluid is motionless.

A heater is placed on the surface of a channel's wall. A thermal boundary layer forms in the flowing gas in the vicinity of the heater (see Figure 2). The thickness of this boundary layer is proportional to $(\alpha/\omega)^{1/2}$, where ω is the angular frequency [4]. Hence, by increasing the frequency, most of the heat exchange is confined to a narrow region of low flow velocity close to the channel's wall. Due to the non-slip condition, the local velocity is invariably close to zero regardless of the flow rate, as long as the flow regime stays laminar.

Hong and Kim [4] exploited this to determine the thermal conductivity of flowing liquids using the 3ω method provided that the following criterion is held:

$$2u/(D\omega) < 2.5, \qquad (2)$$

where u is the average flow speed and D the hydraulic diameter of the channel.

The main drawback of the 3ω method, as mentioned above, is that it requires sweeping over a range of frequencies, thus increasing the measuring time. Here, a single-frequency heating signal is proposed. The measurement signals are the amplitude $|\theta_{CT}|$ and the phase shift ϕ_{CT} of the measured temperature oscillations. This phase shift is measured with respect to the heating signal.

Since the heater and the central thermistor are very close to each other, it is expected that the amplitude $|\theta_{CT}|$ and the phase shift ϕ_{CT} depend only on the thermal properties of the gas regardless of the flow rate, that is, they can be expressed as $|\theta_{CT}| = f(k, \rho c_p; a_i)$ and $\phi_{CT} = g(k, \rho c_p; b_i)$, where a_i and b_i are parameters that only depend on the geometry and properties of the sensor itself.

MODEL

A simple analytical model is proposed in order to determine the relationship between the thermal properties of the gas and the signals $|\theta_{CT}|$ and ϕ_{CT} in a similar fashion as the model proposed by Beigelbeck et al. [3]. *Figure* 3 shows the corresponding simplified two-dimensional geometry. It features a central thermistor surrounded by two sections of the heater; both structures have an infinitesimal thickness and are embedded inside the membrane. The model considers four different regions: the membrane sections over and under the heater, the channel region, and the stagnant gas region below the membrane. The same gas occupies the regions above and below the membrane, thus maximizing the sensitivity to the thermal properties.

Since the excitation frequency is assumed to be large, based on Hong's criterion (Eq. 2), the effect of the flow rate is negligible. Hence, the flow rate in the channel above the membrane is assumed to be zero. Hence, the model solves the heat equation in the frequency domain without the convection term (second term in Eq. 1), that is, its Fourier transform:

$$\frac{\partial^2 \theta_i}{\partial x^2} + \frac{\partial^2 \theta_i}{\partial y^2} - \frac{j\rho_i c_{p,i}\omega}{k_i}\theta_i = 0 \qquad (3)$$

where θ represents the temperature field in the frequency domain. Solving Equation (3) requires numerical integration.

MEASUREMENT METHOD

Figure 4 presents the resulting contour plots relating $|\theta_{CT}|$ (left) and ϕ_{CT} (right) to k and ρc_p of the gas for an average heating power of 0.5 mW and a frequency of 200 Hz. For a wide channel with a height of 600 µm, this frequency guarantees flow independency for average flow velocities up to about 2 m/s (see Eq. 2). Plots in Figure 4 correspond to the parameters summarized in the Table 1. Since the
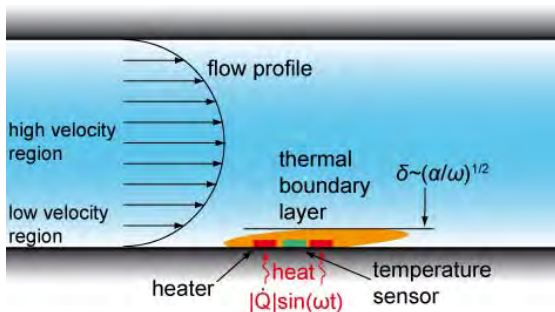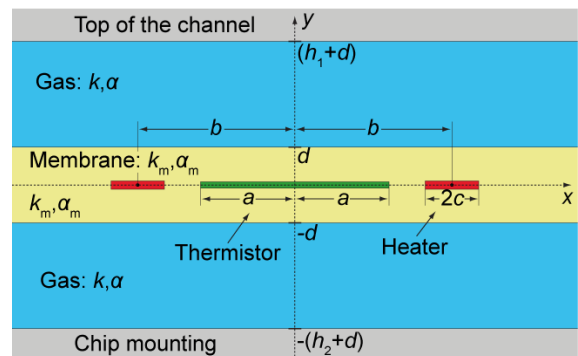

Figure 2: Modulation of the thermal penetration by means of the frequency of the heating signal. The thermal boundary layer is confined to a region of low flow velocity.

Figure 3. Simplified representation of the analytical AC model

2. Actuators   Poster or Presentation
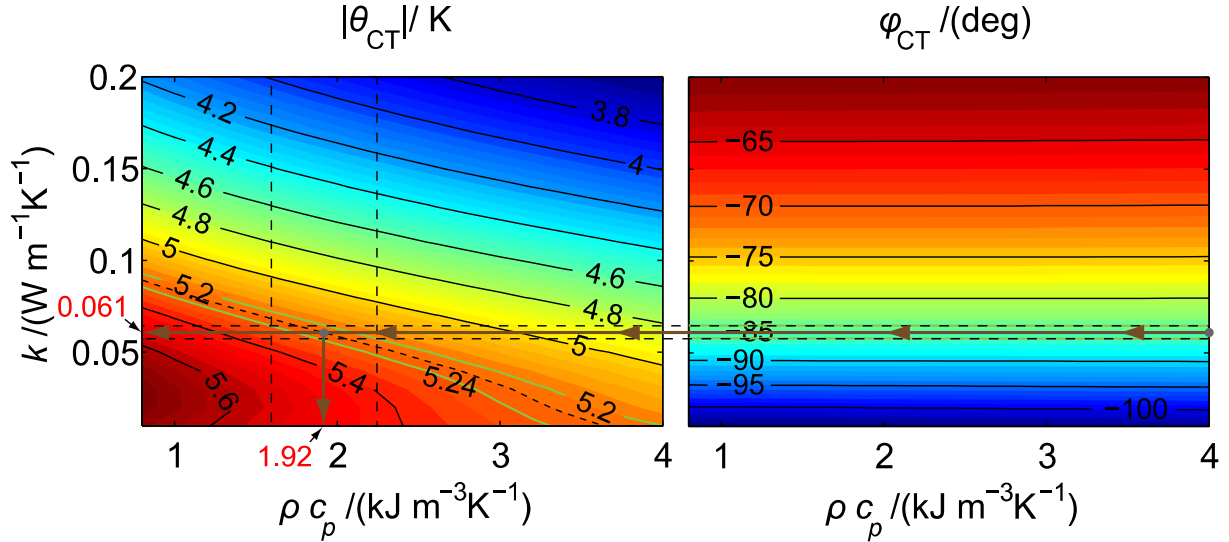(please choose category from list)   (if requesting poster)

Figure 4. Graphical representation of the procedure to determine the thermal properties of an unknown gas using thermal excitation at 200 Hz.

phase contour lines (right panel) are completely horizontal, the phase signal solely depends on the thermal conductivity. This relationship is found to be

$$\phi_{CT} = -a + b\ln(k+c) \qquad (4)$$

with a, b, and c being sensor-specific constants. Given the parameters in Table 1, these constants are found to be $a = 210.38°$, $b = 27.417°$, and $c = 36$ with k in $Wm^{-1}K^{-1}$. Equation (3) allows for direct determination of the thermal conductivity of a gas under flow conditions.

On the other hand, the contour lines corresponding to the amplitude signal $|\theta_{CT}|$ depend on both k and ρc_p (see left panel in Figure 4). Since the slopes of the contour lines are rather small, the thermal conductivity is the dominant parameter on the amplitude signal.

Nevertheless, both contour plots in Figure 4 can be used to determine ρc_p. For instance, let us assume that the heater harmonically generates heat at 200 Hz with an average power of 0.5 mW. A measurement of the amplitude $|\theta_{CT}|$ and phase ϕ_{CT} of the temperature oscillations at the central thermistor gives 5.24 K and

−85°, respectively. Now, the thermal conductivity can be directly determined using Equation (4), that is, $0.061 \ Wm^{-1}K^{-1}$. Then, a horizontal (brown) line can be projected from the right panel into the left panel until it intersects the amplitude contour line corresponding to 5.24 K. This point corresponds to the volumetric heat capacity of the gas, in this case, $1.92 \ kJm^{-3}K^{-1}$, obtained by projecting a vertical line from the point of intersection down to the ρc_p-axis.

Let us suppose that the measurement error on the amplitude and phase signals is about 1%. The corresponding error regions are delimited by the black dashed lines in Figure 4. The resulting relative error on the thermal conductivity is about 5%. On other hand the error on the volumetric heat capacity goes as high as 33%, which is rather high. This large error on ρc_p results from the fact that most of the contour lines in Figure 4 form a small angle with the ρc_p-axis, thus making the thermal conductivity the dominant parameter as mentioned before.

As a comparison, if the error on $|\theta_{CT}|$ and ϕ_{CT} is 0.5%, then the relative error on the thermal conductivity is about 2.5%, and on the volumetric heat capacity about 16.7%, which is still rather high.

Table 1: Parameters from the model in Figure 3 used to obtain the plots in Figure 4

Parameter	Value
a	57.5 µm
b	65 µm
c	1.75 µm
d	0.75 µm
h_1	600 µm
h_2	1000 µm

EXPERIMENTAL

To verify the behavior described by the analytical model, the flow sensor was placed in the bottom of a small flow channel ($14 \times 0.6 \ mm^2$). Two mass flow controllers regulate the amount of gas coming from two different gas bottles in to a mixing tube, which is connected to the inlet of the channel. The channel's outlet leads to open space (1 atm, 25°C). Several pure inert gases and some binary mixtures have been used.

Gases were selected to cover a wide range of thermal conductivity and volumetric heat capacity. The flow rate inside the channel was varied from 20 sccm up to 1000 sccm, which corresponds to an average velocity of 2 m/s. Under these conditions and for all gases, laminar flow regime is guaranteed.

The temperature at the central thermistor is measured with a trans-impedance amplifier. The resulting voltage signal is then digitally acquired. A lock-in amplifier implemented in LabVIEW was used to determine the amplitude and phase shift of the acquired signal.

Figure 5 depicts the phase shift ϕ_{CT} measured by the central thermistor in terms of the thermal conductivity of the gas. Error bars around each point represent the total variation of ϕ_{CT} as the flow rate was increased from 20 sccm up to 1000 sccm; for all points, this variation is under 2.5%. Helium shows the largest error due to its low density, which allows the atmospheric air to enter into the channel across the outlet at low flow rates.

Equation (4) was subsequently used to fit the data points in Figure 5. A least-squares regression results in the black dashed line. This fit successfully matches all measuring points. Therefore, the validity of Equation (4) is confirmed. The resulting regression parameters are a = -191.7, b = 27.05 and c = 27.83. These values differ from the theoretical values obtained in the previous section because the analytical model only considers a two-dimensional geometry.
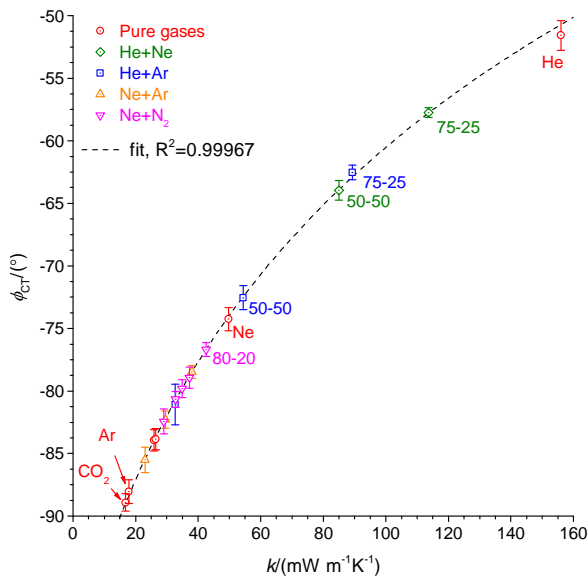

Figure 5. ϕ_{CT} vs. k at 200 Hz for various gases and flow rates up to 1000 sccm. The label numbers represent the mole percentage of the corresponding binary gas mixtures. The dashed line corresponds to the least squares fit on the experimental data.

Yet, the model is able to predict the general behavior of the sensor.

Since the thermal conductivity is the dominant parameter over the amplitude $|\theta_{CT}|$ (Figure 4), the measurement error required on $|\theta_{CT}|$ has to be very small. Therefore, for the measurement setup used, it was not possible to determine the thermal conductivity based on the method presented in the previous section.

CONCLUSION

Determination of the thermal properties of flowing gases is possible by means of sinusoidal heat excitation. The criterion proposed by Hong [4] for liquids was verified also for gases.

Although the volumetric heat capacity cannot be yet determined with the presented sensor, this should be possible by improving the measurement error and the analytical model, which should consider a three-dimensional geometry.

REFERENCES

[1] J. H. Lienhard IV and J. H. Lienhard V, *A heat transfer textbook*, Phlogiston Press, Cambridge, Massachusetts, U.S.A., 3rd edition, 2008.

[2] J. Kuntner, F. Kohl, B. Jakoby, "Simultaneous thermal conductivity and diffusivity sensing in liquids using a micromachined device," Sens. and Act. A: Phys., 130-131 (0), pp. 62–67, 2006.

[3] R. Beigelbeck, F. Kohl, S. Cerimovic, A. Talic, F. Keplinger, B. Jakoby, "Thermal property determination of laminar-flowing fluids utilizing the frequency response of a calorimetric flow sensor", *Proc. 2008 IEEE Sensors Conference*, pp. 518–521, 2008.

[4] J. Hong, D. Kim, "Measuring the Thermal Conductivity of Flowing Liquid Samples Using the Three Omega Method", Journal of Heat Transfer, Vol. 134 (9), pp. 094502, 2012.

[5] I. K. Moon, Y. H. Jeong, S. I. Kwun, "The 3ω technique for measuring dynamic specific heat and thermal conductivity of a liquid or solid," Review of Scientific Instruments, 67(1), p. 29, 1996.

[6] S. Gauthier, A. Giani, P. Combette. "Gas thermal conductivity measurement using the three-omega method," Sens. and Act. A: Phys., 195, pp. 50–55, 2013.

[7] M. Grinstein, J. Y. Mantinband, S. Bentov, M. Adler, "Flow rate meter," US Patent Application US 20130041234 A1, 2013.

CONTACT

* D. F. Reyes-Romero, diego.reyes@ist-ag.com, reyes@imtek.de

4. Fluidic control systems or 5. Applications   Presentation

MICRO FLOW STANDARD FOR STEADY AND PULSATING FLOW

H. Bissig ,M. Tschannen and M. de Huu
Federal Institute of Metrology METAS, Bern-Wabern, Switzerland

ABSTRACT

Micro and nano flow calibrations are important in several applications such as volumetric dosage or drug delivery where the exact amount of the delivered volume or a stable flow rate is crucial for the efficient operation. However, international traceability in the micro and nano flow is not validated up to date in Europe for flow rate ranges below 33 µl/min. METAS develops in the framework of the EMRP project "HLT07 Metrology for Drug Delivery" [1, 2] a primary standard to cover the flow rate range from 1 ml/min down to 100 nl/min with uncertainties in the range from 0.1 % to 0.6 % and calibration of pulsating flow rates from 1 ml/min down to 1 µl/min with measurement uncertainties from 0.2 % to 2.7 %. (coverage factor 95 %).

KEYWORDS

Micro flow, liquid, dynamic gravimetric calibration, pulsating flow

DESIGN OF THE FACILITY

To realize such small flow rates with the appropriate flow rate stability METAS applies the principle of generating the flow by means of a constant pressure drop over a capillary tube according to the law of Hagen-Poiseuille. As shown in Fig. 1 and Fig. 2, a metallic bellow is immerged into a water tank where the water pressure is controlled by expanding or compressing the metallic bellow by means of adjusting the air pressure inside the bellow with a pressure controller. For this part, the air pressure inside the bellow is adjusted according to the signal of a pressure sensor inside the water tank in order to reach the desired water pressure in the tank. The stability of the water pressure is guaranteed by means of a regulation loop controlled by software. The pressure drop from the water tank to the atmospheric pressure at the outlet needle and the size of the capillary tube determine the flow rate.

The facility is designed in such a way that the water pressure upstream the DUT (Device Under Test) can be varied to some extent. In one mode, the water flows from the capillary tube through the DUT and finally in the measurement beaker on the balance. The main pressure drop occurs over the capillary tube and this means that the pressure difference with respect to the ambient pressure upstream the DUT is very small. In a second mode, the water is first guided

through the DUT and then through the capillary tube and in the measurement beaker on the balance. In this case the water pressure upstream the DUT is similar to the water pressure in the water tank.
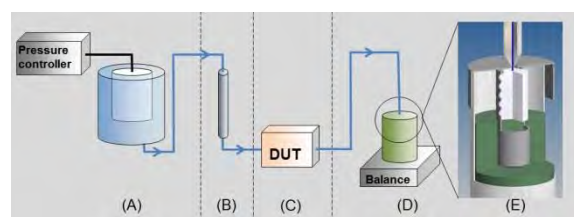

Figure 1: Simplified drawing of the working principle of the facility. (A) water tank with immerged metallic bellow and pressure controller, (B) capillary tube, (C) device under test (DUT), (D) measurement beaker on the balance, (E) detailed cross-section of the top part of the measurement beaker.
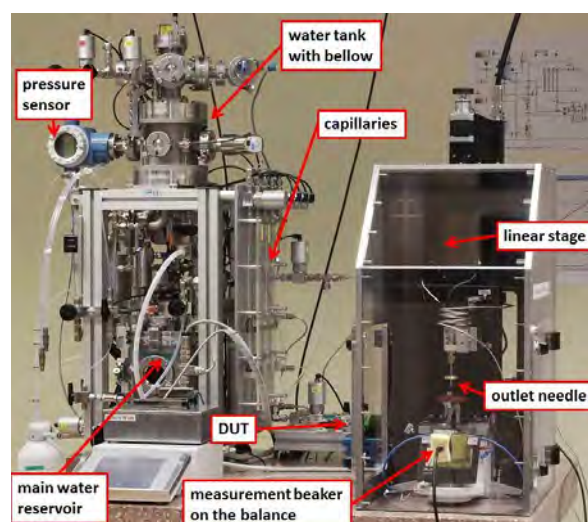

Figure 2: Photograph of the facility with the main components: water tank with metallic bellow, capillary tubes, device under test (DUT), measurement beaker on the balance, main water reservoir.

Evaporation rate

An important issue is the evaporation rate of the water in the beaker during the measurement. To control this process we apply the conventional method of adding water in an evaporation trap in the weighing zone where the air is then saturated with humidity. Additionally, we have built a special measurement beaker as drawn in the detailed cross-section in Fig. 1 (E). The outlet needle is positioned above the glass filter (white disc) where the water enters the measurement beaker. The capillary force in the glass filter sucks the water in before any droplet can be

formed at the surface. The water cleaves its way through the glass filter and continues in the water-absorbing foam into the bulk. This prevents the water to be at the surface. With this setup we get stable evaporation rates of (3.15 ± 0.50) µg/min or (3.16 ± 0.50) nl/min respectively and (3.42 ± 1.00) µg/min or (3.43 ± 1.00) nl/min respectively depending on the porosity of the glass filters used.

Gravimetric flying start-stop method

The measurements are performed by means of the dynamic gravimetric flying start-stop method. This means that the desired flow rate is set and the data acquisition is only started once the flow rate has reached a steady state. Therefore, the measurement beaker is continuously filled with water and the weighing data are continuously collected with the time stamp of the balance at an acquisition rate of 10 Hz.

Determination of flow rate

The collected weighing data are then fitted by means of the "Trust-region Levenberg-Marquardt algorithm" [3] where the uncertainties in the dependent as well as the independent variable are taken into account. To perform the fit, we use the Software IGOR Pro and the fitting function "Orthogonal Distance Regression (ODR)" [3, 4].

Flow rate determination is best explained using an example. We choose a fixed time window of 23 minutes for the flow rate shown in Fig. 3 as white and light gray portion and perform an ODR linear fit on the collected data. The resulting mass flow rates are then converted to volume flow rates and are shown in Fig. 4 as black empty circle and light gray full triangle with their uncertainties. The time stamp of the determined volume flow rate of each fixed time window is the center time of these data. This guarantees that any strong change in the flow rate is detected at the occurring time independently on the chosen fixed time window. By increasing the starting time of this fixed time window by time steps corresponding to the acquisition rate of 10 Hz we can follow the evolution of the flow rate in time. Applying this to the collected weighing data shown in Fig. 3 we get the evolution in time of the volume flow rate as shown in Fig. 4.
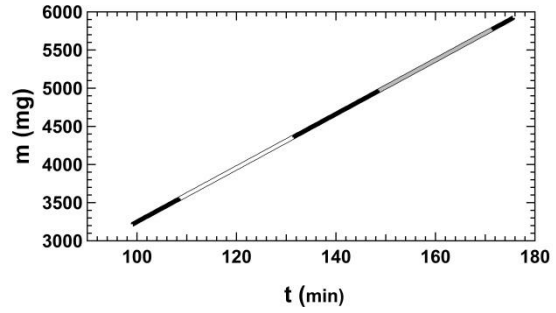

Figure 3: Increase of mass as a function of time. Two time window of 23 minutes are shown in white and light gray.
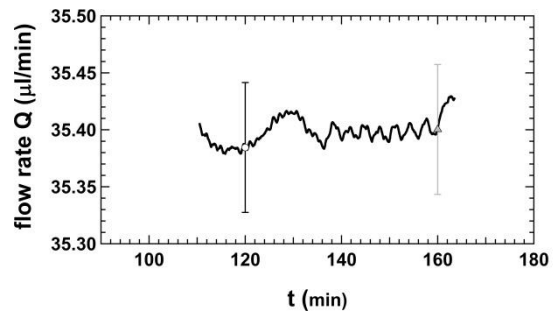

Figure 4: The determined volume flow rate as a function of time. The black empty circle and light gray full triangle are the determined volume flow rates corresponding to the data in the time windows (white and light gray) in Fig. 3.

Flow rate stability

As mentioned in the beginning, the flow rate stability is very important. In Fig. 5, we show the evolution in time of the reference volume flow rate already shown in Fig. 4 and the corresponding data of the DUT (mini Cori-Flow M12P from Bronkhorst, flow rate at 1 % of full scale [5]) where the deviations to the mean reference volume flow rate of 35.42 µl/min are plotted as a function of time. To illustrate the flow rate stability, the uncertainty (k=2) of the reference volume flow rate of 0.16 % is added on the Fig. 5 as black dashed lines and we observe the fluctuations being clearly within the uncertainties.

The histograms of the data shown in Fig. 5 are plotted in Fig. 6 in order to better visualize the flow rate stability of the reference volume flow rate as well as the volume flow rate of the DUT. We can clearly observe that the stability is very good and we obtain a distribution with $\sigma = 0.032$ % for the reference volume flow rate, as seen in Fig. 6.
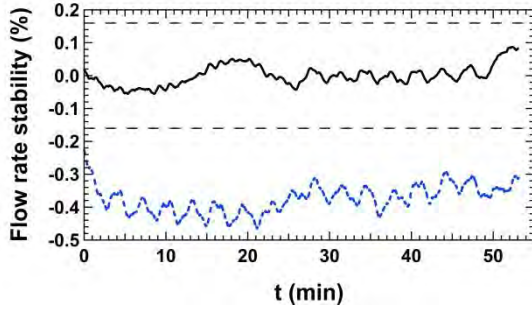
Figure 5: Evolution in time of the relative deviation of the reference volume flow rate (solid black line) from the mean value of 35.42 μl/min and the corresponding relative deviation of the DUT (doted blue line). To illustrate the flow rate stability, the uncertainty (k=2) of the reference volume flow rate of 0.16 % (dashed black line) is added where the fluctuations are clearly within the uncertainties.
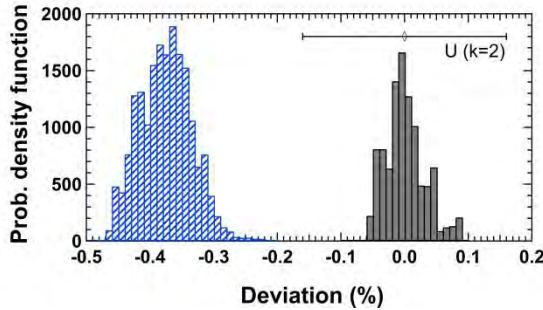

Figure 6: Histogram of the data shown in Fig. 5. (Full dark gray bars) Distribution of the reference volume flow rate with σ = 0.032 % and the corresponding uncertainty (k=2) of the reference volume flow rate. (Dashed blue bars) Distribution of the volume flow rate of the DUT.

CALIBRATION OF FLOW METER IN STEADY FLOW

In Fig. 7 and 8, calibration results for steady flow of commercially available Coriolis flow meters and thermal flow meters are shown, which highlight the repeatability and the reproducibility of the facility.
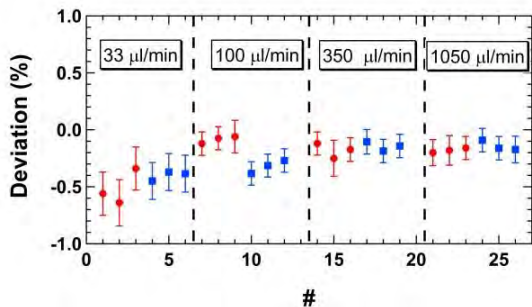

Figure 7: Calibration of a commercially available Coriolis flow meter "mini Cori-Flow M12P" from Bronkhorst High-Tech B.V. [5]. The red circles and the blue squares represent repeatability measurements whereas the different color codes represent the reproducibility measurements in the flow rate range from 1 ml/min to 33 μl/min.
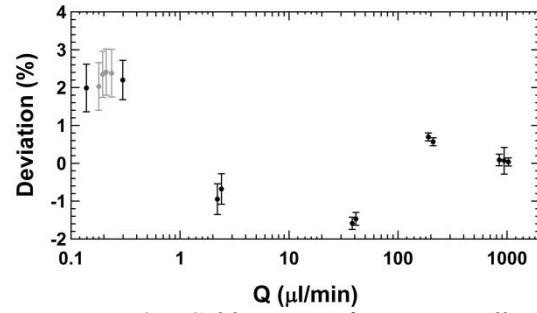

Figure 8: Calibration of commercially available thermal flow meters "SLG1430-025", "SLI-0430" and "SLI-1000" from Sensirion AG [6]. The black and gray full circles represent repeatability measurements whereas the different color codes in the range of 0.1 μl/min to 0.3 μl/min represent the reproducibility measurements in this flow rate range.

CALIBRATION AT PULSATING FLOW

Furthermore, the facility can generate unsteady flow by means of varying the water pressure in the water tank according to a desired pattern. This enables us to calibrate flow sensors under unsteady flow conditions in the flow rate range of 1 ml/min down to 1 μl/min.

Moreover, flow generators can be connected to the facility and calibrated in the same way. In Fig. 9, three calibration curves of a commercially available syringe pump are shown. The selected flow rate at the syringe pump is 100 μl/min and the instantaneous deviations to the reference flow rates are reported as a function of the syringe plunger position.

A reoccurring pattern of pulsating flow can be observed (highlighted in gray) where the cycles correspond to full rotations of the spindle of the syringe pump.

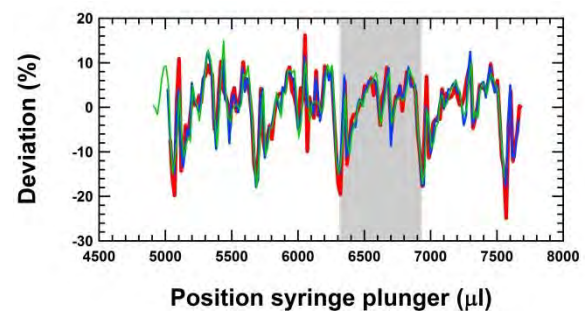*Figure 9: Three calibration curves of a commercially available syringe pump (NEXUS 3000 [7]) at the selected flow rate of 100 μl/min. The instantaneous deviations to the reference flow rates are reported as a function of the syringe plunger position. The reoccurring pattern of pulsating flow due to the full rotation of the spindle is highlighted in gray.*
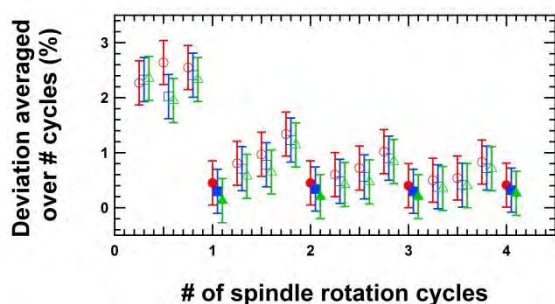
Figure 10: Mean deviation averaged over fractional value of spindle rotation cycles starting from the syringe plunger position of 7550 μl. The red circles, the blue squares and the green triangles are the mean deviations from the corresponding data shown in Fig. 9. Full symbols correspond to integer numbers of the spindle rotation cycles, whereas the empty symbols represent fractional values of spindle rotation cycles. The blue squares are shifted by 0.05 and the green triangles are shifted by 0.10 in the x-axis for clarity.

The average flow rate or the average deviation is then determined over an integer number of these cycles. To illustrate the significance of the average over an integer number of spindle rotation cycles, we show in Fig. 10 the averaged deviation as a function of the fractional value of the spindle rotation cycles starting from the syringe plunger position of 7550 μl. The red circles, the blue squares and the green triangles are the mean deviations from the corresponding data shown in Fig. 9. Full symbols correspond to integer numbers of the spindle rotation cycles, whereas the empty symbols represent fractional values of spindle rotation cycles. The blue squares are shifted by 0.05 and the green triangles are shifted by 0.10 in the x-axis for clarity. We can observe that the average over an integer value of the spindle rotation time leads to reproducible deviations, whereas fractional values of spindle rotation cycles can lead to erroneous deviations. Obviously, if the fractional value of spindle rotation cycles becomes larger, the erroneous discrepancy becomes smaller, even within the stated uncertainty of 0.4 % for this case.

CONCLUSIONS

The micro flow facility at METAS is developed to perform calibrations of steady flow rates from 1 ml/min down to 100 nl/min with measurement uncertainties from 0.1 % to 0.6 % and calibration of pulsating flow rates from 1 ml/min down to 1 μl/min with measurement uncertainties from 0.2 % to 2.7 %.

The flow rate range from 1 ml/min down to 10 μl/min has already been validated by means of an inter-comparison within the EMRP project [2, 8]. The lower flow rate range from 10 μl/min down to 100 nl/min is currently in the validation process where a research inter-comparison takes place within Euramet [9].

So far promising results of repeatability and reproducibility measurements of Coriolis and thermal flow meters as well as flow generators have been reported.

REFERENCES

[1] EMRP Call 2011 - Health, SI Broader Scope & New Technologies, HLT07 Metrology for drug delivery, www.euramet.org

[2] Website of the EMRP Project HLT07 MeDD, http://www.drugmetrology.com/

[3] IGOR Pro, WaveMetrics Inc., Version 6.21, ODRPACK95, Manual Version 6.21, Volume III, p. 229 Curve Fitting References

[4] W. Press, S. Teukolsky, W. Vetterling, B. Flannery, Numerical Recipes in C, New York: Cambridge University Press, 1992, ch. 15.3 Straight-Line Data with Errors in Both Coordinates, pp. 666 – 670, ch. 15.5 Nonlinear Models – Levenberg-Marquardt Method, pp. 681 – 688.

[5] Bronkhorst High-Tech B.V., www.bronkhorst.com

[6] Sensirion AG, www.sensirion.com

[7] Chemyx Datasheet NEXUS 3000 syringe pump, Chemyx Inc. www.chemyx.com

[8] Christopher David, Claus Melvad, Hugo Bissig and Elsa Batista. Research inter-comparison for small liquid flow rates (2 g/h to 600 g/h). Proceedings of Flomeko 2013, A10.4 – 314.

[9] Euramet, TC-F Projects, research inter-comparison E-1291. Comparison between recently developed primary standards. www.euramet.org

CONTACT

* H. Bissig, Hugo.Bissig@metas.ch

1. Sensors

DETECTION OF GAS KIND AND FLOW SPEED USING THERMAL FLOW SENSORS WITH DC EXCITATION IN A FLOWING FLUID

C.J. Hepp[1], F.T. Krogmann[1] and G.A. Urban[2]
[1]Innovative Sensor Technology IST AG, Ebnat-Kappel, Switzerland
[2]University of Freiburg, Freiburg Institute for Advanced Studies, Freiburg, Germany

ABSTRACT

A method for measuring flow speed and simultaneously thermal conductivity is presented in this contribution. The value of the thermal conductivity can be used to determine the gas concentration of binary gas mixtures. The chosen materials offer the possibility to excite the heating element in two different DC-modes – temperature and power. It is shown that thermal conductivity can be extracted from a flowing fluid by power excitation. Flow speed is determined afterwards by the use of temperature excitation. This procedure offers new application options for thermal flow sensors like use in biogas or breath gas analysis.

KEYWORDS

Calorimetric flow sensor, flow speed, thermal conductivity, gas concentration.

INTRODUCTION

The first thermal micro machined thermal flow sensor was presented over 40 years ago [1], since that time recent research has been done in this topic. Various applications use thermal flow sensors due to very low power consumption and excellent long-term stability [2]. In the market place, thermal flow meters are well established in different fields like process control and medical engineering. There are three main working principles [3]:

Sensors used in anemometers consist of at least one element, which can be used as joule heater and temperature senor. These sensors use the effect that a heated element is cooled by flow. There are several electronics available to monitor the flow rate; most common is the constant temperature anemometer (CTA). The electronic sets a constant temperature difference between heater and ambient by readjusting the power, which corresponds to the flow rate.

Calorimetric flow sensors feature usually one heater, which is surrounded by an upstream and downstream temperature sensor. The fluid is heated by the centered element and the heat distribution is detected. The temperature difference between up- and downstream element corresponds to the flow rate.

Sensors measuring the flow rate by the time of flight principle consist of a heater and distant temperature sensor located downstream. The time a heat plus needs between these two elements corresponds to the flow rate.

Thermal flow sensors are as well sensitive to thermal properties of the gas, where they are applied in. This demands a calibration to the application in order to achieve an accurate flow speed measurement. Table 1 shows thermal properties of several gases. It can be seen, how large the differences between the gases are.

By reason of this drawback, thermal flow sensors cannot be used in applications where the gas composition is varying over time, because this will lead to a significant measurement error. On the other hand, the detection of gas type or concentration and flow speed simultaneously allows new applications. Furthermore, the measurement of two parameters leads to unique features for the user. These sensors can be applied in anaerobic digestions or breath gas analysis. By flow speed and gas concentration measurement the fuel value of the fluid can be calculated or different medical examinations can be combined.

*Table 1. Thermal properties of analyzed gases at $T=20°C$; * at $T=25°C$ and $p=1bar$ [4].*

Gas	Thermal conductivity [mW / m K]	Spe. heat capacity [J / kg K]	Density [kg / m³]
CO_2	16.79	825	1.773
N_2	25.97	1041	1.123
Ar	17.84	521.5	1.603
Ne*	49.00	1030	0.828
Air	26.38	1007	1.161
O_2	26.49	919.9	1.284
He	156.0	5193	0.160

In this contribution, we present a sensor measuring flow speed and thermal conductivity simultaneously using one single chip. The heater is excited in direct mode contrary to other research groups addressing the investigation towards a thermal gas independent flow meter. They are usually using an alternating [5] or pulsating excitation. In our case, power excitation is used to determine the gas thermal conductivity and therewith the gas concentration; constant temperature to measure flow speed.

SENSOR

The sensor design is based on a calorimetric flow sensor. The chip has a size of

$3.4mm \times 3.9mm \times 0.51mm$. Foturan glass serves as substrate material. This photosensitive glass is etchable with hydrofluoric acid and defines therewith the membrane area (size: $1mm \times 2mm$). The membrane is fabricated with polyimide. A detailed view of the membrane area is depicted in Figure 1. In this paper the flow rate is according to the x-axes (from left to right, the resistors are labeled accordingly). The layout consists of two temperature sensors and a centered heating element. They are designed as resistance temperature detectors (RTD); all elements are made of platinum and embedded in a polymer membrane. The polymer membrane is a high temperature type and applicable to temperatures around 250°C. The low thermal conductivity (0.15W/mK) of this material reduces significant the heat transfer through the membrane. The centered element serves as joule heater. In order to minimize the supplied electrical power to this element, it is designed as two resistors, which are connected in parallel. Platinum can be heated and simultaneously the resistance can be measured, due to the defined temperature coefficient of resistance (TCR). This effect offers the possibility to excite the heating element in two different modes. Regardless of flow rate and medium, temperature or power on the heating element can be held constant by a controller.

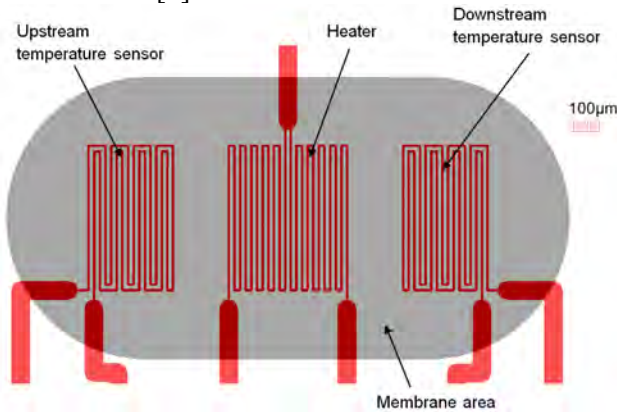The fabrication process was already presented in previous work [6].

Figure 1: Detailed view of sensor structure – membrane area. Labeling according to flow direction.

SIMULATION MODEL
Physics and Geometry

The numerical model is set up in COMSOL Multiphysics, which offers a coupling between different physical problems. The FEM-model combines the Heat Transfer (ht-mode) and incompressible Navier Stokes (spf-mode) equation in stationary domain. The coupling is chosen in order to respect changes in thermal properties of the fluid due to temperature variations. The geometry is outlined in three dimensions. Due to simplification reasons the

model is designed symmetrically to the z-axes. The flow channel's height is 1mm, width is 1mm and length is 4mm. Several common gases are modeled as flowing medium (see Table 1). The flow is assumed to be parallel to the x-axes with boundaries in no slip condition. The average flow speed is varied between 10^{-4} and 1.5 m/s.

The sensor is designed underneath the channel. The cavity is filled with stagnant air. The resistor areas are embedded in the membrane and designed as areas of platinum using the highly conductive layer option. As the RTDs are designed with meander lines (see Figure 1), the thermal properties of these areas are calculated according to the area percentage of platinum and polyimide.

No traces are built due to simple terms. The boundaries of the model are set to a constant temperature of 26°C. The centered element is used as joule heater operating with constant power of 12mW (DC). The average temperature of the downstream element is analyzed as response signal.

Theoretical Results

A fully developed laminar, parabolic flow profile is established inside the channel regardless the tested gas. Figure 2 shows the temperature difference between downstream temperature sensor and ambient using power excitation. The temperature is increasing, before a flat region is established. The temperature values in this region differ significant between the gases if they have a different thermal conductivity. The temperature values in the flow region between 0.25 and 1.5m/s show a variation of less then 0.6% between minimum and maximum. This variation will be even less if the flow region is constricted. Hence, the temperature in this region can be seen as flow independent, but gas type dependent.
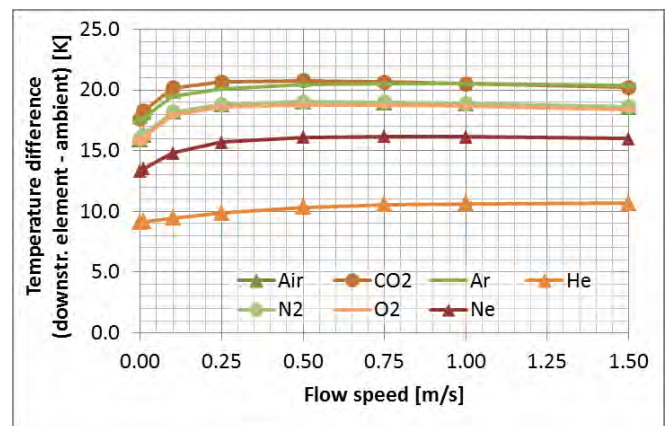

Figure 2: Temperature of downstream temp. sensor by power excitation of heating element – Simulation result.

The simulation results of the flow independent region suggest, that the temperature value of the

downstream element is correlating to the gas thermal conductivity by:

$$y = A \cdot e^{-bx}$$
(1)

where A and b are fitting parameters, x is the temperature of the downstream element [°C] and y is value of thermal conductivity [mW/(m*K)]. Figure 3 shows the fitting curve according to Equation 1 with A=1425.56 [mW/(m*K)], b=0.2123[K^{-1}] and R^2=0.9996.
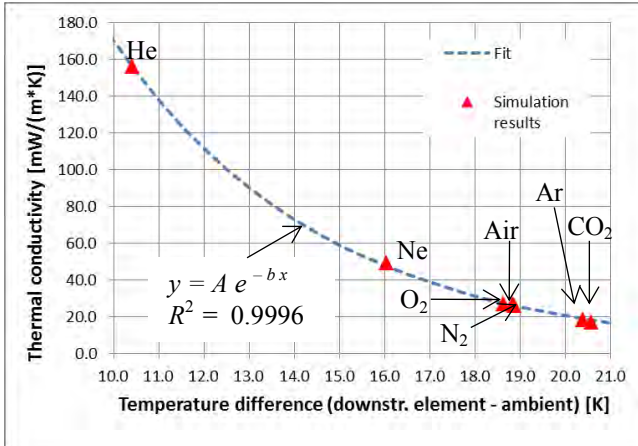

Figure 3: Correlation between thermal conductivity and temperature of downstream element in the flow independent region (0.25 – 1.5 m/s) according to Equation 1 (ambient temperature subtracted).

MEASUREMENTS
Experimental Setup

For verifying the simulations, the chip is mounted in a cavity of a printed circuit board (PCB). The topside of the PCB and sensor form the bottom side of a flow channel. Above the PCB, a channel is attached, analog to the simulation model. The flow channel's length is 40.8mm. A bonding process does the electrical connection sensor to PCB. The volume flow is adjusted with a Mass Flow Controller (MFC); the average flow speed in the channel is adjusted between 0 and 1.8m/s.

Electronics

The heating element can excite in two different modes (DC) – constant power and temperature – using a controller implemented in LABVIEW. The power is set up to 12mW, and 75°C temperature difference between heater and ambient, respectively.

The current through the downstream element is 0.1mA, to avoid self-heating effects. The voltage drop is acquired with a data acquisition card (NI USB-6225). For the resistance to temperature conversion the TCR and the resistance at 0°C are used. These resistor specific parameters have been obtained by carrying out a resistance-temperature measurement between 5 and 85°C and a curve fitting by least

squares.

Experimental Results

The temperature of the downstream element is depicted in Figure 4 for power excitation, Figure 5 for temperature excitation respectively. The curve progressions between the different excitation modes vary significantly. A flow independent region is observed by power excitation according to the simulation results. The difference from simulations and measurements comparing nitrogen is smaller than 12% and shows therefore a very good accordance. The temperature value is only affected by gas type in the flow region between 0.25 and 1.25m/s. Temperature excitation leads to a continuously increasing signal, which is a function of flow speed and gas type.

Figure 4: Temperature of downstream temp. sensor. Excitation of heating element with constant power – measurement results.

By correlating the thermal conductivity to gas concentration of a binary mixture as shown in Figure 6, the concentration can be obtained, if the components are known in advance. Furthermore, the gas type can be determined based on the thermal conductivity. However, gases cannot be distinguished if they have the same thermal conductivity.

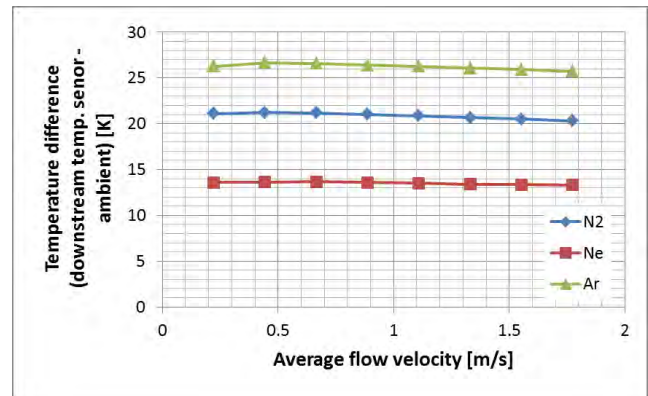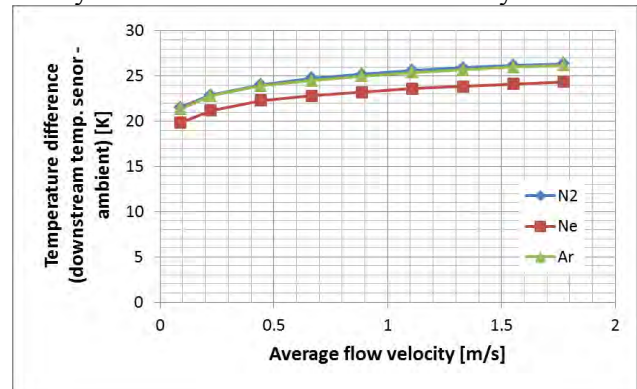*Figure 5: Temperature of downstream temp. sensor. Excitation of heating element with constant temperature – measurement results.*
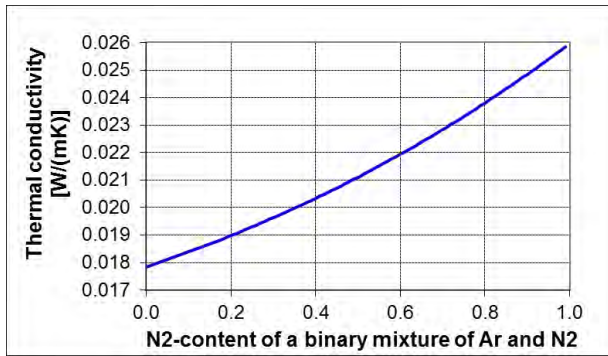
Figure 6: Theoretical progress of thermal conductivity in a binary gas mixture (argon and nitrogen).

DISCUSSION

Theoretical and experimental results show a procedure to determine thermal conductivity and flow speed simultaneously by using a simple chip layout with a heater and a downstream temperature sensor. First, thermal conductivity is extracted by power excitation. By knowing the gas thermal conductivity, a corrected flow speed value is obtained by switching to temperature excitation. Hence, thermal conductivity and flow speed can be obtained. The concentration of binary mixtures can be obtained if the components are known and differ in thermal conductivity; this is achieved by correlating the thermal conductivity to the gas concentration. The concentration measurement mixture with argon and nitrogen can be obtained with a resolution of +/- 8% (calculated with experimental results). An even better resolution can be achieved, if the difference in thermal conductivity of gases is lager, e.g. mixture of carbon dioxide and methane or neon.

Several effects obtain the flow independent region: Sensor design, cooling of the heating element and shift of the heat diffusion downstream by flow. The gas thermal conductivity affects the heater temperature, a low thermal conductivity corresponds to a high temperature value. The cooling of the heater temperature is affected by thermal conductivity and density times specific heat capacity. The higher density times specific heat capacity, the higher the temperature decreases. But this difference is not transferred to the downstream resistor in the desired flow range. As rule of thumb, it can be concluded that gases with a same value in thermal conductivity times specific heat capacity and a difference in thermal conductivity have a corresponding cooling. Due to the increase of downstream temperature, it can be assumed that the penetration depth is larger than the stagnant boundary layer, which establishes close to the wall. This can lead to a shift of the heat diffusion further downstream.

CONCLUSIONS

A novel procedure to determine flow speed and simultaneously gas type or gas concentration is presented in this contribution. Compared to other approaches, we showed that a time-independent excitation procedure is sufficient to detect a quantitative and qualitative measure. The sensor layout only requires a heating element and a downstream temperature sensor. Using power excitation, a flow independent region is established on the downstream element. This region is used to detect thermal gas conductivity. The gas concentration is obtained by correlating this value with the thermal conductivity. By the use of temperature excitation flow speed is measured and can be corrected afterwards, because the thermal conductivity is known. However, flow direction cannot be observed with this simple layout. In a further study, the upstream element will be investigated in order to determine also the flow direction. Approaches to improve the resolution have to be discussed as well.

REFERENCES

[1] A. van Putten, S. Middelhoek, "Integrated silicon anemometer", Electronic Letters, Vol. 19, No. 21, pp. 425-426, 1974.

[2] A. Cubukcu, E. Zernickel, U. Buerklin, G. Urban, "A 2D Thermal Flow Sensor with sub-mW power consumption", Sensors and Actuators A: Physical, Vol. 163, pp. 449-456, 2010.

[3] M. Ashauer, H. Glosch, F. Hedrich, N. Hey, H. Sandmaier, W. Lang, "Thermal flow sensor for liquids and gases based on the combinations of two principles", Sensors and Actuators A: Physical, Vol. 73, pp. 7-13, 1998.

[4] D. R. Lide, ed., "CRC Handbook of Chemistry and Physics", 90th edition, CRC Press/Taylor and Francis, Boca Raton, 2010.

[5] D. Reyes, K. Kogan, A. Cubukcu, G. Urban, "Simultaneous flow and thermal conductivity measurement of gases utilizing a calorimetric flow sensor", Sensors and Actuators A: Physical, Vol. 203, pp. 225-233, 2013.

[6] C. Hepp, F. Krogmann, J. Polak, M. Lehmann, G. Urban, "AC Characterisation of Thermal Flow sensors with Fluid Characterisation Feature", *Proc. of 16th Transducers*, June 5-9, 2011, pp. 1084-1087.

CONTACT

Christoph J. Hepp, christoph.hepp@ist-ag.com

1. Sensors

TRULY CALORIMETRIC FLOW SENSOR CHIP BASED ON SURFACE CHANNEL TECHNOLOGY

W. Sparreboom[1], E.J. van der Wouden[1], T.S.J. Lammerink[2],*
and J.C. Lötters[1,2]
[1] Bronkhorst High-Tech BV, Ruurlo, The Netherlands
[2] University of Twente, Transducers Science and Technology, Enschede, The Netherlands

ABSTRACT

In this paper we present a truly calorimetric flow sensor. The technology to fabricate the sensor is based on surface channel technology. The nominal measurable air flow is 0.8 ml_n/min. The material of the sensor element is silicon nitride which is resistant to most commonly applied chemicals.

The measurement tube is freely suspended and has a wall thickness of only 1 micron. This gives the tube an extremely low thermal mass which facilitates true calorimetric flow sensing. Calorimetric flow sensing allows for conversion between different gases based on their density and heat capacity product (ρ-C_p). This was checked experimentally for several common gases. Conversion between gases was found to be within 2%.

Figure 1: SEM picture of a surface channel fabricated by buried channel technology.

KEYWORDS

Thermal flow sensor, MEMS, Microfluidics

INTRODUCTION

Calorimetric flow sensors have the interesting property of ρ-C_p conversion between gases. This facilitates calibration on a single gas (e.g. nitrogen) and conversion to other gases simply by ρ-C_p for volumetric flow and C_p for mass flow. For decades these sensors have been manufactured mainly in steel. Since steel sensors typically have a relatively large thermal mass, these sensors have a response time typically higher than 1 s.

FLOW SENSOR DESCRIPTION

Novelty

Here we present a truly calorimetric MEMS gas flow sensor as opposed to semi calorimetric sensors introduced in literature before [1]. It has a nominal air flow of 0.8 ml_n/min. It has a fast response time in the order of milliseconds and is chemically inert to most common gases.

Chip

The sensor chip is based on the technology developed by Dijkstra et al [2]. With this technology buried channels can be fabricated. In figure 1 a scanning electron microscope (SEM) picture of a buried channel fabricated with this technology is given. A SEM picture of the functional part of the chip is depicted in figure 2. Here two tubes can be observed. The tubes are etched free from the substrate. Both tubes contain metal resistors that act as heaters and temperature sensors. Flow enters the tube in the bottom left of the picture via a surface channel inside the substrate. On the top right end of the picture a surface channel continuously (i.e. without steps in diameter) connects the two tubes. The free hanging tubes have an inner diameter of approximately 40 µm and a wall thickness of approximately 1 µm. Channels are fabricated using surface channel fabrication as described in [3,4]. The channel wall is silicon rich LPCVD silicon nitride. This material is chemically very resistive and allows for a broad range of applications. The material of the resistors is 200 nm

gold with 15 nm chromium for adhesion. They are sputtered on top of the nitride channels and are therefore galvanically separated from the medium.
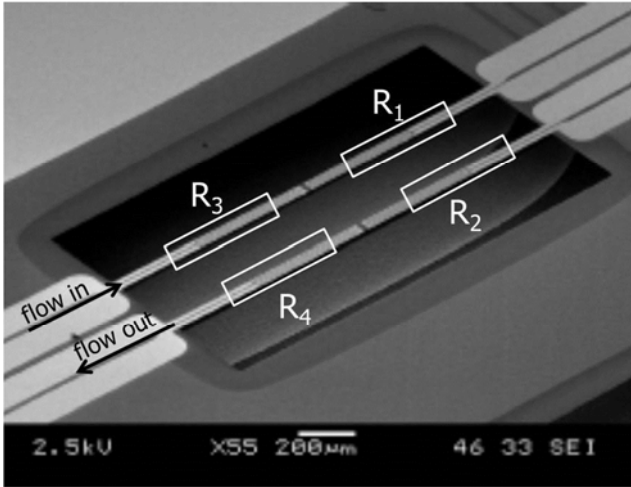

Figure 2: SEM picture of the chip with schematic representation of the gold resistors and the flow direction.
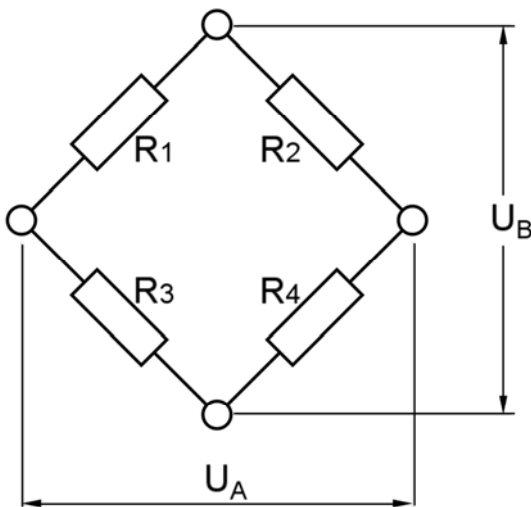

Figure 3: Heater / temperature sensor resistors in a Wheatstone bridge. The resistor numbers correspond to the definition in figure 2. A voltage is placed between U_B, the resulting voltage difference is measured at U_A.

Electrical and fluidic interface

The chip has four temperature dependent resistors (figure 2) which are placed in a Wheatstone configuration (figure 3). A 100 mV potential is placed across the bridge (U_B in figure 3) using a digitally controlled voltage supply. The thus occurring electrical power heats up the resistors. If a flow is applied in the direction given in figure 2 a voltage difference occurs between the midsection of the left side and the right side branch of the bridge. This

voltage difference is a function of flow. It is measured in the midsection (U_A in figure 3) using a high impedance differential amplifier. The temperature dependent resistors have a DC value of approximately 100 Ω at T = 25°C. The analog signals are digitized using a 24 bits analog to digital converter (ADC). This is then converted to an RS-232 signal in a microcontroller for communication with a computer.
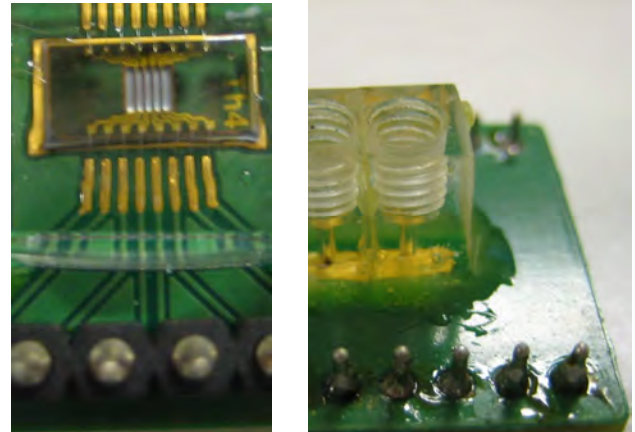
Figure 4: Left: Electrical chip interface. The chip looks distorted, because of an optical effect caused by the plastic cover. Right: Fluidic chip interface.

EXPERIMENTAL
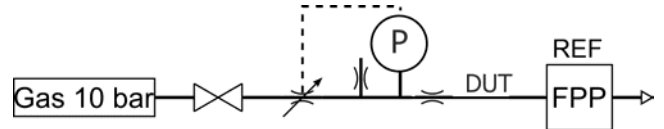
Figure 5: Schematic view of the setup. Gas pressure is delivered using a mechanical pressure controller at 10 bara. A pressure meter (P) is used to electronically control the pressure using an electromagnetic valve. Between the device under test (DUT) a restriction is placed and as a reference a 50 ml_n/min piston prover (FPP) is used

The setup we used to characterize this system is given in figure 5. Gas flow is generated by an electronically controlled pressure at the inlet. We use a pressure controller for this (Bronkhorst, EL-PRESS) and a constant leak. The outlet is at atmospheric pressure which is also monitored during the experiment using a pressure sensor. As a volumetric flow reference we use a 50 mln/min piston prover (Bronkhorst, FPP-050). Before the DUT (device under test) we placed a restriction (10 cm long stainless steel tube with an inner diameter of 125 μm). In this way the range of the pressure controller is more efficiently used. This in turn gives a higher resolution for the pressure control. We tested the sensor chip with 4 different gases, Argon (Ar), Helium (He), Nitrogen (N_2) and Carbon dioxide (CO_2).

RESULTS

In this section we present and discuss the results obtained with the setup described above. We measured the resulting sensor signals as a function of the reference flow measured by the piston prover. An example of such a curve, measured with N_2 is given in figure 6.

Figure 6. Measured sensor signal for N_2 as a function of reference flow by a 50 mln/min piston prover. The fit is a 3rd order odd function polynomial fitted by the least square method. The fit is reasonable up to approximately 0.8 ml_n/min, which we define as its nominal flow rate.
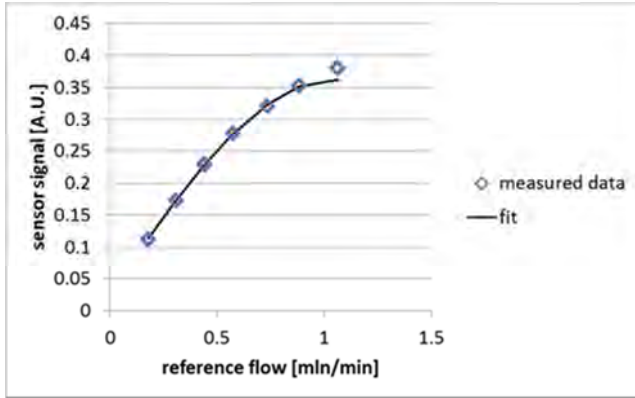
We fitted the data with a third order odd function polynomial. This means we only used the first and third order term. This fit was found to describe the sensor signal most effectively. Later this polynomial function can also be applied to linearize the sensor response. The coefficient of the first order or linear part of the fit is used as the sensor sensitivity, S_x, for a specific gas, x. If we plot this sensitivity as a function of ρ-C_p for different gases we find a linear fit (figure 7). This is expected since we suppose S_x is indeed a linear function of ρ-C_p.

Moreover we find that Ar and He show similar sensitivities, which is expected since they have a similar ρ-C_p product. To prove that the sensor sensitivity is a function of ρ-C_p we define two types of conversion factors, a theoretical conversion factor TCF_x and an empirical conversion factor ECF_x. These are then used to directly compare the measured values with theory for each gas. In equation (1) TCF_x is defined.

$$TCF_x = \frac{\rho_x C_{p,x}}{\rho_{N_2} C_{p,N_2}} \qquad (1)$$

In TCF_x the ratio of ρ-C_p product of the gas of interest to the ρ-C_p product of N_2 is determined.
ECF_x is defined in equation 2.

$$ECF_x = \frac{S_x}{S_{N_2}} \qquad (2)$$

Here the ratio of the empirical sensitivity of the gas of interest and the empirical sensitivity of N_2 is determined. The theoretical and empirical conversion factors can be compared to determine the accuracy of conversion solely based on the ρ-C_p product.
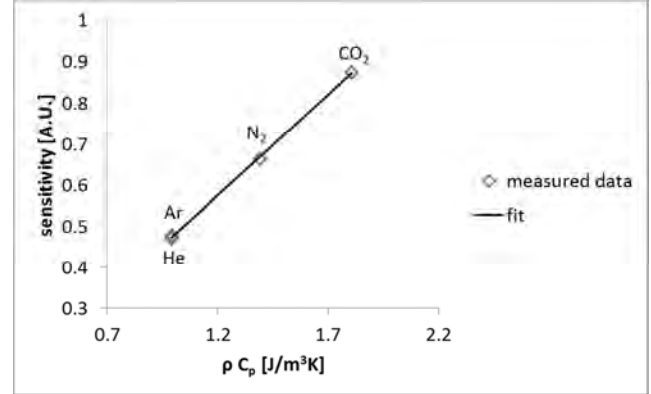
Figure 7. Measured sensitivity (slope of the linear part of the fit in figure 6) as a function of the theoretical ρ-C_p product at 1.2 bar(a) and 30°C (average pressure and temperature inside the sensor).

In table 1 we show the conversion factors for different gases. Also the deviation between the theoretical and the empirical conversion factors is given. The deviation is well below 2% which is good enough for a proof of principle. Not only does this facilitate conversion between gases, it will also result in reproducible behavior between chips when applying gas mixtures that vary in composition during a measurement.

Table 1: Measured and theoretical conversion factors with respect to N_2

	ECF_x [measured]	TCF_x [theoretical]	deviation [%]
He	0.707	0.711	-0.57
Ar	0.719	0.714	0.69
CO_2	1.317	1.298	1.43

CONCLUSION

To conclude we presented a truly calorimetric flow sensor chip. The sensor element is made of silicon nitride and the heaters are galvanically separated from the inner part of the sensor element. This makes the sensor chemically resistant to most gases. We tested this chip with several common gases and found predictable behavior. Moreover we found a

ρ-C_p relation between different gases. This eliminates the need for calibration with actual gases and opens up the road to measuring various mixtures reproducibly between sensor chips.

ACKNOWLEDGEMENTS

REFERENCES

[1] J.T.W. Kuo, L. Yu, E. Meng, "Micromachined Thermal Flow Sensors – A Review", Micromachines, 3 (2012), 550-573.

[2] M. Dijkstra, M.J. de Boer, J.W. Berenschot, T.S.J. Lammerink, R.J. Wiegerink, M. Elwenspoek, "A versatile surface channel concept for microfluidic applications", J. Micromech. Microeng., 17 (2007) 1971-1977.

[3] M. Dijkstra, M.J. de Boer, J.W. Berenschot, T.S.J. Lammerink, R.J. Wiegerink, M. Elwenspoek, "Miniaturized thermal flow sensor with planar integrated sensor structures on semicircular surface channels", Sensor. Actuat. A-Phys., 143 (2008) 1-6.

[4] T.S.J. Lammerink, J.C. Lötters, R.J. Wiegerink, J. Groenesteijn, J. Haneveld. "Single chip flow sensing system with a dynamic flow range of more than 4 decades", 16th International Solid-State Sensors, Actuators and Microsystems Conference, TRANSDUCERS 2011, 890-893 (2011).

CONTACT

*W. Sparreboom, w.sparreboom@bronkhorst.com

2. Actuators   **Presentation**

STARJET-BASED, PNEUMATICALLY ACTUATED LIQUID METAL DROPLET PRINTING AT UP TO 500 °C

B. Gerdes[1], N. Lass[1], L. Riegger[1], R. Zengerle[1] and P. Koltay[1]

[1]Laboratory for MEMS Applications, IMTEK, University of Freiburg, Freiburg, Germany

SUMMARY

In this work, we present a novel generation of pneumatically actuated printheads based on the StarJet technology which have been successfully applied for the direct non-contact printing of droplets from molten metal [1, 2]. This paper reports the technological advances of the newly designed printhead V3 which for the first time has been fabricated by selective laser melting (SLM). The StarJet technology features an inert rinse gas that surrounds the droplets inside the nozzle. V3 features an integrated heating for rinse gas which prevents the droplets from fast solidification and oxidation after ejection, as they are surrounded by hot nitrogen gas. The feasibility of the StarJet technology is demonstrated for printing at temperatures up to 500 °C. Moreover, the angular deviation of the droplets' flight path has been investigated. A maximum angular deviation of 0.89° has been evaluated. The droplets' velocity after ejection and the influence of the different pressures on this parameter have been investigated.

KEYWORDS

StarJet, Molten Metal Droplets, 3D Printing, Rapid Prototyping

INTRODUCTION

The direct non-contact printing of liquid metal droplets offers a large number of possible industrial applications, and has the potential to replace currently established processes. This includes direct metallization of solar cells, formation of electrical contacts on printed circuit boards (PCBs), 3D integration of microelectronics in hybrid packages as well as the fabrication of micro structured metal layers on polymers for molded interconnect devices (MIDs) [3]. Especially the direct placement of solder balls on PCBs is of high interest in this field [4].

It is however still challenging to generate droplets from molten metals in the micrometer scale. The StarJet technology utilizes a star-shaped nozzle which forms and centers the droplet of molten metal inside the orifice before it is ejected [1]. Figure 1 depicts an SEM view of a StarJet nozzle chip with the star-shaped orifice and the rinse gas channels surrounding it.

The chip is attached to the printhead which is pneumatically actuated and features two gas inlets for e.g. nitrogen. For the generation of droplets, two individual gas pressures are used: The actuation pressure is used to apply a short pressure pulse on top of the molten metal reservoir to push metal in the nozzle.
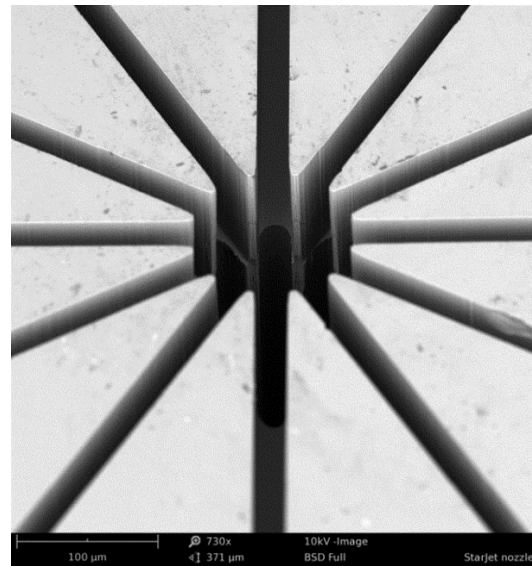
Figure 1: SEM view of a StarJet nozzle chip made from Si with star-shaped nozzle orifice (center) and surrounding rinse gas channels.

The rinse gas pressure results in an even flow through the bypass channels of the chip, surrounds the droplets in the nozzle and directs its path after ejection. It also prevents oxidation of the droplets. This technology currently enables the direct printing of metal droplets with diameters down to 60 μm.

The pneumatic actuation principle has several advantages over other actuation principles such as piezoelectrically driven devices, which are limited in their maximum operating temperature due to depolarization of the actuator above their Curie temperature. This usually limits the operating temperatures to below 350 °C or requires complex thermal shielding above this temperature for the actuator [5, 6, 7]. The maximum operating temperature of the StarJet technology is however only limited by the melting temperatures of the printhead material. The technology is therefore not inherently limited but in principle feasible for the direct printing of

higher melting metals.

In this work, the pneumatic actuation principle has been further improved over the previously developed printhead V2 to allow for higher printing temperatures.

For industrial applications a high repeatability and low deviation of the droplets' flight paths are of importance as these enable precise placement of droplets on substrates. Therefore, the angular deviation of the droplets after ejection, depending on rinse and actuation gas pressures, has been investigated.

FABRICATION AND EXPERIMENTAL SETUP

Like the previous version V2 of the actuator [2], the novel version V3 is made of stainless steel to ensure high temperature stability. However, for V3, the fabrication technology selective laser melting (SLM) is used. Figure 2 depicts an exploded view of printhead V3.
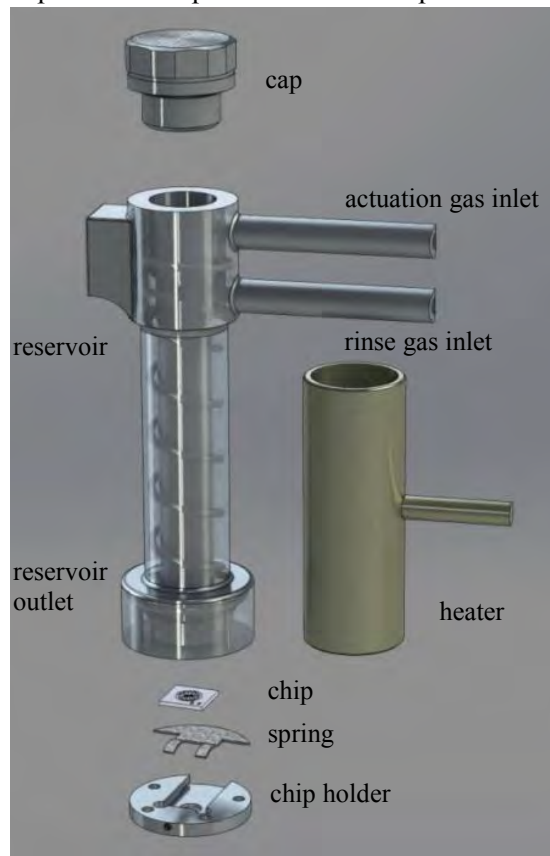

Figure 2: Exploded view of StarJet V3 actuator with integrated heating channels for rinse gas surrounding the reservoir.

The SLM process enables the fabrication of gas channels in the side-walls of the printhead (Figure 2), which allows for pre-heating of the rinse gas before it comes in contact with the molten metal. This not only reduces the risk of oxidation but also effectively prevents an undesired cooling of the metal droplets, which is especially important for high printing temperatures.

The StarJet nozzle chips are fabricated from silicone by deep reactive ion etching (DRIE) processes and are attached below the outlet of the main reservoir which has a small reservoir outlet tube with a diameter of 400 μm. The droplet diameter primarily depends on the chip orifice diameter and can thus be tuned by exchanging the nozzle chip. For the desired droplet diameter, a chip with a suitable orifice diameter can be chosen. Typical orifice diameters of chips in operation range from 50 - 200 μm. The newly developed chip holder for printhead V3 features a spring which presses the chip under the reservoir outlet. The chip can be slid into the chip holder from the side. This allows for nozzle chip exchange without dismounting the chip holder. The printhead has been miniaturized in comparison to the previously developed V2, to allow for easier system integration. The reservoir features a volume of 1500 mm^3. To melt the metal inside the reservoir, the complete printhead assembly is heated up to the necessary temperature by a heater which surrounds the printhead as depicted in the explosion view (Figure 2).

Like the previous version, V3 can be used in two different operation modes. In the Continuous Mode, a constant rinse gas pressure and a constant actuation pressure are applied to the chip and reservoir. This leads to a continuous formation of droplets at high frequencies of up to 11 kHz. The second operation mode is the Drop-on-Demand mode, where a constant rinse gas pressure is applied and short actuation pressure pulses on top of the reservoir lead to the formation of individual droplets. For the pressure pulses a pneumatic high speed valve was used (Type*: MHE2MS1H-3/2G-M7-K, Festo, Germany*) which is opened for 5 ms for each individual droplet. Presented results were created using Drop-on-Demand mode. For printhead V3, low pressures in the range of some 10 mbar for the actuation pressure and some 100 mbar for the rinse gas pressure have to be applied.

The droplet ejection and flight path are investigated with a high speed camera (*MotionBlitz, Mikrotron, Germany*), by visualizing the nozzle outlet and the first

millimeters of flight path. For this, the deviation from the straight path is evaluated after 1 mm distance from the nozzle, which is a typical distance between nozzle and substrate when printing structures.

EXPERIMENTS

Printing at 500 °C

The maximum operating temperature of the StarJet technology has been extended from previously 350 °C to up to 500 °C. At 350 °C the technology is limited to the direct printing of solder balls. Based on the technology, it was possible to produce droplets of molten metal from the alloy Zamak (Zn96Al4) in Drop-on-Demand mode (Figure 3). To achieve this, the printhead had to be heated up to 500 °C. The depicted droplets were printed with a nozzle chip orifice diameter of $d_{orifice} = 140$ µm, leading to droplet diameters of $d_{droplet} = 180$ µm.

Figure 3: Droplets from Zamak (d = 180 µm), printed using the StarJet technology.

Velocity and angular deviation analysis

Moreover, the deviation in flight path for printed solder droplets in Drop-on-Demand mode was further investigated, as the precision of droplet placing is crucial for industrial applications. In the same series of experiments, the velocity of the droplets after ejection and the correlation with adjusting the rinse gas pressure for a constant actuation pressure was also investigated. A chip with nozzle diameter $d_{nozzle} = 183$ µm was used for these experiments. The rinse gas pressure can be adjusted independently from the actuation gas pressure. The droplet generation is possible in a certain parameter range for actuation pressure and rinse pressure and possible combinations mainly depend on the diameter of the nozzle orifice. For the experiments, a variable rinse gas pressure and

a constant actuation pressure of $p_{actuation} = 0.02$ bar were applied in order to investigate the impact of a variable rinse gas pressure on droplet ejection. For a given actuation pressure, the rinse pressure can be varied in the range of some 10 mbar and has a direct influence on the velocity of the droplets. Figure 4 shows the ejection of one single solder droplet from a chip with $d_{orifice} = 183$ µm ($p_{rinse} = 0.11$ bar, $p_{actuation} = 0.02$ bar).

For the actuation pressure $p_{actuation} = 0.02$ bar, the rinse gas pressures 0.11 bar, 0.12 bar and 0.13 bar were each applied to create 10 individual droplets. Figure 5 displays the results from these measurements. The droplet velocity for a constant actuation pressure rises for an increasing rinse pressure. This indicates that the droplet velocity can be directly influenced by adjusting the rinse gas pressure in a certain parameter range.

Moreover, it was investigated in this context if different rinse gas pressures for constant actuation pressures have an impact on the flight path of the droplets. Table 1 shows the mean deviation in flight path for three different rinse pressures 1 mm after ejection. For each run, ten droplets were generated.
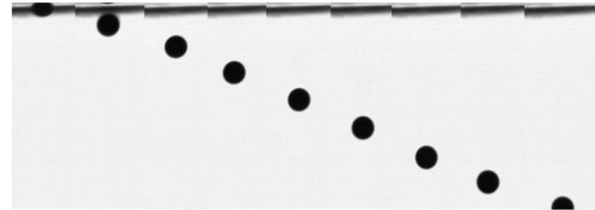

Figure 4: Image series of an ejected solder droplet from the StarJet printhead V3.
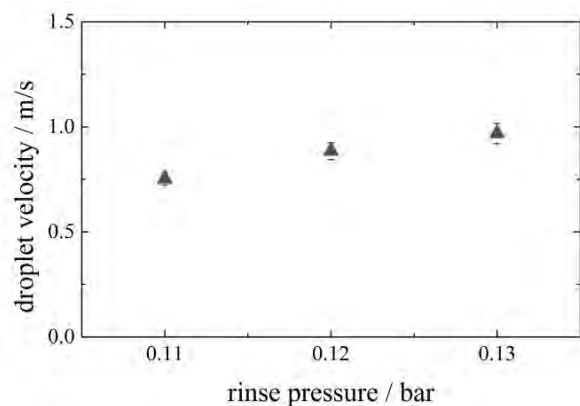

Figure 5: The droplet velocity for increasing rinse pressure and constant actuation pressure of $p_{actuation} = 0.02$ bar.

The angular deviation slightly decreases for higher rinse gas pressures in this series of

measurements. This indicates that a higher rinse gas pressure can lead to a better guiding of the droplet after ejection. Comparing the deviation of the droplets with the droplet diameters, it can be stated that the deviation is relatively small. The mean value is in the range of 10 μm, whereas the droplet diameter is around 200 μm. There are however some outliers and the maximum deviation in flight path for $p_{actuation} = 0.02$ bar amounts to 26 μm, which explains the standard deviations for the measurement (Table 1). Moreover, in this measurement, for higher rinse gas pressures (0.13 bar), the number of outliners decreases significantly, as the lower standard deviation indicates.

Table 1: Standard deviation of droplets' flight path after ejection depending on different rinse gas pressures for $p_{actuation} = 0.02$ bar.

Actuation pressure / bar	Mean deviation / μm	Standard deviation / μm
0.11	13.2	9.8
0.12	11.1	6.7
0.13	7.3	4.4

The experiments have been extended to a series with different actuation pressures and the deviations have been investigated. A maximum angular deviation of 0.89° was found over a series of experiments with different rinse and actuation gas pressures. The mean angular deviation was found to be even smaller at 0.26°.

CONCLUSION

The StarJet technology currently allows for the drop-wise printing of molten metals at up to 500 °C while in general exhibiting a very low angular deviation in droplet flight path. The droplets are pneumatically generated with the two independent gas pressures, rinse gas and actuation gas. These two gas pressures allow for a direct control of droplet generation and have an influence on the droplets' velocity after ejection. It is indicated that for a given actuation pressure, the rinse gas pressure can be used to control the droplets' velocity after ejection from the nozzle. The mean angular deviation of the droplets' flight path has been found to be only 0.26° and the maximum angular deviation is only 0.89° for a given series of experiments. This high accuracy and repeatability show that the StarJet technology has the potential to be used in industrial applications, where the precise placement of metal droplets is required.

Further research is carried out in order to enable droplet printing at even higher temperatures than shown here, targeting aluminum or silver at up to 1000 °C. This ultimately may pave the way for new approaches for the fabrication of 3D interconnects.

REFERENCES

[1] T. Metz, G. Birkle, R. Zengerle, P. Koltay, "StarJet: Pneumatic dispensing of nano- to picoliter droplets of liquid metal", *Proc. IEEE MEMS 2009, Sorrento, Italy,* January 25-29, pp.43-46.

[2] N. Lass, L. Riegger, R. Zengerle, P. Koltay, "Enhanced liquid metal micro droplet generation by pneumatic actuation based on the StarJet technology", Micromachines, Vol. 4, pp. 49-66, 2013.

[3] P. Khuntontong, T. Blaser, W. K. Schomburg, „Fabrication of molded interconnection devices by ultrasonic hot embossing on thin polymer films", IEEE Transactions on Electronics Packaging Manufacturing , Vol. 32, No. 4, pp. 152-156, 2009.

[4] A. Strandjord, T. Teutsch, G. Azdasht, „Laser based assembly of ultra finepitch bumped ICs for chip-to-chip proximity coupled application", *IMAP Synopsis, 2009, San Diego, USA, November 3-5.*

[5] B. Lemmermeyer, "Ein hochtemperatur-beständiger Einzeltropfenerzeuger für flüssige Metalle", *2006, Technische Universität München.*

[6] T. Ottnad, M. Kagerer, F. Irlinger, T. C. Lueth, "Modification and further development of a drop-on-demand printhead for wax, enabling future 3D printing and rapid prototyping", *The 2012 IEEE/ASME International Conference on advanced intelligent Mechatronics, 2012, Kaohsiung, Taiwan, July 11-14.*

[7] D. J. Hayes, W. R. Cox, "Micro-Jet printing of polymers for electronics interconnections", *Proc. of 3rd International Conference on Adhesive Joining and Coating Technology in Electronics Manufacturing, 1998, Binghamton, USA, September 28-30.*

ACKNOWLEDGEMENTS

CONTACT

Björn Gerdes, Tel. +49 (0) 761 203 73265, bjoern.gerdes@imtek.de

DYNAMIC BEHAVIOUR OF A PIEZOELECTRIC MICROPUMP ACTUATOR

C. W. Jenke[1], M. Köhn[1], M. Wackerle[1], C. Kutter[1], M. Richter[1]
[1] Fraunhofer Research Institution for Modular Solid State Technologies EMFT,
Munich, Germany

Introduction

A novel MEMS micropump has been developed to achieve improved bubble tolerance for liquids and high pressures for gases, as shown in Figure 1. By reducing the pump chamber height down to 3µm, the dead volume has been decreased, hence achieving a higher compression ratio. With decreasing pump chamber height, the viscous fluidic resistance increases exponentially, becoming the dominant damping effect for actuators of micropumps for liquids.

For precise dosing, both the operating mode dependent performance and its statistical behavior have to be understood, taking this viscous effect into account.
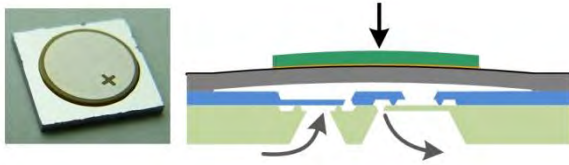

Figure 1: Micropump with its cross section and measurement point at diaphragm center

State of the art

The operating parameters to vary pump performance are mainly the driving voltage and the frequency of the piezoelectric actuator [1] but also the driving signal. The best pump performance can be achieved with a rectangular driving signal.

The applied voltage varies the displacement and the displacement volume with a theoretically linear relation [2] but is limited by the maximum allowed electric field for example 2kV/mm in polarization direction and 0.4kV/mm in the opposite direction for the PIC151 of PI Ceramics. Furthermore, the electric field induced and pressure induced strain is governed by hysteresis effects as described by Uchino [3] for different piezoelectric materials.

According to Zengerle *et al.* [4] and Yang *et al.* [5] the flow rate of displacement pumps can be calculated as the product of the pump stroke and the operating frequency:

$$\Phi = f V_{disp} \qquad (1)$$

In general this relation gives a high degree of freedom to change the flow rate in combination with the operability of the piezo actuator up to high frequencies of more than 1kHz. This equation assumes the pump stroke to be constant over the considered frequency range. Zengerle *et al.* explained that the stroke volume depends on hydrostatic pressures at inlet and outlet,

the properties of the passive check valves and the operation frequencies. Moreover, they describe that the actuator displacement corresponds to the rectangular electrical supply voltage while neglecting internal damping effects of the actuator, which has been investigated by Gomes to predict resonance frequencies [6]. Here internal damping accounted for 5% of the 20% overestimation.

Furthermore, no feedback from the dynamics of the pump was assumed [4]. Consequently, any frequency dependence would need to result from valve behavior or fluid dynamics not affecting the actuation. Junwu *et al.* followed this thought and held the phase shift of the valves accountable for the whole frequency dependence of the flow rate [7]. Although this might be the major effect for high frequencies of the investigated pumps, this is not the only effect present in micropumps. Particularly once reaching shallow pump chambers of only 3µm a squeeze film will be generated with effects investigated in this paper. Maillefer et al. avoided important squeeze film effects by patterning the ground to reach a defined position, touching the ground, thus keeping the stroke volume constant [8]. The actuator behavior under feedback effects of the fluid dynamics has not yet been studied thoroughly.

To achieve precise dosing reliably, the short term repeatability and long term stability of the actuator movement are of major importance. One effect altering the stroke displacement is the time dependent creeping effect present in piezo ceramics [3].

In general good reliability can be achieved with piezoelectric actuators [1], however according to Uchino "little repeatability test have been performed so far" [3]. Even though that quote has been stated in 1998, so far no data has been found on the repeatability of circular unimorph actuators including the statistical analysis, nor on the frequency dependent actuator stability.

Research goal

The goal of this research was to investigate the statistical dynamic behavior of piezoelectric unimorph actuators in micropumps.

This includes the investigation of the frequency dependence of actuator displacement and flow rate. In addition, the predictability of the actuator displacement and flow rate shall be inspected.

In order to get a measureof the reliability of the micropump operation, the short term repeatability of the actuator displacement needs to be evaluated and described statistically.

With the mapped frequency dependent micropump performance, the desired flow rate can be set

accordingly to the needs. The piezoelectric, mechanical and fluidic effects and their interactions lead to a dynamic non-linear behavior of the actuator and micropump that needs to be investigated. Practically, the understanding of fluidic damping effects at low pump chamber heights is useful to balance pump performance with bubble tolerance [9].

Experimental Setup
The goal of the experimental setup was to monitor the actuator displacement in real time and to obtain averaged flow rate values.
The investigated micropump, shown in Figure 1 pumps clean water and is driven at different frequencies in the ranges of 1 to 20Hz. Each frequency is maintained for about 100 seconds before changing to the next higher one. The electric voltage has been set to 175V/-75V for a piezo thickness of 190μm.
The measurements of the actuator displacement have been performed with a profilometer (FRT MicroProf with CWL X 300 μm Sensor) at 3,2kHz at the center of the diaphragm. The raw data is either used directly, or processed, identifying the jump point between pressure and suction stroke, which gives the absolute displacement of the actuator. The flow rate has been determined by measuring the weight over time of the pumped fluid with a scale (Sartorius MC 410S).
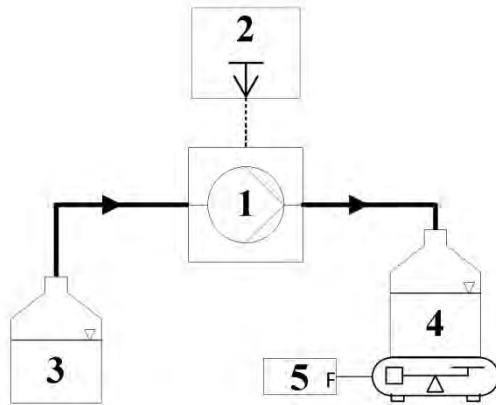

Figure 2: Experimental setup: 1-micropump, 2-profilometer, 3-reservoir, 4-tank on scale, 5-flow calculation

Results and Discussion
In Figure 2 one can see the displacement curve of an actuator, driven by a rectangular electric signal at 1Hz. Each pump stroke is followed by a suction stroke, which resets the actuator to its initial position. The diaphragm is working against water. Considering the time course of the curve, it is obvious that the stroke volume cannot be indifferent of the frequency, which effectively reduces the stroke time. In addition, the frequency dependency has to arise starting right from 1Hz as the static displacement needs more than 500ms to reach its final position.
As the actuator exhibits this damping effect to a larger extent in pump mode than in suction mode, the

damping has to result from fluid dynamics inside the pump chamber. As the diaphragm is sensitive to pressure, a higher pump chamber pressure would lead to reduced actuator motion. The pump chamber pressure depends on the inward and outward flow resistance and on fluid inertia. The outlet valve is positioned symmetrically to the center of the diaphragm in a distance of 1.2mm to the inlet valve. With a very low central pump chamber height of about 0.5μm in the final position of the pump stroke, a squeeze film is generated, exponentially increasing fluid resistance to the outlet valve.
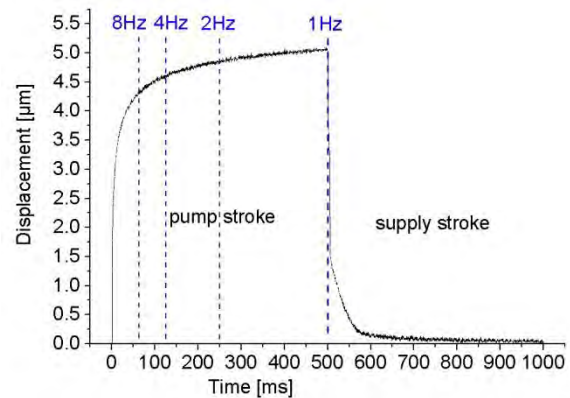
Figure 3: Single displacement curve with indicated prediction at certain frequencies (blue)

Based on the demonstrated motion curve of the pump stroke in Figure 3, the frequency dependent actuator displacement has been predicted. For the prediction, shown as blue dots in Figure 4, the displacement values of the motion curve have been calculated to be plotted over the frequency:

$$d_{predict}(f) = d_{measure}(t = \frac{500ms}{f}) \quad (2)$$

To compare the prediction with measured data, the actuator displacement has been evaluated for different frequencies of 1-20Hz with the method described in the section of the experimental setup. The results have been plotted in Figure 4 in black including the standard deviation. While the initial position at the suction stroke stays the same, the pump stroke, approaching the chamber ground, decreases with advancing frequency.
Both prediction and measurement describe a 1/x curve. However, the real stroke shows lower values than expected. To quantify the error of prediction, the differences between both have been plotted in Figure 5, showing a linear increase over frequency.
The hypothesis was that the prediction made will equal the measurement but, even though the method is able to describe the major part of the decrease of the actuator displacement, the left part is yet unexplained. There has to be an additional effect causing a linearly increasing reduction of stroke. Possible explanations are fluid inertia or fluidic resistance of the tubing at

the outlet, though this has yet to be investigated.
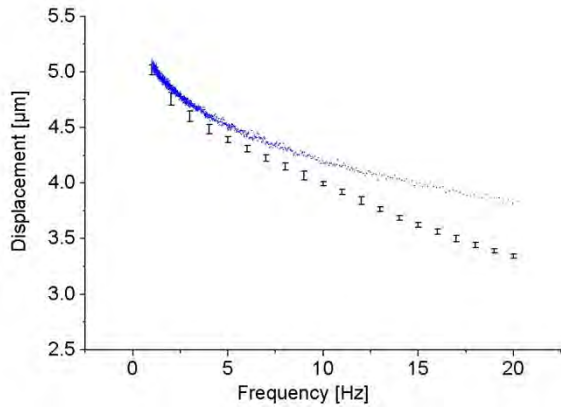

Figure 4: Relative displacement of measured data (black) and prediction (blue)
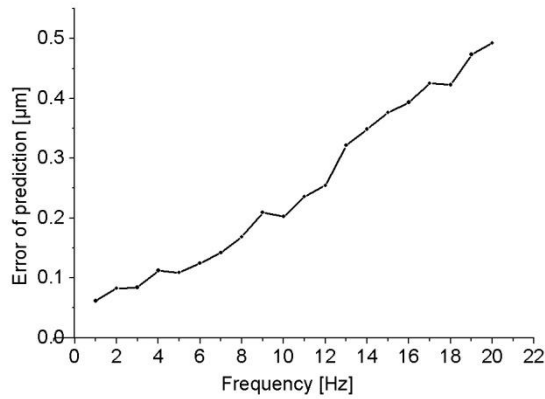

Figure 5: Error of prediction compared to measurement

In order to predict the flow rate based on the center displacement, one needs to know the stroke volume per displacement. The relation between stroke and stroke volume is linear as described by the model of Prasad [2] and validated with quasi static line measurements of the actuator displacement. One example of these measurements can be seen in Figure 6 describing the position difference between 0 and 100V. The displacement has been fitted with a 4th order polynomial fit. To get the stroke volume the fit function y(x) has to be shifted to the center and integrated over 180° within the borders of the diaphragm -3.15mm to 0mm and 0 to 3.15mm:

$$V_{disp} = \pi \int_a^b x \cdot y(x) dx \qquad (3)$$

According to this calculation, a stroke of 1µm corresponds to a stroke volume of 12.5nl. The flow rate has been predicted by multiplying the measured displacement in Figure 4 with the frequency and the constant ratio of volume per stroke:

$$\Phi_{predict} = d_{measure} f \cdot 12.5 \frac{nl}{\mu m} \qquad (4)$$

The measured flow rate has been corrected with the previous measured evaporation of 0.45µl/min. Both flow rates are displayed in Figure 7.

The comparison shows a good match in low frequencies up to 10Hz but diverges continually. The left errors can be explained with an inaccurately determined stroke volume per displacement or valve leakage in backwards direction. For higher frequencies, the phase shift of the valve opening behavior as explained by Junwu *et al.* can cause the increasing differences and has yet to be investigated.
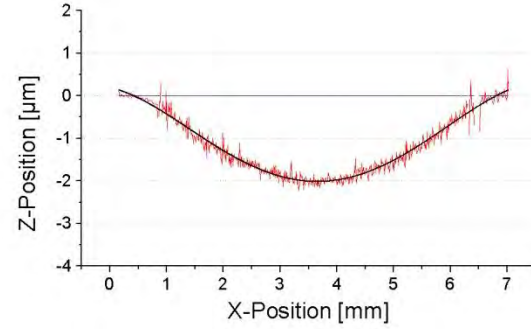
Figure 6: Static line measurement of distance between 0 and 100V(red) with polynomial fit(black)
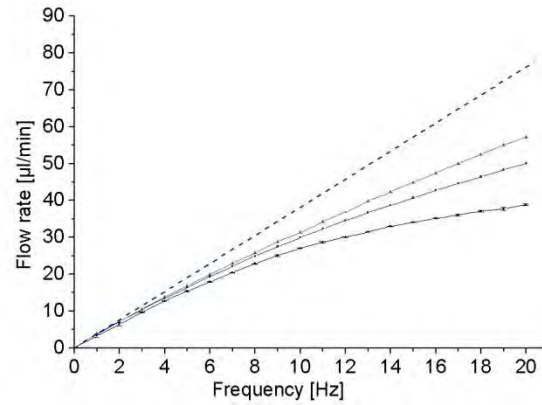
Figure 7: Frequency dependent flowrate: measured(black), prediction based on stroke measurement(blue), prediction based on motion curve(green) and the linear comparison(blue dashed)

In order to predict the flow rate of a piezoelectric micropump, not only the general frequency dependent behavior needs to be understood, but also the repeatability of the actuator movement. Not before showing that the stroke can be maintained within a narrow band, precise dosing can be achieved.

Therefore, the statistical distribution of the stroke has been displayed in Figure 7, exhibiting a normal distribution with standard deviations of 0.015µm at 1Hz and remains there even for higher frequencies, as can be seen in Figure 8.

The observed variations in actuator displacement are mainly due to the available measurement technique with an accuracy of +-0.1µm. That means that the stroke permanence is most likely even better than stated.
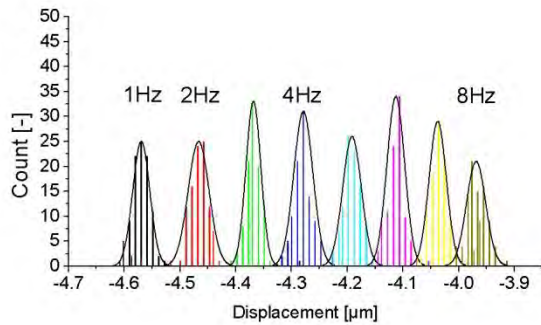
Figure 8: Typical statistical distribution of displacement for frequencies 1-8Hz
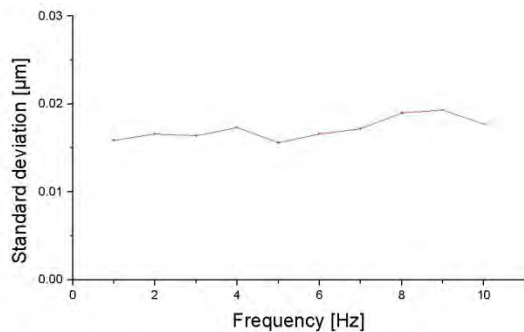
Figure 9: Standard deviation over frequency

Conclusion

To achieve improved bubble tolerance the compression ratio has been increased by reducing the pump chamber height. This leads to an effect of strong viscous damping of the actuator, resulting in a frequency dependent behavior of stroke and flow rate, which has been investigated here.

First, a method to measure the dynamic motion of the actuator has been developed exhibiting the motion curve at 1Hz with the damping effect becoming apparent. Based on this curve, a prediction of the frequency dependent actuator displacement has been compared to its measurement. Furthermore, the measured data has been used to predict the frequency dependent flow rate, also compared with its experimental values. For both steps of prediction, the viscous damping is responsible for the major part of the change. However significant parts remain unexplained and only assumptions are given.

The statistical behavior has been investigated to understand in what range a reliable operation is possible. A low standard deviation, stable over the measured frequency range was found. This implies that the relative deviation will worsen with higher frequencies, as the absolute displacement declines. As the measurement method only has a specified accuracy of +-0.1µm, which can be seen as noise in the displacement, the real deviation will probably even be better.

The gained understanding can help in designing new micro dosing systems applications specifically in terms of balancing flow rates, bubble tolerance and repeatability.

Outlook

The analysis revealed more dynamic effects to be present inside a micropump, which needs to be further conceived. Therefore new experiments are planned to distinguish between actuator, and valve behavior in connection with fluidic effects. Repeatability has only been checked for a small frequency range suitable for liquid pumps. As the pump can achieve high flow rates and pressures with air, too a far higher frequency range up to kHz, this should be looked at. The long term reliability under influence of strain is also a necessary field of research to ensure usage in a broader field of application.

REFERENCES:

[1]   D.J. Laser, J.G. Santiago, "A review of micropumps", J. Micromech. Microeng., Vol. 14, R35-R64, 2004

[2]   S.A.N. Prasad, "Two-Port Electroacoustic Model of Piezoelectric Composite Circular Plate", M.S. Thesis, Univ. of Florida, Gainesville, FL, 2002

[3]   K. Uchino, "Materials issues in design and performance of piezoelectric actuators: An overview", Acta mater., Vol. 46, No. 11, pp.3745-3753, 1998

[4]   R. Zengerle and M. Richter, "Simulation of microfluidic systems", J. Micromech. Microeng, Vol 4, No. 4, pp.192-204, 1994

[5]   R. Yang, M. Zhang, T. Tarn, "Dynamic Modeling and Control of a Micro-needle Integrated Piezoelectric Micro-pump for Diabetes Care", *Nanotechnology 2006 IEEE-NANO*, June 17-20, 2006, pp.146-149

[6]   L. Gomes, "Effect of damping and relaxed clamping on a new vibration theory of piezoelectric diaphragms", Sensors and Actuators A, Vol. 169, pp.12– 17, 2011

[7]   K. Junwu, Y. Zhigang, P. Taijiang, C. Guangming, W. Boda, "Design and test of a high-performance piezoelectric micropump for drug delivery", Sensors and Actuators A, Vol. 121, pp.156-161, 2005

[8]   D. Maillefer, S. Gamper, B. Frehner, P. Balmer, H. van Lintel, P. Renaud, „A high-performance silicon micropump for disposable drug delivery systems", *MEMS 2001, Interlaken, Switzerland*, January 21-25, 2001, pp.413-417

[9]   M. Richter, R. Linnemann, P. Woias, „Robust design of gas and liquid micropumps", Sensors and Actuators A, Vol. 68, pp.480-486, 1998

Contact information

Email: christoph.jenke@emft.fraunhofer.de
Tel.: +49 89 54759 159

2. Actuators   Presentation

A DISPOSABLE, DISPENSING VALVE FOR NON-CONTACT MICROLITER APPLICATIONS IN 96-WELL PLATE FORMAT

S. Kartmann[1], R. Zengerle[1], P. Koltay[1,2] and A. Ernst[1,2]
[1] University of Freiburg, Lab for MEMS Applications, Freiburg, Germany
[2] BioFluidix GmbH, Freiburg, Germany

ABSTRACT

We present a miniaturized, disposable dispensing valve for the microliter range, applicable as consumable to process 96-well plates. The new valve design is adapted to fit into a 9 mm grid and derives from the miniaturization study of a previous functional model [1]. The outer diameter of the valve, including actuating coil, was reduced from 16 mm to 8.5 mm without performance restrictions, thus made compatible for 96-well plate processing. Also the actuation current was reduced from 10 A to 5 A. The valve enables the dosage of target volumes in the range between 230 nL and 5 µL with coefficients of variation (CVs) below 2%. The current performance coincides with similar commercially available systems with the decisive advantage of material costs below 1 €

KEYWORDS

non-contact dispensing, electromagnetic valve, normally closed, disposable, 96-well plate format

INTRODUCTION

The requirements concerning dispensing performance of liquid handling systems in terms of precision and trueness are increasingly growing. Also the risk of cross-contamination and the need of expensive cleaning steps are omnipresent issues. Therefore, disposable components and non-contact dispensing technologies are preferred, which are hardly available on market.
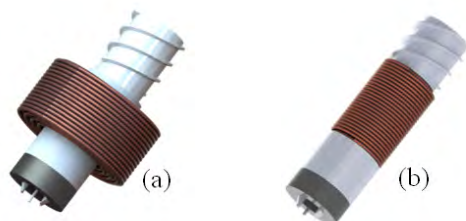

Figure 1: Schematic drawing of the functional model (a) [1] and the novel miniaturized (b) design of the disposable, non-contact dispensing valve.

In a previous work [1], we developed a disposable, normally-closed, non-contact dispensing valve focused on requirements given from industry and research [2]. The major drawbacks of that functional model were the large size with an overall outer diameter of 16 mm (including actuation coil, see fig. 1(a)), and the heat coupling, induced by the required high actuation currents. For pressure-time controlled valves, the flow rate and therefore the dispensed volume is depending on the nozzle dimension and the fluid properties. In this case, the coil is in direct contact with the valve body, so a high actuation current will heat up the valve and the containing fluid. The temperature will influence the viscosity of the fluid which will lead to a higher flow rate, thus an increased dispensed volume for pressure-time controlled systems. Therefore, the actuation current has to be reduced in order to minimize this influence on the dosing performance.

MINATURISATION STUDY

To enable a parallel application of multiple valves, in order to process 96-well plates by individual channels, the geometry of the valve requires an outer diameter of below 9 mm which was a crucial issue for the realization of the presented work. Also the actuation currents had to be reduced to lower the heat coupling into the liquid.

Working principle and acting forces

The miniaturization study is based on the theoretical consideration of three general forces acting on the valve plunger during actuation [3]. The individual forces are: a) the force between the coil and the plunger $F_{plunger}$, b) the force between the normally-closed (NC) ring magnet and the plunger $F_{RingMagnet}$ and c) the pressure force $F_{pressure(open)}$ as illustrated in fig. 2.

The movement of the plunger is controlled by the coil current and the induced opening force $F_{plunger}$ which is dependent on the distance between the coil and the plunger and their dimensions. In the normally closed state, the plunger is contact with the valve seat because of the attractive force $F_{RingMagnet}$ exerted by the NC magnet and the pressure force $F_{pressure(open)}$ as illustrated in figure 2. In order to open the valve, the two closing forces have to be overcome by applying a positive current pulse, whereby a magnetic field is generated, which exerts a force on the plunger higher than the closing forces and opens the valve. After the current is turned off, the plunger moves downwards again (see figure 2). The dispensed volume can be

controlled by either varying the applied external actuating pressure, the nozzle dimensions or the current pulse length.
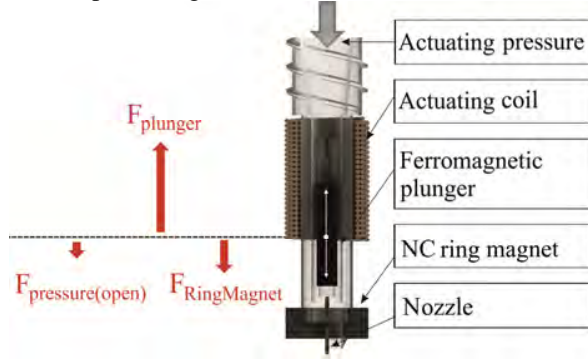

Figure 2: Cross section of the disposable, electromagnetic dispensing valve and the three main forces acting on the ferromagnetic plunger.

$F_{Plunger}$ acts as opening force which needs to overcome the closing force ($F_{RingMagnet}$ + $F_{pressure(open)}$) to enable the movement of the plunger and the actuation of the valve. These three forces can be calculated analytically with focus on the geometrical miniaturization of the valve.

Force between two permanent magnets

First, the force $F_{RingMagnet}$ between a permanent ring magnet and a permanent cylindrical magnet, both with axial magnetization is calculated. In Ravaud et. al. [3] the force between two permanent ring magnets is calculated by using the charge model. This model can be used due to the constant magnetization of the permanent magnets. Each magnet can be described by two charged planes located on the upper and lower surface of the magnet. Analogically, the force between a ring magnet and a cylindrical magnet can be calculated. $F_{RingMagnet}$ is depending on the dimensions of the magnet and the magnitude of the magnetization.

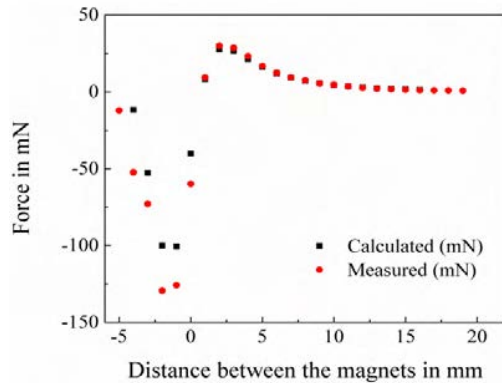*Figure 3: Measured (red) and calculated (black) force $F_{RingMagnet}$ between a plunger and a NC magnet in correlation with the distance between the magnets.*

Using a hard ferrite as NC ring magnet with an inner diameter of 4 mm, an outer diameter of 8 mm and a height of 3 mm and a NdFeB magnet with an outer diameter of 2 mm and a height of 10 mm as plunger (cf. figure 2) leads to a maximum calculated force $F_{RingMagnet}$ of 30.11 mN at a distance of 2 mm between attractive planes of the two magnets (cf. fig. 3).

Pressure force

The second closing force is the pressure force which appears from the external actuating pressure required to drive the valve. Therefore, the pressure force $F_{pressure(open)}$ can be calculated with the following formula:

$$d\vec{F}_{pressure(open)} = \int_A p \, d\vec{A} \qquad (1)$$

where $F_{pressure(open)}$ is the pressure force in N, p is the pressure in bar and A is the surface in m².

In the normally-closed state the plunger is in contact with the valve seat. The upper side of the plunger is exposed to a pressure force $F_{pressure(open)}$ acting on the whole surface $\pi r^2_{plunger}$. This force is determined as positive. On the other side of the plunger which is in contact with valve seat, the pressure force acts in the opposite direction (negative). On this side, the force acts on the cross section which is not in contact with the valve seat $\pi(r^2_{plunger} - r^2_{nozzle})$. After adding these forces one gets the pressure force acting on the cross section of the outer diameter of the nozzle in direction of the external applied pressure:

$$F_{pressure(open)} = p_{ext}\pi r^2_{nozzle} \qquad (2)$$

Force between coil and plunger

In [4] the force between a coil and a permanent magnet is calculated by using the charge model described in [3]. The force $F_{Plunger}$ is dependent on the coil dimensions (windings, height, length, inner and outer diameter and wire diameter), the distance between the coil and the plunger, the current and the plunger properties and dimensions. For this study, a NdFeB magnet with an outer diameter of 2 mm and a height of 10 mm was used as plunger, and the minimized target current was set to 5 A. A pressure of 2 bar is specified to be the maximum applicable actuation pressure.

The required opening force $F_{Plunger}$ can then be calculated by:

$$F_{Plunger} > F_{RingMagnet} + F_{pressure(open)}$$
$$> 30.11 \text{ mN} + 101.1 \text{ mN} = 131.81 \text{mN} \quad (3)$$

$F_{plunger}$ needs to overcome the maximum calculated closing force of 131.81mN, to guarantee a reliable functionality of the valve for the entire actuation pressure range. The outer diameter of the coil was set to 8.5 mm. By reducing the inner diameter of the coil, the opening force could be increased. But this dimension could not be reduced to an arbitrarily low value, because of the minimal required wall thickness of the valve which was set to 1.2 mm to guarantee no deformations for actuating pressures of 2 bar. Based on theoretical considerations in [4], the design rules for the valve miniaturization could be identified, which are listed in table 1. This configuration entails a maximum opening force of $F_{plunger}$ of 150.15 mN.

Table 1: Comparison of the dimensions of the old [1] and the new design of the disposable, electromagnetic dispensing valve.

	Old design [1]	New design
Outer diameter coil	16 mm	8.5 mm
Inner diameter coil	9 mm	5.5 mm
Length coil	8.5. mm	12 mm
Number of windings	105	72
Peak current	10 A	5 A
Overall length valve	27.1 mm	29.35 mm

FABRICATION

Based on the investigated design rules, a first prototype was fabricated. The two parts of the valve body are fabricated with a 3D-printer working with the MultiJet Moldeling (MJM) technology, where high viscose urethane acrylate printed structures become solid three-dimensional bodies after a UV curing process. The used transparent material is "Visijet EX 200".

In figure 5, an exploded drawing of the valve body is shown. The body consists of two individual parts, whereas part one consists of a Luer Lock connection to the reservoir, the magnet stop and the duct structures for the plunger, necessary to minimize the tilting, lower the friction and to guarantee a parallel movement of the plunger. Part two consists of the clamps for the NC magnet and a hole to mount the nozzle. The nozzle is made of a either a PI or steel capillary tube which is glued inside the hole with a defined height of 0.5 mm of the valve seat.
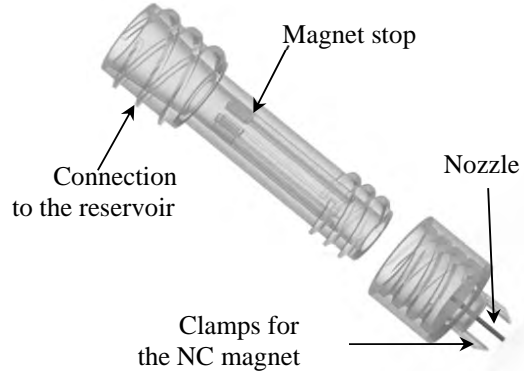
Figure 5. Exploded drawing of the two-part valve body with mounted nozzle.

The used magnet stop defines the maximum stroke length of the plunger to 2.5 mm. The plunger is coated with a Parylene C layer and a 1mm thick silicone sealing layer, with a shore hardness of A60, is glued on top of the plunger. Afterwards, the plunger is inserted into part one which was previously inserted into the actuation coil. Finally, the assembly is closed by part two by a Luer-Lock thread.

Figure 6: Prototype of the disposable, non-contact dispensing valve fabricated applying a 3D printing process.

In order to cover a wide area of applications, different nozzles are used to obtain different minimum volumes and flow rates, cf. table 2.

Table 2: Influence of the dimensions of the nozzle at a constant actuating pressure of 200 mbar on the flow rate and the volume range of the dispensing valve.

ID nozzle	Length nozzle	Flow rate	Min. volume
200 µm	16.5 mm	43 µL/s	200 nL
200 µm	5.5. mm	80 µL/s	400 nL
230 µm	5.5 mm	130 µL/s	1 µL

RESULTS

In order to characterize the droplet ejection process, the droplet volume has to be determined gravimetrically. The dispensing performance was characterized applying the GRM method [5].

The first characterization study focuses on the reproducibility of the valve, expressed by the coefficient of variation (CV) given in percent. It describes the ration between the standard deviation s and the mean volume $\bar{V}$ of 24 individual measurements.

$$CV_{intra-run} = \frac{s}{\bar{V}} = \frac{\sqrt{\frac{1}{n-1}\sum_{i=1}^{n}(d_i - \bar{V})}}{\bar{V}} = \quad (4)$$

Where d_i is the volume of a single dispense in nL and n the number of dispense.

As nozzle we used a metal capillary with an inner diameter of 200 µm and a length of 5.5 mm. The actuation pressure wars set to 160 mbar to guarantee a suitable droplet tear-off. The number of dispenses per run were set to 24 dispenses to get a reliable statistic. The actuation time of the valve was varied between 1 and 60 ms.

In figure 7, each measured volume point in the diagram states the mean volume $\bar{V}$ of one run with 24 dispenses. The valve reveals an excellent performance for water as dispensing medium, cf. figure 7. The CV varies between 0.3% and 2.0% for a volume range between 400 nL and 4.2 µL.
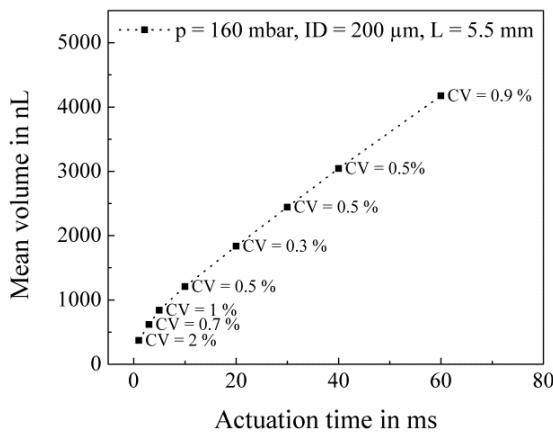

Figure 7: The dispensing performance shows a linear dependency between the actuation time and the dispensed mean volume. Each data point represents the mean volume of one run of 24 individual measurements. Percentages state the respective CV.

As shown in figure 7, the mean volume $\bar{V}$ and the actuation time t show a linear correlation for an actuation time above 10 ms. In order to evaluate the non-linear behavior for t < 10 ms, the flow profile was recorded by a flow sensor from the Sensirion AG mounted between the reservoir and the dispensing valve. We examined that for actuation times less than 10 ms, the flow profile is not fully established. This behavior explains the non-linear range in figure 7 for an actuation time between 1 ms and 10 ms.

SUMMARY

In summary, we successfully miniaturized the functional model of the existing valve to an allover outer diameter of 8.5 mm without any performance restrictions, implying the arrayability of the valve in a 9 mm pitch for 96-well plate applications. The decrease of the actuation current by 50% entails less heat transfer to the sample liquid, thus improves the valve accuracy and reproducibility. Furthermore, we were able to adjust the desired volume range and flow rate by using nozzles with different dimensions. The performance of the developed prototype can already compete with commercially available dispensing valves, implying a cost effective and clean application and the possibility of fabrication by injection molding processes.

REFERENCE

[1] S. Bammesberger, S. Kartmann, L. Tanguy, D. Liang, K. Mutschler, A. Ernst, R. Zengerle, P. Koltay, "A Low-Cost, Normally Closed, Solenoid Valve for Non-Contact Dispensing in the Sub-µL Range", Micromachines, Vol. 4, pp. 9-21, 2013.

[2] F. Kong, L. Yuan, Y. F. Zheng, and W. Chen, "Automatic Liquid Handling for Life Science: A Critical Review of the Current State of the Art", Journal of Laboratory Automation Vol. 17, pp. 169-185, 2012

[3] R. Ravaud, G. Lemarquand, and V. Lemarquand. Force and stiffness of passive magnetic bearings using permanent magnets. part 1: Axial magnetization. Magnetics, IEEE Transactions on, 45(7):2996 –3002, july 2009.

[4] K. Mutschler, S. Dwivedi, S. Kartmann, S. Bammesberger, P. Koltay, R. Zengerle, L. Tanguy, "Multi physics network simulation of a solenoid dispensing valve", Mechatronics, Vol. 24, pp. 209-221, 2014.

[5] D. Liang, C. Steinert, S. Bammesberger, L. Tanguy, A. Ernst, R. Zengerle, P. Koltay, "Novel gravimetric measurement technique for quantitative volume calibration in the sub-microliter range", Meas. Sci. Technol., Vol. 24, 2013.

CONTACT
* S. Kartmann, sabrina.kartmann@imtek.de

2. Actuators   Presentation

VOLUME CONTROLLABLE SEQUENTAIL GENERATION OF THREE DIFFERENT REAGENTS INCUBATED IN MICRO DROPLETS FOR DIGITAL FLOW SYNTHESIS

Afshan Jamshaid[1,3], D.H.Yoon[1], T.Sekiguchi[2,] S.Shoji[1]
[1]Waseda University Tokyo, JAPAN
[2]Nano Technology Research Center, Waseda University Tokyo, JAPAN
[3]Department of Physics, Syed Baber Ali School of Science & Engineering, Lahore University of Management Sciences(LUMS), Pakistan
afshan@toki.waseda.jp

ABSTRACT

We demonstrate the novel microfluidics device for volume controllable and sequential three different reagents incubated micro droplet generation with high performance. The device consists of three Co-flowing generation with different widths of channels. The frequency of droplets flow and prevent from merging at joining point in main channel are controlled by different resistances of three channels. Moreover, we successfully achieved individually controlled volume range from 300nl to 50pl per droplet in multiple sequences of three droplets in different and equal diameters by varying flow rates of carrier and disperse phase. Rapidly and controllably incubating of reagents in different and low volumes makes this device more effective in the chemicals synthesis and drugs discoveries using with our droplet merging device.

KEYWORDS

Micro Droplets, Generation, Flow Resistances, Reagents, Sequential.

INTRODUCTION

Microdroplets in microfluidics offer a great number of opportunities in chemical and biological research. They provide a compartment in which reactions can be isolated. They are Monodispersed and suitable for quantitative studies [1]. Droplet formation of multiple immiscible fluids in microchannels has attracted extensive attentions due to its wide range of applications, such as food and pharmaceutical products [2].Therefore, chemical processes occurring on the fluid/fluid interface can be studied and enhanced by means of efficient droplet generation. An increasing demand is emerging for effortless different reagents microdroplets generation. In response to this demand, the viability of our device to be used as controllable different reagents microdroplets generator.

DEVICE CONCEPT

Concept of device is illustrated in Figure 1. As we know the area is inversely proportional to the resistance. Therefore, with the large area of channel, the resistance will be small of that channel and with the small area of channel the resistance will be high. By using this phenomena we designed this three droplets generation device. With the different resistances of three channels we generated the different three reagents incubated droplets sequentially.

Moreover, carrier flow in channel I (Q_1) is higher than channel II (Q_2). Similarly carrier flow in channel II (Q_2) is higher than channel III (Q_3) because of their different flow resistances. However, Rhodamine B droplet (D_R) flow is slow in channel II and flow of Methylene blue droplets (D_M) is faster in channel I as well in channel III Fluorescein droplet (D_Y) flow is two times slower than Methylene blue droplets (D_M). Therefore, with this technique we will successfully generate three different reagents sequential droplets in multiple combinations by the controlled velocity of these three droplets.

D_M =Methylene Blue Droplet
D_R= (Rhodamine B Droplet)
D_Y=Fluorescein (Sodium Salt) Droplet
Q=Carrier Flow (Oil Flow)
Q_1=Disperse Phase Flow I (Methylene Blue Flow)
Q_2= Disperse Phase Flow II (Fluorescent Dye)
Q_3= Disperse Phase Flow III (Rhodmine B Flow)

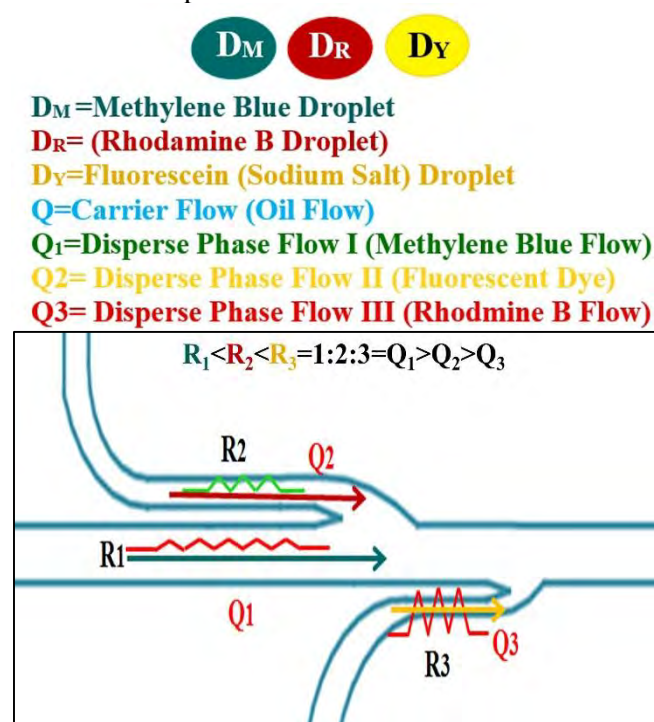$R_1 < R_2 < R_3 = 1:2:3 = Q_1 > Q_2 > Q_3$

Figure 1: Working principle of three reagents droplets Generation device

DESIGN AND FABRICATION
Design

Figure 2 shows the top view and detailed dimensions of the whole droplet generation device. In this design, the generation part is consist of three Cross-

flowing generation, in which width of the channel I is 200μm and channel II has width of 100 μm, and 50 μm width of channel III for the purpose to generate the synchronized three colors droplets. Height of all structure is 85μm. The generated three reagents incubated droplets observed in the main channel for analysis. Where the width of main channel is also 200 μm to provide the low resistance flow path to generated three reagents droplets. This three droplets generation device is too simple and easy to fabricate for different chemical analysis.
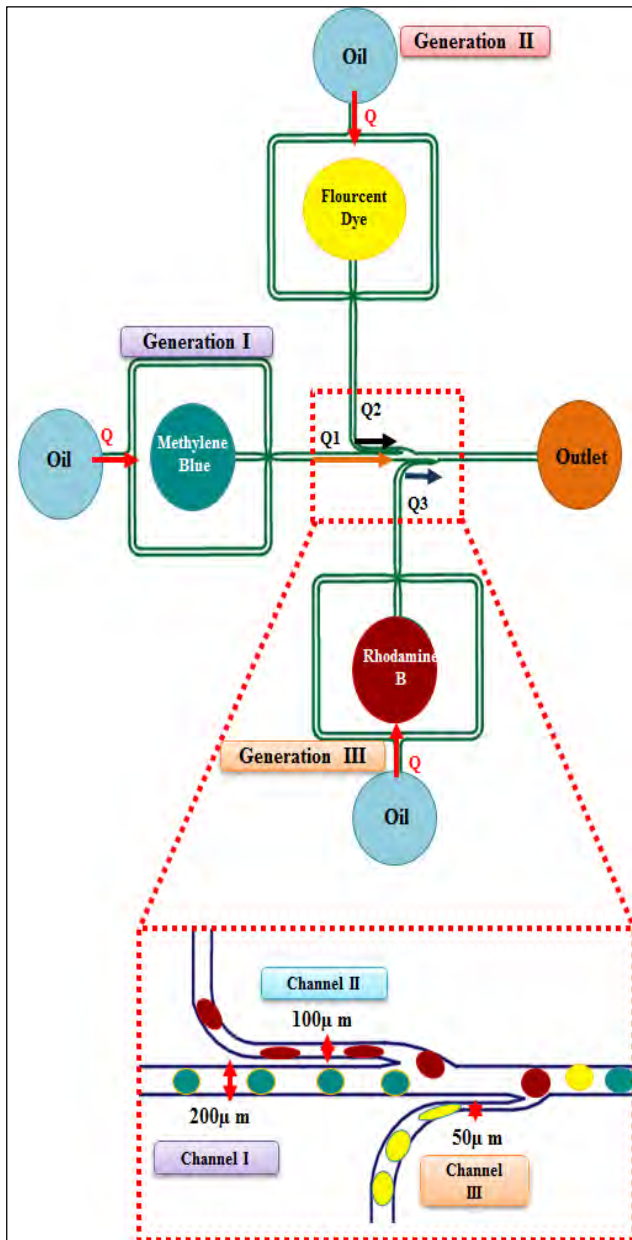

Figure 2: Design of controllable three reagents droplets generation device.

Fabrication

The Si wafer is coated with SU-8 (3050 negative photoresist) using the recipe of the spinner as slope for 5sec, 1500rpm for 30sec, again slope for 5sec and then at last the 3000rpm for 0.5sec to make the photoresist coating on edges of the wafer equal to the middle on the wafer. After coating and baking the photoresist, we used the photo mask for transferring the system pattern on the wafer using standard soft lithographic technique structured PDMS layer, PDMS base and curing agent were mixed in a ratio of 15: 1, degassed and decanted onto an SU-8 master mold. The resulting structure was cured for 90min in an oven at 75ºC and then kept overnight. On the other day the polymer layer was peeled off the master mold. This layer is then bonded with a flat PDMS layer using O_2 plasma treatment. After plasma bonding the surface of PDMS has become hydrophilic, to make it hydrophobic we baked the microfluidics device at 70ºC for 30min in oven and kept for one week on room temperature to form the completed micro device.

The SEM images of SU-8 mold of droplets generation device and PDMS replica of SU-8 mold droplets generation device illustrated in Figure 3 (a) and (b).
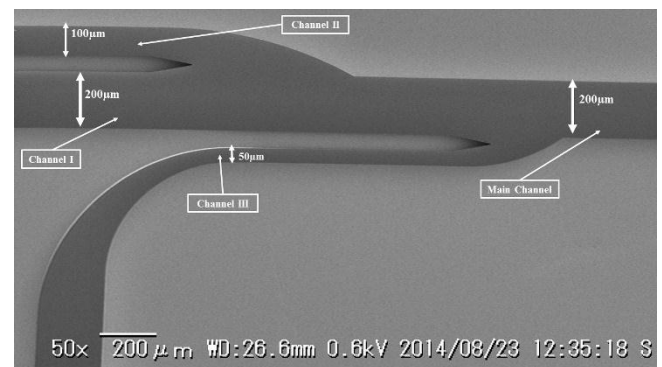
(a) Su-8 mold
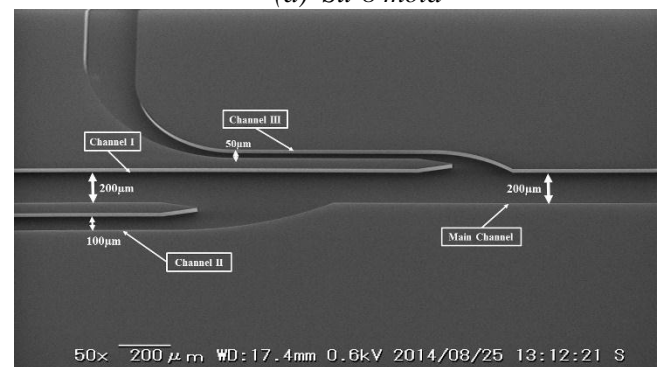
(b) PDMS device
Figure 3: SEM images of device

EXPERIMENTAL SETUP

For fluidic experiments, a syringe pump (KDS210, kd Scientific) and a syringe (1725CX HAMILTON) were used to control volumetric flow rates of oil as carrier, Rhodamine B, Methylene Blue and Fluorescein droplet. In order to evaluate the generation rate and the diameter of micro droplets, the high speed CCD camera

(PHOTRON FASTCAM-NEO32KC) was used. This camera system and a data processing computer were utilized for visualization and storage of the three colors droplets behaviors in generation part for different sizes and different volumes as shown in Figure 4.

Figure 4: The experimental setup

RESULTS AND DISCUSSION

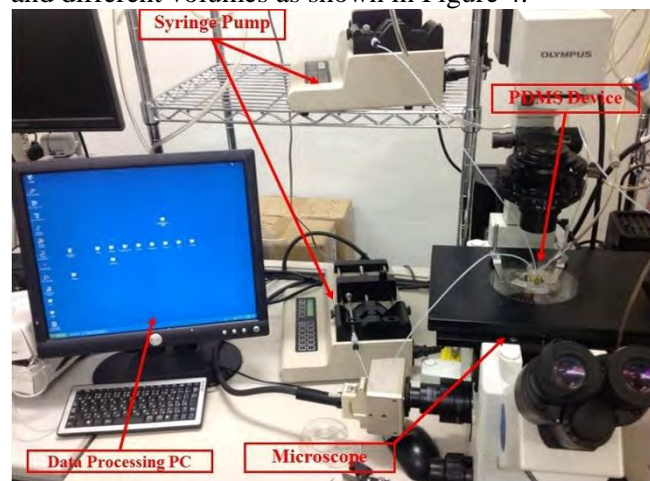Figure 5 provides a detailed analysis of multiple combinations of large, medium and small D_M (Methylene Blue), D_R (Rhodamine B) and D_Y (Fluorescein or Sodium Salt) in different and equal diameter droplets. Process of scaling of the size of the discrete fluid produced in channels geometries over a range of typical values of flow rates of oil and fluid. Resistances of three channels are fixed and different from each other, through which surface tension and the flow frequency of droplets are controlled and not to infuse at the joining point in main channel. Figure 5 (a) demonstrates the equal and large droplets (D_R, D_Y, D_M) inside micro channels with the flow rate of 0.5μl/min of carrier flow and 0.5μl/min of Rhodamine B, Methylen blue and Fluorescein. Where Figure 5 (b,c,d) shows the medium and small three droplets generation in different ratios by varying the flow rates of oil and three reagents. These three different reagents droplets are generated sequentially without changing the channels resistances. With only varying the flow rates of carrier flow and disperse phases we successfully achieved the multiple combinations of three different droplets in equal and different diameters. With these results we can generate droplets of three chemicals in various volumes on demand for multiple applications.

Moreover, Graph in Figure 6 depicts the results of generation of three reagents Microdroplets in multiple diameters with different flow rates of carrier (oil) and methylene blue, Rhodamine B and Fluorescein.

Comparing the other mechanisms such as electrical generation can damage chemical or biological fluids. Hence, our device will be more productive when applying microdroplets to digital flow synthesis and can be effectively used for multiple applications in drugs discoveries and different cells analysis at the same time and in same device. In future, this three droplets generation device will be effectively used for chemical analysis by integrating with our droplets merging device [1].

(a) $Q=0.5\mu l/min$, $Q_1= Q_2= Q_3=0.5\mu l/min$

(b) $Q=0.9\mu l/min$, $Q_1=0.5\mu l/min$, $Q_3=0.7\mu l/min$ $Q_2=0.1\mu l/min$

(c) $Q=0.8\mu l/min$, $Q_1= Q_3=0.6\mu l/min$ $Q_1=0.01\mu l/min$

(d) $Q=0.6\mu l/min$, $Q_2= Q_3=0.02\mu l/min$, $Q_3=0.2\mu l/min$
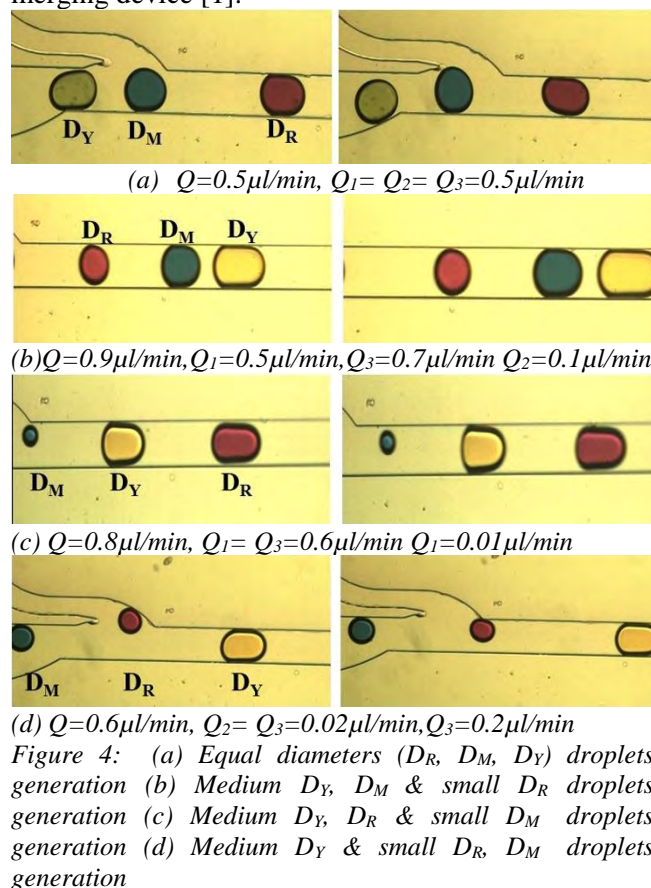
Figure 4: (a) Equal diameters (D_R, D_M, D_Y) droplets generation (b) Medium D_Y, D_M & small D_R droplets generation (c) Medium D_Y, D_R & small D_M droplets generation (d) Medium D_Y & small D_R, D_M droplets generation
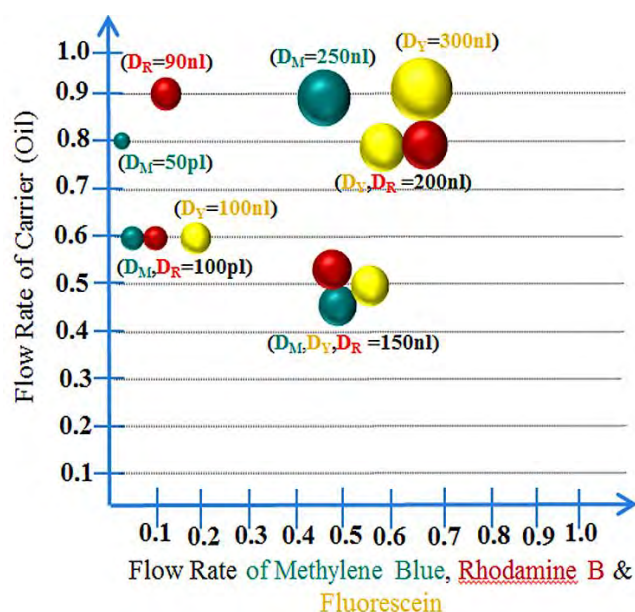
Figure 6: Graphical representation of generation of three reagents microdroplets in multiple diameters

CONCLUSION

With these results we can generate droplets of three reagents in various volumes of Pico and Nano liters on demand. The numbers and volumes of generated droplets were controlled by without changing the channels resistances. Furthermore, the reagents will not be affected by any external forces in micro channels, which makes this droplets generation device more effective choice rather than using other droplets generation mechanisms such as electric field or magnetic field controlled and Ultrasonic waves can damage chemicals and biological species incubated in micro droplets for analysis.

REFERENCES

[1] Afshan Jamshaid , Masaya Igaki, Dong Hyun Yoon, Tetsushi,Sekiguchi and Shuichi,Shoji"Controll able active droplets merging device using horizontal pneumatic micro valves" Micromachines 2013, 4(1), 34-48; doi:10.3390/mi4010034

[2] West J, Becker M, Tombrink S, Manz A. "Micro Total Analysis System" Latest Achievements, Anal Chem. 2008 Jun 15;80(12):4403-19. doi: 10.1021/ac800680j.

CONTACT

* afshan@toki.waseda.jp

2. Actuators   Presentation

DECOUPLED MICROFLUIDIC FLUID HANDLING SYSTEM FOR COMBINATORIAL GENOME SEGMENT ASSEMBLY

M. Kersaudy-Kerhoas[1], F. Amalou[1], M.P.Y. Desmulliez[2] and W. Shu[1]*

[1] Heriot-Watt University, Institute of Biological Chemistry, Biophysics and Bioengineering, Edinburgh, Scotland
[2] Heriot-Watt University, Institute of Signals, Sensors and Systems, Edinburgh, Scotland

ABSTRACT

The aim of synthetic biology is to remodel living units from building blocks such as genes in order to optimize the production of value-added products such as pharmaceutical products, or simply develop a better understanding of biological processes. For this purpose, genes of several hundreds of base–pairs are produced *de-novo* via oligonucleotide synthesis to create libraries. However, to develop a full or partial genome requires the assembly of genes, or genome segments. Testing hundreds of different genome segment combinations demand complex and expensive robotic fluid handling systems. We propose a decoupled microfluidic handling system which could lower the costs of combinatorial genome segment assembly. The platform and disposable chips are validated against a bench protocol using a 5 part assembly.

KEYWORDS

Decoupling, pneumatic actuation, droplets, synthetic biology, combinatorial assembly

INTRODUCTION

Synthetic Biology is emerging as one of the potential solutions to several global issues including food and energy scarcity, and environmental pollution monitoring [1]. The concept of synthetic biology is to engineer living organisms using standardized DNA parts in order to produce individual organisms capable of producing novel pharmaceutical, nutritional, or fuel compounds or function as biosensors. An important feature of synthetic organism production is the efficient automation of DNA part assembly. In order to re-engineer bacteria, a bioengineer must use library constructs or synthetize new constructs (parts) and assemble them into a plasmid, or genomic backbone. A number of ways to assemble DNA parts have been devised, some of which, such as ligation allow pooling assembly [1]. This enables rapid combinatorial assemblies from an existing DNA parts library. Unlike in electronics or mechanics, the constructs composed of several parts cannot yet be simulated or well predicted based on reliable datasheets. As a result, building new constructs requires extensive trial and error, and the capacity to rapidly assemble parts in various order is crucial.

Fluid handling robots (Fig.1) are commonly used by synthetic biologists to assemble parts; however these tools have limitations due to their cost, and limited integration capabilities. Microfluidics is recognised as an enabling technology capable of solving some of these issues and producing alternative high-throughput approach for DNA segments assembly [1,2]. De-novo DNA synthesis has been demonstrated on microfluidic platforms, however the size of the constructs was limited to 1kb [3, 4].

We have proposed an integrated microfluidic platform which uses a decoupling concept (Fig.2) to isolate the fluidic layer from integrated actuators which enable complex biological protocols without increasing the cost of the disposable microfluidic chip [2]. In an earlier publication, we demonstrated the purification of up to four genome segments in parallel. In this present paper we propose a novel module capable of combinatorial assembly of genome segments encapsulated in aqueous droplets and transported in an oil phase.
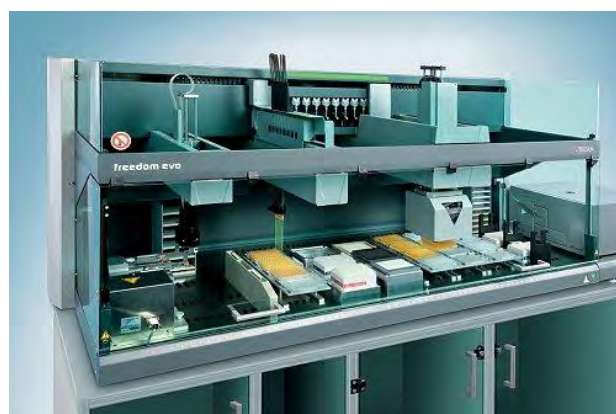
Figure 1: A fluid handling robot (Freedom Evo) from Tecan (USA) pictured here can cost around from 50k€ refurbished to several 100k€ depending on the modularity of the instrument. Reproduced from www.tecan.com.

DESIGN

The decoupled concept was described extensively in [2]. Briefly, it features a rigid layer (Fig.2, part A) for the accurate alignment of the chip with the underlying platform, combined with an elastic and deformable layer (Fig.2, part B) acting as

a membrane for closing valves via pneumatic actuation as well as sealing the chip and isolating it from the platform. The flow inside the microfluidic channels is accurately controlled by a separate underlying control platform (Fig.2, C). No tubing connection is necessary on the microfluidic chip and the disposable passive part is simply clamped on a layer of silicone O-rings embedded in the integrated control platform.
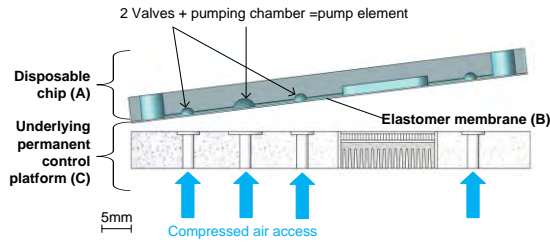
Figure 2: Decoupled concept detailed in [2]. An elastomer membrane (B) acts both as a seal to close a disposable chip and a flexible membrane actuated via compressed air through an underlying control platform (C).

Here we propose a novel chip design for the assembly of up to 2x6 parts in 2 parallel channels, using a two-phase approach with oil as a carrier, and DNA parts in a water-based buffer. The chip design illustrated in Fig.3, includes two main channels filled with mineral oil and 14 individual channels containing the genome segments, ligase buffer or water. Two types of valves and pumps were used: a regular spherical cap type was used for the pump seat, while a thin valve was used at the junction or the nozzle between the aqueous channel and the oil main channel (Fig.3.B). A cross-section of this valve is presented in Fig.3C. The theoretical thickness of the valve was 50 μm, although once opened the membrane exposed on the pneumatic access side can be slightly deformed by the upcoming flow. Using one or several pump strokes, DNA parts are encapsulated in an aqueous droplet floating in the main channel and flowed to the output well using the oil carrier pump strokes where it naturally coalesces with other droplets from different DNA parts channels and the ligase buffer to form the assembly ready to be transformed into competent cells.

DEVICE FABRICATION

The 4 mm PMMA rigid layer featuring the channels, pump and valves was manufactured using laser cutting and computer numerical control (CNC) milling, and assembled using a process described in [2]. In particular, for this design the output wells were chambered in order to trap the final product droplet at the bottom of the well (top-view photograph and cross-section, Fig 4B). Double coated adhesive transfer tape (467MP, 3M) was used

to bond the layers. This rapid-prototyping technique has been widely used and reported by other groups and is straightforward, reliable and cost-effective compared to surface modification techniques such as the use of oxygen plasma.

In addition, to ensure that no adhesive is obstructing the membrane in the valve and chambers area, which would otherwise impair the functionality of the chip, the adhesive layer was laser-cut prior to assembly. A 0.5 mm thick PMMA back layer coated with a layer of double sided transfer tape was also applied to the membrane to support the channels.
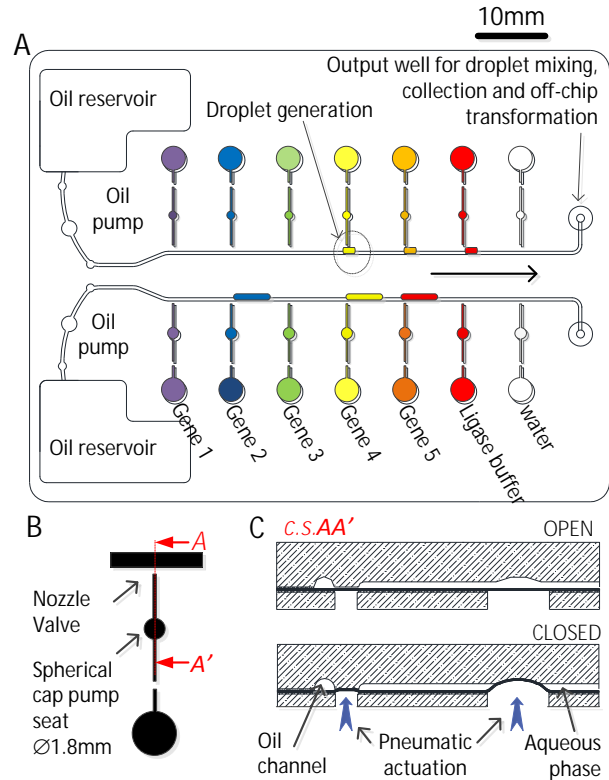
Figure 3: Microfluidic chip for combinatorial assembly of up to 5 DNA parts. A) Chip design featuring two parallel main channels (filled with mineral oil) with 6 channels containing DNA parts (water-based). The upper channels have a pump seat diameter of 1.2 mm and the bottom channels a maximum pump seat diameter of 1.8 mm. B) Detail of an individual pump system comprising two valves and a spherical cap pump seat. C) Cross-section of a pump system with nozzle valve and spherical cap pump seat.
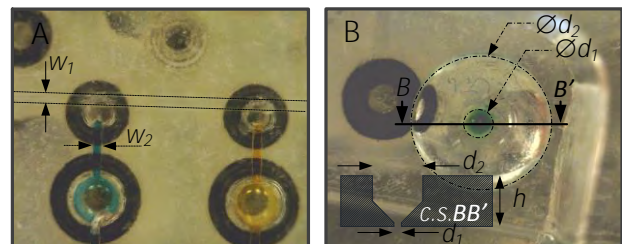
Figure 4: Details of microfluidic chip prototypes A) Channels and valves for droplet delivery. The dashed line highlight the edges of the main channel (width w_1=0.5

mm), the channels ($w_2=0.3$ mm) containing DNA parts are filled with food dyes (blue and yellow). The black circles on the photos are O-rings enabling a tight seal between the disposable chip (clamped) and the platform. B) Photograph showing the chamfered output well for droplets mixing and collection. In insert a cross-section of the well, $d_1=4$ mm, $d_2=0.5$ mm, $h=4$ mm.

EXPERIMENTAL METHODS

Biological materials were provided by Ginkgo Bioworks Inc. (MA, USA), and included a 5 parts assembly kit containing parts coding for red fluorescent protein (RFP), green fluorescent protein (GFP), kanamycin resistance (KanR), ampicillin resistance (AmpR), a plasmid backbone (psC101) and a ligation buffer. On-chip and off-chip protocols developed jointly with Ginkgo Bioworks are described in Table.1. For the on-chip experiment the valves were closed and the 5 parts, buffer and water were placed into the input wells as indicated in Fig. 3. In this experiment, we generated 4 products: P1 was the on-chip experiment and P2 the on-chip negative control. Two controls were performed off-chip by assembly directly all parts and buffer in an Eppendorf tube. To investigate the effect of food dyes and oil on the assembly efficiency, we placed 0.5 µL of food dye and the same amount of oil into the assembly mix prior to transformation. P3 the off-chip (or bench) control (P1, P2, P3 and P4). The results were validated indirectly by transforming *E.Coli* competent cells (NEB, USA) with these products. Cells were then plated onto Agar Plates containing kanamycin and ampicillin antibiotics (Technova, USA) and incubated over night at 37ºC. Colonies were inspected by eye and under fluorescent light. Counting was performed using an Image J macro.

RESULTS AND DISCUSSION

Droplet generation

The droplet production in the chip is illustrated in Fig. 4 using water mixed with food dyes. The droplets produced by a single pump stroke with a pump seat of 1.8 mm and 1.2 mm have a surface area respectively, around 0.72 mm^2 and 1.68 mm^2 (Fig. 5). The desired number of bubbles is produced in the main channel and oil flow is activated to push the droplets in the output well. Once into the output well, the droplets stay at the bottom of the well, and coalesce naturally in a few seconds. After coalescence, the product is ready to be pipetted out of the chip. Fig. 6 illustrates the droplet coalescence under the injection of new bubbles in a series of photographs with an interval of ~30 s.

Two different types of pumping modes were used. A single stroke of the pump system allowed the formation of a single droplet with a volume corresponding to the volume of the pump seat and valve seat. In a second "continuous" mode, several strokes of the pump allowed the formation of much larger volume of sub-products, corresponding to the number of pump strokes.
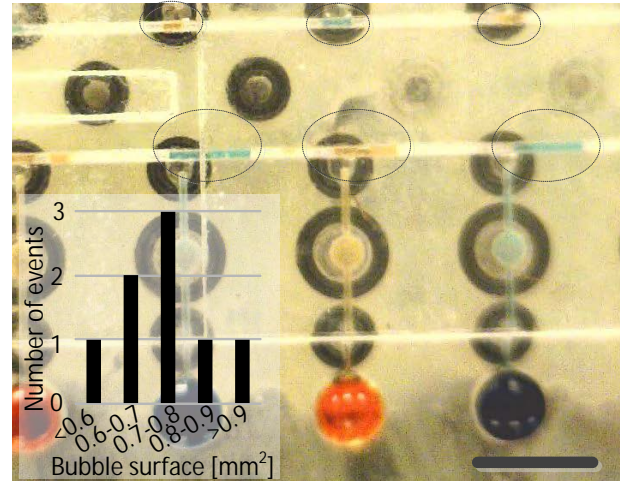
Figure 5: Droplet generation at the nozzle of input channels with pump seat of 1.2 and 1.8 mm. In insert, the range of bubble surface for 1.2 mm pump seat over n=8 with a single droplet generation mode.
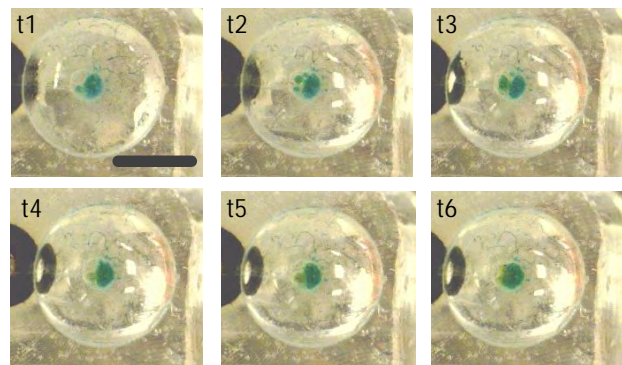
Figure 6: A sequence of 6 photos at an interval of approximately 30 seconds showing droplet coalescence in the output well. An additional droplet of yellow food dye mixed with water was injected into the well via the main channel (on the left of the output well) between each image which explains why the gradient from blue to green in the final product droplet. As oil is the carrier fluid, the amount of oil is increasing after each droplet is added. The scale bar is 250 µm.

Biological validation

Cell colonies were observed on all P1, P3 and P4 plates as illustrated in Fig. 7. The negative control P2 did not have any colonies. The yield in P1, P3 and P4 are of the same order of magnitude, although the on-chip yield is about 41% lower than the off-chip control. It can be noticed that the off-chip control with oil and food dyes has a yield

slightly higher (6%) than the control without oil and food dyes. Ideally, colonies could have been extracted; DNA purified and separated using gel electrophoresis to check for the size of the product as another control of assembly. This was not performed at the time of the project.

Table 1. DNA parts assembly on-chip and off-chip protocols for four products

Reagents and Parts and Sequences		
On-chip	0.5 µL of ligation buffer, 0.5 µL of each parts including the plasmid, were pumped sequentially into the main channel, pushed into the output well and collected with a pipette	P1
	1 µL of water from the water well was pumped into the output channel and pipetted off the chip to waste. Another 1µL of water was then pumped and formed final product	P2
Off-chip	0.5 µL of buffer, 0.5 µL of each part, 0.5 µL of mineral oil, and 1µL of blue and yellow dye were pipetted in a 0. 5mL tube and gently mixed	P3
	0.5 µL Buffer, 0.5 µL of each parts were pipetted in a 0.5 mL tube and gently mixed	P4

Figure 7: Agar plates from P1, P2, P3 and P4 including approximated yield calculated from 2 random windows in each plate. Yield Inserts show a close-up view of the cell colonies under UV light (no image processing).

CONCLUSION AND OUTLOOK
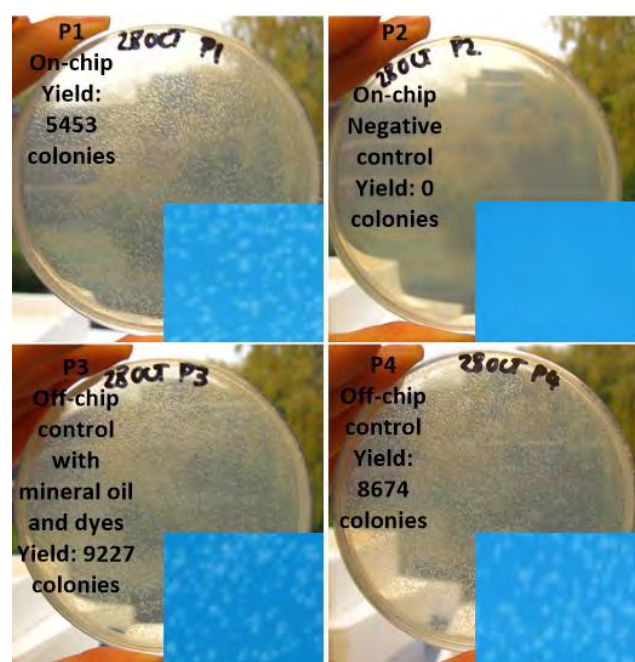
In conclusion, although lacking a thorough statistical analysis, these preliminary findings highlight the possibility of performing complex combinatorial assembly without the need for a high number of pipetting steps and expensive liquid handling solutions. A scale-up version of this chip, including a total of 48 channels was produced by a design company and used to produce a 10 part assembly which resulted in black colonies. This demonstrated the scalability of the design, however the reliability of the chip still need improvement, specifically we found that the time for the membrane to be release from the bottom of the spherical cap was variable. Improvement in general reliability and droplet area/volume may come from manufacturing the chip using photolithography rather than laser etching and milling. However the ability to produce the chips rapidly without masks and from affordable material has the appeal of fast turn-around from idea to test.

Together with our previous module for parts purification [2], this combinatorial assembly chip forms a flexible and affordable platform for synthetic biology applications as well as general high-throughput nucleic acids manipulation.

CONTACT

*w.shu@hw.ac.uk

REFERENCES:

[1] P.A. Carr and G.M. Church, "Genome Engineering", Nature Biotechnology, pp 1151-1163, 2009

[2] H. Huang and D. Densmore "Integration of microfluidics into the synthetic biology workflow", Lab On Chip, pp, 2014

[3] D.S. Kong, P.A.Carr, C.Lu, S.Zhang, J.M. Jacobson "Parallel gene synthesis in a microfluidic device", Nucleic Acids Research, p. e61, 2007

[4] C.-C. Lee, T.M. Snyder and S.R. Quake, Nucleic Acids Research, p e61, 2007

[5] M. Kersaudy-Kerhoas, F. Amalou, A. Che, J. Kelly, Y. Liu, M.P.Y. Desmulliez and W. Shu, "Validation of a fully integrated platform and disposable microfluidic chips enabling parallel purification of genome segments for assembly", Biotechnol. Bioeng, pp 1627-1637, 2014

4. Fluidic control systems   Presentation&Poster

MICROFLUIDIC DROPLET HANDLING BY ACOUSTOPHORESIS ON BULK ACOUSTIC WAVE (BAW) DEVICES

I. Leibacher*, P. Reichert* and J. Dual
Swiss Federal Institute of Technology (ETH Zurich), Institute of Mechanical Systems (IMES), Zurich, Switzerland

ABSTRACT

Droplet microfluidics has emerged into a promising field for fluid handling on lab-on-a-chip devices, where fluidic droplets serve as liquid vessels e. g. for biochemical reagents. Key to the applications is a set of unit operations for droplet handling, i.e. droplet fusion, sorting, medium exchange and storage. In the following, we present a method to provide these unit operations for droplets of about 200 µm size. The acoustophoretic method is applied in bulk acoustic wave (BAW) devices, where water-in-oil droplets can be generated and manipulated with acoustic operating frequencies around 0.5 MHz.

KEYWORDS

Droplet microfluidics, acoustophoresis, ultrasonic standing wave, droplet sorting, droplet fusion, piezoelectric transducer

INTRODUCTION

The miniaturization of fluid handling systems has led to the field of "droplet microfluidics" [1]. Discrete fluid droplets are thereby the vessels for biological-chemical laboratory procedures, which are operated in lab-on-a-chip systems. Favored by low Reynolds and Weber numbers, the droplet format offers many advantages for fluid handling on the micro scale, once the droplet handling is enabled [2]. Therefore, we propose the contactless handling of droplets by ultrasonic waves for unit operations such as droplet fusion, sorting, medium exchange and storage [3]. This fluid handling method is enabled by bulk acoustic wave (BAW) devices with the method of acoustophoresis [4].

Regarding acoustic droplet handling, most work so far has been dealing with surface acoustic waves (SAW). Thereby, an acoustic field in PDMS microchannels is generated on a piezoelectric ground plate with interdigitated transducers (IDT), which acts on droplets by acoustic radiation forces [5] or by the drag forces of acoustic streaming [6]. Compared to this earlier work, our method differs as it builds on a bulk acoustic wave (BAW) approach. In our microfluidic channel, a standing acoustic wave is generated by a bulk piezoelectric transducer rather than IDTs. The piezoelectric transducer allows to excite bulk waves and mechanical resonance in acoustically hard silicon

devices. Whereas SAW approaches are restricted by a piezoelectric ground plate and PDMS channels, the BAW approach allows quite a free transducer placement on any acoustically hard microfluidic channel. The resulting method is simple in terms of fabrication, versatile in applications and geometrically compact.

SETUP AND OPERATION PRINCIPLE

The proposed fluid handling method operates on a micromachined silicon/glass chip (Figure 1) with a main channel of 1 mm width and 200 µm height. Both the droplet generation and the subsequent acoustophoretic manipulation were conducted on this chip. Water-in-oil droplets (silicone oil, Dow Corning 200) with diameters ranging from 50 µm to 250 µm were generated with T-junction and flow focusing geometries in a flow rate range of 15 to 40 µl/min. To actuate acoustophoresis, a bulk piezoelectric transducer for the excitation of ultrasonic waves was glued on the back side of the devices (Figure 2). The transducer was excited by a function generator (Tektronix AFG 3022B) and an amplifier (ENI 2100L) at channel resonance frequencies in the range of 400 kHz to 2 MHz with 20-35 V_{rms} amplitude. The transducer requires only low power. Therefore it is suitable to be integrated on portable devices, as desired in the lab-on-a-chip concept.

The experiments were monitored by a high speed camera (HiSpec 1 Mono, Fastec Imaging) in bright field and fluorescent microscopy. Fluid flows were actuated by up to 4 syringe pumps (Cetoni Nemesys). The experimental setup is illustrated in Figure 3.
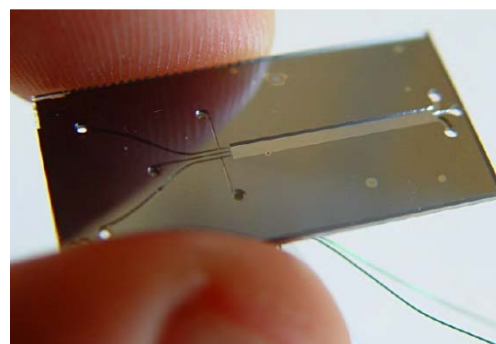

Figure 1: Front side of a 8 mm x 24 mm *silicon chip with microfluidic channels for droplet generation and manipulation.*
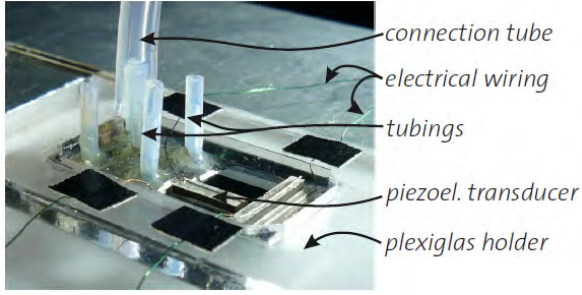
Figure 2: Back side of the chip from Figure 1 with fluidic and electrical connections.
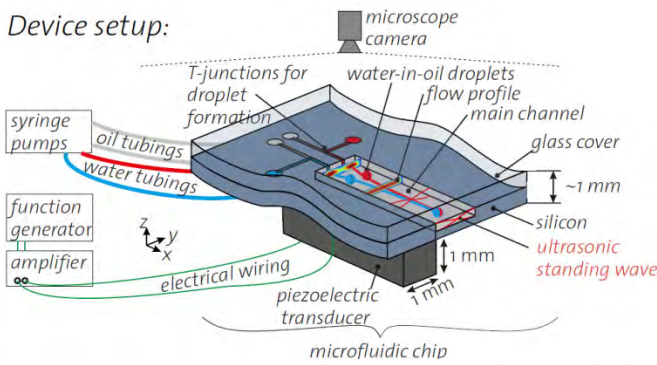

Figure 3: Experimental setup on and around the microfluidic chip.

Bounded by the mismatch of the characteristic acoustic impedance $Z=\rho c$ at the silicon/silicone oil interface (modeled as hard wall condition), certain fluid resonance modes across the channel width are feasible, when multiples of $\lambda/2$ fit between left and right channel wall with $\lambda = c_{oil}/f$ for the wavelength λ, the speed of sound c_{oil} in silicone oil and the actuation frequency f. If the transducer is tuned to such a fluid resonance frequency, this leads to the formation of an ultrasonic standing wave in the fluid. As an example, the first and second resonance modes of $\lambda/2$ and λ are shown in Figure 4.

These standing wave fields exert acoustic radiation forces on acoustically contrasting dispensed droplets within the suspending liquid. For spherical droplets with radius $r \ll \lambda$ (long-wavelength range), the acoustic radiation force $\mathbf{F}$ can be calculated with the Gor'kov potential [7] in the acoustic domain. For a droplet in a 1D standing wave field, the analytic calculation yields [8]

$$\mathbf{F} = F \cdot \boldsymbol{e}_y = 4\pi\Phi k_y r^3 E_{ac}\sin(2k_y y) \quad (1)$$

with the acoustic contrast factor $\Phi=f_1/3+f_2/2$ [9], the acoustic energy density $E_{ac}= p_a^2 /(4\ \rho_{oil}\ c_{oil}^2)$, the pressure amplitude p_a, the density ρ_{oil} and speed of

sound c_{oil} in the suspending silicone oil and the wave number k_y. For droplets in fluid, the first factor f_1 yields

$$f_1 = 1 - \frac{\kappa_{wa}}{\kappa_{oil}} = 1 - \frac{\rho_{oil}c_{oil}^2}{\rho_{wa}c_{wa}^2} \quad (2)$$

with the compressibility κ_{wa} of the water droplet and κ_{oil} of the surrounding silicone oil.

The second factor f_2 determines the influence of the velocity field in the Gor'kov potential. It is given as

$$f_2 = \frac{2(\rho_{wa}-\rho_{oil})}{2\rho_{wa}+\rho_{oil}} \quad (3)$$

In our experiments, the material parameters of water and silicone oil lead to the factors $f_1=0.57$, $f_2=0.03$ and a positive acoustic contrast factor $\Phi>0$. Therefore, droplets will be attracted to the pressure nodes in the standing wave, which correspond to the velocity antinodes as known from linear acoustics of standing waves.

Figure 4: Sketch of the operating principle for BAW acoustophoretic droplet handling with a standing acoustic wave. The lowest two resonance modes with $\lambda/2$ and λ in y-direction are illustrated. (They occur at two different resonance frequencies.)

RESULTS AND DISCUSSION

Droplet Fusion

For droplet fusion experiments, two water-in-oil droplets were generated in a temporally synchronized manner. The droplets were generated at microfluidic T-junctions [10, 11] as shown in Figure 5. For visualization, the water - inflowing from above - was dyed with fluorescein and appears white in the shown high-speed fluorescence microscopy images. The silicone oil is flowing in from the left side and pinches off a discrete water droplet. The water droplet is then flowing to the right side and finally into a larger channel of 1 mm width for ultrasonic manipulation, as

shown in Figure 6, which was captured by bright field microscopy.

Figure 5: Generation of microfluidic water-in-oil droplets in a T-junction with 40 μm channel width, captured by fluorescent imaging.

Further downwards in the channel of Figure 6, the one-to-one fusion of droplets in a continuous flow is induced by focusing them on the channel centerline with acoustophoresis. A resonance mode with a standing pressure wave of $\lambda/2$ across the channel width was found by tuning the transducer frequency to 464 kHz. With the speed of sound $c_{oil} \approx 1000$ m/s of silicone oil, this frequency value approximately matches the expectation of the first resonance frequency $f = c_{oil}/\lambda = 1000$ m/s / 2 mm = 500 kHz, where a $\lambda/2$ mode will be generated in the channel of 1 mm width as shown in Figure 4. Reasons for the difference between calculated and experimentally found resonance frequency are the compliance of the silicon boundary (which was neglected by the hard wall assumption) and the influence of the mechanical/piezoelectric device parts which couple with the fluidic resonance.

Besides the acoustic forces, the droplet fusion also depends on the fluid dynamics. Droplets of larger size showed a slower velocity due to an increase of friction at the top/bottom channel boundaries. Because of this velocity difference, the droplets from the upper and lower T-junction were found to self-synchronize: the smaller droplets (dark dyed) catch up with the larger droplets (lighter color, undyed), until both droplets came into contact and merged.

Compared to other droplet fusion methods, acoustic methods show several benefits: they allow active on/off control (unlike passive hydrodynamic fusion), they are simple to fabricate (simpler than electrodes for fusion by electric fields), they can easily be integrated on chip-level (unlike laser-assisted methods), and they work for many combinations of dispersed and continuous phase liquid as long as they are acoustically contrasting (no dependency on magnetic/dielectric properties). As a disadvantage of this acoustic method, it is less suited for fusion of strongly surfactant-stabilized droplets.

The shown active droplet fusion method allows fluid sample mixing operations on the micro scale. It allows e. g. reaction initiation, droplet dilution and cell-in-droplet handling, which are of interest for biochemical applications of droplet microfluidics.

Figure 6: Acoustophoretic droplet fusion induced by piezoelectric ultrasonic excitation, which results in a pressure standing wave in the microfluidic channel.

Droplet sorting

Acoustophoresis is a suitable method for droplet sorting tasks [5,6]. As shown in Figure 8, by turning the ultrasound transducer on/off, droplet paths can actively be switched between upper/lower outlet by the same BAW method as for the droplet fusion of the last section.

Alternatively to turning the transducer on/off, the resonance frequency might be switched between the $\lambda/2$ and $\lambda/2$ mode as shown in Figure 4 to achieve droplet sorting in an upper/lower outlet.

This valve-like operation might allow controlled droplet sorting, when a further upstream sensor is installed to characterize the inflowing droplets. Depending on the measured droplet characteristics, they can then be guided through the upper or lower outlet and collected further downstream. Future efforts are aiming at an increase of the sorting speed to meet the requirements of high-speed droplet handling with increased throughput.

Figure 8: Droplet sorting between the two outlet channels by switching the $\lambda/2$ mode on in b), whereas ultrasound was turned off in a).

Medium change

As a third droplet handling unit operation, it is often desired to transfer droplets to another continuous phase for washing, for droplet concentration or to expose them to another surfactant in the continuous phase.

In Figure 9b, droplets experience an exchange of their suspending continuous phase from the dyed oil (center) to the undyed oil in the lower third of the channel. This is feasible because the acoustic radiation force acts selectively on the dispersed water because it is acoustically contrasting to the continuous phase, namely the silicone oil. This method enables e. g. to stabilize droplets by moving them from a surfactant-free continuous liquid to a surfactant-blended continuous liquid.

Figure 9: Exchange of the continuous phase of dispersed droplets (Ø~150µm). A droplet in dyed oil without ultrasound in a) is deflected into a different oil phase in b) with acoustophoresis.

CONCLUSION

The presented acoustophoretic droplet handling enables a range of fluid handling operations for droplet microfluidics. This is feasible becau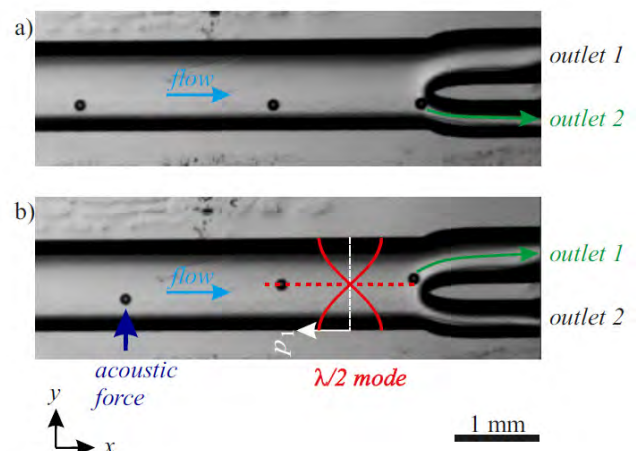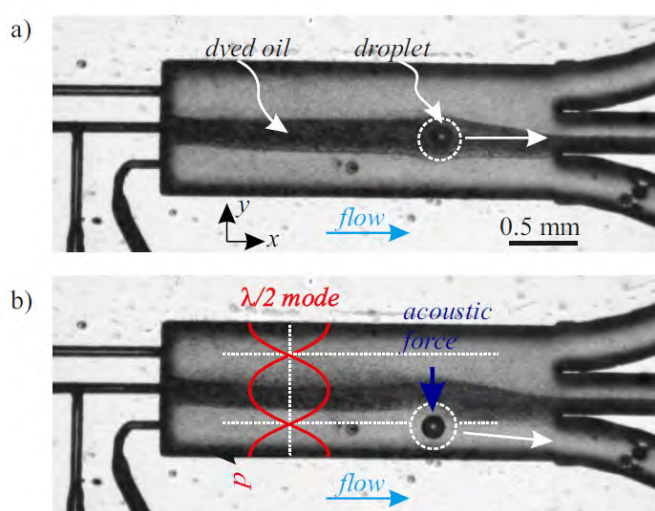se the acoustic radiation force acts selectively on dispersed water droplets due to their acoustically contrasting fluid.

Compared to the alternative surface acoustic wave (SAW) method [5,6], the BAW method has a simpler setup. The lower operation frequency of the BAW method leads to higher wavelengths, which allow the handling of larger droplets from ~1 µm up to ~500 µm size. The method is ideally suited for active droplet handling tasks in portable, low-power lab-on-a-chip systems.

In view of applications, the shown fluid sample handling by ultrasonic waves offers significant benefits for the contact-free fluid handling e.g. in laboratory diagnostics/analytics and biochemical research.

REFERENCES

[1] S. Y. Teh, R. Lin, L. H. Hung, A. P. Lee, „Droplet microfluidics", Lab on a Chip, 8(2), 198-220, 2008.

[2] X. Casadevall i Solvas, A. de Mello, "Droplet microfluidics: recent developments and future applications", Chemical communications, 47(7), 1936–1942, 2011.

[3] I. Leibacher & P. Reichert, J. Dual, "Continuous flow droplet acoustophoresis with bulk acoustic waves", *Flow14 Conference*, *Enschede, Netherlands*, May 18-21, 2014.

[4] H. Bruus, J. Dual, J. Hawkes, M. Hill, T. Laurell, J. Nilsson, S. Radel, S. Sadhal, M. Wiklund, "Forthcoming Lab on a Chip tutorial series on acoustofluidics: Acoustofluidics - exploiting ultrasonic standing wave forces and acoustic streaming in microfluidic systems for cell and particle manipulation", Lab on a Chip, 11(21), 3579-3580, 2011.

[5] S. Li, et al, "An on-chip, multichannel droplet sorter using standing surface acoustic waves", Analytical chemistry 85(11), 5468-5474, 2012.

[6] T. Franke, A. R. Abate, D. A. Weitz, A. Wixforth, „Surface acoustic wave (SAW) directed droplet flow in microfluidics for PDMS devices", Lab on a Chip, 9(18), 2625-2627, 2009.

[7] L. P. Gor'kov, "On the forces acting on a small particle in an acoustical field in an ideal fluid", Soviet Physics Doklady. Vol. 6., 773-775, 1962.

[8] H. Bruus, "Acoustofluidics 7: The acoustic radiation force on small particles", Lab on a Chip, 12(6), 1014-1021, 2012.

[9] K. Yosioka, Y. Kawasima, "Acoustic radiation pressure on a compressible sphere", Acta Acustica united with Acustica, 5(3), 167-173, 1955.

[10] G. F. Christopher, S. L. Anna, "Microfluidic methods for generating continuous droplet streams", Journal of Physics D: Applied Physics, 40(19), R319, 2007.

[11] T. Thorsen, R. W. Roberts, F. H. Arnold, S. R. Quake, "Dynamic pattern formation in a vesicle-generating microfluidic device", Physical review letters, 86(18), 4163, 2001.

CONTACT

* I. Leibacher, leibacher@
P. Reichert, reichert@ — imes.mavt.ethz.ch
J. Dual, dual@

2. Actuators   **Presentation**

A DISPENSING SYSTEM FOR SEDIMENTING METAL MICROPARTICLE SOLUTIONS BASED ON A CIRCULATION MIXER METHOD

L. Riegger [1, 2], *A. Ernst* [1, 2] *and P. Koltay* [1, 2]

[1] BioFluidix GmbH, Freiburg, Germany

[2] University of Freiburg, Lab for MEMS Applications, Freiburg, Germany

ABSTRACT

We present a novel method for the ejection of sedimenting microparticle solutions by a non-contact drop-on-demand dispensing system with integrated mixing technology. The system enables the generation of single liquid droplets in the nanoliter range containing similar amounts of solids. The system is evaluated for a process time of more than 4 h and is applied to produce particle layers with homogeneous layer thicknesses in the micrometer range.

KEYWORDS

sedimenting microparticle solution, mixing, contact-free micro dispensing

INTRODUCTION

A specific application for the use of homogeneous metal particle layers is the production of electrical connections by printing and subsequent laser sintering for high performance electronics and small footprint PCBs. Thereby, the layer thickness needs to be in the high micrometer range ($>= 20$ μm) thus enabling a feasible conductance for high currents. This largely exceeds the thickness typically achievable by inkjet printers with nanoparticle inks in printed electronics [1,2] without executing 100+ printing cycles. Also, the reduction of costs per sample due to the use of microparticles instead of nanoparticles is a non-negligible issue. The handling of metal microparticle solutions is however critical due to sedimentation issues as stabilizing a dispersion based on high specific gravity microparticles poses a significant challenge. Additionally, dispensing systems which are capable to handle microparticle solutions can hardly be found on the market. An applicable dispensing technology is the PipeJet [3] dispenser from BioFluidix [4]. In contrast to standard dispensing valves, the open, direct volume displacement method is resistant against deposition of particles at the wall inside of the system. However, sedimentation of microparticles inside the nozzle implies clogging after a few minutes. Also, concentration gradients appear which lead to unreproducible and inhomogeneous layers. Therefore, a circular mixing procedure not only in the reservoir but also in close proximity to the nozzle is required, keeping the particles continuously in movement, without changing the pressure boundary inside the nozzle.
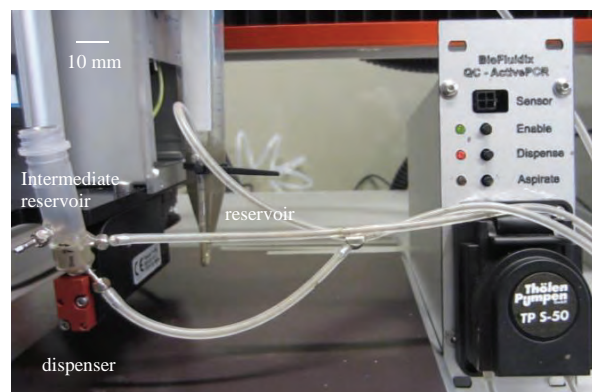
Figure 1: Experimental setup to demonstrate functionality of the circulation mixer. It comprises a PipeJet P9 dispenser (left) mounted on a XYZ stage (BioSpot BT600, BioFluidix, Germany), a first prototype of the intermediate reservoir, the main reservoir containing the dispersion as well as a peristaltic pump (right) to circulate the liquid.

The presented circular mixing method is based on the continuous circulation of the particle solution by a standard peristaltic pump, c.f. figure 1. The entire system consist of a main reservoir, containing the particle solution, a roller pump with disposable pump chamber, a PipeJet P9 dispenser and the intermediate reservoir, which is the integral part, keeping the solution in a homogeneous mixing state. All components are connected by the fluidic pathway (silicone tubes) as shown in fig. 1.

WORKING PRINCIPLE

The intermediate reservoir provides an inlet and outlet connection for the circulation system, as well as a connector to the dispenser nozzle, refer to figure 2. The open concept prevents pressure changes inside the system rendering it highly suitable for the PipeJet technology.
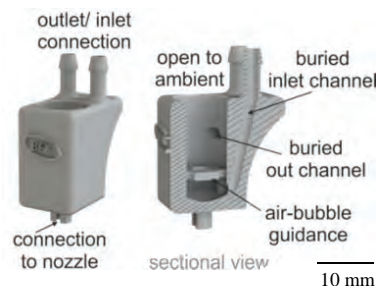
Figure 2: Design of the intermediate reservoir (second prototype). The outlet and inlet connections are guided by buried channels to the reservoir inside to enable a small mounting size. The air-bubble guidance prevents the nozzle inlet from clogging by air.

The working principle of the circulation mixer can be explained *via* the schematic in figure 3. Due to the continuous circulation of the solution, the filling level in the intermediate reservoir and thus the hydrostatic pressure at the nozzle stays constant. Surplus liquid is sucked in at 5 and mixed with small air-bubbles. These bubbles additionally lead to a mixing effect even while the liquid is transported through the fluid path. Ejected liquid out of the nozzle is refilled from the main reservoir continuously. This self-sustaining process is guaranteed due to the well adapted fluidic resistance ratio in the tubing system, connected at 3 and 4. The supply of solution including small air-bubbles, entering into the intermediate reservoir at the bottom side and passing the air-bubble guidance delivers the required mixing effect.
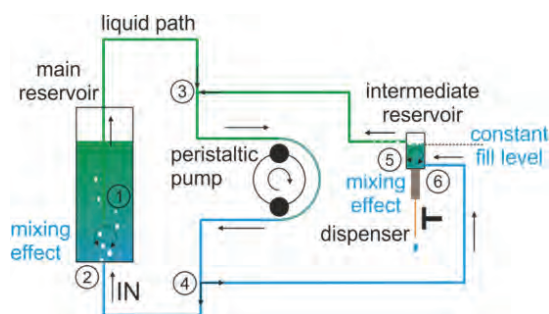
*Figure 3: Principle schematic of the circulation method and the liquid pathway. The size of the main reservoir is independent whereas the filling height of the intermediate reservoir must not surpass a certain height (depending on surface tension of the sample).*

EXPERIMENTAL CHARACTERIZATION

To evaluate the system performance we used Ag dispersion as listed in table 1.

Table 1: Applied Ag microparticle dispersion

solution	KTD 6078, FEW Chemicals, Germany
particle size	d= 0.5 - 1 µm
concentration	20 wt% Ag
contents	polymer stabilizer
(full) sedimentation time	1 hour

Applying the presented method kept the system operational for over 4 hours without any clogging effect. As circulation flow rate, a setting of 10 µL/s was chosen however operation could be demonstrated for lower and higher flow rates, too. We took several samples at identical dispensing parameters to evaluate the constancy of the particle concentration over time, c.f. figure 4. The method was further applied to produce Ag layers as shown in figure 5. For that instance, droplet patterns comprising 50 dispenses (5X * 10Y) of 50 nL droplets arrayed with a 1 mm pitch were printed. This procedure was repeated up to three times with a variable delay to allow for partial or complete drying. The printing of a layer based on the current process parameters and a single dispenser nozzle took about 15 s.
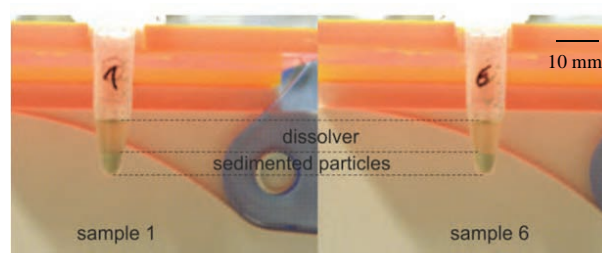
Figure 4: Evaluation of the concentration homogeneity over time. Several samples were taken from the running system by dispensing a constant number of droplets into the test vessel. The pictures are taken after a sedimentation time of 1h. A comparable amount of solids is found in the test vessel.

The patterns were then evaluated with an optical microsocope (Zeiss Axioplan 2 Light / Fluorescence Microscope, Zeiss, Germany) and e.g. a thickness of 23 µm and a deviation of +/- 2 µm was measured for the dual-layer coating. The illustration shows two batches of printed dual-layers with a downtime of 2 hours in between.
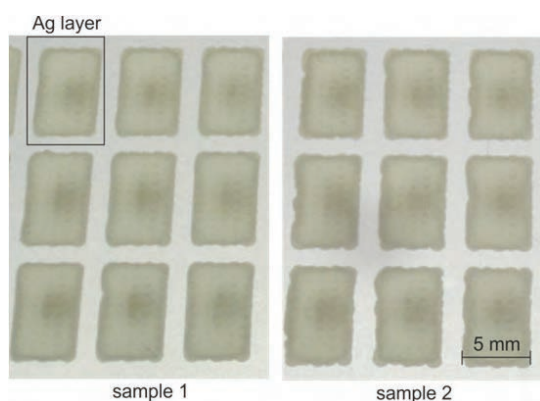
Figure 5: Ag microlayers fabricated by the presented circulation mixer dispensing system. For all layers, similar process parameters were applied. The nine patterns on the right side were printed 2 hours after the patterns on the left side. All layers feature an average thickness of 23 µm +/- 2 µm. The limited edge quality is correlated to the low-pinning substrate surface.

SUMMARY

In summary we presented a novel dispenser/mixer hybrid system for the handling of sedimenting media. The concept was successfully implemented on a dispensing process for the fabrication of homogeneous micro layers using sedimenting silver microparticle solutions. Future work will focus on the printing process optimization and the production of electrical conductors based on Ag and Cu dispersions. Additionally, different particle dispersions with varying fluidic properties will be tested to assess the performance of the circulation mixed in other application scenarios.

REFERENCES:

[1] Moira M. Nir, Dov Zamir, Ilana Haymov, Limor Ben-Asher, Orit Cohen, Bill Faulkner, and Fernando de la Vega, "Electrically conductive inks for inkjet printing", The chemistry of inkjet inks, chapter 12, ISBN-13 978-981-281-821-8.

[2] Sawyer B. Fuller, Eric J. Wilhelm, and Joseph M. Jacobson, "Ink-Jet Printed Nanoparticle Microelectromechanical Systems", *Journal of Microelectromechanical Systems*, Vol. 11, No. 1, 2002

[3] W. Streule, T. Lindemann, G. Birkle, R. Zengerle, and P. Koltay, "PipeJet: a simple disposable dispenser for the nano- and microliter range," *Journal of the Association for Laboratory Automation* (JALA), Vol. 9 Issue 5, pp. 300-306, 2004.

[4] BioFluidix GmbH, Georges Köhler Allee 103, 79110 Freiburg, Germany, http://www.biofluidix.com

CONTACT

Lutz Riegger, Tel. +49 (0) 761 458938 50, lutz.riegger@biofluidix.com

4. Fluidic control systems

A PICOLITER DISPENSER WITH DISPOSABLE CARTRIDGES FOR PRECISE AND CONTACT-FREE INJECTION OF DNA INTO OPEN MICROFLUIDIC STRUCTURES

J. Riba[1], L. Gutzweiler[1], L. Riegger[1,2], P. Koltay[1,2], R. Zengerle[1] and A. Gross[1]
[1] University of Freiburg, Lab for MEMS Applications, Freiburg, Germany
[2] BioFluidix GmbH, Freiburg, Germany

ABSTRACT

We present a new disposable liquid handling system addressing the lower picoliter volume range and allowing for precise and contact-free injection of biopolymer samples into open microfluidic structures. Droplet placement precision of single stranded DNA (ssDNA) solutions up to 50 µM and a DNA reference ladder is investigated by high resolution optical monitoring. We present three different sample injection methods that account for evaporation protection of picoliter samples. Finally, we show the applicability of the dispenser by a successful electrophoretic separation *via* injecting ~70 pL of a DNA solution into a 200-300 µm wide gel line.

KEYWORDS

contact-free picoliter dispenser; open microfluidic gel electrophoresis; DNA injection.

INTRODUCTION

Open microfluidics (OM) has evolved as a promising technology in which fluidic structures are generated and accessed on planar substrates without rigid-rigid interfaces like micro-fabricated channels [1]. The concept allows for low-cost rapid prototyping of fluidic structures [2]. Recently, electrophoretic separation of DNA in direct-written open gel lines has been demonstrated [3]. The two key steps for reproducible separations in such structures are the generation of liquid separation channels and the precise contact-free sample injection. Here, resolution of electrophoretic separations is mainly determined by the injected sample plug length and hence is inversely related to its volume. Therefore, a dispenser capable of precisely injecting picoliter samples in a non-contact manner is highly desirable. Due to the open interface it is necessary to provide protection against evaporation of liquids which becomes more important the smaller the liquid volumes of the assay are. A successful strategy is to cool the substrate close to the dew point and to cover liquids with oil [3]. It is therefore crucial that the sample injection method is compatible with the evaporation protection.

Here, we present a non-contact drop-on-demand dispenser that is capable of reproducibly placing droplets down to 35 pL into open microfluidic gel lines. We propose a method to measure and quantify placement precision and investigate three different sample injection methods that account for the evaporation protection of the liquid gel line and the sample. Further, the presented dispenser features low-cost disposable cartridges, has no thermal impact on the sample, and can be applied to biopolymer and salt solutions. Here, we present data for ssDNA concentrations up to 50 µM and for a standard DNA ladder.

DISPENSER TECHNOLOGY

The dispenser chip is a silicon-glass compound comprising a dosage chamber with a backside membrane, a fluidic inlet, and a 20x20 µm² orifice (Fig. 1 a-b). In brief, the silicon-glass chips were fabricated on a wafer level as follows: After lithographic structuring of a photoresist, the fluidic chamber was 20 µm deep etched into the silicon by deep-reactive ion etching (DRIE). Through-holes for the fluidic inlet in the glass (Pyrex) were fabricated by a wet etching process. Both wafers were bonded anodically and subsequently diced. The disposable cartridge is finally assembled by gluing the silicon-glass chip to CNC-milled chip holders that comprise the medium reservoir (Fig.1 d). Both, chip and holder undergo a specific cleaning procedure to minimize organic contamination. To prevent wetting of the nozzle, the exterior of the chip is coated by a vapor phase deposited organo-silane after O_2-plasma treatment: A highly hydrophobic monolayer is formed on the silicon/glass surface preventing precipitation of solutes ensuring reliable and reproducible droplet generation of salt and polymer solutions. The cartridge is operated in a direct-displacement mode where a piezoelectric driver (BioFluidix P9) deflects the silicon membrane resulting in on-demand single droplet generation. Droplet volume is adjustable within a specific range, mainly depending on orifice dimensions, and the piezo stroke-length [4].
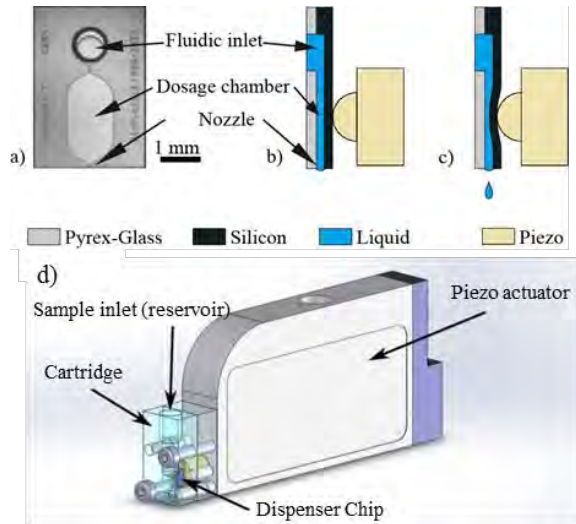
Figure 1: The dispenser chip (a) consists of a micro-fabricated silicon-glass compound (b). Droplets are generated by deflecting silicon membrane driven by a piezo actuator (c). The CAD model (d) illustrates the disposable cartridge comprising the dispenser chip assembled with the piezo actuator (BioFluidix P9).

Droplet volume

Droplet volume is measured by the gravimetric method introduced in [5]. In brief, we dispense into a weighing dish which is prefilled with silicone oil to prevent evaporation of the dispensed droplets. For each measurement point 600 droplets were dispensed at a frequency of 40 Hz. Thereby, we derive a highly accurate measure of the average droplet volume. Fig. 2 illustrates the characteristic dosage curve of our dispenser for water based solutions of 30 & 70 basepair (bp) ssDNA with equimolar concentrations ranging from 0.1 µM to 50 µM. Further, we used a DNA ladder (25-500 bp / 9 fragments; 576 nM all together in TE-buffer).
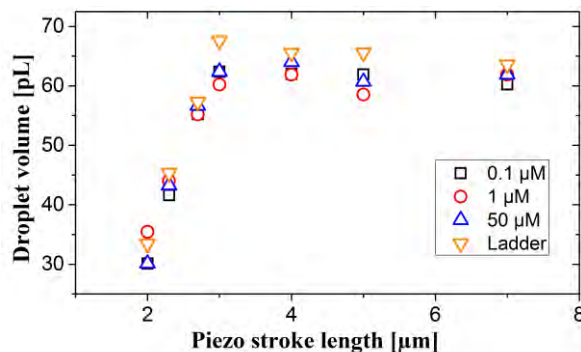
Figure 3: Dosage curves of the dispenser chip with ssDNA concentrations ranging from 100 nM to 50 µM (30 & 70 bp, equimolar) and a standard DNA ladder (576 nM). 600 droplets were dispensed for each data point and measured with the gravimetric setup. The droplet volume can be tuned between 30-60 pL.

Varying the piezo stroke-length between 2-3 µm volumes ranging from 30 to 60 pL are obtained. At higher stroke lengths a characteristic plateau in the droplet volumes is observed. In this regime we frequently observe formation of satellite droplets. The volumes vary between the different DNA samples by 9 % CV for ~ 35 pL droplets and 2 % CV for ~ 50 pL.

Droplet stability & placement precision

In order to investigate reproducibility and placement precision, droplets are dispensed on a glass slide (working distance: 2.5 mm) which is continuously monitored by a camera from below with a lateral resolution of approximately 2 µm. The glass slide was rendered hydrophobic with windshield treatment (rain-x original glass treatment) which improves the contrast of the images. For each sample we determined the center of 100 subsequently dispensed droplets with Matlab using a custom image processing script. The setup and workflow is illustrated in Fig. 4. In order to quantify placement precision of the dispenser we calculate the deviation of two consecutively dispensed droplets which we refer to as drop-to-drop deviation d_{mean} (averaged over 100 droplets) and d_{max} (maximum out of 100 droplets). Further, we define the scattering radius (eq. 1)

$$R_{2\sigma} = 2 \cdot d_{std,} \qquad (1)$$

where d_{std} is the standard deviation of the droplet position and therefore $R_{2\sigma}$ reflects the size of the circle in which 95 % of the dispensed droplets are located considering a normal distribution. In Fig. 4 c) $R_{2\sigma}$ is illustrated as a red circle. It ranges from 4 µm (DNA ladder) to 7 µm (50 µm ssDNA). The maximum drop-to-drop deviation d_{max} for DNA ladder is below the setup's detection limit and was highest for 50 µM ssDNA (5.9 µm). The resulting values are summarized in Table 1.

Table 1: Scattering radius $R_{2\sigma}$, mean and maximum drop-to-drop deviation (d_{mean} & d_{max}) for 100 subsequently dispensed droplets of the tested samples. All values are given in µm. Entries marked with an asterisk are below the detection limit.

Sample	$R_{2\sigma}$	d_{mean}	d_{max}
100 nM ssDNA	4.8	2.7	4.3
1 µM ssDNA	5.1	2.8	5.5
50 µM ssDNA	7.0	2.3	5.9
DNA ladder	4.0	*	*

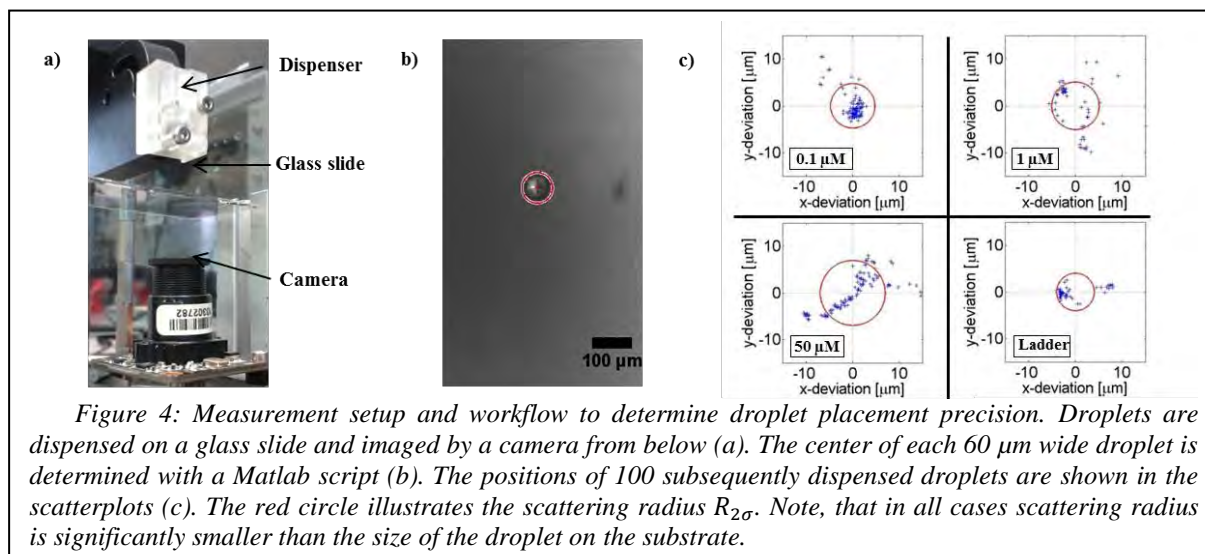Figure 4: Measurement setup and workflow to determine droplet placement precision. Droplets are dispensed on a glass slide and imaged by a camera from below (a). The center of each 60 μm wide droplet is determined with a Matlab script (b). The positions of 100 subsequently dispensed droplets are shown in the scatterplots (c). The red circle illustrates the scattering radius $R_{2\sigma}$. Note, that in all cases scattering radius is significantly smaller than the size of the droplet on the substrate.
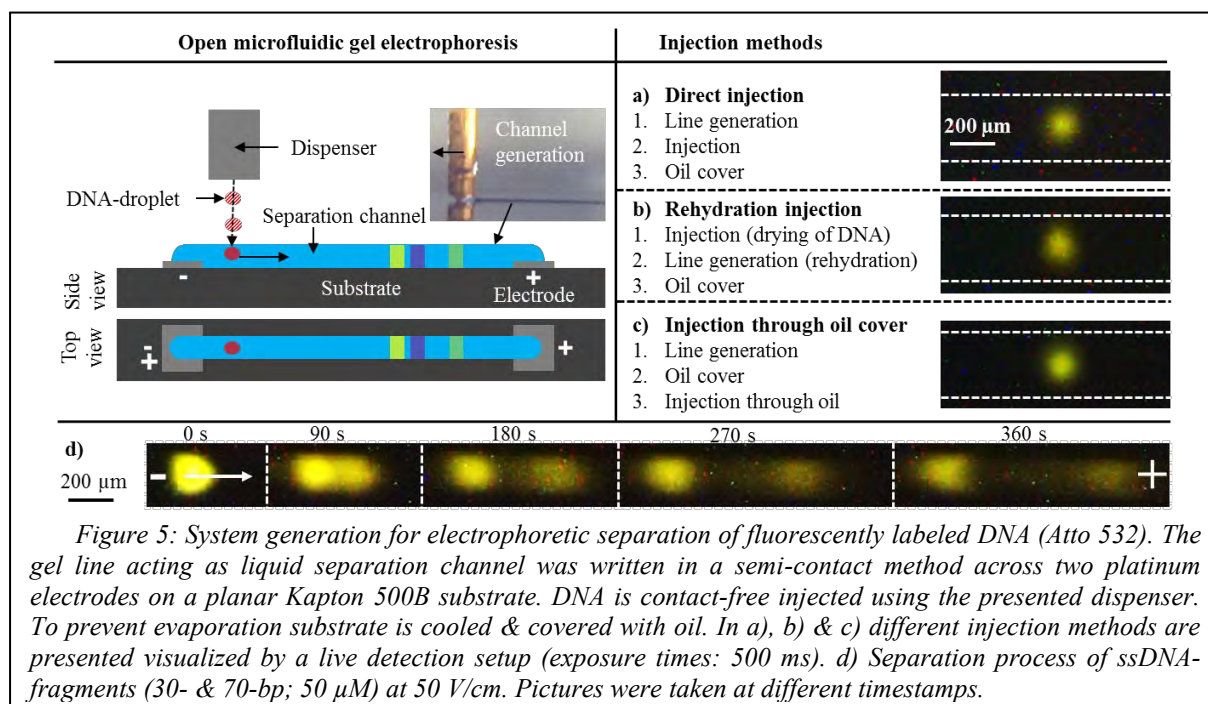
Sample injection in open microfluidics

To perform electrophoretic separations in open microfluidics key features are the generation of a liquid separation channel across two electrodes on a planar substrate, the contact-free sample injection, and evaporation protection realized by a covering oil layer and cooling. Here, the separation channel is made by direct writing of a linear polyacrylamide hydrogel [3]. In order to inject DNA into open microfluidic structures the presented dispenser was mounted to the 3-axis robot that is responsible for structure generation. By the use of a non-contact dispenser as injector the injection plug length is defined by the droplet volume and is an indicator for resolution. Thus, small volumes are beneficial for a good separation performance as long as detector signals are significant. During impact of droplets on the channel liquid their transferred kinetic energy results in liquid spilled around and injection length is larger compared to the initial droplet diameter. Hence, volume and kinetic energy of injected droplets should be small. Using the presented dispenser three injection methods have been identified to inject small amounts of only 35 pL ($d_{droplet} \approx 41$ μm) into 200-300 μm wide gel lines. Fig. 5 shows the fundamental process of open microfluidic system prototyping (left) and the three different injection methods investigated in this study (right). To illustrate the applicability of the dispenser we injected single ~35 pL droplets of fluorescently labeled (Atto 532) ssDNA sample (30 & 70 bp, 50 μM) exhibiting constant injection lengths of only ~150 μm as shown in Fig. 5 a-c.

Spatial drop-to-drop deviation of DNA was compensated by a referencing method before each injection, whereby all droplets were placed sufficiently close to the center of the line. In Fig. 5 a) DNA was directly dispensed into the gel after line generation, followed by oil coating. In Fig. 5 b) a rehydrated injection spot can be seen. Here, the DNA sample was first dispensed onto the blank substrate and then dried. Next, the gel line was written over the dried spot which leads to rehydration of the DNA, followed by coating with oil. Finally, in Fig. 5 c) the dispenser was used to directly inject the DNA sample into the oil coated line. Here, we added 0.1 % (v/v) of a surfactant (Span 80) to the silicone oil (200 Fluid, Dow Corning) in order to decrease surface tension which allows for rapid penetration of the dispensed sample droplet into the oil layer. Due to the fact that in most cases open microfluidic systems are non-equilibrated immediately after line generation, the injected DNA spot sometimes smears out when applying injection method a). Longer idle-times before injection and oil coating are disadvantageous due to evaporation. Method b) is reproducible but only applicable for biomolecules that are stable during drying and that can be rehydrated like DNA. Method c) is applicable for all biomolecule solutions but reproducibility must be evaluated in the future. In Fig. 5 d) the live separation of the aforementioned DNA mixture is demonstrated using injection method c) applying an electric field of 50 V/cm. Due to the low sensitive live detection setup comprising a green DPSS laser ($\lambda_{ex} = 532$ nm, 4 mW, Blau Optoelektronik GmbH) with line optics and a CMOS camera with a pre-mounted long-pass filter ($\lambda_{cutoff} = 550$ nm) 70 pL were injected for a better visualization of the live migration. First separation is achieved 90 s after applying the electric field at a migration distance of ~3 mm.

Figure 5: System generation for electrophoretic separation of fluorescently labeled DNA (Atto 532). The gel line acting as liquid separation channel was written in a semi-contact method across two platinum electrodes on a planar Kapton 500B substrate. DNA is contact-free injected using the presented dispenser. To prevent evaporation substrate is cooled & covered with oil. In a), b) & c) different injection methods are presented visualized by a live detection setup (exposure times: 500 ms). d) Separation process of ssDNA-fragments (30- & 70-bp; 50 µM) at 50 V/cm. Pictures were taken at different timestamps.

CONCLUSION

We presented a new dispenser for the lower picoliter range that can be used to precisely deliver biopolymer solutions contact-free without any thermal impact on the sample. We proposed a new method to evaluate placement precision by high resolution optical monitoring. Droplet volume and precision for various DNA samples have been evaluated. Three different methods have been identified and investigated that were successfully used for the injection of DNA samples in open microfluidic structures. In practice the injection through a previously placed oil cover might prove to be the most universal and reliable method, as it is likely to be compatible with other samples like proteins and limits the time the open gel line is exposed to air. Even quite high concentrated biopolymer solutions (50 µM DNA, 2x25 µM respectively) could be reproducibly injected into OM structures exhibiting injection lengths as small as ~150 µm followed by successful electrophoretic separation. Given the high placement precision of the dispenser we can operate from a fairly large working distance of 2.5 mm. All 35 pL droplets (diameter ~41 µm) were sufficiently placed in the center of 200-300 µm wide gel lines. The high dispensing precision allows for controlled DNA injection into even narrower structures, whereby separation performance could be improved. Summed up, the presented dispenser is capable to reproducibly dispense droplets with volumes down to 30 pL exhibiting exceptionally high placement precisions from large working distances with even high DNA concentrations.

In future we will further exploit the methodology of placement precision measurement and the range of applicable samples. Since a calibration-free dispenser could be beneficial for many applications, the variation within different disposable cartridges needs to be fully characterized as proposed in [6]. From our point of view, precise contact-free injection of picoliter samples combined with protective oil covers are not only of interest for OM electrophoresis but also for other biochemical assays such as solid phase DNA amplification or single cell studies in oil protected droplet arrays.

REFERENCES:

[1] Pfohl, T. et al., ChemPhysChem, *4*(12), pp. 1291-1298, 2003.
[2] Gutzweiler, L. et al*., MicroTAS 2013, 17th International Conference*, pp. 1409 – 1411.
[3] Tanguy, L. et al., *TRANSDUCERS 2013, 17th International Conference*, pp. 1223-1226.
[4] Koltay, P. et al., *SPIE's MICRO/MEMS*, 2001, pp. 195-203.
[5] Liang, D. et al., Measurement Science and Technology, 24(2), 02530, 2013.
[6] Bammesberger, S. et al., Drug discovery today, *18*(9), pp. 435-446, 2013.

CONTACT

* J. Riba, Julian.Riba@imtek.de

NANO-WORKBENCH: A COMBINED AFM-FEMTOPIPETTE AND ROBOTIC NANOMANIPULATOR

H.H. Perez Garza*, M.K. Ghatkesar* and U. Staufer
Delft University of Technology, Delft, THE NETHERLANDS

ABSTRACT

As the nanoscale world presents a considerable amount of challenges and obstacles, robotic systems are required to perform manipulation, characterization and assembly of these nanoscale objects. These robotic systems require a correct actuation and precise control approaches in order to reach the required positioning accuracy and perform the desired manipulation. To address such needs, we have developed a robotics-based nano-manipulation platform termed as Nano-Workbench (NWB). It encompasses the usage of different robots that have been equipped with the hollow atomic force microscope cantilevers. We demonstrate the capability of NWB with two experiments. First, clamping graphene on a microsystem, and second, nanoparticle synthesis by mixing femto-liter volumes of liquids.

KEYWORDS

Nano-Workbench, Femtopipette, Nanorobot, Nanomanipulation, Microfluidics, Nanodispensing.

INTRODUCTION

The ultimate goal within the field of nanotechnology is to develop a novel system and device with unconventional properties that usual methods cannot achieve. One of the prerequisites to accomplish this goal is the capability of manipulating objects at nanoscale with extreme precision and resolution. In order to satisfy such critical requirement, different tools have been developed, among which the atomic force microscope (AFM) started attracting widespread attention due to numerous applications in biological and materials science technologies. Soon after the invention of AFM, its further capabilities than pure imaging were realized. Consequently, researchers worldwide pushed the AFM-based nanomanipulation into a major technique for different research purposes [1]. However, the conventional AFM cantilevers have one sharp tip as the end-effector, and can only apply a point force to the nano-object during manipulation. This limits the possibilities of manipulation that can be explored. In order to overcome those limitations, the AFM-Femtopipette [2] was developed. It could typically be used not only to interact with objects and surfaces by mechanical contact manipulation, but also to explore the possibilities of precise functionalization, local/controlled synthesis of nanoparticles and dispensing/aspirating of different reagents. Therefore, the latter device could represent a pioneer for nano-manufacturing. Nevertheless, this demands an extreme degree of accuracy. As a result, robotics-based nanomanipulation has recently emerged as a new field that encompasses the design, modeling and fabrication of different nanotools to be used by robots, hence obtaining a programmable manipulation of matter at the nanoscale. These robotic systems require a correct actuation and precise control approaches in order to reach the required positioning accuracy and perform the desired manipulation. Up to now, different groups have demonstrated initial AFM based robotic manipulation of particles [3]. The techniques used in these studies mostly involved switching the servo feedback off or sometimes decreasing the distance between the substrate and the tip by reducing the voltage set-point. Therefore, the particles are mechanically manipulated rather than the tip of the AFM cantilever jumping over them. However, this type of manipulation still offers little control and reliability could become a problem. To increase the versatility over previously shown AFM based nanomanipulation, this work focuses on the development of a flexible nanorobot-based workstation for micro and nano-manipulation, referred to as the nano-workbench (NWB).

MATERIALS AND METHODS

a) Nano-Workbench

In order to achieve high precision and accuracy during manipulation, we used the commercially available robots from Imina Technologies (Fig. 1a). Such robot is a mobile nanomanipulator with 4 degrees of freedom (DoF), two translations and two rotations. It combines long traveling range displacements with nanometric resolution. The vertical displacements are made by means of the piezo-actuator inside to move the arm, and horizontal displacements through piezo-actuator located beneath the robot. In order to equip the robot with a versatile tool for innovative manipulations, the previously developed femtopipette was mounted on the arm (Fig.1b). The latter comprises of a hollow AFM cantilever pipette [2], made of SiO_2, which can be used to dispense and aspirate liquids in the sub-femtoliter regime. As shown in Fig.1c, our device resembles a commercial AFM-chip, additionally with an integrated fluidic inlet located on the upper side, which is connected to an outlet located at the tip via the hollow cantilever. When the inlet is filled, the

liquid travels through the integrated capillaries until the nano-aperture at the AFM tip. The device can be used to dispense and aspirate in the sub-femtoliter regime, as well as for weighing and imaging[2]. The chip was mounted in such way that the cantilever tip would always point downwards, such that the aperture located in the tip could be brought in contact with the intended sample/surface to manipulate.
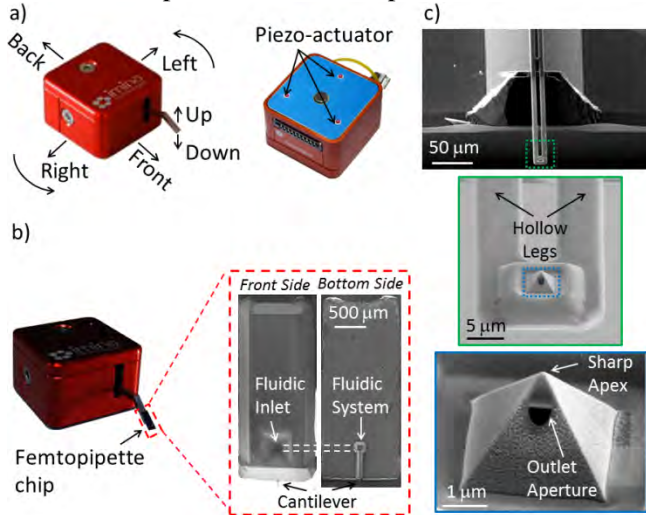
Figure 1: Combined Femtopipette-Robotic Nanomanipulator System. (a) The robot has 4 DoF which gives it the versatility to move and/or position the mounted tool (i.e. femtopipette) in the required place. (b) The femtopipette was mounted on the arm, allowing us to remotely control the location of its cantilever and very importantly, the exact position on which a given reagent could be dispensed through the aperture. (c) The cantilever connects the on-chip fluidic inlet to an outlet aperture located at the tip. A close-up view of the hollow cantilever is shown. The outlet aperture is milled using Focused Ion Beam on the side of the pyramid, to preserve the sharp apex for AFM purposes.

A control pad, which was plugged into a USB slot of the computer, allowed to remotely control the nanomanipulators by increasing/decreasing the frequency and amplitude of the actuators for the vertical and horizontal motions. The external electronics, also plugged to the computer via a USB cable, was used for the control of piezoelectric actuators via flex cables. The robotic arena over which the robots were operating was made of a steel plate. An overview of the interconnections of the different components is shown in Fig. 2. To monitor the performance of both the robot and femtopipette during manipulation, the robotic arena has been mounted on top of an inverted fluorescent microscope. A top view lens helped to increase the visual control during manipulation.
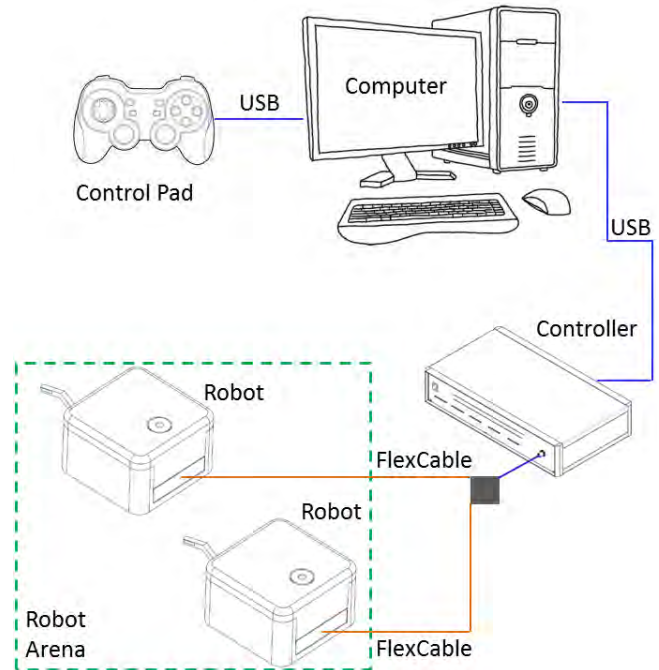
Figure 2: Interconnections to control the nanomanipulators. This figure depicts an overview of the interconnection between the components that allow to control the individual nanomanipulators.

The speed and the resolution of positioning of the robot could be tuned by varying the frequency and the amplitude of the driving signals.

b) Experiments using the Nano-Workbench

To demonstrate the capability and accuracy of using the NWB, we have used the robot and the femtopipette to perform two different experiments (Fig. 3). In the first experiment, we have locally dispensed epoxy for clamping a graphene flake to be strained using a tensile MEMS device. The device had two suspended shuttles bridged by the graphene were actuated such that the graphene would experience a pulling effect. However, the graphene was always slipping away as the tensile force was overcoming the existing adhesion due to van der walls forces between graphene and shuttle surface. To prevent this, the femtopipette was accurately brought to the point of interest by means of the remotely controlled robot. Once positioned in the vicinity of the graphene, the robot arm displaced the femto-pipette slowly and accurately towards the edge of the graphene. Then, the femtopipette was snapped-in multiple times to locally dispense the epoxy along the edge of the shuttle over an area ranging about 10µm x 10µm. This area covered the entire graphene edge on the shuttle. The process was repeated on both edges.

For the second experiment, we used the NWB to enable local deposition and controlled synthesis of gold nanoparticles. We have used a chip containing a

transmission electron microscopy (TEM) window of 50nm thick Si_3N_4 and two different robots which were equipped with their own femtopipette. One of them was filled with a metallic salt (chloroauric acid – $AuCl_4$), while the other was filled with a reducing agent (sodium azide – NaN_3). We first brought the robot carrying the metallic salt near the TEM chip and approached the femtopipette towards the membrane window to dispense a droplet of controlled volume. After deposition, we brought the second robot containing the reducing agent and a droplet with the same volume was dispensed, allowing both reagents to coalesce and mix. Nanoparticles were synthesized in different droplet volumes ranging from 2.4fL to 0.25fLin equal quantities of both reagents. The results of the triggered chemical mixture to synthesize nanoparticles were analyzed under the TEM.
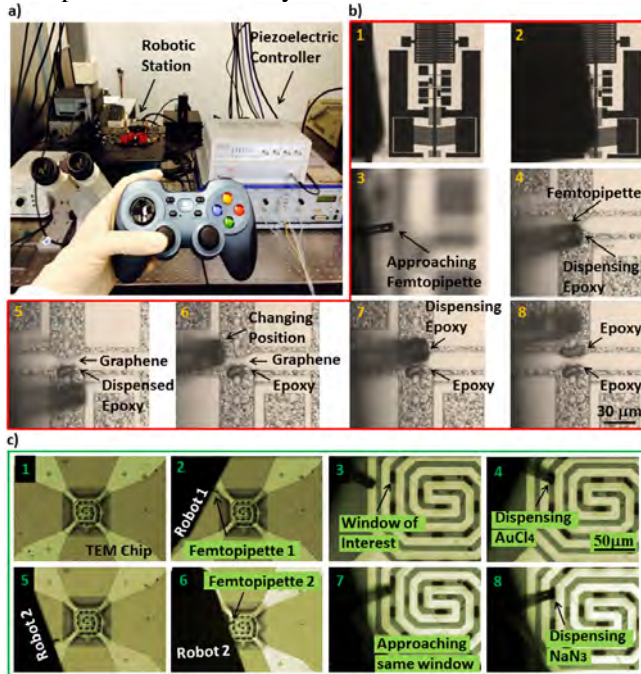

Figure 3: Experiments done with NWB. (a) The robot-femtopipette complex were remotely controlled. (b) For the first experiment we accurately clamped a suspended graphene by dispensing epoxy. (c) For the second experiment we locally synthesized nanoparticles.

RESULTS

a) Nano-Workbench

The assembly of the NWB resulted in a well mounted robotic arena on top of the inverted microscope which had an opened window in the center, such that the lens from the inverted microscope could have access to view the sample during manipulation (Fig. 4). Similarly, the resulting working distance of 2cm between the arena and the top camera allowed the robots to move their arms up and down freely without the problem of a potential crash. During operation, it was found that the travel range of the robot in stepping mode was of X:25mm,

Y:25mm and Z:8mm. Whereas in scanning mode it was found to be X:150nm, Y:150nm and Z:300nm. As for the positioning resolution, in stepping mode it was found to be X:50-150nm, Y: 50-150nm and Z: 50-150nm. Similarly, in scanning mode it was found to be X:5nm, Y:5nm, Z:5nm. The controller of the piezoactuators gave an output frequency of 0.7Hz to 23.5kHz and an output voltages of 55V-185V (AC) and 0V-185V (DC).
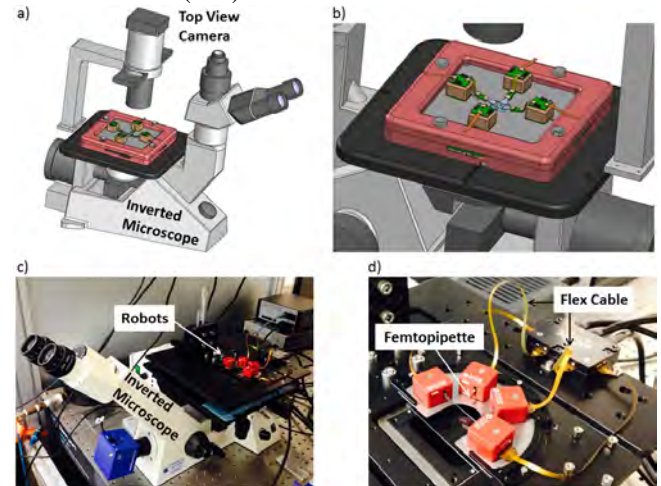
Figure4: NanoWork Bench. (a) Schematic of the working platform which was mounted on an inverted microscope. (b) The robotic arena was occupied by different robots. (c) A photograph of the NWB is shown. (d) Each robot was equipped with a femtopipette.

b) Experimenting with the Nano-Workbench

The successful clamping of the graphene using the developed NWB (Fig. 5), allowed to achieve extreme strains in graphene, which were 1 order of magnitude higher than the previously reported values [4]. Before clamping, a maximum strain of ~1.3% had been achieved, after clamping we could achieve strains of ~14%. In the synthesis experiment, the local dispensing of the metallic salt and reducing agent with equal volumes helped us explore the possibility of controlled synthesis of gold nanoparticles (AuNPs) with 20nm in diameter and homogeneous distribution [5].
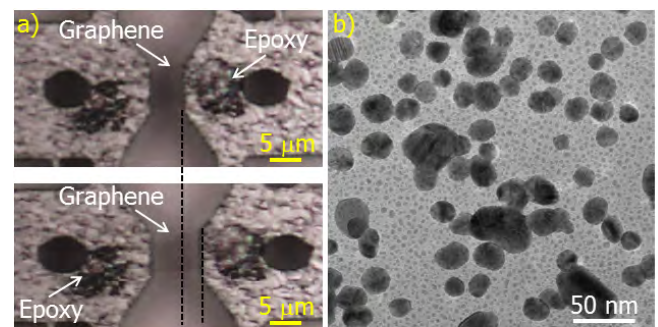
Figure5: Results obtained after using Nano-Workbench. (a) The accurately dispensed epoxy helped us achieve record levels of strains in graphene, due to the

strong clamping. (b) The precise positioning of the femtopipette on top of the TEM window helped us dispensed controlled volumes of AuCl₄ and NaN₃ to enable local deposition and controlled synthesis of AuNPs.

DISCUSSION

The robots' ability to position in a given spot and move the arm up and down was thanks to the working principle of the piezoelectric actuators. Basically, the actuators could rely on inertia and friction, in a mode referred to as the stick-and-slip mode. Due to the typically limited displacement of the actuators, stick-slip offered the possibility to combine very high resolutions with very large range of displacements. Therefore, if the robot needed to be driven over large distances, the piezo-stick-slip actuator generated a series of small steps, each with hundreds of nanometers in displacement. This is also referred to as the stepping mode. When high resolution was needed, the robot could be positioned within one step with a resolution of a few nanometers depending on the electronics used. This is called the scanning mode.

The volume of the dispensed droplet was separately measured using force distance curves on an AFM setup. The mass of the liquid loaded inside the cantilever was measured from the shift in the resonance frequency. The dispensed droplets for the nanoparticle synthesis being in the femto-liter domain, they are prone to evaporate in less than a second. Therefore these experiments were performed in non-condensing high humidity environment. This was not a problem for epoxy, due to its low vapor pressure and high viscosity.

SUMMARY AND CONCLUSIONS

In conclusion, the femtopipettes mounted on the robots can be used to locally and accurately dispense/remove material on/from target sites. This opens the window to a whole new opportunity of manipulating matter (including liquid) that up to now has been very difficult to achieve. To begin with, the developed NWB could be used to study the mechanical properties (buckling, adhesion) of different samples (i.e. carbon nanotubes, graphene) and/or also to evaluate the behavior of a biological cell as a function of mechanical/chemical stimuli. In fact, there is an increasing interest among biologists in the capability to manipulate both cells and smaller intracellular components, hence giving them the chance to perform "nano-surgery" that could be used to create incisions in the cell membrane, cut single cytoskeleton filaments, isolate organelles and to perform in-situ dissections of cell walls. Other examples of manipulation of matter at this particular scale might include nano-functionalization and assembly of micro and nano-electromechanical systems, which should be demonstrable with the NWM. A summary with the technical specifications of our NWB is shown in Table 1.

Table 1. Summary of technical specifications

Femtopipette
Resonance Frequency: 153.94kHz
Spring Constant: 3.48N/m
Typical dispensed volume: 30fL
Storage volume: 20nL
Robot
Travelling Range
a) Stepping Mode: X:25mm, Y:25mm, Z:8mm
b) Scanning Mode: X:150nm, Y:150nm, Z:300nm
Positioning resolution
a) Stepping Mode: X:50-150nm, Y: 50-150nm, Z: 50-150nm
b) Scanning Mode: X:5nm, Y:5nm, Z:5nm
Controller
Output Frequency: 0.7Hz to 23.5kHz
Output Voltage: 55V-185V (AC) and 0V-185V (DC)
Slew Rate: 500V/µs – with 0nF load, 185V/µs – with 1nF load

ACKNOWLEDGEMENTS

REFERENCES

[1] B. Mokaberi and A.A.G.Requicha, "Drift compensation for automatic nanomanipulation with scanning probe microscopes", *IEEE Transactions on Automation Science and Engineering*, **3**(3): p. 199-207, 2006.

[2] M.K. Ghatkesar, H.H. Perez Garza and U. Staufer, "Hollow AFM cantilever pipette", *Microelectronic Engineering*, **124**: p. 22-25, 2014.

[3] C. Baur, et al., "Robotic nanomanipulation with a scanning probe microscope in a networked computing environment". *Journal of Vacuum Science & Technology B*, **15**(4): p. 1577-1580, 1997.

[4] H.H.Perez Garza et al., "Controlled, Reversible, and Nondestructive Generation of Uniaxial Extreme Strains (>10%) in Graphene". *Nano Letters*, **14**(7): p. 4107-4113, 2014.

[5] H.H.Perez Garza et al., "Enabling Local Deposition and Controlled Synthesis of Au-Nanoparticles Using a Femtopipette". *IEEE NEMS'14 Conference, Waikiki, Hawaii, USA*, 2014.

CONTACTS

* H.H.PerezGarza@tudelft.nl, M.K.Ghatkesar@tudelft.nl

FEEDBACK CONTROLLED MICRODOSING SYSTEM FOR NANOLITER PER SECOND DOSING RATES USING A CAPACITIVE PHASE BOUNDARY TIME-OF-FLIGHT FLOW SENSOR

S. Kibler[1], L. Hassan[1], M. Richter[1] and C. Kutter[1]

[1] Fraunhofer Research Institution for Modular Solid State Technologies EMFT, Munich, Germany

ABSTRACT

A stand-alone micro dosing system is presented, that enables closed loop controlled micro dosing of flow rates from 2.5 nl/s up to 30 nl/s by using capacitive time-of-flight measurement of moving phase boundaries of a two-phase gas-liquid slug flow in a micro fluidic channel.

KEYWORDS

Micro dosing, nanoliter per second, two-phase flow, capacitive measurement, feedback control.

INTRODUCTION

The presented micro dosing system is developed for feedback controlled dosing in the application field of micro lubrication with low viscous oil in high speed bearings of machine spindles. It was shown to precisely deliver flow rates from 2 nl/s up to 50 nl/s with two different sensor designs [3].

Within this work the system with small sized sensor for flow rates from 2.5 nl/s to 30 nl/s will be presented in detail.

The flow metering is based on time-of-flight measurement of moving phase boundaries of a two-phase gas-liquid slug flow in a micro fluidic channel that is generated by two silicon micro pumps. By using capacitive measurement with an array of segmented electrodes a tracking of phase boundaries is simply realized (see fig. 1).
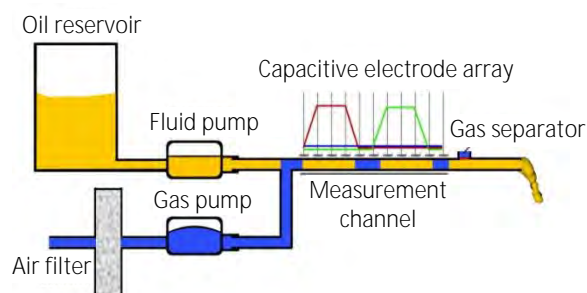
Figure 1: Micro dosing principle with segmented capacitive electrode array for time-of-flight measurement of gas-liquid phase boundaries.

STATE OF THE ART

Non-capacitive measurement of micro flow by observing moving phase boundaries is known from a non-portable laboratory setup, using microscopy and video analysis for optical time-of-flight measurement of an air bubble in a micro channel for nanoliter flow detection [5].

A second flow sensor concept [4] is detecting a moving phase boundary resistively with two electrodes at flow rates from 2 to 200 μl/min, according to a lowest detection level of about 33 nl/s.

IMPLEMENTATION

The stand-alone micro dosing system (see fig. 2) is based on two Piezo-electrically driven silicon micro pumps with a stroke volume of 80 nl, that are used for oil and gas injection. The micro fluidic channel is designed as a T-cross section wherein the so called slug flow is observed via a segmented array of capacitive measuring electrodes.
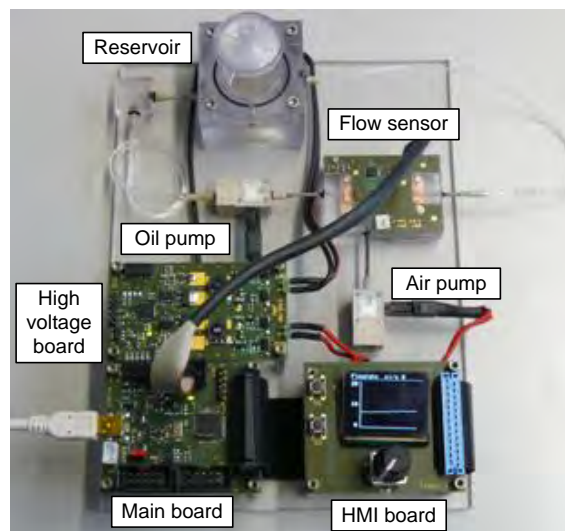
Figure 2: Realized stand-alone micro dosing system.

Capacitive measurement, signal analysis, micro pump control and data communication is provided by a modular electronic. The electronic is designed for autarkic control of the complete dosing system consisting of following subsystems:

- A high voltage driver board for driving the piezo ceramic actuators of the silicon micro pumps
- A sensor pcb board with a capacitance to digital converter directly attached to the microfluidic measurement channel. The capacitance to digital converter IC AD7142 of Analog Devices [2] provides a relative resolution of about 30 atto Farad for capacitance readout
- An operating interface board (HMI) with an OLED-display for data and parameter display and input buttons for parameter settings
- A mainboard with a 16-bit micro-controller to enable the algorithmic calculations for flow measurement, controlling the micro pump high voltage drivers and the display board

SENSOR DESIGN

The realized small sensor design is produced by micro milling of two halves of the micro fluidic channel that are assembled afterwards.
A top polycarbonate block covers a bottom driving electrode made of copper. Opposing to the bottom electrode the capacitive array of measuring electrodes is placed on a pcb-board on top of the micro fluidic channel (see fig. 3).
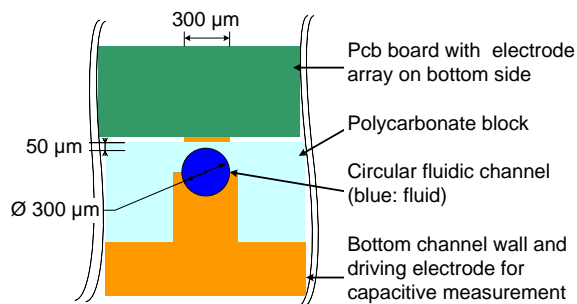
Figure 3: Schematic cross section of small flow sensor design.

The sensor is designed to have a circular channel cross section of 300 μm inner diameter. The corresponding capacitive sensor pcb-board has 10 electrodes with 300 μm width and 1100 μm length that are separated by a 100 μm space (see fig. 4). Each electrode observes a channel volume of 80 nl. The capacitive level change from oil to air is less than 4 nano Farads that is measured by a capacitance-to-digital converter of Analog Devices [2].
As milling in those small dimensions is related to tolerances respectively, the real cross sections of

the micro fluidic channels are not perfect circles and have about 20% bigger cross sectional areas than intended (see fig. 5).
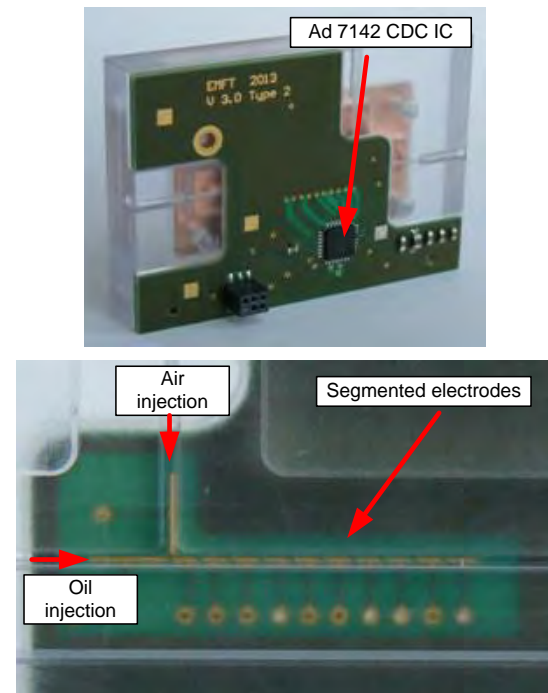
Figure 4: above: small flow sensor version top view; below: bottom view into fluidic channel T cross section with segmented electrodes.
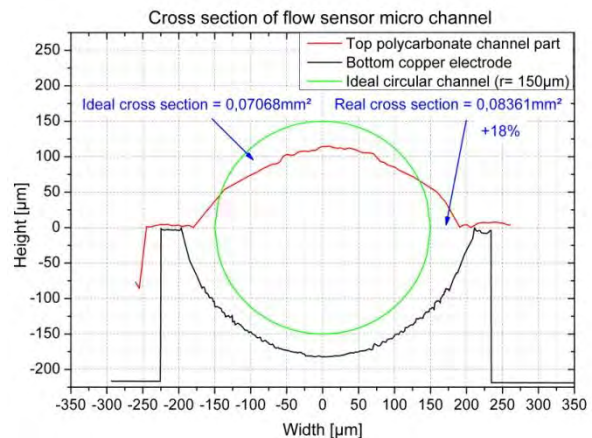
Figure 5: Measured cross section profile of a produced sensor channel.

FLUIDIC CHARACTERISTICS

Slug flow is achieved if two separate liquid, gaseous or solid phases inside a tubing, pipe or micro channel are not mixing with each other and keep permanently separated while moving. In this case with using oil and air an oleophilic surface of tubing or micro channel walls is required [1].

Accuracy of this measurement principle is mainly limited by surface tension and geometrical channel and electrode resolution: First, a remaining liquid film on the hydrophilic or oleophilic channel surfaces has to be considered when a gas bubble is passing by. It can be **estimated using Bretherton's formula** [6] and numerical simulation [7]. It is related to the Capillary number Ca of a gas bubble in surrounding liquid inside a micro channel, which is depending on kinematic viscosity μ, moving speed U and surface tension σ of the liquid (1).

$$Ca = \frac{\mu U}{\sigma} \qquad (1)$$

The theoretical approach of Bretherton predicts a film thickness b related to the channel width w (2).

$$\frac{b}{w} = 0.321 \left(3\frac{\mu U}{\sigma}\right)^{2/3} \qquad (2)$$

For very low phase moving speeds in this application from 0.01 mm/s to 0.5 mm/s this liquid film is expected to be less than 0.5 μm in thickness (see fig. 6).
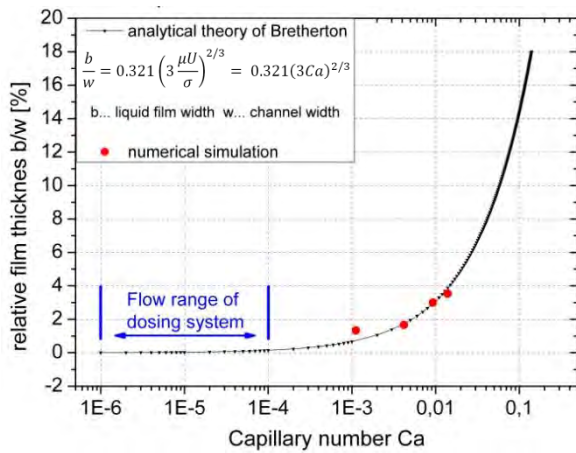
Figure 6: Relative surrounding liquid film thickness of a gas bubble in a two-phase flow related to the Capillary number.

Secondly, as gas-liquid phase boundaries build curved meniscus shapes, the measured volume under each electrode has to be recalibrated in accordance to the real displaced volume (see fig. 7). In addition, this calibration is depending on the current number of phase-boundaries inside the measurement channel.
Third, displacement volume of the micro pumps, the geometrical volume resolution of the segmented electrode array and its corresponding fluidic channel are limiting the resolution of the dosing system.
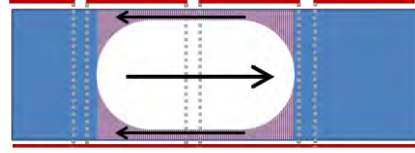
Figure 7: Sketch view of a moving gas bubble (white) in surrounding liquid (blue); accuracy is limited by the remaining not displaced liquid volume (red shaded).

RESULTS

Characterization of the dosing system is done by gravimetrical reference control via a micro scale with measurement precision of ±0,3 nl/s for one system and with further two systems for measurement of the feedback control behavior. Figure 8 shows the performance of the micro dosing system, where a linear behavior can be observed. With this characterization a linear sensor calibration is done. Main influence on a need of linear adaption is explained in figure 5. The cross section deviation from design to reality is about 20%, whereas the deviation in figure 8 is about 30% when using the displayed fit curve. The remaining 10% seems to be related to the curved meniscus front, but this still has to be examined.
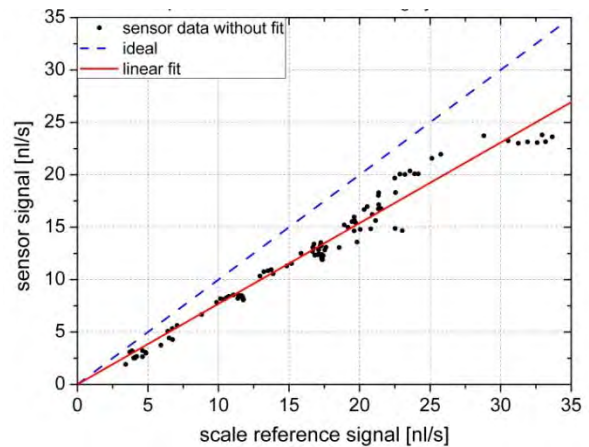
Figure 8: Sensor performance in comparison to a reference scale

Figure 9 shows the absolute measurement of the sensor according to the reference scale when using the linear calibration fit. For flow rates from 2.5 nl/s to 15 nl/s an absolute error less than 1 nl/s can be achieved. For higher flow rates up to 30 nl/s this error is still less than 4 nl/s.
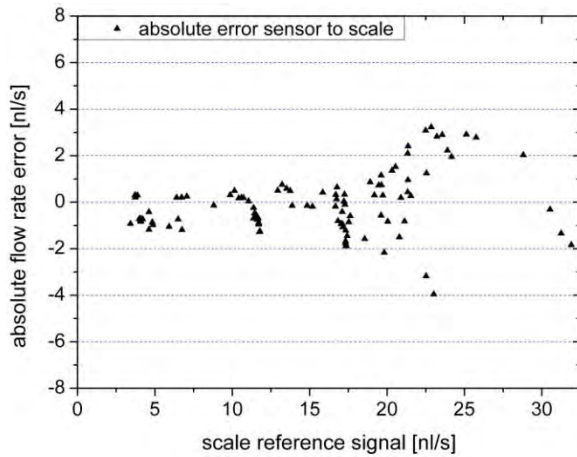
Figure 9: Absolute measurement error of sensor.

Figure 12: Absolute error of feedback control algorithm according to lead flow rate values. Data of three micro dosing systems.

Feedback control ability was tested with three produced dosing systems. Figures 10 and 11 show a long time measurement over more than 16 hours and an enlarged view into it, where the system had to control onto a lead value of flow rate that was varied in repeated steps from 2.5 to 30 nl/s.
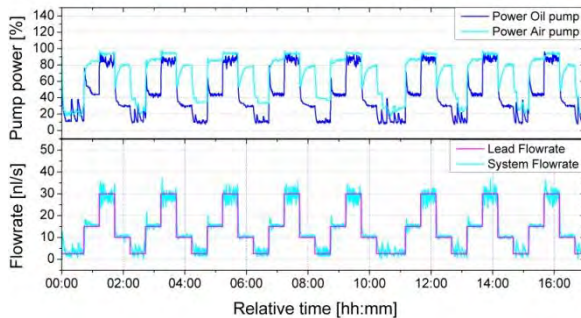
Figure 10: Long time measurement with feedback control. Upper half: power values of the two micro pumps that are adapted by the feedback algorithm. Lower half: Lead flow rate steps and achieved flow rate of the dosing system
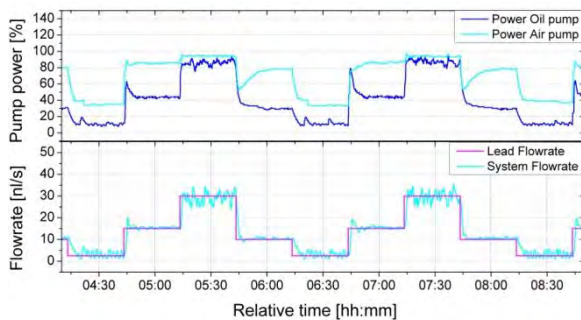
Figure 11: Feedback control at lead flow rate steps. Enlarged view of figure 10.

REFERENCES:

[1] T. Cubaud, U. Ulmanella, C.-M. Ho, *Two-phase flow in microchannels with surface modifications*, in Fluid Dynamics Research 38, pp. 772-786, 2006.

[2] J. Dowd, A. Callanan, G. Banarie, E. Company-Bosch, *Capacitive sensor interfacing using sigma-delta techniques*, in IEEE Sensors 2005, pp. 951-954, 2005.

[3] S. Kibler, B. Möller, M. Richter, C. Kutter, *Closed loop micro dosing for oil lubrication of precision bearings in high speed machine spindles using capacitive flow metering*, Sensoren und Messsysteme 03.-04.06.2014, Nürnberg, ISBN 978-3-8007-3622-5.

[4] J. M. Lippmann, A. P. Pisano, *Simple, High-Precision, microliter per minute, fluid-flow sensor*, in MEMS2011, pp. 1197-1200, 2011.

[5] B. Nestler, S. Klein, A. Opp, D. Wuttig, *Dosierung und Messung kleiner Volumenströme als Voraussetzung für die Realisierung eines implantierbaren Mikroinfusionssystems*, in Impulse, Volume 10, S. 65-73, 2005, ISSN 1618-5528.

[6] F. P. Bretherton, *The motion of long bubbles in tubes*, Journal of Fluid Mechanics 10, pp. 166-188, 1961

[7] D. A. Hoang et al., *Modeling of LowCapillary Number Segmented Flows in Microchannels Using OpenFoam*, in AIP Conf. Proc. 1479, pp. 86-89, 2012

CONTACT
Email: sebastian.kibler@emft.fraunhofer.de
Tel.: +49 89 54759 227

SEMI-CONTACT WRITING TECHNOLOGY & APPLICATIONS

L. Gutzweiler[1], T. Gleichmann[1], P. Koltay[1,2], R. Zengerle[1] and L. Riegger[1,2]
[1] University of Freiburg, Lab for MEMS Applications, Freiburg, Germany
[2] BioFluidix GmbH, Freiburg, Germany

ABSTRACT

We present an adaption of a direct ink writing approach to facilitate prevalent standard applications like fabricating masters for PDMS casting, conducting path structuring and generation of open microfluidic structures towards gel electrophoresis. In all presented applications, flexibility is increased and standard structuring processes can be substituted offering the ability for low-cost fabrication with less required expertise. In contrast to existing approaches low to medium viscous liquids are applied due to passive capillary forces.

KEYWORDS

Open microfluidics; Semi-contact writing; Droplet jetting

INTRODUCTION

In the past direct ink writing approaches have been presented to satisfy the need for flexible and low-cost material structuring [1] across various disciplines like physics, chemistry or biology enabling the implementation of customized structure designs in a fast and comfortable manner. Structures are generated using a viscous paste released out of a nozzle during pressure application to the dispensing system. A more common method for structure generation based on low viscous materials is droplet jetting/dispensing where structures are realized by merging of subsequently dispensed droplets (Fig. 1 a) [2]. A related method is droplet dispensing in pre-fabricated open channels, where structures are formed by capillary forces. While direct ink writing methods primarily address pasty materials, droplet jetting of low viscous liquids is challenging owed to the adjustment of optimum droplet spacing. The semi-contact writing (SCW) approach presented here is a convenient method to process low or even medium viscous liquids onto a variety of common substrate materials.

SEMI-CONTACT WRITING TECHNOLOGY

Figure 1 b represents the SCW working principle. Here, the nozzle (ID: 200 µm) of a PipeJet[TM]-dispenser (BioFluidix GmbH,

Germany) [3] mounted to a software-controlled 3-axis robot is primed with the desired structural liquid and moved in close proximity (~100 µm) to a planar substrate (perpendicular to the nozzle orifice). The ejection of a single droplet bridges the detached dispenser nozzle and the substrate surface. Due to controlled nozzle-displacement in x- & y-direction liquid is released out of the nozzle by capillary force, only. Previously, similar techniques have been demonstrated by pressure-driven release of viscous liquids or pastes [1]. Using the SCW-method, structure width and height largely depend on the liquid-substrate combination (attributed by contact angle and viscosity) and can be controlled by process parameters like displacement-velocity, hydrostatic pressure, nozzle diameter & nozzle-substrate-distance. Varying these parameters
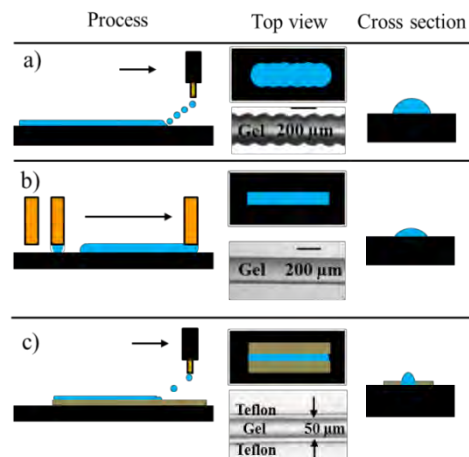
Figure 1: a) Periodic droplet jetting to produce linear structures on planar substrates. b) Semi-contact writing method. The nozzle of a dispenser is moved close to the substrate (~100 µm). The ejection of a single droplet establishes a capillary bridge between nozzle and substrate. Complex fluidic structures are generated due to capillary flow by controlled displacement of the substrate along the x-y-plane. c) Combined method of the SCW-technology and droplet jetting.

enables processing of liquids with viscosities up to 500 mPas as demonstrated for polyacrylic acid (50 wt-%) (PAA) on planar Polyimide (PI) substrates exhibiting widths down to 120 µm. Narrower structures can be achieved by decreasing the nozzle diameter which in turn complicates the process due to an increased
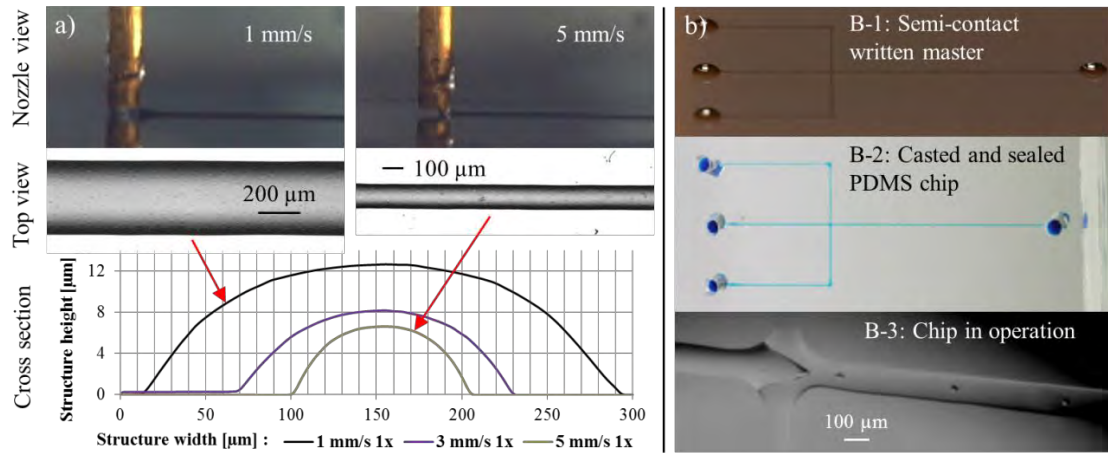
Figure 2: a) Nozzle observation during line generation process (Polacrylic acid 50 w-% on a Polyimide foil substrate) and profiler cross sections at different displacement velocities. Stacking structures on top of each other leads to a linear increase in height. b) Processing steps for PDMS prototyping. B-1) Written master-structure (5 mm/s; 5 stacks) for PDMS casting ($A_{channel}$: 100x35 μm²). B-2) Casted, sealed and ink-filled PDMS chip. B-3) Microfluidic droplet generator in operation.

fluidic resistance restricting the flow out of the nozzle. To overcome these challenges SCW- & droplet jetting methods are combined writing hydrophobic boundary structures (Teflon®, Dupont, USA) in parallel at an in-between distance of about 50 μm using SCW (Fig. 1 c). The formed space is filled up *via* liquid dispensing (droplet jetting) resulting in droplet merging to form line shaped structures, for instance. Thus structure width can be further decreased while the impact of the structural liquid on dimensions is reduced as dimensions mainly depend on the generated boundary geometry.

APPLICATIONS
PDMS prototyping

The SCW-method can be used to fabricate master-structures in conventional PDMS prototyping [5]. The integration of SCW allows for the rapid change of chip designs bypassing cleanroom facilities and time-consuming mask fabrication which also reduces required expertise. For this purpose, an aqueous polyacrylic acid solution (50 wt-%) was applied to a standard Polyimide foil substrate using a software-based implemented design. After master fabrication Parylene-C was vapor deposited on the structures to prevent liquefaction and adhesion during PDMS casting enabling multiple casting procedures using the same master. The applicability of the process was demonstrated by fabricating a microfluidic droplet generator within less than 4 hours (from individual design to chip, Fig. 2b). Adjusting flow rates to 30 μL/h for water and 200 μL/h for two perpendicularly

crossing oil streams periodic droplet generation can be observed with a frequency of ~60 Hz and a volume of about 15 pL per single droplet. Summarized, the process features the following specifications:

- Stack width ∝ displacement velocity (Fig 2a)
- Stacking of structures (multiple writing cycles) → linear increase in height without significant structure broadening (max. aspect ratio for PAA on PI: 0.36)
- Local height adjustment possible *via* selective structure stacking
- Channel width: 100-500 μm
- Channel height: 7-200 μm
- Semi-circular cross-section
- Multiple casting due to hydrophobic coating

To demonstrate the accuracy of SCW-based fabrication two fluids of differing physico-chemical properties where applied upon a PI substrate to form channels, junctions, corners and intersections (Fig. 3). Implementation of velocity
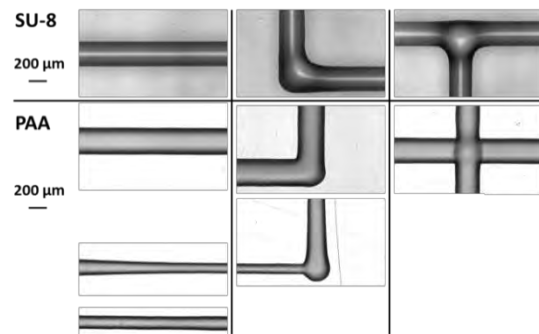

Figure 3: Structure examples generated using the semi-contact writing method applying SU-8 photo resist and PAA as structural material on PI.

gradients during nozzle displacement leads to the formation of tapered channel structures (Fig. 3, PAA bottom left).

Reproducibility was tested by writing 5 lines (length: 5 cm) next to each other with a certain pitch and multiple writing cycles (structure stacking) on a microscopic glass slide. Effects of displacement velocity and the number of stacks on channel dimensions are shown in Table 1.

Table 1: Structure dimensions in dependence on displacement velocity and number of stacks.

Displacement velocity [mm/s]	No. of stacks *n*	Mean structure width [µm]	Mean structure height [µm]
1	10	396 ± 6	88 ± 4.5
3	8	278 ± 3.7	47.5 ± 0.9

Conducting path & substrate prototyping

As described for PDMS prototyping, SCW was used to generate simple conducting paths upon flexible, isolating polymer foils. A sintering-customized ink containing silver nanoparticles (Metalon JS-B25HV, Novacentrix) was used as basic conductive material and was modified towards our purpose. The alcoholic solvent was replaced by water to achieve desired wetting properties. For the use of Kapton 500B as substrate material the silver nanoparticles were centrifuged and alcohol was removed *via* pipetting and desiccation. Afterwards, silver particles were rehydrated with equal amounts of DI-water in respect to the removed solvent, resulting in a similar viscosity as the stock ink but with substrate-adapted surface properties. During processing substrates are mounted to a substrate carrier with small through-holes and buried channels to implement vacuum fixation. Thus a planar substrate surface is ensured whereas no substrate displacement takes place.

Linear structures of different widths are generated by single semi-contact writing, larger areas could be realized by line merging of side by side written liquid structures.

Fig. 4a displays conducting paths directly after generation on a Kapton 500B substrate. Following solvent evaporation (~5 min), common soldering paste was used to mount a SMD resistor and a SMD LED on the fabricated circuit. Both, nanoparticles and paste were soldered during a single standard reflow process within about 10 minutes.

The SCW-method presented here enables simple and rapid prototyping of low-cost
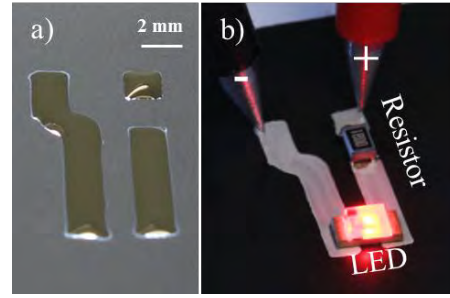
Figure 4: Semi-contact writing method was used to apply a water-based silver-nanoparticle ink on a planar Kapton 500B substrate. To achieve area structures multiple lines were written side by side with a pitch of 300 µm. a) Silver-ink right after structure generation. b) Silver nanoparticle layer after solvent evaporation with mounted SMD-electronics via soldering paste.

customized and compact electric circuits especially for low to medium unit numbers, where specifically designed printed circuit boards (PCB) are not cost-efficient, e.g. when fabricating prototypes. Moreover, it can be used to modify standard circuit boards in case of adding additional components or to prototype flexible PCBs.

Structure generation in open microfluidics

A third application is the generation of liquid structures in open microfluidics [6] like separation channels in open microfluidic gel electrophoresis (OMGE) [7] (Fig. 4). Using the SCW-method a ~200 µm wide channel of linear acrylamide is written across two flat platinum-electrodes on a planar Kapton 500B substrate. To perform electrophoretic separations the open microfluidic system requires two additional dispensers, one to handle the sample and a second to cover the structure with oil to prevent evaporation. A Nano-Jet [8] module is used as a picoliter-dispenser for the contact-free injection of the sample into the separation channel. In this case 150 pL of a fluorescently labeled (Cy5) ssDNA-fragments mixture at a concentration of 1 µM (56-&112-bp, equimolar) was injected. The other dispenser is a conventional syringe pump to apply the oil (Mineral oil PCR Reagent, Sigma-Aldrich). Due to small channel dimensions the substrate needs to be temperature controlled (here: ~14°C) to prevent evaporation during the SCW-process. Furthermore, gel reservoirs were established on both electrodes for an enhanced coupling of the electric field and to prevent charge carrier depletion during electrophoretic separation. Fig. 4 details the process flow (a) and
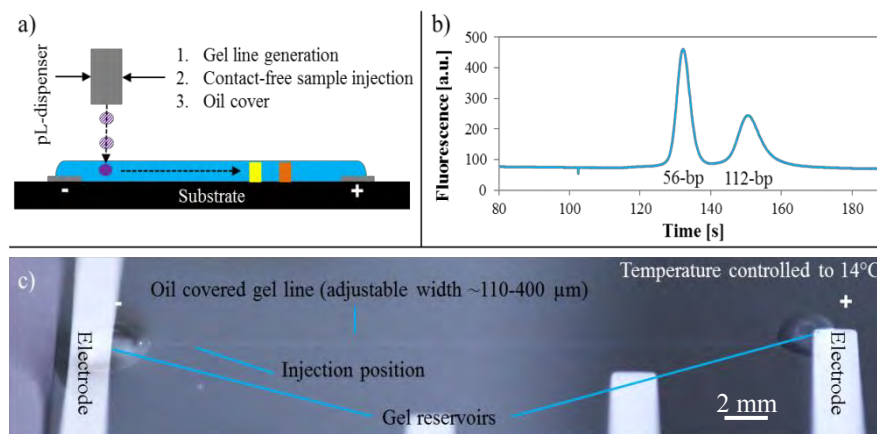
Figure 5: Semi-contact writing used to generate gel separation channels for capillary electrophoresis in open microfluidics. After line generation a DNA sample is injected via non-contact dispensing into the channel and separated by an electrical field with a field strength of E = 200 V/cm. To prevent evaporation the channel is cooled and covered with an oil layer. Migrating DNA was point-detected via LIF near the cathode.

represents an example of an oil covered open microfluidic structure (c). After fabricating the microfluidic system an electrical field of 200 V/cm was applied along the separation channel and separated ssDNA-fragments were detected *via* end-point laser-induced fluorescence about 15 mm downstream the injection position (λ_{ex}= 635 nm, λ_{em}= 685 nm) (Fig. 4 b). Together, the process took about 5 min from fabricating the open microfluidic structure to signal detection.

Applying the SCW-method in open microfluidic gel electrophoresis is a fast, low cost, low volume consuming and on-demand method for conducting electrophoretic separations. The software based customized design implementation increases flexibility while multiplexing is enabled due to the modular setup.

CONCLUSION & OUTLOOK

The semi-contact writing method is a modification of existing direct ink writing technologies and was successfully transferred to a variety of applications, like fabrication of masters in conventional PDMS prototyping, conducting path and electrode fabrication or open microfluidic gel electrophoresis. SCW enables accurate fabrication of structures exhibiting semicircular cross sections in a fast, convenient and low-cost manner. All presented applications benefit from SCW by increased flexibility, decreased process time & costs as well as less required expertise. In future, the SCW application spectrum will be extended and presented applications will be studied in more detail.

REFERENCES

[1] Lewis, J.A., "Direct Ink Writing of 3D Functional Materials", Adv. Funct. Mater., vol. 16, pp. 2193-2204, 2006.

[2] Derby, B., "Inkjet Printing of Functional and Structural Materials: Fluid Property Requirements, Feature Stability, and Resolution", Annu. Rev. Mater. Res., vol. 40, pp. 395-414, 2010.

[3] Streule, W. et al., "Pipejet: a simple disposable dispenser for the nano- and microliter range", JALA, vol. 9, pp. 300-306, 2004.

[4] McDonald, J.C. et al., "Fabrication of microfluidic systems in poly(dimethylsiloxane)", Electrophoresis, vol. 21, pp. 27-40, 2000.

[5] Gutzweiler, L. et al., "A flexible method for rapid prototyping of PDMS microfluidic chips using direct written polymer master structures", *MicroTAS 2013, 17th International Conference* pp. 1409-1411.

[6] Pfohl, T. et al., "Trends in Microfluidics with Complex Fluids", Chemphyschem, vol. 4, pp. 1291-1298, 2003.

[7] Tanguy, L. et al., "On-demand electrophoretic separation of DNA in written gel lines on planar substrates", *TRANSDUCERS 2013, 17th International Conference*, pp. 1223-1226.

[8] Koltay, P. et al., "Highly parallel and accurate nanoliter dispenser for high-throughput-synthesis of chemical compounds", *Proc. International MEMS Workshop (I-MEMS) 2001*, pp. 115-124.

CONTACT

* L. Gutzweiler, ludwig.gutzweiler@imtek.de

5. Applications   **Presentation**

MICROFLUIDIC SAMPLE PREPARATION CHIP FOR RNA-BASED PATHOGEN DETECTION

H. Hubbe[1], S. Hakenberg[1], G. Dame[1] and G. Urban[1,2]
[1] University of Freiburg, Lab for Sensors, Freiburg, Germany
[2] University of Freiburg, Freiburg Institute for Advanced Studies, Freiburg, Germany

We report the development of a microfluidic sample preparation chip (fig. 1). It provides preconcentration, thermoelectrical lysis and nucleic acid purification without manual interventions. Total process time is less than 15 minutes.

Hours of processing time, manifold laboratory equipment and tedious manual work are involved, when gene-based pathogen detection is done today [1]. It is the objective of this work, to reduce time and effort to a minimum and provide a point-of-care compatible device for sample preparation. This chip is an integration of a previously presented preconcentration chip [2] into a lysis and nucleic acid purification chip [3,4].
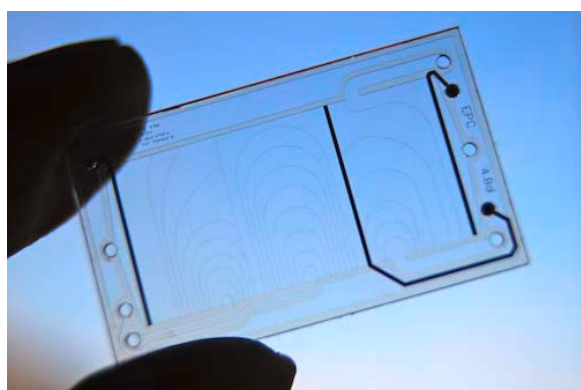
Fig. 1: Microfluidic sample preparation chip in top view

The chip consists of two fluidic compartments with multifunctional thin-film electrodes (fig. 2). A hydrogel separates the compartments from each other. Compartment (A) is used for the enrichment and subsequent lysis. The sample solution continuously flows through the chamber. Two electrodes create an electrical field, accumulating bacteria at the hydrogel surface and increasing their concentration in the device.

An AC voltage lyses the bacteria directly after the preconcentration. Purification of the released nucleic acids follows immediately through integrated gel electrophoresis. The nucleic acids migrate through the hydrogel and are eluted from the opposite compartment (B).

E. Coli is used as a model. The functionality is shown with fluorescence observation of a green fluorescent protein modified strain and quantitative RT-PCR of the eluate.
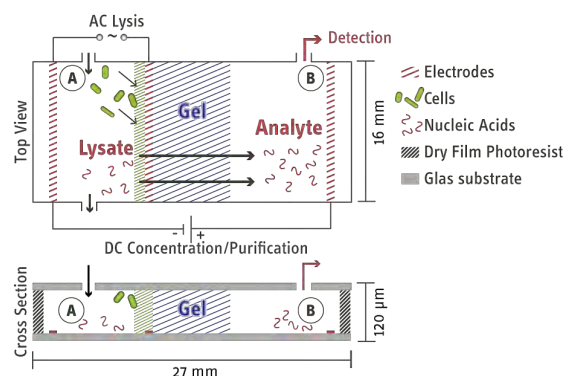
Fig. 2: Simplified model of sample preparation chip in top view and cross section

Fluorescence imaging demonstrates the accumulation of bacteria. Results of quantitative RT-PCR show lower c_t values for longer preconcentration time, indicating higher amounts of RNA.
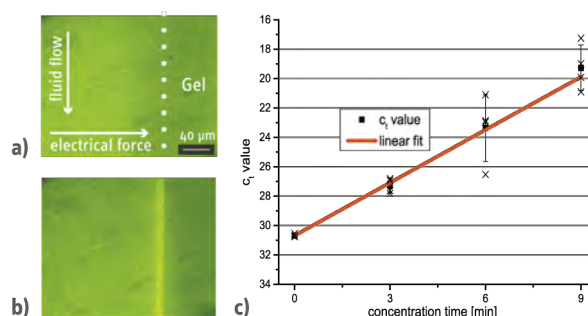
Fig. 3: Fluorescence images of preconcentration process at a) 0s and b) 200 s. c) results of quantitative RT-PCR of eluates processed for different concentration times.

Preconcentration has shown to be effective and has the potential to lower detection limits. The device does not require manual intermediate steps. It is able to prepare a bacterial sample for RNA detection in less than 15 minutes. These novel features illustrate a high potential for future point-of-care diagnostic devices for pathogen detection.

References
[1] "Microfluidic Systems for Pathogen Sensing: A Review.", J. Mairhofer et al., Sensors, 9(6) 4804 (2009).
[2] "Enrichment of viable bacteria in a micro- volume by free-flow electrophoresis", S. Podszun et al. Lab on a chip, 3, 451 (2012).

[3] "A Lab-on-a-Chip for automated RNA extraction from bacteria", P. Vulto, Dissertation, Albert-Ludwigs-Universität Freiburg, 2008.
[4] "A microfluidic approach for high efficiency extraction of low molecular weight RNA" P. Vulto, et al., Lab on a chip, 5, 610 (2010).

Applications   Presentation

ASTROBIONIBBLER: MICROFLUIDIC SUBCRITICAL WATER EXTRACTION OF ORGANICS FROM PLANETARY SAMPLES

A. C. Noell[1], M. C. Lee[1], A. M. Stockton[1], N. Takano[1,2], D. Elleman[1,3], J. Hasenoehrl[1,4], S. Sherrit[1], and F. Grunthaner[1]

[1] Jet Propulsion Laboratory, California Institute of Technology, Pasadena, CA, USA
[2] California State Polytechnic University, Pomona, CA, USA
[3] Tulsa Community College, Tulsa, OK, USA
[4] University of Idaho, Moscow, ID, USA

ABSTRACT

Given a long, problematic history of attempted Martian organic analysis using thermal volatilization (pyrolysis) to extract organics from Martian regolith samples, it has become clear that liquid-based extraction is an attractive alternative in need of further development. Subcritical water extraction (SCWE) has been widely used for extractions here on Earth. In this work, we develop an end-to-end microfluidic SCWE instrument for potential application to planetary exploration. The instrument includes three primary modules: (1) sample acceptance and slurry preparation, (2) on-chip microfluidic SCWE, and (3) H-Cell sample concentration and detection.

KEYWORDS

Microfluidics, subcritical water extraction, planetary exploration, astrobiology, organic analysis, laminar flow diffusion interface

INTRODUCTION

Searching for trace levels of organic molecules on Mars or other rocky bodies presents a formidable challenge for robotic instrumentation. Many organic molecules of specific interest, including potential biomarkers such as amino acids, are not ideally suited for identification via gas chromatography and mass spectrometry (GC/MS) the current robotic state of the art. Liquid chemical methods such as liquid chromatography (LC) and capillary electrophoresis (CE) are typically used for analysis on Earth, and because of this automated microfluidic versions of LC and CE capable of separation and sensitive detection of a broad variety of organic molecules are already demonstrated or under development [1, 2].

What is currently lacking however, is a reliable, small sample extraction and concentration instrument which can deliver liquid extracts to microfluidic devices. The Astrobionibbler instrument (ABN) meets these needs and can be conceptually broken into three functional modules: 1. Sample acceptance and slurry preparation 2. Extraction of organics from the soil via subcritical water extraction (SCWE) performed on chip. 3. Organic concentration via a laminar flow diffusion interface (H-Cell) and detection.

BACKGROUND

An ideal organic extraction method will efficiently extract a wide range of organic molecules from solid matrices without degradation. The development of SCWE for this purpose is based on the fact that the dielectric constant of water changes dramatically with temperature making it a polar solvent at room temperature but becoming increasing nonpolar with increasing temperature, especially above 100°C [3]. Furthermore, at the pressures necessary to keep water subcritical at temperatures above its boiling point, the hot pressurized fluid will be able to penetrate pores in solid matrices to more efficiently extract the material within. Both amino acids and polycyclic aromatic hydrocarbons have been extracted from Atacama soils using SCWE [3, 4].

Given the likelihood that if organics are present in accessible planetary samples they will be so at trace levels, a concentration step after extraction will greatly increase the probability of down-stream detection. Laminar flow diffusion interfaces (LFDI) take advantage of the lack of turbulent mixing in side by side laminar flows to allow diffusion of an analyte from one flow to another. Microfluidic H-Cells easily create LFDIs that can be tuned for the desired properties by design of the microfluidic chip [5, 6].

INSTRUMENT DESIGN AND EVALUATION

First prototypes of each of the three functional subsystems of ABN have been developed and tested: 1. The sample acceptance and slurry preparation module. 2. The microfluidic subcritical water extractor (SCWE) microdevice. 3.The H-cell organic concentrator.

Sample acceptance and slurry preparation

Initially mechanical mixing using a stir bar created homogenous slurries for peristaltic pumping tests, but in a reusable cup a noncontact method of mixing is preferable. Therefore a small cup with a piezoelectric driven nebulizer on the bottom was designed to allow mixing via sonication (Figure 1). Complete mixing was observed with the piezo nebulizer cup, and mechanical mixing is no longer needed.
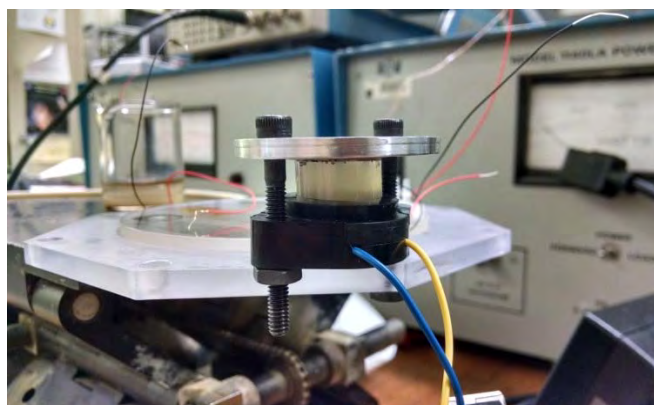
Figure 1. Piezo driven nebulizer with sample cup.

Using a peristaltic pump it was possible to reproducibly and homogenously move slurries up to 20% weight from the sample cups to the microdevice. Observed flow profiles within the microdevice matched models (Figure 2). Semi-dead space is created by eddies at rapid flow rates (>10 mL/min), while at lower flow rates (< 5 mL/min) clogging of the miniature peristaltic pump and/or the microfluidic channel becomes problematic. This indicates that careful design of device geometry will be required to obtain adequate sample volume while minimizing dead-space and clogging concerns.
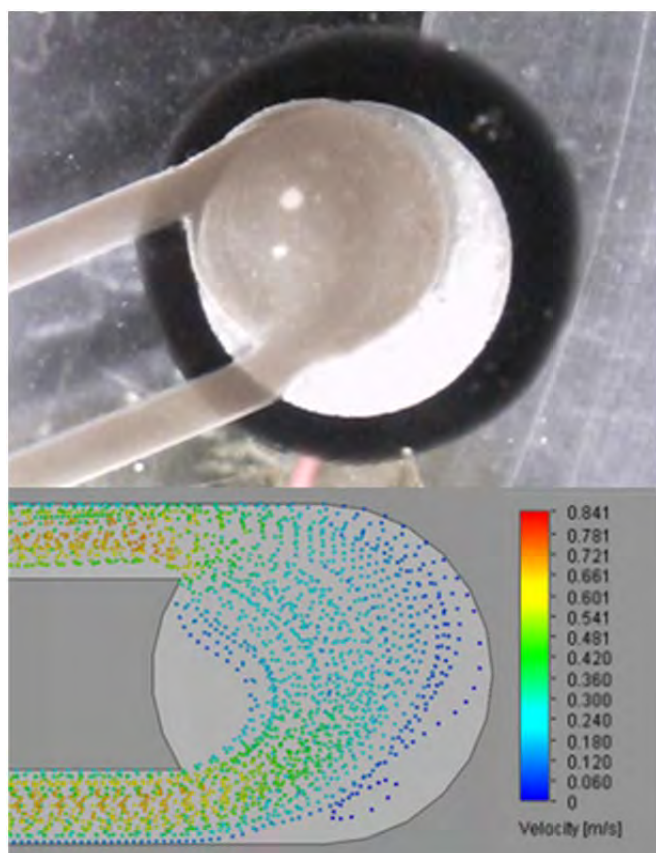
Figure 2. (Top) Photograph of microdevice during 10 mL/min pumping of a 10% by weight slurry of JSC-Mars1 simulant in water. (Bottom) Flow modeled in Solid Works.
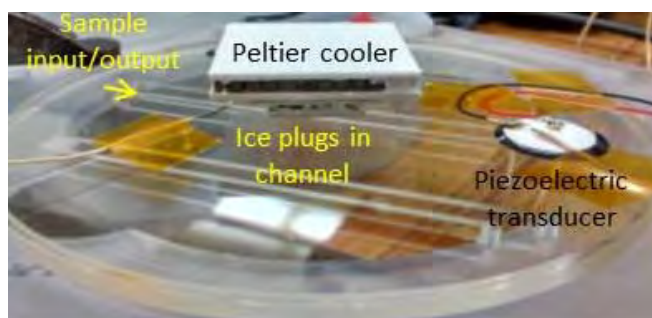
Figure 3. Image of subcritical water extraction (SCWE) microdevice set-up.

Microfluidic subcritical water extraction (SCWE) microdevice

A significant challenge in creating a SCWE instrument is withstanding the pressures and temperatures required during extraction. A bonded glass chip of sufficient thickness has the inherent strength, but creating pressurized seals at the interfaces that are easily automatable is non-trivial. The ABN prototype extraction chip overcomes this by using ice plugs in the microfluidic channels as a sealing mechanism while ultrasonication is used to locally heat a SCWE extraction chamber defined on the chip. The ice plugs are formed reversibly via Thermo Electric Coolers (TEC) attached to the exterior glass surface. The instrument set-up is shown in Figure 3.

Frozen plugs can be maintained and the chamber heated to $\geq 150°C$ with both pure water and slurry solutions. The pressures built up during heating to subcritical temperatures can be sufficient to break the glass devices, particularly after repeated extractions. This was mitigated by going from a 200 µm thick backing wafer to a 5 mm thick backing wafer. Tests of preliminary SCWE chip sealing and extractions are ongoing.

Sample concentration using an H-Cell

Prototype microfluidic devices for testing diffusion transport of amino acids in H-Cells have been built. Preliminary data demonstrating the development of the laminar flow diffusion interface (LFDI) under laminar flow conditions has been demonstrated and tests of the desired flow conditions to allow optimal diffusion have begun.

The LFDI is clearly visualized by using two different colored dyes (Figure 4). In order to quantify diffusion and to serve as a detector for the final system, a custom laser-induced fluorescence detection (LIF) system with three translational degrees of freedom was built (Figure 5). This system was demonstrated to have sensitivity to less than 3 nM fluorescamine-labeled glycine (Figure 6). Using
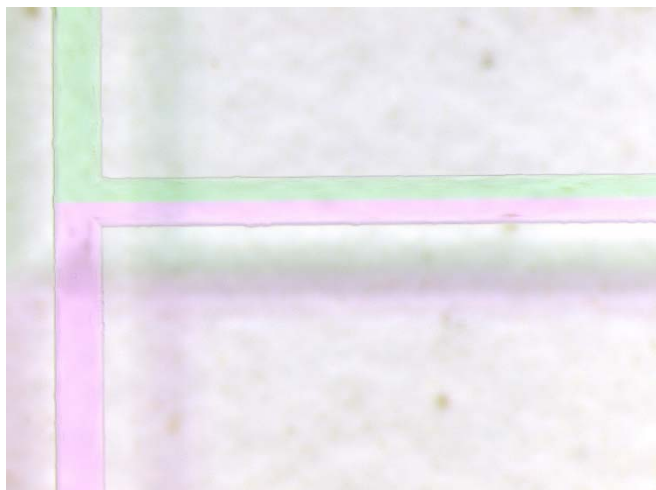
Figure 4. Red and green food coloring in laminar flow, visually demonstrating the lack of turbulent mixing in H-Cell devices.
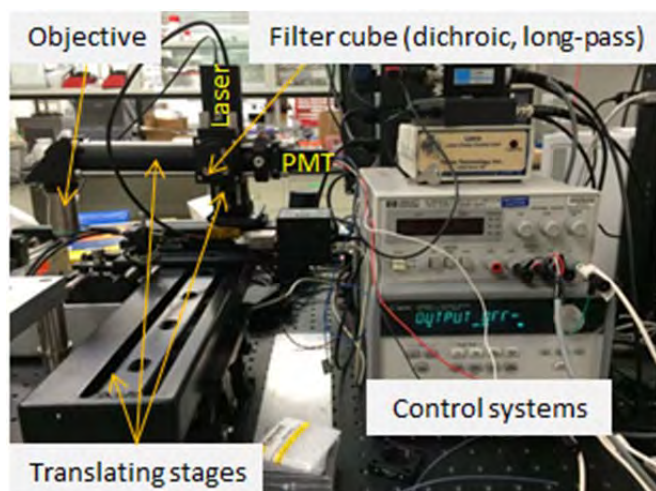
Figure 5. Custom-built laser-induced fluorescence detection (LIF) system.
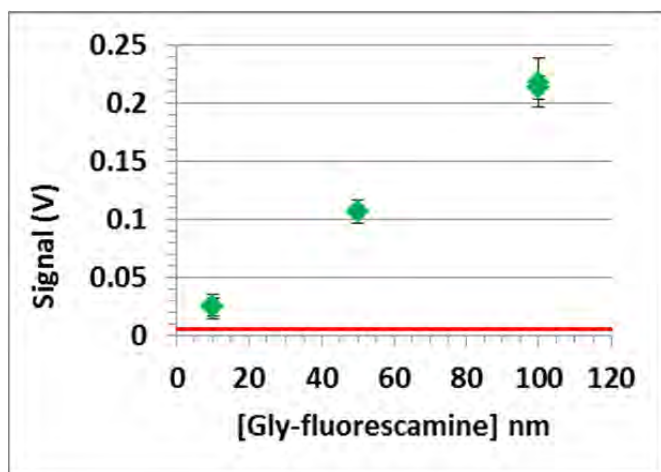
Figure 6. Glycine limit of detection was found to be 3 nM using fluorescamine and the custom LIF system.

determined that 110s is required to enable sufficient diffusion of target analytes across the LFDI. In order to maintain sufficient flow rates to avoid photobleaching of fluorescent probes by the LIF system, LFDI channel length must be greatly extended beyond the current 2.5 cm.

The next version of the H-Cell devices will include a significantly longer diffusion channel and a loop on one half of the H-Cell to allow recirculation of the concentrating flow as it continuously strips the analyte of interest from the sample flow.

CONCLUSIONS

A first prototype of all three subsystems of the ABN have been designed and tested, and initial integration between two subsystems has been tested. Critically, the challenges of performing SCWE on chip because of the temperature and pressures accessed has been met through the use of local heating via sonication and sealing of the SCWE chamber via reversible frozen plug valves in the entrance and exit microchannels. This work has led to multiple technology reports and a provisional patent [7-9]. Continued testing and integration of all three subsystems will lead to a small instrument for extraction and concentration of organics from solid powder samples.

REFERENCES

[1] M. F. Mora, A. M. Stockton, P. A. Willis, "Microchip Capillary Electrophoresis Instrumentation for In Situ Analysis in the Search for Extraterrestrial Life," *Electrophoresis*, **2012**, *33*, 2624-2638.

[2] A. M. Skelley, A. D. Aubrey, P. A. Willis, X. Amashukeli, P. Ehrenfreund, J. L. Bada, F. J. Grunthaner, R. A. Mathies, "Organic amine biomarker detection in the Yungay region of the Atacama Desert with the Urey instrument," *J. Geophys. Res.*, **2007**, *112*, G04S11.

[3] X. Amashukeli, C. C. Pelletier, J. P. Kirby, F. J. Grunthaner, "Subcritical water extraction of amino acids from Atacama Desert soils," *J. Geophys. Res.,* 2007, 112, G04S16.

[4] A. M. Stockton, T. N. Chiesl, J. R. Scherer, R. A. Mathies, "Polycyclic Aromatic Hydrocarbon (PAH) Analysis with the Mars Organic Analyzer Microchip Capillary Electrophoresis System," *Anal. Chem.*, **2009**, *81*, 790-796.

[5] A. E. Kamholz, E. A. Schilling, P. Yager, "Optical measurement of transverse molecular diffusion in a microchannel," *Biophys. J.*, **2001**, *80*, 1967-1972.

[6] A. E. Kamholz, P. Yager, "Theoretical analysis of molecular diffusion in pressure-driven laminar flow in microfluidic channels," *Biophys. J.*,

2001, *80*, 155-160.

[7] S. Sherrit, M.C. Lee, A.C Noell, A.D. Aubrey, J.L. Hasenoehrl, N. Takano, F. Grunthaner, "Micro Acoustic resonant chambers for heating/agitating/mixing (MARCHAM)," NPO # 49130, April 2013, U. S. Provisional Patent, California Institute of Technology.

[8] M. C. Lee, S. Sherrit, A.C Noell, J.L. Hasenoehrl, N. Takano, F. Grunthaner, "Frozen plugs as microfluidic valves (FRO-FLO)," NPO # 49220, Nov 8, 2013

[9] F. Grunthaner, S. Sherrit, M. Lee, A. Noell, A. Aubrey, "AstroBioNibbler - A Sensitive Microfluidic Amino Acid Detector," NPO # 49395, Nov 18, 2013.

CONTACT
Stewart Sherrit, ssherrit@jpl.nasa.gov

4. Fluidic control systems   Presentation

TOWARDS SYSTEM-LEVEL MODELING AND CHARACTERIZATION OF COMPONENTS FOR INTRAVENOUS THERAPY

D. Alveringh[1], R.J. Wiegerink[1], and J.C. Lötters[1,2]
[1] MESA+ Institute for Nanotechnology, University of Twente, Enschede, The Netherlands
[2] Bronkhorst High-Tech BV, Ruurlo, The Netherlands

ABSTRACT

Problems occur regularly with intravenous therapy, especially with the flow behavior. A mechanical model can predict which components of intravenous therapy systems introduce non-ideal effects in the flow. This study concentrates on gaining quantitative information of each separate component for intravenous therapy, characterize its non-ideal effects and combine these quantities in one system-level model. The model will help in the development of a mass flow sensor which can be used in a control system for intravenous therapy.

KEYWORDS

intravenous therapy, flow sensor, infusion, Coriolis

INTRODUCTION

According to reference [1], between 2005 and 2009, the FDA (US Food and Drug Administration) received more than 56,000 reports of problems associated with infusion pumps. To find the health risks for intravenous therapy, measurements have been done in the past on infusion pumps, tubes and other components. Reference [2], for example, summarizes the main problems based on a literature study. However, to understand all non-ideal effects and predict the behavior of intravenous therapy, the entire system must be described in one model.

Our study concentrates on gaining quantitative information of each separate component, characterize its non-ideal effects and combine these quantities in one system-level model. This model is part of the development of a new micro Coriolis mass flow sensor based on reference [3], which can be used for real-time monitoring or as a calibration method for systems for intravenous therapy, leading to safer infusions.

(a) Practical infusion setup.
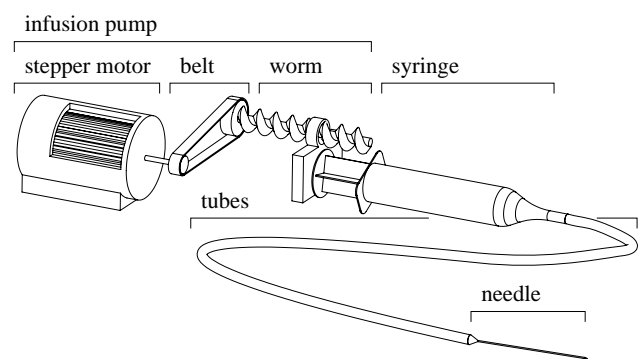
(b) Schematic overview of the components
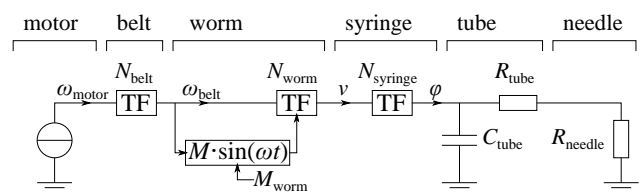
(c) System-level lumped elements model.

Figure 1: Intravenous therapy.

MODEL OVERVIEW

Systems for intravenous therapy consist of infusion pumps, syringes, tubes and needles. Infusion pumps consist of stepper motors, belts and worm wheels (Figure 1b). A stepper motor generates an angular velocity ω_{motor}. This angular velocity is transmitted via a belt (ω_{belt}) to a worm, which transforms it into a velocity v of the plunger. The syringe transforms the velocity into a fluid flow ϕ.

The mentioned components can be modeled with lumped elements (Figure 1c), where each component is modeled as an equivalent electronic resistor (R), capacitor (C) or transformer (N). This method for modeling dynamical systems is done in many applications; the modeling of micropumps [4], for example. For equivalent resistors (e.g. a small needle), the following equations hold:

$$F(t) = R_{\text{t}} \cdot v(t), \tag{1}$$

$$T(t) = R_{\text{r}} \cdot \omega(t), \tag{2}$$

$$P(t) = R_{\text{f}} \cdot \phi(t). \tag{3}$$

with t the time, F the force, T the torque and P the pressure. And for equivalent capacitors (e.g. a compiant tube), the following equations hold:

$$F(t) = \frac{1}{C_{\text{t}}} \int v(t)\,\mathrm{d}t, \tag{4}$$

$$T(t) = \frac{1}{C_{\text{r}}} \int \omega(t)\,\mathrm{d}t, \tag{5}$$

$$P(t) = \frac{1}{C_{\text{f}}} \int \phi(t)\,\mathrm{d}t. \tag{6}$$

Transformers (e.g. a syringe converts a velocity to a flow) are two-ports, and obey following equation:

$$e_{\text{out}}(t) = \frac{1}{N} e_{\text{in}}(t), \quad \text{with} \ \ e = F \vee T \vee P, \tag{7}$$

$$f_{\text{out}}(t) = N f_{\text{in}}(t), \quad \text{with} \ \ f = v \vee \omega \vee \phi. \tag{8}$$

In Figure 1c, the major parts of an intravenous therapy system are represented using the described elements.

The sine-block in Figure 1c models the shape of a bent worm, modeled by a sine wave with amplitude M_{worm} and frequency dependent of the angular velocity of the worm.

MODEL PARAMETERS

All parameters are estimated using calculations,

finite element simulations and measurements on commercially available components.

Stepper motor

Stepper motors rotate by actuating the rotor in steps. This allows good control of the angular velocity, but may introduce non-smooth transitions between steps. Therefore, measurements where done using a 10-bit contactless magnetic angular encoder (Avago AEAT-6600-T16) on a stepper motor (17H130HM) from an infusion pump (NE-300), using the measurement setup in Figure 2a. Oversampling of 30 times was used to increase the resolution. As shown in Figure 3, there where no significant steps or other non-ideal effects observed, which means that the stepper motor can be modeled as a straight-forward source of angular velocity.

(a)   *(b)*
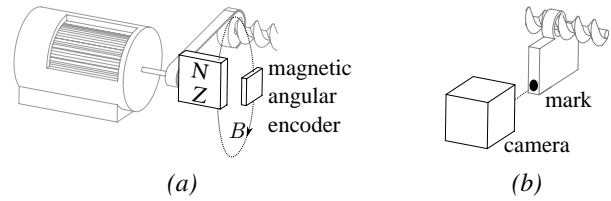
Figure 2: Measurement setup for the characterization of the infusion pump, with (a) contactless motor angle measurement and (b) displacement measurement.
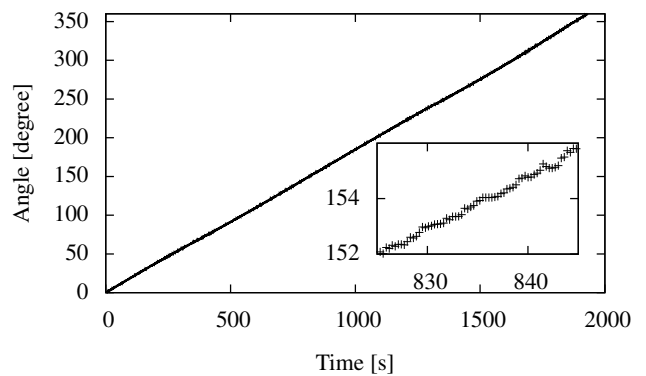
Figure 3: Characterization results of the stepper motor with an equivalent pumping speed of 0.49 mL h^{-1} at 100 Hz and 30× oversampling.

Worm

Non-ideal transformation effects of the worm were found using video measurements. By recording (640×480 pixels, 15 FPS) the movement of the cart on the worm wheel, the displacement over time is measured. Figure 2b

shows schematically the measurement setup. A moving average filter (31) is applied on the data, the result and its derivative are shown in Figure 4.

Figure 4: *Characterization results of the worm with an equivalent pumping speed of $49\,mL\,h^{-1}$.*

It can be concluded that the the influence of the non-ideal shape of the worm on the velocity is more than 75 %. This value is expected to be much smaller for most infusion pumps, since this measurement was done on a worn infusion pump. The measurement setup will be used to characterize the worms of different infusion pumps in the future.

Tubes and needles

Characterization of two types of tubes and needles is done using the setups in Figure 5.

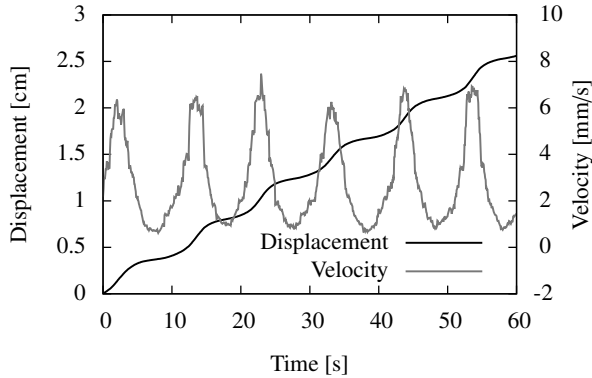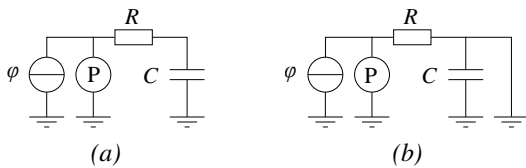

Figure 5: *Measurement setup for the characterization of tubes, with (a) capacitive measurement and (b) resistance measurement.*

The capacitances have been measured by filling the tubes with water, clamping one end while expanding the tubes with constant flow of water. The equivalent capacitance can be calculated from Equation 6. For constant flow, this is related to the flow, time and pressure as shown in following equations:

$$C_f(t) = \phi \frac{t}{P(t)}. \tag{9}$$

The resistances have been measured by pumping a

constant flow and measuring the pressure. This can be calculated by deriving the following equation from Equation 3:

$$R_f(t) = \frac{P(t)}{\phi}. \tag{10}$$

The measurement results for two frequently used tubes and needles are available in Table 1. The results were checked using finite element simulations for the capacitive values and Hagen-Poiseuille calculations for the resistive values. The values correspond in the same order of magnitude.

Table 1: *Resistance and capacitance measurements of infusion tubes and needles.*

	Resistance	Capacitance
Tube 1[a]	$1.3 \cdot 10^{10}\,\mathrm{Pa\,s\,m^{-3}}$	$2.3 \cdot 10^{-12}\,\mathrm{m^3\,Pa^{-1}}$
Tube 2[b]	$4.8 \cdot 10^{10}\,\mathrm{Pa\,s\,m^{-3}}$	$3.5 \cdot 10^{-13}\,\mathrm{m^3\,Pa^{-1}}$
Needle 1[c]	$3.3 \cdot 10^{10}\,\mathrm{Pa\,s\,m^{-3}}$	
Needle 2[d]	$1.3 \cdot 10^{12}\,\mathrm{Pa\,s\,m^{-3}}$	
Flow sensor[e]	$\approx 1 \cdot 10^{13}\,\mathrm{Pa\,s\,m^{-3}}$	

[a] Clinico Medical Sp. z o.o PVC Infusion Line (2 m).
[b] Biocath PE/PVC Extension Line (2 m).
[c] BD Microlance 3 0.8×25 mm needle.
[d] BD Microlance 3 0.3×13 mm needle.
[e] Bronkhorst L01 flow sensor, derived from datasheet.

Other parameters

The resistance of the plunger is connected in series with the source of velocity, hence, this will not influence the flow. The compliance of the plunger is, according to finite element simulations, also not significant compared to the compliance of the tubes. The compliance of the belt, the inertia of the worm and the compliance of the needle are assumed not significant compared to the other resistances and compliances in the system. For the rest, the used flow meter consists of a stainless steel tube that is similar to a needle.

SIMULATION

The parameters used in the model of Figure 1c are printed in Table 2. The simulation software 20-sim was used to simulate the model. The set point changes from $0\,\mathrm{mL\,h^{-1}}$ to $1\,\mathrm{mL\,h^{-1}}$ and back to $0\,\mathrm{mL\,h^{-1}}$, which simulates a practical medical situation. Results are shown in Figure 6. It is clear that the RC-effect and the modulation effect have a major influence on the flow.

2$^{\mathrm{nd}}$ International Conference on MicroFluidic Handling Systems
8 – 10 October 2014, University of Freiburg, Germany

108

Table 2: Values used in the model of Figure 1c.

Parameter	Value	Description
N_{belt}	0.5	Ratio of belt[a]
N_{worm}	$1.3 \cdot 10^{-4}$ m rad^{-1}	Ratio of worm[a]
M_{worm}	5 %	Worm modulation[b]
$N_{syringe}$	$6.2 \cdot 10^{-4}$ m^2	Ratio of syringe[c]
R_{tube}	$1.3 \cdot 10^{10}$ Pa s m^{-3}	Tube 1[d]
C_{tube}	$2.3 \cdot 10^{-12}$ m^3 Pa^{-1}	Tube 1[d]
R_{needle}	$1 \cdot 10^{13}$ Pa s m^{-3}	Flow sensor[d]

[a] Calculated from the results in Figure 3 and Figure 4.
[b] Expected, to be specified in future work.
[c] Calculated from the section area of a syringe.
[d] From the results in table 1.
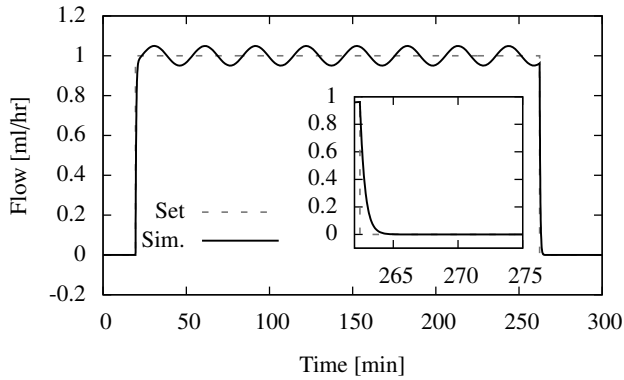
Figure 6: Simulation results, with a clear RC-effect of tube and needle combination and the modulation effect of a non-ideal worm.

MEASUREMENTS

To validate the model, measurements of the complete system were done. The setup in Figure 1b was used, where the needle is replaced by a a flow sensor. Purified water was used for the fluid flow. The results are shown in Figure 7.

It can be concluded that there are differences between the model and the measurements: the frequency of the modulation of the worm is higher in the simulation. Besides, the RC-time is lower. Latter may be because of the connection tubes between flow sensor and setup. Nevertheless, the model supports the major non-ideal effects.

CONCLUSION

The first system-level model for intravenous therapy systems is realized. A stepper motor and worm of an infusion pump as well as two different tubes and needles
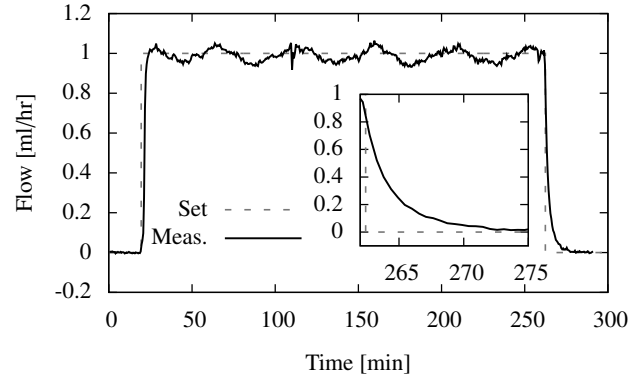
Figure 7: Measurement results, also with a clear RC-effect of tube and needle combination and the modulation effect of a non-ideal worm.

are characterized and included in the simulation. The RC-time as a result of the compliance and resistance of the tube and needle and the modulation as a result of the shape of the worm have major influences on the flow. Measurements on a complete intravenous therapy system agree with these observations.

Future work will focus on further characterization of different systems for intravenous therapy, improving the model and the development of a new mass flow sensor can be used in a control system for intravenous therapy.

ACKNOWLEDGEMENTS

REFERENCES

[1] T. Agres, "FDA seeking safer infusion pumps," *Pharmacy Practice News*, may 4th 2010.

[2] A. C. van der Eijk *et al.*, "A literature review on flow-rate variability in neonatal iv therapy," *Pediatric Anesthesia*, vol. 23, no. 1, pp. 9–21, 2013.

[3] J. Haneveld *et al.*, "Modeling, design, fabrication and characterization of a micro coriolis mass flow sensor," *Journal of Micromechanics and Microengineering*, vol. 20, no. 12, p. 125001, 2010.

[4] T. Bourouina *et al.*, "Modeling micropumps with electrical equivalent networks," *Journal of Micromechanics and Microengineering*, vol. 6, no. 4, p. 398, 1996.

CELL SIZE DISCRIMINATION BASED ON THE MEASUREMENT OF THE EQUILIBRIUM VELOCITY IN RECTANGULAR MICROCHANNELS FOR POINT OF CARE DIAGNOSTICS

L. Schott[1], C. Sommer[1], T. Walther[2] and M. Baßler[1]
[1] Fraunhofer ICT-IMM, Mainz, Germany
[2] Technische Universität Darmstadt, Darmstadt, Germany

ABSTRACT

In this work we measure fluorescently stained SUP-B15 cells using spatially modulated fluorescence emission (SME). We demonstrate that the experimental apparatus is able to detect cells and that the results are comparable to the ones obtained by the commercially available CASY® TT Counter. Furthermore, by examining the velocity distribution of the cells, we are able to distinguish between different cell conditions in the cell suspension. Additionally, our setup is also capable of determining the viability of cells in suspension. The SME technique presented within this paper is a promising method for cell counting and viability characterization in point of care (PoC) diagnostics.

KEYWORDS

Equilibrium velocity, spatially modulated fluorescence emission, Point of Care, Cell Counter

INTRODUCTION

In conventional flow cytometry the physical cell size is derived from scattered excitation light. To obtain scattered excitation light from individual cells, such devices use a narrow laser spot causing high alignment effort and resulting in the need for complex imaging optics. Thus, miniaturization of conventional flow cytometry for PoC applications is difficult.

A different approach to flow cytometry called "spatially modulated fluorescence emission" (SME) was introduced by Kiesel *et al.* [1]. The spatial modulation of the fluorescent cell signal is realized by placing a spatially modulated mask (see Figure 4) with alternating transparent and opaque features in the optical path of the fluorescence light leading to an amplitude modulation of the detector signal (see Figure 5). This modulation is equivalent to a fingerprint of a cell being recovered during the signal analysis procedure by correlation techniques. As Kiesel *et al.* pointed out, the SME technique is well suited for PoC applications. The SME technique provides a very precise intrinsic velocity measurement. This was used in recent work by Sommer *et al.* [2] to measure the size dependence of the so-called "equilibrium velocity" of rigid particles while being transported in microfluidic channels.

In this paper the measurement of cell size via the equilibrium velocity is demonstrated. A suspension of SUP-B15 cells is measured in the experimental setup of Sommer *et al.* as well as in a commercial CASY® TT Counter (Roche Diagnostics, Germany) and the results are compared.
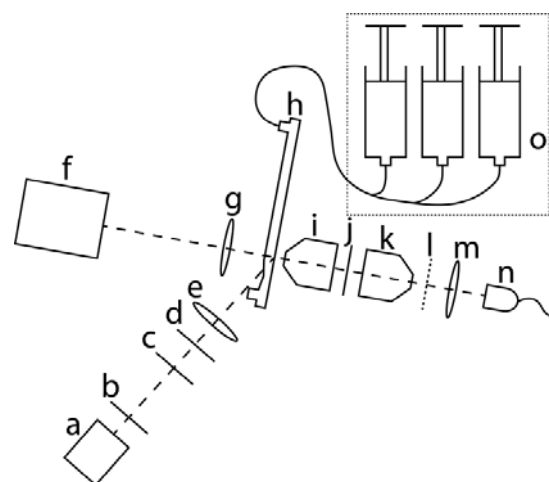
Figure 1: Sketch of the experimental apparatus. a) 488 nm laser, b) iris diaphragm, c) interference filter, d) λ/2-plate, e) cylindrical lens, f) alignment camera, g) spherical lens, h) microfluidic chip, i) & k) microscope objective, j) interference filter, l) spatially modulated mask, m) spherical lens, n) photo diode, o) syringe pump.

EXPERIMENTAL SETUP

A sketch of the experimental apparatus for the measurements of Sommer *et al.* is shown in Figure 1. The beam of the 488 nm laser a) is formed by the optical components b) to e) to an elliptical spot ($388\ mW/mm^2$) which illuminates the detection zone (see Figure 2) in the measurement channel of the microfluidic chip h). In order to align particles at their equilibrium position they must be transported under precisely controlled hydrodynamic conditions at a channel Reynolds number of Re = 14.9 in a constant parabolic flow profile. Therefore, the cells are hydrodynamically focused into a small segment (transport region, see Figure 3) of the rectangular cross section of the measurement channel ($488 \times 12\ \mu m^2$). This region is essentially free of any hydrodynamic effects caused by the left and right boundaries of the channel. Particles in this region are therefore subject to a purely parabolic flow profile. Sheath flow was set to $2 \times 96\ \mu l/min$ and sample flow to $8\ \mu l/min$ to achieve

the desired focusing. With these settings we obtained a 20 μm width of the sample flow and a total flow rate of 200 μL/min. The detection zone is placed 47.5 mm downstream after the focusing junction.
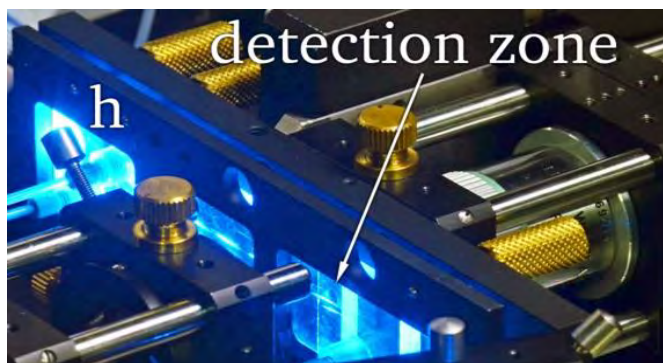
Figure 2: Microfluidic chip (h) installed in the experimental apparatus during measurement. The detection zone is located at the tip of the arrow.

While microscope objective i) captures the fluorescence light, objective k) projects it on the spatially modulated mask l) after being transmitted through the filter j). The spatial mask is sketched in Figure 4. The binary sequence of the mask has a length of 50 digits. The sequence is [1-1,-1,1,-1,1,1,-1,1,-1,1,1,1,-1,-1,-1,1,-1,1,1,-1,1,-1,1,1,1,1,-1,1,1,1,-1,-1,1,1,1,-1,-1,-1,-1,1,1,1,1,1,1,-1,-1,1,1,1,1,1,1,1,1,-1], where "1" stands for transparent and "-1" for opaque. The detector n) records the modulated signal of a cell, an example of such a signal is given in Figure 5. The SME signal analysis procedure based on correlation techniques ultimately measures the time the cell needs to traverse the whole mask. Using the known physical length of the mask the velocity of the cell can be calculated. Clearly, the higher the sampling rate the better the velocity resolution. For a sampling rate of 333 ksps, a minimal velocity resolution of $\Delta v = 0.7$ mm/s is achieved.

CELL PREPARATION

Human B cell precursor leukemia cell line SUP-B15 was obtained from the German Collection of Microorganism and Cell Cultures (DSMZ) and cultured in MC COSY 5a Medium containing 20% heat inactivated fetal calf serum (FCS, SigmaAldrich) and 1% GIBCO® GlutaMAX™ (dilution 1:100, Life Technologies). The cells where incubated in humidified atmosphere at 37 °C containing 5% of CO_2 and harvested at a concentration of about $1.5 \cdot 10^6$ cells/mL by centrifugation at 450 g for 5 minutes at room temperature. To stain the cells with a fluorescent dye, the pellet was re-suspended in 1 mL phosphate-buffered saline (PBS, Applichem, Germany) and 2 μL of 5 mM carboxyfluorescein suc-

cinimidyl ester (CFSE, Invitrogen) and incubated in a water bath at 37 °C for 15 minutes. Afterwards the cells were re-pelleted by centrifugation and re-suspended in 1 mL of fresh PBS and transferred to the syringe pump of the experimental apparatus.

To compare the quality of our results with an established cell counter, we choose the CASY® TT Cytometer. The CASY® Counter measures size and condition of a cell using the Electrical Current Exclusion (ECE) principle. The intact cell membrane of a viable cell excludes the electrical current so that the true cell volume is determined. The broken cell membrane of a dead cell is permeable for this electrical current and therefore only the size of the nucleolus is measured [3]. For comparable measurements the same passage of cell suspension was analyzed by the CASY® Counter and the SME technique
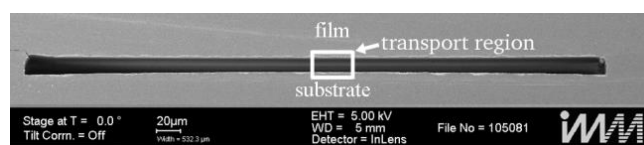
Figure 3: REM picture of the channel cross section of the measurement channel. The highlighted rectangular frame indicates the transport region that contains the actual particles. The large regions to the left and right carry only sheath liquid.
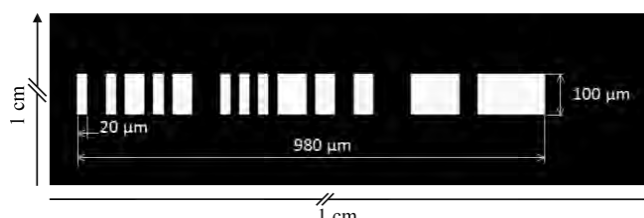
Figure 4: Sketch of the spatially modulated mask complying with a 50-digit binary sequence. The width of each digit is 20 μm. The total mask length is 980 μm starting left of the open feature (#1) and ending right of the last open feature (#49). The first feature (#50) is opaque and therefore not distinguishable from the mask body.

RESULTS AND DISCUSSION

Figure 5 shows a scatter plot of the velocity versus the intensity of rigid spherical particles. The data contain results for particle mean diameters of 5.51 μm, 3.30 μm and 0.84 μm. The 0.84 μm as well as the 5.51 μm particles are used to probe the flow profile: The population of 0.84 μm particles provides information about v_{max} (see inset in figure 6) while viscosity variations across different measurements are monitored via the equilibrium velocity of the 5.51 μm population. Comparing the 5.51 μm and 3.30 μm population shows that both populations appear at

clearly different velocities with $\Delta v = 12$ mm/s (v(5.51 µm)=467±2 mm/s, v(3.30 µm)=579±2 mm/s at $v_{max} = 660$ mm/s).
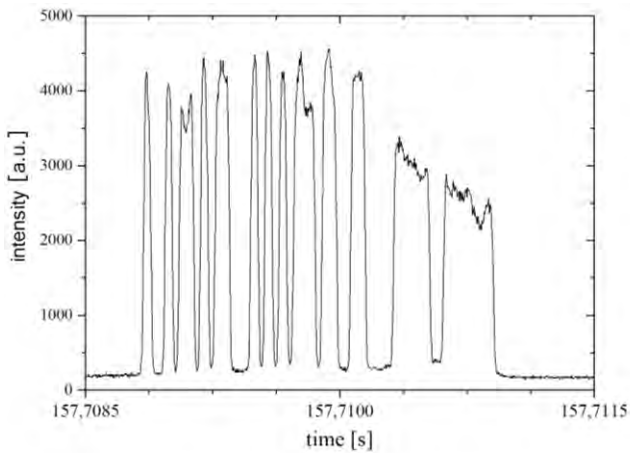
Figure 5: Modulated detector signal of a CFSE stained SUP-B15 cell traversing the modulated mask. The cell needs ~2 ms to pass the mask length of 980 µm which evaluates to a velocity of 490 mm/s.
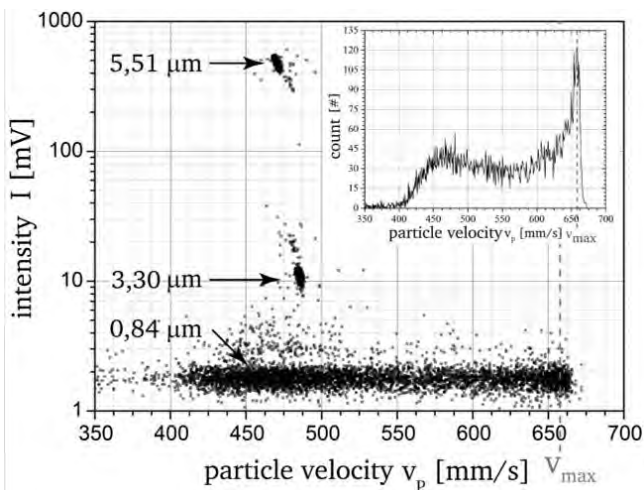
Figure 6: Intensity versus particle velocity plot of a suspension containing particle populations with mean diameters of 5.51 µm, 3.30 µm and 0.84 µm. In the field of flow cytometry such a plot is called a scatter plot. The vertical dashed line is an auxiliary line showing the maximum theoretical channel velocity of the center stream line.

Size discrimination of cells is similarly possible by measuring the velocity as evidenced by means of the scatter plot in Figure 7. Three dominating populations can be distinguished by intensity as well as by velocity and they are denominated in the plot as "viable cells", "dead cells" and "debris". The size distribution of the SUP-B15 cell suspension measured with the CASY® Counter is shown for comparison in figure 8 (a). According to the specifications the

CASY® Counter assigns viable cells in the range between the solid lines, dead cells in the range between the left dashed line (3.5 µm) and the solid line (9 µm) in the middle of figure 8. Cell debris is found left of the dashed line for a size of 3.5 µm and smaller. Thus, the CASY® Counter measurement results in a total cell count of $1.35 \cdot 10^6$, a viable cells count of $1.15 \cdot 10^6$ leading to a cell viability of 85%.

Table 1: Measured values of Figure 7.

Population	SUP-B15 cell line	
	velocity [mm/s]	intensity [mV]
Viable cells	501.4	695.4
Dead cells	463.6	181.3
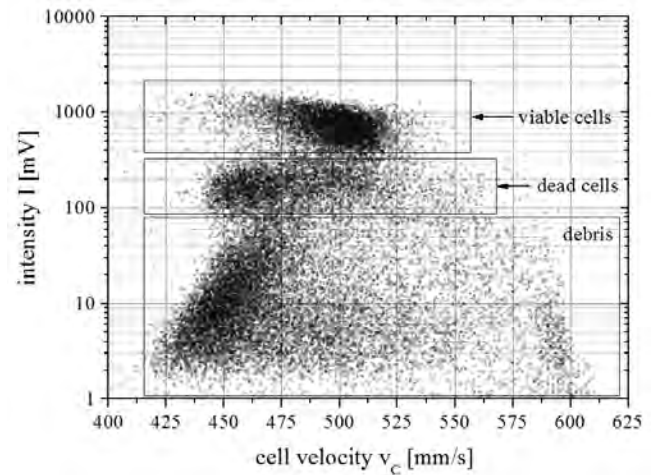
Figure 7:Intensity versus cell velocity Scatter plot of a SUP-B15 cell suspension stained with CFSE and measured with the SME method. Each dot corresponds to a measured cell passing the detection zone. The scatter plot shows three different populations: population 1: viable cells, population 2: dead cells, population 3: debris.

Viable cells are the tallest cells in this suspension. The membrane of these cells is intact and the whole cell membrane and the cytoplasm are stained with the fluorescent dye CFSE. Therefore, these cells are assumed to be brightest and we attribute the brightest population with a mean intensity of 695.4 mV in the SME scatterplot to the viable cells. The viable cells pass the microfluidic channel with a mean velocity of 501.4 mm/s.

The second population identified in the SME plot is the dead cells. In the CASY® Counter the signal from dead cells is dominated by the size of the cell nucleolus due to the principle of Electrical Current Exclusion. The cell membrane of dead cells is broken and it shrinks according to the loss of cytoplasm. In the SME results this has two effects: (1) Dead cells

have lower fluorescence intensity due to the loss of stained cytoplasm and fragments of the cell membrane. Consequently, the dimmer population distributed around a fluorescent intensity of 181.3 mV is attributed to the dead cells. (2) The shrinking of the cells affects the hydrodynamic transport conditions, resulting in the shift (-37.8 mm/s) of the average velocity of the dead cell population (463.6 mm/s) with respect to the viable cells.
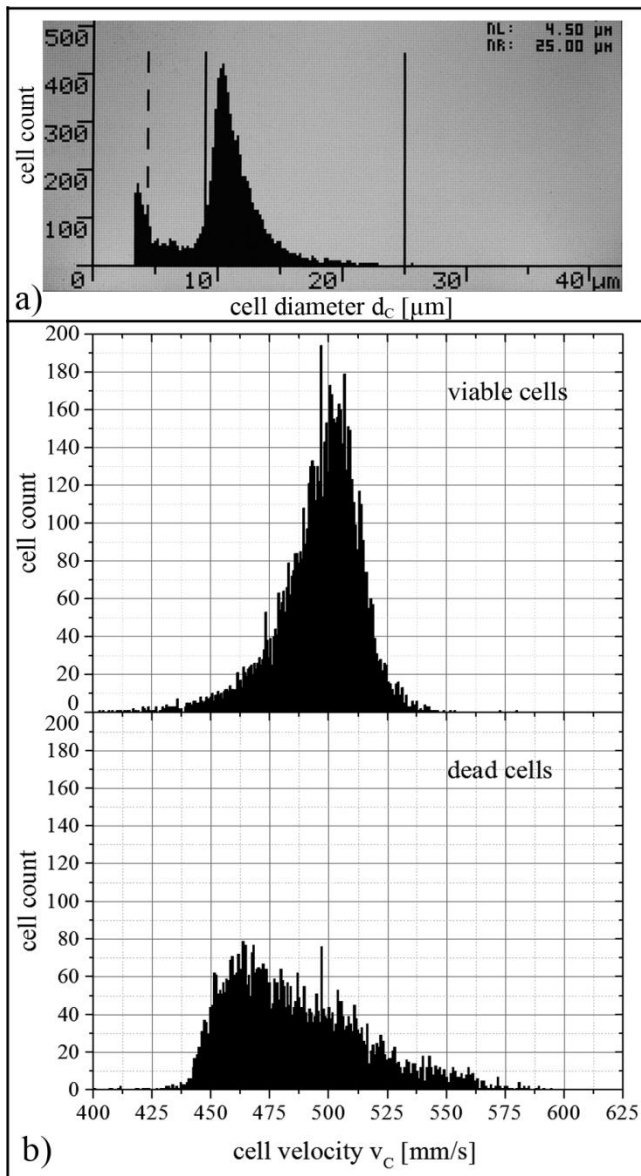
Figure 8 (a) SUP-B15 size distribution of a CASY® Counter measurement. The viable cells have their size maximum at 11 μm, dead cells are measured between the dashed and consistent lines at a size between 9 and 4,5 μm. The debris were measured from a size of 4.5 μm. and smaller (b) Velocity distribution of viable and dead Sup-B15 cells measured with the experimental setup. Viable cells have their velocity maximum at 501.4 mm/s, dead cells at 463.6 mm/s.

The third population measured by the experimental apparatus is the cell debris. Cell debris is composed of fragments of the membrane and has a wide range of sizes and thus shows a broad distribution in velocity as well as in fluorescent intensity. This is the reason for the diagonal skew of the detected population in the scatter plot.

Comparing the measured cell viability of the CASY® Counter with the cell viability of the experimental apparatus, we recognize that the CASY® Counter measures a viability of 85% while the SME System records only 55%. This indicates that the cells are exposed to physical stress before they reach the detection zone. An ongoing task is to identify the location in the microfluidic structure causing the cell damage. Furthermore, the viable cell and dead cell distributions overlap, in contrast to spherical rigid particles (compare figure 6) where the differently sized particle population appear at different velocities. At higher channel Reynolds number, the distance between the velocity distributions for rigid particles increases further [4]. Thus, we expect even clearer results for cell viability assessment at higher channel Reynolds number, as long as there is no overlap in physical cell size between viable and dead cells.

SUMMARY

Our results show that cell velocity contains valuable information about physical cell properties such as size. This information can be used to distinguish between different cell conditions. The results of the SME technique are in that sense comparable with those of the commercially available CASY® TT Counter. Thus, velocimetry offers access to additional parameters for microfluidic point of care flow cytometers without adding significant cost or complexity to the system, especially when using the SME technique.

REFERENCES:
[1] P. Kiesel, M. Bassler, M. Beck and N. Johnson, *Appl. Phys. Lett.*, 2009, 94, p. 41107.

[2] C. Sommer, S. Quint, P. Spang, T. Walther and M. Baßler, *Lab Chip*, 2014, 14, p. 2319

[3] Roche Diagnostics Corporation, CASY Model TTC - Cell Counter and Analyzer. 2010

[4] C. Sommer, S. Quint, P. Spang, T. Walther, and M. Baßler, Advances in Fluid Mechanics X, 2014, 82, p. 265.

5. Applications   Poster

OXYGEN SUPPLY FOR CELL CULTURE SYSTEMS – CHARACTERIZED WITH FLUORESCENCE LIFETIME ANALYSIS AND MODELLED USING SIMULATIONX

M. Busek[1], F. Schmieder[1], S. Grünzner[1], K. Hofmann[2], U. Grätz[2], F. Sonntag[1]
[1] Fraunhofer IWS, Dresden, Germany
[2] ITI GmbH, Dresden, Germany

ABSTRACT

We present a model for oxygen supply, transport and consumption in microfluidic 3D cell culture systems with active perfusion. The oxygen content was characterized using fluorescence lifetime imaging with immobilized oxygen sensitive microbeads. A pneumatically actuated, membrane-based peristaltic pump was used for active oxygenation and de-oxygenation. Simulation results and experimental data were compared to determine oxygen permeation constants for the pump membranes. The presented tool is useful to calculate the oxygen supply for cell culture systems and the formation of oxygen gradients for cell differentiation.

KEYWORDS

Mass transport; oxygen supply; modelling; cell culture; microfluidic

INTRODUCTION

Microfluidic 3D cell culture systems are getting more and more important in biotechnology. Due to new EU regulations animal experimentation for substance testing should be replaced within the next few years. Nevertheless a lot of these experiments are necessary during that period caused by the new REACH regulation. This issue may be resolved by organ-on-a-chip devices predicted by Baker [1]. The complexity of those systems makes modelling necessary for the design process to maintain sufficient nutrient supply and the stability of gradients within the system. In conventional static systems oxygen is only transported via diffusion which limits the cell density and tissue size [2, 3]. Therefore more and more perfused cell culture systems are presented in literature enabling real 3D cell culture and organ-on-chip systems [3]. One of these developments is the so called multi-organ-chip (MOC) [4]. It was used to cultivate several human tissues e.g. skin [5] and liver [6] equivalents, endothelial cells [7] and hair follicles [8] within one closed microfluidic circuit. A pneumatically actuated peristaltic micropump was integrated in the system to ensure sufficient nutrient supply to the cultivated cells. The cell culture media is oxygenated by the pump and circulated through the culture chambers. Hereby presented is a model for the oxygen supply, transport and consumption in this device. Together with models of the fluidic network

and the micropump the complete system should be simulated in the future.

MATERIALS AND METHODS
Microfluidic system

Microchannels, reservoirs and membranes for pumping and oxygenation were produced with a well-established Polydimethylsiloxane (PDMS) molding process [9]. Fig. 1a shows a rendered cross-sectional view of the system. The flow cell is casted at a connection plate (CP) including several cell culture chambers and pneumatic connections and sealed with a plasma-bonded glass slide. After the fabrication process the microsystem is mounted in a heatable support to ensure a stable temperature for cell cultivation. The system is filled with distilled water by mounting a syringe at the cell culture inserts which are also used as liquid reservoirs. The micropump schematically shown in Fig. 1b can be operated with compressed air or other gases to oxygenate or de-oxygenate the cell culture media. It is operated by sequential application of pressure and vacuum to three pump chambers placed in a row. The first and the last chamber are designed as valves. A controlling device ensures pump functionality and measures pressure and vacuum. The fluidic layout used for the experiments is widely used for cell culture experiments [5-8]. It features a closed fluidic loop with one pump and two cell culture-inserts. The inserts are designed to house a single membrane culture compartment of a standard 96-transwell plate [5] for cell culture of skin models for example. The oxygen sensitive beads were immobilized in PDMS droplets printed at the glass slide. Those oxygen sensitive spots can be found in both inserts.

Optical oxygen measurement

Optical sensor systems based on fluorescence lifetime analysis [10] are widely used to measure the oxygen content in human tissues [11]. We used the commercial available *OPAL* device from Colibri Photonics to detect the oxygen content within our microfluidic platform. A modified optical sensor [12] is used to measure the fluorescence lifetime. To ensure the right position of sensor focus a 3D portal-robotic system with an auto-tuning function was used to maximize the signal of the immobilized beads with oxygen sensitive dye.
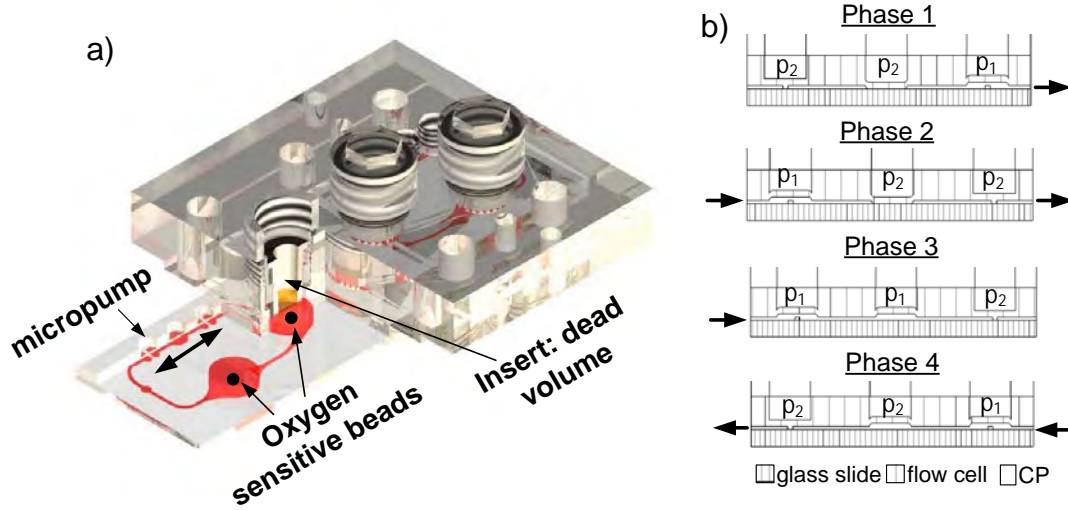
Figure 1: a) Rendered view of the microsystem; b) cross-sectional view and peristaltic pumping principle

Mathematic model for oxygen transport

In general the oxygen flux J in the microfluidic system consists of a diffusive part J_D and a convective part J_C. Convection is driven by the micropump and corresponds with the flow velocity. Micro-Particle-Image-Velocimetry (μPIV) [13] can be used to measure this effect. It has been successfully applied to the presented microfluidic systems [14]. In contrast to that, the diffusive flux is driven by concentration gradients and can be formulated using Fick's law:

$$J_D = -D \cdot \nabla c \tag{1}$$

The peristaltic pump transports a maximum amount of 3 μL s^{-1} [7]. The channel volume (red circuit in Fig. 1a) is in total 15 μL. Furthermore each insert has an additional dead volume which depends on the reservoir mounted on top of the device. In our experiments each insert has a dead volume of 7.5 μL which means that the total volume is 30 μL. Hence the whole fluid is recirculated every 10 seconds by the pump and the system can be seen as ideally mixed meaning that there are no concentration gradients within the channels. Therefore oxygen is only transported via convection. From particular interest is the gas exchange at the PDMS pump membrane. Fig. 2 illustrates the oxygen flux in the pump chambers.
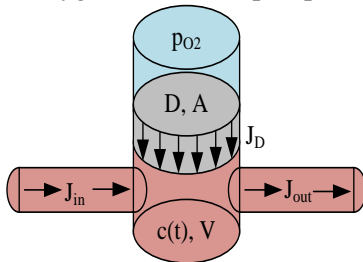
Figure 2: Oxygen fluxes at the pump chamber (blue), pump membrane (grey) and the fluidic system (red).

The permeation is driven by the oxygen applied to the membrane from the controlling device. This is represented by the oxygen partial pressure p_{O2}. Due to pumping process each membrane is sequentially pressurized with p_2 and de-pressurized with the vacuum p_1. The amount of oxygen in air normally is 20.95 vol. %. Therefore the mean oxygen partial pressure can be calculated by following equation:

$$p_{O2} = 0.2095 \cdot \frac{p_2 + p_1}{2} \tag{2}$$

The solubility of gases in liquids is described by Henry's law. Considering that the concentration of dissolved oxygen depends on its partial pressure and the solubility λ:

$$c_{O2} = \lambda \cdot p_{O2} \tag{3}$$

Now the total diffusive oxygen flux through a membrane with a thickness of b and gas diffusion coefficient of D_{O2} can be described as:

$$J = D_{O2} \cdot \frac{c_{O2} - c(t)}{b} \tag{4}$$

The concentration gradient is replaced by the difference between applied c_{O2} and dissolved oxygen $c(t)$. The convective oxygen flux is represented by J_{in} and J_{out}. For an ideally mixed system they can be neglected because the amount of oxygen entering and leaving the system is nearly the same. Therefore the mass flux through the membrane (area A) is:

$$\dot{m}(t) = J \cdot A = V \cdot \dot{c}(t) \tag{5}$$

By substituting the mass flow with the oxygen concentration and the fluid volume V one can devise following differential equation for the concentration:

$$\dot{c}(t) = \frac{A \cdot D_{O2}}{V \cdot b}\left(c_{O2} - c(t)\right) \tag{6}$$

With the starting condition $c(t=0)=0$ the following solution can be obtained:

$$c(t) = \lambda \cdot p_{O2}\left(1 - e^{-\frac{A \cdot D_{O2}}{V \cdot b}}\right) \tag{7}$$

SimulationX model

The multi-domain CAE (computer aided engineering) modelling software *SimulationX* [15] with its network approach is perfectly suited for calculating the complete fluidic system. Based on the analytical findings a model for the membrane is implemented using the *Modelica* model description language [16]. The fluidic circuit consisting of a pump, liquid reservoirs and interconnecting channels has been developed as shown in Fig. 3.
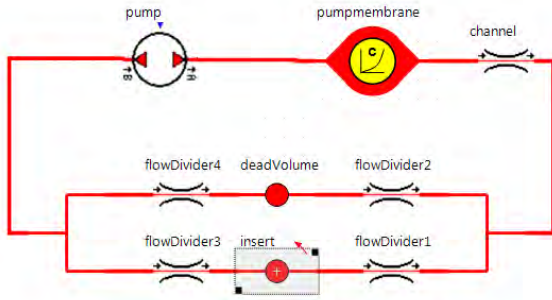
Figure 3: Mass-transport model in SimulationX.

The channel is 500 µm wide, 100 µm high and in total 36 mm long. Both inserts are summarized to one. Furthermore an additional parallel fluidic path has been implemented in the model to reconstruct the fluidic behavior of the liquid reservoirs mounted on top of the channels. As shown in the CFD-Simulation picture in Fig. 4 most of the liquid is flowing near the bottom of the insert whereby a large amount of the fluid isn't moved at all. A large amount of dissolved oxygen is stored in this dead Volume and will be released very slowly. Considering that in the model the reservoir is separated into two different entities. "deadVolume" with a volume of 38.5 µL and "insert" with 8.4 µL. The perfusion of each entity can be influenced by varying "flowDivider1/2". This mimics that the dead volume is perfused with a lower flow rate than the insert volume near the channel bottom.
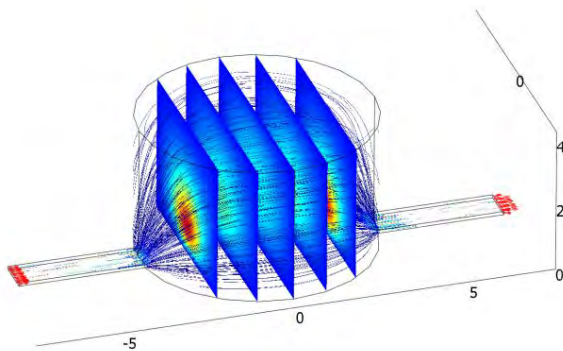
Figure 4: CFD model of the insert generated with Comsol Multiphysics 3.4. Shown is the flow velocity normalized to its maximum.

Only a very small amount (0.0025 µL s^{-1}) of the total 3 µl s^{-1} pumped through the circuit is flowing in the dead volume.

RESULTS

Oxygen input by pump

The oxygen input of the pump was determined using following experimental setting:

1. Calibration of the O_2-sensitive beads by flushing the complete fluidic with nitrogen (0 vol. % O_2) and air (21 vol. % O_2).
2. Afterwards the system was filled with distilled water, so oxygen is now solved in the media. The saturation concentration corresponds to an O_2 content of 100 %.
3. De-oxygenation of the media (distilled water) by pressuring the pump with nitrogen and applying nitrogen to the incubation chamber around the microsystem (O_2 content: 2.5 %).
4. Switching from nitrogen as pumping and incubation gas to compressed air for the gas permeation experiment.

Following pump configuration has been used for the experiment: p_1: 1750 atm; p_2: 250 atm; pumping frequency 2.4 Hz. This corresponds to a mean flow rate of 3 µL s^{-1}. Each of the three pump membranes has a diameter of 3 mm and a thickness of 500 µm. The diffusion constant of oxygen in PDMS was found to be $3*10^{-9}$ m^2 s^{-1} [17]. According to Eq. 2 the mean oxygen partial pressure at all pump membranes is 0.2095 atm. Together with a solubility λ of 0.0416 g L^{-1} atm^{-1} the saturation concentration of oxygen in distilled water is 8.74 mg L^{-1}, according to Eq. 3. A comparison between calculated (analytical model from Eq. 7, SimulationX model) and measured oxygen contents is shown in Fig. 5.
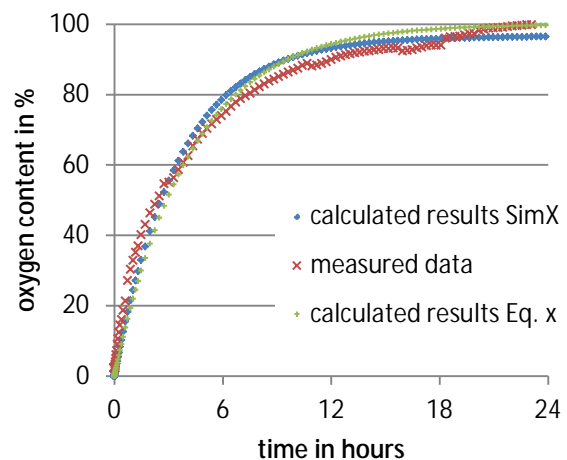
Figure 5: Simulated vs. measured oxygen contents for oxygenation by micropump.

The parameter *V* (total Volume) in the analytical model (Eq. 7) should correspond with the value used in the SimulationX model. Indeed the mixing behavior of the dead volume is not considered in the analytical model. The system cannot be seen is ideally mixed. Therefore a fitting algorithm based on least square minimizing was used to determine this value to 1910 µL. The curve shown in Fig. 5 was obtained with this value.

CONCLUSION

The aim of this work was to simulate the oxygenation of the microfluidic system by the integrated micropump. Based on mathematic considerations an analytic model and a network model in SimulationX have been developed. The gas transport was then measured with fluorescence life time analysis. Therefore the pump was first operated with nitrogen for complete de-oxygenation of the fluidic system. Thereafter the driving gas was changed to compressed air and the oxygen content was measured over 24 hours.

The modelled results fit the experimental data with a coefficient of determination of R^2=0.995. In future experiments the influence of pumping parameters e.g. pressure, vacuum and speed should be further investigated. Considering Eq. 2 the oxygenation of the cell cultures can be controlled by varying pumping pressure and vacuum. This allows the evaluation of hypoxia to cultured cells. Furthermore the analytical model should be refined to mimic the non-ideal mixing behavior of the liquid reservoirs.

REFERENCES

[1] M. Baker: "A Living system on a chip", Nature, 471, 664-665, 2011.

[2] R.L. Carrier, et al.: "Effects of oxygen on engineered cardiac muscle", Biotechnol Bioeng., 78 (6), 617–25, 2002.

[3] E. Volkmer et al: "Overcoming hypoxia in 3D culture systems for tissue engineering of bone in-vitro using an automated, oxygen-triggered feedback loop", Journal of Materials Science: Materials in Medicine 23.11, 2793-2801, 2012.

[4] U. Marx, et al: "Human-on-a-chip Develop-ments: A Translational Cutting-edge Alternative to Systemic Safety Assessment and Efficiency Evaluation of Substances in Laboratory Animals and Man?", ATLA, 40, 235–257, 2012.

[5] I. Wagner, E.-M. Materne, et al.: "A dynamic multi-organ-chip for long-term cultivation and substance testing proven by 3D human liver and skin tissue co-culture", Lab Chip, 13, 3538-3547, 2013.

[6] E.-M. Materne, A. Tonevitsky, U. Marx: "Chip-based liver equivalents for toxicity testing – organo-typicalness versus cost-efficient high throughput", Lab Chip, 13, 3481-3495, 2013.

[7] M. Busek and K. Schimek, et al: "Integrating biological vasculature into a multi-organ-chip microsystem", Lab Chip, 13, 3588-3598, 2013.

[8] B. Atac, et al: "Skin and hair on-a-chip: in vitro skin models versus ex vivo tissue maintenance with dynamic perfusion", Lab Chip, 13, 3555-3561, 2013.

[9] D. J. Campbell, et al: "Replication and Compression of Bulk and Surface Structures with Polydimethylsiloxane Elastomer", Journal of Chemical Education, 75, 537-541, 1999

[10] Y. Amao, et al: "Oxygen sensing based on lifetime of photoexcited triplet state of platinum porphyrin-polystyrene film using time-resolved spectroscopy", J. of Porphyrins and Phthalocyanines, 4.3, 292-299, 2000.

[11] K. Koren, et al: "Complexes of IrIII-Octaethylporphyrin with Peptides as Probes for Sensing Cellular O2", ChemBioChem, 13.8., 1184-1190, 2012.

[12] F. Schmieder, et al: "Automated universal chip platform for fluorescence based cellular assays." 2012.

[13] Lindken: "Micro-particle image velocimetry (µPIV): Recent developments, applications, and guidelines", Lab Chip, 9, 2551–2567, 2009.

[14] M. Busek, et al: "Automated Micro-PIV measure-ment in Lab-on-a-Chip systems", Biomed Tech, 57, 927-930, 2012.

[15] ITI GmbH: "User Manual SimulationX", Version 3, 2009

[16] Modelica Association: "Modelica - A Unified Object-Oriented Language for Systems Modeling", Language Specification, Version 3.3, 2012

[17] D. A. Markov, et al: "Variation in diffusion of gases through PDMS due to plasma surface treatment and storage conditions", Biomed Microdevices, 16(1), 91-97, 2013.

1. Sensors   Poster

SIMULATION STUDY OF A NOVEL CAPACITIVE PRESSURE SENSOR CONCEPT BASED ON THE GEOMETRICAL DEFORMATION OF AN ELASTIC MEASURING CELL

S. Kartmann[1], M. Kellermann[1], R. Zengerle,[1] P. Koltay[1,2] and A. Ernst[1,2]
[1] University of Freiburg, Lab for MEMS Applications, Freiburg, Germany
[2] BioFluidix GmbH, Freiburg, Germany

ABSTRACT

We present the simulative investigation of design rules for a novel pressure transducer to realize a disposable pressure sensor for medical applications. The presented simulation study is based on a three-dimensional CFD-ACE+ model, which describes the expansion behavior of tubular, elastic measuring cells at varying inner hydrostatic pressures for and different boundary conditions like material properties or size. The elastic measuring cell is exposed to an electric field which is sensitive to the implied geometrical deformation, thus transduces a pressure change to a change in capacitance.

KEYWORDS

Disposable pressure sensor, capacitive sensor, CFD-ACE+ model, medical

INTRODUCTION

In general, pressure sensors have a wide range of applications, for example in the petrochemical industry, automotive industry, consumer electronics, process technology and in medical industry. Medical applications particularly require disposable low-cost pressure sensors. They are used for monitoring infusion systems or blood pressure measurements, but also in the in vitro diagnostics (IVD) pressure sensors are applied for monitoring the dispensing process and providing qualitative information back to the system whether the process was successful or not. Standard IVD test systems are based on mechanically operated pipetting systems, which are controlled by robotic arms without sensor feedback. Significant disadvantages of these systems are the large size, the risk of cross-contamination, the costly cleaning steps of the pipette tips, and the large volume of liquid that is applied per test. In order to improve these systems, we want to combine a disposable, non-contact dispensing valve, like [1], with the presented low-cost pressure sensor. Non-contact dispensing systems are able to dispense smaller volume in a shorter process time and avoid cross contamination. A particular advantage of disposable dispensing systems is the lack of necessity of time and cost consuming washing steps. The demand for reliable and inexpensive sensors is rapidly increasing pushing the development of new technologies, especially based on micro- and nanotechnology [2, 3].

Most commercially available pressure sensors are based on the piezoresistive measuring principle [2]. The novelty of the presented sensor approach is the contactless capacitive measurement of the deformation of an elastic measurement cell which depends on the change of the inner hydrodynamic or hydrostatic pressure inside the cell. The sensor is designed for the measurement of liquid pressures, whereas the liquid itself acts at dielectric. All liquid contaminated parts can be disposed, whereas the expensive amplification electronics and electrodes can be used again. In contrast to prior art capacitive sensors, the measuring principle is based on a change in the amount and distribution of the dielectric in the sensor. Standard capacitive sensor concepts are based on the change of the distance of two or more electrodes relative to each other. In this concept, it is difficult to separate the electronics from the fluid-carrying components.

WORKING PRINCIPLE

The presented work introduces a novel concept of a low-cost pressure sensor where a pressure change is measured by a change in capacitance due to the deformation of an elastic measuring cell, cf. fig. 1.
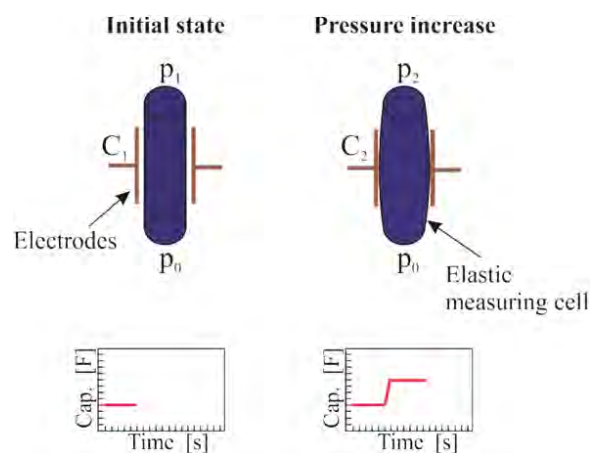

Figure 1: Schematic sketch of two states of the disposable capacitive pressure sensor comprising an elastic measuring cell mounted between two electrodes and filled with a medium acting as dielectric material (initial state). A pressure increase results in an expansion of the cell and therefore in a change of capacity.

The desired modular construction of the

disposable micro-dosing system should consist of a disposable dispensing valve and low-cost pressure sensor integrated in the fluid path between the reservoir and the valve. The sensor is illustrated in figure 1 consisting of a cell, presented as a tube shaped cell, which is mounted concentrically between two electrodes by local fixations on the inlet and outlet side. The cell is connected to the fluid line which is focused to be measured, thus filled with the medium of interest acting as dielectric material. An applied hydrodynamic pressure for an open outlet or an applied hydrostatic pressure for a closed outlet results in geometrical deformation of the elastic measuring cell which implies a change in capacitance of the electrode arrangement due to the increasing amount and the change of distribution of dielectric material in the electric field. Thus, a maximum growth in the cell's diameter at a certain pressure increase implements maximum sensitivity.

THERORETICAL INVESTIGATION

The theoretical investigation focuses of the expansion behavior depending on the applied inner hydrostatic pressure of the tubular, elastic measuring cell. CFD-ACE+ is applied as simulation tool to identify design rules for an enhanced sensitivity considering certain boundary conditions. Especially the influence of the cell's length - distance in-between the fixation - and the young's modulus of the cell material were in focus. The influence of the length in the range from 1.5 to 5 mm and a variable Young's modulus in the range of 1 MPa to 12 MPa were investigated at different applied pressures from 0 to 1 bar.
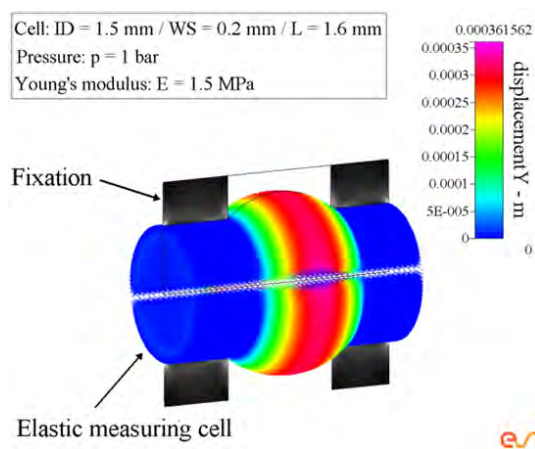
Figure 2: Illustration of the three-dimensional CFD-ACE+ simulation result for an elastic, tubular measuring cell at an inner hydrostatic pressure of 1 bar (Type A (see table 1), L = 1.6 mm).

As a boundary condition of the simulation it is determined that the flexible measuring cell is firmly clamped at both ends, where on one side the pressure is applied and the other is closed. For the material of the measuring cell, we assumed linear material properties and a constant Young's modulus.

RESULTS OF THE THEORETICAL INVESTIGATION

Influence of the Young's modulus

Here, the influence of the young's modulus on the expansion behavior was investigated. Therefore, the Young's modulus for flexible round measuring cells with a fixed geometry was varied between 1 and 14 MPa. The inner hydrostatic pressure was increased in steps of 50 mbar from 0 to 1 bar and the change of the maximal outer diameter of the arched-shaped expansion profile of the measuring cell is plotted. The change of the maximal outer diameter in correlation to the applied pressure shows a linear dependency for the assumption of a linear Young's modulus and material properties.

In order to illustrate the dependency of the material properties, the maximal displacement per applied pressure (slope in µm/bar) was plotted against the Young's modulus (cf. fig. 3). The simulation study revealed an allometric relationship between the Young's modulus and the cell expansion at constant hydrodynamic pressure. Therefore for maximum sensitivity, a cell material with low Young's modulus is preferred.
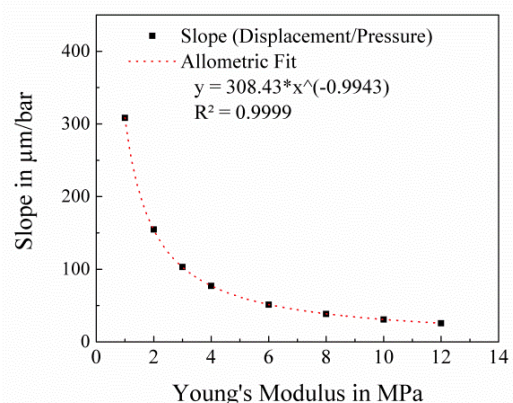
Figure 3: The change of the maximal outer diameter per applied pressure (slope) is plotted in dependency of the Young's Modulus for cell type A with a length of 1.6 mm.

Influence of the length of the measuring cell

Also, the influence of the length on the expansion behavior was examined. The comparison of different lengths showed increase of maximal expansion for

longer measuring cells. It was found that the maximal expansion per applied pressure of the measuring cell converges for increasing tube lengths to a maximum change in an asymptotic manner (cf. fig. 4). For a cell length > 4 mm, the influence of the length is negligible because the expansion profile shows a plateau for longer cells.
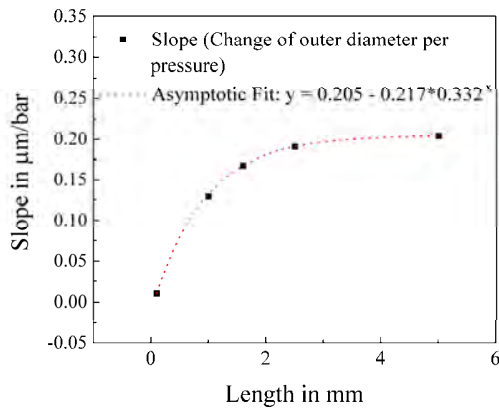
Figure 4: The change of the outer diameter in µm in correlation to the applied pressure in mbar (slope) shows a linear dependency. The slope converges for increasing tube lengths to a maximum change in an asymptotic manner. Here, plotted for cell type C.

Influence of inner diameter and wall thickness

The variation of inner diameter (ID) to wall thickness (WS) ratio showed that the expansion increases, the greater the ID / WS ratio at constant ID. In addition, the expansion increases at a constant ID / WS ratio, the larger the inner diameter is. For a high sensitivity - maximal expansion per applied pressure - we are searching for a measuring cell with a big ID, combined with large ID / WS ratio. The influence of the ID / WS ratio should also be validated experimentally.

EXPERIMENTAL SET-UP

Three different commercially available silicone rubber tubes were selected (see table 1) to emulate the simulation model of the elastic measuring cell by experiment.

Table1: Variants of the tubular measuring cell made of silicone rubber used for experimental validation. The Young's modulus was determined experimentally.

Type	Inner diameter	Wall thickness	Young's modulus
A	1.5±0.1 mm	0.2±0.1 mm	3.85 MPa
B	1.9±0.03	0.1±0.03 mm	4.64 MPa
C	2.5±0.1 mm	0.2±0.1 mm	3.62 MPa

The experimental characterization of the change of the outer diameter of the tube per applied hydrostatic pressure was realized by the laser scan micrometer optoCONTROL 2600 from MICRO-EPSILON featuring a geometrical resolution of 0.6 µm (cf. fig. 5). The both sided clamped silicone tube is left pressurized by a pressure control valve from FESTO and has a dead end at the right. The tube and its holder are mounted on a stepper motor and are placed inside the laser scan micrometer. The outer diameter was measured at eight different position 0 to 7 distributed evenly over the entire length of the tube. Position 0 and 7 are located at the beginning and end of the tube respectively. The pressure and the movement of the stepper motor were controlled via software.
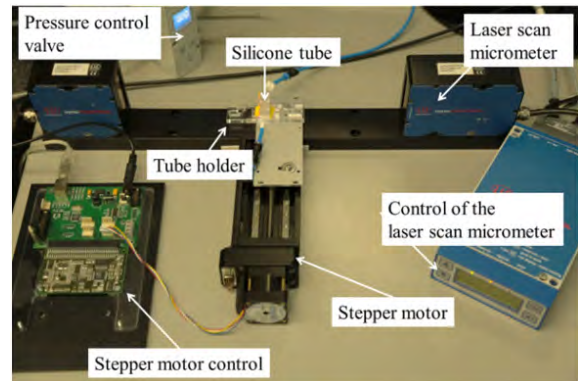
Figure 5: Illustration of the experimental set-up, with a laser scan micrometer of the company MicroEPSILON, a stepper motor, control electronics of the stepper motor and the pressure control valve. Not shown is the control electronic of the pressure control valve and the control software.

In order to experimentally determine the reproducibility of the expansion behavior, we increased the inner hydrostatic pressure from 0 bar to a defined target pressure following a specific measuring loop as illustrated in figure 6. The defined target pressures are set to: 250 mbar, 500 mbar, 750 mbar and 1000 mbar. At the beginning of the loop, the pressure is set to 0 bar and the outer diameter is measured at position 0 to 7. The first pressure increase to a certain target pressure is again followed by the measurement of the outer diameter as described above. The pressure change from 0 bar to the target pressure is repeated six times (cf. fig. 6). This measurement loop for one target pressure is then repeated for the other set of target pressures. Successively, we repeated the loop five times to verify the permanent elasticity and reproducibility of the deformation behavior. After that, the complete loop is performed with two other tubes of the same geometry.
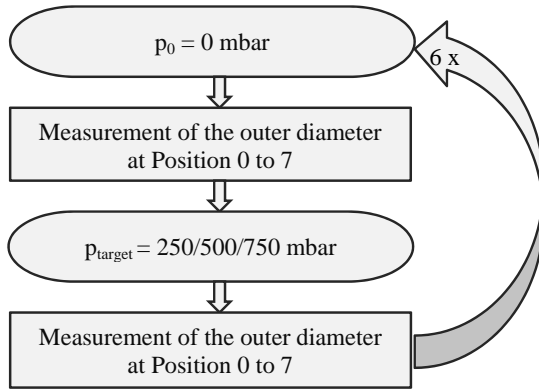
Figure 6: Schematic representation of a measuring loop for the experimental determination of the reproducibility of the expansion behavior of an elastic measuring cell.

EXPERIMENTAL RESULTS

The gained experimental results are depicted in figure 8 showing the results of all three tubular measuring cell types with the length 5 mm in comparison with the simulation results. In order to compare the simulation and the experimental results, we take the mean outer diameter over position 2 to 5 and not the maximal outer diameter. An individual data point represents the mean of the individual changes in outer diameter of position 2 to 5 of three different tubes. The error bars correspond to the standard deviation of a complete measuring loop.
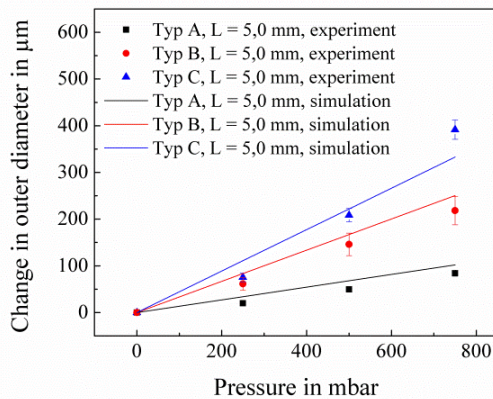
Figure 7: Experimental validation of the simulated expansion behavior of the elastic, tubular measuring cell for three different silicone tubes.

The evaluation showed that the tube type C showed the highest sensitivity with an outer diameter increase of 17.3% at a pressure of 1 bar, where type A only increases by 5.2% and type B by 9.8%. All tube types do not show a linear expansion behavior like the simulation. The deviation of the simulation results from the experimental values can be explained by the non-linear stress/stain behavior of silicone. The

biggest difference between the simulation and the experiment exists for of type C, length 5.0 mm, at 500 mbar. Here, the experimentally determined value of the change in outer diameter is 64 µm (27%) bigger than the simulated value. The error bars for applied inner hydrodynamic pressures above 500 mbar are higher, because silicone shows a viscoelastic behavior. The viscoelasticity is characterized by a partially elastic, partially viscous behavior. In figure 8 a measured cyclic stress/strain curve is plotted, where we applied a hydrodynamic pressure and the released it in 250 mbar steps from 0 to 750 mbar.
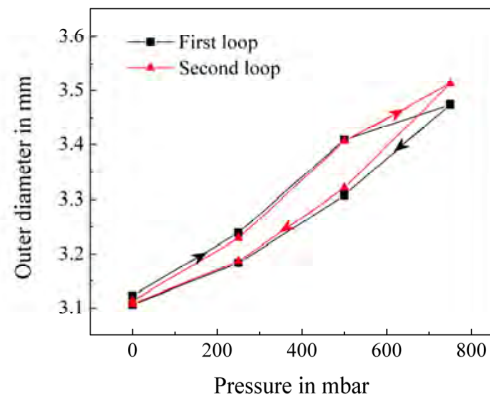
Figure 8: Cyclic load and unloading of tube type C for a pressure range between 0 and 750 mbar.

SUMMARY

In summary, we successfully implemented a model to approximate the expansion behavior of tubular ideal linear measuring cells. Optimized design rules were defined and verified by experiment. In future work, we will extent the model by the implementation of the non-linear viscoelastic behavior and add electrodes to the described model to enable the simulation of the change in capacitance caused by deformation of the measuring cell.

REFERENCES

[1] S. Bammesberger, S. Kartmann, L. Tanguy, D. Liang, K. Mutschler, A. Ernst, R. Zengerle, P. Koltay, "A Low-Cost, Normally Closed, Solenoid Valve for Non-Contact Dispensing in the Sub-µL Range", Micromachines, Vol. 4, pp. 9-21, 2013.

[2] W. P. Eaton, J. H. Smith, "Micromachined pressure sensors: review and recent developments", Smart Structures and Materials, Vol. 6, 1997.

[3] R. Eibl, D. Eibl, "Single-Use Technology in Biopharmaceutical Manufacture", 1st edition, John Wiley & Sons, 2011.

CONTACT

* S. Kartmann, sabrina.kartmann@imtek.de

1. Sensors   Poster

HOLLOW FIBER-BASED LAB-ON-A-CHIP PERFUSION SYSTEM WITH INTEGRATED FLUORESCENCE-BASED OXYGEN MONITORING

F. Schmieder[1], S. Grünzner[1], C. Winkelmann[1] and F. Sonntag[1]
[1] Fraunhofer Institute for Material and Beam Technology IWS, Dresden, Germany

ABSTRACT

Here we present a perfused hollow fiber based microfluidic system that mimics oxygen uptake by the artificial consumer glucose oxidase (GOD). Therefore the different parts of the system will be discussed concerning their ability to store, release or convert oxygen. The influence of permeation for the oxygen supply through the integrated hollow fiber network is shown as well as the opportunity to vary the concentration of GOD for simulating different types of consumers.

KEYWORDS

Oxygen supply, Hollow fiber, Perfusion, Lab-on-chip, 3D-cell culture, Simulated hypoxia

INTRODUCTION

The hollow fiber-based lab-on-a-chip perfusion system is derived from the established microfluidic platform, which was developed in cooperation between the Fraunhofer IWS and the Institute of Biotechnology at the Technical University of Berlin [1,2,4-7]. It includes a pneumatically actuated peristaltic micro-pump, several built-in fluidic reservoirs, micro valves and cell culture chambers, which are connected by an integrated microfluidic channel system. Different technologies for cultivation of various human cell cultures or even micro organs such as skin [4], liver [5], endothelial tissue [6] and hair follicles [7] have been successfully developed and established. The challenge is to build and maintain a biological 3D microenvironment. Therefore artificial structures like hydrogel blocks or membranes are needed to ensure interactions between different cell types or tissues. To build an extended artificial skin model the combination of both epithelial cells cultured on a membrane and fibroblasts embedded in a hydrogel block underneath these cells is necessary. For nutrition and oxygen supply the integration of a hollow fiber network, which acts as artificial vessels, would be suitable. The integration of such a network into a micro perfusion bioreactor is shown in figure 1. This bioreactor ensures the perfusion of the whole system by the use of a peristaltic micro pump that is integrated in the microfluidic circuit [8].
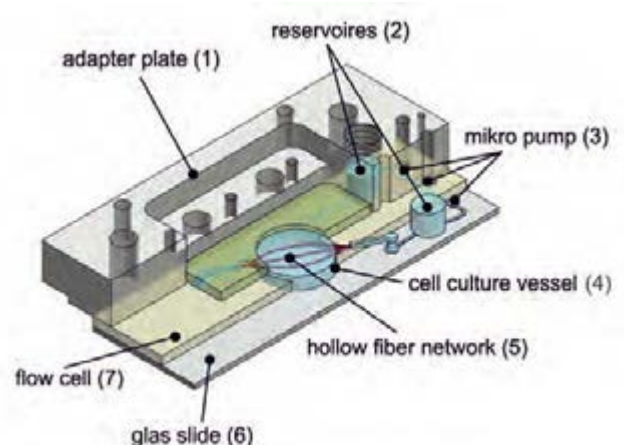
Figure 1: Design of the hollow fiber-based lab-on-a-chip perfusion bioreactor with perfusion circuit (blue) and integrated hollow fiber (red)

MATERIALS AND METHODS

Microfluidic system

The microfluidic system consists of reservoirs for the storage of cell culture media (2), microchannels, membranes for pumping and oxygenation (3), an adapter plate to fuse all the other components and pneumatic connectors to plug on the tubing. Microchannels and pumping membranes were produced in a well-established polydimethylsiloxane (PDMS) casting process that is described elsewhere [9]. Reservoirs and adapter plate were made of different plastics by milling. The flow cell (7) is casted on the adapter plate (1) including several cell culture vessels (4) as well as reservoirs (2) and is sealed with a glass slide by a plasma bonding process (6). To ensure the precise adjustment of the oxygen sensor the microsystem is mounted in a mechanical support which was later integrated in a laboratory automation system. The basic fluidic system was filled with PBS solution (1 M, amresco, USA) by mounting a syringe at the liquid reservoirs.

As an artificial oxygen consumer glucose oxidase (GOD VII from aspergillus niger 100.000 U/g, Sigma-Aldrich, USA) was used in the microfluidic system. For keeping GOD inside of the cell culture vessel a dialysis membrane (MWCO = 400 Da) was glued to the reservoir with biocompatible adhesive (Loctite 4011, Henkel, Germany) forming a barrier that can be passed by oxygen and glucose but is impermeable for GOD. To protect GOD against degradation by hydrogen peroxide that is formed in the reaction horse reddish peroxidase (300 U/mL, AppliChem,

Germany) was added to the GOD solution.

For the integration of a hollow fiber network microporous polyethersulfon hollow fibers (capillary membrane MicroPES®, Membrana GmbH, Germany) were glued into the system with a mixture of polydimethylsiloxane (PDMS, Sylgard®184, Dow Corning, USA) and silica (HDK® - pyrogene Kieselsäure, WACKER, Germany).Figure 2 shows the fluidic system with the integrated hollow fiber. To realize an adequate oxygen supply of the artificial consumer, the hollow fiber network is placed underneath the GOD filled reservoir.

Figure 2: Lab-on-a-chip perfusion system with integrated hollow fiber.

The mode of operation as well as the setting of the micropump is described in detail by Busek et al. [10]. Oxygen sensitive beads were immobilized in the microfluidic circuit by printing PDMS droplets with the beads on the glass slide at the bottom of the microfluidic circuit. The oxygen sensitive spot is placed next to the hollow fiber network underneath the GOD filled reservoir.

Optical oxygen measurement

Optical sensor systems based on fluorescence lifetime analysis [11] are widely used to measure the oxygen content in human tissues [12]. We used the commercial available OPAL [9] device from Colibri Photonics to detect the oxygen content within our microfluidic platform. A modified optical sensor [13] is used to measure the fluorescence lifetime. To ensure the right position of the sensor focus a laboratory automation system with an auto tuning function was used to maximize the signal of the immobilized, oxygen sensitive beads. To observe the functionality of the whole system the laboratory automation system also includes a microscope. Figure 3 shows the setup for optical noninvasive oxygen measurement. The oxygen content is declared in percent, where one hundred percent air saturation denotes the oxygen content of air-saturated water, which is in equilibrium to water-vapor saturated air

(compare [14]). Considering effects like temperature, ion concentration pressure etc. the calibration of the system took place under the same conditions as the experiments.
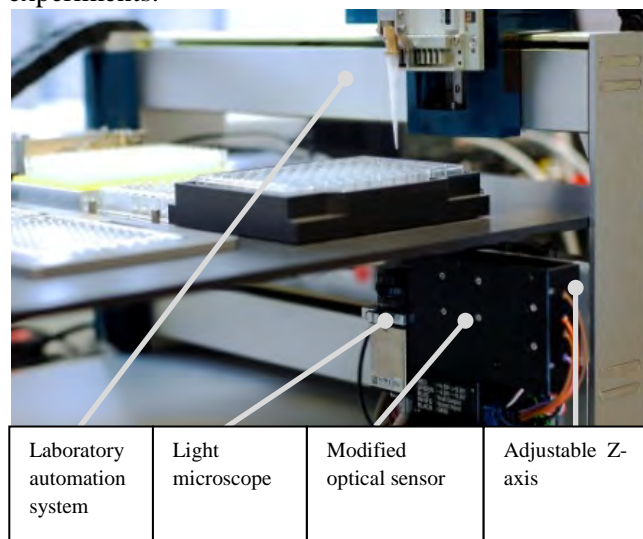
Figure 3: Miniaturized automated fluorescence lifetime-based measurement technology.

RESULTS
Experimental setup

Mimicking the cellular oxygen consumption with an artificial consumer like GOD means to exclude several cellular functions like cell growth and metabolic changes. Nevertheless it depends on the setup how the oxygen consumer acts in the microfluidic circuit. Considering that the following setup was used:

1. Calibration of the O_2-sensitive beads by flushing the complete fluidic with nitrogen (0 vol. % O_2 content) and air (100 vol. % O_2 content).
2. Filling the system with oxygen saturated PBS solution (O_2 content: 100%)
3. Filling the dialysis membrane reservoir with 300 µL GOD solution
   A.) 500 U*mL^{-1}
   B.) 500 U*mL^{-1}/50 U*mL^{-1}
4. Filling the media reservoir (between micro pump and cell culture vessel, figure 4 b) with glucose solution (5 g*L^{-1} in 1 M PBS)
5. **A.)** Operating the pump (process gas: air) just for 30 seconds (to induce an almost equal distribution of glucose in the whole microfluidic system) and again after equilibrium state is reached
   B.) Operating the pump (process gas: air) during the whole experiment

Figure 4 shows a schematic sketch of the fluidic circuit. The arrows indicate oxygen and glucose uptake and consumption as well as the direction of

flow. As one can see, the circuit is divided into 4 main stages for conversion and permeation of both species. The small red arrows show the diffusive input of oxygen through the PDMS layer of the microfluidic device as described by Metha et al [15].
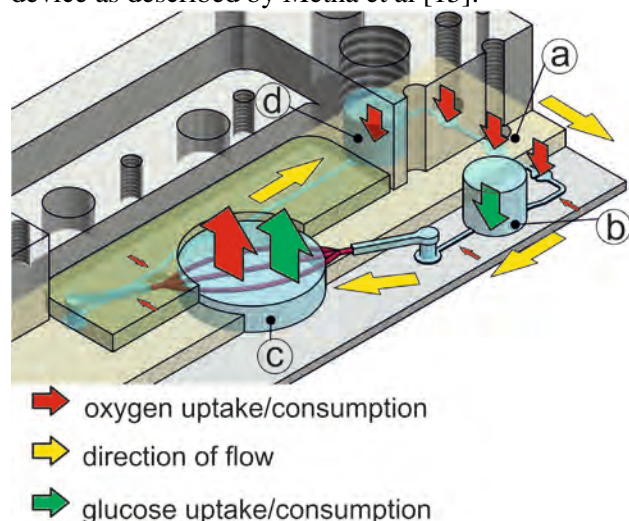
Figure 4: Schematic sketch of the microfluidic circuit. Arrows are indicating oxygen/glucose uptake/consumption and flow direction

a.) Oxygen input by pump

The oxygen input of the pump (Figure 4 stage »a«) was determined by Busek et al. and is described elsewhere [16].

b.) Glucose uptake

Compared to the size of the channels, the volume of the reservoir filled with glucose solution is large (300 µL). That means convection takes place just in the small part of the reservoir next to the bottom of the fluidic. From this it follows that the glucose is distributed slowly to the circuit limited by the diffusion process in the rest of the reservoir. This is useful in cell culture experiments where the supply with nutrients over a long period of time is required.

c.) Oxygen/Glucose consumption

The cell culture vessel is feeded with nutrients by the hollow fiber network underneath the membrane. Unfortunately oxygen can yet just be measured underneath the hollow fibers. That means transport processes like diffusion and permeation take place next to the oxygen sensitive spot at the same time and cannot be separated by measurements.

d.) Oxygen uptake

Taking the second media reservoir (Figure 4 stage »d«) of the microfluidic circuit into account one can imagine that the amount of stored oxygen in the media of that vessel is large compared to the dissolved oxygen in the microfluidic circle. That means that not only the pump is distributing fresh oxygen to the cell culture vessel.

As previously described the oxygen sensitive particles are immobilized in the cell culture vessel (Figure 4 stage »c«). This means the content of oxygen is just measured at a single point underneath the hollow fiber network and the GOD filled reservoir (stage »c«). For setup »A« the oxygen content as a function of time is shown in figure 5. The measurements were started after the first pump operation. Because GOD catalyzed reaction still took place during this period the measured oxygen content starts at 85 %.
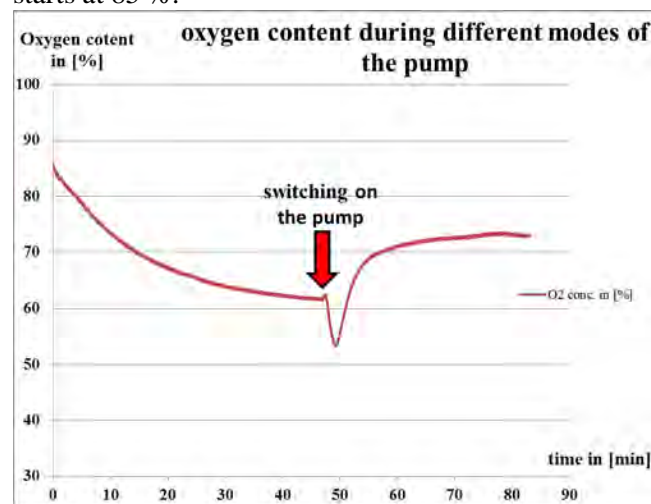
Figure 5: Oxygen contents during different operating modes of the pump.

While reaction takes place the oxygen concentration is decreasing. Nevertheless the supply of reactive species at stage »c« is limited by diffusion. Thus the equilibrium concentration of oxygen remains at 63 %. After switching on the pump again the oxygen concentration is dropping because glucose is brought to the consumer (»c«) from the reservoir (»b«). After a short period of time oxygen is delivered from the pump (»a«) and the second reservoir (»d«) so the concentration of oxygen is rising to the new equilibrium state at 73 %. These findings could be reproduced three times. Taking that into account new modes of operation of the system could be used to produce well-defined hypoxic conditions in the cell culture vessel. Furthermore these findings could be used to determine the amount of enzyme that is necessary to create a well-defined oxygen concentration far from zero percent. Therefore different concentrations of enzyme solution where prepared and used for measurements like described in setup »B«. Figure 6 shows the results of these measurements. As one can see the concentration of oxygen under perfusion is decreasing during the first hours of the experiments. Afterwards, depending on the GOD concentration, the consumption of oxygen in

the cell culture vessel during the reaction is:
   a.) higher than the oxygen uptake (red line, GOD 500 U/mL),
   b.) lower than the oxygen uptake (green line, GOD 50 U/mL).

The increasing oxygen concentration after some hours is the result of the decreasing glucose concentration in the whole microfluidic circuit. After 20 hours all glucose is converted to gluconolactone and the PBS solution is saturated with oxygen.
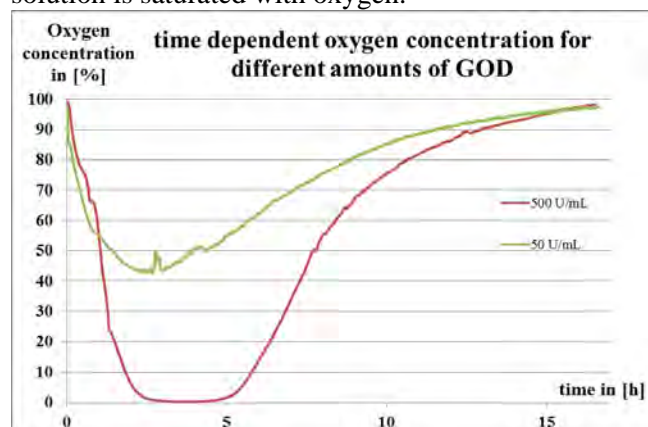
Figure 6: Time dependent oxygen concentration for different amounts of GOD.

CONCLUSION

The aim of this work was to show the influence of permeation to the oxygen supply by a hollow fiber network in a PDMS based perfusion cell culture platform. Therefore the different parts of the system where discussed concerning their ability to store, release ore convert oxygen. Based on those findings the variation of permeation showed the expected equilibrium states at the point of measurement. Furthermore the opportunity to adjust different conditions in the cell culture vessel like hypoxia was shown. With an optimized artificial consumer it was possible to create well defined equilibrium states in the cell culture vessel.

Further investigations should include multistage oxygen measurements to show the spatial resolution of oxygen within the cell culture vessel. Moreover mathematical modeling tools like SimulationX or Comsol Multiphysics should be applied to the measured data to create a model for the whole micro perfusion system.

REFERENCES

[1] M. Baker: "A Living system on a chip", Nature, 471, 664-665, 2011.

[2] U. Marx, et al.: "Human-on-a-chip Developments: A Translational Cutting-edge Alternative to Systemic Safety Assessment and Efficiency Evaluation of Substances in Laboratory Animals and Man?", ATLA, 40, 235-257, 2012.

[3] L. E. Bertassoni, et al.: "Hydrogel bioprinted microchannel networks for vascularization of tissue engineering constructs", Lab Chip, 14, 2202, 2014.

[4] I. Wagner, et al.: "A dynamic multi-organ-chip for long-term cultivation and substance testing proven by 3D human liver and skin tissue co-culture", Lab Chip, 13, 3538-3547, 2013.

[5] E.-M. Materne, A. Tonevitsky, U. Marx: "Chip-based liver equivalents for toxicity testing – organo-typicalness versus cost-efficient high throughput", Lab Chip, 13, 3481-3495, 2013.

[6] M. Busek and K. Schimek, et al.: "Integrating biological vasculature into a multi-organ-chip microsystem", Lab Chip, 13, 3588-3598, 2013.

[7] B. Atac, et al.: "Skin and hair on-a-chip: in vitro skin models versus ex vivo tissue maintenance with dynamic perfusion", Lab Chip, 13, 3555-3561, 2013.

[8] M. Busek et al.: "Peristaltic pneumatic pump - characterisation via µPIV, non-invasive pressure measurement and simulation", J. Sens. Sens. Syst., 2, 165–169, 2013.

[9] F. Schmieder et al.: "Automated universal chip platform for fluorescence based cellular assays", Biomed Tech 57 (Suppl. 1), 2012.

[10] M. Busek, et al.: "Automated Micro-PIV measurement in Lab-on-a-Chip systems", Biomedical Engineering (2012).

[11] Y. Amao, et al.: "Oxygen sensing based on lifetime of photoexcited triplet state of platinum porphyrin-polystyrene film using time-resolved spectroscopy", J. of Porphyrins and Phthalocyanines, 4.3, 292-299, 2000.

[12] K. Koren et al.: "Complexes of IrIII-Octaethylporphyrin with Peptides as Probes for Sensing Cellular O2", ChemBioChem, 13.8., 1184-1190, 2012.

[13] R. Lindken, et al.: "Micro-particle image velocimetry (µPIV): Recent developments, applications, and guidelines", Lab Chip, 9, 2551–2567, 2009.

[14] E. Schmälzlin, et al. "Monitoring hormone-induced oxygen consumption in the salivary glands of the blowfly, *Calliphora vicina*, by use of luminescent microbeads." Sensors and Actuators B: Chemical 119.1, 251-254, 2006.

[15] Mehta, G.et al: "Quantitative measurement and control of oxygen levels in microfluidic poly (dimethylsiloxane) bioreactors during cell culture", Biomedical microdevices, 9(2), 123-134, 2007.

[16] M. Busek, et al.: "Oxygen supply for cell-culture-systems-characterized with fluorescence-life time analysis and modelled using SimulationX in press, 2012.

MODELLING AND CHARACTERIZATION OF A MULTIPARAMETER HOT DISK SENSOR FOR DETERMINATION OF FLUID MIXTURE PROPERTIES

B. Schmitt, K. Sauer, A. Schütze
Saarland University, Laboratory for Measurement Technology, Saarbrücken, Germany

ABSTRACT

The mathematical modelling of a measurement principle based on the transient hot disk method is presented, giving the possibility to measure mixture ratio and flow rate of binary fluid mixtures simultaneously. Measurements of methanol/water-mixtures are shown with and without an applied fluid flow, while the measurement results are compared with the theoretical model. Using this extended hot disk sensor in stopped-flow condition, multiple thermal properties of the fluid mixture are evaluated, enabling the self-test of the sensor and the detection of a possible deception. The latter aspect is of interest especially for characterization of aqueous urea solutions used in selective catalytic reduction systems to reduce exhaust emissions of diesel engines.

KEYWORDS

Microthermal sensor, hot disk method, mathematical modelling, concentration sensor, flow sensor, DMFC, urea

INTRODUCTION

In many technical systems monitoring and control of binary fluid mixtures is important for proper operation. Often, low cost and robust sensors are required. One possible application can be seen in direct methanol fuel cells (DMFC) to enable the control of a constant methanol concentration in water of less than 4.2 % (V/V) [1], depending on the currently required output power of the system. The exhaust aftertreatment of diesel engines using selective catalytic reduction (SCR) is another important application. Here, a mixture of 32.5 % (W/W) urea dissolved in water is injected in the exhaust stream where urea reacts at high temperatures with water to ammonia which reduces nitrogen oxide to nitrogen and water. To ensure correct operation of the system a sensor is needed to monitor the urea concentration while a deception of the system using, e. g., only (salt-) water has to be prevented. Furthermore, a self-test of the sensor is desired to ensure correct operation.

MEASUREMENT PRINCIPLE

The sensor principle that has been developed and successfully evaluated is based on the transient hot disk method [2], which is primarily used to thermally characterize solid materials. Here, a small heater covered with the unknown binary mixture is heated with a short power pulse. In stopped-flow measurements the temperature increase after a given time is affected by the thermal properties of the fluid, thus reflecting the mixture ratio if the two components in the mixture are known [3]. This measurement principle is well-known but has some limitations for the use in DMFC or SCR systems. First of all, if a fluid flow is present additional heat is dissipated from the heater due to forced convection, reducing the heater's temperature and thus prohibiting the measurement of the mixture ratio if the flow velocity is unknown. Furthermore, since only one parameter (the temperature of the heater) is measured, different fluids or fluid compositions can cause the same sensor response. Especially in the case of SCR systems a possible deception of the sensor must be prohibited to ensure correct operation of the exhaust aftertreatment. Finally, using only one measurement parameter a drift of the sensor cannot be detected.

To overcome these drawbacks, a sensor layout as shown in Fig. 1 has been realized, using one central heater with four-terminal sensing of its resistance and four surrounding temperature sensors to simultaneously measure the temperature increase of the heater and the spreading of the induced temperature pulse, as both properties are influenced by different thermal properties.
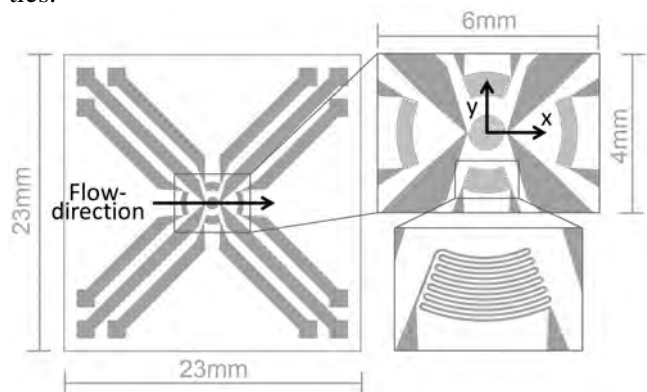
Figure 1: Layout of the realized sensors with central heater and surrounding temperature sensors [3].

The flow velocity is measured using a modified type of pulsed wire anemometry [4]. Here, a temperature pulse induced by the heater is dissipated downstream by the flow and can be measured with a temperature sensor placed behind the heater. The time needed for the temperature pulse to reach the sensor is inversely proportional to the flow velocity and nearly independent of the thermal properties of the fluid, as will be shown later.

MATHEMATICAL MODELLING

Neglecting the temperature dependence of the material properties, the equation for heat conduction in a non-moving, isotropic and incompressible material [5] can be written as:

$$\alpha \nabla^2 T(\boldsymbol{x}, t) + \frac{Q(\boldsymbol{x}, t)}{\rho c_v} = \frac{\partial T(\boldsymbol{x}, t)}{\partial t} \qquad (1)$$

Here, $\alpha = \lambda/(\rho c_v)$ denotes the thermal diffusivity with thermal conductivity λ, density ρ and isochoric heat capacity c_v that can be approximated using the isobaric heat capacity c_p [6]. $\nabla^2 = \nabla \cdot \nabla$ stands for the Laplace operator, $T(\boldsymbol{x}, t)$ for the temperature at point $\boldsymbol{x} = [x, y, z]$ at time t and $Q(\boldsymbol{x}, t)$ for the power induced per volume.

If a fluid flow with average flow velocity $\boldsymbol{v}$ is present, causing forced convection, a convection (or advection) term has to be considered in eq. (1), giving the so-called *advection-* or *convection-diffusion equation* [5],[7]:

$$\alpha \nabla^2 T + \frac{Q}{\rho c_v} = \frac{\partial T}{\partial t} + \nabla \cdot (\boldsymbol{v} T) \qquad (2)$$

Assuming $Q(\boldsymbol{x}, t) = 0$ and with the initial and boundary conditions $T(\boldsymbol{x}, 0) = 0$ and $T(\infty, 0) = 0$, the fundamental solution $G(\boldsymbol{x}, t)$ of eq. (2) is [7]

$$G(\boldsymbol{x}, t) = \frac{1}{(4\pi\alpha t)^{3/2}} \exp\left(-\frac{||\boldsymbol{x} - \boldsymbol{v}t||^2}{4\alpha t}\right) \qquad (3)$$

with the Euclidean norm $||\boldsymbol{x}|| = \sqrt{x^2 + y^2 + z^2}$. In the case of an initial temperature $T(\boldsymbol{x}, 0) = T_0$ and a source $Q(\boldsymbol{x}, t) \neq 0$, the solution of eq. (2) is given by the convolution of the initial temperature and the source $Q(\boldsymbol{x}, t)/(\rho c_p)$ with eq. (3) [7]. The temperature increase $\Delta T(\boldsymbol{x}, t) = T(\boldsymbol{x}, t) - T_0$ then follows to:

$$\Delta T(\boldsymbol{x}, t) = \int_0^t \int_{V'} \frac{Q(\boldsymbol{x}', t')}{\rho c_p} \frac{1}{[4\pi\alpha(t - t')]^{3/2}}$$
$$\times \exp\left(-\frac{||\boldsymbol{x} - \boldsymbol{x}' - \boldsymbol{v}(t - t')||^2}{4\alpha(t - t')}\right) d^3\boldsymbol{x}' dt' \qquad (4)$$

For the sensor layout shown in Fig. 1 and an applied constant heater power P switched on at $t = 0$, finite element simulations using Comsol Multiphysics® (Comsol AB) showed that the heat source can be approximated using a two-dimensional Gaussian distribution with

$$Q(\boldsymbol{x}, t) = \frac{P}{2\pi\omega_0^2} \exp\left(-\frac{x^2 + y^2}{2\omega_0^2}\right) \delta(z)\Theta(t) \qquad (5)$$

where ω_0 can be approximated with the radius of the used heater [8]. $\delta(\cdot)$ and $\Theta(\cdot)$ represent the Dirac delta function and the Heaviside step function, respectively.

With eq. (4) and (5) and assuming that the flow is only occurring in the x-direction and constant with $\boldsymbol{v} = v\,\boldsymbol{e_x}$ (see Fig. 1), the temperature increase ΔT_G in the xy-plane due to the Gaussian distribution of the surface power density of the heater can be calculated by integration, giving

$$\Delta T_G(x, y, 0, t) = \frac{2P}{4\pi^{3/2}b} \int_0^t \frac{1}{\sqrt{t - t'}}$$
$$\times \frac{1}{2\alpha(t - t') + \omega_0^2}$$
$$\times \exp\left(-\frac{(x - v(t - ts))^2 + y^2}{4\alpha(t - t') + 2\omega_0^2}\right) dt' \qquad (6)$$

with the thermal effusivity $b = \sqrt{\lambda \rho c_p}$. The additional factor 2 is used since it can be assumed for simplification that the heat is mainly dissipated in the half-space of the liquid covering the heater because of the thin polyimide substrate and the very low thermal effusivity of air beneath the substrate. Thus, with a given heater power only α and b have an influence on the temperature increase while ω_0 can be regarded as independent of the thermal properties for simplification. In contrast to b, α is included in the integral and coupled with the position $\boldsymbol{x}$, offering the possibility to adapt the sensor position to maximize the influence of α.

In the center of the heater (at $\boldsymbol{x} = \boldsymbol{0}$) and if no flow is present ($v = 0$) the temperature increase is given by

$$\Delta T(\boldsymbol{0}, t) = \frac{2\,P}{(2\pi)^{3/2}\lambda\omega_0} \arctan\left(\sqrt{\frac{2\alpha t}{\omega_0^2}}\right), \qquad (7)$$

which for long times t converges to

$$\lim_{t \to +\infty} \Delta T(\boldsymbol{0}, t) = \frac{2\,P}{4\sqrt{2\pi}\lambda\omega_0} \qquad . \qquad (8)$$

Thus, in the stationary case only the thermal conductivity λ influences the temperature increase. Using eq. (8) the stationary temperature increase after a long heating time or the needed heating power to reach a certain temperature can easily be estimated.

Finally, since the measurement of the resistances of the heater and the surrounding temperature sensors only gives the mean temperatures in the relevant areas, these mean values can be estimated by integrating the temperature distribution in the xy-plane (see eq. (6)) over the area of the heater and the temperature sensors, respectively. The mean temperature increase $\Delta \overline{T}_H = \overline{T}_H - T_0$ (with mean temperature $\overline{T}_H$) over

the heater area $A_H = \pi r_h^2$ with radius r_h can be calculated with

$$\Delta \overline{T}_H(t) = \frac{1}{A_H} \int\limits_{-r_h}^{r_h} \int\limits_{-a}^{a} \Delta T_G(x, y, 0, t)\, \mathrm{d}y\, \mathrm{d}x \qquad (9)$$

with $a = \sqrt{r_h^2 - x^2}$. The mean temperature increase of the sensors $\Delta \overline{T}_S$ can be estimated using a rectangular area for simplification. With their respective dimension in x- and y-direction from x_1 to x_2 and y_1 to y_2 and the subsequent area of $A_S = (x_2 - x_1)(y_2 - y_1)$, $\Delta \overline{T}_S$ can be written as:

$$\Delta \overline{T}_S(t) = \frac{1}{A_S} \int\limits_{x_1}^{x_2} \int\limits_{y_1}^{y_2} \Delta T_G(x, y, 0, t)\, \mathrm{d}y\, \mathrm{d}x \qquad (10)$$

Fig. 2 shows the calculated temperature increase of the heater and of two points with different distances from the heater's center for four different combinations of thermal diffusivities and effusivities covering the range of methanol/water-mixtures, normalized with respect to the final temperature with combination α_1 and b_1 (comparable to water).

At a difference of 0.5 mm from the heater's center the initial temperature increase is nearly only depending on b as is the case of the heater's initial temperature increase. At larger distances and time α becomes more important. It can be said that by evaluating the temperature at different distances from the heater both thermal properties can be evaluated to enable higher resolution or prohibit the deception of the sensor.
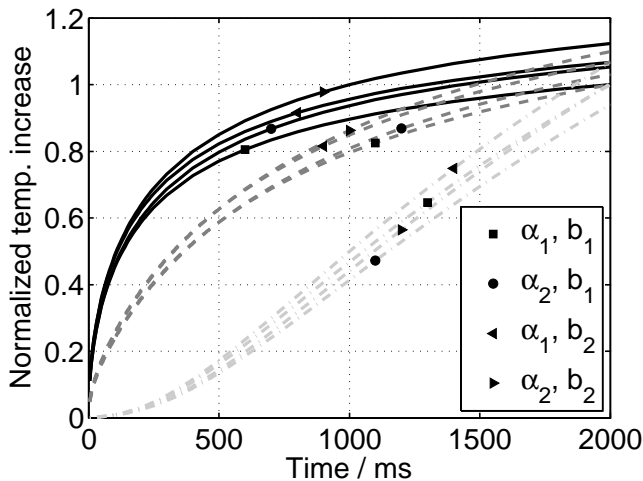
Figure 2: Calculated temp. increase of the heater (–) and at two points with distances of 0.5 mm (- -) and 1 mm (··) from the heater's center without fluid flow for values of $\{\alpha_1, \alpha_2\}=\{15,13\} \times 10^{-8}\, m^2/s$ and $\{b_1, b_2\}=\{1600, 1500\}\, W\sqrt{s}/(m^2 K)$.

MEASUREMENT RESULTS

Fig. 3 shows the measured temperature increase of the central heater with a diameter of 0.5 mm with an applied heater power of 30 mW for different methanol concentrations in water. As the thermal effusivity of the mixture decreases with increasing methanol concentration, the temperature increases as well. Additionally, a fit of the temperature increase of water based on eq. (7) is presented, showing the validity of the used assumptions. Using literature data for water at 25 °C and neglecting the heat dissipation into the substrate to estimate the temperature increase of the heater's center (ref. eq. (7)), the expected function was $\Delta \overline{T}_H(t) = 29.9\, \mathrm{atan}(2.4\, \sqrt{x})$, what is in satisfactory agreement with the measured increase. Here, a value of $\omega_0 = 0.22$ mm was used, based on the finite element simulations [8]. The calculated mean temperature in-
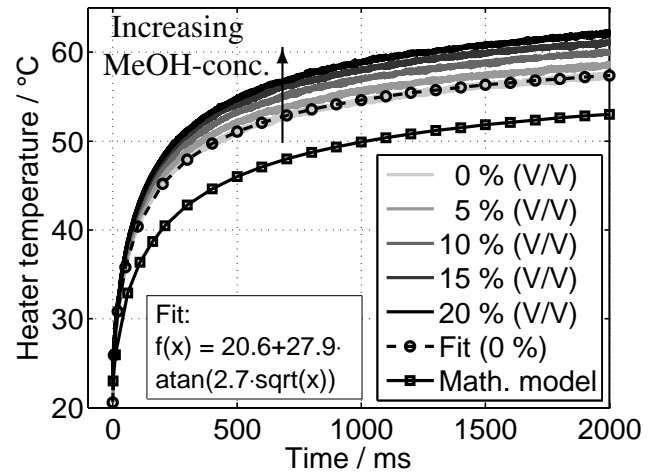
Figure 3: Temperature increase of the heater without fluid flow for different methanol concentrations [8].

crease of the heater using eq. (9) and literature data for water at 25 °C is also shown. The trend of the measured increase is approximated rather well. The difference can be attributed to the used passivation on top of the heater (approx. 5 µm of Polyamide-imide) which encapsulates the heater and increases the thermal resistance.

In Fig. 4 the measured as well as the calculated (using eq. (9)) temperature increases of the heater in fluid flow condition with a heater power of 40 mW are shown for water and 10 % (V/V) of methanol. Due to the cross section of the chamber with 1x8 mm², the flow rates of 94 and 188 ml/h correspond to mean flow velocities of 3.26 and 6.53 mm/s, respectively. With increasing flow velocity, the temperature increase of the heater reduces due to an increase of forced convection. The temperature difference caused by the methanol concentration can be described satisfactorily by the developed model. The absolute temperature increase cannot be calculated by the mean flow velocity in the chamber because of the

2nd International Conference on MicroFluidic Handling Systems
8 – 10 October 2014, University of Freiburg, Germany

128

Figure 4: Measured (–) and calculated (- -) temp. increase of the heater for different flow rates (and their respective mean flow velocities) and volume concentrations of methanol in water (acc. to [3]).

Figure 5: Measured (–) and calculated (- -) temp. increase of a sensor 1.7 mm behind the heater for flow rates and their respective flow velocities of 0 ml/h (■,●), 50 ml/h (▲,▼), 100 ml/h (◄,►) and 200 ml/h (♦,✕) for 0 and 10 % (V/V) of methanol in water, respectively.

strong influence of the flow profile, reducing the effective flow velocity over the heater.

Fig. 5 shows the influence of the applied flow rate on the temperature increase of a sensor located 1.7 mm behind a larger heater with 1 mm diameter, using a constant heater power of 55 mW. As can be seen from the measurements and the calculated curves, the initial temperature increase of the sensor is mainly depending on the applied flow rate and, more importantly, nearly unaffected by the methanol concentration, offering the possibility to determine the flow rate independently of the fluid properties by evaluating the time needed for the sensor temperature to reach a certain threshold value. Thus, the influence of the flow rate on the temperature increase of the heater can be compensated to determine the methanol concentration and flow rate independently. Without fluid flow the developed model describes the temperature increase very accurately. If a fluid flow is present, the shape of the curves cannot be described very precisely since the flow profile is not considered.
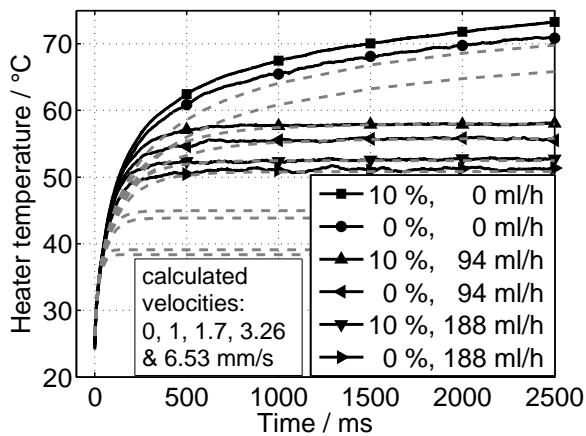
CONCLUSION AND OUTLOOK

The mathematical model for a novel measurement principle based on the transient hot disk method has been presented, providing a suitable description of the measured temperature increase in stopped-flow conditions. If a fluid flow is present, the respective temperature increases of heater and adjacent temperature sensors can only be approximated as the model does not consider the flow profile. However, the model shows that by using temperature sensors in addition to the heater itself, different thermal properties, mainly thermal diffusivity and effusivity, of a fluid mixture can be
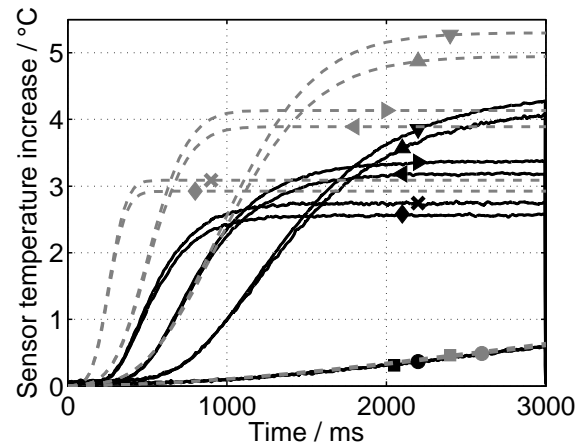
determined and, in addition, the simultaneous measurement of the flow rate is also possible.

REFERENCES

[1] X. Ren et al., "Recent advances in direct methanol fuel cells at Los Alamos National Laboratory", J. Power Sources, Vol. 86 (1-2), pp. 111-116, 2000.

[2] S. E. Gustafsson, "Transient plane source techniques for thermal conductivity and thermal diffusivity measurements of solid materials", Rev. Sci. Instrum. 62 (3), pp. 797-804, 1991.

[3] B. Schmitt, C. Kiefer, A. Schütze, "Microthermal sensors for determining fluid composition and flow rate in fluidic systems", Microsystem Technol., Vol. 20 (4-5), pp. 641-652, 2014.

[4] C. G. Lomas, "Fundamentals of Hot Wire Anemometry", Cambridge University Press, 2011.

[5] H. S. Carslaw, J. C. Jaeger, "Conduction of heat in solids", Clarendon Press, Oxford, 1959.

[6] W. M. Haynes, D. R. Lide, T. J. Bruno ed., "CRC Handbook of Chemistry and Physics", 95th edition, CRC Press, Taylor & Francis Group, 2014.

[7] R. Poprawe, "Lasertechnik für die Fertigung", Springer-Verlag Berlin Heidelberg, 2005.

[8] B. Schmitt, K. Sauer, A. Schütze, "Analytische Beschreibung von Hot Disk-Sensoren zur Bestimmung von Methanolkonzentration und Strömungsgeschwindigkeit für Direktmethanolbrennstoffzellen", XXVIII. Messtechnisches Symposium, Saarbrücken, Germany, September 18-20, 2014, pp. 15-24.

CONTACT

* B. Schmitt, b.schmitt@lmt.uni-saarland.de

1. Sensors   Poster

OPTO-ELECTRONIC FLOW SENSOR - VERY THIN IN DIRECTION OF FLOW

R. Müller[1], D. Petrak[2], J. Zosel[3] and O. Brodersen[1]*
[1] CiS Forschungsinstitut für Mikrosensorik und Photovoltaik GmbH, Erfurt, Germany
[2] Ingenieurbüro FlowSensor GbR, Weimar, Germany
[3] Kurt-Schwabe-Institut für Mess- und Sensortechnik e.V. Meinsberg, Waldheim, Germany

ABSTRACT

In this work a prototype of an integrated fiber-free optical flow sensor based on the spatial filtering technique is presented, which is suited for the inline measurement of hydrodynamically induced purging of microstructures in galvanic plating baths. The measuring principle requires tracer particles in the fluid. The sensor contains a Vertical Cavity Surface Emitting Laser (VCSEL), a 2 mm long capillary as the microstructure to be measured (inner diameter: 0.15 mm; outer diameter: 5 mm) and a special silicon chip, which was developed at CiS Forschungsinstitut. Laboratory based characterization of the sensor parameters prove its suitability for the desired application.

KEYWORDS

Flow sensor, opto-electronic spatial filter, micro-structure, galvanic plating, free impinging jet flow

INTRODUCTION

Modern plants for electrochemical plating of metallic microstructures have to be optimized hydrodynamically to ensure convective mass transfer rates into the microstructures above lower limits depending on the side conditions [1]. Due to the complex situation especially in horizontal facilities for galvanic plating with various nozzles and mountings, it is not possible to predict the electrolyte flow in microstructures to be plated during the passage of the bath. Therefore, sensors are needed to enable flow measurements in microstructures passing plating baths with free impinging nozzle jets at practical side conditions [2],[3].

For this purpose a new integrated fiber-free optical flow sensor (IFOFS) based on the spatial filtering technique is presented. Due to its thickness in the lower mm range, a multi-sensor array can be integrated into a printed circuit board for inline measurements during passage of plating facilities. The sensor requires the presence of tracer particles in the liquid for signal generation.

MEASUREMENT PRINCIPLE

The flow rate q_v of fully developed laminar pipe flows of Newtonian fluids can be calculated from the maximum flow velocity U_{max} in the pipe centre which is equal to the double mean velocity u_m. With a known cross-sectional area of the capillary, the flow is equal to the product of the mean velocity u_m and the pipe cross-sectional area. With the newly developed sensor U_{max} is determined with an optoelectronic spatial frequency filter. The fluid contains tracer particles whose velocities are measured by means of this optical spatial filter. In detail, the tracer particles are illuminated with a laser so that the particle shadow falls on the optical spatial filter. A differential spatial filter consisting of two identical spatial filters which are shifted by half of the spatial filter constant g is mounted directly on the outer wall of the capillary. The velocity U and thus U_{max} is the result of:

$$U = \frac{g}{T} \quad (1)$$

whereby T is the period length for the differential signal of both spatial filters during particle passage.

More detailed descriptions of the measurement principle are contained in [4].

LAYOUT OF THE SENSOR

A special silicon chip was developed for the sensor (see Figure 1).
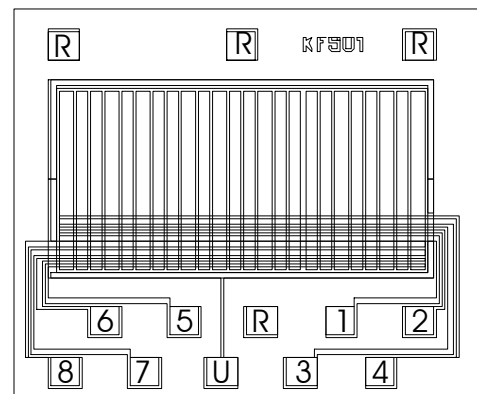
Figure 1: Layout for the silicon photodiode chip developed with the possibility to switch the grid constant, 1…8 anode contacts, R back side contacts.

The chip contains 24 stripes of photodiodes with the width of 50 microns/stripe. The micro-optical sensor is manufactured on a glass slide of 10×20 mm^2, which carry the signal preprocessing. A glassy wiring substrate which carries the Si chip (flip-chip) is positioned perpendicular to the glass slide. The wiring

on the glass was realized by means of a layer system made of CrNi-Al-FeNi-Au. Figure 2 shows a schema of the design approach.
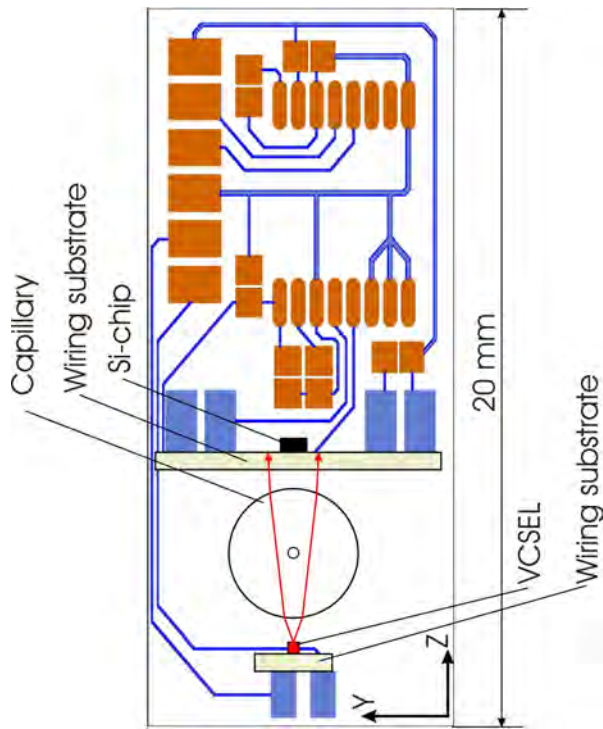
Figure 2: Design for the sensor, viewed from above, the thickness of the module in the X-direction: 2.5 mm.

In Figure 3, a first functional arrangement is shown. The entire sensor is inserted into a 6 mm thick PMMA plate ($100 \times 60 \times 6$ mm^3) and completely sealed. The capillary piece has a length of 2 mm and is terminated with the top of the PMMA plate. The outer diameter of the capillary tube is 5 mm and the inner diameter is 150 microns.

SIGNAL PROCESSING

The outputs of the two spatial filters (anodes) are guided to transimpedance amplifiers in two separate channels with adjustable gain factors. The two output voltages are guided through two active low pass 2nd order Sallen-Key-filters with individually adjustable cut-off frequencies. Subsequently, the signals are guided through active high-pass Sallen-Key-filters cutting of all unwanted low-frequency components. The difference between the two signals (channels) is finally amplified with an instrument amplifier circuit. Then the signals were recorded and stored with a DL750 Scope Corder (Yokogawa Electric Corporation, Tokyo). A real signal with one particle in the measuring volume is shown in Figure 4. The trigger level was adjusted for ensuring sufficient data rates.

The upper limit frequency of the low-pass filters was adjusted to approx. 5 times the maximum signal frequency, while the sampling rate was set to approx. 10 times the maximum signal frequency. Subsequently, the recorded signals were evaluated automatically with newly developed software algorithm counting the number of periods in the time domain and evaluating the peak-to-peak ratio in the power spectrum.
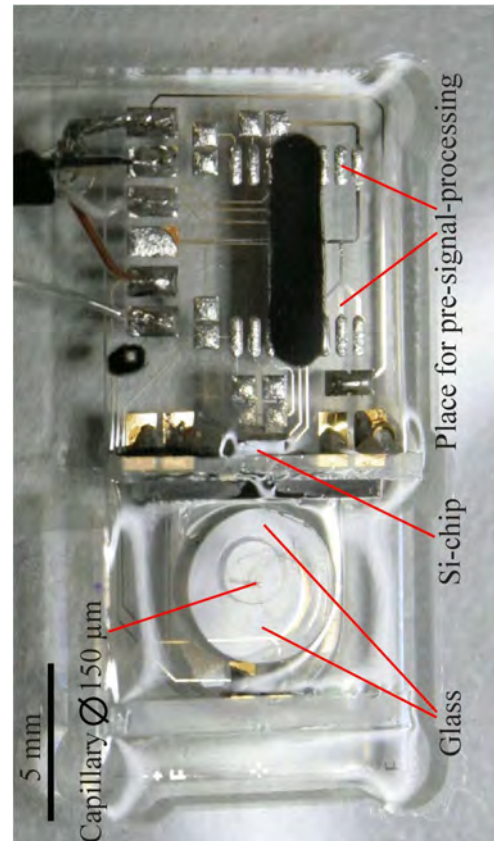
Figure 3: A photographic illustration of a first functional design of the flow rate sensor for free oncoming flow embedded in a 6 mm thick PMMA plate.
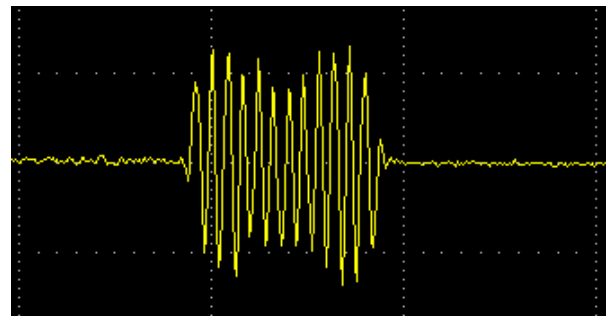
Figure 4: Exemplary sensor signal, lattice constant 120 microns, particles: 10 micron hollow glass beads, flow: 20 ml / h, the time interval shown is 6 ms.

EXPERIMENTAL

Before the characterization of two newly developed IFOFS in free impinging jet flows, they were calibrated using a tube pressed onto the front end of the sensor capillary to establish a forced flow with defined flow rate in the range of 5 ... 140 ml/h coming from a syringe pump. The medium used for calibration as well as for investigation in free impinging jet flows was deionised water containing glass beads as tracer particles with the diameter of $10 \, \mu m$. The tracer concentration was adjusted at a value which ensures the maximum number of particles in the measuring volume of the capillary equal to one.

After the calibration of the IFOFS measurements were taken in a flow chamber according to Figure 5, described in more detail in [4] with free impinging nozzle jets at different impinging angles and jet velocities, as the following experimental conditions indicate:

- nozzle flow rate: 19-1300 ml/min
- pump induced flow rate variation: < 5 %
- nozzle diameter: 0,94 mm
- distance nozzle outlet – sensor: 25 mm
- bath volume: ca. 0,5 l
- impinging angle: 30°; 15°; 0°

The adjustable nozzle position was optically fixed at the point where the jet center meets the sensor capillary.
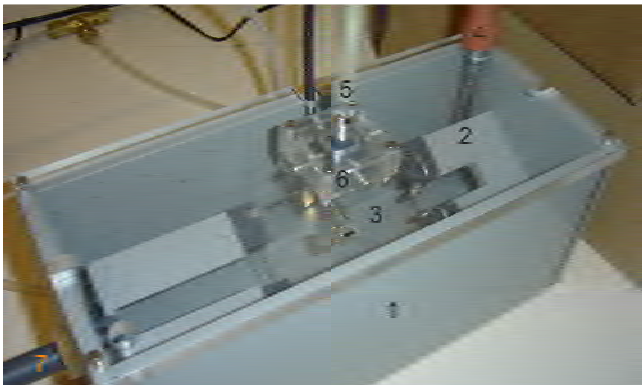
Figure 5: Setup for the investigation of IFOFS in free impinging nozzle jets with different impinging angles: 1 flow chamber, 2 rotatable sensor holder, 3 IFOFS, 4 fluid outlet, 5 nozzle inlet, 6 nozzle adjustment, 7 angle adjustment.

RESULTS

Before the characterization of two newly developed IFOFS in free impinging jet flows, they were calibrated (described above). The corresponding calibration curves are illustrated in Figure 6.
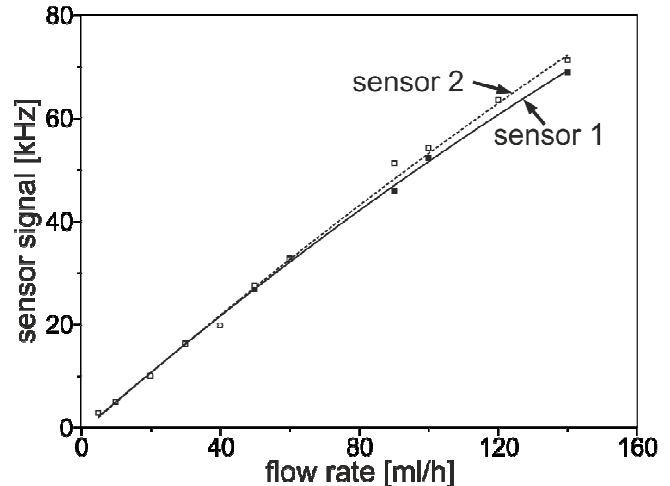
Figure 6: Calibration of two investigated IFOFS with forced flow rates from a syringe pump.

They indicate that the sensor signal is determined completely by the geometric parameters, enabling relatively small tolerances with the used manufacturing technology. The results given in Fig. 6 were taken for a second order regression of a calibration function $dV/dt = f$ (sensor signal [Hz)]). The small deviation of the signal from the linear path at higher flow rates is caused by the entrance length of the sensor capillary which is too short for establishing a fully developed laminar profile.

After the calibration of the IFOFS, measurements were carried out under the influence of a free impinging jet. The results given in Figure 7 prove that the sensor can resolve the flow in a microcapillary flushed by a free impinging jet. With response times $t_{90} < 30$ s it is possible to translate a multisensor panel through a horizontal bath at acceptable velocity. The flow rate through the micro capillary increases nonlinearly with the mean velocity of the impinging jet at the nozzle outlet. The differences between IFOFS 1 and 2 found at free jet flow come from inaccuracies of the sensor positioning in the flow chamber with respect to the jet position. The investigations prove also that through hole capillaries are maximally purged at frontal impingement (angle = 0°).
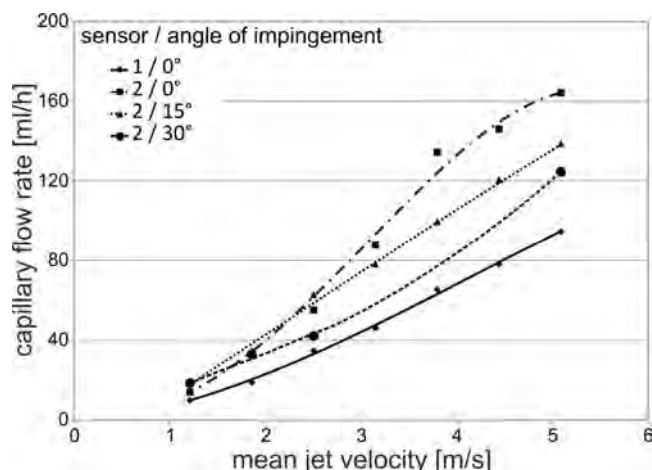
Figure 7: Capillary flow rate through the two FFOFS at flushing in a free impinging nozzle jet with different angles of impingement and jet velocities.

SUMMARY

An integrated fiber-free optical flow sensor for characterising and optimizing hydrodynamic conditions in complex facilities for electrochemical plating of metallic microstructures was developed and tested at practical conditions of free impinging jet flows. Providing a drift free signal created by an opto-physical measuring principle, an appropriate response time and attractive geometric measures the sensor is completely suited for the investigation of hydrodynamic conditions in through holes with diameters in the µm range and can be used for the manufacturing of multi sensor arrays integrated in printed circuit boards.

The results of laboratory calibration reveal that the signal establishing parameters can be controlled by the adapted micro technologies in a way that the systematic deviation in the interesting measuring range is smaller than 5 %. Investigations in a model flow chamber with free impinging jet flows at different impinging angles and jet velocities prove, that the sensor can resolve the parameters of interest for the characterization of plating baths at appropriate spatial, temporal and quantitative resolutions.

REFERENCES

[1] J. Zosel, U. Guth, A. Thies, B. Reents, "Flow measurements in micro holes with electrochemical and optical methods", Electrochimica Acta, Vol. 48, pp. 3299-3305, 2003.

[2] R. Müller, D. Petrak, O. Brodersen, "Volumenstrommessung in Kapillaren mit einem optischen Sensor", *Proc. Conference "11. Chemnitzer Fachtagung Mikromechanik & Mikroelektronik"*, Chemnitz, Oct. 23–24, 2012, ISBN-978-3-00-039162-0.

[3] H. Rauh, J. Zosel, D. Petrak, "OPTISCHER SENSOR ZUR STRÖMUNGSMESSUNG IN MIKROSTRUKTUREN", *Proc. Conference "Laser-methoden in der Strömungsmesstechnik"*, Karlsruhe, Sept. 9–11, 2008, pp. 47/1-47/9.

[4] D. Petrak, J. Zosel, H. Rauh, „Optische Durchflussmessung in einer frei angeströmten Mikrobohrung", tm Technisches Messen Vol. 76, pp. 432-440, 2009.

ACKNOWLEDGEMENTS

CONTACT

* Ralf Müller, rmueller@cismst.de

2. Sensors

A ROBUST ELECTRICAL SENSOR FOR CONTACTLESS CONTROL OF MOVING PLUGS IN MICROFLUIDIC SYSTEMS WITH HIGH ACCURACY

A. Hoffmann,[1,2], K. Potje-Kamloth[1], S. Hardt[2], and M. Bassler[1]
[1] Fraunhofer ICT-IMM, Mainz, Germany
[2] Technische Universität Darmstadt, Darmstadt, Germany

ABSTRACT

Real-time detection of fluid plugs is of fundamental interest for process control in biomedical and microfluidic applications. We present a simple, planar electrode configuration for contactless measurement of plug front position and velocity. Our setup guarantees non-intrusive detection inside of disposable microfluidic cartridges while the sensor can be reused. The sensor operates even at a large distance of up to 1.5 mm. This sensor is theoretically validated with simulations and experimentally demonstrated for various liquids, sensor configurations and distances to the fluid plug front.

KEYWORDS

Process control, fluid plug detection, microfluidic systems

INTRODUCTION

The transfer of biological or medical laboratory assays to microfluidic cartridges is a common goal in point of care research. From the microfluidic point of view, an assay is a composition of various fluidic actions, regularly requiring complex routines resulting in complex microfluidic channel circuitry. Liquids within the circuitry are handled in defined amounts – fluid plugs – that are actuated inside the cartridge structure by external or internal pumps. Often the assay requires the plug to be pumped over long distances compared to its length, for instance to enable repeatedly processed subroutines. However, fabrication methods always yield deviations in channel geometries. Further, common pumps do not reach the precision to run a microfluidic assay purely based on instrument settings for volumes and flow rates. Therefore, sensors to monitor the plug position at selected positions are needed. As the majority of microfluidic cartridges is for single use, the sensors should not be part of the cartridge to avoid extra cost. Instead, it is preferred to provide the sensing functionality within the instrument.

Usually optical detection methods like light barriers or camera systems [1] are used to detect plug positions from the outside of the channel. However,

the range of applications for optical sensors is restricted to transparent cartridges. Besides the opacity, texture, roughness and wetting state of the channel walls impede the use of light barriers and tend to cause erroneous sensor events. Therefore, an alternative sensor principle for reliable plug detection in both transparent and opaque cartridges is of great interest. In addition, a low cost solution is preferred, which enables easy mounting and independence of the cartridge itself.

Here, we present our approach for a capacitance based sensor for both the plug front position and the flow velocity. The contactless detection uses capacitively coupled electrodes. It detects the fluid interfaces on the basis of dielectric permittivity [4].

EXPERIMENTAL SETUP

The sensor configuration consists of two coplanar electrodes surrounded by a guarding electrode (Figure 1b) on a two-layered PC board (copper layer thickness: 35 μm). The copper backplane of the PCB acts as additional guarding electrode.
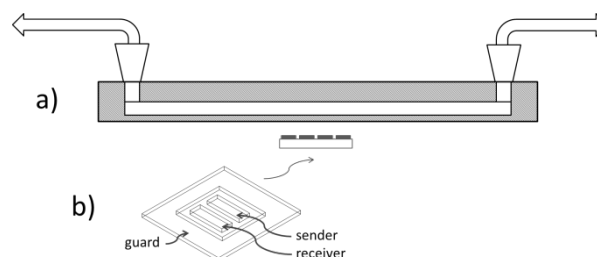
Figure 1. a) Microfluidic test channel and external sensor position .b) Configuration of contactless sensor comprising two coplanar electrodes surrounded by a framing electrode.

The sensor is driven with an AC signal of fixed frequency and voltage applied to one of the rectangular electrodes ("sender"). The second electrode ("receiver") is used to measure the capacitively induced signal. Both guard electrodes are grounded. The sensor footprint is 1 cm², and the electrodes have dimensions of 1 mm x 4 mm. For plug detection, the sensor is mounted on the outside of disposable microfluidic cartridges. Thus the sensor is

2. Sensors

part of the reusable apparatus (Figure 1a).

All experimental results shown here are based on a frequency of 400 kHz and signal amplitude of 38 V rms, which resulted in the optimal signal-to-noise ratio for our experimental setup. The voltage source is a Novocontrol Impedance Spectrometer with voltage range extender HVB300. Initially, the spectrometer itself was used to record the system response. Later experiments are based on a customized measurement circuit and associated data processing and evaluation software. The tested liquids were DI-water for its high permittivity of about $\varepsilon = 80$, and on the contrary oil with $\varepsilon = 2$. The microfluidic test channels were milled in PMMA substrates with square cross-sections ranging from 100 µm to 1 mm. To cover the channels a self-adhesive foil (110 µm) was used.

SIMULATIONS

The experimental results (see below) revealed an unexpectedly high accuracy in detecting the plug position. There are attempts to describe the electric field between coplanar electrodes analytically with conformal mapping [2, 5]. However, for more complex geometries, especially for three-dimensional configurations, no analytical solutions exist and simplifications were not satisfactory to describe our results. FEM simulations provide a reasonable alternative to analyze the electric field distribution. The presented simulation study was performed with the *Electrostatics Module (ES)* of the Comsol Multiphysics software. The geometry was defined according to the experimental dimensions of the electrodes. Tests have shown that varying the material properties of the channel does not significantly influence the qualitative signal characteristic. Therefore, to simplify and speed up the simulations, the material properties of air were assumed for the channel (square cross-section 1 mm). Water was used as liquid.

Two sensor configurations were simulated. A basic coplanar capacitor and a coplanar capacitor with surrounding guard electrode, as depicted in Figure 2. The inset in Figure 2 shows a simulated signal response of the basic coplanar sensor configuration (Figure 1b) without frame). The signal caused while the liquid fills the channel above the planar electrode follows a characteristic error-function starting at low capacitance for the empty channel and ending at high capacitance for the completely filled channel. The steady-state capacitances are directly proportional to the permittivity difference between liquid and air but with a correction factor compared to the case of

parallel plates. The precision of liquid-plug front detection with the basic coplanar sensor complies with the distance between the two coplanar plates. For higher accuracy the distance needs to be decreased implying higher production efforts.
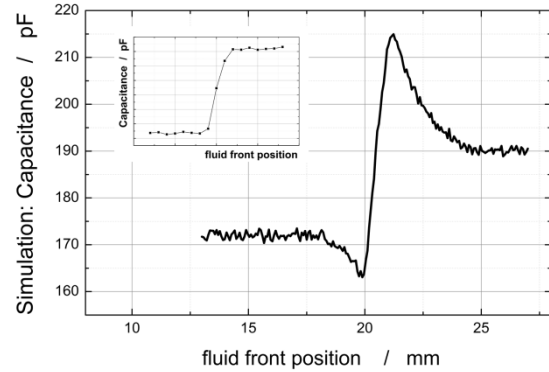
Figure 2. Simulated sensor signal for a liquid plug filling the channel. The insert shows a simulated response of a pair of coplanar electrodes without the framing electrode: no extrema are observed.

Expanding the basic geometry using a frame-shaped guard electrode (Figure 1b)) shows an unexpected but useful change in the signal as shown in the simulation in Figure 2. Two extrema appear: a minimum located between the lower steady state capacitance and the steep signal rise, and a maximum after which the signal drops to the higher steady state capacitance.

For physical understanding of the signal shape the electric field distribution is shown for various locations of the liquid plug front (Figure 3). (I) is the steady state distribution of the electric field for an empty channel. Originating from the sending electrode, the field spreads out symmetrically. The electric field couples into the receiving electrode and the guarding frame around.

In the second line (II), a liquid plug enters from the left as indicated by the arrow. The approaching liquid draws the field lines towards the guard. As these field lines are effectively removed from the receiving electrode the measured field strength reduces and the sensor signal decreases. The minimal coupling to the receiving electrode is reached when the liquid front has fully passed the receiver, and consequently the minimum in the signal is obtained.

The third line (III) shows the steep rise of the sensor signal between the two extrema. The liquid above the two sensing electrodes switches the field back to the receiving electrode. Further, the increased permittivity draws more charges to the electrode

2. Sensors

resulting in a rising sensor signal, comparable to the situation for the planar pair of electrodes. The maximum in the signal is reached when the liquid front has fully passed the sender electrode and the strongest coupling between both electrodes occurs.
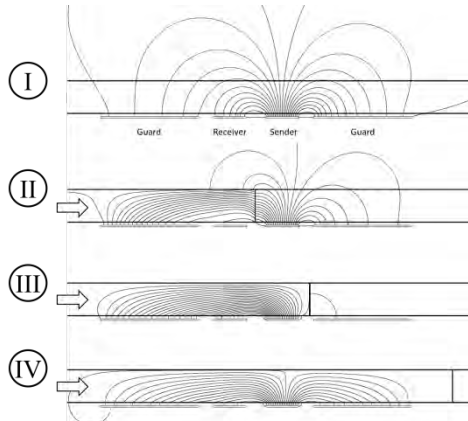
Figure 3. Electric field distribution in dependence of the liquid front position: I) equilibrium state with empty channel. II) Liquid moving in from the left; field lines shift from the coplanar electrodes to the frame until the minimum in the signal is reached. III) Liquid front moving over the second coplanar electrode; the increased permittivity causes a steep rise of the signal towards maximum. IV) Liquid front leaves sensor area and field relaxes (final equilibrium state).

When the liquid front has passed the sender electrode (line (IV)) the signal decreases again to a second steady state for a filled channel. A part of the electric field is removed from the receiving electrode and couples through the liquid directly to the guard electrode on the right, resulting in a lowered charge on the receiving electrode.

The guarding electrode framing the sender and receiver electrodes is the key feature for the changed signal characteristics. Depending on the fluid interface position the guard is able to attract a larger or smaller share of the electric field. The turning points of this effect are directly reflected in the signal reaching a minimum or a maximum.

EXPERIMENTS

Figure 4a) shows the experimental counterpart of the simulations results. The measured signal shows the same pronounced extrema as seen in the simulation. Both measured and simulated data in Figure 4a) are qualitatively in very good agreement. The different signal levels are due to the simplification in material parameters in the simulation as mentioned above. In addition, thicker electrodes are

assumed in the simulation due to meshing constraints.
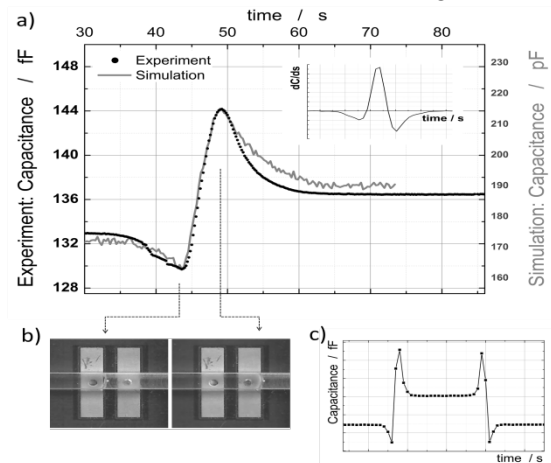
Figure 4. a) Sensor signal for a liquid plug filling the channel (black: measurement, gray: simulation). The inset shows the derivate signal. The width between the zero-crossing is used for velocity measurements. b) Relation of the signal extrema to the liquid-front position over the sensor (liquids enter from the left). Minimum: liquid completely covers the left electrode; maximum: both electrodes are covered. c) Reversibility of the sensor for filling the channel and withdrawing the plug.

Figure 4a) and b) reveal the relationship between the liquid front, the sensor position and the signal shape for a liquid entering the channel from the left. The sensor is aligned with the long side of the electrode pair orthogonal to the fluid channel, as visible in Figure 4b). This arrangement allows for a greater tolerance concerning alignment errors on the vertical axis. When the liquid plug approaches the first electrode, the sensor signal starts to decline until it reaches a minimal capacitance value, Figure 4a). The signal minimum corresponds to the liquid plug fully covering the left electrode (left image, Figure 4b)). The maximum is reached when the liquid plug has fully moved over the right electrode (right image, Figure 4b)). Figure 4c) demonstrates the independence from the filling mode in the channel during a cycle of filling and withdrawing the liquid, contrary to laser-based erroneous detections due to pre-wetting.

The signal can be easily analyzed using the two characteristic points as long as they are global extrema. A further simplification is achieved by the derivative signal shown in the inset in Figure 4a). The characteristic zero-crossing in the derivative of the signal can be directly used for plug detection and velocity measurement.

2. Sensors
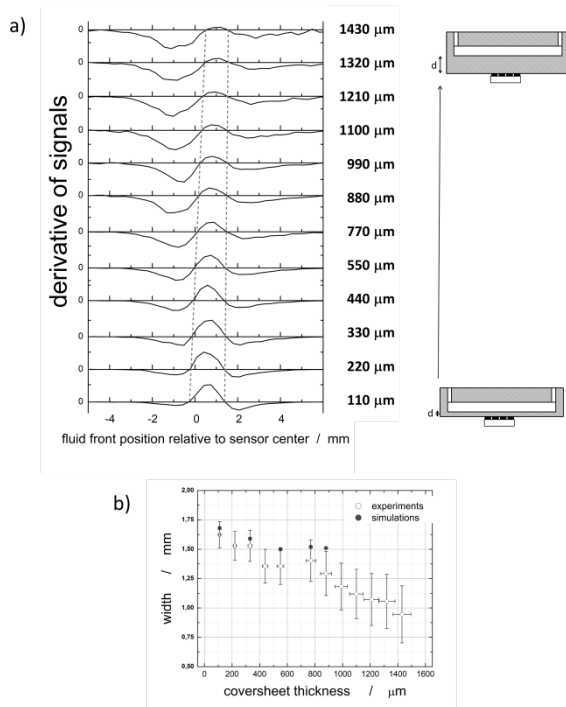
Figure 5. a) Sensor performance as a function of distance to the microfluidic channel. The position of the liquid front which is represented by the first zero crossing has been calibrated by simulation data. With increasing distance to the sensor the first zero-crossing shifts to the right. The experimental data and the simulations in b) demonstrate that the distance between both zero-crossing shrinks by approx. 30%. However, the data demonstrate the wide range of operability of the sensor configuration.

DISCUSSION

A key parameter of the sensor performance and operability is the sensitivity at various distances between sensor and channel. Figure 5a) shows the evolution of the derivative signal shape for distances between 100 µm and 1400 µm.

The dotted trend lines indicate a shift of the zero-crossing of the derivate sensor signal – reflecting the two extrema. Both zero-crossings shift to larger *x*-values as the distance is increased, and it appears that the minimum shifts more than the maximum. The left zero crossing shifts by approx. 700 µm, the right zero-crossing only by about 190 µm. Obviously, the maximum is very suitable for plug position measurement. The correlation between the appearance of the maximum and a certain liquid front position shows a very small drift over the wide distance range. The width of the sensor signal (distance between both zero-crossings) drops by approx. 30% (Figure 5a)). As this width can be used to calculate the velocity of the liquid plug, the distance needs to be known to obtain precise velocity measurements.

Video analysis and simulations with Comsol determine the spatial precision to be better than ± 100 µm, which is approximately the extension of the liquid meniscus in our experiments. Assuming a sensor positioning accuracy of ± 50 µm, the relative error in measuring the plug front velocity turns out to be below 2 %, calculated from the slope of the width in Figure 5b). State of the art electronics with appropriate sampling rate (1-10 kHz) makes it possible to detect plugs at flow velocities up to 10 cm/s, which is well within the requirements for common biomedical applications.

SUMMARY

In summary, we have presented a robust and highly accurate electrical sensor configuration with major advantages compared to common plug detection systems such as light barriers or integrated electrodes: minimized footprint on cartridge, contactless detection, combined and highly accurate measurement of plug position (± 100 µm) and velocity (error < 2 %), low cost fabrication, calibration based on geometry factors, easy mounting, wide range of geometric operability, and applicability for opaque materials.

REFERENCES

[1] R. Gransee, T. Schneider, D. Elyorgun,,,Fluorescence detection in Lab-on-a-chip systems using ultrafast nucleic acid amplification methods", Proc. of SPIE Vol. 9107, 91070P

[2] P. Linderholm, P. Renaud, J. Hong and D. S. Yoon, ''AC frequency characteristics of coplanar impedance sensors as design parameters'', Lab Chip, Vol. 5, pp.1416–1418, 2005

[3] M. Demori, V. Ferrari, P. Poesio, D. Strazza, "A microfluidic capacitance sensor for fluid discrimination and characterization", Sensors and Actuators A: Physical, Vol. 172, pp.212-219, 2011,

[4] X. Niu, M. Zhang, S. Peng, W. Wen, P. Sheng, "Real-time detection, control, and sorting of microfluidic droplets", Biomicrofluidics 1, pp. 1–12, 2007.

[5] J.Z. Chen et al,"Capacitive sensing of droplets for micro fluidic devices based on thermocapillary actuatuon", Lab chip, Vol. 4, pp.473-480, 2004

CONTACT

* A. Hoffmann,
   Almuth.Hoffmann@imm.fraunhofer.de

2. Actuators   Poster

PNEUMATICALLY ACTUATED PERISTALTIC MICROPUMP – CHARACTERIZED WITH µPIV AND MODELLED USING SIMULATIONX

M. Busek[1], K. Hofmann[2], U. Grätz[2], F. Sonntag[1]
[1] Fraunhofer IWS, Dresden, Germany
[2] ITI GmbH, Dresden, Germany

ABSTRACT

Hereby presented is a model for peristaltic micropumps with pneumatic actuation which can be integrated in human 3D cell culture systems for active perfusion. The flow in a branched microfluidic device is measured using Micro Particle Image Velocimetry (µPIV) and matched with simulation results. Furthermore the influence of non-Newtonian flow behavior is examined using a transparent blood surrogate. The presented tool is useful to test and optimize different fluidic layouts and pump designs to generate more in-vivo like cell culture models.

KEYWORDS

Micropump; Modelling; µPIV; cell culture; branched microfluidic systems

INTRODUCTION

Microfluidic 3D cell culture systems are getting more and more important in biotechnology. Due to new EU regulations animal experimentation for substance testing should be replaced within the next few years. Nevertheless a lot of these experiments are necessary during that period caused by the new REACH regulation. This issue may be solved by organ-on-a-chip devices predicted by Baker [1]. The complexity of those systems makes modelling for the design process necessary to maintain sufficient nutrient supply and the stability of gradients within the system. Hereby presented is a model for an in-vivo like peristaltic micropump integrated in a cell culture system. Together with other models e.g. substance and oxygen transport, metabolism and excretion the complete system should be simulated in future.

MATERIALS AND METHODS
Microfluidic system

Within the last years a microfluidic platform including a pneumatically actuated peristaltic micro-pump as well as several valves, cell culture chambers, fluidic reservoirs and connecting channels has been developed. The fluidic structure is produced by casting of Polydimethylsiloxane (PDMS). Fig. 1a shows an exploded view of an exemplary device. By
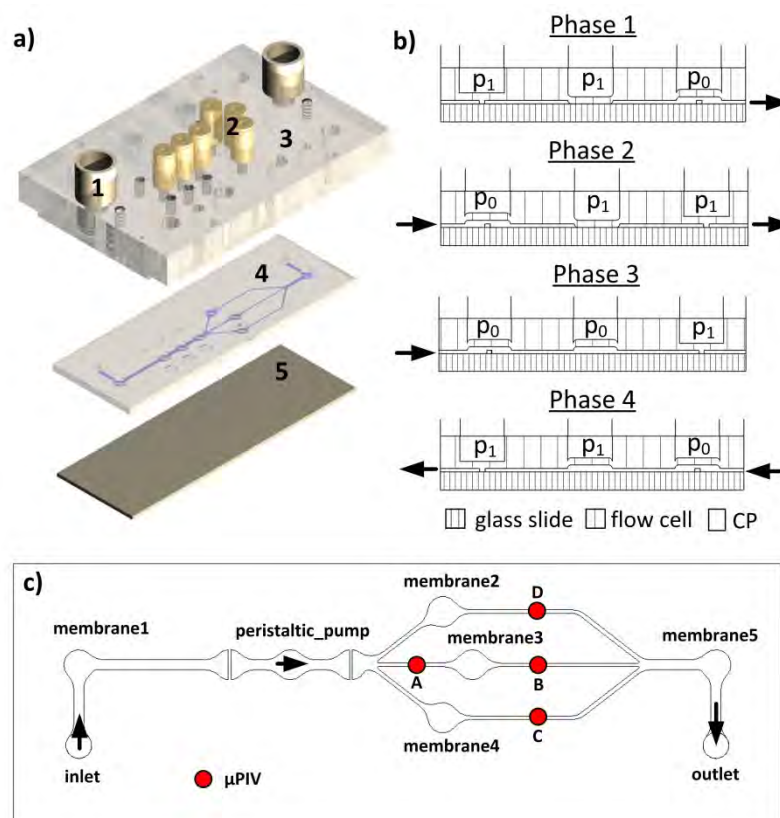

Figure 1: a) Exploded view of the microfluidic system; b) Peristaltic pumping principle; c) Fluidic layout used for simulation and µPIV

replacing the molding master structure the fluidic layout can easily be changed. The flow cell (4) is casted at a connection plate (3) including fluidic (1) and pneumatic (2) connectors. At the bottom side the PDMS is plasma-bonded to a glass slide (5) which allows easy optical access. Several human cell cultures have been successfully cultivated within this so-called multi-organ-chip (MOC) e.g. skin [2] and liver [3] equivalents, endothelial cells [4] and hair-follicles [5]. Oxygenated media is pumped through the microfluidic device by an integrated peristaltic pump [6] consisting of three pumping chambers in a row. Each is actuated one after another by applying pressure or vacuum. As shown in Fig. 1b, the first and the last chambers are designed as valves. In phase 1 the pump chamber is actuated with closed inlet and opened outlet which results in a main pump pulse. Afterwards both valve states are switched which causes a smaller pulse. Phase 3 represents the filling state of the pump chamber. Since the outlet valve is closed no fluid movement can be observed in pumping direction. In the last phase both valves are switched again which results in a back-flow because fluid fills the outlet valve chamber.

The branched fluidic layout shown in Fig. 1c was used for the experiments and modelling and the flow velocity was examined at different spots (red dots). A big channel (width: 1 mm, height: 150 µm) splits in three smaller channels (width: 300 µm, height: 150 µm). Pressure can be applied to the three membranes to throttle the flow in each channel segment.

Flow measurement with µPIV

Flow measurement was done using the non-invasive Micro Particle Image Velocimetry (µPIV) [7]. The experimental setup consists of an inverting microscope with LED illumination coupled to a high-speed CMOS camera [8]. The images were processed with a developed software which calculates the peak velocity at the channel center with a time resolution of about 100 µs.

Mathematic model of the pump

In a previous work [8] the mathematical model of the pump had an analytical approach consisting of the following two parts:
1. Airflow from the outputs of the control unit to the pump chamber, resulting in a deflection of the pump membrane.
2. Due to the movement of the membrane liquid volume is displaced and flows through a small, cylindrical channel to a reservoir.

With this estimation one single pump pulse could

be described. The approach is now further refined by modelling the complete pump with three changeable fluidic reservoirs closed by a displaceable membrane where pressure is applied to. Between each chamber a valve is placed which closes when the pressure reaches a specific threshold. Fig. 2 clarifies this pneumatic-hydraulic coupling.
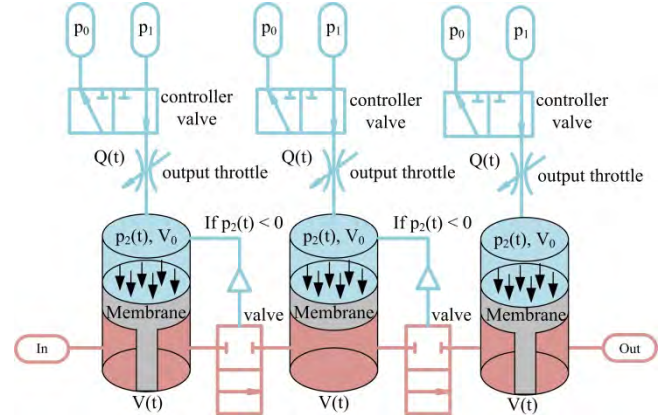
Figure 2: Model of the peristaltic micro pump.

At the top one can see the pneumatic switching circuits (blue) and the throttles regulating the mass air flow $m'(t)$ to the pneumatic chambers with the dead volumes V_0 at the membrane. The volume V_0 is constant. Described is the moment when the valve switches from p_0 to p_1. Now the air inside the pneumatic chamber is compressed, which leads to a pressure and density increase. The universal gas law describes this behavior:

$$p_2(t) = p_0 + R_s \cdot T \cdot \left(\rho(t) - \rho_0\right) = p_0 + \frac{R_s \cdot T}{V_0} \cdot \int_o^t m'(t)\, dt \qquad (1)$$

The pressure can be calculated with the universal gas constant R_s, the temperature T and the density ρ. The mass air flow through the throttle is represented by the Hagen-Poiseuille law:

$$m'(t) = \frac{\rho_1 \cdot \pi \cdot a^4 \cdot \Delta p}{8 \cdot \eta_L \cdot b} = \rho_1 \cdot k \cdot \left(p_1 - p_2(t)\right) \qquad (2)$$

The geometrical properties of the throttle (a…radius, b…length) as well as the dynamic viscosity of air η_L are summarized as the coefficient k. The air flow through the throttle is therefore directly proportional to the pressure drop between both sides. The following linear differential equation describes the time-dependent pressure behavior:

$$p_2'(t) = k \cdot \frac{p_1}{V_0} \cdot \left(p_1 - p_2(t)\right) \qquad (3)$$

This solution can be assumed:

$$p_2(t) = e^{-\frac{k \cdot p_1 \cdot t}{V_0}}\left[p_0 + p_1\left(e^{\frac{k \cdot p_1 \cdot t}{V_0}} - 1 \right)\right] \qquad (4)$$

Under a constant pressure the membrane is deflected. Following formula describes the deflection of a round membrane with clamped edges [9]:

$$z(r) = z_{max}\left(1 - \frac{r^2}{r_0^2}\right)^2 \qquad (5)$$

Here z_{max} describes the maximum of the elongation at the center, r is the position at the membrane and r_0 represents the membrane radius. The flow within the micro channel is equal to the displaced volume per time which can be determined by integrating this equation over the two cylindrical-space dimensions r and φ:

$$V(t) = \iint z(r,t)\,d\phi\,dr = \frac{\pi}{3}\cdot r_o^2 \cdot z_{max}(p_2(t)) \qquad (6)$$

If the deflection is small compared to the thickness of the membrane than z_{max} is directly proportional to the applied pressure p_2 and the displaced volume is:

$$V(t) = \frac{\pi}{3}\cdot r_o^2 \cdot c \cdot p_2(t) \qquad (7)$$

The factor c describes the membrane stiffness [10]. For larger deflections the developed optical membrane based pressure sensor could be used [11].

RESULTS
SimulationX model

Beside the membrane stiffness following additional phenomena has to be considered if the pump is integrated in a microfluidic system:

- Wall friction of the moving fluid leads to a pressure drop over the channels.
- The integrated membranes and reservoirs act as damping elements.
- The membrane stiffness of the valve is higher and the chamber volume is lower than that one of the pump element.
- Membrane deflection is constrained in positive direction by the channel height.

The multi-domain CAE (computer aided engineering) simulation software *SimulationX* [12] with its network approach is perfectly suited for modelling this complete fluidic system. The mathematical behavior of the pump is implemented using the *Modelica* model description language [13]. A controlling device switches the two valves and the pump chamber according to the programmed sequence. Model library development was done focusing on non-Newtonian fluids e.g. blood as flowing liquids. Therefore several elements of the hydraulic library have to be modified to represent their specific non-Newtonian flow behavior. In Fig. 3 the complete SimulationX model of the micro fluidic device is shown. The channels were replaced by fluidic resistances (throttles) and the reservoirs are modelled by fluidic capacitors (liquid reservoir closed by a flexible membrane). A pressure increase in the channels results in a membrane deflection, which dampens the flow.

Model validation

Model validation was done using the described µPIV measuring setup. By reducing the field of view (1024x100 pixels) a high frame rate (3205 fps) could be achieved while the exposure time was set to 4µs. Therefore a low magnification (4x) was chosen so one pixel is about 2.15 microns. An image stack with a size of 15000 was recorded and afterwards analyzed with the developed algorithm. This corresponds with a measurement time of 4s. To examine the influence of non-Newtonian liquid flow on the velocity-time-curve a blood surrogate derived from literature was chosen [14]. This replacement has the same rheological behavior as it is described for blood [15] but still has good optical characteristics as it is needed for µPIV measurements. The surrogate is a mixture composed of 46.140 wt. % distilled water, 47.566 wt. % of glycerin, 6.292 wt. % of sodium chloride and 0.002 wt. % of xanthan gum particles. Polystyrene beads with a size of 10 microns were chosen as velocity tracers. Fig. 4 compares modelled to measured velocity-time curves metered at spot c for distilled water (top) and blood surrogate (bottom) as flowing liquid.
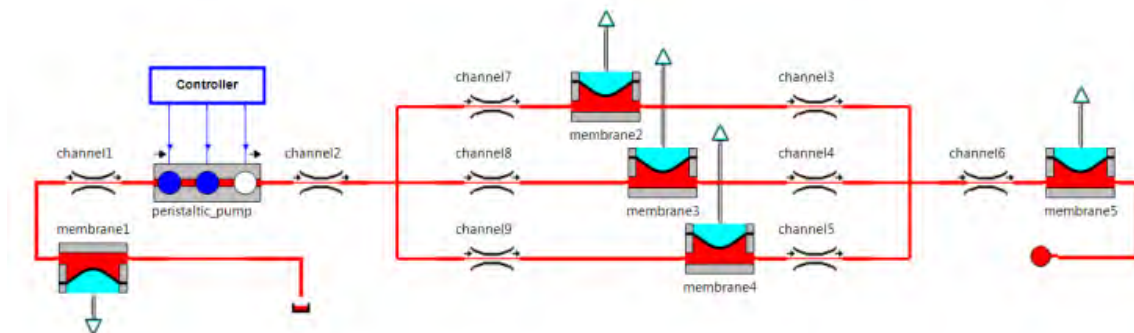

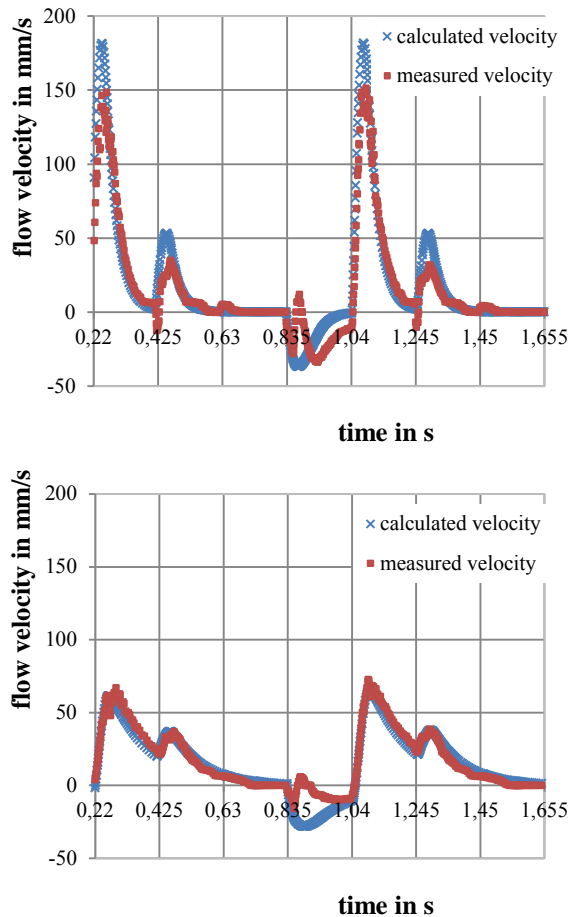*Figure 3:* SimulationX model of the fluidic network shown in Fig. 1c

Figure 4: Measured vs calculated velocity at spot c (position shown Fig. 1c) for deionized water (top) and blood surrogate (bottom)

The observed channel has a height of 150 microns and a width of 300 microns. The following pump configuration was used for the experiments: pressure: 650 mbar; vacuum: −750 mbar; pumping frequency 1.2 Hz and air flow: 1.41 L min^{-1} at 1800 mbar.

CONCLUSION

Both graphs show a good correlation (coefficient of determination: $R^2 = 0.79$ for water and $R^2 = 0.85$ for the surrogate) so the developed model is suited to simulate liquid flow in the micro-fluidic system. Furthermore the non-Newtonian flow behavior of the blood surrogate and the higher viscosity compared to water leads to a damping effect of the pump pulses reducing the peak velocities from more than 160 mm s^{-1} to values below 80 mm s^{-1} and smoothing the velocity-time curve. In both graphs the experimental results show an abnormality during the negative pump pulse. The negative pulse appears during pump phase 4 (Fig. 1b), when the inlet valve opens and the outlet valve closes. Fluid is sucked backwards to fill the chamber of the valve. Flow measurements showed an

additional positive peak which may be caused because both valves differ in their filling and closing behavior. This effect was not described before [4] and may be further investigated. In future developments the pump model features such asymmetric behavior.

REFERENCES

[1] M. Baker: "A Living system on a chip", Nature, 471, 664-665, 2011.

[2] I. Wagner, E.-M. Materne, et al.: "A dynamic multi-organ-chip for long-term cultivation and substance testing proven by 3D human liver and skin tissue co-culture", Lab Chip, 13, 3538-3547, 2013.

[3] E.-M. Materne, A. Tonevitsky, U. Marx: "Chip-based liver equivalents for toxicity testing – organo-typicalness versus cost-efficient high throughput", Lab Chip, 13, 3481-3495, 2013.

[4] M. Busek and K. Schimek, et al: "Integrating biological vasculature into a multi-organ-chip microsystem", Lab Chip, 13, 3588-3598, 2013.

[5] B. Atac, et al: "Skin and hair on-a-chip: in vitro skin models versus ex vivo tissue maintenance with dynamic perfusion", Lab Chip, 13, 3555-3561, 2013.

[6] C.-W. Huang, et al: "Pneumatic micropumps with serially connected actuation chambers": J. Micromech. Microeng., 16, 2265–2272, 2006.

[7] Lindken: "Micro-particle image velocimetry (µPIV): Recent developments, applications, and guidelines", Lab Chip, 9, 2551–2567, 2009.

[8] M. Busek, et al: "Automated Micro-PIV measurement in Lab-on-a-Chip systems", Biomed Tech, 57, 927-930, 2012.

[9] M. Busek, M. Nötzel, C. Polk, F. Sonntag: "Characterization and simulation of peristaltic micropumps", J. Sens. Sens. Syst., 2, 1–5, 2013.

[10] A.L. Thangawng, et al: "An ultra-thin PDMS membrane as a bio/micro–nano interface: fabrication and characterization", Biomed. M., 9, 587-595, 2007.

[11] M. Nötzel, M. Busek, F. Sonntag: „Nicht-invasive optische Druckmessung in Lab-on-a-Chip Systemen" , Dresdner Sensor-Symposium, 11, 394 – 397, 2013.

[12] ITI GmbH: "User Manual SimulationX", Version 3, 2009

[13] Modelica Association: "Modelica - A Unified Object-Oriented Language for Systems Modeling", Language Specification, Version 3.3, 2012

[14] C. Roloff, et al.: "Investigation of the velocity field in a full-scale model of a cerebral aneurysm", International Journal of Heat and Fluid Flow, 43, 212-219, 2013.

[15] H. Chmiel, B. Stornier: „Zur Rheologie des Blutes", Biomedizinische Technik, Band 17, 5, 1972

MICROFLUIDIC DEVICE COMPONENTS FOR MULTISTEP ASSAYS

E.X. Vrouwe, M. Brivio and M.T. Blom
Micronit Microfluidics BV, Enschede, The Netherlands

ABSTRACT

In order to perform multistep assays inside a microfluidic device multiple functional components need to be integrated and work in unison. The entire device should be low cost and require few or no external hardware to operate. In this work we show examples of filter membrane integration for sample cleanup, integrated magnetic stirrers for mixing and the use of capillary burst valves that are triggered electrostatically or with a second fluid.

KEYWORDS

Burst valve, electrostatic actuation, filter membrane, magnetic stirrer

INTRODUCTION

There is a growing need for microfluidic devices that can perform complex assays, consisting of multiple steps, integrating as much of the sample handling on-chip as possible. Depending on the application there are different options to accomplish a certain function. For example, devices aimed at point-of-care (PoC) testing should be disposable and the devices and hardware have to be cheap enough for the end-users to compete with existing solutions. Conversely, devices that are used in a lab environment can utilize more complex hardware with the goal of minimizing the use of sample and reagents. In this paper we will present a selection of pumping methods, integrated valves and mixers that we have fabricated. The devices shown are fabricated from glass, polymers or a combination of the two. The aim is show functional components that need as little external hardware as possible to operate.

PUMPING AND FLOW CONTROL

All-glass hydrophilic capillary burst valves

One of the advantages of glass is that it is very hydrophilic and thereby contributes to excellent and reliable wetting of aqueous samples without having to pretreat the surface first. For applications relying solely on capillary force for liquid transport this is a definite advantage. For many applications liquid has to be stopped temporarily inside a device and capillary burst valves are excellent candidates for this [1].

Geometrically defined burst valves rely solely on a sharp edge at which the meniscus pins and stop it from advancing. This type of valve is traditionally made using high aspect ratio etching of for example

silicon [2]. For improved robustness a PDMS capping layer was used. We recently showed that such a valve can be made completely from glass using a relatively cheap wet etching process. Figure 1 shows a cross-section through a burst valve that is formed from three glass wafers fusion bonded together. Channels are wet etched in the middle layer from both the top and bottom side and where channels cross a passage forms between the layers. Owing to the sharp angle created the hole acts as a valve.
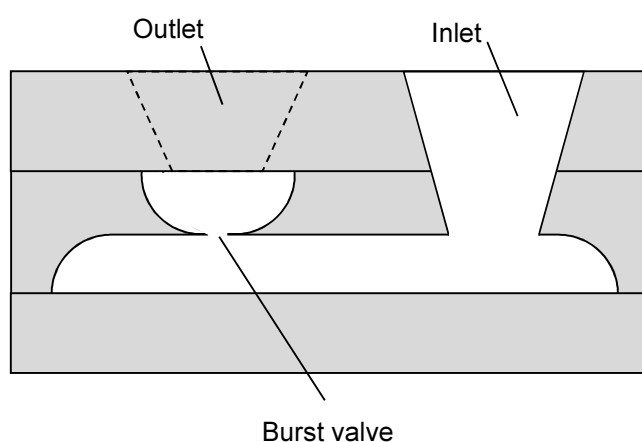
Figure 1: Schematic representation of an out-of-plane burst valve viewed from the side and made by wet etching glass.
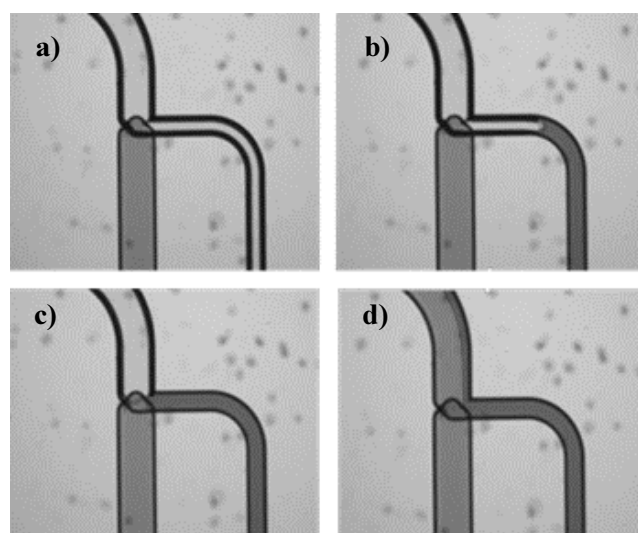

Figure 2: Image sequence starting with one fluid stopped at an out-of plane valve, which is triggered by a second fluid approaching from the right. The interval between the photographs is 0.25 s. The channels are 400 and 210 µm wide respectively and 105 µm deep. The diameter of the through hole at the intersection is approximately 45 µm.

Figure 2 shows an example of a device made completely from glass without any treatment to reduce hydrophilicity. The liquid has stopped at the valve and a second liquid enters from a second channel to trigger the valve causing the first liquid to continue further into the device.

A different approach was taken for device shown in Figure 3a, which is fabricated from two instead of three glass wafers. Here a 5 μm shallow channel is isotropically etched in both the top and then bottom wafer emerging in a 200 μm deep part. The transition in the channel depth creates steep walls at the end of the shallow channel creating the requirements for a burst valve. This is shown in Figure 3b where the first liquid entering from the left has stopped and a second trigger liquid is approaching from the bottom.
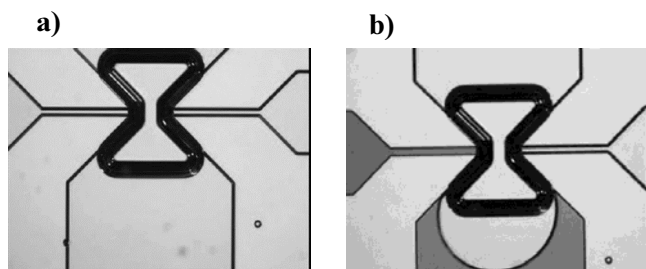

a)   b)

Figure 3: Image sequence of an in-plane valve. In a) liquid has not reached the valve and in b) the first liquid coming from the left has stopped at the valve and a second trigger liquid is approaching from the bottom. The inside of the hourglass shape is etched deeper than the other regions.

Electrostatically triggered valve

Triggering liquid stopped at a burst valves with a second liquid as shown above offers the possibility of running a pre-programmed sequence autonomously on a device without having to supply power. Inevitably, a small amount of the second liquid mixes with the first liquid and that may pose a problem. Furthermore, for certain applications precise control over the moment a valve is triggered is needed. These requirements led to the development of electrostatically triggered burst valves.

The concept of stopping the fluid remains the same as discussed before, but a pair of electrodes is added to the device (see Fig. 4). One of the electrodes is in contact with the liquid and the second electrode is positioned opposite of the meniscus when stopped at the valve. An attractive electrostatic force can be generated between the meniscus and the second electrode by applying a voltage. If the resulting deflection of the meniscus is sufficient the liquid will be pulled through the valve and continue to flow further inside the device.
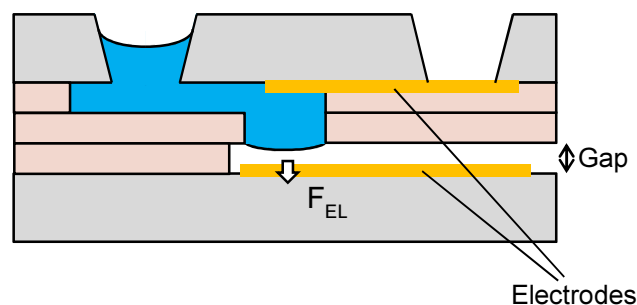
Figure 4: Conceptual drawing of an electrostatically actuated valve. Cross-section.

A working device is shown in Figure 5, which is made from a glass top and bottom substrate with patterned thin film electrodes made from gold. The microfluidic channels and valve are made using a photo patternable permanent resist foil (45 μm thick TMMF, Tokyo Ohka Kogyo). The device is equipped with three inlets that are filled with liquid at the start of the experiment. Each liquid enters the microfluidic channels by capillary force until the first set of valves is reached. At that moment any of the three valves can be triggered by momentarily applying a voltage pulse (e.g. 700 V) to the correct electrodes causing the liquid to continue further into the device. At the outlet a sorbent pad is placed to absorb all liquid thus, completely draining the serpentine channel from liquid. At that point one of the remaining liquids can be triggered and the cycle repeats. By using short voltage pulses (e.g. 0.2 s) the extend of any electrochemical reactions occurring at the electrodes such as gas formation are minimized.
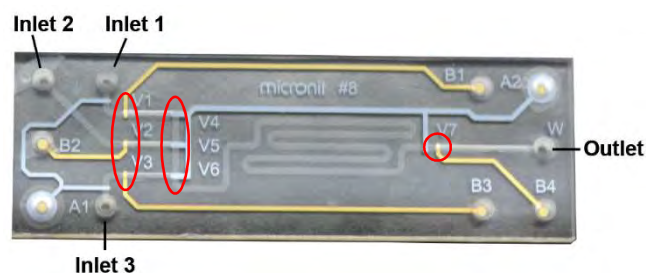
Figure 5: Photograph of a chip equipped with electrostatically triggered valves (inside the red circles) used to flow three liquids in sequence through the device.

Pneumatically actuated membrane valves and pumps

Various types of pneumatically actuated membrane valves have been well described in literature [1]. Typically these consist of a microfluidic structure combined with a flexible elastomeric

structure made from e.g. silicone rubber that can be deformed to seal the microfluidic channel using external actuation. For applications where inertness is critical we have made all glass valves using a 100 μm thin glass membrane as the moving part. Because of the high Youngs modulus a pressure of several bars is needed to close the valve and even the leakage is relatively high because the membrane does not conform to the valve seat. Elastomeric materials provide good sealing performance but if inertness is critical then the use of cyclic olefin copolymers (COC) could be used. An example is shown later in the section on mixing.

SAMPLE PROCESSING

Next to pumping and stopping fluids, certain actions need to be performed on the fluid, for example to add and mix precise amounts of reagents or to clean-up samples.

Filtration

Filtration is an important step for example to remove cells from blood samples, for concentrating particulates or to remove suspended particles that may block microfluidic structures. One of the options that was explored was to bond various membranes between microstructured plastic parts. An example is shown in figure 6 where a polysulfone membrane is bonded at the inlet of a microfluidic channel to remove blood cells from whole blood.
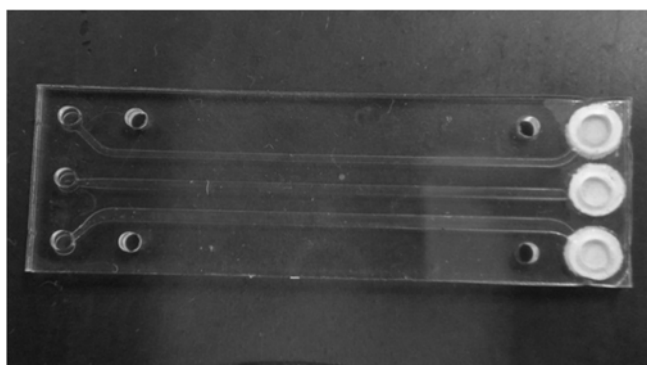
Figure 6: Photograph of a chip made from polycarbonate with polysulfone membrane discs sandwiched between the fluid inlet and the channels. Microfluidic chip (dimensions 15x45 mm²).

Volume metering

Metering specific volumes is a prerequisite for many applications, especially in case quantitative results are generated. On-chip volume metering can be accomplished using the capillary burst valves presented above. The device shown in figure 7 contains a chamber that fills by capillary action until it reaches a burst valve. Close to the inlet of the chamber any excess liquid is directed to a sorbent pad wicking up excess liquid until an isolated amount of liquid is created shown by the blue dye in figure 7. Any further operation can be performed on the liquid by triggering for example the valve at the outlet using a secondary liquid or by using electrostatic force if electrodes are integrated.
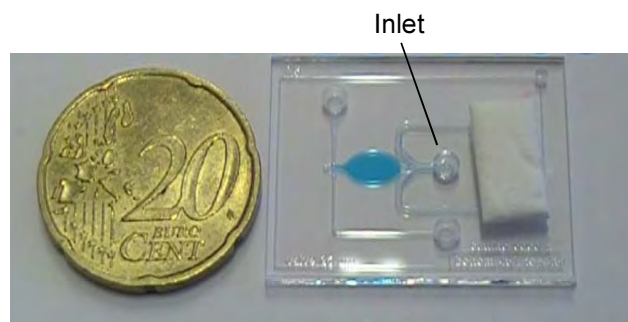
Figure 7: Photograph of a structure that can be used to meter a specific volume of liquid. A blue dye has been loaded and the excess has been absorbed by the white wicking pad on top.

Mixing (Magnetic stirrer)

Asymmetric mixing of fluids at ratios higher than 1:2 is often required in multistep molecular assays. This is difficult to achieve in microfluidic devices where mixing generally relies on slow diffusion of molecules. To enable uniform mixing of asymmetric ratios on-chip requires non-passive techniques, such as pumping or stirring. Stirring can be created using on-chip magnetic stirring, whilst, pumping can be created using on-chip membrane valves in conjunction with carefully designed geometries to pump fluids and create uniform mixing.

Successful mixing of fluid ratios 1:10 has been in a monolithic COC chip. The chip enabled fluids to be loaded into an on-chip mixing chamber using peristaltic pumping and was subsequently mixed using a magnetic stirrer. The chamber was filled pumping using an array of COC membrane valves, once the chamber was filled it was sealed using valves at either side. The two fluids in a 1:10 ratio were then mixed in less than 5 seconds to form a homogenized mixture.
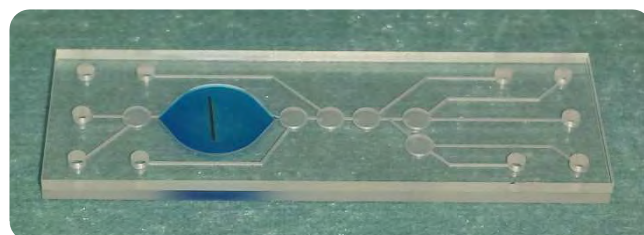
Figure 8: Microfluidic chip (dimensions 15x45 mm²) used to demonstrate complete mixing of a 1:10 ratio of fluids (clear and stained water).

CONCLUSION

We have presented a number of microfluidic components that can contribute to the development of microfluidic devices for performing multistep assays. The amount of external control that is needed greatly influences whether a device is feasible that does not require any external actuation and runs by virtue of the capillary action alone. A simple actuation methods have been developed to trigger capillary burst valves using electrostatic force, requiring no mechanical parts.

REFERENCES

[1] A.K. Au, H. Lai, B.R. Utela, A. Folch, "Microvalves and Micropumps for BioMEMS", Micromachines, 2, 179-220, 2011

[2] M. Zimmermann, P. Hunziker, E. Delamarche "Valves for autonomous capillary systems", Microfluid Nanofluid 5, 395-402, 2008

2. Actuators   Poster

UNIBODY THREE CHANNELS INJECTOR WITH INTEGRATED MANUAL PUMPS

A. Suska, G. Comina and D. Filippini*
Optical Devices Laboratory, IFM – Linköping University, Sweden.

ABSTRACT

Emerging chemical sensing on cell phones [1,2] poses specific demands on the development of complementary devices necessary for chemical interfacing. One particular approach relies entirely on disposable devices [2,3] to assist the cell phone optical detection, and thus defines challenging demands for what can be integrated. Sample transport and conditioning are, however, essential to provide comprehensive autonomous or semi-autonomous solutions.

Here we present a disposable manual action three channels injector for lab-on-a-chip (LOC) sample handling. In this work the unibody LOC fast micro prototyping concept [4] is used to configure an injection system with integrated manual pumps, check valves and fixed volume reservoirs.

KEYWORDS

3D printer, lab-on-a-chip, manual pumps, injector, fast prototyping, unibody.

INTRODUCTION

Unibody-LOCs (ULOC) are built around a single 3D printed monolithic structure (unibody), which accommodates all the complementary functions [4]. The devices in this work were fabricated with a consumer grade stereo-lithography (SL) 3D printer (Miicraft), which enables prototype fabrication typically under 30 min and by less than 0.5 US$ / piece. Unibody designs are conceived to exploit the low surface roughness (< 200 nm) achievable with this kind of printer, which allows direct sealing with regular adhesive tape. In this way, channels can be configured with one open side, which allows uniform arbitrarily long channels at the resolution limit (50 μm), since unexposed resin can be easily removed from the open side.

Adhesive tape strongly adheres to the unibody, which is relevant for manual pumping, since the devices should endure the varied range of pressure stimuli produced by manual actuation.

In this work, we investigate the ability of ULOC to configure a three channel disposable delivery system capable of sequential sample injection and volume insolation with air droplets.

EXPERIMENTAL

Device fabrication

Device structures were designed with free CAD software for Mac Os X 10.8.3 (Autodesk® Inventor® Fusion, Autodesk Inc.) on a MacBook Air computer (13-inch, late 2010, 1.86 GHz Intel Core 2 Duo, 4 GB 1067 MHz).

The devices were fabricated with a Miicraft® 3D printer, which is a stereo lithography (SL) platform (2299 US$) with 450ppi (~56μm) lateral resolution, and 50μm resolution in the vertical direction.

CADs were exported as .stl mesh files and converted to bitmap exposure patterns by the Miicraft® Suite software provided with the 3D printer. Further details of these recourses have been published elsewhere [4,5].

After optimization, devices were printed in the following conditions of exposure time, printing speed and vertical step size: 7s, 2cm/hour, 50μm. After printing, the devices were sonicated (FinnSonic m15) in industrial grade ethanol for 20s, and air-dried.

The printer uses a proprietary resin (138 US$ / 500 ml), with undisclosed formulations of a modified acrylate oligomer and monomer in combination with an epoxy monomer, a photo initiator, and additives.

The average device weight was 1.5 gr, which for the resin cost corresponded to 0.41 US$/device.

Surface roughness was measured with a stylus profiler (Dektak 6, Veeco Instrument Inc.) along 1mm tracks resolved in 6000 points. The average roughness was 182nm for the finished templates, which enables direct sealing with adhesive tape. Unibody designs exploit this aspect by simplifying the fabrication to a single monolithic 3D printed structure, or unibody [4], around which the device is assembled.

The same low surface roughness enabled efficient sealing with flat polydimethylsiloxane (PDMS) film, which was used to create the integrated check-valves (Fig.1).

To fabricate the PDMS film, Dow Corning Sylgard 184 base and curing agent were mixed in 10:1 proportion and stirred in a cup for 2 min. The mixture was degassed in a desiccator connected to a rotary pump for 30 min, and subsequently poured on glass and cured at 65 °C for 2 h in an environmental oven

(Gallem Kamp incubator). The PDMS elements of the check-valves were cut with a blade and placed in the unibody seats with a tweezer.

The devices were subsequently sealed with adhesive tape (3M Ruban Adhesive Scotch® Nastro Adhesive). Excess tape was trimmed with a cutter and the tape was pressed against the unibody surface with a cotton tip in order to eliminate trapped air in small blisters. The total fabrication time, including the PDMS assembly and sealing, to produce a device ready for testing was less than 30 min.

Device characterization

The device reservoirs were filled with pink (rhodamine), yellow (fluorescein) and blue (food colorant) aqueous solutions using a 5 ml syringe. Injection could be sufficiently controlled to avoid reaching the manifold. Residual excess solution, leaked to the tubing can be easily sucked with the same syringe, since the check-valves prevent backward flow.

Pressure pulses were manually applied to the silicone tubing while the device was imaged using a Samsung Galaxy Note 2, 8 Mpix rear side camera operating in full HD video acquisition (30 fps). Background illumination was provided by an iPod Touch screen (4th generation, 960 × 640 pixel screen resolution, with iOS 6) running Led Torch v1.37 app (www.smallte.ch), set to pure white (rgb 255, 255, 255).

Reference pressure pulses were also used to determine minimal operating conditions, with the aid of a pressure micro-injector (PMI-200, Dagan Corporation, USA), set to 10 psi, 100 ms pulses.

For quantification purposes the video was decomposed in individual frames using Adapter 2.1.0 for Mac. Each video frame corresponds to a 33.3 ms interval from the previous frame, and enabled the quantification of the distance displaced by each pressure pulse by subtracting subsequent frames. Image J was used for image subtraction (Fig. 2) and to measure the displaced distances.

Since the channel dimensions are known, the average displaced volume and corresponding flow rates could be calculated.

RESULTS AND DISCUSSION

The injector consists of three independent channels connected to a manifold (Fig. 1a). Each line has its own manual pump and fixed-volume reservoir confined between two check-valves, which secure unidirectional flow when the line is pressurized. Fig. 1b shows the unibody design, the image of one reservoir with valves and the cross section highlighting the asymmetric geometry used to create

the uni-directional flow. The sealing element of these check-valves is a blade cut polydimethylsiloxane (PDMS) film. The design is tolerant to variability in the PDMS dimensions, provided that it does not touch the walls of the valve seat, created in the unibody. Average forward flows of 1.22 ml/min, for a reference minimal pressure pulse of 10 psi for 100 ms, have been registered, whereas the manual pumping with the silicone tubing connected to the unibody terminals show a resolution of 0.5 µl/pulse.

In conventional continuous flow designs the accuracy of the sample flow is relevant, whereas the present concept relies on fixed volumes defined by the reservoirs and the ability to expose the detection region of the LOC to such substance volumes.
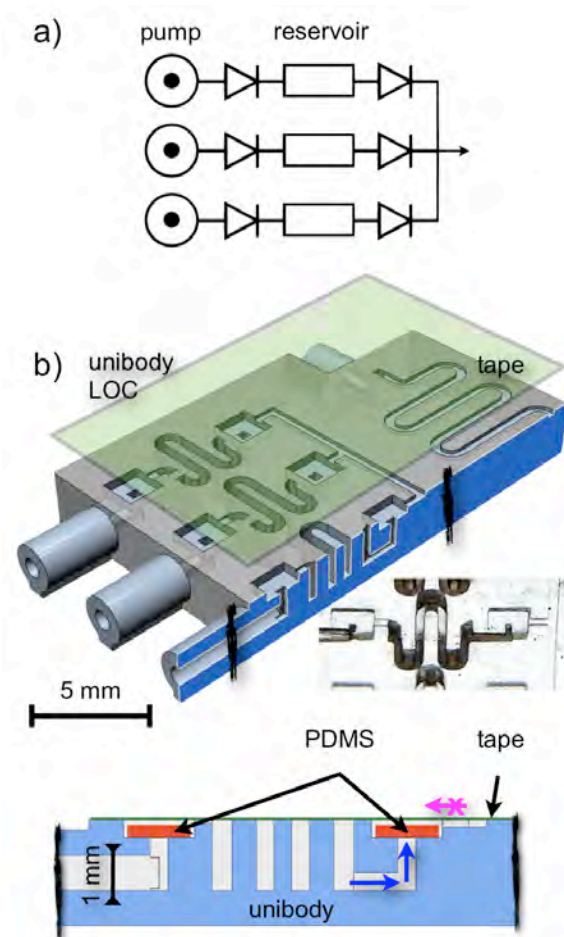

Fig. 1a) Schematics of the injector system indicating three separated lines with their own manual pumps, all converging to a manifold. b) CAD of the unibody design with cross section underscoring the asymmetric geometry used to configure the check-valves. The inset is the actual image of the reservoir with the connection to the valve seats.

Fig. 2a shows the finished injector with 1.5 mm I.D. silicone tubing pumps and filled with three colored solutions. The reservoirs are separately filed by injection through the tubing (Fig. 2b-d). The distal check-valve of each line prevents reflow and isolate solutions within each reservoir. The only mixing in this design occurs in the manifold, and constitutes a lost volume of 0.7 µl, in the present design.

The valves are entirely unidirectional (zero backward flow up to 100 psi), making unnecessary to equalize the different manifold paths, thus simplifying design and saving layout footprint.

By pulsing the tubing, air is pushed through the proximal valve and reservoir. The proximal valve prevents back flow when the tubing is released, thus conveying an effective forward flow. Fig. 2e-g shows the sequential injection of 1 µl from left to right. By choosing the injection sequence the mixed volume in the manifold can be reduced, and in addition large volume and flows of washing solution can be easily delivered by overriding any channel with a syringe connected to the silicone tubing.

Furthermore, the same injector design can be configured to create air pockets setting well-defined volumes (Fig. 2h) or to separate different solutions (Fig. 2i,j) with different droplet volumes depending on the number of pulses, thus canceling mixing in the manifold. In this alternative on reservoir can be left empty or used for this purpose after been emptied, which in such case do not limit the number of substances that can be integrated in the device.

This work demonstrated the capabilities of the ULOC concept to create a flexible delivery system with integrated manually actuated pumps. Systems like this can constitute the sample handling component necessary for integration into disposable autonomous LOCs, such as those deemed suitable with cell phone detection [2,3].
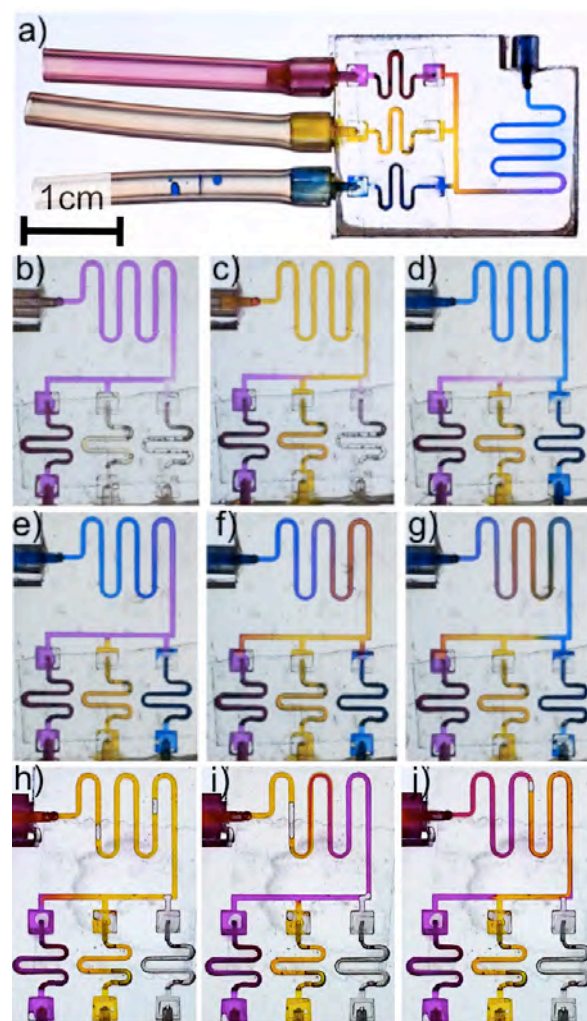
Fig. 2a) Three channels unibody injector with manual silicone tubing pumps. b-d) Independent filling of the three reservoirs. e-g) Sequential pumping of three different colored solutions. No reflow within non-active reservoirs. h) Setting of a defined solution volume using air bubbles as spacers and i-j) Separation of different solutions with air pocket of different volume, defined by the number of air pulses.

CONCLUSIONS

A Unibody-LOC device has been demonstrated as a cost-effective fast-prototyping alternative to create essential functionalities for practical sample handling.

The three-channel injector with integrated manually actuated pumps is a versatile platform to deliver different sample/reagents sequences and fixed volumes to a detection region. It also enables to introduce air pockets for sample separation and it can incorporate large volume/flows in the workflow by simple overriding any channel.

ULOC provides a hybrid fabrication concept where is natural to blend 3D mechanical design with classical planar configurations, and in this case at a cost of 0.41 US$/prototype.

REFERENCES

[1] A. Vashist, O. Mudanyali, E. Schneider, R. Zengerle, A. Ozcan, Cellphone-based devices for bioanalytical sciences, Anal Bioanal Chem, DOI 10.1007/s00216-013-7473-1.

[2] P. Preechaburana, A. Suska, D. Filippini, Biosensing with cell phones, Trends in Biotech 32 (2014), 351-355.

[3] P. Preechaburana, M. Collado Gonzalez, A. Suska, D. Filippini, "Surface Plasmon resonance chemical sensing on cell phones", Angewandte Chemie 52, 2012, 11585-11588.

[4] G. Comina, A. Suska, D. Filippini, Low cost lab-on-a-chip prototyping with a consumer grade 3D printer, Lab Chip (2014), DOI: 10.1039/c4lc00394b.

[5] G. Comina, A. Suska, D. Filippini, "PDMS lab-on-a-chip fabrication using 3D printed templates", Lab Chip 14, 2014, 424-430.

CONTACT

* D. Filippini, danfi@ifm.liu.se

2. Actuators   Poster

INTEGRATED PASSIVE CHECK-VALVES FOR 3D PRINTED FLUIDICS

G. Comina, A. Suska and D. Filippini*

Optical Devices Laboratory, IFM – Linköping University, Sweden.

ABSTRACT

Fast and low cost micro-prototyping of lab-on-a-chip (LOC) devices is possible using last generation consumer grade stereo lithography (SL) 3D printers. Printed monolithic elements (unibody-LOC, ULOC) concentrate complex features and allow simplified integration of complementary parts.

Here we demonstrate the first passive check-valves for ULOC devices. The valves are strictly unidirectional up to 100psi and show an exponential forward flow behavior up to 70psi.

KEYWORDS

3D printer, lab-on-a-chip, check-valves, fast prototyping, unibody.

INTRODUCTION

Disposable LOCs for ubiquitous readout [1] require integrated sample conditioning to support advanced autonomous [2] analyses. A central function in benchmark target assays, such as immunosorbent assays or surface plasmon resonance measurements [1], is the ability to sequentially deliver unidirectional flows [3] of samples and reagents to the detection area. Robust passive check-valves suitable with integration in ULOCs are thus key components to avoid reflows, and need to operate within a broad range of pressures to allow simple pressurization mechanisms, such as manually operated pumps.

In this work we investigate the design of check-valves that exploit the characteristics of the ULOC principles for cost-effective fast-prototyping and integration of common LOC materials such as polydimethylsiloxane (PDMS) for the valve action.

EXPERIMENTAL
Device fabrication

Device structures were designed with free CAD software for Mac Os X 10.8.3 (Autodesk® Inventor® Fusion, Autodesk Inc.) on a MacBook Air computer (13-inch, late 2010, 1.86 GHz Intel Core 2 Duo, 4 GB 1067 MHz).

The devices were fabricated with a Miicraft® 3D printer, which is a stereo lithography (SL) platform (2299 US$) with 450ppi (~56µm) lateral resolution, and 50µm resolution in the vertical direction.

CADs were exported as .stl mesh files and converted to bitmap exposure patterns by the Miicraft® Suite software provided with the 3D printer. Further details of these recourses have been published elsewhere [6,7].

After optimization, devices were printed in the following conditions of exposure time, printing speed and vertical step size: 7s, 2cm/hour, 50µm. After printing, the devices were sonicated (FinnSonic m15) in industrial grade ethanol for 20s, and air-dried.

The printer uses a proprietary resin (138 US$ / 500 ml), with undisclosed formulations of a modified acrylate oligomer and monomer in combination with an epoxy monomer, a photo initiator, and additives.

The average device weight was 3 gr, which for the resin cost corresponded to 0.82 US$/device.

Surface roughness was measured with a stylus profiler (Dektak 6, Veeco Instrument Inc.) along 1mm tracks resolved in 6000 points. The average roughness was 182nm for the finished templates, which enables direct sealing with adhesive tape. Designs are conceived to exploit this aspect and simplify the fabrication to a single monolithic 3D printed body, or unibody [6], around which the device is assembled.

The same low surface roughness enabled efficient sealing with flat polydimethylsiloxane (PDMS) film, which was used to create the check-valves (Fig.1).

To fabricate the PDMS film, Dow Corning Sylgard 184 base and curing agent were mixed in 10:1 proportion and stirred in a cup for 2 min. The mixture was degassed in a desiccator connected to a rotary pump for 30 min, and subsequently poured on glass and cured at 65 °C for 2 h in an environmental oven (Gallem Kamp incubator). The PDMS elements of the check-valves were cut with a blade and placed in the unibody seats with a tweezer.

The devices were subsequently sealed with adhesive tape (3M Ruban Adhesive Scotch® Nastro Adhesive). Excess tape was trimmed with a cutter and the tape was pressed against the unibody surface with a cotton tip in order to eliminate trapped air in small blisters. The total fabrication time, including the PDMS assembly and sealing, to produce a device ready for testing was less than 30 min.

Device characterization

The device in Fig.1 was specifically designed to optically characterize the forward and backward check-valve behavior simultaneously.

The device was connected to two reservoirs containing rhodamine and fluorescein aqueous solutions. The reservoirs were connected to mechanical valves and to a manifold supplied by a pressure micro-injector (PMI-200, Dagan Corporation, USA). The injector delivered 100 ms pressure pulses to only one reservoir at time (the second one blocked with its corresponding valve), between 10 and 70psi, at 10 psi intervals.

Every time a pressure pulse was applied one check-valve was tested in the forward direction and simultaneously the opposite in the backward direction.

The device was video recorded during the experiment using a Samsung Galaxy Note 2, 8 Mpix rear side camera operating in full HD video acquisition (30 fps). Background illumination was provided by an iPod Touch screen (4th generation, 960 × 640 pixel screen resolution, with iOS 6) running Led Torch v1.37 app (www.smallte.ch), set to pure white (rgb 255, 255, 255).

For quantification purposes, the video was decomposed in individual frames using Adapter 2.1.0 for Mac. Each video frame corresponds to a 33.3 ms interval from the previous, which enabled measuring of the distance displaced by each pressure pulse by subtracting subsequent frames. Image J was used for image subtraction (Fig. 2) and to measured displaced distances.

Since the channel dimensions are known, the flow rates corresponding to the displacements could be calculated.

RESULTS AND DISCUSSION

Fig. 1 shows the ULOC design used for characterization of our passive check-valves. The 3D printed (Miicraft SL-3D printer [4], ~50x50x50µm resolution, <200 nm surface roughness in the x-y plane, 2299 US$) unibody integrates tight connectors to 1.5 mm ID silicone tubing and the seats for polydimethylsiloxane (PDMS) film valves working in opposition, thus allowing the simultaneous characterization of forward and backward behavior of each valve.

The valve seat is a 1 mm deep, 2 x 3 mm rectangular sector with a square 500 µm side orifice in one side. The 3D printer enables to create this asymmetric geometry where the PDMS sits. Due to the low surface roughness, a flat PDMS layer efficiently seals the orifice when pressurized in the backwards direction, whereas this element easily bends upwards when the flow comes from the orifice,

thus offering little forward resistance.

The nozzle connects to a 500 µm wide, 200 µm deep channels. The low surface roughness has additional benefits: it enables to simply seal the channels with a layer of adhesive tape, and this aspect is exploited in ULOC design. Simple sealing permits the fabrication of reliably formed and arbitrarily long channels, since they can be constructed with an open side, which secures the removal of unexposed resin [6]. In addition, the channel bottom enjoys the same surface finishing along its entire extension.
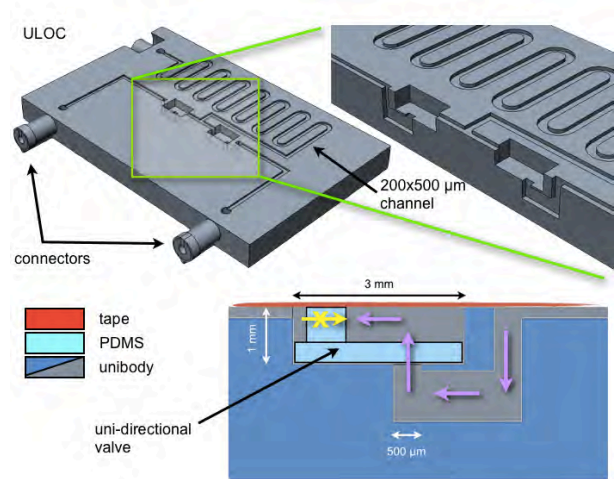
Fig. 1. CAD design of ULOC device for simultaneous characterization of two opposed check-valves. The unibody has integrated connectors and uses blade cut PDMS films as valves sitting on the 3D printed asymmetric geometric confinement. The device was sealed with regular adhesive tape, costs 0.82 US$ and took less than 30min to fabricate.

Valves were characterized using 100 ms pressure pulses delivered by a micro-injector. Pressures were increased in steps of 10 psi, from 10 psi to 70 psi and alternatively applied to the left and right valve, with the aid of two mechanical valves in line with the inputs.

The entire experiment was captured in video at 30fps, enabling the characterization of the flow rate by measuring the displacement of colored aqueous solutions with a 33.3 ms resolution. The quantification of the displacement was done by image subtraction of video frames corresponding to known time intervals.

Fig. 2 illustrates this procedure for 70 psi. At t_0 pressure is applied to the left valve, and 1 s later the yellow solution has reached almost the distal end of the device. The difference between these 2 frames highlights the displaced volume in blue, from which the displaced distance can be measured. This distance is then used to compute the average forward flow rate for this pressure.

Simultaneously, the backward behavior of the

opposed valve is captured. As can be seen in the subtracted image at 70 psi, no fluorescein solution has leaked into the rhodamine channel, corresponding to zero backward flow in this direction.

Only the PDMS seat chamber is flooded with fluorescein solution, thus defining a dead volume of about 3 µL in the present design. The motivation for the size of the PMDS elements relates to the smallest elements that can be easily cut by hand. Using a laser cutter could significantly reduce the dimension of these valves, and the consequent dead volume.

Although the long exit channel implies that essentially the 70 psi are applied to the valve in backward configuration, an additional experiment was run with the exit channel blocked, which confirmed zero leakage in the backward direction, up to 100 psi.
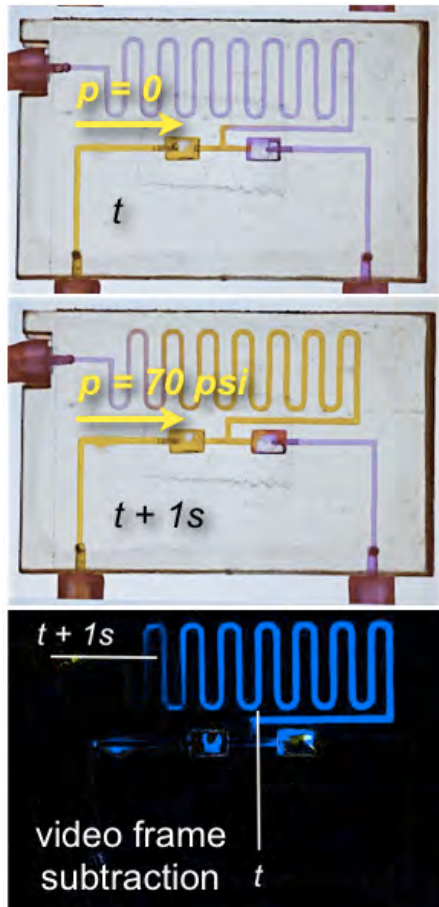

Fig. 2. Example of simultaneous forward and back-flow rate measurement after a 100ms pressure pulse of 70psi, in this case. The images correspond to two 1080p video frames separated by 1s interval, and the image subtraction was used to quantify the displaced volume and flow rate.

Fig. 3 collects the characterization of both valves under forward and back-pressures up to 70psi. Above 70 psi, the forward behavior departed from the exponential trend, whereas the back-flow of both valves remained identically zero up to 100psi.

The different forward response depends on the PDMS element width, which in one case was 500µm wider, and behaved according to similar valve designs [5]. The ability of this simple feature to introduce differences in forward response is the key to allow pressure regulated sequential injection in a compact and robust way.
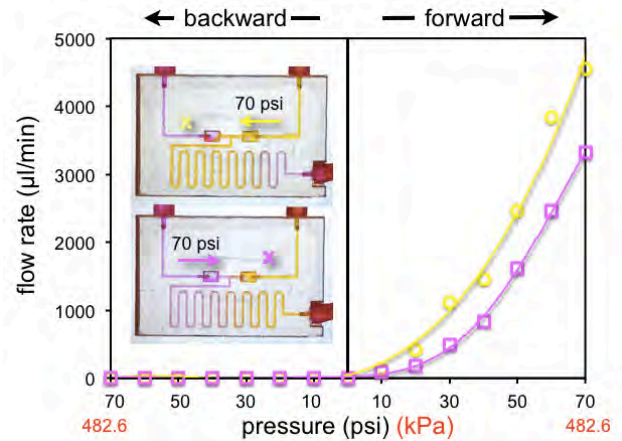
Fig. 3. Forward and back-pressure vs. flow rate behavior for both check-valves. The inset show selected video frames underscoring the strictly 0 backward flow rate of both valves at 70psi.

This work demonstrated a simple to fabricate crucial component for passive control, which can be integrated in disposable unibody-LOCs prototypes rendering these devices suitable with logic processing in autonomous or semi-autonomous configurations. [5]. Present dimensions are compatible with manual configuration of the PDMS elements, which were convenient for this proof of concept, but can be significantly reduced by molding them with the same 3D printing technology [6,7] or using classical methods.

CONCLUSIONS

Cost-effective fast-prototyping of check-valves integrated to unibody-LOC devices have been demonstrated and characterized.

Fabrication costs under one US$/prototype and fabrication times shorter than 30 min, as regularly present in 3D printed approaches [6,7] are also achievable in the present case.

Flexible PDMS elements provide variable forward flow resistance, according to described expectations [5] and complete PDMS/ULOC sealing is achieved in the backward direction up to 100 psi.

REFERENCES

[1] P. Preechaburana, M. Collado Gonzalez, A. Suska, D. Filippini, "Surface Plasmon resonance chemical sensing on cell phones", Angewandte Chemie 52, 2012, 11585-11588.

[2] R. Bharadwaj, A. Singh, Autonomous Lab-on-a-Chip Technologies, in Autonomous Sensor Networks: Collective Sensing Strategies for Analytical Purposes, D. Filippini (Ed.), Springer Series on Chemical Sensors and Biosensors (Series Ed. G. Urban), Volume 13, 2013, 217–236.

[3] B. Yang, Q. Lin, "Planar micro-check valves exploiting large polymer compliance", Sensors and Actuators A 134, 2007, 186–193.

[4] MiiCraft®, MiiCraft 3D Printer, http://www.miicraft.com/products/

[5] B. Mosadegh, C. Kuo, Y.Tung, Y. Torisawa, S. Takayama, "A monolithic passive check-valve for systematic control of temporal actuation in microfluidic devices", Twelfth International Conference on Miniaturized Systems for Chemistry and Life Sciences October 12 - 16, 2008, San Diego, California, USA, 826-828.

[6] G. Comina, A. Suska, D. Filippini, "Low cost lab-on-a-chip prototyping with a consumer grade 3D printer", Lab Chip 14, 2014, 2978-2982.

[7] G. Comina, A. Suska, D. Filippini, " PDMS lab-on-a-chip fabrication using 3D printed templates", Lab Chip 14, 2014, 424-430.

CONTACT

* D. Filippini, danfi@ifm.liu.se

2. Actuators   **Poster or Presentation**

EMULSION PREPARATION USING STAINLESS STEEL EDGE MICROFLUIDIC DEVICES

O. Bliznyuk, S. Sahin and K. Schroën
Food Process Engineering Group,
Wageningen University, The Netherlands

Large part of the food and cosmetic products we use on a daily base are emulsions: mixtures of two immiscible liquids stabilized by various emulsifiers. Most of the commercially available emulsions are prepared in large scale operations: first two liquids are mixed to create a coarse emulsion with relatively large droplets that is further refined in rotor-stator systems, high pressure or ultrasound homogenizers to the desired droplet size which is mostly in the submicrometer range. This approach requires a large energy input in production of the emulsions from which more than 90% may be lost in form of heat. The resulting emulsion is polydisperse which may be acceptable or even desirable in multiple applications, although monodisperse emulsions are intrinsically more stable. The large energy losses represent always a major drawback.

Producing emulsions using microfluidic devices offers an attractive alternative with such benefits as low energy consumption, related to the low pressures applied and narrow droplet size distributions. However, a major drawback of the existing microfluidic devices is that droplet production rate is too low to be used in large scale applications. Upscaling of the existing microfluidic devices through mass parallelization is one of the major challenges that the field of the microfluidics is facing today. One of the promising solutions is developing systems capable of producing multiple droplets simultaneously from a single droplet formation unit.

We have recently introduced a new spontaneous droplet formation technique called EDGE (Edge-based Droplet GEneration), where the dispersed phase is confined onto a shallow plateau before it reaches a deeper channel with the continuous phase where droplet formation starts (see Figures 1 and 2) [1]. The produced emulsions exhibit a coefficient of variation of less than 10% (very monodisperse) within a fairly large working pressure range for both silicon and glass chips. Moreover, the EDGE system appears to be fairly robust to fouling and can be easily parallelized on a chip level (see Figure 3; [2]). Nevertheless, in industrial applications metal and specifically stainless steel (SS) is required. Our recent experiments with the semi-metal Cu and CuNi EDGE systems (see Figure 4; [3]) shown how the performance of a system changes once metals are used [2], and interestingly enough the performance appears to be enhanced. Specifically, metal surface roughness and interactions with ingredients from the oil/emulsifier/water system used appear to be critical for a stable droplet formation process and deeper understanding of processes taking place in the vicinity of the surface is part of our investigations. Using stainless steel represents additional challenges due to the heterogeneous chemical composition of its surface. Furthermore, macroscopic parameters such as plateau length and width appear to have important impact on the resulting working range. We report successful formation of emulsions using semi metal SS EDGE and compare the obtained results with previously collected data on other types of chips, and relate that to scalability of the current design.

Word Count: 502
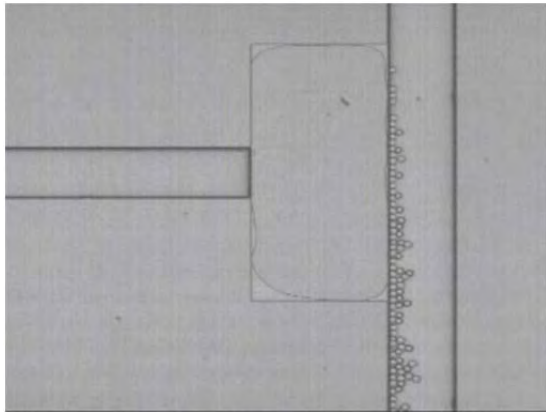
Figure 1: Microscopic image of and EDGE chip making monodisperse droplets
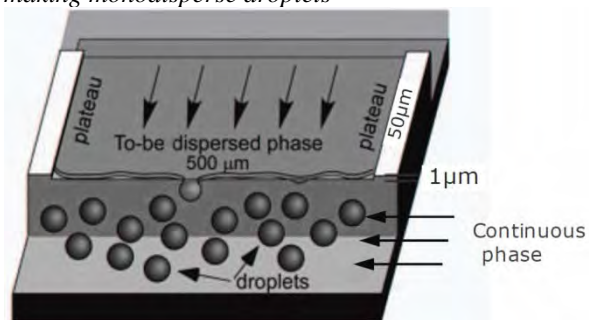
Figure 2. An artist's impression of the plateau at which droplet formation takes place
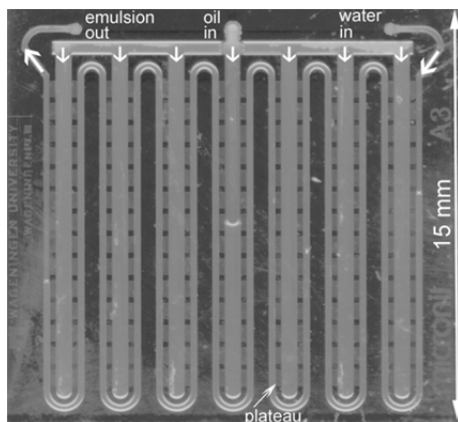
Figure 3. Up-scaled EDGE chip, containing many plateaus that all work in parallel

Figure 4. up-scaled EDGE chip containing copper parts as a first step toward fully metal emulsification micro systems

REFERENCES:

[1]   K. C. van Dijke, G. Veldhuis, K. Schroën, R. M. Boom, "Simultaneous formation of many droplets in a single microfluidic droplet formation unit", *AIChE Journal*, **2010**, 56, 833-836.

[2]   K. C. van Dijke, G. Veldhuis, K. Schroën, R. M. Boom, "Parallelized edge-based droplet generation (EDGE) devices", *Lab on a Chip* (**2009**), 9, 2824-2830.

[3]   A. A. Maan, K. Schroën, R. M. Boom, "Monodispersed water-in-oil emulsions prepared with semi-metal microfluidic EDGE systems", *Microfluid Nanofluid*, **2013**, 14, 187–196.

2. Actuators   Poster

FREQUENCY AND VOLTAGE CHARACTERISTICS OF A PIEZOELECTRIC DIAPHRAGM PUMP

T. Li, Y. Wang, L.B. Kong, H.H. Hng, and P.S. Lee
School of Materials Science and Engineering, Nanyang Technological University, Singapore

ABSTRACT

The piezoelectric diaphragm pump is small, compact and low cost. However, for precision liquid handling applications, the flow rate must be precise and accurate. In this paper, the accuracy and limitations of the piezoelectric pump were studied. Frequency and voltage are the two controlling parameters. It was found and concluded that the dependence of flow rate on frequency and voltage are nonlinear. With fine adjusting these two parameters, sub-mL/min flow rate and sub-(mL/min)/(Hz or Vpp) sensitivity can be obtained. The accuracy of the pump is largely limited by the response of the check valve, the vibration velocity and displacement of the piezoelectric actuator.

KEYWORDS

Piezoelectric; Pump; Actuator; Control; Frequency; Voltage

INTRODUCTION

For precision liquid handling applications, the syringe and peristaltic pumps have been widely used in the industries. However, these two types of pumps were usually bulky and unportable. Therefore, people are continuous to strive for low cost, compact and high efficiency pumps. The piezoelectric diaphragm pump shines a light on this issue. Compared with the syringe and peristaltic pump, the advantages of the piezoelectric pumps are small size, cheap, portable and low power consumption [1, 2]. Table 1 gives a comparison between different pumps.

Table 1. Comparison of different pumps

Type of pump	Parameters					
	Size	Power	Cost	Pressure ripple	Liquid cycling	Response speed
Peristaltic	Large	High	High	Yes high	Yes	Low
Syringe	Large	High	High	Rely on motor	No	Low
Piezoelectric	Small	Low	Low	Yes low	Yes	Fast

The piezoelectric pump has history for a few decades. Now, there are a few companies all over the world developing the pump for different market potentials. However, for practical applications, the flow rate of a pump shall be accurate, precise and stable. This paper hence studies the voltage and frequency characteristics of a piezoelectric diaphragm pump, which provides the basis for the control of flow rate. The pump used in this paper was developed in the previous references [1, 2]. It was diaphragm type and driven by a unimorph type piezoelectric actuator. The pump is able to generate a flow rate more than 100 mL/min under free flow condition and a pressure head up to 5 mH_2O. Another important feature of the pump is the stable output performance when subject to different external loadings.

EXPERIMENTAL

Fig. 1 shows the experimental setup in this paper. The frequency and voltage were controlled by a function generator (FG300) and a power amplifier (PZD2000). The inlet of the pump was connected to a water source and the outlet was connected to a micro channel. The channel has an inner diameter of 0.5 mm and length 250 mm. The flow rate was measured using a measuring cylinder. Practically, this setup is used in author's lab for nano materials study. The advantage of the piezo pump here is the quick response, capability of handling large quantity of liquid and recycling abilities.
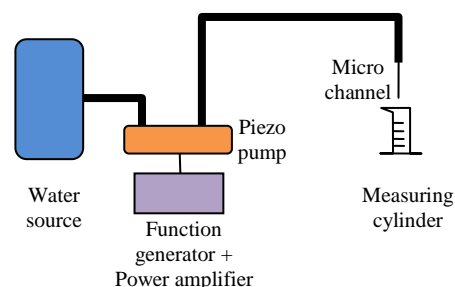
Figure 1: Experimental setup

RESULTS AND DISCUSSION

Figs. 2 and 3 show the experimental results. Fig. 2 is the frequency effect and Fig. 3 is the voltage effect. In Fig. 2, the voltage was fixed at 400 Vpp. Then, the frequency was varied from 200 Hz down to the cut-off frequency, below which there is no visible flow. The

maximum flow rate is about 25 mL/min, much lower than 100 mL/min mentioned earlier for the free flow condition. This is because of the resistance from the micro channel. From 200 Hz, the flow rate gradually decreases as the frequency reduces. However, the change rate or gradient of the flow rate is not linear and different in different frequency range as shown in the dashed line of Fig. 2. At both high and low frequency range, the gradient is smaller. However, in between, there is a peak. The peak value is around 0.35 (mL/min)/Hz, which means there is a 0.35 mL/min flow rate change when the frequency was adjusted by 1 Hz at the peak location. This phenomenon suggests that flow rate by frequency control is most sensitive in the peak range and less sensitive at two ends. The reason can be analyzed as: at higher frequency ends, the lower sensitivity can be attributed to the response of the check valve and vibration velocity of the piezo actuator [1, 2]. Due to the resonance properties of the check valve, the excitation of the piezo actuator and the response of the check valve may be out of phase, which results in the back flow leakage of the liquid. Furthermore, at higher frequencies, the vibration velocity of the actuator, which is proportional to the flow rate, does not increase anymore. The net result is the saturation and flattening of the flow rate, i.e. lower gradient or lower frequency sensitivity. On the other hand, at lower frequency end, the lower sensitivity might be due to the back flow of the liquid because of the slow closing of the check valves. In this test case, the minimum flow rate of 0.1 mL/min was obtained at 4 Hz. Below it, only water dancing was observed due to the valve limitation, i.e., in response to the on/off state of the valve, the forward flow and back flow are balanced. Compared with the syringe pump, which is able to reach μL/min accuracy, the accuracy of 0.1 mL/min, or sub-mL/min is not so high. However, it has been good enough for many practical applications, such as delivering continuous liquid for thin film fabrication.
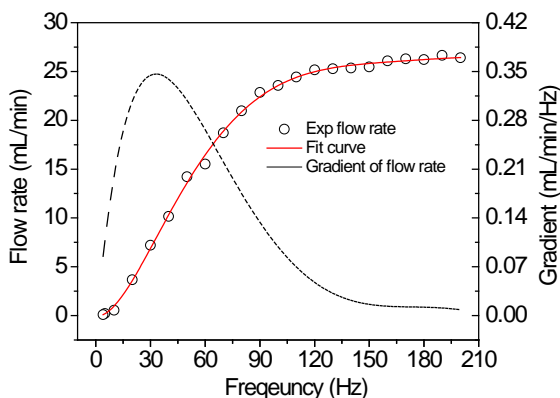
From the above analysis, it is known that to achieve the lowest flow rate, the frequency must be very low. This induces a problem, i.e., pressure ripple. This is because in the frequency control, the driving voltage of the actuator is 400 Vpp, i.e., maximum input, which produces large the displacement and liquid pressure. If the frequency is low at this time, the pressure ripple will become obvious and significant. For some applications, this periodical phenomenon might be a disadvantage. To minimize this, the voltage control is a choice.

Fig. 3 shows the result of voltage control. In this experiment, the frequency was fixed at 200 Hz. However, the voltage was decreased from 400 Vpp down to the cut-off voltage, which is 69.6 Vpp, below which there was no visible flow. At this voltage, 0.06 mL/min flow rate was obtained. Similarly as the frequency effect, there is a gradient or sensitivity peak on the flow rate curve. The maximum sensitivity is about 0.11 (mL/min)/Vpp. This observation can be explained as: the displacement of the piezo actuator and accordingly the liquid pressure inside the pump chamber is not varied linearly in response to the driving voltage. The liquid pressure is mainly determined by the displacement to pump chamber height ratio. At higher voltage end, the ratio is large and tends to saturate, which flattens the flow rate – voltage curve, as a result, decreases the gradient or sensitivity. On the contrary, at the lower voltage end, the ratio approaches zero. The pressure is smaller. Comparatively, the flow resistance becomes larger. Hence, the flow rate becomes flattened and shows lower gradient or sensitivity.
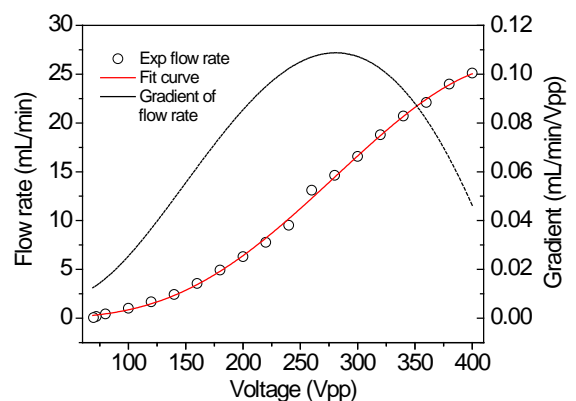

Figure 3. Voltage effect on the flow rate

From the above analysis, it is known that for the piezo pump used in this study, for both frequency control and voltage control, the accuracy of sub-mL/min flow rate can be obtained. The sensitivity is also in range of sub-(mL/min)/(Hz or Vpp). The flow

Figure 2: Frequency effect on the flow rate

rate curve is not linear in response to either frequency or driving voltage. In both cases, there are sensitivity peaks. For practical applications, ideally, the flow rate shall be able to be fine tuned by either frequency or voltages. From the earlier analysis, it is known that to achieve a lower flow rate, either parameter shall be small. This may produce problems, such as low pressure or pressure ripple, which may affect some applications. So to achieve the best control result, the high frequency and high voltage mechanism shall be applied. However, this is highly associated with the pump physical design parameters. So it will be achieved in the future work.

CONCLUSIONS

Both frequency and voltage can be used to control the flow rate. Sub-mL/min flow rate and sub-(mL/min)/(Hz or Vpp) tuning sensitivity can be achieved in the current study. The dependence of flow rate on frequency and voltage are not linear. There are sensitivity peaks. A few parameters will affect the accuracy of the flow rate, including the response of the valve, the actuator velocity, and the displacement to chamber depth ratio.

ACKNOWLEDGEMENT

REFERENCES

[1] T. Li, C.F. Goh, J. Ma, "Development of Piezoelectric Diaphragm Pump", Solid State Phenomena, Vol.185, pp.18-20, 2012.

[2] T. Li, Y. Wang, P.S. Lee, "Power Transducer and Piezoelectric Pump: Modeling, Simulation, Design and Characterization", LAP Lambert academic publishing, 2012.

CONTACT

* T. Li, TLI@ntu.edu.sg

2. Actuators   **Poster**

A STUDY ON SINGLE AND MULTILAYER MICROVALVES AND THEIR APPLICATION TO ANALYZE INFECTION PROBABILITY OF *P. FALCIPARUM*

W. Zhai, E. Nugent, A. Grigore and P. Cicuta[1]
[1] University of Cambridge, Cavendish Laboratory, Cambridge, UK

Human malaria is caused by one of the 4 species of malaria parasites, of which *P.falciparum* is the most severe. Recent studies of the infected red blood cells (iRBCs) in microfluidic channels have indicated that the biophysical and biochemical changes in the iRBCs play a major role [1] [2]. Microfluidic devices can offer dynamic constrictions for cells in the channel [3], and the flow rate of iRBCs can be addressed directly using our device proposed for malaria infection probability studies. Moreover, the PDMS material displays higher elastic property and is gas permeable, which allows longer time observation of the interactions between parasites and RBCs [4]. Overall, microfluidic devices allow high throughput studies on a large number of samples containing malaria parasite and erythrocytes.

Introducing microvalves into microfluidic devices enables the control of the fluid flow for complex functionalities [5]. In this paper, we study the pneumatically driven single and multi-layer microvalves and explore their potential to be incorporated into microfluidic designs those study the infection probability of *Plasmodium (P) falciparum*.
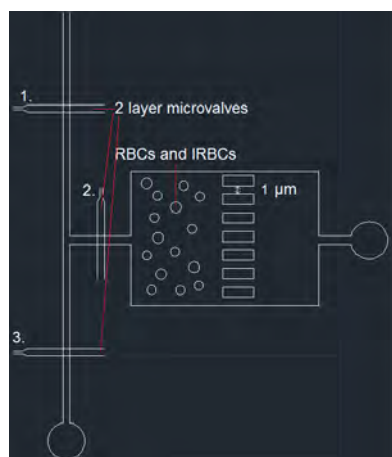

Figure 1: Preliminary design of the 2 layer microvalves for measuring the infection probability of malaria parasites. With valves 1 and 2 open, and valve 3 closed, a mixture of healthy and infected RBCs are directed to a capture chamber, where infection probability can be computed as a function of the flow rate. Diagram not drawn to scale.

Two types of pneumatic microvalves were tested out with the microfluidic design [5] [6]. Normally-open (N.O.) 1 layer valves were constructed with a PDMS base/curing agent ratio of 20:1 to ensure a flexible membrane that can be easily deflected with an applied pressure. N.O. 1 layer valves sealing the flow channel by applying a fluid pressure is shown in Fig. 2. Thus

by applying and removing the control channel pressure, we can control the fluid flow in a section of the channel, and its applications will be discussed in the later sections.
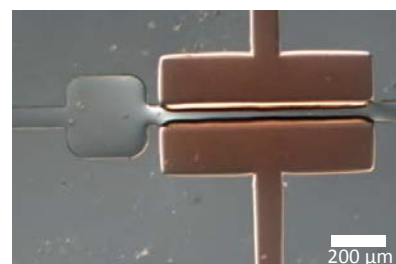
Figure 2: Image of N.O. 1 layer valve closing at 500 µl/min.

Though N.O. 1 layer valves avoid the complication in multilayer bonding and assembly, it does not ensure complete sealing for wider channels. Normally-open 2 layer valves shown in Fig. 3 offer a higher flexibility in terms of channel width. It is also considered as the primary design to be implemented into malaria studies, as it could selectively close a section of the flow channel, allowing cells at a particular flow rate to be diverted into a capture chamber where they could be further analysed to calculate infection rates. The pressure applied to the control channel can be adjusted using a Fluigent set-up with input pressure ranging from 0.1 to 7 bars. Thus, by employing the N.O. 2 layer valves, we could control the routing and the separation of the fluid containing malaria parasites and erythrocytes in the microfluidic device.
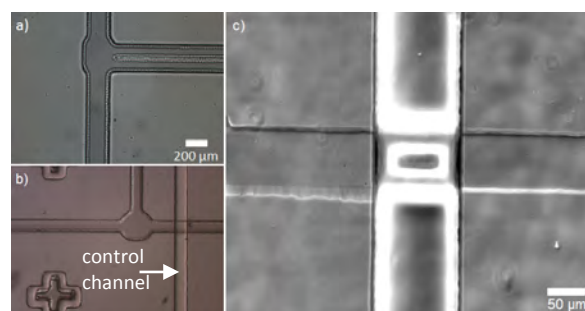
Figure 3: Images of N.O. 2 layer valves a) flow channel, b) microscope aligned control channel on top of flow channel and c) N.O. 2 layer control channel sealing the flow channel at 2 bar.

For N.O. 1 layer valves, as the pressure is applied and removed from the control channel, it closes and re-opens corresponding. Thus, this set-up offers a novel application by dynamically introducing symmetric or asymmetric constrictions to mimic blood vessel

blockages. As the fluid pressure was applied and removed from the control channel, the flow of the RBCs changed correspondingly as shown in Fig. 4. This proves that our single layer microvalve device is able to controllably introduce and release a blockage, and thus enables us to observe the change in infection probability as a function of the flow rate. By counting the percentage of infection of the healthy RBCs in the capture chamber, we could evaluate the effect of introducing constrictions on the probability of infection of malaria parasites in the future.
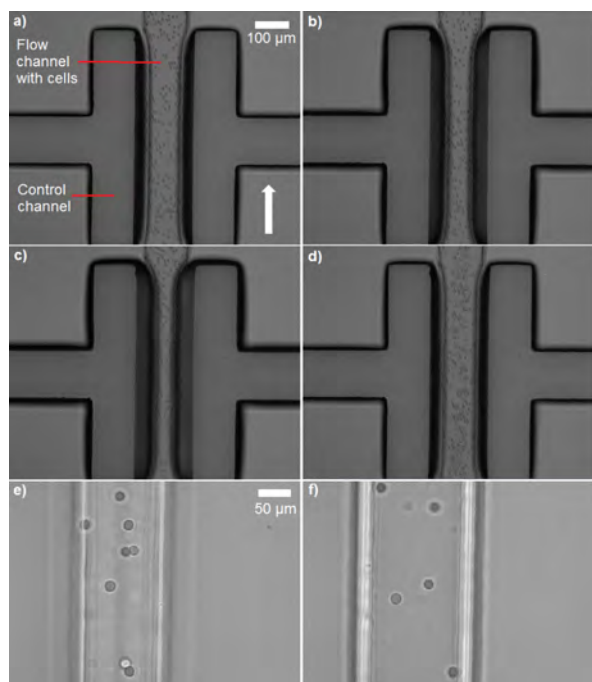
Figure 4. A sequence of images displaying a change in the concentration of red blood cells in a section of the flow channel when the pressure is applied and withdrawn from the control channel. a) to c) die is pumped into the control channel at a flow rate of 800 μl/minute, d) pressure was withdrawn and e), f) higher resolution images showing RBCs clamped in between control channels and the concentration of cells decreased as the pressure was released in f).

Word Count: 638

REFERENCES:

[1] H. Fujioka, "Malaria Parasite and Disease – Structure and Lifestyle", *Chem. Immunol.*, 2002, Vol.80, pp1-26
[2] A. Crick *et al.*, "An automated live imaging platform for studying merozoite egress-invasion in malaria cultures", *Biophys. J.,* 2013, 104(5) pp.997-1005
[3] J. P. Shelby *et al.*, A microfluidic model for single-cell capillary obstruction by plasmodium falciparum-infected erythrocytes", PNAS, 2003, 100, pp.14618-14622
[4] M. Antia, "Microfluidic Approach to Malaria Pathogenesis", *Cell. Microbiol*, 2008, Vol.10, pp1968-1974
[5] A.K. Au, H. Lai, E.R. Utela and A. Folch, "Microvalves and Micropumps for BioMEMS", *Micromachines*, 2011, Vol.2, pp.179-220
[6] M.A. Unger et al., "Monolithic Microfabricated Valves and Pumps by Multilayer Soft Lithography", Science, 2000, Vol. 288, pp113-116

4. Fluid control systems

SMART OPEN MICROFLUIDICS: AN AUTOMATED PLATFORM FOR THE DYNAMIC GENERATION OF FLUIDIC STRUCTURES DOWN TO THE SUB-nL-RANGE

T. Gleichmann[1], L. Gutzweiler[1], P. Koltay[1,2], R. Zengerle[1] and L. Riegger[1,2]
[1] University of Freiburg, Lab for MEMS Applications, Freiburg, Germany
[2] BioFluidix GmbH, Freiburg, Germany

ABSTRACT

We developed an open microfluidic (OM) [1] platform for the computer-assisted generation of fluidic structures virtually on demand. On using a set of piezo-driven dispenser modules, namely PipeJet[TM] [2] and Nano-Jet [3] (BioFluidix GmbH, Freiburg, Germany), and a peristaltic pump as well the system enables handling of liquids from the mL- down to the pL-range covering up to nine orders of magnitude in volume. The integration of multiple structuring methods like semi-contact writing (SCW) or non-contact dispensing allows for processing droplet arrays or continuous geometries of desired dimension, using low to medium viscous fluids and a number of different substrate materials.

KEYWORDS

Open microfluidics, non-contact dispensing, semi-contact writing, picoliter injection

MOTIVATION & INTRODUCTION

Since most microfluidic chips comprise a repertoire of common structures and operational units like reservoirs or channels one drawback is the necessity to structure such elements into silicon/glass or polymers. Thus，if a design flaw becomes obvious, redesign of the underlying structure is required and often accompanied with a time consuming or even expensive process chain.

Open microfluidics counteracts this disadvantage by creating fluidic elements on an open surface providing the ability of dynamic structure design and modifications. For this purpose we developed an integrated device to design, redesign or simply to repeat the application of almost arbitrary fluidic structures giving users the ability to test new fluidic approaches or to establish them using this platform.

While certainly not any microfluidic device or mechanism can be processed by such a system, a few promising applications have been identified covering PDMS prototyping, capillary gel electrophoresis or droplet-based PCR.

DEVICE CONFIGURATION

Serving as platform for process-automation, the 3-axis manipulator Biospot-BT600[TM] (Bio-Fluidix GmbH, Freiburg, Germany), was modified towards OM-requirements (Fig. 1 A). The axes-bound printhead was equipped with a 5-dispenser-slot to install either PipeJet[TM]- or Nano-Jet-modules in accordance to properties and volumes of desired liquids (Fig. 2 B). Based on a piezo-driven piston droplets are released *via* direct liquid displacement either through a poly-imide tube nozzle (PipeJet[TM]) of varying diameter addressing the nL-range from 200 nL to about 2 nL or a silicon micro-machined nozzle of a chip (Nano-Jet) with nozzle-diameters of 100x70 µm² down to 10x20 µm² covering volume-ranges of several 100 pL down to 30 pL. While Pipe-Jet[TM]- and Nano-Jet-modules address the range from nL to pL, larger volumes can be released by an integrated peristaltic pump exhibiting a flow rate up to 50 ml/min (Fig. 1 C).

Moreover, single dispenser can be moved pneumatically along a second z-axis to handle several PipeJet[TM]-modules simultaneously required for semi-contact writing as explained later on [4][5].

Two high-resolution cameras (5 Mpx) were introduced for process observation but also giving the opportunity to acquire visual data. The substrate – a planar polymer or glass slide for instance – is mounted on the substrate carrier which encloses a FPH1-1270AC Peltier element (Z-Max Co. Ltd., Tokyo, Japan) to adjust the surface temperature between -5°C and 60°C. As surface-cooling helps to reduce evaporation, possible issues due to condensation are avoided by a dew-point-based feedback-regulation. Heat is drained both passively and actively by a heat-sink and a multi-fan rack as well. In order to ensure a planar processing surface the substrate is fixed by vacuum aspiration. A three-point screw adjustment with fine threads enables substrate leveling to set a constant dispenser-to-substrate distance supported by lateral camera-observation along the x-y plane.
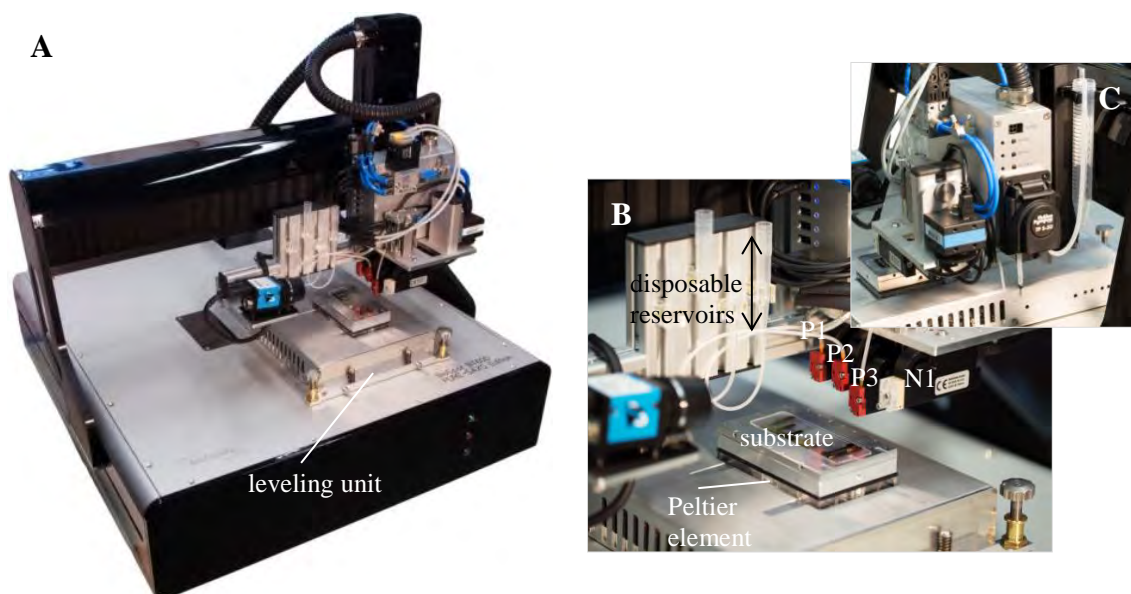
Figure 1: Custom made liquid handling device configured for electrophoretic applications. (A) Total view of the processing platform: a BioSpot-BT600^{TM} (Biofluidix GmbH) serves as basic 3-axis manipulator. Substrate carrier is fixed by a spring-loaded passive 3-point leveling unit. (B) Close-up of the OM-adapted print-head and substrate carrier including a pL-nL-dispenser rack (1x fixed PipeJet^{TM}: P1, 2x lowerable PipeJet^{TM}: P2/P3, 1x Nano-Jet: N1, 1x open slot), an associated reservoir holder and a high-resolution camera for vertical alignment. Planar substrates are fixed by vacuum aspiration on a temperature-adjustable aluminum surface (88x54 mm). (C) Peristaltic pump with disposable reservoir for high-volume supply and second camera for process observation and horizontal alignment.

PROCESSING
System Initialization

Desired substrates with a maximum area of 88x54 mm² (just restricted by current design) are mounted onto the substrate carrier workspace. Vacuum aspiration is turned on to fix flexible substrates onto the metal surface. Dispensers are supplied with liquids *via* silicone tubing and standard pipet tips as reservoirs for PipeJet^{TM}-modules, the integrated reservoir of the Nano-Jet cartridge (80 µL) or 15-mL Falcon tubes connected to the pump. Especially when working with multiple PipeJet^{TM}-modules and tubes of different length an adequate z-alignment is important. Working with multiple fluids one would like to stack structures or inject droplets into an existing reservoir or channel, inherently possible with the presented device. For this purpose, a precise x-y alignment of each dispenser module to a reference point and thus to each other is conducted. Both vertical (z) and horizontal alignment (x-y) can be realized by camera-based optical inspection or image pattern recognition.

Fluidic elements are designed using an integrated visual batch-processor were the user is able to define droplet-, plane- or channel-based structures or even to combine them. Once the desired surface temperature is reached the batch can be executed to process the fluidic elements previously defined.

Generating Fluidic Structures

Fluidic structures are applied onto substrates either as single droplets of dynamic volume dispensed in a non-contact manner or deposited forming a liquid bridge between the pipe-nozzle of a PipeJet^{TM}-dispenser and the substrate surface (Fig. 2). The later method, namely SCW enables the generation of arbitrary planar structures as channels or filaments by continuous capillary flow out of the dispenser nozzle while displacing the axis-mounted dispenser. Usually supported by a software integrated batch processor, even more complex structures as grids or reservoir coupled injection channels as well as arbitrary sized droplet-arrays can be generated (Fig. 3). Moreover, planar filled areas of particular extension are applied by writing overlapping channel-structures side-by-side. Hydrostatic pressure can be adjusted by raising or lowering dispenser-associated reservoirs. By additionally adapting displacement velocity the flow rates affecting channel diameter can be set dynamically. Especially when handling aqueous solutions in the sub-µL range evaporation might cause issues as open fluidic compartments become unstable. For this purpose, if necessary, OM structures are
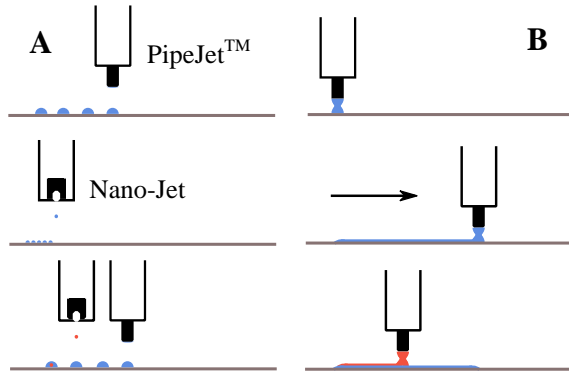
Figure 2: Strategies for open fluidic structure design. (A) Droplet ejection in non-contact mode either by PipeJet[TM] or Nano-Jet dispenser. The bottom sketch exemplifies a combined use of both dispenser types: pL-injection into nL-droplets. (B) Once a liquid bridge is formed (top) between the substrate and the pipe-nozzle dispenser displacement allows for the generation of continuous structures (middle). Stacking of structures (bottom) is used to protect functional fluidic elements from evaporation or to enlarge dimensions.

Figure 3: Examples of open microfluidic structures generated with the presented device. (A) Semi-contact written grid structure of alginate on polyimide used as delineation for cell culturing. (B) DMSO volume-gradient array on cooled cyclic-olefin copolymer foil (~10 °C). Array was generated in non-contact mode using a Nano-Jet-dispenser. Droplets are multitudes of 130 pL starting with n=1, where n is the number of single-spot dispensed droplets, up to n=400 corresponding to an overall volume of about 50 nL. For purpose of illustration a black polyimide foil was inserted between substrate foil and mounting plate.

covered with immiscible liquids like protective oil layers deposited by the peristaltic pump supplementary to the Peltier-cooled surface.

APPLICATION EXAMPLES

To demonstrate system capabilities we designed and processed a variety of structures of different size and geometries using SCW, non-contact dispensing or droplet injection. We combined aqueous solutions, oil and gel-like fluids upon polymer or glass substrates.

Figure 3 exemplifies two common structures. An alginate-grid was designed to form squared traps for cell-culturing (Fig. 3A) by SCW (tube diameter: 200 µm). Reducing the pitch down to 200 µm between two parallel channels results in stable squares with wall heights of about 7 µm (width: 100 µm / 10 stacks) after processing and up to 50 times higher after rehydration in a CaCl-solution (alginate-structure previously dried). DMSO was used to print a 19x22 droplet array by non-contact dispensing with a 20x40 µm² nozzle-chip of a Nano-Jet-module at a nozzle-to-surface distance of ~1 mm (Fig. 3B). Volumes of single droplets were determined by gravimetric measurement techniques as shown by *Liang* et al. [5].

Finally, combined PipeJet[TM] and Nano-Jet droplet dispensing was used to demonstrate the ability for OM droplet-based PCR by droplet encapsulation. An arbitrary sized array (here 1000) of oil droplets (~5 nL each) was applied on

standard microscopic glass slides first using a 200 µm tube of a PipeJet[TM]-dispenser (Fig. 4A). Simulating the PCR-reaction mixture a Nano-Jet
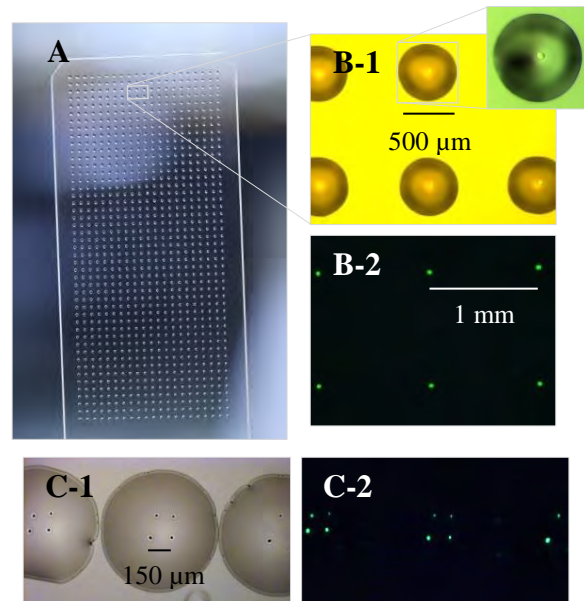
Figure 4: Precise nL-injection of an aqueous Fluorescein solution into oil arrays printed on standard microscopic glass slides. (A) 1000x-spot array applied with a PipeJet[TM]; 0.5 mm nozzle-to-surface distance. (B-1) Close-up of (A) at incident light acquired by inverted fluorescence microscopy. (B-2) Close-up of (A) without incident light and fluorescence excitation of the enclosed ~60 pL spots previously injected by a Nano-Jet-dispenser. (C-1)(C-2) Nested arrays demonstrated by inverted fluorescence microscopy. The continuous shift between the upper and lower row might be owed to an axis backlash which can be compensated by optimizing the batch processing.

equipped with a 20x20 μm² nozzle was used to inject an aqueous solution of about ~60 pL into the oil droplets forming distinct phase boundaries (Fig. 4B-1, close-up). Here, we used a 3 μM Fluorescein solution from Fluorescein sodium salt (Sigma-Aldrich Inc., Saint-Louis, USA) for better visualization of the injection precision, exciting and observing the oil-enclosed droplets with a OLYMPUS CKX41 (Olympus Corporation, Tokyo, Japan) inverted fluorescence microscope (Fig. 4B-2). Increasing the level of complexity nested arrays of oil and the mentioned Fluorescein solution were processed (Fig. 4 C-1 & C-2), thus one can imagine to place several compartments of a single reaction next to each other. The reaction is started by fusing those compartments by gentle vibrations. Due to the integrated Peltier-cooling down to sub-zero degrees nested arrays of such a composition could be frozen (using DMSO for cryo-conservation in case of proteins or cells) and stored subsequently at e.g. -80 °C for later use.

CONCLUSION & OUTLOOK

Taken together the OM-platform presented here provides a plurality of integrated and combinable features to handle liquids. Among others:

- three species of liquid dispenser covering 9 orders of magnitude in volume
- on demand design of fluidic structures in non-contact or semi-contact mode
- processing liquids of various physicochemical properties like low to medium viscosity
- using substrates of diverse materials in accordance with the demands of the user e.g. to process microarrays

Based on the work of *Tanguy* et. al. [6] open capillary gel-electrophoresis of proteins should be realized in the near future using the open microfluidic platform. Further applications might include medium to high-throughput droplet-based PCR – even of single cells [7] – using droplet-injection as demonstrated here.

ACKNOWLEDGEMENT

REFERENCES

[1] T. Pfohl, F. Mugele, R. Seemann and S. Herminghaus. Trends in Microfluidics with Complex Fluids, ChemPhysChem, 2003.

[2] W. Streule, T. Lindemann, G. Birkle, R. Zengerle, P. Koltay. PipeJet: A Simple Disposable Dispenser for the Nano- and Microliter Range, Journal of the Association for Laboratory Automation (JALA), 2004.

[3] P. Koltay, G. Birkle, R. Steger, H. Kuhn, M. Mayer, H. Sandmaier, R. Zengerle. „Highly Parallel and Accurate Nanoliter Dispenser for High-Throughput-Synthesis of Chemical Compounds", IMEMS Workshop, Singapore, July 4-6, 2001.

[4] L. Gutzweiler, F. Stumpf, L. Riegger, P. Koltay, R. Zengerle, L. Tanguy, „A flexible method for rapid-prototyping of PDMS microfluidic chips using direct-written polymer-master-structures", *MicroTAS '13 Conference, Freiburg, Germany,* October 27-31, 2013 , pp.1409 – 1411.

[5] D. Liang, C. Steinert, S. Bammesberger, L. Tanguy, A. Ernst, R. Zengerle, P. Koltay, „Novel gravimetric measuremnt technigue for quantitative volume calibration in the sub-microliter range! ‚Measurement Science and Technology, 2013.

[6] L. Tanguy, L. Gutzweiler, P. Koltay, R. Zengerle, L. Riegger, "On-demand electrophoretic separation of DNA in written gel lines on planar substrates", *Transducer '13 Conference, Barcelona, Spain,* June 16-18, 2013, pp.1223 – 1226.

[7] A. Gross, J. Schöndube, S. Niekrawitz, W. Streule, L. Riegger, R. Zengerle, P. Koltay, „Single-Cell Printer: Automated, On Demand, and Label Free" , Journal of the Association for Laboratory Automation (JALA), 2013.

CONTACT
* T. Gleichmann tobias.gleichmann@imtek.de

4. Systems

LOW FLOW LIQUID CALIBRATION SETUP

*T.H. Platenkamp[*1], W. Sparreboom[1], G.H.J.M. Ratering[1], M.R. Katerberg[1] and J.C. Lötters[1,2]*
[1] Bronkhorst High-Tech BV, Ruurlo, The Netherlands
[2] University of Twente, Transducers Science and Technology, Enschede, The Netherlands

ABSTRACT
This article describes a primary calibration setup and its uncertainty for low flow liquid calibrations at Bronkhorst High-Tech, which is traceable to international standards. It will be used to calibrate reference flow meters from 1 to 200 g/h. By setting up an uncertainty budget for this setup, the calibration of the instruments will be traceable. The uncertainty budget consists of mass, time and mass flow uncertainties/corrections that need to be taken in account for determining the real mass flow. By participating in an laboratory intercomparison the accuracy and calculated uncertainty of this setup is traceable to international standards at several European national metrology labs.

KEYWORDS
Liquid mass flow, calibration, uncertainty budget.

INTRODUCTION
Worldwide there is an increasing demand for low flow liquid mass flow meters. Because applications require traceable accuracy of these instruments, they need to be calibrated by a reference that is traceable to a primary standard. Today there is no primary standard for low liquid mass flows smaller than 200 g/h. Therefore, we started to develop a setup that is able to calibrate mass flow meters in the range of 1 to 200 g/h with a traceable uncertainty. A unique feature in this setup is that the DUT (device under test) itself will establish a stable flow.

THEORY
From mass to mass flow
In the calibration setup a high precision balance is used as mass flow reference. This is done by differentiating its measured mass (Δm) to measured time (Δt). The resulting output is mass flow ($\dot{m}$), as shown in equation (1) below.

$$\dot{m} = \lim_{\Delta t \to 0} \frac{\Delta m}{\Delta t} = \frac{m_r}{t_r} \qquad (1)$$

Where m_r and t_r are respectively the reference mass and reference time.

An RS232 balance interface is used between the balance and the data acquisition computer. This interface combines each mass sample with the correct time sample, resulting in a mass flow. This way the flow of the DUT (device under test) can be directly compared to the flow indicated by the reference (balance). The method of directly comparing measured flow to reference flow is called "flying-method". The uncertainty on mass and time of the balance is known and used to determine the total uncertainty of the setup.

Actual mass flow and uncertainty
Besides the mass- and time- (m_r and t_r) uncertainties of the reference, there are also extra mass flow uncertainties ($\dot{m}_{unc}$) due to environmental effects and interactions between tube and fluid. An absolute correction on mass is needed due to buoyant interaction forces [1] (m_{cor}). The actual mass flow is then given by equation (2) below;

$$\dot{m} = \left(\frac{m_r + m_{cor}}{t_r}\right) \pm \dot{m}_{unc} \qquad (2)$$

As can be seen in the equation above the actual mass flow consists of four components; m_r, m_{cor}, t_r and $\dot{m}_{unc}$. Therefore the uncertainty budget is divided into four groups. Each group has its own uncertainties. The uncertainties are combined into a total uncertainty [2] on mass flow with a confidence level of k=2 (95%).

Buoyant interaction forces
The standard Buoyancy correction due to density differences between calibration and measurement (m_{cor1}) is shown in the equation below. Besides the initial mass (m_r), the correction depends on the difference in mass- and air density during calibration (ρ_{mass_cal} and ρ_{air_cal}) and measurement (ρ_{object} and ρ_{air}). During calibration the weighted mass is a calibrated weight. During measurement the weighted mass is a beaker with liquid, called "object" in equation (3) below.

$$m_{cor1} = \frac{m_r * \left(1 - \frac{\rho_{air\_cal}}{\rho_{mass\_cal}}\right)}{\left(1 - \frac{\rho_{air}}{\rho_{object}}\right)} - m_r \qquad (3)$$

Because a tube is used to deliver the liquid in the beaker on the balance and is partly submerged in the liquid, another buoyant force will make the weighted object appear heavier. For a submerged body the buoyancy force of the fluid is equal to the weight of displaced fluid [1]. Because the tube is fixed and the surface of beaker and tube are constant, the extra weight will rise constantly when the liquid rises in the beaker. This results in a second mass correction needed to determine the actual mass. The correction depends on the difference between tube- and beaker surface (A_{tube} and A_{beaker}) and the initial mass (m_r).

$$m_{cor2} = (m_r * (1 - \frac{A_{tube}}{A_{beaker}})) - m_r \qquad (4)$$

Combining equation (3) and (4) results in a total mass correction (m_{cor}) for the collected mass (equation (5)).

$$m_{cor} = \frac{m_r * \left(1 - \frac{\rho_{air-cal}}{\rho_{mass-cal}}\right)}{\left(1 - \frac{\rho_{air}}{\rho_{object}}\right)} * \left(1 - \frac{A_{tube}}{A_{beaker}}\right) \quad (5)$$

SETUP

The setup consists of a pressurized liquid tank, filter, degasser, pressure sensor, DUT with control valve, balance and valves with small internal volume. All parts in the setup are connected by 1/16" tubes. In Figure 1 a schematic of the setup is shown. It is placed on a granite table with shock absorbing blocks to reduce vibration interference from the environment. The complete setup with table is installed in a box to reduce fast temperature changes.

Pure liquid

The flow path situated before the control valve of the DUT consists of parts to create a pure liquid flow; this is needed to create a stable flow.

Particle contamination in the liquid is prevented by using demineralized water (grade 3) and a 0.5μm SS filter. The filter has a large surface to reduce pressure drop (Figure 2).

Figure 2. Low delta p 0.5μm SS filter with 1/16" SS connectors.

Besides possible contamination by particles, the liquid is also contaminated by dissolved gas. As the dissolved gas undergoes a pressure drop the gas bubbles will expand and could get stuck in the flow path acting as a hydraulic spring damper. This causes major flow errors between DUT and reference. By pressurizing the liquid with Helium (low solubility in water) and the use of a degasser, the amount of dissolved gas in the liquid is reduced to a minimum.
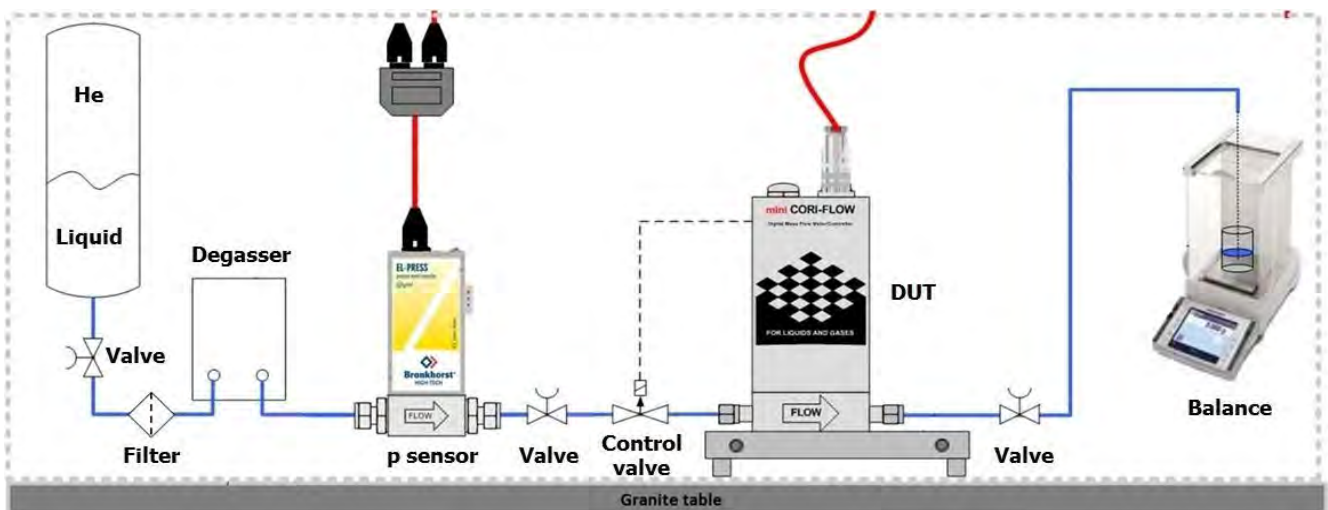

Figure 1. Schematic of the setup

Stable mass flow

A stable mass flow is created by using the DUT to control the valve. The control valve is situated upstream from the DUT to eliminate its influence on the comparison between DUT and balance. This is a unique way of establishing a stable low liquid mass flow during calibration. To prevent control instability of the flow, pressure fluctuations may not exceed 5 mbar/min. The flow path downstream from the control valve is led, by a small tube, to the balance. The tube transports the liquid into a beaker on the balance. The outlet of the tube must stay under the water surface in the beaker to prevent droplet formation. Doing so results in a continuous and stable flow towards the balance. The uncertainty budget is based on equation (2) and the flow path downstream from the control valve.

Environmental influences

The environmental temperature can have a big influence on measurements during calibration. Liquid and tube volumes that shrink or expand in a short time will create flow fluctuations, resulting in flow errors between DUT and reference. Because fast temperature changes have a big influence, the setup is fitted in a box that prevents this. Besides keeping the temperature stable, the liquid volumes in the setup should be kept small as possible to reduce the temperature influence on the mass flow measurement even further. Typical changes measured inside the box of the setup in the lab are shown in Figure 3.
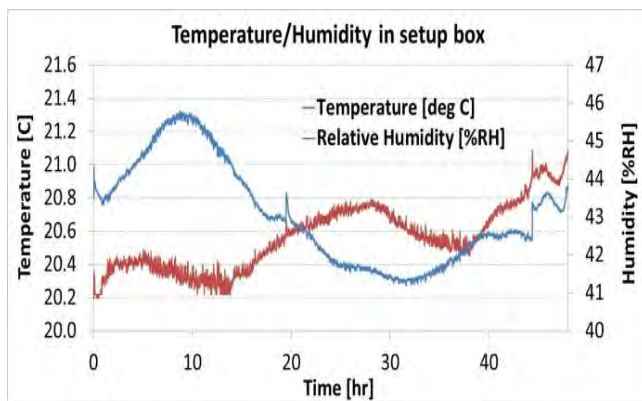

Figure 3. Temperature and humidity in the lab. The temperature is stable within 1 degrees Celsius over 48 hours. It shows no fast temperature changes.

INTERCOMPARISON RESULTS

By participation in an intercomparison between national labs, this setup and method has been validated [3]. In this comparison two Bronkhorst flow meters (M12p and M13) where used as transfer standard. The M12p was used in the flow range 2 to 200 g/h, the M13 for 200 g/h. The average result of three participating labs is compared with the average result of Bronkhorst and its trumpet curve (Figure 4).
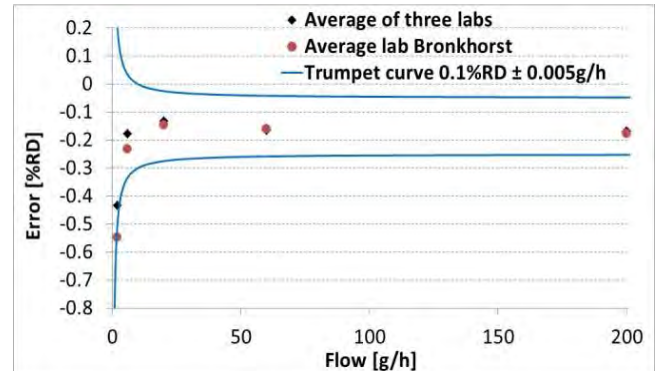
Figure 4. Comparison of average flow error for the M12p.

This trumpet curve shows the boundaries of the accuracy ± zero stability. All points within it meet the stated accuracy and zero stability. The intercomparison showed that the measurements and accompanying uncertainty budget are consistent (Table 1). The E_n values are the result of comparing the mean value obtained by this setup to the mean value of all labs. This value should be < 1 to be consistent.

Table 1. Average results and E_n values for the M12p in the intercomparison.

Bronkhorst results

flow rate (g/h)	error (%)	uncertainty (%)	E_n value (-)
2	-0.55	0.31	0.05
6	-0.23	0.11	0.21
20	-0.14	0.06	0.05
60	-0.16	0.06	0.10
200	-0.17	0.10	0.14

By comparing our measured points on each flow it is shown that the repeatability is well within the uncertainty of the setup and trumpet curve of 0.1%RD ±0.005 g/h (Figure 5).
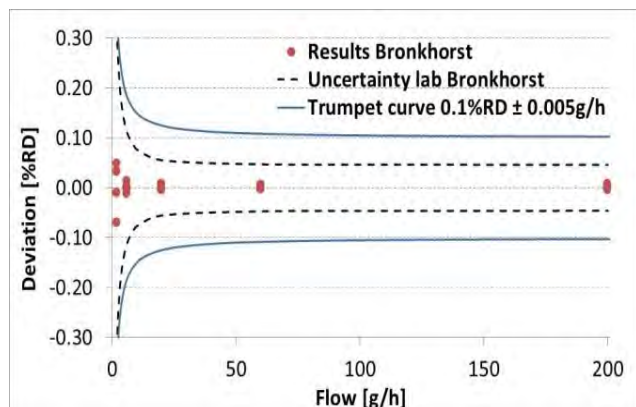
Figure 5. Repeatability of the M12p measured by Bronkhorst.

It shows that the repeatability is well within the given uncertainty. The uncertainty is within the trumpet curve of 0.1%RD ±0.005g/h, which will be used as reference for calibrations. Both flow meters (M12p and M13) are found repeatable and reproducible enough as transfer standard [4] (Table 1 and Figure 5).

CONCLUSION

A low flow liquid setup is build and validated. With this setup one is able to perform calibrations on mass flow meters in the range from 1 to 200 g/h. It is found that the uncertainty of this setup is within a 0.1%RD ±0.005 g/h trumpet curve with a 95% confidence level. This is validated by the results of the intercomparison, in which Bronkhorst participated. The M12p and M13 are both found repeatable and reproducible enough as transfer standards.

REFERENCES:

[1] Robert W. Fox, Alan T. McDonald, Philip J. Pritchard, "Introduction to Fluid Mechanics", 6th edition, 2004.

[2] Iosif I. Shinder, Iryna V. Marfenko., "NIST calibration services for water flowmeters", *water flow calibrationfacility,* special publication 250, August 2006.

[3] Peter Lucas, "MeDD - Task 1.1. Intercomparison supplement report", May 2014.

[4] Christopher David, "MeDD - Task 1.1. Intercomparison report", December 2013.

CONTACT

*T.H. Platenkamp, t.platenkamp@bronkhorst.com

4. Systems   **Poster**

LOW FLOW CORIOLIS FLOW CONTROLLER WITH PIEZO OPERATED CONTROL VALVE

M.R. Katerberg[1], G.H.J.M. Ratering[1], T.H. Platenkamp[1]
J.W. van de Geest[1], S. Klein Hesselink[1], J.C. Lötters[1,2]
[1] Bronkhorst High-Tech BV, Ruurlo, The Netherlands
[2] University of Twente, Transducers Science and Technology, Enschede, The Netherlands

Abstract

We developed a compact conventional steel tube Coriolis mass flow controller for low flow rates down to 10mg/min and up to 3g/min in one instrument. The mechanical construction of the flow controller has been optimized to have a low internal dead volume for control speed and stability. An on board piezo actuated control valve is used as actuator to control the flow. The advantage of this valve principle is the lack of internal volume, high stiffness and very little self-heating. A dedicated setup is used to validate the performance of the Coriolis flow controller. The instrument is capable of controlling 30mg/min over 25hrs within 1% peak to peak of reading. Due to the small internal volume and stiffness of the actuator the flow controller response time within 1% accuracy is <6s on the reference. On different liquids the flow controller shows an accuracy of better than 0.1mg/min ± 0.2% of reading.

Keywords

Coriolis low flow controlled piezo valve .

Introduction

Coriolis flow meters and controllers are widely used in various types of industrial applications. Conventional steel tube sensor technology with the latest state of the art signal processing enables highly accurate and medium independent flow measurement over a wide flow range with various tube sizes. Since 2008 Bronkhorst High-Tech offers a Coriolis mass flow meter with contactless actuators and sensors based on the technology as described in [1]. This known and commercially available technology enables accurate low flow measurement and control down to 160mg/min. Current control valves strategies are usually based on small electromagnetic control valves. The internal volume and self-heating of these valves result in slower and unstable flow and batch control for lower flow rates. There are

current market demands for even lower flow control with high accuracy as well as for fast batch dosing. These requirements can be found in e.g. food and pharmaceutical applications where traceable and direct mass measurement for the dosage of additives is a must.

Novelty

We developed a compact steel tube Coriolis mass flow controller for low flow rates with an on board piezo actuated control valve and electronic driver for the piezo actuator. This enables a stably measured and controlled mass flow down to 10mg/min and up to 3mg/min for liquids and gasses. The controller response time is <6s. This creates opportunities for the accurate and fast dosing of small batches. Figure 1 shows the inside of the flow controller with on board piezo valve.

Figure 1. Inside of the flow controller with visible piezo valve

Internal volume

When it comes to accurately controlling low liquid flow rates the used devices and liquid must be free of entrapped gas bubbles. Any gas bubble acts as a hydraulic spring damper resulting in reduced system response time and inaccurate mass flow measurement. Commercially available degassers can provide the system with bubble free liquid. However the filling of a dry system without entrapped bubbles demands not only bubble free liquid but also a construction without any dead volume. In order to achieve the lowest dead volume we redesigned the construction. The sensor tubes are continuously and directly led into the inlet of the flow controller and the inlet of the control valve There are no right-angled bore holes, or other dead volumes. Figure 2 shows a detailed photo of the sensor part and piezo valve and the hydraulic interconnection.
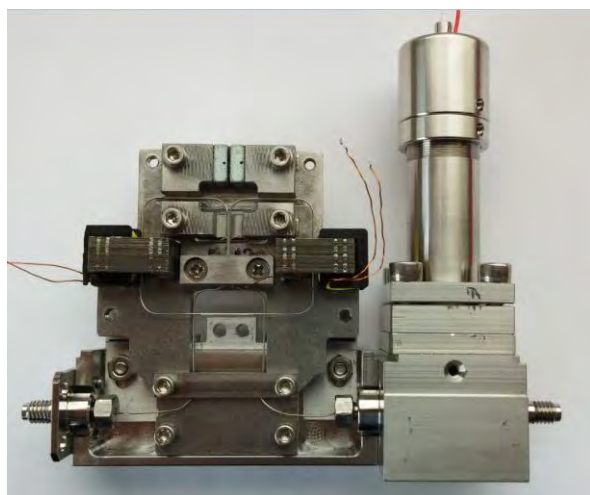

Figure 2. Detail photo of the sensor part and piezo valve without electronics. The rectangle thin sensor tube is clearly visible.

Piezo actuated control valve

For the fast control of small flow rates conventional electromagnetic control valves with elastomeric seal have limited force and stiffness. The elastomeric seal results in non-reproducible behavior and suffers from aging and sticking behavior. These valve principles also suffer from self-heating due to copper losses and have a significant internal volume. The self-heating and internal volume lead to unwanted fluid expansion. This causes an unstable flow at the outlet of the flow controller, especially for very low flow rates. In order to eliminate this we developed a piezo control valve with steel membrane that has almost no self-heating a high stiffness and little dead volume.

Experimental

The setup we used to characterize this system is given in figure 3. The inlet of the flow controller is connected to a pressurized liquid source. Helium is used to pressurize the liquid as it dissolves less into the liquid than nitrogen or air. This helps to prevent issues with gas bubbles. In between the liquid source and the flow controller is a commercially available degasser to remove any leftover dissolved gas bubbles. The tested Coriolis flow controller provides a stable flow that will be checked by an electronic balance. The electronic balance RS232 output signal is continuously differentiated and filtered to calculate the actual reference mass flow. This signal is compared to the measured flow of the flow controller.
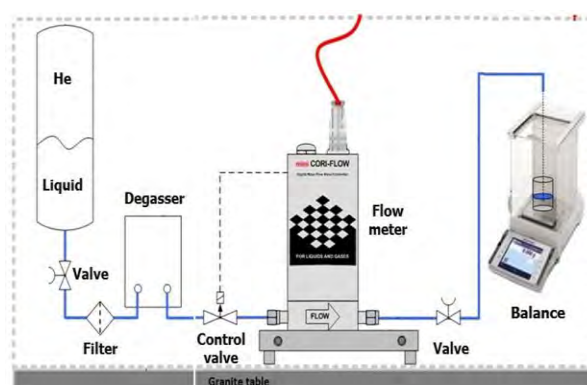
Figure 3. Schematic view of the test setup to measure the stability of the flow controller.

The setup is used to investigate the performance on response time, long term stability and medium independence.

Results on response time

To measure the step response of the flow controller the setpoint value is compared to the reference flow on the electronic balance. As the electronic balance suffers from noise due to limited resolution some filtering is necessary. The used filter is an averaging filter over 60s. As filtering also results in a phase delay of the

signal an anti causal filter is chosen to show a quick response of the filtered value. This means that offline data is used to calculate the average over 60s of future samples. In figure 4 the result of the step response is shown for a setpoint change from 0 tot 30mg/min at t=0s. The time scale is logarithmic to show the quick response and the longer term stability during the measurement. The figure shows a response time of 6s on the reference flow within 1%.

Figure 4. Response time of the flowcontroller of <6s within 1% at 30mg/min compared to filtered reference flow

Results on long term stability

The result of a long term stability measurement is depicted in figure 4. It shows the stability of the instrument at 30mg/min over 25hrs. The measured value of the electronic balance is average filtered over 60s. This signal is used as the reference value and stays within 1% of reading peak to peak during the entire measurement. The measurement is carried out with ethyl benzoate.
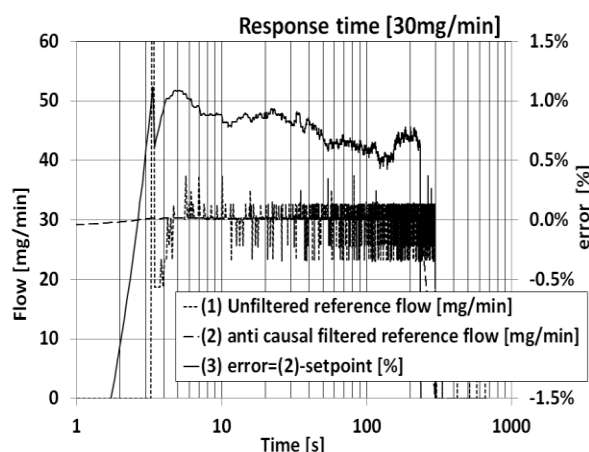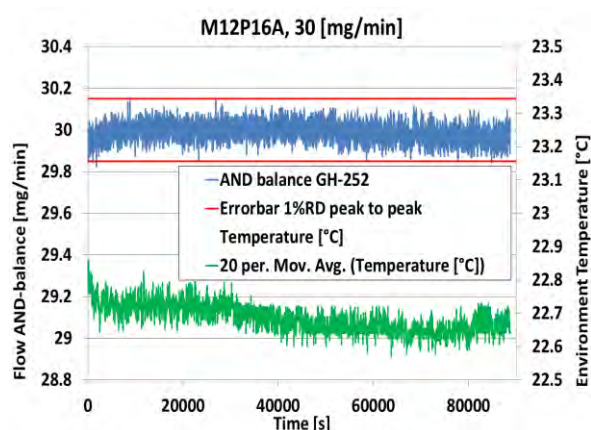

Figure 4. Measurement results long term stability at 30mg/min on electronic balance as reference with 1min averaging

Results on medium independence

A advantage of the Coriolis measurement principle is its direct mass flow, independent of medium properties. In order to investigate the performance on this subject the flow controller is calibrated with different media. The same setup as depicted in figure 3 is used to validate the accuracy on different media and on different flow rates. The measured data is compared to the reference flow and the error percentage is calculated. The experiment is carried out for water, isopropanol and ethylbenzoate. Before each measurement the instrument is zeroed. The investigated flow range starts from 10mg/min to 3g/min. The results are depicted in figure 5. The outcome is that the accuracy of the instrument is medium independent and shows a performance on accuracy over all measured points within 0.1mg/min $\pm$ 0.2% of reading.
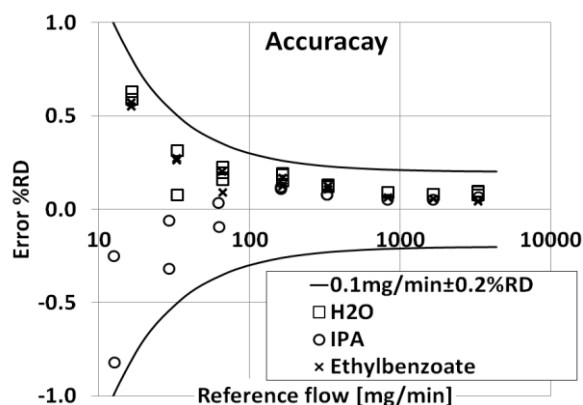
Figure 5. Accuracy of the flow controller for various liquids.

Conclusion

To conclude we presented a compact coriolis flow controller with no dead volume and a on board piezo actuated control valve. The stainless steel tube and piezo controlled valve result in an all wetted parts stainless steel instrument. The controlled flow rate goes down to 10mg/min and up to 3g/min. The response time of the flow controller is <6s within 1% accuracy. The long term stability measurements show a 1% accuracy over 25hours at 30mg/min. On different liquids the instrument shows an accuracy of better than 0.1mg/min ± 0.2% of reading over the entire range. The flow controller can be used in any application where medium independence, direct mass flow, accuracy and fast dosing is required.

Word Count: 1252

REFERENCES:
[1] A. Mehendale, "Coriolis mass flow rate meters for low flows", Phd Thesis, 2008

4. Fluidic control systems   Presentation&Poster

MICROFLUIDIC DROPLET HANDLING BY ACOUSTOPHORESIS ON BULK ACOUSTIC WAVE (BAW) DEVICES

I. Leibacher*, P. Reichert* and J. Dual

Swiss Federal Institute of Technology (ETH Zurich), Institute of Mechanical Systems (IMES), Zurich, Switzerland

ABSTRACT

Droplet microfluidics has emerged into a promising field for fluid handling on lab-on-a-chip devices, where fluidic droplets serve as liquid vessels e. g. for biochemical reagents. Key to the applications is a set of unit operations for droplet handling, i.e. droplet fusion, sorting, medium exchange and storage. In the following, we present a method to provide these unit operations for droplets of about 200 µm size. The acoustophoretic method is applied in bulk acoustic wave (BAW) devices, where water-in-oil droplets can be generated and manipulated with acoustic operating frequencies around 0.5 MHz.

KEYWORDS

Droplet microfluidics, acoustophoresis, ultrasonic standing wave, droplet sorting, droplet fusion, piezoelectric transducer

INTRODUCTION

The miniaturization of fluid handling systems has led to the field of "droplet microfluidics" [1]. Discrete fluid droplets are thereby the vessels for biological-chemical laboratory procedures, which are operated in lab-on-a-chip systems. Favored by low Reynolds and Weber numbers, the droplet format offers many advantages for fluid handling on the micro scale, once the droplet handling is enabled [2]. Therefore, we propose the contactless handling of droplets by ultrasonic waves for unit operations such as droplet fusion, sorting, medium exchange and storage [3]. This fluid handling method is enabled by bulk acoustic wave (BAW) devices with the method of acoustophoresis [4].

Regarding acoustic droplet handling, most work so far has been dealing with surface acoustic waves (SAW). Thereby, an acoustic field in PDMS microchannels is generated on a piezoelectric ground plate with interdigitated transducers (IDT), which acts on droplets by acoustic radiation forces [5] or by the drag forces of acoustic streaming [6]. Compared to this earlier work, our method differs as it builds on a bulk acoustic wave (BAW) approach. In our microfluidic channel, a standing acoustic wave is generated by a bulk piezoelectric transducer rather than IDTs. The piezoelectric transducer allows to excite bulk waves and mechanical resonance in acoustically hard silicon devices. Whereas SAW approaches are restricted by a piezoelectric ground plate and PDMS channels, the BAW approach allows quite a free transducer placement on any acoustically hard microfluidic channel. The resulting method is simple in terms of fabrication, versatile in applications and geometrically compact.

SETUP AND OPERATION PRINCIPLE

The proposed fluid handling method operates on a micromachined silicon/glass chip (Figure 1) with a main channel of 1 mm width and 200 µm height. Both the droplet generation and the subsequent acoustophoretic manipulation were conducted on this chip. Water-in-oil droplets (silicone oil, Dow Corning 200) with diameters ranging from 50 μm to 250 μm were generated with T-junction and flow focusing geometries in a flow rate range of 15 to 40 μl/min. To actuate acoustophoresis, a bulk piezoelectric transducer for the excitation of ultrasonic waves was glued on the back side of the devices (Figure 2). The transducer was excited by a function generator (Tektronix AFG 3022B) and an amplifier (ENI 2100L) at channel resonance frequencies in the range of 400 kHz to 2 MHz with 20-35 V_{rms} amplitude. The transducer requires only low power. Therefore it is suitable to be integrated on portable devices, as desired in the lab-on-a-chip concept.

The experiments were monitored by a high speed camera (HiSpec 1 Mono, Fastec Imaging) in bright field and fluorescent microscopy. Fluid flows were actuated by up to 4 syringe pumps (Cetoni Nemesys). The experimental setup is illustrated in Figure 3.
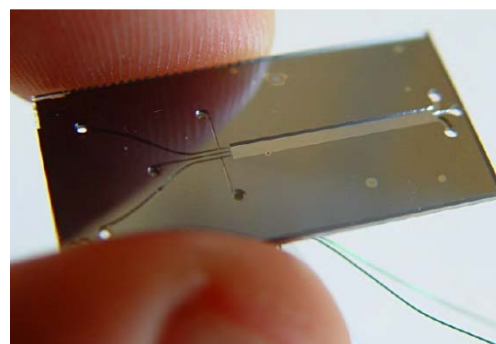

Figure 1: Front side of a 8 mm x 24 mm *silicon chip with microfluidic channels for droplet generation and manipulation.*
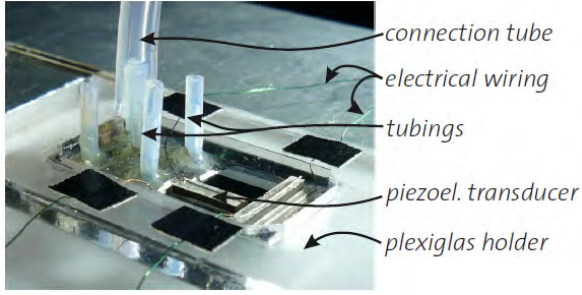
* joint first authors

Figure 2: Back side of the chip from Figure 1 with fluidic and electrical connections.
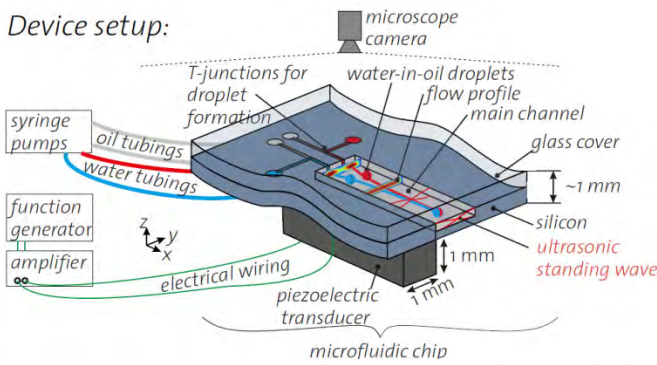

Figure 3: Experimental setup on and around the microfluidic chip.

Bounded by the mismatch of the characteristic acoustic impedance $Z=\rho c$ at the silicon/silicone oil interface (modeled as hard wall condition), certain fluid resonance modes across the channel width are feasible, when multiples of $\lambda/2$ fit between left and right channel wall with $\lambda = c_{oil}/f$ for the wavelength λ, the speed of sound c_{oil} in silicone oil and the actuation frequency f. If the transducer is tuned to such a fluid resonance frequency, this leads to the formation of an ultrasonic standing wave in the fluid. As an example, the first and second resonance modes of $\lambda/2$ and λ are shown in Figure 4.

These standing wave fields exert acoustic radiation forces on acoustically contrasting dispensed droplets within the suspending liquid. For spherical droplets with radius $r \ll \lambda$ (long-wavelength range), the acoustic radiation force $\mathbf{F}$ can be calculated with the Gor'kov potential [7] in the acoustic domain. For a droplet in a 1D standing wave field, the analytic calculation yields [8]

$$\mathbf{F} = F \cdot \boldsymbol{e}_y = 4\pi\Phi k_y r^3 E_{ac}\sin(2k_y y) \quad (1)$$

with the acoustic contrast factor $\Phi=f_1/3+f_2/2$ [9], the acoustic energy density $E_{ac}= p_a^2 /(4\ \rho_{oil}\ c_{oil}^2)$, the pressure amplitude p_a, the density ρ_{oil} and speed of

sound c_{oil} in the suspending silicone oil and the wave number k_y. For droplets in fluid, the first factor f_1 yields

$$f_1 = 1 - \frac{\kappa_{wa}}{\kappa_{oil}} = 1 - \frac{\rho_{oil}c_{oil}^2}{\rho_{wa}c_{wa}^2} \quad (2)$$

with the compressibility κ_{wa} of the water droplet and κ_{oil} of the surrounding silicone oil.

The second factor f_2 determines the influence of the velocity field in the Gor'kov potential. It is given as

$$f_2 = \frac{2(\rho_{wa}-\rho_{oil})}{2\rho_{wa}+\rho_{oil}} \quad (3)$$

In our experiments, the material parameters of water and silicone oil lead to the factors f_1=0.57, f_2=0.03 and a positive acoustic contrast factor Φ>0. Therefore, droplets will be attracted to the pressure nodes in the standing wave, which correspond to the velocity antinodes as known from linear acoustics of standing waves.

Figure 4: Sketch of the operating principle for BAW acoustophoretic droplet handling with a standing acoustic wave. The lowest two resonance modes with $\lambda/2$ and λ in y-direction are illustrated. (They occur at two different resonance frequencies.)

RESULTS AND DISCUSSION

Droplet Fusion

For droplet fusion experiments, two water-in-oil droplets were generated in a temporally synchronized manner. The droplets were generated at microfluidic T-junctions [10, 11] as shown in Figure 5. For visualization, the water - inflowing from above - was dyed with fluorescein and appears white in the shown high-speed fluorescence microscopy images. The silicone oil is flowing in from the left side and pinches off a discrete water droplet. The water droplet is then flowing to the right side and finally into a larger channel of 1 mm width for ultrasonic manipulation, as

shown in Figure 6, which was captured by bright field microscopy.

Figure 5: Generation of microfluidic water-in-oil droplets in a T-junction with 40 μm channel width, captured by fluorescent imaging.

Further downwards in the channel of Figure 6, the one-to-one fusion of droplets in a continuous flow is induced by focusing them on the channel centerline with acoustophoresis. A resonance mode with a standing pressure wave of $\lambda/2$ across the channel width was found by tuning the transducer frequency to 464 kHz. With the speed of sound $c_{oil} \approx 1000$ m/s of silicone oil, this frequency value approximately matches the expectation of the first resonance frequency $f = c_{oil}/\lambda = 1000$ m/s / 2 mm= 500 kHz, where a $\lambda/2$ mode will be generated in the channel of 1 mm width as shown in Figure 4. Reasons for the difference between calculated and experimentally found resonance frequency are the compliance of the silicon boundary (which was neglected by the hard wall assumption) and the influence of the mechanical/piezoelectric device parts which couple with the fluidic resonance.

Besides the acoustic forces, the droplet fusion also depends on the fluid dynamics. Droplets of larger size showed a slower velocity due to an increase of friction at the top/bottom channel boundaries. Because of this velocity difference, the droplets from the upper and lower T-junction were found to self-synchronize: the smaller droplets (dark dyed) catch up with the larger droplets (lighter color, undyed), until both droplets came into contact and merged.

Compared to other droplet fusion methods, acoustic methods show several benefits: they allow active on/off control (unlike passive hydrodynamic fusion), they are simple to fabricate (simpler than electrodes for fusion by electric fields), they can easily be integrated on chip-level (unlike laser-assisted methods), and they work for many combinations of dispersed and continuous phase liquid as long as they are acoustically contrasting (no dependency on magnetic/dielectric properties). As a disadvantage of this acoustic method, it is less suited for fusion of strongly surfactant-stabilized droplets.

The shown active droplet fusion method allows fluid sample mixing operations on the micro scale. It allows e. g. reaction initiation, droplet dilution and cell-in-droplet handling, which are of interest for biochemical applications of droplet microfluidics.

Figure 6: Acoustophoretic droplet fusion induced by piezoelectric ultrasonic excitation, which results in a pressure standing wave in the microfluidic channel.

Droplet sorting

Acoustophoresis is a suitable method for droplet sorting tasks [5,6]. As shown in Figure 8, by turning the ultrasound transducer on/off, droplet paths can actively be switched between upper/lower outlet by the same BAW method as for the droplet fusion of the last section.

Alternatively to turning the transducer on/off, the resonance frequency might be switched between the $\lambda/2$ and $\lambda/2$ mode as shown in Figure 4 to achieve droplet sorting in an upper/lower outlet.

This valve-like operation might allow controlled droplet sorting, when a further upstream sensor is installed to characterize the inflowing droplets. Depending on the measured droplet characteristics, they can then be guided through the upper or lower outlet and collected further downstream. Future efforts are aiming at an increase of the sorting speed to meet the requirements of high-speed droplet handling with increased throughput.

Figure 8: Droplet sorting between the two outlet channels by switching the $\lambda/2$ mode on in b), whereas ultrasound was turned off in a).

Medium change

As a third droplet handling unit operation, it is often desired to transfer droplets to another continuous phase for washing, for droplet concentration or to expose them to another surfactant in the continuous phase.

In Figure 9b, droplets experience an exchange of their suspending continuous phase from the dyed oil (center) to the undyed oil in the lower third of the channel. This is feasible because the acoustic radiation force acts selectively on the dispersed water because it is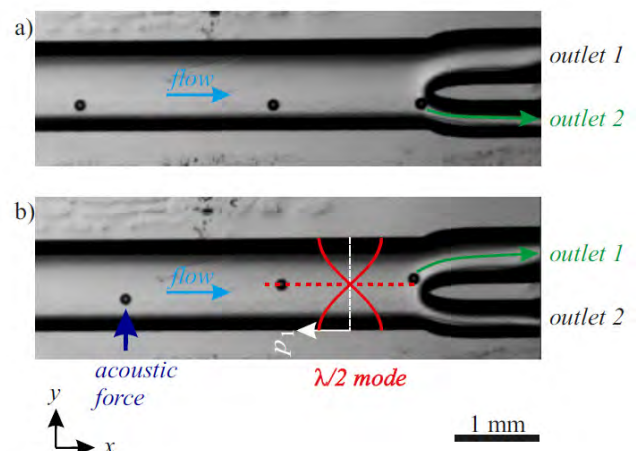 acoustically contrasting to the continuous phase, namely the silicone oil. This method enables e. g. to stabilize droplets by moving them from a surfactant-free continuous liquid to a surfactant-blended continuous liquid.
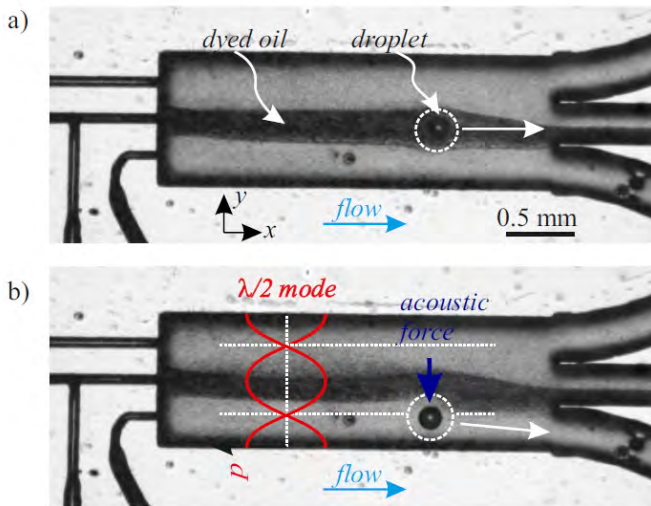

Figure 9: Exchange of the continuous phase of dispersed droplets (Ø~150µm). A droplet in dyed oil without ultrasound in a) is deflected into a different oil phase in b) with acoustophoresis.

CONCLUSION

The presented acoustophoretic droplet handling enables a range of fluid handling operations for droplet microfluidics. This is feasible because the acoustic radiation force acts selectively on dispersed water droplets due to their acoustically contrasting fluid.

Compared to the alternative surface acoustic wave (SAW) method [5,6], the BAW method has a simpler setup. The lower operation frequency of the BAW method leads to higher wavelengths, which allow the handling of larger droplets from ~1 µm up to ~500 µm size. The method is ideally suited for active droplet handling tasks in portable, low-power lab-on-a-chip systems.

In view of applications, the shown fluid sample handling by ultrasonic waves offers significant benefits for the contact-free fluid handling e.g. in laboratory diagnostics/analytics and biochemical research.

REFERENCES

[1] S. Y. Teh, R. Lin, L. H. Hung, A. P. Lee, „Droplet microfluidics", Lab on a Chip, 8(2), 198-220, 2008.

[2] X. Casadevall i Solvas, A. de Mello, "Droplet microfluidics: recent developments and future applications", Chemical communications, 47(7), 1936–1942, 2011.

[3] I. Leibacher & P. Reichert, J. Dual, "Continuous flow droplet acoustophoresis with bulk acoustic waves", *Flow14 Conference*, *Enschede, Netherlands*, May 18-21, 2014.

[4] H. Bruus, J. Dual, J. Hawkes, M. Hill, T. Laurell, J. Nilsson, S. Radel, S. Sadhal, M. Wiklund, "Forthcoming Lab on a Chip tutorial series on acoustofluidics: Acoustofluidics - exploiting ultrasonic standing wave forces and acoustic streaming in microfluidic systems for cell and particle manipulation", Lab on a Chip, 11(21), 3579-3580, 2011.

[5] S. Li, et al, "An on-chip, multichannel droplet sorter using standing surface acoustic waves", Analytical chemistry 85(11), 5468-5474, 2012.

[6] T. Franke, A. R. Abate, D. A. Weitz, A. Wixforth, „Surface acoustic wave (SAW) directed droplet flow in microfluidics for PDMS devices", Lab on a Chip, 9(18), 2625-2627, 2009.

[7] L. P. Gor'kov, "On the forces acting on a small particle in an acoustical field in an ideal fluid", Soviet Physics Doklady. Vol. 6., 773-775, 1962.

[8] H. Bruus, "Acoustofluidics 7: The acoustic radiation force on small particles", Lab on a Chip, 12(6), 1014-1021, 2012.

[9] K. Yosioka, Y. Kawasima, "Acoustic radiation pressure on a compressible sphere", Acta Acustica united with Acustica, 5(3), 167-173, 1955.

[10] G. F. Christopher, S. L. Anna, "Microfluidic methods for generating continuous droplet streams", Journal of Physics D: Applied Physics, 40(19), R319, 2007.

[11] T. Thorsen, R. W. Roberts, F. H. Arnold, S. R. Quake, "Dynamic pattern formation in a vesicle-generating microfluidic device", Physical review letters, 86(18), 4163, 2001.

CONTACT

* I. Leibacher, leibacher@
  P. Reichert, reichert@ — imes.mavt.ethz.ch
  J. Dual, dual@

2. Fluidic control systems   **Poster**

COMPUTATIONAL DESIGN OF WETTING AND SPREADING BEHAVIOUR FOR ENHANCED IN-VITRO-DIAGNOSTIC APPLICATIONS

Adham Hashibon, Matthias Gurr, Pit Polfer, Frank Burmeister, Torsten Kraft
Fraunhofer Institute for Mechanics of Materials IWM,
Woehlerstr. 11, 79108 Freiburg, Germany

Abstract

In this study we demonstrate that by a combination of theory, computational fluid dynamics (CFD) calculations and experimental verification, a successful design of superhydrophobic surfaces for microfluidic applications can be achieved. This design approach enables control of the wetting and spreading properties without chemical surface modifications for a variety of applications, including in-vitro diagnostics (IVD) and digital microfluidics.

Introduction

Automated micro-dosing systems for in-vitro diagnostics (IVD) and high-throughput screening require efficient and exact handling of minute amounts of fluidic samples. Some of the challenges are precise control of transport and storage of small fluid quantities ($<\sim 1\mu l$) as well as loss-free, i.e., complete transfer of minute fluid portions. This also holds particularly for droplet-based lab-on-chip devices, including open digital microfluidic systems where liquid drops are used as micro-reactors confining and transporting samples [1, 2]. In these systems there is a need to precisely control the transport, mixing, separation and dispersion of single drops on surfaces with intricate networks of channels and patterns.

The transport and storage of the liquid through capillary channels and particularly in droplet-based microfluidic systems are strongly limited by the wetting and spreading behaviour of the liquid and the surface properties of the miniaturized containers and sample holders like multiwell-plates. Hence, the control of wetting and spreading properties in these systems is one of the most important factors that govern their efficiency and successful application.

In this contribution, we demonstrate that by combining computational modelling, surface microstructuring and experimental characterization, a new design of surface structures can be achieved changing the component's wetting properties with regard to water solutions from slightly hydrophobic to superhydrophobic, thus allowing the precise control of wetting on approved biomedical materials. This is achieved through micro and nano-structuring of the surfaces in a prescribed manner and by further control of the geometrical shape of the containers.

Tailoring wetting and spreading

Wetting and spreading are determined by the static and dynamic properties of the interfaces between the liquid and the solid surfaces as well as between the liquids themselves (liquid, oil or air), see Figure 1. The effect of surface tension is apparent in microfluidic applications since the capillary number (Ca) expressing the ratio between the viscous and surface tension forces:

$$Ca = \mu\, V / \gamma \qquad (1)$$

where μ is the viscosity, V the velocity and γ the surface tension of the liquid/air interface, is very small. When, for example, capillary driven flows which are purely governed by surface tension forces are used for microfluidics the wetting property of the microchannels has a significant effect on the liquid flow behaviour. This can readily be seen by

$$\gamma_{lv}\cos\theta + \gamma_{sl} = \gamma_{sv}$$
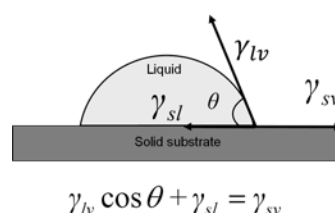
Figure 1: A schematic of a sessile drop on a substrate and the Young equation showing the relation between the wetting angle and surface tensions.

considering the spreading rate of the liquid in a capillary channel given by the Lucas–Washburn Model [3]. The time traversed by the meniscus front according to this model is proportional to $(\gamma\, t)^{1/2}$. Therefore by controlling γ, i.e., the wetting properties, it is possible to control the flow in capillary systems, at least in the impregnation phase. Namely, a hydrophilic surface will assist fluid motion, whereas a hydrophobic surface will retard the fluid motion inside a microchannel.

Tailoring the wettability of the microfluidic channels in order to control the flow behaviour can in general be achieved by two main approaches, namely by chemical surface modifications to increase or decrease the free surface energy and surface patterning to change the wetting state. Chemical modifications are achieved by coating the surface with polar molecules (e.g. salinization) [4]. However, such coatings are in general not desired as they may interact with the specimens. Moreover, there are strict biomedical regulations that usually limit the choice of possible materials down to a few approved plastic (e.g. polystyrene) or glass varieties. This poses in turn

further challenges to the optimization of the microfluidic components, since it severely limits possible surface modifications.

Surface patterning

Research on patterned surfaces reveals interesting phenomena that can be exploited to control liquid motions in microfluidic devices [5, 6, 7, 8]. Hydrophobic and hydrophilic regions inside microchannels can be patterned through various nanofabrication techniques, e.g., laser based additive manufacturing, hot embossing and micromachining.

In order to obtain stick-free surfaces by tuning wetting properties, there are basically two completely different approaches. The first approach aims at the production of a perfectly smooth and highly wetting surface, namely a superhydrophilic surface. Such surfaces are characterized by a very low contact angle of less than about 10°. For the definition of the contact angle see Figure 1. In such systems, a lubricating immiscible liquid film can be introduced [9]. However, the motion of the liquid is often hampered by pinning or hysteresis effects and evaporation. In the second, surfaces are patterned in such a way that a superhydrophobic wetting behaviour is obtained. Nature exhibits many such examples where specific hierarchical patterning on the micro and nano scales leads to superhydrophobic systems. In these systems the wetting angle is larger than about 150° and due to the small contact area between the liquid and the solid, hysteresis effects are negligible, hence the drop is not pinned. A prototypical example from nature is the Lotus plant leaf. Numerous studies aimed at the replication of the lotus leaf surface and similar natural structures in order to produce self-cleaning stick-free surfaces. However, designing and fabrication of robust patterned surfaces for practical applications is still very challenging. Furthermore, the exact wetting behaviour on the patterned surfaces is still hard to predict based only on analytical approaches.

A prerequisite for producing such superhydrophobic patterns is that the flat un-patterned surface has a wetting angle which is above 90°. That means the surface must be already hydrophobic, otherwise the liquid drop will wet and penetrate the grooves between the patterns and will be hard to transport it out of it. In general, the more hydrophobic the material the easier it is to produce a superhydrophobic surface. Polystyrene (PS) and Polymethyl methacrylate (PMMA) based materials are widely used for assays and biomedical IVD applications [10]. This is mainly due to low price, known and approved medical compliance and advantages of mass manufacturing, e.g. by injection moulding [11]. However both materials do not exhibit particularly pronounced hydrophobic behaviour on flat surfaces. For example, the reported wetting angles of water on such polymer substrates ranges from 80° to 97°

depending on the composition and environment [12, 13]. PS and PMMA pose therefore a serious challenge to producing such superhydrophobic surfaces. Alternative more hydrophobic materials such as Polydimethyl siloxane (PDMS) suffer from higher material cost, the need for more demanding fabrication techniques and enhanced adsorption of hydrophobic drugs [10].

Design principles

The main aim is to design surfaces with pillar shapes distributed on the surface in a specific pattern so as to minimize the contact area between the liquid and the solid. The wetting angle of a liquid drop on a superhydrophobic patterned surface, as shown on the right side of Figure 2 is given by the well-known Cassie-Baxter equation:

$$\cos \theta^* = -1 + \phi_s \left(\cos \theta + 1\right) \qquad (3)$$

where θ^* is the apparent contact angle and ϕ_s is the solid-liquid area fraction. From Equation (3) it is clear that, as the area fraction between the liquid-solid, ϕ_s, is smaller, then the apparent wetting angle increases. The area fraction can be tuned by specific geometrical structures, as shown in the right of Figure 2. Nevertheless, even for very small ϕ_s, the actual wetting state may be more correctly described by the so called Wenzel state, where the liquid penetrates the grooves between the patterns as shown in the left of Figure 2. In this case the apparent contact angle is given according to the Wenzel equation:

$$\cos \theta^* = r \cos \theta \qquad (4)$$

where r is the roughness of the surface defined as the ratio of the apparent contact area to the projected one underneath the droplet. In fact it can be shown that the Wenzel state, also known as the homogenous wetting state, will always be the thermodynamically more stable state with respect to the Cassie-Baxter state, also known as heterogeneous wetting [3], as schematically shown in Figure 2. The requirement for a successful application of a stable and robust superhydrophobic surface is therefore to design a pillar configuration that renders the Cassie-Baxter state sufficiently metastable with respect to the Wenzel state for practical applications as shown schematically in the middle panel of Figure 2.

The basic underlying physics is rather straight forward and consists of comparing the energies of a configuration in which the droplet is completely wetting the surface (Wenzel state in Figure 2) and that in which the drop is sitting on top of the patterns (Cassie-Baxter state in Figure 2). A derivation can be found, e.g., in the classic texts of [3, 5]. The condition for a metastable Cassie-Baxter state is that the contact angle of the patterned surface is larger than a critical wetting angle θ_c given by:

$$\cos \theta_c \geq \frac{\phi_s - 1}{r - \phi_s} \qquad (2)$$

However, this is normally not sufficient since in practical systems, other factors need to be considered. The above theoretical treatment assumes a rotationally invariant system and excludes both impurities and the intricate shape of the triple line and the complex shape of the solid-air-liquid interface beneath the drop. Such factors are not amenable to simple analytical solutions and therefore need to be calculated numerically.

Computational Methods

Several computational fluid dynamics (CFD) approaches have been developed to deal with multiphase liquids. These include Eulerian methods, such as the finite-volume-method with the volume-of-fluid (VOF) framework [14] and Lagrangian methods, such as the smoothed particle hydrodynamics (SPH) [15]. Both methods have the ability to handle flows that undergo arbitrary topologic transformations including surface tension effects. In this study, the simulations of droplets on patterned-surface are performed using a VOF formalism using the OpenFOAM® code.
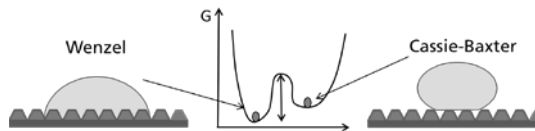

Figure 2: Schematics showing the Wenzel or homogenous wetting Vs. Cassie-Baxter or heterogeneuous wetting states.The Wenzel state is the most stable one, but Cassie-Baxter can be made metastable by specific design.

Results

Computational VOF calculations have been performed for several candidate pattern structures chosen first according to Equation (2). Figure (3) shows one such candidate system. It is clear from Figure (2) that the actual wetting state in this system is more complex that that suggested by simple theoretical predictions, and that the actual state is a mixture of both Cassie-Baxter and Wenzel states.
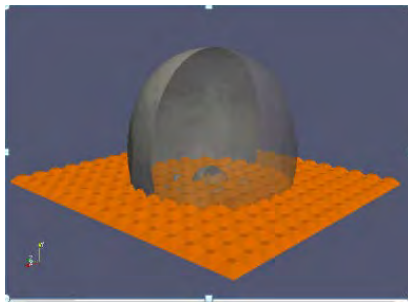

Figure 3: a simulation of a water droplet on a structured surface showing a mixture of Cassie-Baxter and Wenzel states.

In the second stage of this study, the most superhydrophobic candidate systems found by the CFD simulations have been manufactured using micromachining methods and a series of experiments to test the stability of the system have been conducted. The exact details of the patterned surfaces and the manufactured process will be publishes elsewhere. Figure 4 shows a comparison between the wetting behaviour of a droplet deposited on a flat polystyrene surface and a patterned one. While in Figure 4(a) the droplet remains stuck on the inclined surface on the flat surface, in figure 4(b) it rolls out of the optimal patterned surface. For comparison, a droplet deposited on a Teflon substrate, one of the most hydrophobic materials is shown in Figure 4(c), where again the droplet remains stuck on the inclined surface.
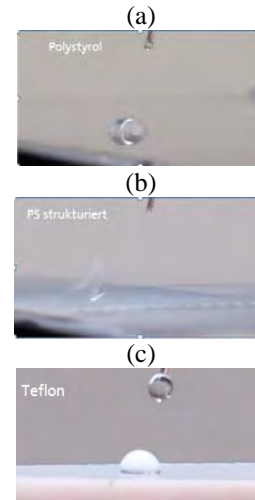
Figure 4: A water drop is deposited on a flat polystyrene surface (a); a pattered superhydrophobic polystyrene surface (b); and a Teflon surface for comparison (c). The surfaces are inclined by 10°.

Summary and outlook

In this work we have demonstrated a procedure to control the wetting properties of surfaces using only patterning of the surface on the micro- and nanoscales. Superhydrophobic systems where designed and produced without any chemical modifications to the surface complying with biomedical requirements. The main challenge thereby was the reconciliation of feasible and machinable structures with theoretically ideal surface geometries derived from numerical calculations and verified using experiments. This approach, based on multi-scale modelling and experimental characterization can reduce the time to optimize and discover novel micro and nano-fluidic systems and has a great potential for applications in IVD systems and digital microfluidics.

Acknowledgements

REFERENCES:

[1] C. N. Baroud, F. Gallaire, R. Dangla, "Dynamics of microfluidic droplets". Lab on a chip, 10(16), 2032, (2010).

[2] J. Liu, N. T. Nguyen, "Numerical Simulation of Droplet-Based Microfluidics - A Review". Micro and Nanosystemse, 2(3), 193, (2010).

[3] Pierre-Gilles de Gennes, Francoise Brochard-Wyart, David Quéré, "Capillarity and Wetting Phenomena, Drops, Bubbles, Pearls, Waves". Springer, New York, USA (2004).

[4] J. B. Brzoska, N. Shahidzadeh, F. Rondelez, "Evidence of a transition temperature for the optimum deposition of grafted monolayer coatings", Nature 360, 719, (1992).

[5] D. Quéré, "Non-sticking drops. Reports on Progress in Physics, 68(11), 2495, (2001).

[6] M. Nosonovsky, B. Bhushan, "Hierarchical roughness optimization for biomimetic superhydrophobic surfaces". Ultramicroscopy, 107(10-11), 969, (2007).

[7] A. A. Saha, S. K. Mitra, "Numerical study of capillary flow in microchannels with alternate hydrophilic-hydrophobic bottom wall". *Journal of Fluids Engineering*, *131*(6), 061202, (2009).

[8] R. Blossey, "Self-cleaning surfaces-virtual realities". Nature materials, 2(5), 301, (1996).

[9] A. Lafuma, D. Quéré, "Slippery pre-suffused surfaces". Europhysics Letters, 96(5), 56001, (2011).

[10] P. M. van Midwoud, A. Janse, M. T. Merema, G. M. M. Groothuis, E. Verpoorte, "Comparison of Biocompatibility and Adsorption Properties of Different Plastics for Advanced Microfluidic Cell and Tissue Culture Models". Anal. Chem. 84(9), 3938, (2012).

[11] C. D. Chin, V. Linder, S. K. Sia, „Commercialization of Microfluidic Point-of-Care Diagnositc devices". Lab Chip, 12, 2118, (2012).

[12] L. Yuan, J. Q. Pham, K. P. Johnston, P. F. Green, "Contact angle of water on polystyrene thin films: effects of CO_2 environment and film thickness", Langmuir 23(19), 9785, (2001)

[13] T. Yasuda, T. Okuno, H. Yasuda, "Contact angle of water on polymer surfaces", Langmuir 10(7), 2435, (1994).

[14] C. W. Hirt, B. D. Nichols, "Volume of fluid (VOF) method for the dynamics of free boundaries," J. Comput. Phys., 39, pp. 201, (1981).

[15] T. Breinlinger, P. Polfer, A. Hashibon , T. Kraft, "Surface tension and wetting effects with smoothed particle hydrodynamics". Journal of Computational Physics, 243:14–27, (2013).

2. Application   Poster

FAST PROTOTYPING OF MULTISENSOR CELL-CULTURE CHIPS USING ULTRA-SHORT PULSE-LASER ABLATION AND MICROMILLING

S.M. Bonk [1], P. Oldorf [2], R. Peters [2], W. Baumann [1] and J. Gimsa [1*]*
[1] University of Rostock, Chair of Biophysics, Rostock, Germany
[2] Schweißtechnische Lehr- und Versuchsanstalt Mecklenburg-Vorpommern GmbH, Germany

ABSTRACT

We developed a sensor chip with sensors for acidification, oxygen consumption and adhesion measurements inside a microfluidic system for long-term cell culturing. The sensors were directly produced from a Pt layer on a microscopic slide carrier by ultra-short pulse-laser ablation. The processing time for a chip surface of 11.5 cm² was less than 3 min. The external body of the system and the PDMS-molding forms for the microfluidics were manufactured by micro milling using a CNC-isolation-milling machine commonly used in the prototyping of circuit boards (PCB). Our approach allows for fast prototyping of sensorized microfluidic systems and avoids the use of photolithographic techniques.

KEYWORDS

Rapid-prototyping, micro milling, sensor-chip, ITO, oxygen, pH, pico-second-laser, cell monitoring system

INTRODUCTION

The development of microfluidic cell-monitoring systems call for the integration of multiple sensors and actuators. Manufacturing of electrical sensors, actuators, heating elements or other components is usually realized by the well-established microelectronic fabrication techniques. Even the production of microfluidic components is often based on photolithography processes [1].

For the mass production of microfluidic systems and also for basic research mostly polymer technologies are used. While for the mass production of microfluidic systems injection molding is unrivaled, lithography is used for the processing of electrical components. Micro-injection molding, hot embossing or hot shaping are the alternative methods in low volume production or prototyping. [2]

For biotech and medical applications additional requirements such as the biocompatibility of materials have to be taken into account. Especially for cell-monitoring systems, lab-on-chip devices or in micro-reaction techniques also requirements such as the temperature or chemical stabilities are very challenging. [3]

The use of glass as the material of choice requires adaptation of the microchip-production methods [4].

Photolithographic production techniques are time and cost extensive due to their high number of processing steps. For the realization of prototypes and low volume production (which is usually the case in basic research) the possibility of the fast implementation design changes is a must. Flexible and fast microsystem production technologies are necessary to reduce costs, increase flexibility and shorten the times for the development of microfluidic systems. As a consequence, rapid prototyping techniques are gaining increasing importance in the field.

The presented laser-based prototyping technology enables the direct production of thin layer sensor structures on different substrates. The technology reduces manufacturing times and avoids the use of toxic or harmful chemicals as well as clean rooms. With our technology, platinum, titanium, silicon-nitride (Si_3N_4) or indium-tin oxide (ITO) structures were made down to a width of 20 µm and an edge roughness below 2 µm. The amperometric Clark oxygen sensors, potentiometric pH and impedimetric cell adhesion sensors (interdigitating electrode structures, IDES) used on the chip were originally produced by photolithographic techniques and have been redesigned for the new system [5] (fig. 1). The newly developed potentiometric pH sensor features a 60 nm Si_3N_4, pH-sensitive substrate layer as it is usually used in ISFETs [6].

PRODUCTION
Structuring platinum and ITO

The microscopic slides were cleaned with 10 % aqueous Tickopur W77-cleaning solution (BANDELIN electronic GmbH & Co. KG, Germany) in an ultrasonic bath and dried by compressed air. The slides were sputtered with 130 nm platinum on a 15 nm titanium adhesion layer using a magnetron-sputter system (Ardenne LA-320S, www.vonardenne.biz). Subsequently the chips were structured by laser ablation with a pico-second laser (TRUMP TruMicro 5x50) which was incorporated into a high-precision micromachining system (GFH GmbH, www.gfh-gmbh.de). The system has a positioning precision better than 1 µm and allows for a direct import of DXF-data files [7]. The structures were designed in AutoCAD 2010 (www.autodesk.com) and exported as

DXF-files into the laser-control system which drew the structures directly onto the chip with a 343 nm laser. The laser was programmed to ablate not required material starting with outlining the structures at a slow scan velocity of 100 mm/s. All AutoCAD files were modified by an offset of 6 µm to compensate for the radius of the laser spot of approx. 10 µm in its focus area. Consecutively, the not required platinum layer was removed in bidirectional stripes with up to 1000 mm/s on the rest of the microscope slide. For ITO structures, the second step could be omitted for its optical transparency (Fig. 1.).
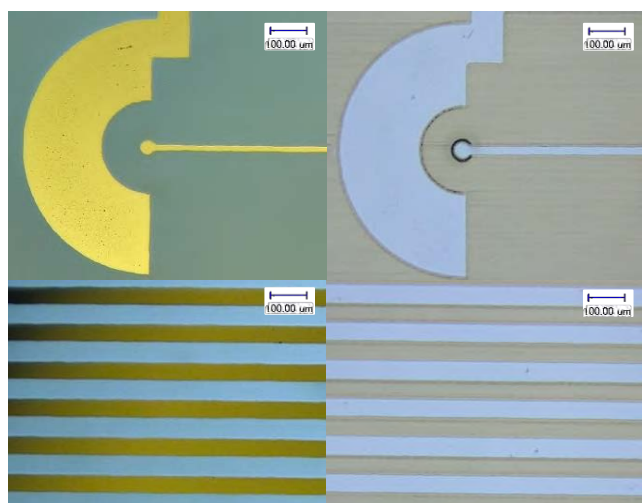

Figure 1: Top: working electrode of the oxygen sensor with engulfing counter electrode; bottom: IDES-sensor area with interdigitated electrodes (distance/width: 50µm/50µm); right: the same structures made of ITO with equal laser protocol.

Structuring silicon nitride

After another cleaning step (see above), the ablated chips were fully passivated in the sputter system with a 60 nm Si_3N_4 layer. For test purposes, a second batch was passivated with 1000 nm Si_3N_4 using a PE-CVD process by GeSiM (www.gesim.de). Si_3N_4 was chosen because of its biocompatibility and electrical and optical properties. Another reason was that Si_3N_4 was also used as the ion-sensitive substrate for the pH sensors in our chips. For opening the passivation above contact and metallic-sensor surfaces (IDES and the oxygen sensor), a second laser-processing step was executed.

Microfluidic fabrication

The whole cell-culture system comprises an external polycarbonate body with fluidic connectors carrying an internal PDMS structure with fluidic channels which were sealed by the sensor chip (fig. 2). The system and the PDMS molding tools for imprinting the microfluidic structure were milled by a PCB-micro milling machine (CCD 2, www.bungard.de) in polycarbonate (PC) or PMMA. Body and lid were designed in AutoCAD 2010 and milled in an 8 mm PC plate, while the molding cast was milled in PMMA because of its better cutting behavior especially for smaller milling tools (<500 µm diameter).
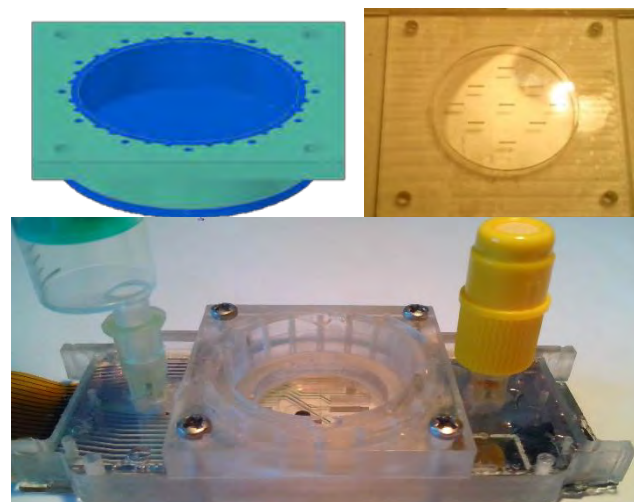

Figure 2. Top-left: PC system lid (light green) with PDMS fluidic part (blue). Top-right: Molding cast for the fluidic lid milled in PMMA. Bottom: PC cell culture body with chip, flexible circuit board connector (left), as well as filling syringe on the left and port cap on the right inlets.

For molding, the PDMS monomers (Sylgard 184, www.dowcorning.com) were degassed, injected in the molding cast and cured for 4 h at 70°C. After removing the molding parts, the bottom side of the case PDMS was coated manually with a fine layer of uncured PDMS and pressure-fixed to the chip before a second curing step. For better PDMS adhesion, the PC parts and the chip surfaces were coated with bonding agent (GRUN G790, Wacker Silicones, www.wacker.com) before PDMS injection. After curing the PDMS the microfluidic connectors were glued to the body. The connectors consisted of syringe tips with shortened cannulas which were fixed in cross shaped notches to enable the use of the Luer-Lock connecting system (see fig 2.) The removable lid enables easy cleaning of the culture area or input and exchange of 3D-scaffolds.

Cell culture

The mouse-osteoblast precursor-cell line (MC3T3-E1), a model system for bone regeneration, was used to verify the biocompatibility. The cell line was obtained from the German collection of microorganisms and cell culture (www.dsmz.de). The cells were cultured in an incubator at 37 °C, 95% humidity and 5% CO_2 atmosphere. The cells were let grown to confluence in 50 ml cell-culture flasks (25 cm^2; Greiner bio-one,

Frickenhausen, Germany) in alpha medium (ord. No. F 0925) supplemented with 1% penicillin/streptomycin (stem solution: 100 U/ml penicillin/100 µg/ml streptomycin) and 10% fetal bovine serum (all purchased from Biochrom AG, Berlin, Germany). Cells grown to confluence were trypsinated (0.05% Trypsin + EDTA 0.02%, PAN Biotech GmbH, Aidenbach, Germany) and diluted before subculture or transfer to the microfluidic system.

For cell seeding 500.000 cells/ml (corresponding to 50.000 cells per system) were injected by flushing 500 µl cell suspension through the system. The system was closed with a syringe filled with 6 ml medium at one inlet and a cap with a cannula-injection port at the outlet (see fig.2). Carbonate-free alpha medium (P03-2510, Pan Biotech, Aidenbach, Germany) with the supplements of a standard alpha medium was buffered with 20 mM HEPES and used for cell culture in the closed system. For medium exchange, the needle of a syringe without piston was introduced through the cap before 500 µl of fresh medium of the filled syringe was flushed through the system.

RESULTS
Structuring platinum and ITO

Structuring of platinum was easy after several tests were conducted in order to find the ideal settings for power, speed and overlap of the laser spot for the thin structures. It was sufficient to attach the chip to the arrester of the work bench inside the machine. Laser processing required less than 3 min for processing the chip area of 11.5 cm². Structures with less than 20 µm width and minimal distances of 10 µm between them could be manufactured. The smallest structures on our chips were the working electrodes of the oxygen sensors with 40 µm diameter and a conducting path width of 20 µm. To compensate for the spot size, the designed structures were modified by a 6 µm offset using the AutoCAD function "offset". The edge roughness of the structures depends on shape and material, but was generally in the range of ± 1.5 µm (fig. 3). We think that the edge roughness of the platinum structures was primarily the consequence of pulsing and local effects at the ablation spot rather than of the beam guidance. Negligible mismatches between design and manufactured structures were mainly caused by an insufficient offset. This effect is obvious in fig. 3 where the distance between the IDES fingers was approx. 2 µm wider than expected, while their widths was approx. 2 µm too small. Nevertheless, such mismatches can be corrected by changing the offset in the redesign phase. Small circular structures were especially problematic to produce because the laser scan speed was relatively slow resulting in an excessive removal of material, sometimes even of the glass

carrier (see fig. 1. top-right oxygen electrode). We were informed that this problem should be solved by the laser-manufacturer in the next update of the software.

Structuring Si_3N_4

For the processing the Si_3N_4 passivation it was necessary to laser on existing structures (IDES, oxygen sensor). This limited the feasible laser parameters to a very small window in order to ablate the Si_3N_4 layer without damaging the platinum structures. In principle, it was possible to remove 200 nm thick layers of Si_3N_4 without platinum removal [7]. Removing the Si_3N_4 usually led to a roughening of the platinum surface due to punctual ablation (see IDES fig.3.). Further, the ablation rate was depending on the underlying substrate. For optimal Si_3N_4 ablation on glass, the parameters had to be modified with respect to the optimal parameters found for the removal of Si_3N_4 above platinum. Possible reasons for a more efficient ablation above platinum could be the different energy coupling into the Si_3N_4 layer especially in the immediate vicinity to the platinum surface or different properties of Si_3N_4 adhesion to platinum and glass. This view was supported by the finding that the 1000 nm Si_3N_4 layers produced by GeSiM could be removed from platinum surfaces using the same parameters as 60 nm Si_3N_4 layers. These effects require further investigation.
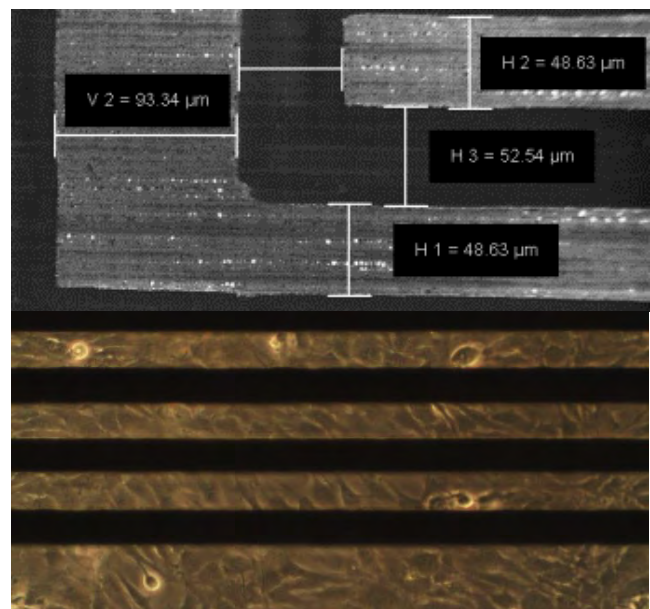

Figure 3: Pictures of the Pt-IDES: REM with dimensions (top), with cells in the system (bottom)

Cell culture

MC3T3-E1 cells showed a good proliferation in the systems reaching confluence approx. three days after seeding. No adhesion coatings were necessary. The cells adhered to Si_3N_4 surface as well as to platinum.

Rough surfaces caused by the laser ablation even seemed to improve cell adhesion.

Interestingly, bubble formation inside the cell culture medium by external covering of the PDMS lid with deionized water. This allowed for cell culturing times longer than 10 days.
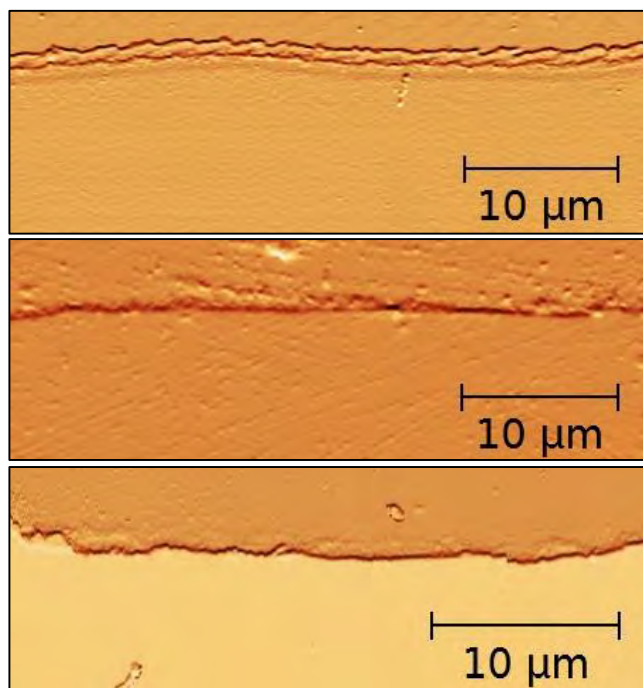

Figure 4: AFM image of an IDES-finger edge. Top: ITO on glass; Middle: platinum on glass; Bottom: photolithographically produced platinum structure (GeSiM®).

CONCLUSION

We show that laser ablation allows for the production of structures comparable to photolithographic resolutions (fig. 4). With ITO layers (CEC020, www.pgo-online.com) fabrication times are reduced because also non-ablated areas are microscopically accessible. While our laser system has a maximum speed of 2000 mm/s next generation systems are even faster which will further be decrease processing times and personal costs. Currently a man-hour cost approx. 300 €, making chip prices (slide) of 5 € possible (30s per ITO Slide + exchange time; 60 chip batch). The laser also can be used to produce holes or recesses for advanced microfluidic designs.

The chips are well suitable for cell culture. Cell adhesion to laser-manufactured chips is very good. For cell-culture systems, the gas permeability of PDMS has to be taken into account. The system can be vapor sterilized and easily modified by remolding the PDMS-lid structure. Combination of pulse-laser micromachining of the chips, micromachining of the body as well as molding tools combined with the well-established PDMS technology enables the fast prototyping of complex microfluidic systems with electrochemical sensors avoiding photolithographic processes. In future, very small fluidic designs can be produced using ultra-short pulse-laser techniques to produce casts for PDMS molding or even hot embossing of PMMA. In first tests, we produced casts for PDMS molding from Polyoxymethylene (POM) and stainless steel sheets for hot embossing.

REFERENCES

[1] M. S. Chiriacò, E. Primiceri, E. D'Amone, R. E. Ionescu, R. Rinaldi, and G. Maruccio, "EIS microfluidic chips for flow immunoassay and ultrasensitive cholera toxin detection," *Lab Chip*, 2011.

[2] J. J. Shah, J. Geist, L. E. Locascio, M. Gaitan, M. V. Rao, and W. N. Vreeland, "Capillarity induced solvent-actuated bonding of polymeric microfluidic devices," *Analytical chemistry*, vol. 78, no. 10, pp. 3348–3353, 2006.

[3] M. L. Kovarik, P. C. Gach, D. M. Ornoff, Y. Wang, J. Balowski, L. Farrag, and N. L. Allbritton, "Micro Total Analysis Systems for Cell Biology and Biochemical Assays," *Analytical Chemistry*, vol. 84, no. 2, pp. 516–540, Jan. 2012.

[4] C. Khan Malek, L. Robert, J.-J. Boy, and P. Blind, "Deep microstructuring in glass for microfluidic applications," *Microsystem Technologies*, vol. 13, no. 5–6, pp. 447–453, May 2006.

[5] S. M. Buehler, M. Stubbe, U. Gimsa, W. Baumann, and J. Gimsa, "A decrease of intracellular ATP is compensated by increased respiration and acidification at sub-lethal parathion concentrations in murine embryonic neuronal cells: Measurements in metabolic cell-culture chips," *Toxicology Letters*, vol. 207, no. 2, pp. 182–190, Nov. 2011.

[6] L. Bousse, S. Mostarshed, B. van der Schoot, and N. F. De Rooij, "Comparison of the hysteresis of Ta2O5 and Si3N4 pH-sensing insulators," *Sensors and Actuators B: Chemical*, vol. 17, no. 2, pp. 157–164, 1994.

[7] R. Peters and P. Oldorf, "Novel Applications of Ultra-short Pulsed Lasers," *Optik & Photonik*, vol. 7, no. 4, pp. 30–33, 2012.

CONTACT

* S.M. Bonk, sebastian.bonk@uni-rostock.de
* J. Gimsa, jan.gimsa@uni-rostock.de

LIVE IMAGING STUDIES OF *P. FALCIPARUM* EGRESS AND INVASION OF ERYTHROCYTES BY USING MICROFLUIDIC DEVICES

*Yen-Chun Lin[1], **Weichao Zhai[1]**, Eileen Nugent[1], Alex Crick[1], Teresa Tiffert[2], Virgilio Lew[2], Julian Rayner[3] & Pietro Cicuta[1]*

[1] Cavendish Laboratory, University of Cambridge
[2] Department of Physiology, Development and Neuroscience, University of Cambridge
[3] Wellcome Trust Sanger Institute, Wellcome Trust Genome Campus, Cambridge,

Severe malaria by *Plasmodium falciparum* is a leading cause of death in many developing countries [1]. In the blood stage of the disease, the merozoite invasion of erythrocytes is a repetitive intraerythrocytic cycle with a ~ 48-hour period. Infection of healthy blood cells after parasite egress takes only a few minutes and is a critical point in the progression of the disease. [2].

We aim to understand better this stage of the malarial infection by monitoring egress-invasion sequences in live cultures under controlled conditions. PDMS microfluidic channels are optically transparent, non-toxic structures that mimic the environment of the microcirculation in blood vessels [3] and which enable live imaging studies of host cells and malaria infected red blood cells (iRBCs). We develop the microfluidics with two aims: to approximate better the physiological conditions of micro-circulation, and to achieve higher throughput than in stationary cultures.

In this study we develop microfluidic devices with dimensions close to that of blood capillaries and produce controlled flows in these channels at physiological flow speeds. As shown in fig 1, two inlets (one with a constriction) are combined into one serpentine channel of 100 to 300 turns where infections in flow are expected to occur. IRBCs are delivered to the constriction, which blocks these relatively stiff cells and ensures the observation of fresh parasites which are released from iRBCs invasion in flow. RBCs are delivered to the second (non-constricted) input and manage to pass unhindered to the serpentine output, where they co-flow with the egressed parasites.

In addition, the development of a fully automated, robotic imaging platform [4] enables us to identify infected red cells pre-egression, and record their egress and subsequent parasite movement via a high-speed camera. Our results, shown in figure 2 and 3, are that healthy RBCs pass through the channel while iRBCs block the entrance of channels, where they burst and release the parasites. In addition, the custom software written in-house to run the microscopy enables us to combine Matlab functions to track RBCs. In our study, Matlab code is capable of identifying the RBC followed by the movement of microscope stage follow the flowing RBC in the channels. Furthermore, another Matlab code is written to track RBCs to enable us to analyse the RBCs property of velocity in microchannels after being recorded by video.

Finally, in our group, by using optical tweezers we are quantifying the strength of interactions between merozoites and erythrocytes. To do this we measure the extent of erythrocyte elongation when a merozoite is forcibly detached, as shown in figure 4 and 5. By subtracting, L_0, the cell length in the relaxed state from L, the elongated length, we calculate the detachment force $F = \kappa \Delta L$ to be 40 ± 8 pN, where κ is the cell stiffness [5].

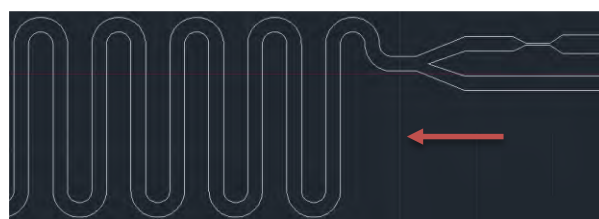*Figure 1. Schematic of microfluidic chip. RBCs and iRBCs are introduced into two separate inputs and combined RBCs and egressed parasites are combined in a long serpentine channel, the red arrow is flow direction.*
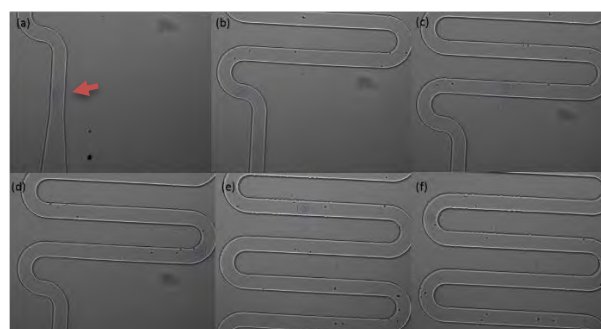

Fig. 2 a)– f) Images of a healthy RBC (red arrow) flowing through the channel, the movement is tracked using custom written matlab routines (cell tracking results are showns as blue circles).
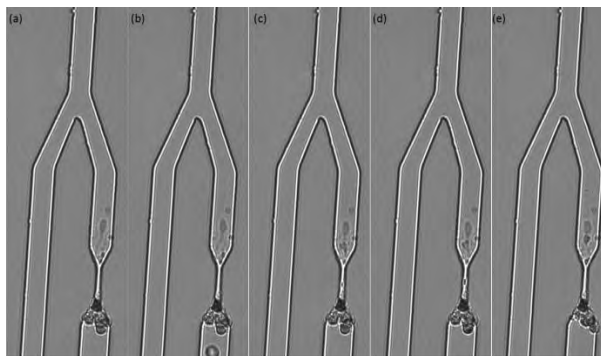
Fig. 3 a) – e) Sequence of images showing iRBCs and parasites being trapped and released from a 4 μm constriction.
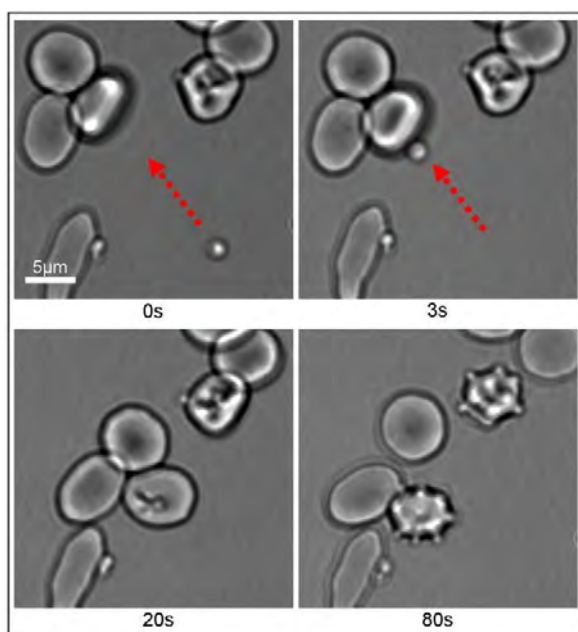
Fig. 4 Image sequence showing how a freshly released merozite was trapped and moved along the path indicated by the red arrow. It attaches to an erythrocyte at 3s. Cell invasion is observed at 20s and a post invasion image taken at 80s is also shown [5].
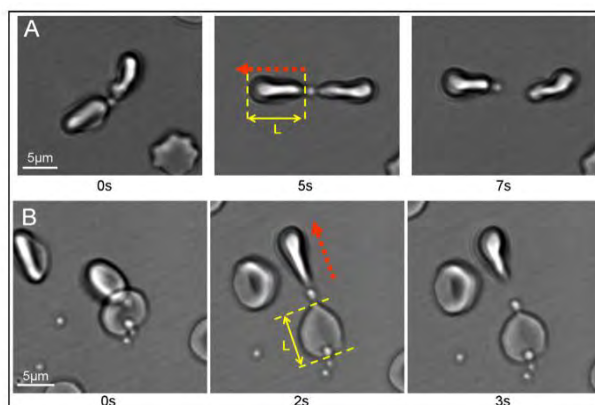
Fig. 5 Images showing detachment of a merozite from one of two initially attached erythrocytes using optical

tweezers. Directed movements are indicated [5].

REFERENCES:

[1]	Miller, L. H., Baruch, D. I., Marsh, K., and Doumbo, O. K. "The pathogenic basis of malaria", Nature 415, 673-679, 2002.
[2]	Cowman, A. F., and Crabb, B. S. "Invasion of red blood cells by malaria parasites", Cell 124, 755-766, 2006.
[3]	Becker, H., and Gärtner, C. "Polymer microfabrication methods for microfluidic analytical applications", Electrophoresis 21, 12-26, 2000.
[4]	Crick, A.J., Tiffert, T., Shah, S.M. Kotar, J., Lew, V.L., and Cicuta, P.. "An Automated Live Imaging Platform for Studying Merozoite Egress-Invasion in Malaria Cultures", Biophys. J. 104, 997-1005, 2013
[5]	Crick, A.J., Theron, M., Tiffert, T., Lew, V.L., Cicuta, P.. "Quantitation of Malaria Parasite-Erythrocyte Cell-Cell Interactions Using Optical Tweezers", Biophys. J. 107 (4), 846-853, 2014

OPTIMIZATION OF THE MICROFLUIDIC DESIGN OF A MINIATURIZED COUNTER-CURRENT FLAME IONIZATION DETECTOR

W.J. Kuipers[1], M. Deilmann[1], C. Koch[2] and J. Müller[3]
[1] KROHNE Messtechnik GmbH, Duisburg, Germany
[2] KROHNE Innovation GmbH, Duisburg, Germany
[3] Hamburg University of Technology, Hamburg, Germany

ABSTRACT
The flame ionization detector (FID) measures traces amounts of hydrocarbon substances. A novel counter-current micro FID (cc-µFID) with reduced gas consumption is expected to allow for a true industrial field device. This work is concerned with the simulation-based optimization and experimental verification of the geometrical design of the cc-µFID. As predicted by the model and verified by experiment, sensitivity increases with decreasing dimensions. The optimized µFID-design allows for conventional FID-sensitivity at considerably reduced gas consumption.

KEYWORDS
Flame Ionization Detector (FID), Total Hydrocarbon Analysis, MEMS, Microsystems Technology, Computational Fluid Dynamics (CFD)

INTRODUCTION
The flame ionization detector (FID) measures trace amounts of hydrocarbon components [1]. Ions resulting from flame ionization of organic substances introduced into an otherwise non-conductive hydrogen flame are collected using an electrical field. The thereby obtained ion current is proportional to the mass flow of hydrogen-bonded carbon.

It is either used in gas chromatography to analyze individual compounds after separation or as a stand-alone device to quantify the total amount of hydrocarbons. The latter is relevant in case of emission monitoring, monitoring of the lower explosive limit or process analysis.

Due to the need for large amounts of hydrogen (approx. 30 ml/min) and synthetic air (approx. 300 ml/min) and the corresponding gas infrastructure, complex FID devices are commonly installed centrally in an industrial facility, from which they operate several multiplexed measuring points. The resulting measurement delay and discontinuity challenge process control and safety-related monitoring.

In order to obtain a true FID field device, which can be directly installed at every single measuring point, gas consumption has to be reduced considerably. This work presents a MEMS-based counter-current FID (cc-µFID). The supply of hydrogen and oxygen from opposite directions allows

for stable miniature flames [2] with reduced hydrogen and pure oxygen consumption of 10 ml/min or less. Since the influence of operating parameters on device performance has been presented elsewhere [3], this contribution focuses on the simulation-based optimization and experimental verification of the geometrical design of the microsystem.

GENERAL DESIGN
The counter-current diffusion flame burns in the silicon plane of a glass-silicon-glass sandwich (Figure 1 and Figure 2). The miniaturized design allows for reasonable sensitivity at hydrogen flows as low as 5 ml/min.
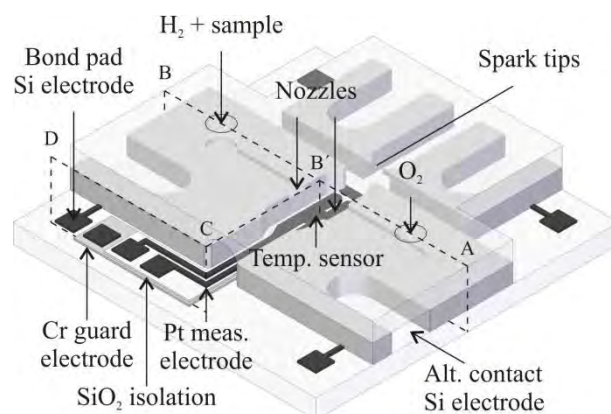
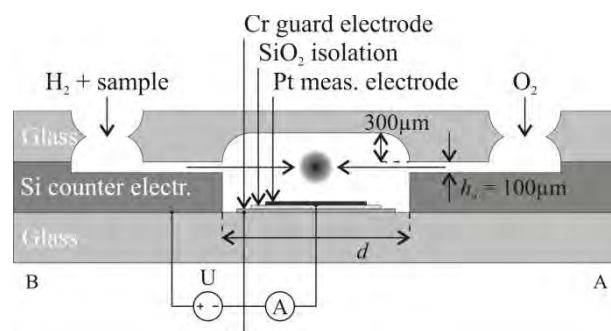*Figure 1 3D representation of the cc-µFID. The dice measures 8 mm x 8 mm*

Figure 2 Cross-section of the cc-µFID. The cross-section AB corresponds with the cut indicated in Figure 1. Each substrate is 500 µm thick.

Orthogonal dimensions of the micro-burner, including wafer thickness (500 µm), the nozzle height (100 µm) and the depth of the cavity in the top glass substrate (300 µm), are based on preliminary results [3]. The

outlet width measures 700 μm. Other in plane dimensions, such as the width of the nozzles and the distance between the nozzles are chosen after simulations of flow and convection inside the micro-burner, as will be explained in this paper.

As in conventional FIDs, the sample is premixed with the hydrogen. Therefore, only two gas inlets suffice. The inlets are realized orthogonally by etching through the top glass substrate.

The polarization voltage is applied between the silicon counter electrode and a platinum thin film measurement electrode on the bottom glass substrate.

SIMULATION-BASED OPTIMIZATION
Model

To predict the location and the ionizing power of the flame an CFD model has been developed. It is expected that flames will burn in the vicinity of the stagnation point, because only at very low flow velocities, mixing of hydrogen and oxygen can take place by diffusion. This behavior is described by the Péclet number:

$$Pe = \frac{L \cdot V}{D} \qquad (1)$$

where L is a characteristic length, V the magnitude of the velocity vector (speed) and D the diffusion coefficient. Only when the Péclet number is small ($Pe < 1$) a flammable mixture is formed by diffusion. The confinement of the flammable mixture is expected to relate to the strength (brightness and sensitivity) of the flame.

The following model considers the behavior of two different gases impinging onto each other, without reacting with each other, at 273 K and in two dimensions only. Because of the two different gases, it is not sufficient to model gas flow only, but there has to be accounted for convection (diffusion and advection) too.

The MEMS module of Comsol Multiphysics[R] [4] offers application modes for different kinds of flow and also for convection. In addition, flow can be coupled to convection, which is then called "flow with species transport". The model described here is based on the incompressible Navier-Stokes equations [5]:

$$\nabla p - \mu \nabla^2 \vec{V} + \rho \vec{V} \cdot \nabla \vec{V} = \rho \vec{g} \qquad (2)$$
$$\nabla \cdot \vec{V} = 0 \qquad (3)$$

where μ is the (dynamic) viscosity, ρ is the density and $\bar{g}$ the gravity vector. Pressure p and the components of the mass velocity vector $\bar{V}$ are the dependent variables. Equation (2) is found when applying Newton's second law to an infinitesimal mass element. Equation (3) is the result of mass conservation and is called the continuity equation.

Due to conservation of species (no reaction) at steady state, the divergence of the molar flux of species A (in a binary mixture of species A and B) $\bar{N}_A$ equals zero:

$$\nabla \cdot \vec{N}_A = \nabla \cdot \left(-D_{AB} \nabla C_A + C_A \vec{V} \right) = 0 \qquad (4)$$

The first part of N_A [6] is Fick's law, in which D_{AB} is the binary diffusion coefficient and C_A is the concentration of species A, and represents mass transport by diffusion. The second part represents mass transport by advection of a dilute mixture [4].

In the COMSOL Multiphysics[R] application mode "flow with species transport", Equations (2), (3) and (4) are coupled. For two dimensions, this results in four equations and four dependent variables: V_x, V_y, p and C_A. Viscosity μ and density ρ depend on the composition of the gas mixture. Both can be approximated by a concentration based weighed average.

The two dimensional plane of interest corresponds with the top side of the silicon substrate, including nozzles, flame chamber and outlets (Figure 1). Because of symmetry, only half the system has to be considered.

To account for friction forces at top and bottom boundaries, the MEMS module of Comsol Multiphysics[R] offers the "shallow channel approximation" (SCA). Based on a certain value for the third orthogonal dimension (height), a drag force is added to the two dimensional problem, which represents the effect of friction [4]. To obtain results, which represent the maximum effect of friction, the additional parameter height has to be set equal to the minimal distance between different top and bottom boundaries. From Figure 2 it can be seen that this distance corresponds to the nozzle height, $h_n = 100$ μm. If the SCA is not applied, the effect of friction on the simulation is minimal (zero). In this way two extreme cases of the effect of friction are simulated. It can be expected that the actual behavior lies somewhere in between.

Simulations are performed for equal hydrogen and oxygen flows of 7.5 ml/min. Consequently, an error is induced by Equation (4), which holds for dilute solutions.

Results

Figure 3 shows simulation results for configuration L2 (Table 1). The left hand side depicts the simulation results with SCA. The contour plot represents the magnitude of gas velocity. Maximum gas velocity is colored red and found at the nozzles. Consequently, dark blue (half) circles in between the nozzles indicate the position of the stagnation point with zero flow velocity. The surface plot indicates the relative

hydrogen concentration. 33 % hydrogen (67 % oxygen) is colored blue. Red indicates 67 % hydrogen (33 % oxygen). The region with relative hydrogen concentrations between 33 and 67 % is referred to as the "1/3 zone". More directly than the Péclet number, the width of the 1/3 zone $w_{1/3}$ is also a measure for the confinement of the flammable mixture.
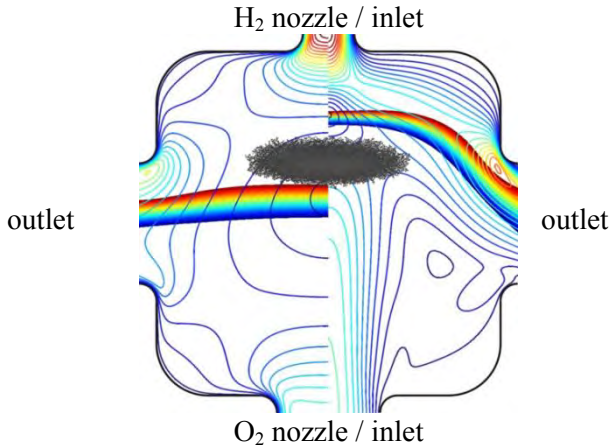

H$_2$ nozzle / inlet

outlet   outlet

O$_2$ nozzle / inlet

Figure 3 Simulation results for a type L2 (Table 1) micro-burner compared with the actual flame position. (H$_2$ flow = O$_2$ flow = 7.5 ml/min). Left hand side: with SCA, right hand side: without SCA.

Table 1 Overview of micro-burner geometries.

System	Parameters		
	Distance between nozzles (mm)	H$_2$ nozzle width (µm)	O$_2$ nozzle width (µm)
L1	2	600	600
L2	2	300	600
S1	1	600	600
S2	1	300	600
S3	1	300	300
S4	1	150	300

In general, the stagnation points are located off-center, closer to the hydrogen nozzle. This can be explained by the 16 times larger molecular weight of the oxygen compared to the hydrogen. For L2 (Figure 3) the smaller hydrogen nozzle somewhat compensates for the momentum difference at equal volume flow. During FID operation, the sample is premixed with the hydrogen. This not only guarantees maximum ion yield, but also increases the momentum of the gas flow from the hydrogen nozzle.

Since the momentum effect is damped by the additional volume forces of the SCA, the corresponding stagnation points are located closer to the flame chamber center (left hand side of Figure 3), than when the SCA is not applied (right hand side of Figure 3).

From Figure 3 it can be seen that mixing by diffusion takes place only after gas flows have slowed down to negligible flow velocities, i.e. in the vicinity of the stagnation point. This is confirmed by the Péclet number (Figure 4), which, for a characteristic length of 1 mm, is large at the nozzles (> 30) and is smaller than unity in the direct vicinity (± 50 µm) of the stagnation point only. Therefore, the location of the flame is determined by the stagnation point. Figure 5 compares normalized values of $1/w_{1/3}$ (with and without SCA) for all six geometries from Table 1.
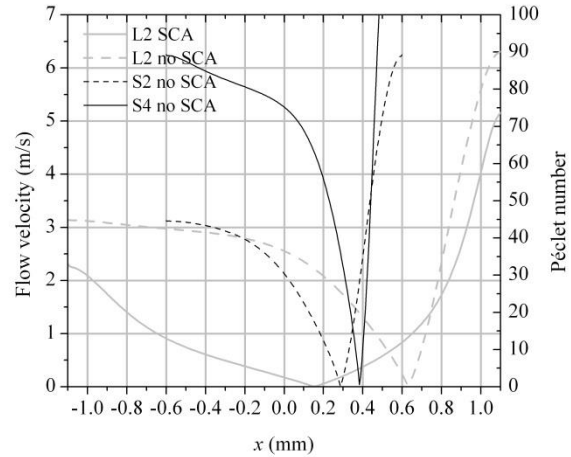
Figure 4 Magnitude of the gas flow velocity and the Péclet number as a function of the distance to the flame chamber center x.
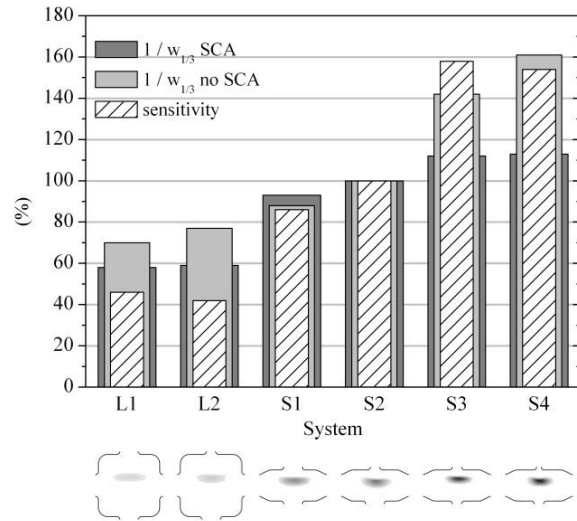
Figure 5 Comparison of I) the simulated degree of confinement with and without SCA with II) measured FID sensitivity (Figure 6) and III) flame brightness for different micro-burner geometries (Table 1).

Based on these simulation results, a micro-burner with a small nozzle distance and small nozzles produces the most confined flammable mixture. However, to verify the model, all six configurations are fabricated and characterized by experiment (flame observations and sensitivity measurements). Since the nozzle width and distance are mask design parameters, all systems can be fabricated simultaneously on a single set of

substrates (glass – silicon – glass).

EXPERIMENTAL

FID sensitivity is defined as the ion current (in A) measured, divided by the carbon mass flow (in gC/s) and is thereby expressed in C/gC. The ion current was measured for four different carbon mass flows, including zero (offset correction). The different carbon mass flows were obtained by changing the gas flows of a calibration gas (1 % CH_4 in N_2) and pure nitrogen, keeping the total sample gas flow constant at 2.0 ml/min. Largest carbon mass flow used for these measurements was obtained with 1.5 ml/min calibration gas and 0.5 ml/min pure nitrogen (0.75 % CH_4 in N_2). Then, the calibration gas was diluted in tree equal steps of 0.5 ml/min to pure nitrogen.

All measurements were performed with an applied polarization voltage of 50 V as well as equal hydrogen and oxygen flows of 7.5 ml/min.

Mass flows were controlled by mass flow controllers (MFCs) (Bronkhorst EL-FLOW F201CV). FID electronics were provided by a picoammeter with integrated voltage source (Keithley 487).

RESULTS AND DISCUSSION

Figure 6 shows the results of ion current vs. carbon mass flow measurements. In general, sensitivity (slope) increases with decreasing dimensions. Since the sensitivities of S1 and 2, S3 and 4, and L1 and 2 do not vary much, it can be concluded that sensitivity is primarily determined by the nozzle distance and the size of the oxygen nozzle.
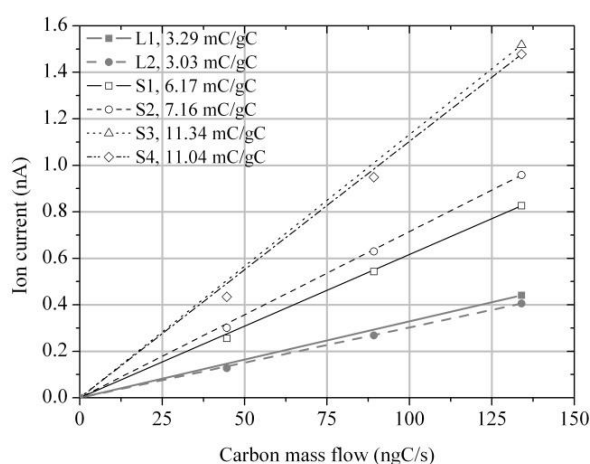

Figure 6 Ion current as a function of carbon mass flow for different geometries (Table 1).

In Figure 5 the measured sensitivities are compared with the simulation results (with and without SCA). At the bottom of the figure also photographs of the corresponding flames are shown. It can be concluded that like sensitivity also flame brightness and the simulated confinement of the flammable mixture

(expressed as the inverse of the 1/3 zone width) increase with decreasing distance between the nozzles and decreasing size of the oxygen nozzle.

In addition, counter-current diffusion flames are indeed located in between the two simulated extreme stagnation points Figure 3.

CONCLUSIONS

This paper presents a 2D CFD model of a cc-µFID to predict flame location and FID sensitivity as a function of e.g. distance between opposing nozzles and nozzle width. Experimental verification of the simulation results confirms the applicability of the model as a useful design tool. As predicted by the model and verified by experiment, sensitivity increases with decreasing distance between the nozzles and decreasing width of the oxygen nozzle.

At 7.5 ml/min hydrogen and oxygen maximum sensitivity measures 11.3 mC/gC (S3), which is comparable with typical FID sensitivity of 15 mC/gC [1]. With 1 pA peak-to-peak noise, the minimum detectable limit (defined as two times peak-to-peak noise divided by sensitivity) is somewhat higher than conventionally ($1.8 \cdot 10^{-10}$ gC/s vs. $< 1 \cdot 10^{-10}$ gC/s).

Future work will focus on packaging and long-term stability as demanded by process industrial applications.

ACKNOWLEDGEMENT

REFERENCES

[1] D.G McMinn, H.H. Hill, The Flame Ionization Detector, in: H.H. Hill, D.G. McMinn (Eds.), Detectors for Capillary Chromatography, John Wiley & Sons, New York, 1992, p. 7.

[2] T.C. Hayward, K.B. Thurbide, Talanta 73 (2007) 583.

[3] W.J. Kuipers and J. Müller, J. Chrom. A 1218-14 (2011) pp. 1891-1898.

[4] COMSOL Multiphysics® Version 3.5a MEMS Module User's Guide, 2008.

[5] B.R. Munson, D.F. Young and T.H. Okiishi, Fundamentals of Fluid Mechanics, third ed., Wiley, New York, 1998.

[6] F.P Incropera and D.P. DeWitt, Fundamentals of Heat and Mass Transfer, sixth ed., Wiley, Hoboken, 2007.

CONTACT

∗   W.J. Kuipers, w.kuipers@krohne.com

5. Applications   **Poster**

DEVELOPMENT OF A PORTABLE MULTI-PARAMETER CENTRIFUGAL MICROFLUIDIC ANALYSIS SYSTEM (CMAS) FOR WATER QUALITY MONITORING

Patrick Floris[1], Thomas Glennon[1], Conor O'Quigley[1], Eoghan Mc Namara[1], Yang Yang[1], Jens Ducrée[2], Alan Smeaton[1], Dermot Diamond[1] and Kevin J. Fraser[1]*

[1] Insight Centre for Data Analytics, National Centre for Sensor Research, Dublin City University, Dublin 9, Ireland

[2] Biomedical Diagnostics Institute. National Centre for Sensor Research, Dublin City University, Dublin 9, Ireland

ABSTRACT

In this paper we report the development of a multi-parameter low-cost (< 100 EUR) portable Centrifugal Microfluidic Analysis System (CMAS) for the in-situ colorimetric analysis of nutrients. Microfluidic discs consisting of three PMMA (Poly(methyl methacrylate)) layers bonded together by two PSA (Pressure Sensitive Adhesive) layers were prepared. A 3D-printed housing was produced for hosting the microfluidic discs which incorporated a low-cost optical sensor for colorimetric detection and a motor which generated the centrifugal force necessary to carry out the tests. Limits of detections of 0.233 ppm, 0.189 ppm and 0.050 ppm were obtained for ammonia, orthophosphate and nitrite respectively.

KEYWORDS

Centrifugal Microfluidics, Lab-on-a-disc, Colorimetric Analysis, Environmental Monitoring, Water Quality.

INTRODUCTION

The environmental monitoring of inorganic nutrients in water traditionally involved the collection of samples which would then be subsequently analysed in the laboratory using automated methods such as flow injection analysis coupled with spectroscopic detection of light absorbing species [1, 2]. These methods however, rely on the use of expensive equipment which requires the processing of large sample and reagent volumes, resulting in a costly and time-consuming process that can take up to two weeks in some cases. Recently, there has been a growing interest, and demand for, real time in-situ monitoring for situations that require rapid access to time-critical data which led to the development of portable analysis systems. Most of the commercially available devices have restricted applicability due to either high manufacturing costs or lack of data logging functions. Microfluidic discs have increasingly been used as a platform for performing complex biological and chemical reactions which involve multi-step mixing processes, such as colorimetric assays, with similar performance to conventional benchtop instrumentation [3]. By applying a centrifugal force, the displacement of complex fluid mixtures is achieved using a single motor, without the need of external pumps. Reports describing the development of micro Total Analysis Systems (µTAS) for environmental monitoring applications have recently emerged, with the benefit of reducing sample volume requirements to µL amounts [3-5]. For example, Hwang *et al.* [6] recently reported the development of a microfluidic system for the simultaneous determination of several nutrients in water such as nitrite, nitrate, ammonium orthophosphate and silicate. Optical detection was achieved using a benchtop fiber-coupled spectrophotometer which restricted the portability of the device hence making it unsuitable for remote water quality monitoring purposes.

Here, we report the development of a portable multi-parameter low-cost Centrifugal Microfluidic Analysis System (CMAS) for in situ water quality evaluation (shown in Figure 1). The portability of the system was facilitated by the incorporation of a low cost/power-efficient detection system based on LEDs-photodiode [7] and by allowing complete control of the device via a conventional Android tablet.
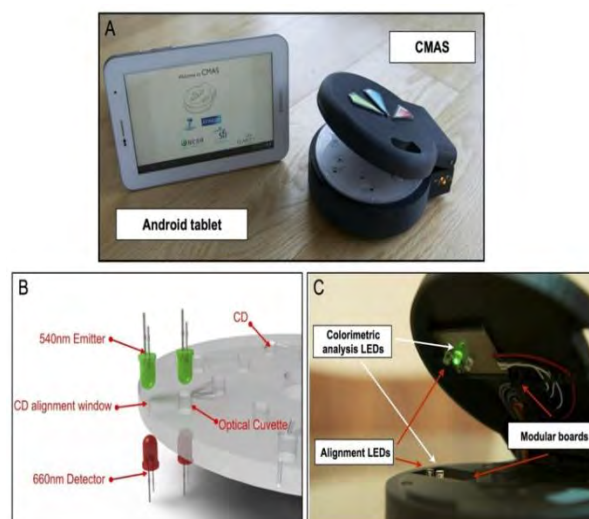

Figure 1: (A) Portable Android controller and CMAS, (B) schematic representation of the alignment/emitter/detector LEDs and (C) CMAS LED configuration specific to a nitrite CD (bottom right) [3].

EXPERIMENTAL
Microfluidic discs fabrication

Microfluidic discs were prepared consisting of three PMMA (Poly(methyl methacrylate)) layers bonded together by two PSA (Pressure Sensitive Adhesive) layers (see Figure 2). The layers are designed using CAD software before being manufactured with an Epilog Zing Laser (PMMA layers) and a Graphtec cutting plotter (PSA layers). Each disc was designed with six test areas consisting of a sample chamber and either single/dual reagent chambers connected, by 400 µm channels in 86 µm PSA, to a common reaction/detection chamber.
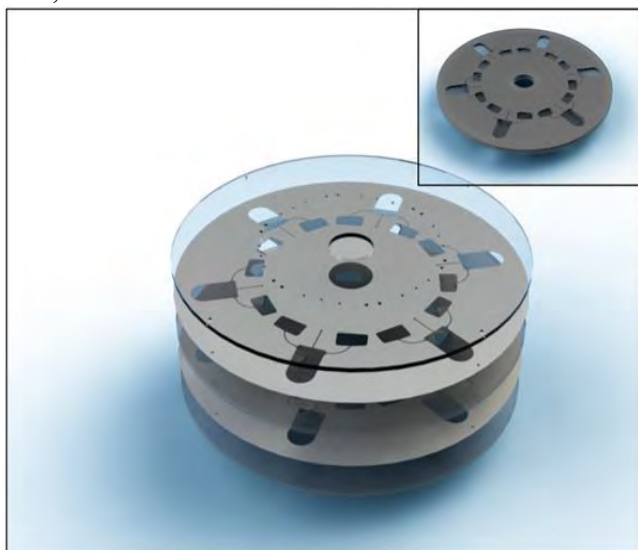

Figure 2: An exploded view of the microfluidic detection disc with the three transparent PMMA layers bonded by the PSA Layers. The top PMMA layer (1.5mm) contains the loading and vent holes, the top PSA (0.086mm) contains provides the connecting and venting channels, the middle PMMA (2mm) provides the reservoirs, and the bottom PSA (0.086mm) is used to bond the sealing base layer of PMMA (1.5mm). These layers are assembled to form the resulting centrifugal microfluidic cartridge (inset).

Nutrients analysis

The analysis of nitrite, ammonia and orthophosphate was performed using colorimetric methods on microfluidic discs. All reagents were stored in amber glass containers and aliquoted on the microfluidic discs prior to analysis, where they were mixed in a 1:1 v/v ratio with the standards. Nitrite determinations involved the formation of a diazonium salt that reacts with chromotropic acid to form a red/orange complex with a strong λ_{max} at 515 nm. The reagent was found to be stable for at least 4 weeks if protected from ambient light. The analysis of orthophosphate involved the formation of a molybdophosphoric acid complex by reacting phosphate with ammonium molybdate in an acidic medium. Reduction by stannous chloride led to a molybdenum blue complex with a λ_{max} at 685 nm. The reagents were found to be stable for 3 months if kept separately. Finally, the analysis of ammonia was based on a modified Berthelot method [8]. A green coloured complex (λ_{max} 660 nm) formed when salicylate reacted with hypochlorite under alkaline conditions in the presence of a nitroprusside catalyst. The reagents were stored separately in amber containers for improved stability.

Development of detection system

The optical sensor consisted of multiple LEDs of different wavelengths (515nm, 660 nm and 685 nm for nitrite, ammonia and orthophosphate respectively) which were selected as a light source depending on the analyte, using variable resistors to adjust the light intensity. A photodiode was placed in the direct path of the light from the LED and the detection chambers of the CDs. The concentration-dependent output voltage was measured using the on-board Arduino Analog-to-Digital controller (ADC).

CMAS hardware fabrication

A bespoke 3D-printed housing, shown in Figure 3, was produced for hosting the microfluidic discs which incorporated a low-cost optical sensor for colorimetric detection and a stepper motor which generated the centrifugal force necessary to carry out the tests.

Figure 3: Computer generated exploded view of the CMAS components

Operational conditions

Microfluidic discs were spun at 1200 rpm for 30 seconds to deliver 100 µL each of sample and reagent to the detection chamber. Mixing was then carried out by alternating between high and low spin speeds (1200 rpm and 12 rpm) repeatedly for 30 seconds prior to analysis.

RESULTS AND DISCUSSION

Preliminary experiments aimed at demonstrating the applicability of CMAS as a point of need analytical device involved an evaluation of colorimetric methods for the detection of orthophosphate, ammonia and nitrite with the microfluidic discs. For calibration purposes, microfluidic discs were designed to accommodate 6 detection chambers each with an effective path length of 2 mm and a sample volume of 260 µL. These detection chambers were connected to a sample chamber (into which the analyte standards were aliquoted) and connected to either a single or dual reagent chambers. An example of a microfluidic disc containing a single reagent chamber is shown in Figure 4. The analysis of nitrite was based on a diazotization method which required a single liquid reagent while the determination of orthophosphate and ammonia required two reagents to be separately added to the sample. The displacement of both standards and reagents into the detection chambers was achieved by spinning the microfluidic discs at 1200 rpm for 30 seconds using a stepper motor, followed by the alternation of high and low speeds for 3 times (a further 30 seconds in total) to allow mixing of standards and reagents. Depending on the target analyte, different waiting periods were required to allow full color development indicative of reaction completion. A summary of experimental data is shown in Table 1. The LOD values obtained were ca. 4-times higher for all three analytes than values obtained via similar experiments performed using a traditional UV-Vis spectrophotometer. This was attributed to fundamental differences between the two techniques such as the reduced path length (2 mm) present on microfluidic discs and the resolution of Analog-to-Digital controller which affected the discrimination for colorimetric detection.

Table 1: Summary of data for the analysis of nutrients on microfluidic discs.

Target analyte	Calibration range (ppm)	LOD (ppm)	Reaction time (min)
NH_3	0-2	0.233	20
NO_2^-	0-2	0.050	15
PO_4^{3-}	0-5	0.189	5

The quantification of the target analytes was achieved using a LED-photodiode detection system. As illustrated in Figure 4, the required LED was placed in a 3D-printed holder with the photodiode detector held in position below the detection chamber.

For our purposes, manual alignment was required for the correct positioning of the LED over the detection chambers. Optimisation of LED intensity was also required prior to each test and an auto-calibration feature was developed to facilitate this process. This was achieved using a digital resistor which allowed a pre-defined value to be set for blank measurements. The auto-calibration feature involved setting the initial LED intensity as high as possible and then checking the photodiode reading, which was then compared to a pre-set bracket. If the reading was too high, the digital resistor increased in value until the intensity of the LED signal was reduced to a satisfactory level.
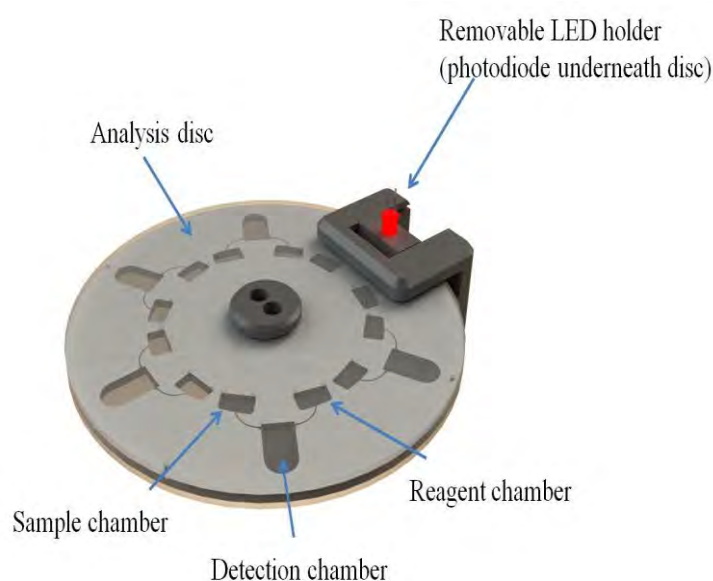
Figure 4: Image showing a 3D-printed prototype system for LED-photodiode detection system on microfluidic discs.

Depending on the light absorbed by the sample, an output voltage was generated and measured by the ADC. These values were converted to absorbance using a Beer's law type equation [9]:

$$A = -\log\left(\frac{\text{sample intensity}}{\text{blank intensity}}\right) \quad (1)$$

As shown in Figure 5, absorbance values were plotted against concentration for each analyte achieving excellent linearity in each case (lowest R^2 value of 0.9802 for ammonia).

CONCLUSION AND FUTURE WORK

The development of a portable microfluidic system suitable for in situ water quality analysis has been described. Preliminary experiments suggest these methods, implemented on microfluidic dics, can be successfully applied for the analysis of nutrients. Further research is in progress to develop and validate

a single disc capable of performing automatic simultaneous detection of these analytes from a single sample aliquot. A fully automated alignment function will also be integrated which will require minimum user manipulation hence minimising human error and improving analysis accuracy.
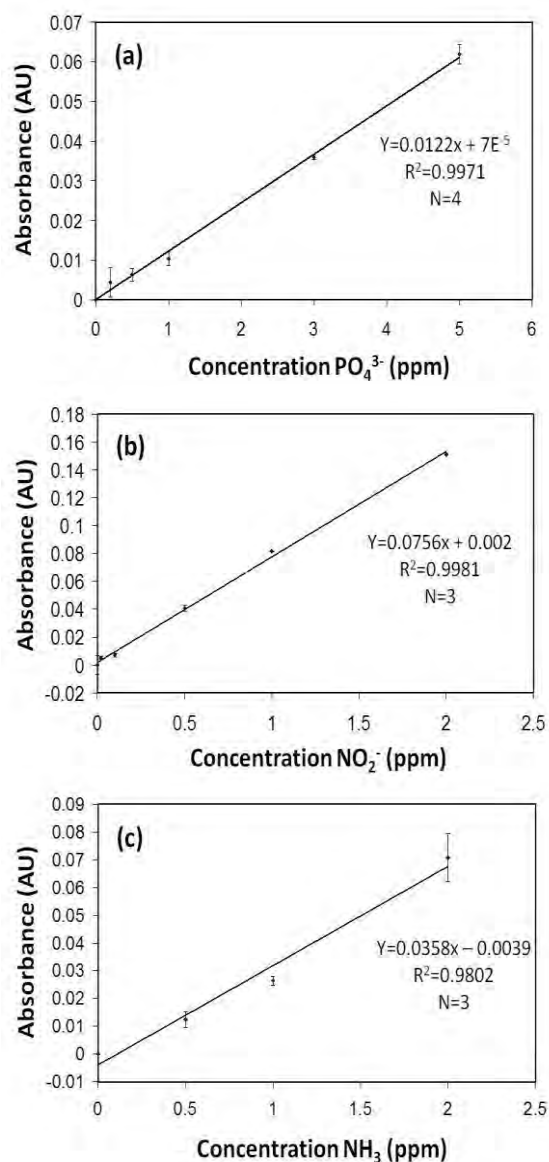

Figure 5: Calibration plots for the determination of (a) orthophosphate, (b) nitrite and (c) ammonia on microfluidic discs.

ACKNOWLEDGMENTS

REFERENCES

[1] A.C. Ariza, P. Linares, M.D. de Castro, M. Valcárcel, ''Flow-injection analysis for on-line monitoring of nutrients (ammonia and nitrite) in aquaculture'', J. Automat. Chem., vol. 14, pp. 181-183, 1992.

[2] P. J. Worsfold, R. Clough, M. C. Lohan, P. Monbet, P. S. Ellis, C. R. Quétel, G. H. Floor and I.D. McKelvie, ''Flow injection analysis as a tool for enhancing oceanographic nutrient measurement-A review'', Anal. Chim. Acta, vol. 803, pp. 15-40, 2013.

[3] M. Czugala, D. Maher, F. Collins, R. Burger, F. Hopfgartner, Y. Yang, J. Zhaou, J. Ducree, A. Smeaton, K. Fraser, F. Benito-Lopez and D. Diamond, ''CMAS: fully integrated portable centrifugal microfluidic analysis system for on-site colorimetric analysis'', RSC Adv., vol. 3, pp. 15928 – 15938, 2013.

[4] M. Czugala, R. Gorkin III, T. Phelan, J. Gaughran, V. F. Curto, J. Ducree, D. Diamond and F. Benito-Lopez, ''Optical sensing system based on wireless paired emitter detector diode device and ionogels for lab-on-a-disc water quality analysis'', Lab on a Chip, vol. 12, pp. 5069-5078, 2012.

[5] C. E. Nwankire, M. Czugala, R. Burger, K. J. Fraser, T. M. O'Connell, T. Glennon, B. E. Onwuliri, I. E. Nduaguibe, D. Diamond and J. Ducrée, ''A portable centrifugal analyser for liver function screening'', Biosens. Bioelectron., 2014, vol. 56, pp. 352-358, 2014.

[6] H. Hwang, Y. Kim, J. Cho, J. Lee, M. Choi and Y. Cho, ''Lab-on-a-Disc for simultaneous determination of nutrients in water'', Anal. Chem., vol. 85, pp. 2954-2960, 2013.

[7] M. O'Toole and D. Diamond, ''Absorbance based light emitting diode optical sensors and sensing device'', Sensors, vol. 8, pp. 2453-2479, 2008.

[8] C.E. Bower and T. Holm-Hansen, ''A salicylate-hypochlorite method for determining ammonia in seawater'', Can. J. of Fish. Aquat. Sci., vol. 37, pp. 794-798, 1980.

[9] M. O'Toole, K.T. Lau, R. Sheperd, C. Slater and D. Diamond, ''Determination of phosphate using a highly sensitive paired emitter-detector diode photometric flow detector'', Anal. Chim. Acta, vol. 597, pp. 290-294, 2007.

2. Applications   Poster
(Bio-analytical systems)

THE LAB-ON-A-CHIP DESIGN & FOUNDRY SERVICE

S. Hin[1], D. Baumann[2], K. Mitsakakis[1,2], V. Klein[1], O. Strohmeier[1,2], M. Keller[1,2], D. Kosse[1,2], R. Zengerle[1,2,3], F. von Stetten[1,2], and D. Mark[1,2]

[1] Laboratory for MEMS Applications, Department of Microsystems Engineering - IMTEK, University of Freiburg, Georges-Koehler-Allee 103, 79110 Freiburg, Germany

[2] HSG-IMIT - Institut für Mikro- und Informationstechnik, Georges-Koehler-Allee 103, 79110 Freiburg, Germany

[3] BIOSS – Centre for Biological Signalling Studies, University of Freiburg, 79110 Freiburg, Germany

ABSTRACT

The Lab-on-a-Chip Design & Foundry Service offers the rapid development of point-of-care systems, which automate diagnostic assays delivered by the customer. The automation is done on a centrifugal microfluidic lab-on-a-chip platform, the LabDisk. The customer profits from the utilization of unit operations in the development process. Those unit operations apply standard rules for the design and production of the cartridges. Unit operations are combined to form process chains for the translation of a manual laboratory protocol into a fully automated analysis. Thus, risk, time, and costs are reduced during the development process, because a well-established production technology is used and existing developments can be re-used. To describe that development process, in this paper the example of a unit operation for liquid reagent release is implemented into a LabDisk for the EU-FP7 project DiscoGnosis. The liquid release is needed in a fluidic structure for nucleic acid extraction from pathogens out of a whole blood sample (50 µl). To implement this unit operation, five different buffer solutions are filled into stickpacks. For each buffer, a research-scale batch of 100 stickpacks is produced. It is demonstrated for all buffers that 4 out of 4 stickpacks release their content in the planned time in the protocol. The time effort for this first design iteration was two weeks, including specification phase, CAD, fabrication, and fluidic validation.

KEYWORDS

Lab-on-a-chip, foundry service, unit operations, centrifugal microfluidics, point-of-care diagnostics

INTRODUCTION

The development of lab-on-a-chip systems for diagnostic applications, such as the detection of infectious diseases, requires extensive knowledge in numerous fields of technology. Microfluidics, production technology, instrumentation, as well as biochemistry and medical knowledge interact with each other. They have to be well controlled and adjusted to achieve optimal performance of the system resulting in maximum benefit for the user. To minimize development effort for new applications, a "toolbox" that offers a set of unit operations is of advantage. Each unit operation represents a standard element for liquid handling to integrate a biochemical assay based on a well-established production technology [1]. By using this strategy we can offer centrifugal microfluidic systems developed with reduced risk, time, and costs.

Development strategy

Based on the customer's specifications, assays are automated on a centrifugal microfluidic platform, the LabDisk. This disposable foil based cartridge has the approximate foot-print of a CD (130 mm diameter) and is operated in a portable processing device, the LabDisk Player (Figure 1). A standard LabDisk Player comprises a motor to rotate the disc and to realize frequency protocols, magnets to handle magnetic particles inside the LabDisk, a heating and cooling unit for temperature control, and a detector for fluorescence and chemiluminescence.

Figure 1: The LabDisk, a foil based unit use cartridge processed by the LabDisk Player. (Source: HSG-IMIT/Bernd Müller)

Development process

At the beginning of a development process (Figure 2) the manual steps from the assay are translated into unit operations, e.g. reagent release, valving, mixing, and aliquoting. Connected to each other, a set of unit operations represents a process chain. A set of process chains is combined to implement a fully automated analysis.
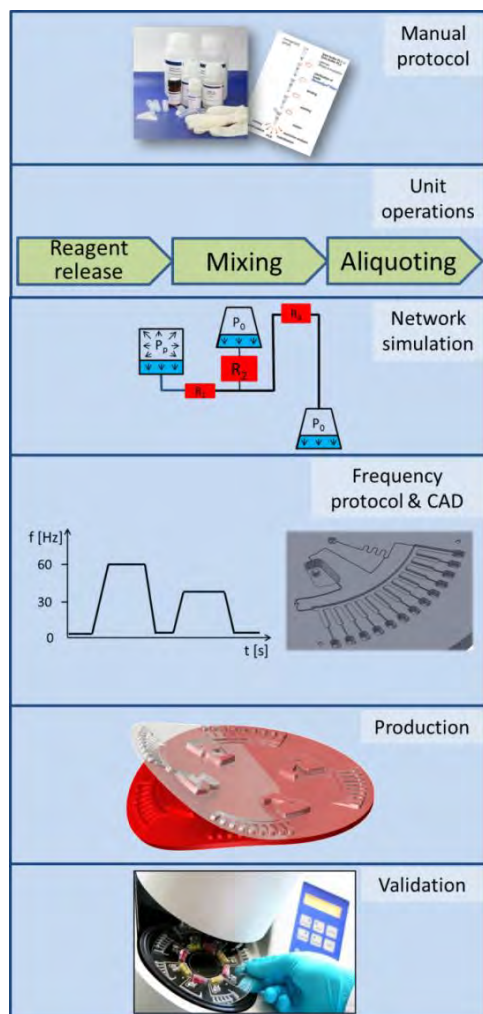

Figure 2: Principle of assay integration into a LabDisk. A manual protocol is translated into unit operations. Then, a network of unit operations is simulated to derive a frequency protocol and a CAD layout. Finally, the LabDisk is produced via micro-thermoforming, and subsequently validated.

Figure 3: Stickpacks for liquid reagent pre-storage and release on demand inserted into a LabDisk.

The interfacing of the unit operations with each other is simulated using microfluidic network simulation, to derive a frequency and temperature protocol for the LabDisk Player and a CAD layout serving as a template for rapid prototyping of the microfluidic structures. Prototyping of the LabDisk is done via micro-thermoforming technology [2], which is adapted from blister production, a low-cost fabrication process used for drug or food packaging. Liquid reagents are pre-stored in stickpacks (Figure 3). These aluminum pouches allow long-term liquid storage and feature frangible seals, which are opened due to liquid pressure under centrifugation [3]. This enables a reagent release on demand at a desired rotational frequency. Dry reagent pre-storage is used for primers and probes in molecular testing, or magnetic beads in sample preparation. Prior to testing, the LabDisk is sealed with a pressure activated adhesive foil. The described production and packaging process enables small scale production of LabDisks (up to 100) for rapid prototyping, as well as pilot production batches for clinical validation (up to tens of thousands). We also offer to accompany our customers in the up-scaling process to mass production.

APPLICATION STUDY

Within the EU-FP7 project DiscoGnosis the Lab-on-a-Chip Design & Foundry Service develops the liquid handling environment [4]. The project DiscoGnosis aims to develop a multiplex diagnostic test to differentiate between tropical diseases causing fever, namely malaria, dengue, typho, and pneumonia. Detection of pathogen-specific nucleic acid targets via loop-mediated isothermal amplification (LAMP) should be performed in parallel with a bead-based heterogeneous immunoassay (Figure 4) on one LabDisk.
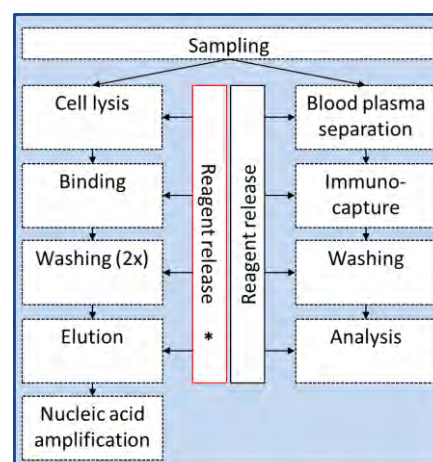

Figure 4: Process chains in DiscoGnosis project. The unit operation described in this paper is the reagent release for the process chains cell lysis, binding, washing, and elution (*).

By this approach, an enlarged diagnostic window is used, since both, nucleic acid targets and protein analytes are measured. All necessary steps are performed in a fully automated manner. This is of great advantage in resource poor settings with low training level of the user.

Task description

The unit operation, which should be implemented for the DiscoGnosis project, is a reagent release for buffers required in the nucleic acid extraction process (prior to LAMP). The reagent pre-storage and release is implemented for five different buffers and performed in parallel. A challenge is posed by the high number of necessary unit operations to perform two assays on one LabDisk. Therefore, a space-saving microfluidic layout is required to achieve the requested integration density. The presented layout solves this problem by placing the stickpacks radially inwards from the chambers to which the respective liquids are supplied (Figure 5).
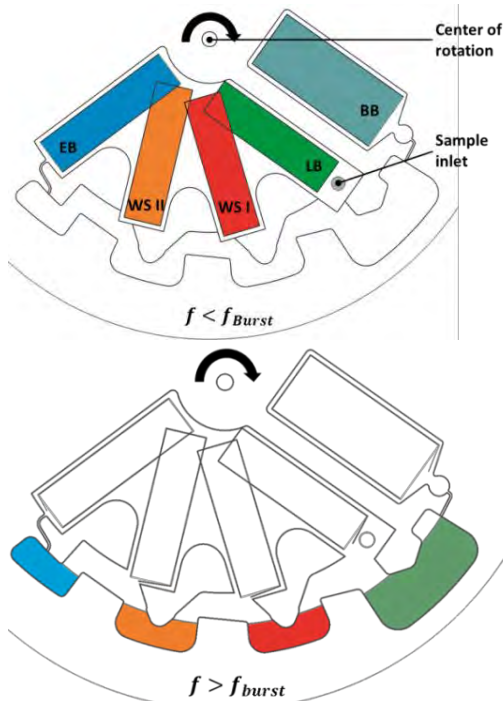

Figure 5: The unit operation of reagent release by stickpacks is shown. In the upper image, stickpacks are closed because the rotation frequency of the LabDisk is lower than the burst frequency. When the burst frequency is reached, stickpacks open and release the liquids to the nucleic acid extraction chambers. BB: Binding buffer; LB: Lysis Buffer; WS I: Washing solution I; WS II: Washing solution II; EB: Elution buffer.

Upon centrifugation of the LabDisk at a specified burst frequency, the stickpacks are opened due to hydrostatic pressure of the liquid acting on the frangible seal at the radially outer side. In this process,

the burst frequency f_{Burst}, at which the stickpacks open, is given by

$$f_{burst} = \frac{1}{2\pi}\sqrt{\frac{2\,p_{liquid}}{\rho*(r_2^2-r_1^2)}} \qquad (1)$$

Where p_{liquid} is the required burst pressure, r_1 is the innermost radius, r_2 is the outermost radius, and ρ the liquid's density.

Specification

The specification process consists in here of three main steps (Table 1): First, the buffer volumes are specified in collaboration with the assay supplier (MagnaMedics Diagnostics B.V., Geleen/ the Netherlands). Then, the burst frequency, at which a stickpack releases its content, is defined by the foundry service based on a frequency protocol (data not shown) for the full process. Finally, the geometrical dimensions are defined in order to achieve a desired hydrostatic pressure according to equation (1).

Table 1: The specified parameters for stickpack production are shown.

Buffer solution	Volume[*] [µl]	Burst frequency[**] [Hz]
Lysis buffer	150	60
Binding buffer	440	75
Wash solution I	200	60
Wash solution II	200	60
Elution buffer	200	60

*: Parameter specified by customer/assay supplier.
**: Parameter specified by fluidic protocol for the complete process.

Fabrication and Validation

The stickpacks are fabricated using a commercial three-side sealing-machine (Merz Verpackungsmaschinen, Lich, Germany). For fluidic validation, stickpacks are centrifuged on a laboratory centrifuge (Sigma1-15P, Sigma Centrifuges, Newtown, UK) at an outermost radial position of r_2=45 mm. On each stickpack, a frequency protocol of 1 min at 40 Hz and 1 min at 60 Hz is applied. After each single step, the integrity on the stickpack is visually checked. When 4/4 stickpacks of a certain type pass this protocol without opening at 40 Hz, but opening at 60 Hz, the test is passed. In this case, another two stickpacks are used for a final check, at which both have to open after 1 min at 60 Hz. This is necessary due to the preliminary applied load in the first test by the 40 Hz step. Thereby, a weakening of the sealing could occur, which would lead to a later falsification of results at the 60 Hz step.

RESULTS

Fabrication resulted in stickpacks with size of 9x33 mm² (washing solutions and elution buffer), 9x30 mm² (lysis buffer), and 15x32 mm² (binding buffer). The validation results are shown in Table 2.

Table 2: Validation results for stickpack burst frequency (opened stickpacks/tested stickpacks).

Buffer solution	Sequentially applied		Directly applied
	1 min 40 Hz	1 min 60 Hz	1 min 60 Hz
Lysis buffer	0/4	4/4	2/2
Binding buffer	0/4	4/4	2/2
Wash solution I	0/4	4/4	2/2
Wash solution II	0/4	4/4	2/2
Elution buffer	0/4	4/4	2/2

It can be seen that all stickpacks open at the desired burst frequency. As shown in Table 1, a burst frequency of 75 Hz is desired for the binding buffer stickpack. This can be achieved by placing that stickpack at a smaller radial position (e.g. r_2=39.5 mm). Then the hydrostatic pressure is comparable to the pressure during the validation experiment. From the data in Table 2 it cannot be concluded whether the stickpacks opened at 60 Hz or at some frequency between 40 Hz and 60 Hz. The time effort for the described task was two weeks. It has to be noted that the present results were obtained in the first iteration. For future projects that have comparable requirements, the development time will significantly reduce, due to the platform-based unit operation approach.

CONCLUSION

The Lab-on-a-Chip Design & Foundry Service offers the possibility to rapidly develop complex lab-on-a-chip systems like in the DiscoGnosis project. Based on the LabDisk platform, manual process steps are translated into unit operations that can also be re-used in further projects. Simulation, layout, production, and validation are offered from one supplier. This significantly minimizes development risk, time, and costs for our customers.

OUTLOOK

Biological validation can be performed in our biological safety level 2 laboratories. As we currently ramp up our production capacities to 50.000-200.000 LabDisks per year, the Lab-on-a-Chip Design & Foundry Service will be able to deliver sufficient numbers of cartridges for clinical validations.

REFERENCES

[1] D. Mark, S. Häberle, G. Roth, F. von Stetten, R. Zengerle, „Microfluidic lab-on-a-chip platforms: requirements, characteristics and applications", Chem Soc Rev, Vol. 39, pp. 1153 – 1182, 2010.

[2] M. Focke, D. Kosse, D. Al-Bamerni, S. Lutz, C. Mueller, H. Reinecke, R. Zengerle, F. von Stetten, „Microthermoforming of microfluidic substrates by soft lithography (µTSL): optimization using design of experiments", J Micromech Microeng, Vol. 21, No. 11, pp. 115001 – 115012, 2011.

[3] T. van Oordt, Y. Barb, J. Smetana, R. Zengerle, F. von Stetten, "Miniature stick-packaging – an industrial technology for pre-storage and release of reagents in lab-on-a-chip systems", Lab Chip, Vol. 13, No. 15, pp. 2888 – 2892, 2013.

[4] K. Mitsakakis, S. Hin, F. von Stetten, R. Zengerle, „Disc-shaped Point-of-Care Platform for Infectious Disease Diagnosis", *The 7th Annual Concertation and Consultation Workshop on Micro-Nano-Bio Convergence Systems (MNBS 2013), Cork, Ireland*, September 24-25 2013.

CONTACT
*S.Hin: sebastian.hin@imtek.de

5. Applications   Poster

POROUS PILLAR ARRAY FORMATION USING ISOTROPIC XENON DIFLUORIDE ETCHING FOR LIQUID CHROMATOGRAPHY MICROCHIP

K. Shih[1], M. Isokawa[2], T. Kanamori[2], D. H. Yoon[1], T. Sekiguchi[3], J. Mizuno[3], T. Funatsu[2], M. Tsunoda[2] and S. Shoji[1]

[1] Major in Nanoscience and Nanoengineering, Waseda University, Tokyo, Japan
[2] Graduate School of Pharmaceutical Sciences, The University of Tokyo, Tokyo, Japan
[3] Nanotechnology Research Center, Waseda University, Tokyo, Japan

ABSTRACT

A method using xenon difluoride (XeF_2) isotropic etching to form porous structure on pillar array column for liquid chromatography (LC) microchip was proposed. This method is a simple technique to form uniform porous structure on pillar surface. The relation of silicon surface condition and the XeF_2 etching behavior was evaluated. The results show that fluorocarbon coated silicon surface has more uniform porous structure than normal silicon after XeF_2 etching. Deep reactive ion etching (DRIE) applied for silicon micro pillars forms fluorocarbon layer on pillar surface. Uniform porous silicon micro pillars were obtained successively by XeF_2 etching without any treatment.

KEYWORDS

Liquid chromatograpy, Xenon difluoride, Porous structure, Isotropic etching, Microfluidics

INTRODUCTION

Development of micro fabrication technology has realized miniaturization in chemical and biological science including chromatographic technologies [1]. Among large number of miniaturized LC systems such as packed bed and monolithic bed capillaries, chip based LC systems has been receiving interest recently [2]. The introduction of micro pillar array as stationery phase presents advantages such as possibility of wafer size fabrication allowing integration with other elements, and controllability of pillar shape and order [3].

Retention ability of analytes in LC microchip is an important performance index which correlates with the surface area of column [4]. Therefore, many approaches have been presented to increase the surface area of micro pillar array. Carbon-nanotube growth [3] and electrochemical anodization [5] have successfully formed porous pillar array increasing the surface area. A method using sol-gel technology is also reported [6]. However, the fabrication processes are relatively complicated or requiring long time. Therefore, a simple method more adaptable to conventional MEMS (Micromechanicalelectro Systems) fabrication technology is requested.

Xenon difluoride etching is a dry etching method widely used in silicon micromachining for three-dimensional microstructure fabrication [7]. It allows plasma-less high rate isotropic etching to silicon. This etching method also increases the surface roughness of silicon forming porous layer [8]. Silicon dioxide can serve as masking material in XeF_2 etching. Hydrofluoric acid treatment must be performed in order to remove the native silicon dioxide immediately before sample loading [9]. Therefore, the surface condition has effect on etching result.

In this research, we consider XeF_2 etching method applicable to porous pillar array formation in LC microchip fabrication process. Since DRIE is the most commonly used method to fabricate silicon micro pillars, fluorocarbon layer usually remains on the pillar sidewall. Therefore, the effect of fluorocarbon layer on silicon surface for XeF_2 etching was evaluated at first, using a handmade XeF_2 etching machine. After evaluating the results, LC microchip with porous pillar array was fabricated.

MATERIALS AND METHODS
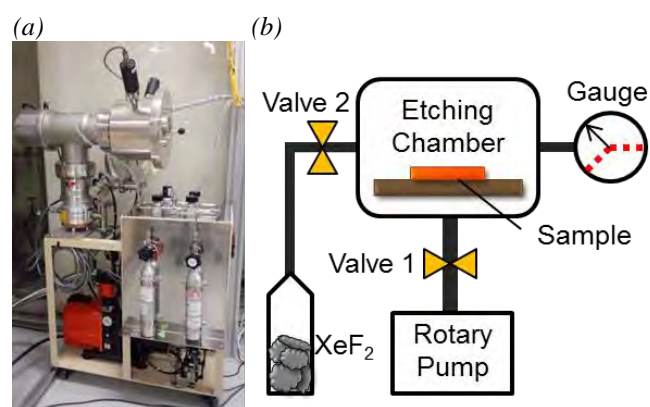
Figure 1: XeF_2 etching machine (a) Photograph of XeF_2 etching machine (b) Schematic of XeF_2 etching machine

In order to compare XeF_2 etching effect on normal silicon and fluorocarbon coated silicon, two types of silicon substrates were prepared. Sulfuric acid cleaning was performed to normal silicon substrate. Fluorocarbon coated silicon was formed using DRIE (RIE-400iPB, Samco, Japan). Etching was stopped at deposition step of DRIE to form fluorocarbon on silicon surface after one etching cycle for cleaning.

Sulfuric acid cleaning was also applied on fluorocarbon coated silicon to make sure both samples are in the same condition.

Table 1: XeF$_2$ etching condition

Upper limit	40 [Pa]
Lower limit	4 [Pa]
Waiting time	1 [s]
Etching cycles	2
Room Temperature	25.8 ℃

Two samples were treated by XeF$_2$ etching. Figure 1 shows the photograph and schematic of the XeF$_2$ etching machine. It consists of an etching chamber, XeF$_2$ source of XsF$_2$ crystal, rotary vacuum pump, and vacuum gauge. First, silicon samples were placed into etching chamber. Valve 1 was opened until the pressure reaches lower pressure limit. Valve 2 then was opened introducing XeF$_2$ vapor into etching chamber. When the pressure reaches the upper limit, valve 1 was closed, and a waiting time can be set for the etching process. After the waiting time, valve 2 was opened again to pump out the gases in etching chamber. These etching steps can be performed repeatedly. Table 1 shows the etching condition. Since the etching rate of XeF$_2$ is fast, the waiting time was set in minimum. Two etching cycles were performed for porous formation.

LC microchip with micro pillar array columns was fabricated using multistep ultraviolet (UV) lithography and DRIE as follows. Twenty millimeter squares silicon substrate with 270 nm of thermal oxidized silicon oxide on both sides was used. First, photoresist (TSMR-V90, Tokyo ohka Kogyo, Japan) was patterned by UV lithography (MA-6, SUSS MicroTec, Germany) for pillar array. The chip was wet etched using buffered hydrofluoric acid (BHF 110U, Daikin Industries, Japan) to transform the pillar array pattern to silicon oxide layer. Second UV lithography process was performed for injection channel patterning. Wet etching of silicon oxide was conducted as well as the first patterning step. This injection channel pattern was etched by DRIE for 30 μm deep. Photoresist was then removed leaving silicon oxide mask of pillar pattern on the surface. DRIE process was performed again to form pillar of 30 μm deep. Through this etching, the depth of injection channel reached 60 μm.

RESULTS AND DISCUSSION

In order to evaluate surface condition, water contact angle of both normal silicon surface and fluorocarbon coated silicon surface were measured as shown in Fig. 2. The contact angle of normal silicon

was 9.9 degree while that of fluorocarbon coated silicon was 59 degree. Since fluorocarbon has hydrophobic characteristic comparing to silicon, we assume that fluorocarbon was formed on silicon surface by DRIE process. Thus these two samples were used for comparison of XeF$_2$ etching effect.

(a)

(b)
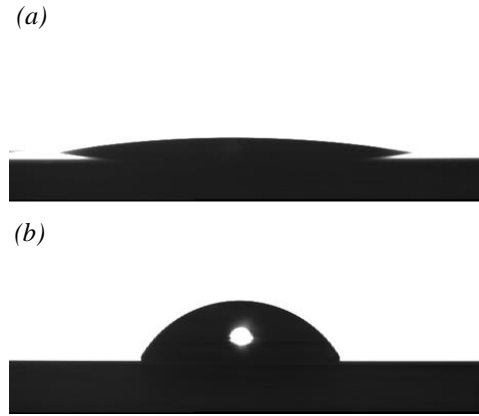
Figure 2: Water contact angle measurement of (a) normal silicon surface and (b) fluorocarbon coated silicon surface
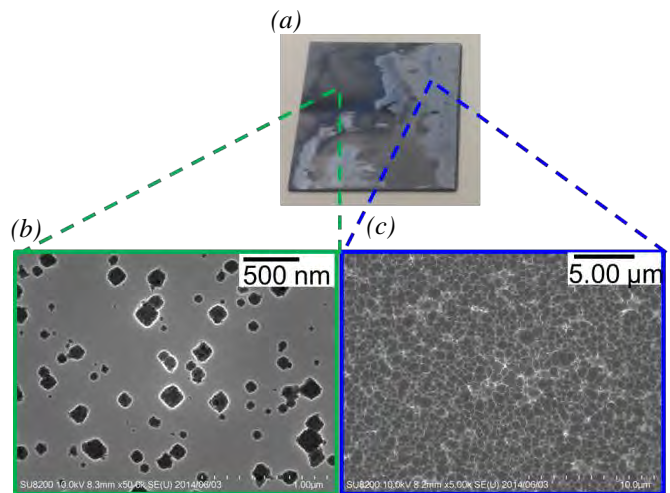
Figure 3: XeF$_2$ Etching results of normal silicon (a) Photograph of whole substrate area (b) SEM observation of deeply etched area (c) SEM observation of lightly etched area
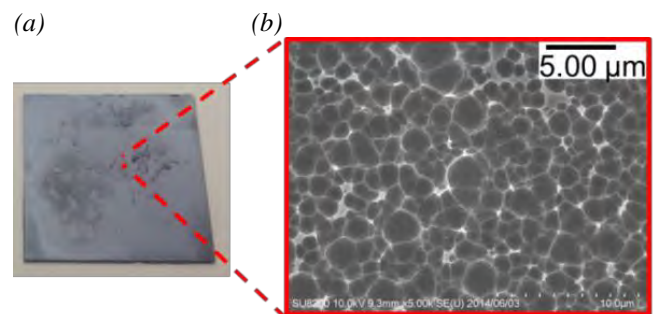
Figure 4: XeF$_2$ etching result of fluorocarbon coated silicon (a) Photograph of whole substrate area (b) SEM image of etched surface

Figure 3 shows the photograph (Fig. 3(a)) and scanning electron microscopic (SEM) images (Fig. 3(b), (c)) of normal silicon after XeF_2 etching. Figure 4 shows the etching results of fluorocarbon coated silicon with same observation methods. Both figures show that porous structure was formed on the surface of substrates. However, the etching result of fluorocarbon coated silicon was uniform throughout whole substrate compared to normal silicon. Inevitable fluorocarbon layer on side wall during LC microchip fabrication helps uniform porous formation using XeF_2 etching without any treatment.

Silicon micro pillar array structure was successfully fabricated as shown in Figure 5 (a). This LC chip was etched by XeF_2 without any pre-treatment that is required for conventional porous formation on silicon surface using XeF_2. Figure 5(b) shows silicon micro pillars with XeF_2 etching treatment. Porous structure was uniformly formed on the surface of micro pillar array (Fig. 5 (b)).

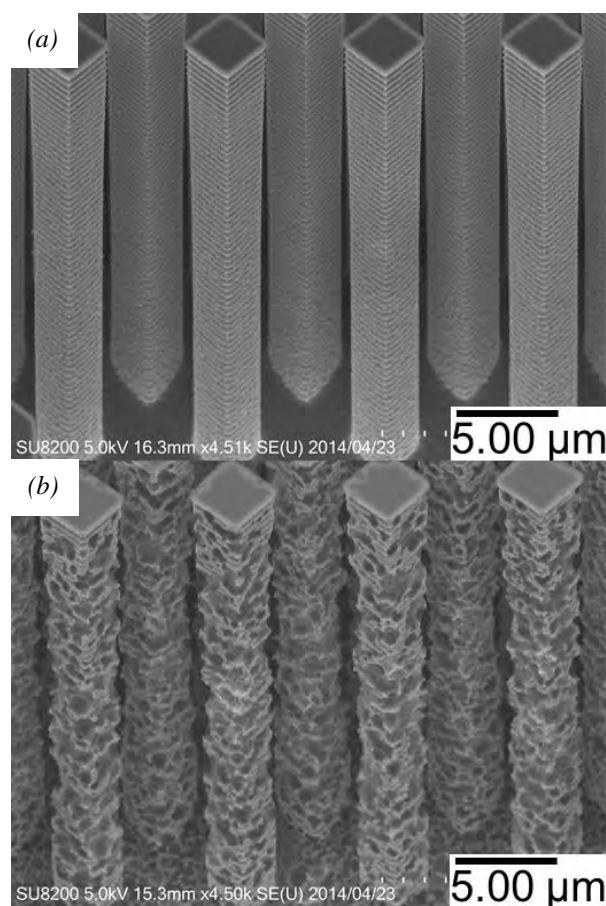*Figure 5: SEM images of silicon micro pillar array (a) untreated pillar array (b) XeF_2 etched pillar array*

CONCLUSIONS

In this paper, a porous pillar array forming method was proposed using XeF_2 isotropic etching. It was shown that fluorocarbon layer formed by DRIE process helps uniform porous formation without any pre-treatment. By using proposed method, uniform porous pillar array was successfully fabricated. As future prospect, pillar design and etching condition must be optimized for practical LC application using this method. The improvement of this porous forming method enables simple fabrication of high performance LC microchip.

REFERENCES
[1] A. J. deMello, "Control and detection of chemical reactions in microfluidic systems," Nature, Vol. 442, pp 394-402, 2006

[2] G. Desmet, S. Eeltink, "Fundamentals of LC Miniaturization", Analytical Chemistry, Vol. 85, Iss. 2, pp.543-556, 2013

[3] A. Fonverrne, C. Demesmay, F. Ricoul, E. Rouviere, J. Dijon, F. Vinet, "New carbon nanotubes growth process in a closed microfabricated channel for liquid chromatography application", Sensors and Actuators A Vol. 167, pp. 517-523, 2011

[4] K. Takatsuki, M. Isokawa, Y. Song, A. Nakahara, D. H. Yoon, T. Sekiguchi, J. Mizuno, T. Funatsu, M. Tsunoda and S. Shoji, "MEMS LC Microchip with Low Dispersion and Low Pressure Drop Turn Structure Using Distribution Controlled micro Pillar Array", *Digest Tech. Papers, MEMS2013 Conference, Taipei, Japan*, January 20-24, pp. 981-984

[5] M. Callewaert, J. Op De Beeck, H. Ottevaere, H. Gardeniers, G. Desmet, W. De malsche, "Integration of Uniform Porous Shell Layers in Microfabricated Pillar Array Columns by Electrochemical Anodization", *Digest Tech. Papers, Transducers2013 Conference, Barcelona, Spain,* June 16-20, pp. 1997-2000

[6] F. Detobel, H. Eghbali, S. De Bruyne, H. Terryn, H. Gardeniers, G. Desmet, "Effect of the presence of an ordered micro-pillar array on the formation of silica monoliths", Journal of Chromatography A, Vol. 1216, pp. 7360-7367, 2009

[7] V. S. Aliev, V. N. Kruchinin, "Development of Si (100) surface roughness at the initial stage of etching in F_2 and XeF_2 gases: ellipsometric study," Surface science, Vol. 442, pp 206-214, 1999

[8] M. Hajj-Hassan, M. Cheung, V. Chodavarapu,

"Dry etching fabrication of porous silicon using xenon difluoride", Micro & nano Letters, Vol. 5, Iss. 2, pp. 63-69, 2010

[9] L. R. Arana, N. de Mas, R. Schmidt, A. J. Franz, M. A. Schmidt, K. F. Jensen, "Isotropic etching of silicon in fluorine gas for MEMS micromachining," Journal of Micromechanics and Microengineering, Vol. 17, pp 384-392, 2007

CONTACT

* K. Shih, kailin@shoji.comm.waseda.ac.jp

5. Applications   Poster

OVERVIEW OF IN VITRO MEASUREMENT STUDIES THAT EXPLORE THE CAUSES OF FLOW RATE VARIABILITY IN INFUSION THERAPY: WHAT ARE THE OPPORTUNITIES FOR MICROFLUIDICS?

R.A. Snijder[1], P. Lucas[2], A.C.G. Egberts[3], J.E.N. Jaspers[1], J.H. Radermacher[1] and A.M.D.E. Timmerman[1]
[1]University Medical Center Utrecht, Medical Technology and Clinical Physics, Utrecht, The Netherlands.
[2]VSL Dutch Metrology Institute, Research, Delft, The Netherlands.
[3]University Medical Center Utrecht, Clinical Pharmacy, Utrecht, The Netherlands.

ABSTRACT

Infusion therapy is both medically and technically challenging. Especially on the intensive care, flow variability may have severe clinical consequences. We present an overview of *in vitro* studies and summarized the physical causes responsible for flow variability in infusion. Subsequently, we discuss the requirements to measure and control this flow variability. The most important physical causes of flow variability were: compliance, dead volume, low flow rate and multi-infusion. Microfluidic technology provides an accurate flow measurement methodology to investigate the physical parameters responsible for flow variability in infusion. In addition, microfluidics might provide innovative possibilities to mitigate flow rate variability.

KEYWORDS

Infusion, review, flowmetry, flow meter, flow variability, medical errors, in vitro, laboratory studies

INTRODUCTION

In health care, infusion therapy is very common. Almost all patients on intensive care units receive continuous infusion therapy. However, infusion technology is also among the most probable sources of technology-related medical errors [1].

Intravenous (IV) drug administration on the intensive care is especially challenging because stable infusion flow rates are necessary. However, these stable flow rates are hard to maintain. There are several reasons for this. First of all, infusion flow rates can be very low. For example, on the neonatal intensive care, flow rates as low as 0.1 ml/h are used to minimize excess fluid delivery. As a consequence, these patients often need very potent pharmaceuticals (drugs). When such potent pharmaceuticals are administered, small variability in infusion flow rate may cause dosing errors. These dosing errors can result in major clinical consequences such as dangerous hypertension (high blood pressure) [2]. Second, intravenous access sites are limited. Usually, only one catheter is available for intravenous drug delivery. Consequently, multiple pumps are combined

on this single catheter, causing the flows from each pump to interact. This principle of joining multiple infusion pumps on one central line has been coined multi-infusion or co-infusion and may be the source of considerable flow rate variability [3]. Third, the total infusion setup consists out of several components, commonly called disposables. While the syringe pumps should produce a relatively accurate outflow, it has been suggested that the physical properties of the components in an infusion setup may still cause an instable and seemingly unpredictable flow rate.

There has been an increased awareness that flow rate variability may be responsible for many of the before mentioned medical errors associated with medical technology. Therefore, in recent years, research has been conducted to trace and assess the origin of infusion flow rate variability. Most of the studies found were *in vitro* laboratory investigations, using various measurement methods. Previous studies have already summarized flow variability studies from a clinical perspective [4]. Recently, Sherwin *et al.* [5] explored infusion studies and stated that the physical variables/causes that affect drug delivery in infusion systems require further exploration. Microfluidics might play an important role in the further investigation of these physical variables by assessing the flow rate characteristics of infusion more accurately. Moreover, when the infusion process is thoroughly understood, innovations and standards that mitigate or eliminate flow rate variability might be developed.

The objective of this study is, therefore, to present an overview of relevant *in vitro* flow rate variability studies. From these studies we will present the physical causes of infusion flow rate variability and the measurement methods that were used. By doing so, we aim to inform researchers and manufacturers about the difficulties and requirements in infusion technology and infusion flow measurement. In addition, we discuss some of the innovative opportunities.

METHODS

We have systematically searched biomedical

literature (Medline, 1994-present) for *in vitro* infusion flow rate variability studies. Only full-text English papers with abstracts were considered. We screened titles and abstracts before reading the entire article. Two sections of information from the studies were retrieved. First, the physical causes of the flow rate variability. Second, the measurement method that was used in the laboratory setup to measure the flow rate variability.

RESULTS

Many cases of flow rate variability have been linked to the infusion components that were used in the infusion setup. Typical components include: syringes, infusion lines (tubing), stop cocks, filters, catheters, cannulae, anti-reflux/check valves and anti-siphon valves [6,7]. However, for each component, there are underlying physical parameters causing the flow rate variability.

Compliance and Resistance

Compliance was often recognized as a physical cause of flow rate variability. Compliance introduces a delayed onset of drug delivery of up to one hour [8]. Compliance can be seen as capacitance, in which volume is stored as the non-rigid infusion components are stretched due to rising pressure applied by the pump. Compliance is defined by equation 1.

$$C = \Delta V/\Delta P \qquad (1)$$

Where C is the compliance, V is the volume increase and P the applied pressure difference. Combined with the resistance of the narrow infusion lines, the infusion setup exhibits typical RC-behaviour. The syringes used in syringe pumps were found to be the most compliant, 2 ml/bar was found using a pressure gauge and a balance [9]. Several infusion lines [10] and syringes [11,12] have been investigated gravimetrically for delayed onset of flow in laboratory studies. The resistance of check valves was investigated with a low flow rate of 0.1 ml/h [6]. The measurements were performed using an accurate thermal mass flow meter suitable for low flow rates. Influence of the cannulae length resistance was also evaluated using a flow meter for relatively high flow rates of 270 ml/min [13]. Contrary to resistance, compliance is mostly problematic for lower flow rates which are also clinically more challenging [4]. Besides the slow onset of the flow, a delayed occlusion alarm is also a problem associated with compliance. The occlusion alarm warns the clinician that an infusion line is obstructed. However, with flow rates of 0.5 ml/h that are used, it can take almost two hours for the pressure to build up sufficiently and

cause an occlusion alarm [14]. Priming the pump to deliver a bolus (a quick single dose) in order to reduce the effective compliance was suggested [15,16]. However, knowledge about physical characteristics of the syringe is needed to perform priming safely.

Dead Volume and Multi-infusion

As was mentioned before, infusion lines are narrow. An important reason for this is to reduce dead volume [17]. Dead volume is the total volume between the pump outflow and the outflow into the patient. When a certain drug concentration is introduced into the infusion line it travels through the dead volume into the patient. Because there is always some distance between the pump and the patient, there are at least a couple of millilitres of dead volume. If multiple infusion pumps are combined on one central line and catheter, the dead space volume is shared between those pumps. In this case, a flow rate change in one pump introduces changes to the entire combined mixture in the central line. A ratio of concentrations introduced in the past is thus administered with the current combined flow rates from all pumps. Flow rate interaction between two syringe pumps was examined [18,19], including the effects of one fast flow (carrier flow) [3,17,20]. Two studies quantified the flow rate variability in two pumps [18] and in three pumps, linking the variability to clinically relevant effects [8]. Absorption-spectrophotometric analysis was used to analyze variability during *in vitro* multi-infusion therapy in real-time. Again, low flow rates are of interest but were hard to measure using absorption spectrophotometry because a balance is needed to measure the total excess fluid. We found that low flow rates (i.e. 0.1 – 5 ml/h) were hard to measure accurately using a balance with a small sample frequency (< 10 seconds) [8].

Miscellaneous

The external conditions of the infusion setup change constantly. For example, temperature may change, affecting the infusion process [21]. Also syringes are renewed, which introduces a sudden interruption of delivery. Although take-over-modes, where one pump proceeds when another pump is empty, may reduce the adverse effects. However, knowledge about the compliance is necessary for one pump to seamlessly take-over another pump. At present, take-over mode is not perfect [22]. The effects of vertical displacement of the pump or patient were also found to cause flow rate variability [23]. Vertical displacement is actually very common as pumps should remain mobile and patients may move as well.

DISCUSSION

Risks of clinical effects due to flow rate variability were especially high on the intensive care. Low flow rates used on the intensive care were hard to maintain and hard to measure. Due to limited vascular access, multi-infusion is used. It was found that this is an important source of flow rate variability. We found multiple physical causes responsible for flow variability. The causes were associated with the infusion components. As the variation in infusion components is substantial, physical assessment of these component may introduce the possibility to predict and control the flow rate variability introduced by the components. In order to do so, adequate measurement techniques and flow sensors are required.

Recommendations

Flow rates from single-pump setups were mostly measured gravimetrically. In multi-infusion measurement, it is necessary to measure the concentration of each drug at the catheter outflow. Most studies used dyes as substitutes for pharmaceuticals and measured those using absorption spectrometric methods. Using spectrometry, it is still necessary to measure the cumulative fluid from all the combined pumps. We have done this gravimetrically [8] but recommend an accurate flow meter suitable for flows between 0.1 – 20 ml/h. In order to accurately assess physical parameters, low sample frequencies of 1 second or lower are required. At those sample frequencies a balance is often not sufficient.

When using flow meters, input pressure should be considered. In some experiments the catheter was immersed in a small amount of water to simulate the intravenous pressure, which could be as low as 5.9 mmHg (0.0079 bar) [23]. Flow meters with an input pressure much higher than the intravenous pressure should be compensated. However, a flow meter with a low input pressure is recommended.

Because of the small size of micro fluidics systems, it is theoretically feasible to employ in-line measurement sensors in clinical practice. Innovations such as a control system might be developed to mitigate or eliminate flow rate variability. Such a control system should be able to control the flow according to real-time measurements in the infusion line. In addition, a flow sensor might be a good alternative for an occlusion alarm. A flow sensor registers an interruption of flow, which follows immediately after obstruction of an infusion line. It has been shown that microfluidic technology is able to measure the flow rates used in clinical practice. As mentioned, besides a good accuracy and precision, a low input pressure should be taken into account.

However, there are some other requirements that need to be considered when developing a clinically applicable infusion sensor. We recommend the following:

- The sensor should be easy to use by clinicians. A clamp-on possibility is an excellent solution.
- If contact with the fluid does occur, the sensor should be either (commercially) disposable or suitable for sterilization.
- Low flow ranges: 0.1 – 20 ml/h are of interest.

If a flow meter is placed in every infusion line, multi-infusion effects due to compliance and dead volume can be largely predicted. However, if a microfluidic sensor can also measure the amount of a certain pharmaceutical in a mixture, only one sensor on the central line is required.

ACKNOWLEGEMENTS

REFERENCES

[1] M. Husch, C. Sullivan, D. Rooney, C. Barnard, M. Fotis, J. Clarke, G. Noskin, "Insights from the sharp end of intravenous medication errors: implications for infusion pump technology," *Qual. Saf. Health. Care*, Vol. 14, no. 2, pp. 80-86, Apr.2005.
[2] C. D. Stowe, S. A. Storgion, K. R. Lee, S. J. Phelps, "Hemodynamic response to intentionally altered flow continuity of dobutamine and dopamine by an infusion pump in infants," *Pharmacotherapy*, Vol. 16, no. 6, pp. 1018-1023, Nov.1996.
[3] B. Decaudin, S. Dewulf, D. Lannoy, N. Simon, A. Secq, C. Barthelemy, B. Debaene, P. Odou, "Impact of multiaccess infusion devices on in vitro drug delivery during multi-infusion therapy," *Anesth. Analg.*, Vol. 109, no. 4, pp. 1147-1155, Oct.2009.
[4] C. M. Sherwin, N. J. Medlicott, D. M. Reith, R. S. Broadbent, "Intravenous drug delivery in neonates: lessons learnt," *Arch. Dis. Child*, Vol. 99, no. 6, pp. 590-594, June2014.
[5] A. C. van der Eijk, R. M. van Rens, J. Dankelman, B. J. Smit, "A literature review on flow-rate variability in neonatal IV therapy," *Paediatr. Anaesth.*, Vol. 23, no. 1, pp. 9-21, Jan.2013.
[6] A. C. van der Eijk, A. J. van der Plas, C. J. van der Palen, J. Dankelman, B. J. Smit, "In vitro measurement of flow rate variability in neonatal IV therapy with and without the use of check valves," *J.*

Neonatal Perinatal. Med., Vol. 7, no. 1, pp. 55-64, 2014.

[7] J. M. Hall and F. L. Roberts, "An investigation into the reduction in flow rate of intravenous fluid by antireflux valves," *Anaesthesia*, Vol. 60, no. 8, pp. 797-800, 2005.

[8] R. A. Snijder, A. C. G. Egberts, P. Lucas, P. M. A. Lemmers, F. van Bel, and A. M. D. E. Timmerman, "Dosing errors and potential clinical impact in preterm infants due to flow rate variability in multi-infusion syringe pump setups: an in vitro inline absorption spectrophotometry study," 2014.

[9] E. Batista et al., "Compliance of drug delivery systems Dependency on several physical parameters and accessories as well as an easy approach for its estimation: EMRP report,"2014.

[10] M. Weiss, O. Banziger, T. Neff, S. Fanconi, "Influence of infusion line compliance on drug delivery rate during acute line loop formation," *Intensive Care Med.*, Vol. 26, no. 6, pp. 776-779, June2000.

[11] D. Neal and J. A. Lin, "The effect of syringe size on reliability and safety of low-flow infusions," *Pediatr. Crit. Care Med.*, Vol. 10, no. 5, pp. 592-596, 2009.

[12] T. Neff, J. Fischer, S. Fehr, O. Baenziger, M. Weiss, "Start-up delays of infusion syringe pumps," *Paediatr. Anaesth.*, Vol. 11, no. 5, pp. 561-565, 2001.

[13] N. V. Jayanthi and H. V. Dabke, "The effect of IV cannula length on the rate of infusion," *Injury*, Vol. 37, no. 1, pp. 41-45, Jan.2006.

[14] A. Donmez, C. Araz, Z. Kayhan, "Syringe pumps take too long to give occlusion alarm," *Paediatr. Anaesth.*, Vol. 15, no. 4, pp. 293-296, Apr.2005.

[15] T. Neff, J. Fischer, S. Fehr, O. Baenziger, M. Weiss, "Evaluation of the FASTSTART mode for reducing start-up delay in syringe pump infusion systems," *Swiss. Med. Wkly.*, Vol. 131, no. 15-16, pp. 219-222, Apr.2001.

[16] J. Y. Kim, B. K. Moon, J. H. Lee, Y. Y. Jo, S. K. Min, "Impact of priming the infusion system on the performance of target-controlled infusion of remifentanil," *Korean J. Anesthesiol.*, Vol. 64, no. 5, pp. 407-413, May2013.

[17] M. A. Lovich, J. Doles, R. A. Peterfreund, "The impact of carrier flow rate and infusion set dead-volume on the dynamics of intravenous drug delivery," *Anesth. Analg.*, Vol. 100, no. 4, pp. 1048-1055, 2005.

[18] A. C. Tsao, M. A. Lovich, M. J. Parker, H. Zheng, R. A. Peterfreund, "Delivery interaction between co-infused medications: An in vitro modeling study of microinfusion," *Paediatr. Anaesth.*, Vol. 23, no. 1, pp. 33-39, 2012.

[19] K. Bartels, D. R. Moss, R. A. Peterfreund, "An analysis of drug delivery dynamics via a pediatric central venous infusion system: quantification of delays in achieving intended doses," *Anesth. Analg.*, Vol. 109, no. 4, pp. 1156-1161, Oct.2009.

[20] D. Lannoy, B. Decaudin, S. Dewulf, N. Simon, A. Secq, C. Barthelemy, B. Debaene, P. Odou, "Infusion set characteristics such as antireflux valve and dead-space volume affect drug delivery: an experimental study designed to enhance infusion sets," *Anesth. Analg.*, Vol. 111, no. 6, pp. 1427-1431, Dec.2010.

[21] Y. Kawabata, "Effect of coefficient of viscosity and ambient temperature on the flow rate of drug solutions in infusion pumps," *Pharm. Dev. Technol.*, Vol. 17, no. 6, pp. 755-762, Nov.2012.

[22] A. Cassano-Piche, M. Fan, S. Sabovitch, C. Masino, A. C. Easty, "Multiple intravenous infusions phase 1b: practice and training scan," *Ont. Health. Technol. Assess. Ser.*, Vol. 12, no. 16, pp. 1-132, 2012.

[23] T. A. Neff, J. E. Fischer, G. Schulz, O. Baenziger, M. Weiss, "Infusion pump performance with vertical displacement: Effect of syringe pump and assembly type," *Intensive Care Med.*, Vol. 27, no. 1, pp. 287-291, 2001.

CONTACT

* R.A.Snijder, R.A.Snijder-2@umcutrecht.nl

5. Applications **Poster**

A MICROFLUIDIC FUEL CELL SIMULATION TO STUDY THE INFLUENCE OF THE POROUS ELECTRODE MORPHOLOGY ON ELECTRODE KINETICS

M. Al-Halhouli[1,2], J. Kieninger[2], P. Daubinger[2], O. Yurchenko[1,2], G. Urban[1,2,3]
[1]University of Freiburg, Freiburg Materials Research Centre - FMF, Freiburg, Germany
[2]University of Freiburg, Department of Microsystems Engineering - IMTEK, Freiburg, Germany
[3]University of Freiburg, Freiburg Institute for Advance Studies, Freiburg, Germany

ABSTRACT

In this work the electrode kinetics of oxidation of organic and bioorganic fuels on a porous electrode (PE) were simulated under microfluidic flow conditions. The influence of the morphology on the current density was investigated and compared with a solid electrode (SE). The pores on PE electrodes provide a three dimensional active area, which results in a high surface area and an increased reaction rates at the electrode [1, 2]. The results show that pore-size and pore-to-pore distance ratio have an influence on the roughness factor of PE surfaces and amplify the current density compared to SE. The observed results are important for fuel cells as well as for sensors applications.

KEYWORDS

Fuel cells, microfluidic, electrode morphology, diffusion, reaction kinetics, current density, COMSOL

INTRODUCTION

A lot of research is ongoing to increase the surface area of electrodes. Porous electrodes and nanowires were used to enhance the roughness factor of the electrode surface, which increases the electrochemical active surface area subsequently [2, 3]. Therefore, the kinetically controlled reaction will take place in an apparent higher reaction rate [2]. Furthermore, one of the most important issues for porous electrode is the low cost. Porous electrodes do not only increase the catalytic activity of electrode surfaces but also decrease the costs due to higher mass activity [2].

In the present paper we investigated the influence of the pore morphology on oxidation current density by means of simulations. Several organic and bioorganic fuels, such as methanol [4], ethanol [5] and glucose [6], can be used in direct fuel cells. Each fuel has its own diffusion and reaction kinetics. We studied diffusion profiles with several pore dimensions. Two values for the diffusion constant at fixed reaction kinetics were used in order to model different fuels.

The simulations of the microfluidic channel were made in 3D mode of COMSOL Multiphysics®. Therefore, two simulation modules were considered. First, transport of diluted species physics, which was used to solve the electrode kinetics, such as reaction kinetics and diffusion at SE and PE. Second, laminar flow physics was applied to solve the microfluidics issues like simulation of flow inside the channel.

The following chemical reaction was used to predict the oxidation taking place on the anode [7]:

$$Re \rightarrow Ox + ne \qquad (1)$$

The mass transport of oxidant and reducing agent inside the microfluidic channel takes place by convection and diffusion. The mass transport by convection was solved by laminar flow physics. Diffusion was solved by the isotropic model of transport of diluted species physics.

Mathematical models of Reaction kinetics

The kinetics of the reactions occurring on the electrode surface is dependent on the electrode potential [8]. The model of Butler-Volmer predicts the currents that results from the overpotential at the electrode [9]. The current-potential characteristic according to Butler-Volmer equation is shown in equation 2:

$$j = Fk^0 \left[C_O \exp\left(\frac{-\alpha F\eta}{RT}\right) - C_R \exp\left(\frac{-\alpha F\eta}{RT}\right) \right] \qquad (2)$$

where j is current density (A/m^2), F is the Faraday constant (C/mol), k^0 is the standard heterogeneous rate constant (m/s), C$_j$ is the concentration of species j (O is oxidant and R is reducing agent) at the electrode surface (mol/m^3), α is the activity constant, η is the overpotential (V), R is the gas constant (J/(mol K)) and T is the absolute temperature (K) [8].

Equation 2 can be rewritten in terms of exchange current density j$_0$ which is defined as the current density at equilibrium, when the overpotential equals 0 V [8]:

$$j_0 = Fk^0 C_O^{1-\alpha} C_R^\alpha = Fk^0 C_{Ref} \qquad (3)$$

where C$_{Ref}$ is reference concentration at which bulk oxidant and reducing agent concentrations are equal.

Mathematical models of Microfluidics

The flow inside the channel is a pressure-driven flow for an incompressible liquid, which leads to a parabolic velocity profile [10]. Three-dimensional

Navier-Stokes equation is used to simulate the incompressible flow inside the channel. The equation is a built-in equation in *single phase flow* (spf) laminar flow physics. Navier-Stockes equation (as in spf module) is as following:

$$\rho(u \cdot \nabla u) = \nabla \cdot \left[-pI + \mu\left(\nabla u + (\nabla u)^T\right)\right] + F \qquad (4)$$

where ρ is liquid density (kg/m^3), u is the vector of liquid velocity (m/s), p is pressure (Pa), μ is liquid viscosity (Pa·s) and F is volume force (N/m^3). Equation 4 represents the influence of pressure gradient, viscous forces and volume force on flow velocity [11].

SIMULATIONS AND METHODS

Finite element simulator, COMSOL Multiphysics® version 4.4, was used to investigate the current density dependency on the pore surface geometry of PE which was integrated in a microfluidic channel of a fuel cell. The surface geometry variations were employed by changing the ratio between the pore-size and the pore-to-pore distance.

Electrochemical simulation

In simulations, 1-electron oxidation of reducing agent was investigated at overpotential of 1 V in all cases. All simulations were made considering phosphate buffered saline (PBS) at pH 7.4. PBS has been applied as reported by Daubinger *et al.* [3]. It consists of 85.2 mM of Na$_2$HPO$_4$·12H$_2$O and 14.8 mM of NaH$_2$PO$_4$·H$_2$O. Then, pH-value was adjusted to 7.4 by adding HCl.
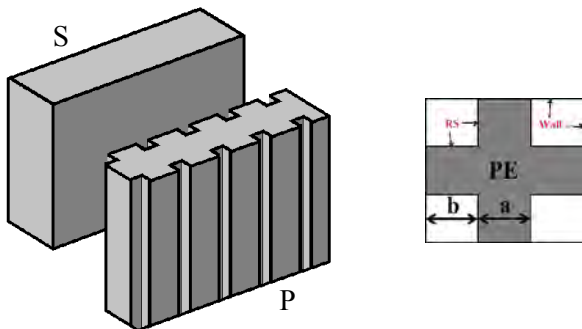

Figure 1. The model of the solid electrode (SE) and the porous electrode (PE) (left) and the boundary conditions for reaction kinetics (right): b is the pore-size, a is the pore-to-pore distance and RS is reaction surface.

The geometries of PE and SE electrodes, which were used in simulations, are presented in Fig. 1. The PE electrode contains 10 pores (5 rows in 2 columns) and SE electrode has a flat surface of equal dimensions as the PE electrode. The pores are square-

holes of pore-size called *b* separated by pore-to-pore distance called *a*.

Microfluidics Simulation

The simulations assumed that the parabolic velocity profile was completely developed and the concentration was homogenous along the inlet. Thus, the parabolic velocity profile was considered as a function of the average velocity and the actual channel thickness. The derivation is as following:

$$u(y) = y(H - y) \cdot z \qquad (5)$$

where u is the velocity inside the fluidic channel, H is channel thickness, y is the distance along the height of the channel and z is a variable which depends on the maximum flow velocity (u_{max}). The value of z can be calculated at the middle of the channel (y = H/2 → u(H/2) = u_{max}). Accordingly, equation 5 will be rewritten as following:

$$u(y) = y(H - y) \cdot (4u_{max}/H^2) \qquad (6)$$

Finding the flow average velocity ($\bar{u}$) by integrating equation 6 and normalizing it by H yields the following equation:

$$u(y) = 6 \cdot \bar{u} \cdot y \cdot (H - y)/H^2 \qquad (7)$$

This equation was used as an input velocity in laminar flow physics to provide a fully developed parabolic profile. Therefore, it was possible to simulate only parts of the channel. The simulated channel was the bottom corner at the inlet of the actual channel (Fig. 2).
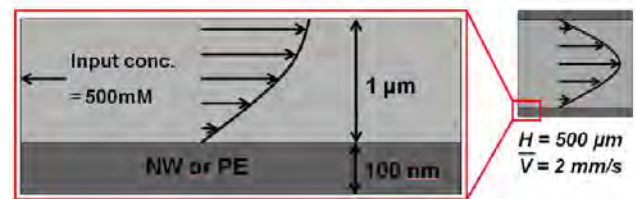

Figure 2. Simulation channel (left) of 100 nm thickness of PE or SE electrode and 1μm microfluidic channel. The simulated channel is part of the actual proposed channel (right). The height of the actual channel is 500μm and the average velocity of the laminar flow is 2 mm/s.

The average velocity of 2 mm/s was applied as a boundary condition for laminar flow. The concentration of the reducing agent at the inlet was 500 mM, as shown in Fig. 2. The height of the actual channel, the simulated microfluidic channel layer and the electrode layer were 500 μm, 1 μm, and 100 nm, respectively. The calculations were performed for

varied pore sizes (3 nm and 6 nm) and different pore-to-pore distances (3 nm, 6 nm, 9 nm, 12 nm and 18 nm).

The approximated values of viscosity and density of water at room temperature, 1 mPa·s and 1000 kg/m^3, respectively, were used. Thus, in a channel with width of 500 μm and thickness of 500 μm Reynolds number Re is 1, which is within the laminar flow range.

SIMULATION APPROACHES
Dependent variables

The concentrations of reducing agent and oxidant are implemented in Butler-Volmer equation (2) and PBS components were implemented in Henderson-Hasselbalch [12] equation (8):

$$pH = pKa + \log \frac{[Na_2HPO_4]}{[NaH_2PO_4]} \qquad (8)$$

Both equations were used in the physics of transport of diluted species as a 3D space. In Navier-Stokes equation (4), the standard dependent variables (pressure and velocity) are applied without applying volume force or any external force.

Surface reactions

The oxidation process takes place at the reaction surface and as result of reaction, the reducing agent is consumed and the oxidant is produced. The reaction rate has been calculated within the simulation by using Faraday's law [9]:

$$Q = \mp nFN_i \qquad (9)$$

Where N_i is the amount of produced or consumed species (mole), Q is the total charge, (C). Negative sign indicates consumption of reducing agent and positive sign indicates the production of oxidant.

Boundary conditions

In the transport of diluted species physics, the inner sides of pores, the top surface of the porous electrode and the top surface of solid electrode (Fig. 1) were defined as a reaction surface (RS).

In laminar flow physics, the pore walls, the top surface of porous electrode and solid electrode were defined as walls. The flow direction is defined as shown in Fig. 2. All other boundaries (simulation channel sides and top) are defined as symmetry boundaries to avoid any hindrance. Symmetry boundaries are important to simulate real conditions since we simulate an inner part of the channel and there is no contact to the channel walls.

RESULTS

Although the length of the simulation channel is too small (27 nm – 102 nm) to develop a parabolic flow profile, a velocity equation (7) was applied to determine the flow based on the average flow velocity. This approach allowed us simulating a completely developed parabolic velocity profile.

Mass transport inside the channel was in two perpendicular directions. Fist direction is from the inlet towards the outlet. The second direction is from the opening of the pore towards its bottom. Therefore, there are two perpendicular directions driven by flow and diffusion. The convection mass transport was solved by Navier-Stockes equation and diffusion was solved by isotropic approach, which is provided by COMSOL.
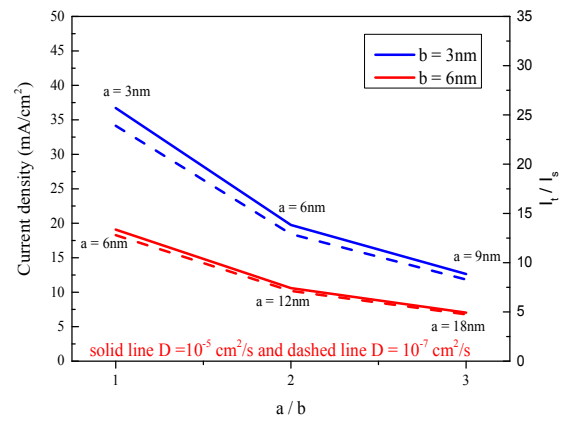

Figure 3. Current density of PE electrode at several a/b ratio, several pore-size and two diffusion values: 10^{-5} cm^2/s (solid lines) and 10^{-7} cm^2/s (dashed lines). PE current magnification is presented and compared with SE (I_t current density for PE, I_s- current density for SE).

The results (Fig. 3) of PE show that both the roughness factor Rf and a/b ratio as well as the pore-size influence the current value. For example, at diffusion constant D = 10^{-5} cm^2/s, the current density for b = 3 nm is higher than for b = 6 nm: for the given pore depth, when a/b ratio is 1, pore-size of 3 nm (Rf = 34.3) and pore-size of 6 nm (Rf =17.6) result current density of 36.7 mA/cm^2 and 19 mA/cm^2. Thus, the current amplification compared to SE is of 27.5 folds and 13.3 folds, respectively.

Moreover, Fig. 3 shows that porous electrode of small pore-size is more sensitive to the diffusion constant. When pores-size is 3 nm, the current density difference between reducing agent with D = 10^{-5} cm^2/s and reducing agent with D = 10^{-7} cm^2/s is bigger than the difference between the same reducing agents when pore-size is 6 nm. For example, when a/b =1, the current density differences between D = 10^{-5} cm^2/s and D = 10^{-7} cm^2/s are 2.6 mA/cm^2 and 0.8 mA/cm^2

for pore-size 3 nm and 6 nm, respectively. This can be explained by the different diffusion distances inside pores.

Additionally, when $D = 10^{-7}$ cm^2/s, the minimal reducing agent concentration obtained for b = 3 nm (a/b = 1) and for b = 3 nm (a/b = 3) are 446 mM and 469 mM, respectively. That means the consumption of reducing agent is faster in smaller pore-size (Fig. 4). The lower reducing agent concentration and the higher current density on porous electrodes by small pore-size are due to the diffusion distance. The diffusion distance in small pores is less than it in big pores.
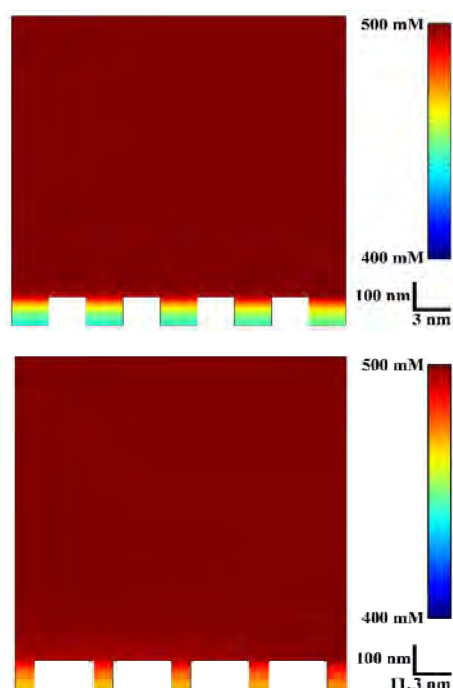

Figure4. Profile of reducing agent (D = 10^{-7} cm^2/s) concentration inside the flow channel for a = 3 nm, b = 3 nm (upper) and for a = 6 nm, b = 18 nm (lower). The concentration scale and the geometrical scale for width and height are show on the right of each figure.

CONCLUSION

In this work, basic theories of microfluidics and electrochemistry were used to solve diffusion, convection, mass transport, and reaction kinetics inside micro- and nanoporous electrodes. The influence of the roughness factor by changing specific characteristics, like the pore-size and pore-to-pore distance, was investigated. The applied procedure can be adapted and expanded in order to study various geometries likes (nanowires, hierarchical structures, and more detailed investigations of electrochemical characteristics).

The simulations of the electrode kinetics for porous electrode show how the tuning of a/b ratio and pore size influence the current density. Further, the geometrical aspects, which influence the roughness factor, were investigated.

REFERENCES:

[1] E. Kjeang, R. Michel, D. A. Harrington, N. Djilali, and D. Sinton, "A microfluidic fuel cell with flow-through porous electrodes", J.Amer.Chem.Soc., Vol. 130, pp. 4000-4006, 2008.

[2] A. Kloke, C. Kohler, A. Dryzga, R. Gerwig, K. Schumann, M. Ade, R. Zengerle, and S. Kerzenmacher, "Fabrication of Highly Porous Platinum by Cyclic Electrodeposition of PtCu Alloys: How do Process Parameters Affect Morphology?", J. Electrochem. Soc., Vol. 160, pp. D111-D118, 2013.

[3] P. Daubinger, J. Kieninger, T. Unmüssig, and G. A. Urban, "Electrochemical characteristics of nanostructured platinum electrodes – a cyclic voltammetry study", Phys. Chem. Chem. Phys., vol. 16, no. 18, pp. 8392–8399, 2014.

[4] H. Liu, C. Song, L. Zhang, J. Zhang, H. Wang, and D. P. Wilkinson, "A review of anode catalysis in the direct methanol fuel cell," J. Power Sources, vol. 155, no. 2, pp. 95–110, 2006.

[5] C. Lamy, S. Rousseau, E. Belgsir, C. Coutanceau, and J.-M. Léger, "Recent progress in the direct ethanol fuel cell: development of new platinum–tin electrocatalysts," Electrochim. Acta, vol. 49, no. 22-23, pp. 3901–3908, 2004.

[6] N. Fujiwara, S.-i. Yamazaki, Z. Siroma, T. Ioroi, H. Senoh, and K. Yasuda, "Nonenzymatic glucose fuel cells with an anion exchange membrane as an electrolyte," Electrochem. Commun., vol. 11, no. 2, pp. 390–392, Feb. 2009.

[7] F. Scholz, "Electroanalytical methods: Guide to experiments and applications", 2nd edition, Springer, 2010.

[8] A. J. Bard and L. R. Faulkner, "Electrochemical methods and applications", 2nd edition, Wiley-Interscience, 2000.

[9] C. G. Zoski, "Handbook of electrochemistry", 1st edition, Elsevier, 2007.

[10] E. Kjeang, N. Djilali, and D. Sinton, "Microfluidic fuel cells: A review," J. Power Sources, Vol. 186, pp. 353–369, 2009.

[11] D. E. Angelescu, "Highly integrated microfluidics design",Artech House, 2011.

[12] Malheiros, Sônia V P, Pinto, Luciana M A, L. Gottardo, D. K. Yokaichiya, L. F. Fraceto, N. C. Meirelles, and E. de Paula, "A new look at the hemolytic effect of local anesthetics, considering their real membrane/water partitioning at pH 7.4", Biophys. Chem, vol. 110, no. 3, pp. 213–221, 2004.

5. Analytical systems

SMALL-ANGLE X-RAY AND NEUTRON SCATTERING IN COMBINATION WITH DROPLET MICROFLUIDICS

S. Seiffert[1,2]
[1] Helmholtz-Zentrum Berlin, Soft Matter and Functional Materials, Berlin, Germany
[2] Freie Universität Berlin, Institute of Chemistry and Biochemistry, Berlin, Germany
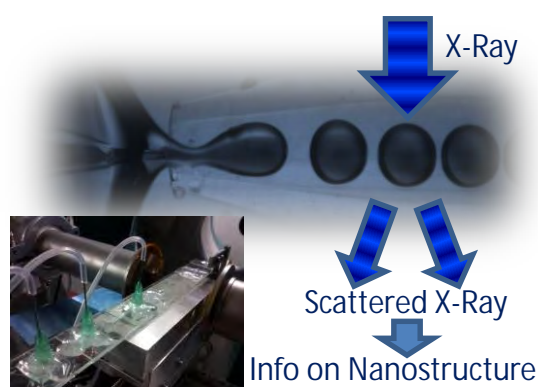
Small-angle X-ray scattering (SAXS) and small-angle neutron scattering (SANS) are powerful techniques to probe nanometer-scale structures. This contribution presents the combination of both SAXS and SANS with multiphase, droplet-based microfluidics.

In one branch of this work, SAXS is implemented within a microfluidic droplet generator to probe nanometer-scale structures in monodisperse emulsion droplets, as illustrated in Figure 1 [1]. In this approach, two different classes of microfluidic devices are used. One class of devices is based on silicone elastomers, serving to form water-in-oil emulsion droplets that contain gold nanoparticles as a model analyte. These emulsion droplets serve as nanoliter-scale compartments that are probed by SAXS off the microfluidic chip. In another class of devices, droplets are both created and probed on the same microfluidic chip that is built from glass microcapillaries. Both variants allow the gold-nanoparticle scattering to be isolated from the raw data; subsequent fitting yields quantitative information on the size, shape, and concentration of the nanoparticles within the compartmentalizing emulsion droplets. In addition, the microfluidic flow parameters scale with the scattering cross-sections in a quantitative fashion. These results foreshadow the utility of this technique for other, more sophisticated tasks such as single-protein analysis or automated assaying.

Figure 1: Small-angle X-ray scatting in droplet-based microfluidics. Main figure: optical micrograph and schematic of in-situ droplet formation and downstream SAXS analysis. Inset: Photograph of a glass micro-capillary device to form and probe microfluidic emulsion droplets by SAXS in situ, placed within an X-ray beam at the ASAXS beamline at BESSY II synchrotron, Helmholtz-Zentrum Berlin.

In the first variant of droplet-based microfluidic SAXS, both is conducted independent of each other. This can be achieved by use of polydimethylsiloxane (PDMS) elastomer-based microfluidic devices to form water-in-oil emulsion droplets that are then pumped through a thin-walled detection glass capillary; this occurs outside the PDMS microfluidic chip. This strategy introduces great flexibility of the experimental implementation, offering custom combinations of channel designs and detection capillaries to be connected in a modular fashion. In the following, the discussion is limited to the use of a 10-µm walled capillary with a cylindrical cross-section of 300 µm (Hilgenberg mark-tube, special glass No. 0140). To demonstrate the utility of this approach, aqueous droplets that contain a suspension of gold nanoparticles at a gold concentration of 98 mg L^{-1} are emulsified by flow-focusing with fluorocarbon oil (HFE 7500, 3M) plus surfactant (Krytox® 157 FSL, DuPont, 1.8 wt.-%) in a 100-µm dropmaking microfluidic device The resulting water-in-oil droplets exit the microfluidic chip and enter the thin-walled detection glass capillary placed within a SAXS setup.

When SAXS is performed on a plain water-in-oil emulsion that does not host any additional load inside its droplets, scattering with $d\sigma/d\Omega \approx 0.05$ cm^{-1} is observed in the range of $q = 0.5$–2.5 nm^{-1}, whereas the scattering at $q = 0.1$–0.5 nm^{-1} is up to one order of magnitude stronger. This scattering can be addressed to several parasitic effects, including scattering by the detection microcapillary, refraction at the droplet interfaces, and scattering due to surfactant micelles in the emulsion. However, if analytes are encapsulated within the droplets, all these contributions superimpose to the analyte scattering in an independent, additive fashion. Thus, the plain-emulsion scattering can be subtracted from the scattering obtained from analyte-laden emulsions to isolate the scattering of the analyte. In the following, this approach is applied to an emulsion that contains gold nanoparticles within its water droplets.

When SAXS is performed on droplets that contain gold nanoparticles, the scattering is about one order of a magnitude stronger than the scattering of the plain water-in-oil carrier emulsion in the range of $q = 0.1$–0.5 nm^{-1}. Subtraction of the plain-emulsion scattering from the scattering of the emulsified gold-nanoparticle suspension yields a curve that corresponds to the form factor of spherical nanoparticles with a Gaussian size distribution. Fitting with this model denotes an average particle radius of $R = (8.1 \pm 1.0)$ nm, in good agreement to dynamic light scattering estimates.

In addition to information on size and structure, SAXS is also suited to probe the concentration of scatterers. This quantity is related to the scattering cross-section, which includes two contributions: the contrast of the scatteres and their number within the detection volume: $d\sigma/d\Omega(q = 0) = n\, r_0^2\, \Delta\rho^2\, V^2 = r_0^2\, \Delta\rho^2\, V\, \Phi$,[1] where n is the density of scatterers in the detection volume, r_0 the electron scattering length (2.8×10^{-13} cm), $\Delta\rho$ the electron density contrast between the scatterers (here: gold particles) and the solvent (here: water), and $V = 4/3\, \pi\, R^3$ ($R = 8.1$ nm) the particle volume. $\Phi = n\, V$ denotes the volume fraction of the scattering particles in the detection volume. In the present approach, this quantity is composed of two contributions: the gold-nanoparticle volume fraction in their aqueous suspension, $\Phi_{Au\text{-}NP}$, and the volume fraction of emulsion droplets wherein which this suspension is compartmentalized, $\Phi_{Droplets}$; thus, $\Phi = \Phi_{Au\text{-}NP}\, \Phi_{Droplets}$. The concentration of gold nanoparticles in the aqueous phase is constant, $\Phi_{Au\text{-}NP} = const.$, but variation of the flow rates of the oil and water phases in the microfluidic experiment varies the droplet size and spacing. Thus, $\Phi_{Droplets} = v_{NP}/(v_{NP} + v_{Oil})$, with v_{NP} the volumetric flow rate of the aqueous nanoparticle suspension and v_{Oil} the volumetric flow rate of the carrying oil. As a result, the macroscopic scattering cross-section scales with the fluid flow rates by $d\sigma/d\Omega(q=0) \sim v_{NP}/(v_{NP} + v_{Oil})$. By taking into account this dependence, one can calculate $\Phi_{Au\text{-}NP} = 6.5 \times 10^6$; this corresponds to a particle concentration of 2.9×10^{12} particles per milliliter and a gold concentration of 94 mg L^{-1}, in excellent agreement to the value used for the synthesis of the nanoparticles (98 mg L^{-1}).

In addition to SAXS analyses on pre-existing gold nanoparticles, the present droplet-based microfluidic approach can also serve to probe particles that are formed in-situ within compartmentalizing emulsion droplets. For this purpose, a glass microcapillary device is constructed that combines mixing, dispersion, and probing of two independent fluids on the same chip, as illustrated in Figure 1. With this device, both fluids are combined within monodisperse emulsion droplets, with a volumetric ratio that is determined by their respective flow rates. About five centimeters downstream, the droplets enter a thin-walled glass capillary that serves for SAXS detection.

When this device is fed with a 1-mM aqueous solution of tetrachloroauric acid and a 2-mM solution of sodium borohydride in 1-mM aqueous NaOH, along with fluorocarbon oil plus surfactant, the resulting emulsion droplets act as nanoliter reaction vessels wherein which gold nanoparticles nucleate and grow. The reacting system is probed 6.6 cm downstream the point of droplet formation, corresponding to a droplet dwell time of 4.2 s at fluid flow rates of 1.5 mL h^{-1} for each aqueous phase and 2 mL h^{-1} for the oil phase. At these flow rates, measurements at different positions of the detection capillary allow dwell times of 3.2–5.0 s to be covered.

Again, the scattering curve of the actual analyte is isolated from the overall scattering signal by subtracting an independent estimate of the signal of plain emulsion droplets that contain 2-mM sodium borohydride in 1-mM aqueous NaOH only. The resulting scattering data can be linearized by a Guinier representation; this analysis yields a Guinier radius of about 14.8 nm, corresponding to a particle radius of 19 nm. The particle concentration can again be calculated as outlined above, yielding a value of 5.3×10^{11} mL^{-1}. Thus, the mixing of the reactants leads to the formation of gold nanoparticles similar to those used in the previous experiment, but this time they are formed in-situ after the droplet pinchoff. This shows that the droplet-based microfluidic sample interfacing is applicable to labile compounds that need to be probed immediately after their formation.
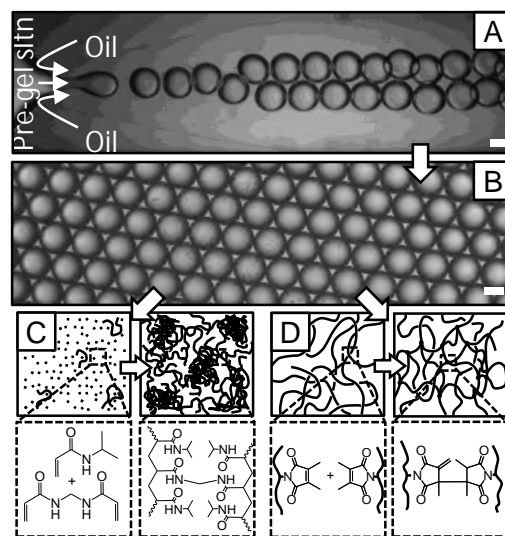
Figure 2. Preparation of thermo-responsive pNIPAAm microgels by droplet-based microfluidics, which are then probed by SANS. The gel homogeneity is varied by different ways of pre-microgel droplet gelation. (A) Glass capillary microfluidic device emulsifying an aqueous pre-gel solution. (B) Monodisperse pre-microgel emulsion droplets. (C) Uncontrolled droplet gelation by free-radical crosslinking copolymerization produces microgels with pronounced nanometer-scale polymer-network heterogeneity (D) Selective inter-connection of pre-polymerized chains that carry photolinkable moieties forms homogeneous microgels. Scalebars are 100 μm. Adopted in part from Ref. [2]. Copyright 2012, 2013, and 2014 Wiley VCH.

In a second branch of this work, droplet-microfluidic reactors are used to fabricate sub-millimeter-sized microgel particles with exquisite, determined and minimized static polymer-network heterogeneity on nanometer lengthscales, as illustrated in Figure 2 [2]. These microgels are then studied by small-angle neutron scattering (SANS) with a particular view to dynamic critical concentration fluctuations, the detectability of which is strongly affected by the co-existing static nanometer-scale polymer network inhomogeneity.

The material basis of this investigation is a set of thermo-sensitive pNIPAAm-based microgel particles that exhibit sizes in the sub-millimeter range, therefore showing considerably fast response to external actuation. In contrast to potentially smaller, micrometer-scale colloidal microgels, such sub-millimeter-scale particles can be made by controlled gelation processes, allowing them to be obtained with minimized and controlled degrees of internal heterogeneity. If this is combined with microfluidic particle templating, the benefit of controlling the microgel homogeneity can be further extended, because potential polymer gel heterogeneity that arises from local heating during the gelation and from insufficient mixing of the gelling precursors is largely suppressed. In addition, the size of the particles obtained by microfluidics, $d \sim 200–350$ μm, covers a perfect range for the studies anticipated: whereas these microgels behave like macroscopic gels in SANS, they can be efficiently heated and cooled on convenient timescales.

Two different types of microgel particles are compared. The first type of particles comprises microgels that are gelled by free-radical crosslinking copolymerization of N-isopropylacrylamide (NIPAAm) and N,N'-methylenebisacrylamide (BIS) in water, as shown in Figure 2C, exhibiting a monomer and crosslinker content that corresponds to the critical composition at the verge between continuous and discontinuous volume phase transitions. Several stocks of these particles are polymerized at different temperatures, $T_{prep} = 10$ °C, 20 °C, and 28 °C, exhibiting 25-°C D$_2$O-swollen sizes in the 220–250-μm domain. The second type of particles comprises microgels that are not gelled by monomer chain-growth gelation but by polymer-analogous gelation of pre-polymerized, macromolecular pNIPAAm in aqueous semidilute solution, as shown in Figure 2D. The precursor polymer is functionalized with photo-crosslinkable dimethylmaleimide moieties in a random sequence that can be selectively interconnected by light-induced dimerization within the templating pre-microgel emulsion droplets. This approach yields a network with a theoretical crosslinking density that resembles the theoretical crosslinking density that can be achieved in the preceding free-radical gelation of NIPAAm and BIS. However, in contrast to free-radical gelation, such polymer-analogous photogelation has been shown to yield networks with greater homogeneity [2].

All these different microgel particles are just narrowly disperse in size, with coefficients of variation of less than ±5%. To quantify their internal nanometer-scale polymer network heterogeneities, proton multiple-quantum NMR at low magnetic fields is used to determine a dipolar coupling constant that is a microscopic observable reflecting the local crosslink density along with its heterogeneity. A strong increase of the relative distribution width, w_Γ, is notable for the microgel sample prepared by free-radical co-polymerization at elevated temperature ($T_{prep} = 28$ °C, $w_\Gamma = 1.09$) compared to the samples prepared at $T_{prep} = 10$ °C ($w_\Gamma = 0.68$) and $T_{prep} = 20$ °C ($w_\Gamma = 0.57$); the microgel batch synthesized by polymer-analogous photogelation exhibits a distribution width comparable to the latter sample ($w_\Gamma = 0.57$).

The preceding analyses reveal that the microgels prepared by free-radical crosslinking copolymerization exhibit marked extents of gel heterogeneity. This is because free-radical chain-growth gelation is accompanied by initial formation of densely crosslinked nanogel clusters that are then loosely interconnected to form a space-filling polymer network. The resulting gel heterogeneity is particularly pronounced at high gel preparation temperature, whereas it is lower at low gel preparation temperature. This is because free-radical crosslinking copolymerization of NIPAAm and BIS is more controlled and less unselective at lower temperatures. In addition, thermo-sensitive pNIPAAm gels exhibit less locked-in concentration fluctuations in their constituent polymer networks if they pass the gel percolation threshold in greater distance to the polymer lower-critical solution temperature. In contrast to these free-radically gelled samples, the microgels made by polymer-analogous precursor gelation are more homogeneous. This is because interconnecting pre-fabricated macromolecular precursor chains in a polymer-analogous process simply locks the homogeneous structure of the semidilute precursor solution.

As a result of their different nanometer-scale polymer-network architectures, the preceding sets of microgels exhibit different mechanical properties. This is revealed by their swelling at low temperatures. Even though all the different microgels are prepared such to exhibit the same molar degree of crosslinks in their constituent polymer networks, the gels prepared by controlled polymer-analogous photogelation exhibit considerably less low-temperature swelling in water (swollen microgel diameter ~200 μm) than those prepared by uncontrolled free-radical crosslinking copolymerization (swollen microgel diameter ~220–250 μm), especially if this is done at high preparation temperature. This finding reveals that in the homogeneous gels, regular distribution of the crosslinkings allows them to equally store mechanical deformation energy, resulting in higher effective crosslinking densities than in those gels with the same average degree of crosslinking if this is heterogeneous.

Nevertheless, when the swelling–deswelling data are normalized such to coincide at both 40 °C and 25 °C, the shape and distinctness of the curves is unaffected by the extent of gel heterogeneity or homogeneity, reflecting the ulitity of mean-field modeling to describe this.

With the present set of microgel particles that exhibit systematic variation of their static polymer-network heterogeneities, along with accompanying variation of their mechanical properties and swelling abilities, small-angle neutron scattering (SANS) can be performed to systematically probe dynamic nanometer-scale concentration fluctuations that occur during their swelling–deswelling volume phase transitions. Each of the different batches of microgels is probed at different temperatures below and above the volume phase transition temperature. The SANS experiments are conducted in both heating and cooling cycles, exhibiting excellent reproducibility.

In this assessment, the scattering cross section, $I(q)$, exhibits steep scaling in the limit of low momentum transfer, $q = 0.002$–0.006 Å^{-1}, whereas at higher q, in the range of $q = 0.006$–0.02 Å^{-1}, shallower Ornstein–Zernike-type scaling is apparent. In all cases, the entire scattering profile is shifted to higher values of $I(q)$ at higher degree of gel heterogeneity: whereas free-radically gelled samples prepared at 28 °C exhibit considerable scattering, polymer-analogously gelled samples exhibit weaker scattering. The high-q Ornstein–Zernike-type scaling of $I(q)$ can be addressed to concentration fluctuations on 1–100 nm lengthscales in the gels, covering both their static polymer-network meshsize ξ and dynamic concentration fluctuations on a scale of ξ_{dyn}. On top of this scattering contribution, there is additional excess low-q scattering that denotes larger clusters and inhomogeneities in the gels, covering another static correlation length ξ_{stat}. This modeling allows the data to be fitted to a combined analytical function that consists of a Guinier-type, a Lorentz-type, or a steep power-law function to represent the low-q scattering, along with an additional Ornstein–Zernike-type function to represent the high-q scattering. This analysis confirms that in heterogeneous gels, static polymer-network heterogeneities and dynamic concentration fluctuations coexist at the volume phase transition and cannot be detected independently in scattering experiments. Whereas ξ_{dyn} diverges at the volume phase transition point, ξ and ξ_{stat} both collapse along with the macroscopically collapsing polymer network. These opposite trends impair the divergence of ξ_{dyn} to be quantified unambiguously from scattering data, even if these are fitted to mathematical models that provide separate terms for both types of fluctuations. Only homogenepous gels provide a model system with less interference of these different quantities.

REFERENCES:

[1]   R. Stehle, G. Goerigk, D. Wallacher, M. Ballauff, S. Seiffert, "Small-angle X-ray scattering in droplet-based microfuidics", *Lab Chip* **2013**, *13*, 1529–1537.

[2]   A. Habicht, W. Schmolke, F. Lange, K. Saalwächter, S. Seiffert, "The Non-Effect of Polymer Network Inhomogeneities in Microgel Volume Phase Transitions: Support for the Mean-Field Perspective." *Macromol. Chem. Phys.* **2014**, *215*, 1116–1133.

2. Actuators   **Poster**

UPSCALING MICROFLUIDIC EDGE DEVICES FOR THE PREPARATION OF LARGE AND SMALL UNIFORM DROPLETS

S. Sahin and K. Schroën
Food Process Engineering Group,
Wageningen University, The Netherlands

Emulsions are widely used in many different product formulations from food to pharmaceuticals, cosmetics and chemicals amongst others. Droplets smaller than 10µm are needed for most applications [1]. In general, conventional emulsification technologies can produce emulsions at high throughput but using brute force, which can degrade heat and shear sensitive formulations [2]. They are highly energy inefficient; energy usage for droplet formation is reported to be as low as 1-5%, and have poor control over the droplet size and size distribution [3,4].

In recent decades, several microfluidic devices, with the ability to produce monodisperse emulsions, have been introduced and studied intensively. They are all superior to conventional emulsification regarding energy usage, and are very suited to process heat and shear sensitive ingredients. However, as most of them are single droplet techniques, their productivity is very low. Besides, mass parallelization of these systems is a challenge due to the necessity for precise flow control of all phases, which is very complex. In comparison, microfluidic EDGE (Edge based Droplet Generation) systems introduced by our group are less sensitive to pressure fluctuations due to the inherent geometry of this droplet formation unit, the so-called plateau which is able to produce multiple monodisperse droplets simultaneously [5]. (Figure 1). The system was parallelized successfully in plane on a chip with 100% efficiency of 196 plateaus, which was a promising start (Figure 2) [6].

As an upscaling approach, we present an adjusted version of the microfluidic EDGE device. In this new design, regularly spaced micron-sized partitions were engineered close to the end of the plateau (Figure 3). With this, remarkably higher pressure stability was obtained, and two orders of magnitude higher droplet formation frequency was achieved. It is important to mention that all micro-partitions were active during droplet formation. A microscopic image of a highly productive partitioned plateau is given in Figure 4, and in Table 1 its productivity is shown. Interestingly, in the partitioned EDGE chip, two different monodisperse droplet formation regions were observed. The average diameters of the droplets produced in these regions were 8.8 and 29 µm, both with a CV < 5%. This brings additional operational flexibility to the new design. Considering possible mass parallelization scenarios (i.e., taking into account the chip layout and required droplet size), the amount of (sunflower) oil can theoretically be emulsified was calculated to be several cubic meters per hour per square meter surface area. With its high throughput potential and ability to produce uniform droplets of different sizes, the partitioned EDGE devices are promising devices to realize larger production throughputs. A suggested layout of possibly upscaled EDGE device is given in Figure 5.
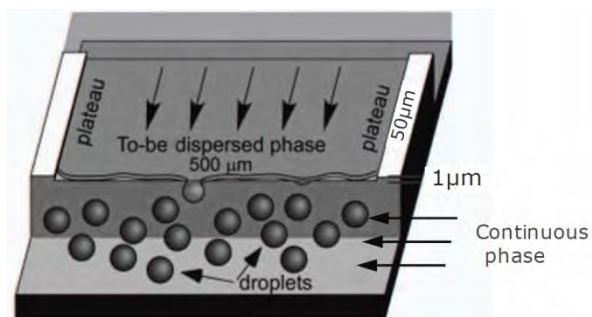
Word Count: 463

Figure 1. Droplet formation unit, the so-called plateau, in microfluidic EDGE devices.
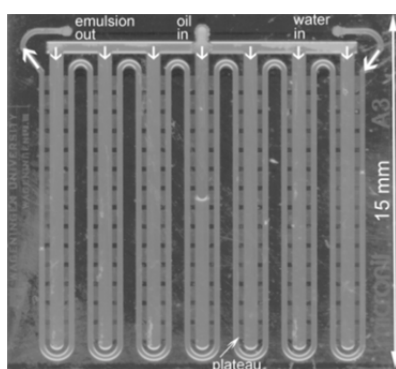

Figure 2. Upscaled EDGE chip, containing many plateaus that all work in parallel.
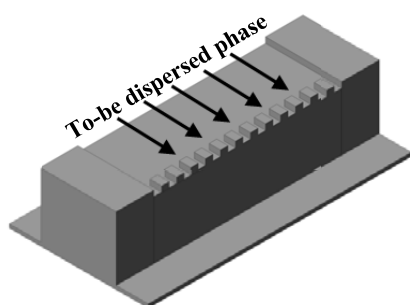

Figure 3. Schematic representation of an adjusted version of the plateau with regularly spaced partitions. Number of partitions is not indicative.
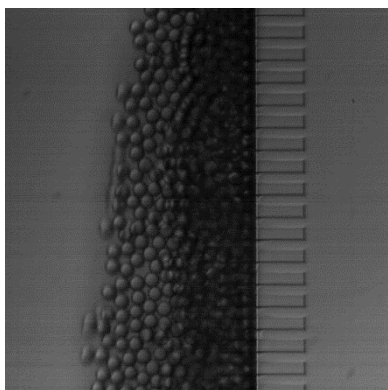

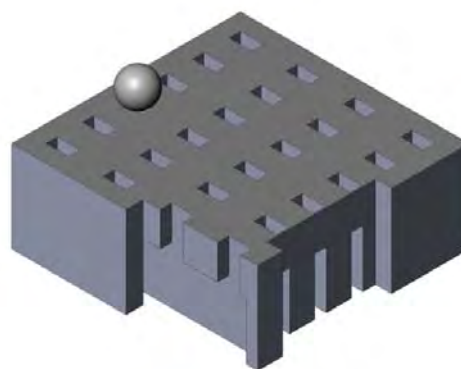*Figure 4: Microscopic image of a partitioned plateau producing many monodisperse droplets at high frequency.*

Figure 5. A suggested layout for an upscaled EDGE device.

Table 1: Productivity of standard (#1) and partitioned (#2) plateaus.

	P_1-P_2 [mbar]	H_{plt} [μm]	D_{drop} [μm]	Scaling ratio	Max frequency per 500μm [Hz]
#1	60-120	2	12	6	160
#2	115-1000	2	8-8.6	4-4.3	36000
	1250->2000	2	29	14.5	5000

REFERENCES:

[1] I. Kobayashi, T. Takano, R. Maeda, Y. Wada, K. Uemura, M. Nakajima, "Straight-through microchannel devices for generating monodisperse emulsion droplets several microns in size", *Microfluidics Nanofluidics*, **2008**, 4(3), 167-177.

[2] C. Charcosset, I. Limayem, H. Fessi, "The membrane emulsification process—a review", *Journal of Chemical Technology & Biotechnology*, **2004**, 79(3), 209-218.

[3] M. Saito, L.-J. Yin, I. Kobayashi, M. Nakajima, "Comparison of stability of bovine serum albumin-stabilized emulsions prepared by microchannel emulsification and homogenization", *Food Hydrocolloids,* **2006**, 20(7), 1020-1028.

[4] K.C. van Dijke, K. Schroën, A. van der Padt, R. Boom, "EDGE emulsification for food-grade dispersions", *Journal of Food Engineering*, **2010a**, 97(3), 348-354.

[5] K.C. van Dijke, G. Veldhuis, K. Schroën, R.M. Boom, "Simultaneous formation of many droplets in a single microfluidic droplet formation unit", *AIChE Journal*, **2010b**, 56(3), 833-836.

[6] K. van Dijke, G. Veldhuis, K. Schroen, R. Boom, "Parallelized edge-based droplet generation (EDGE) devices", *Lab on a Chip*, **2009**, 9(19), 2824-2830.